Transactions of the ASME

Technical Editor
ARTHUR J. WENNERSTROM
Senior Associate Editor
G. K. SEROVY
Associate Editors
Air Pollution Control
H. E. HESKETH
Diesel and Gas Engine Power
G. VanDeMARK
Gas Turbine
G. OPDYKE
Power
R. W. PORTER
Advanced Energy Systems
T. M. BARLOW
Fuels
H. C. ORENDER
Nuclear Engineering
J. SUSNIR

BOARD ON COMMUNICATIONS
Chairman and Vice-President
K. N. REID, JR.

Members-at-Large
W. BEGELL
J. T. COKONIS
W. G. GOTTENBERG
F. LANDIS
J. R. LLOYD
R. E. NICKELL
J. E. ORTLOFF
C. F. PHILLIPS
R. E. REDER
F. W. SCHMIDT

President, L. S. FLETCHER
Executive Director,
PAUL ALLMENDINGER
Treasurer, ROBERT A. BENNETT

PUBLISHING STAFF
Mng. Dir., Publ., J. J. FREY
Dep. Mng. Dir., Pub.,
JOS. SANSONE
Managing Editor,
CORNELIA MONAHAN
Production Editor,
VALERIE WINTERS
Editorial Prod. Asst.
MARISOL ANDINO

The Journal of Engineering for Gas Turbines and Power (ISSN 0022-0825) is published quarterly for $100 per year by The American Society of Mechanical Engineers, 345 East 47th Street, New York, NY 10017. Second class postage paid at New York, NY and additional mailing offices. POSTMASTER: Send address change to The Journal of Engineering for Gas Turbines and Power, c/o The AMERICAN SOCIETY OF MECHANICAL ENGINEERS, 22 Law Drive, Box 2300, Fairfield, NJ 07007-2300.

CHANGES OF ADDRESS must be received at Society headquarters seven weeks before they are to be effective. Please send old label and new address.

PRICES: To members, $24.00, annually; to nonmembers, $100.00. Add $6.00 for postage to countries outside the United States and Canada.

STATEMENT from By-Laws. The Society shall not be responsible for statements or opinions advanced in papers or ... printed in its publications (B 7.1, para. 3).

COPYRIGHT © **1985** by the American Society of Mechanical Engineers. Reprints from this publication may be made on condition that full credit be given the TRANSACTIONS OF THE ASME – JOURNAL OF ENGINEERING FOR POWER, and the author, and date of publication be stated.

INDEXED by the Engineering Index, Inc.

Journal of Engineering for Gas Turbines and Power

Published Quarterly by The American Society of Mechanical Engineers

VOLUME 107 • NUMBER 4 • OCTOBER 1985

TECHNICAL PAPERS

808 Derivative Engines Versus New Engines: What Determines the Choice? (85-GT-190)
D. M. Dix and D. A. Gissendanner

815 F-4 Functional Modernization (85-GT-69)
W. D. Poulin

821 Impingement Starting and Power Boosting of Small Gas Turbines (84-GT-188)
C. Rodgers

828 Experimental Evaluation of Heavy Fan-High-Pressure Compressor Interaction in a Three-Shaft Engine: Part 1 – Experimental Setup and Results (85-GT-173)
A. Schaffler and D. C. Miatt

833 Integrated Flight/Propulsion Control System Considerations for Future Aircraft Application (84-GT-192)
R. W. Vizzini

838 Aircraft Engine Control Mode Analysis (84-GT-262)
H. Brown and J. A. Elgin

845 Design of Noninteracting Multivariable Feedback Control Systems Without Decoupling Filters (84-GT-157)
D. A. Baker and C. J. Maday

851 Fiber Optics for Propulsion Control Systems (84-GT-97)
R. J. Baumbick

856 Cool Water Coal Gasification—a Progress Report (85-GT-55)
D. R. Plumley

861 A Cost-Effective Indirect Coal-Fired Gas Turbine Power and Water-From-Air Cycle (85-GT-54)
P. R. Trumpler

872 Evaluation of Polytropic Calculation Methods for Turbomachinery Performance (85-GT-13)
R. A. Huntington

880 On Thermodynamics of Gas-Turbine Cycles: Part 1 – Second Law Analysis of Combined Cycles (85-GT-129)
M. A. El-Masri

890 Development of Operating Heat Rate Functions for Cyclically Loaded Coal-Fired Power Plants Without In-Plant Computer Systems
T. F. Talty

902 A Theoretical Approach to the Combustion of Fuel-Alcohol Blends
G. Cau and M. P. Pelagagge

908 Comparison of Burning Rates in a Natural-Gas-Fueled Spark Ignition Engine (85-DGP-2)
A. L. Jones and R. L. Evans

914 Dual-Fueling of a Prechamber Diesel Engine With Natural Gas (85-DGP-3)
S. Song and P. G. Hill

922 A Procedure for Calculating Fuel Gas Blend Knock Rating for Large-Bore Gas Engines and Predicting Engine Operation (85-DGP-5)
F. S. Schaub and R. L. Hubbard

931 The Design, Performance and Analysis of a High Work Capacity Transonic Turbine (85-GT-15)
J. D. Bryce, M. R. Litchfield, and N. P. Leversuch

938 High-Temperature Thermocouple and Heat Flux Gauge Using a Unique Thin Film-Hardware Hot Junction (85-GT-18)
C. H. Liebert, R. Holanda, S. A. Hippensteele, and C. A. Andracchio

945 Numerical Analysis of Fully Three-Dimensional Periodic Flows Through a Turbine Stage (85-GT-57)
M. Koya and S. Kotake

953 Local Heat-Transfer Measurements on a Large Scale-Model Turbine Blade Airfoil Using a Composite of a Heater Element and Liquid Crystals (85-GT-59)
S. A. Hippensteele, L. M. Russell, and F. J. Torres

961 Secondary Flows and Losses Downstream of a Turbine Cascade (85-GT-64)
J. Moore and R. Y. Adhye

969 Performance Evaluation of Linear Turbine Cascades Using Three-Dimensional Viscous Flow Calculations (85-GT-65)
J. Moore and J. G. Moore

976 Heat-Transfer Distribution Around a Cylinder in Pulsating Crossflow (85-GT-67)
C. E. Andraka and T. E. Diller

Downloaded 03 Jun 2010 to 171.66.16.159. Redistribution subject to ASME license or copyright; see http://www.asme.org/terms/Terms_Use.cfm

(Contents Continued)

983 Effects of Tip Endwall Contouring on the Three-Dimensional Flow Field in an Annular Turbine Nozzle Guide Vane: Part 1 – Experimental Investigation (85-GT-71)
E. Boletis

991 Short-Duration Measurements and Numerical Simulation of Heat Transfer Along the Suction Side of a Film-Cooled Gas Turbine Blade (85-GT-111)
C. Camci and T. Arts

998 Simulation of the Effects of Shock Wave Passing on a Turbine Rotor Blade (85-GT-112)
D. J. Doorly and M. L. G. Oldfield

1007 Heat Transfer and Fluid Mechanics Measurements in Transitional Boundary Layer Flows (85-GT-113)
T. Wang, T. W. Simon, and J. Buddhavarapu

1016 Experimental Heat Transfer Investigation Around the Film-Cooled Leading Edge of a High-Pressure Gas Turbine Rotor Blade (85-GT-114)
C. Camci and T. Arts

1022 Unsteady Aerodynamic and Heat Transfer Processes in a Transonic Turbine Stage (85-GT-128)
D. A. Ashworth, J. E. LaGraff, D. L. Schultz, and K. J. Grindrod

1031 Secondary Flows in Cascades of Highly Loaded Turbine Blades (85-GT-135)
S. H. Moustapha, G. J. Paron, and J. H. T. Wade

1039 Turbulence Production Due to Secondary Vortex Cutting in a Turbine Rotor (85-GT-193)
A. Binder

DISCUSSION

1047 Discussion of a previously published paper by
M. R. D. Davies and P. J. Bryanston-Cross

1047 Discussion of a previously published paper by
M. V. Casey

1047 Discussion of a previously published paper by
A. I. Kalina

ANNOUNCEMENTS

832 Change of address form for subscribers

860 Mandatory excess-page charge notice

1050 Information for authors

Downloaded 03 Jun 2010 to 171.66.16.159. Redistribution subject to ASME license or copyright; see http://www.asme.org/terms/Terms_Use.cfm

D. M. Dix

D. A. Gissendanner

Office of The Under Secretary
of Defense,
Washington, D.C.

Derivative Engines Versus New Engines: What Determines the Choice?

A choice between a derivative engine or a new engine for either an existing aircraft or a new aircraft is becoming an increasingly frequent one. Although some factors which govern such a choice are necessarily subjective, there are several objective factors which should be considered. Using summaries of recent or current cases as examples, an examination of the many dimensions of capability, cost, and risk identifies twelve of these objective factors, many of which are often not subjected to rational analysis.

Introduction

Although there are several enlightening observations that can be made concerning the history of propulsion systems for military aircraft, there are perhaps two which stand out above all others. The first observation is that propulsion systems (including fuel) have typically accounted for roughly 1/2 of the take-off gross weight of aircraft. From the parochial view of those of us in the propulsion business, this has been the good news, since it has meant that propulsion is one of those unique areas in which relatively modest improvements in propulsion-system performance have a large impact on the military capability and/or cost of aircraft. This fact, coupled with the major role of aircraft in the defense force structure—currently, that portion of the defense budget associated with the development, acquisition, operation and support of aircraft is approaching $100 billion per year—has made improved propulsion systems an area of high military payoff.

The second historical observation is that propulsion systems—engines in particular—have required lengthy and expensive development programs and considerable maintenance expense. As might be expected, this has been the bad news for those of us in the propulsion business. It has produced a natural reluctance on the part of aircraft developers and users, regardless of the potential payoffs offered, to involve themselves with the time, expense and uncertainty associated with obtaining a new and/or improved engine if it can at all be avoided.

These two opposing observations have led to the search for compromise solutions in the selection of engines for aircraft and, not surprisingly, the compromise solution most often offered is the derivative engine. In a larger context, the same compromise solution is also most often offered for aircraft. The derivative engine, or aircraft, is of course intended to offer adequate improvements in military capability at considerably less expense and risk than those associated with new engines or aircraft. Thus, a continuing issue associated with engines is the matter of selecting either a derivative or a new model.

The extent of the derivative versus new engine issue is currently broad. As indicated in Table 1, new and derivative engine alternatives exist for both old and new aircraft. Accordingly, the problem of making a rational choice is a frequent one.

Purpose and Scope

In principle, there are two basic questions which need to be addressed:

1 When is it appropriate to modify an existing aircraft platform, in preference to developing a new one?
2 When is it appropriate to modify an existing engine, in preference to developing a new one? In the context of the subject here—engines—the first question bears on the second, inasmuch as it is obvious that a new plat-

Table 1 Some current examples of derivative and new engine alternatives

Derivative engines for parent aircraft
F100-PW-220/F100 growth for F-15/16
T56-A-427 for E-2C
Derivative engines for other existing aircraft
F404-GE-400 for A-6
New engines for existing aircraft
Joint Advanced Fighter Engine (JAFE) for F-15/16
Modern Technology Engine (MTE) for E-2C/P-3/CH-47
Derivative engines for new aircraft
T64/T701/T55 for JVX
TSE109 for LHX
PW1120 for Israeli LAVI
F404 for Swedish JAS
New engines for new aircraft
JAFE for Advanced Tactical Fighter (ATF)
MTE for JVX
Advanced Technology Engine (ATE) for LHX

Contributed by the Gas Turbine Division of THE AMERICAN SOCIETY OF MECHANICAL ENGINEERS and presented at the 30th International Gas Turbine Conference and Exhibit, Houston, Texas, March 18–21, 1985. Manuscript received at ASME Headquarters, January 16, 1985. Paper No. 85-GT-190.

Copyright © 1985 by ASME
Downloaded 01 Jun 2010 to 171.66.16.71. Redistribution subject to ASME license or copyright; see http://www.asme.org/terms/Terms_Use.cfm

form will increase the likelihood that a new engine is the appropriate choice and an old platform will increase the likelihood that a derivative engine is the appropriate choice.

As it happens, both questions have the same answer: when the costs and risks involved are justified by the increase in capability offered. Unfortunately, this answer contains several subjective elements, as well as objective elements which vary from case to case. Obviously, then, there are no universally applicable, objective answers to these questions and none are offered here.

However, there are several dimensions of capability, cost and risk that are both objective and widely applicable. Our purpose here is to examine these several dimensions with the aim of highlighting those factors which should always be considered in order to arrive at rational case-by-case decisions. Each of the three areas of capability, cost, and risk is examined more or less independently, although their dependence in decision-making will be obvious. For the most part, the examples used will be specific mini-case histories, since it is our intent to highlight the important factors as they relate to current efforts. The primary emphasis throughout is on engine issues, but of necessity the influence of the choice of either an existing or new aircraft platform is also considered to some extent.

Case Histories

For the purposes of discussion, we will selectively summarize three case histories. The first, the Navy's decision to re-engine the E-2C aircraft, is a good example of a decision involving a trade between near-term capability and longer-term capability. The second, the Advanced Joint Vertical Lift Aircraft (JVX) is a typical example of an attempt to define a common aircraft to meet joint Service needs and the difficulties which ensue. The third, the Air Force fighter engine long-range plan, is a case of not only capability but of business strategy and how to balance the two in light of the near-term and long-term needs.

Re-engining the E-2C. In 1966 the Navy established its stated operational need for the E-2C. Not only can today's E-2C not meet these requirements, but on a hot day with one engine out, the aircraft cannot attain a positive rate of climb: a not-too-pleasant picture for those with the distinction of flying the aircraft. So, what do you do? Do you opt for a near-term solution to the problem or do you go for a more long-term solution? The Navy had a choice.

An upgrade to the Allison T56 engine offered the Navy a 22% improvement in endurance, a 24% improvement in hot-day takeoff power, and a 10% improvement in specific fuel consumption. Also, since the Air Force had invested $16.4M in a recent demonstrator engine program to prove the feasibility of T56 engine enhancements, the Navy RDT&E to qualify this derivative (the T56-A-427) could be accomplished for an estimated $113.2M. The first production T56 derivative could be ready in late CY 1987 and the engine fitted within the existing nacelle on the E-2C, thus requiring minimal airframe modifications. The Navy assessment of this T56-A-427 powered E-2C concluded that the aircraft would satisfy the performance requirements of the 1966 Statement of Operational Requirement (SOR) at an aircraft takeoff gross weight (TOGW) consistent with the 1990 aircraft configuration.

On the other hand, the Navy had the option of the Modern Technology Engine (MTE) being considered at that time for the Army JVX program. Being a new centerline engine, the MTE offered some significant performance advantages: a specific fuel consumption (SFC) 15% less than the T56-A-427 at the same power rating; a 17% improvement in endurance/range; and the hot-day takeoff power of MTE is 9% greater. A clear-cut winner? Not so. The MTE development cost was estimated at approximately $250M higher than the derivative and the first production engine would not be available until CY 1992. The E-2C represents a very small portion of the total Navy aviation force structure. While its mission is critical to carrier battle group survival, the Navy concluded that the upgrade program did not warrant the nonrecurring and recurring expenditure associated with MTE application solely to the E-2C. Since the status of the Army JVX program seemed to be unclear, there was no certainty of an MTE production date. The Navy chose to go with the T56-A-427 derivative engine on the basis of adequate performance, lower cost and lower risk.

Engines for the JVX. In late 1981, the Under Secretary of Defense for Research and Engineering directed a tri-Service program for the JVX. This aircraft was envisioned as meeting the common requirements for the Army corps/division electronic warfare and signal intelligence; the Air Force long-range special operations; the Navy and Air Force combat search and rescue; and the Marine Corps assault missions. The program was fraught with problems from the start. Initially, the Army was designated the Executive Service but within one year the Executive Service role was transferred to the Navy, and by May 1983 the very tentative tri-Service Memorandum of Understanding began to break down and the Army withdrew from the program.

From its inception, the JVX program sparked a testy debate within both the aircraft and engine communities between derivative engine advocates and new engine advocates as to the best propulsion approach for the aircraft. The JVX would need a 5000–6000 shp engine to meet the myriad of requirements. There were those who contended that derivatives of the General Electric T64 engine offered the best solution, while others contended that the MTE was the only logical engine approach. Derivative engine advocates based their arguments on shortest development time, lower development cost, lower risk, and the contention that to support a new engine requirement would be the political "kiss of death" to the JVX. New engine advocates based their arguments on lower gross weight system, lower acquisition and life cycle cost, superior system performance (i.e., range, payload, specific fuel consumption), low risk, broad application potential, and the contention that JVX could die without the new engine.

The arguments were difficult to weight. One contributing factor was that the mission requirements for JVX seemed to be in constant flux, particularly the Marine Corps land assault and amphibious assault missions and the Air Force long-range special operations requirements. The bottom line analysis seemed to show that the derivative T64 engines could meet the basic requirements but the MTE could either (1) provide lesser system cost for same mission performance or (2) provide excess capability for all missions. The major hangups with MTE appeared to be the projected development cost and the earliest availability date. Some derivative engine supporters contended that MTE development would cost $300–400M more than the most favored T64 derivative (T64-418B) and that MTE could not meet the Marine Corps IOC date. The MTE supporters pointed to the Army's Modern Technology Demonstrator Engine (MTDE) program and contended that because of the technology base being demonstrated the MTE development cost (at worst) would be $200M more than the T64, and could very well be competitive depending on the contractors' perception of the marketplace and their willingness to cost share. The real problem was that the JVX program was not willing to "hang its hat" on the MTE.

In mid-1984 after considerable struggle within the Services, the Navy issued a competitive RFP for the engine for the

Downloaded 01 Jun 2010 to 171.66.16.71. Redistribution subject to ASME license or copyright; see http://www.asme.org/terms/Terms_Use.cfm

JVX. Four contractors have responded: two with derivative engines and two with MTE. Ironically, the T64-418B which played so heavily in the early mission analysis, cost comparisons, and design baseline was not bid by General Electric. The source selection announcement is not expected until mid-1985, and only then will we see how the derivative versus new engine question resolves itself.

Engines for the Air Force Fighters. In early 1983, the Air Force awarded the initial contracts under the Alternate Fighter Engine (AFE) competition to procure more durable engines for F-15 and F-16 aircraft to be delivered from 1985–1991. Under this competition, the engine buys would be split between General Electric F110-GE-100 and Pratt & Whitney F100-PW-220 engines, derivatives of the F101 B-1 engine and F100 engine, respectively, with −220 engines being used in F-15 aircraft and some mix of engines being used in F-16 aircraft. The ink had hardly dried on the contracts when, for operational reasons, it appeared desirable to increase the aerodynamic performance of future F-15/F-16s by the late 1980s. The Air Force immediately began to formulate an increased performance fighter engine acquisition strategy to provide engines which would permit F-15/F-16 to achieve this desired aerodynamic performance improvement. This proposed program would be performed concurrently with the Joint Advanced Fighter Engine (JAFE) program which is aimed at the Advanced Tactical Fighter (ATF) for the mid-1990s. The question which must be decided is, "Do we provide future F-15/F-16s with an increased performance engine or do we wait for the ATF in the mid-1990s?" If we opt for the increased performance engine today, we have to decide how much performance is enough. Competitive derivatives (of the F100 and F110) are one alternative; the development cost of these engines could be as high as $800M and it would be 1989 before first production. This expense must be borne at the same time the Air Force plans to fund the major new development program for the JAFE for the ATF, a development that could cost $1.06B when one adds the competitive system demonstrator program costs and the full-scale development costs. On the other hand, it might be possible to use the JAFE in the F-15/16s, and at some increase in risk, provide first production engines in 1992.

If the Air Force opts for either increased performance engine, the F-15/F-16 may have aerodynamic performance which under certain conditions could be comparable to the ATF, and some might question the timing for the ATF. If ATF were to slip, and the high-thrust derivative were chosen, the JAFE would be delayed. Even if the aircraft performance were not competitive, the costs for a derivative engine program may be so high as to make it impossible to conduct the increased performance engine development and JAFE full scale development simultaneously. If nothing is done to improve the F-16/F-15, then we must wait 5–6 years for the ATF. How does one decide on the relative priorities? Can both be afforded? Must both be afforded? The answers are not clear cut.

As this case and the preceding two illustrate, there are many considerations involved in making a choice between a derivative engine and a new engine. In the remainder of the text, we endeavor to identify the objective factors by examining the three major areas which influence the choice: (1) capability; (2) cost; and (3) risk.

Capability Considerations

Perhaps the first important point with regard to capability is that, from the national defense point of view, there are two aspects to it: (1) military capability, and (2) industrial capability.

Military Capability. We build military systems for one purpose, to outperform the enemy to the extent that we have the edge—the edge to win. Therefore, performance is important, if not critical, to our weapon systems. Inasmuch as the engine has a lot of leverage in the affordable capability of weapon systems, if ultimate capability were the only factor, a new engine would virtually always be preferred to a derivative. In actuality, however, questions regarding how much it is worth must be addressed. Although there are many subjective issues imbedded in these questions, there are at least three objective factors which are always present.

In the case of existing or derivative aircraft, in particular, the impact of engine performance differences will surface as differences in unit performance: range, payload, speed maneuverability. The value of such differences is, of course, exceedingly difficult to evaluate. A usual approach is to specify a go/no-go threshold for unit performance: Engine options which do not meet this threshold are considered unacceptable, and all options which meet or exceed the threshold are of equal worth. However, it should be borne in mind that superior unit performance will translate into a reduced fleet size requirement to accomplish the same military purpose. Perhaps the simplest example is an aircraft with a transport mission; greater unit payload capabilities obviously require fewer units for the same force capability. Unfortunately, in actual situations, the question of fleet size (or force structure, in military terms) tends to be viewed independently from unit performance. That is, a certain number is claimed to be required regardless of the unit performance level, and a go/no-go threshold is claimed for unit performance level. Although there are, without a doubt, bands of acceptability applicable to both force structure and unit performance, they tend to be rather broad and should be approached accordingly. Specifically, the notion of a go/no-go threshold for unit performance should be viewed with great wariness.

The second factor to be considered is the realization that new versus derivative engine choices will result in tradeoffs between shorter and longer term capabilities. This is simply because resources, specifically resources for engine development and acquisition, are not unlimited. The example of the increased thrust derivative engines for Air Force application to current fighters and the JAFE for ATF is a specific case in point. What it boils down to is the development of an acquisition strategy which balances a perceived need to provide existing aircraft with additional capability in the near-term with the desire to fund the development/acquisition of the next major fighter weapon system to provide greater longer-term capability. The dilemma is that we'd like to have our cake and eat it too, but if we do that then the costs become prohibitive. It becomes extremely difficult to rationalize expenditure of large sums to meet the near-term need because we're dealing with a fixed quantity of aircraft and the use of the derivative engine beyond these aircraft is practically nonexistent. On the other hand, the new engine offers a bigger potential payoff, somewhat delayed, for the funds expended. Although the resolution of this dilemma is not easy, it is important to realize that the near-term–far-term tradeoff exists.

A third factor to be considered is the potential range of applications for engines beyond the specific application under consideration. Too often, there is a tendency to select a particular engine on the basis of only the aircraft system under consideration, with the result that the capability in other potential applications is sacrificed. The E-2C/JVX examples illustrate the point. For example, in the initial decision on selecting an engine for the E-2C upgrade, what would have been the impact if the MTE had been chosen rather than the T56-A-427? In all likelihood, there would have been a clear choice to also put the MTE in the JVX, and both aircraft would have increased capability. Conversely, if an

Downloaded 01 Jun 2010 to 171.66.16.71. Redistribution subject to ASME license or copyright; see http://www.asme.org/terms/Terms_Use.cfm

earlier JVX decision had led to the MTE being chosen, then in all likelihood the MTE would have been picked for the E-2C, with same increased capability. For the most part, this is conjecture because the timing for the E-2C and JVX engine decisions was somewhat different. However, what it clearly points out is that depending on how the initial strategy was derived these decisions could have been strongly interrelated, even though they were not considered in that light. The result is that today the E-2C has chosen the T56-A-427 derivative engine and the JVX is in the throes of a source selection which has both derivative engines and the MTE as potential solutions. Consideration of both applications simultaneously might have produced a different result.

Industrial Base. One factor which we have not discussed thus far in our look at derivative versus new engines for aircraft applicability is the industrial base consideration. Industrial base considerations invariably relate to the determination of an acquisition or business strategy. This has become more pronounced in the past two years because the basic new Department of Defense (DoD) acquisition strategy calls for increased competition on equipment/weapon systems at all levels. The term "competition" we believe has been overused and tends to cloud the more fundamental issue of what competition is for. Competition can be (1) technical, (2) cost, or (3) for risk reduction. From both the technical and cost standpoint, the idea is to ensure that one has some real choices when he needs them, and can exercise these choices at a reasonable risk. There are two basic industrial base characteristics which we want to preserve: (1) a broad enough industrial base to assure true design competition and (2) a balanced industrial base which ensures that there is appropriate production capacity and thus cost competition, and not an overload to just a few contractors. It's not easy to do either of these. We are not advocating socialization in the aircraft engine business; that would be counterproductive. However, the Government's acquisition strategy does have a large influence on which contractors are competitive and on whether desired basic industrial base characteristics can be preserved.

Competition can be based upon technical (design, performance) and/or cost factors. Determining the degree and type of competition determines how far you have to carry more than one company in the R&D and production effort. The Government's view of competition has broadened to the extent that it also implies a willingness on the part of companies to "cost share" or "risk share" in a program. Competition also implies a willingness on the part of the Government to incur increases in cost in a program because of the necessity to carry multiple contractors to a predetermined point. One must determine at the outset whether the benefits of competition warrant the investment and the acquisition strategy must be formulated to ensure that the desired competitive results can be achieved.

Two of the case histories provide examples of the impacts on the industrial base and competition. The JVX engine competition is an interesting example where the Government's acquisition strategy forced "competing" companies to make a decision between derivatives or new engines. The Government indicated that while it might choose to carry more than one engine type into full-scale development, no one contractor could be chosen for both the derivative and the new engine. As a result, two contractors proposed derivative engine solutions and two proposed new engine solutions. Assuming that all evaluation factors are equal, one could conclude that we have four real competitors. From our view, there are perhaps two distinct competitions going on simultaneously: (1) a design/cost competition between the new engine advocates and (2) a cost competition between all four contractors. It's an interesting situation because the companies who proposed the derivative engines may need the business to remain competitive in the future and to utilize existing production capacity more effectively. The new engine advocates may not need the production as much, but they offer the only design competition (i.e., real technology advancement) in this class engine for the future.

The second case is the fighter engine area where General Electric and Pratt & Whitney continue to dominate this class engine, with no immediate prospects of additional competition. The AFE and the increased performance fighter engines are examples of small design competition but major cost competition which will affect production allocations for derivative fighter engines for the near future. The ATF represents both a design and cost competition for the next generation fighter engine. In either fighter engine case, there will be no expansion of the industrial base but a continued perpetuation of a two-man race.

There is not a great deal of flexibility to rectify the industrial base dilemma. Unlike twenty years ago, Government programs are fewer and farther between. It appears to us that the turboprop/turboshaft and small turbofan/turbojet engines offer the best opportunity for enhanced competition. The large fighter and transport turbofans will continue to be dominated by the two big companies.

Clearly, the government must consider many business strategy factors in structuring a program which leads to a decision between a derivative versus a new engine. Some are: (1) How large an industrial base should be preserved? (2) How can this be influenced by the specific program? (3) How can the risk be balanced between companies of unequal capability, where the more capable may be overloaded with work and the less capable may need the work to survive? (4) Is competition desired or not? (5) What kind of competition is desired?

Cost Considerations

General Remarks. As a sweeping generalization, in the consideration of derivative versus new model issues, estimated costs receive more attention than relative capabilities. In our opinion, this is in part due to the more tangible nature of estimated costs as compared to the relative military worth of estimated capabilities, and in part due to the usual presentation of required capabilities in the form of go/no-go thresholds. As we have indicated previously, the go/no-go thresholds, in which alternatives that do not meet the threshold are unacceptable and all alternatives that meet or exceed the threshold are of equal military worth, are in general not a preferred basis for decision-making. This notwithstanding, costs are obviously an important consideration.

A second factor regarding costs is that the up-front costs (in DoD lexicon, the research, development, test, and evaluation, or RDT&E, costs) generally receive predominant consideration. This is simply because these are the first costs incurred.

Advocates of new systems and/or engines tend to be critical of this perceived overemphasis on costs, RDT&E costs in particular, for the obvious reasons that single-minded attention to RDT&E costs will always lead to the selection of a derivative. On the other hand, up-front costs are relatively more important than downstream costs, so the argument should focus on the degree to which this is true.

Return-on-investment (ROI) considerations, or the related discount rates, provide a convenient framework for the assessment of costs. By way of background, the discount rate is, strictly speaking, the rate of return (above inflation) which can be obtained from alternative current investments. It also represents a minimum ROI criterion: A discount rate of, say, 10% implies that investments with less than 10% return will not be made. The discount rate is used to define the present

Downloaded 01 Jun 2010 to 171.66.16.71. Redistribution subject to ASME license or copyright; see http://www.asme.org/terms/Terms_Use.cfm

Table 2 Present value of potential life cycle cost units

	Discount rate			
	0%	5%	10%	15%
RDT&E	1	0.82	0.79	0.70
Procurement	1	0.61	0.38	0.24
O&S	1	0.39	0.17	0.078

Table 3 Engine life cycle cost contribution (percent)

	Discount rate			
	Typical	5%	10%	15%
RDT&E	8%	14	22	31
Procurement	32%	39	42	43
O&M	24%	19	14	10
Fuel	36%	28	22	16

Table 4 Cost reductions required to justify RDT&E investment of $1 billion

	Discount rate			
	0%	5%	10%	15%
Procurement	1.0	0.7	1.1	1.8
O&S	1.0	1.2	2.1	3.4

(or discounted) value of some future cash flow, which is merely the amount of a current investment required to produce the future cash flow. As a practical matter, the value of the discount rate used in investment considerations generally reflects future uncertainties; for example, a possibility of a major conflict during the next ten years would tend to reduce the importance of peacetime support costs relative to the immediate RDT&E investment required. Thus, the actual discount rates used may be high as compared to, for example, the prime rate. Obviously, higher discount rates imply shorter term outlooks, and conversely.

The potential impact of selected discount rates on views of costs is indicated in Table 2, for a typical aircraft life cycle (5-year RDT&E program, 10-year production, 20-year operation). The interpretation of the table is simply, for example, that an average expenditure of one dollar in the Operation and Support (O&S) phase can be provided for by the current investment of 17 cents at an interest rate of 10%. The implications are that: (1) RDT&E costs can be significantly more important on a discounted basis, and (2) in every case, it is important to establish the discount rate, or ROI criterion, to be applied.

The first point is elaborated in Table 3, which indicates the relative contributions of RDT&E, procurement, operations, and maintenance (i.e., O&S costs less fuel) and fuel costs to typical engine life cycle costs. To take the most extreme case in the table, the undiscounted RDT&E portion of 8% of engine life cycle costs rises to 31% for a discount rate of 15%. Looked at differently, the development of a new engine which achieved a reduction of more than 25% in procurement costs as compared to an existing engine would produce an undiscounted life-cycle cost benefit; on the other hand, if the minimum acceptable ROI were 15%, then a 72% reduction in procurement costs would be necessary to justify the development of a new engine on this basis. Clearly, RDT&E costs cannot be downplayed simply because they are only 8% or so of total undiscounted engine life cycle costs.

Discussions of discount rates or ROI criteria tend to rather sterile, particularly in a military context. After all, the military payoff is in increased capability, not in reduced costs. In this context, it is important to appreciate that reduced costs, properly interpreted, equate to increased capability. The simplest illustrative example is that of aircraft designed for the same mission capability with engines of different

Table 5 Aircraft life-cycle cost contributions (percent)

	Typical	Engine contribution
RDT&E	9	25
Procurement	35	25
O&M	44	20
Fuel	12	100

performance levels. The aircraft with the highest engine performance level will yield the smaller airframe, with concomitant reductions in all categories of cost. The magnitude of these reductions is then presumably available to purchase more capability in whatever form. In short, it is capability per unit cost which is the overriding military payoff, and it is quite valid to use cost reductions for the same capability as a measure of this payoff.

Given that cost reductions and capability increases are to some extent interchangeable, some insights into the selection of an ROI, or discount rate, can be gained. For discussion purposes, consider typical cost numbers for a new fighter engine development*:

RDT&E	$1.0 billion
Procurement	$4.0 billion
O&S	$7.5 billion

Table 4 indicates the cost reductions required (in equal percentages of procurement and O&S costs) to justify the RDT&E investment of one billion, at various discount rates. For example, a 5% discount rate will produce a net reduction in costs of $0.9 billion. Viewed in capability terms, this means that an investment of one billion will produce a net increase in capability equivalent to $0.9 billion, some 35 years after the initial part of the RDT&E investment is made. Although any assessment of the proper discount rate to be used is necessarily subjective, it seems to us that 5% is clearly too low. An ROI criterion of 10% would seem to be the minimum acceptable, and perhaps should be higher.

In the context of rates of return, there are two observations which bear on issues involving new versus derivative engines. Firstly, it is in general very difficult to justify the development of a new engine on the basis that engine life-cycle costs alone will be less than those of an existing or modified engine. This is apparent from Table 3, which indicates, for example, that over a 50% reduction in procurement costs would be required to produce a 10% return on investment. O&M cost reductions, of course, offer less return. Secondly and more specifically, it is unlikely that the development of a new military engine can be justified on the basis of fuel savings. Again, Table 3 indicates the difficulty. The net result is that for existing aircraft, if no benefit is attributed to increased unit capability, a new engine is not likely to be a prudent investment. Indeed, it may be difficult to justify a derivative engine in these circumstances.

So, as might be expected, performance differences between engine candidates, and the value of such differences, will be a key ingredient in any rational decision process. The impact of engine performance on airframe capabilities and/or costs is the high leverage item, as can be deduced from Table 5. That is, for example, an engine which permits a greater airframe payload capability will generally be the economic choice, since it is affecting the capability cost relationship of the entire system, rather than affecting merely engine costs.

The final factor related to general ROI considerations concerns establishing competition for potential cost reduction purposes (as in the Alternate Fighter Engine program). It seems clear that if cost reduction is to be the major benefit,

*Obviously, such costs depend on engine size, type, number, usage, fuel costs, etc.; the costs here are merely intended to be representative.

Downloaded 01 Jun 2010 to 171.66.16.71. Redistribution subject to ASME license or copyright; see http://www.asme.org/terms/Terms_Use.cfm

the development of competitive engine configurations will offer a low return on investment. For example, two new engines would require an additional RDT&E investment of about $1 billion, and from Table 4, to obtain even a 5% ROI a reduction of $1.9 billion in procurement and O&S costs would be needed. Such a reduction would be roughly equal to a 17% reduction in procurement and O&S costs, and it is doubtful that this magnitude could be achieved through competition.

RDT&E Costs. It is axiomatic, at least as viewed by the offeror, that any new engine development is a straightforward process of employing standard procedures to incorporate demonstrated technology into an all new engine configuration. It is similarly axiomatic that all derivative engines are virtually trivial modifications of a well-proven product, Although those of us in the engine business have our built-in discount rates to apply to these usual optimistic views, it is not always true that the individuals who make such decisions are similarly enlightened. So, apart from all of the usual assessments attendant to RDT&E costs, there are three factors which should never be far from consciousness.

Firstly, all engine developments—new or derivative—will be aimed at performance levels which are in an uncertainty band of knowledge. That is, for example, component performance goals will typically represent the best ever achieved, suitably interpolated or extrapolated to the specific engine configuration. The reasons this is so are simply that engine performance is such a high payoff quantity, and that engine performance is very sensitive to component performance levels. In our experience, this matter of developing within the uncertainty band is equally likely in either new engine developments or in derivative engine developments. This does not mean that such developments are ill advised; on the contrary, they are necessary to obtain the benefits offered by engines. It does mean, however, that all such developments will involve an appreciable amount of trial-and-error in achieving the desired performance levels. This will obviously influence RDT&E costs.

Secondly, gas-turbine engines are, arguably, the most complex pieces of machinery in existence from an engineeirng viewpoint, and human beings make mistakes. Given the numerous opportunities to make mistakes that engine development provides, mistakes will be made. Further, many of these mistakes will not be discovered until hardware testing begins. Again, this is not a criticism of the development process, but merely indicates that substantial RDT&E costs can be expected. Here, of course, it is quite rational to assume that more mistakes will be made in a new engine development than a derivative one. However, in this context, the concept of scalability deserves comment. The conventional wisdom is that an engine can be scaled "up two" or "down one-half." From an engineering standpoint this is true, given adequate time and funds. But true scaling of an engine means that virtually every part will change, and also provides the opportunity to introduce "improvements"; both of these factors indicate that the development costs will be substantial.

The basic conclusion to be made is that virtually any engine development is a major development undertaking, and has to be treated accordingly. There are no inexpensive engine developments. Two examples are sufficient to close the argument: (1) The development cost of the F100 engine, in 1985 dollars, was approximately $1.3 billion, while the development cost of the improved life derivative (the F100-PW-220) was approximately $250 million; and (2) reasonable estimates, on a consistent basis, for the development of a 5800-hp version of the T64 for the JVX versus an all-new engine for the same application were $120 million and $260 million, respectively. Caveat emptor.

Procurement and O&S Costs. It is not our purpose here to rehash all of the many pitfalls that need to be avoided in estimating procurement and O&S costs of either new or modified engines. However, there is one such potential pitfall which perhaps deserves mention, and this is the matter of costs associated with establishing the logistical support system for the engine. Elements of this support system include spare engines and modules, ground support equipment for base and depot level maintenance and overhaul, initial spare parts for both consumption and shelf stock, technical publications, and training. Typically, the cost of these elements for a new engine is of the order of 20 to 25% of the total O&M costs, or upwards of $500 million for a new fighter engine. Further, these appreciable costs are incurred relatively early in the life cycle, within a few years after the initiation of procurement. Clearly, these costs are an important consideration in derivative versus new engine issues inasmuch as the logistical support costs of a derivative engine (assuming that its parent is in the military inventory) will be less than those associated with a new engine. These costs are also an important factor in evaluating the effectiveness of introducing competitive engine configurations into the operational inventory, as in the case of the Alternate Fighter Engine program. It is doubtful, for example, that the introduction of the F110 into the Air Force inventory could have been justified in the same manner if the parent engine (the F101) were not also to be used.

This slight digression aside, our primary purpose here is to emphasize two areas which often do not receive adequate attention. The first, of course, is the ROI criterion to be used. Regardless of the specific value, procurement costs, and, to an even greater extent, O&M costs must be discounted in assessing alternative RDT&E investments. In general, this discounting will tend to favor the selection of a derivative engine as opposed to a new engine but, on the other hand, it will provide a much better framework than focusing on RDT&E costs alone.

The second area is that of ensuring that the impact of engine performance on aircraft system cost is properly evaluated. For new aircraft, this should be a straightforward process since engine performance will have a direct influence on the size and cost of the airframe. To illustrate the magnitudes involved, consider a more or less typical fighter aircraft which will involve total system life cycle costs of, say, $35 billion. The nature of fighter aircraft is such that, conservatively, engine performance differences of 10% in weight and 5% in specific fuel consumption will produce roughly a 6% difference in system life cycle costs—or on the order of $2 billion. This difference is obviously significant, and will in virtually all cases strongly favor the selection of a new engine over a derivative one. Unfortunately, it is not uncommon for these impacts on total system costs to be overlooked or improperly estimated.

As indicated earlier, in the case of existing or derivative aircraft, the impact of engine performance differences will surface as differences in unit performance: range, payload, speed, maneuverability. Here it is necessary to estimate the value of these differences in unit performance, either in terms of increased force effectiveness or lesser requirements for force size.

A final area related to the impact of engine characteristics on existing airframes which perhaps deserves more attention than it usually receives is that of the airframe structural changes which might be needed to accommodate either a new or derivative engine. If the physical characteristics of the derivative are such that it fits into the existing propulsion volumes, then the related aircraft modifications which will be necessary are of an interface nature (i.e., attach points, plumbing, access, etc.). On the other hand, if the engine size requires major structural changes to existing aircraft, then the additional costs (which can be considerable) to accommodate these changes will be an important factor in the decision.

Downloaded 01 Jun 2010 to 171.66.16.71. Redistribution subject to ASME license or copyright; see http://www.asme.org/terms/Terms_Use.cfm

Similarly, if the weight of the engine results in a large shift in the center of gravity of the aircraft, or in the case of the turboprop or turboshaft results in a significant change in wing or rotor dynamics, then the impact of these on aircraft structure or control have to be assessed.

Risks and Uncertainties

Risk might be defined as the degree of uncertainty that the desired result(s) can be achieved. Risk can be schedule risk, technical risk, or cost risk. These areas of risk are not mutually exclusive but are directly tied to one another. The levels of risk may be different for each of these individual areas.

It is important from the outset (1) to determine the level of risk which you're willing to accept in the program, (2) to adequately characterize the level(s) of risk associated with each alternative approach, and (3) to define a program which to the maximum extent possible recognizes this risk and strives to eliminate or reduce it.

Our case histories provide an opportunity to reflect on risk. In the E-2C decision the technical risk associated with either the T56-A-427 or the MTE may have been equivalent, but based on the desired IOC date, the cost and schedule risk favored the derivative. On the other hand, the derivative may be riskier from the standpoint of meeting future system performance requirements, should the aircraft payload, time on station, or range increase.

For the JVX, the derivative or new engines offer equivalent development risk and under the Navy's acquisition strategy the development cost risk could be comparable. However, the derivative is riskier from a performance standpoint particularly should aircraft weight, payload or range requirements change. The new engines will certainly result in the lowest gross weight, lowest cost weapon system.

In the case of new engines, the technical risks should be relatively easy to identify: How complex is the design mechanically and/or aerodynamically? What types of materials are being proposed? How hot will the engine run? Have the components, designs, technologies previously been demonstrated? Once these technical risks are defined, then the impact in cost and schedule can be determined. Level of competition desired and the development approach will affect the cost and schedule risk as will the degree of concurrency.

The derivative engine could be a bit more difficult to characterize in terms of risk simply because there are such broad ranges of derivatives: (1) repackage, (2) tweek low spool, (3) tweek core, (4) new low spool, or (5) new core. Each of these is characterized by a different level of risk. For whatever reason, there appears to be a tendency to underestimate the level of risk associated with a derivative engine. This is particularly true when comparisons are made between derivative engines and new engines. The fact is that derivative engines can be just as risky or riskier than new engines. History proves this; i.e., J85-21, TF30-P-100, and perhaps the real bottom-line message is that as we begin to make the decision between derivative and new engines we should:

1 determine if there is more than one application which plays in the decision;
2 determine what is more important to the decision: timing, cost, or performance;
3 determine the range of options offered by a given decision;
4 determine if the engine decision will lead to increased airframe costs;
5 characterize the levels of risk associated with each potential solution.

The fighter engine example may offer two more insights into risk assessment. One area has to do with the assumption that a new engine is always riskier than a derivative engine. In the case of the JAFE, we would conclude that the current JAFE program for either F-15/F-16 application or ATF application is not a high-risk effort. There are adequate time and resources to accomplish the objectives. Another observation is that the risk of the derivative fighter engines is directly related to how big an engine you need. Certainly a "cosmic" derivative of either the F100 or the F110 engine for F-15/F-16 could be of significant risk. The opposite side of the coin would be if JAFE application to the F-15/F-16 imposed significant aircraft modifications, then the risk associated with those changes may obviate the new engine approach.

One thing is certain. You can't have it both ways: low cost/schedule and low risk. Big technical jumps generally imply higher risk regardless of whether the engine is a derivative or new engine.

Concluding Remarks

We have attempted to highlight those factors which should be considered in new versus derivative engines and which, in our opinion, do not always receive adequate attention. By way of summary, the major factors in this category are as follows:

- The impact on mid- and far-term military capability, as well as the short-term impact.
- The relationship between unit capability and force structure, as opposed to specific requirements for each.
- The range of potential applications of an engine beyond that under specific consideration.
- The impact on industrial capability, both in terms of maintaining an industrial base and avoiding overload.
- The acquisition strategy to be employed with respect to "competition," and the purposes, attendant economics, and alternatives to same.
- The ROI criterion, or discount rate, to be used, and its application to all cost elements.
- The relatively greater importance of RDT&E costs.
- There is no such thing as an inexpensive engine development for either derivative engines or new engines.
- The applicability of the proposed development/qualification approach to derivative engines, and potential differences in the resulting final product.
- The impact of engine performance levels on total aircraft system costs, including force structure costs associated with aircraft unit performance.
- The impact on the logistical support system.
- The relationship between risk, cost, and time, as opposed to independent assessments.

Although these factors may appear to many readers to be self-evident, it has been our experience that many decisions have been made with little, if any, rational analysis of them.

Downloaded 01 Jun 2010 to 171.66.16.71. Redistribution subject to ASME license or copyright; see http://www.asme.org/terms/Terms_Use.cfm

F-4 Functional Modernization

W. D. Poulin
F-4/PW1120 Program Manager,
Pratt & Whitney,
Government Products Division,
West Palm Beach, FL 33402

Evolving aircraft and engine technologies, as well as advancements in avionics, have resulted in a new generation of fighter aircraft. In order for an air force to remain survivable in such an environment it must face the necessity of either acquiring new aircraft or upgrading its fleet. Today, acquisition of new aircraft may not be an economically or politically viable solution. The newest aircraft, those with a thrust-to-weight ratio exceeding 1 to 1, generally exceed $20 million, exclusive of support costs. Politically, sale of such state-of-the-art aircraft to friendly countries may not be possible given the current FX aircraft export policy, and the fiscal posture of the country. However, there is an alternative to new aircraft acquisition, and that is functional modernization: the modernization of potentially viable systems through the implementation of new and available technologies. The Boeing Military Airplane Company and Pratt & Whitney have teamed in the newest aircraft functional modernization proposal, the F-4 Super Phantom. The full modernization package includes a new centerline conformal fuel tank, new digital avionics, and re-engining with new PW1120 engines. This paper examines the initial feasibility study conducted by Pratt & Whitney and Boeing to determine the feasibility of a functionally modernized F-4.

1 Historical Overview of Re-engining

The re-engining of fighter aircraft that have been in service for some length of time is a concept whose time has come. Airframes now manufactured can remain structurally flyable for up to 50 years. The rapid improvement in gas-turbine performance and durability coupled with the extended aircraft life make re-engining a cost-effective alternative that must be closely evaluated.

There are several examples of successfully re-engined aircraft. Over 1300 Douglas A-4 Skyhawks were produced with the J65W-20 engine. Beginning in 1961, and continuing for another 18 years and 1700 aircraft, the A-4's were re-engined with the J52 engine, realizing a nearly 50% thrust increase and a TSFC improvement of over 25%. Another, more contemporary example is the J57 powered KC135. In 1979, a decision was made to take advantage of gas-turbine technology advancements resulting in lower fuel consumption, lower life-cycle costs, and increased performance. The General Electric CFM56 was chosen as a new engine for the Air Force KC135. An alternate plan was developed for the Air National Guard that included a more comprehensive aircraft upgrade including re-engining with P&W JT3D engines. Both versions of the re-engined KC135 greatly benefited from increased takeoff thrust and dramatically reduced TSFC.

Over 3000 F-4's are presently in active use worldwide and have up to 20 years active service life remaining. The present F-4 powerplant, the J79 developed in the early 1950's, is based on a 30-year-old technology, and has essentially reached its growth limit. Additionally, the J79 is out of production, and its support costs are projected to dramatically increase in the 1990's. The workhorse reputation of the F-4, coupled with its ample remaining service life, prompted an investigation into re-engining with the advanced technology PW1120 engine that would increase the useful life of the aircraft.

II PW1120 Description

The PW1120 is a 20,000 pound thrust class turbojet derivative of the F100 engine, which is presently in use powering the F-15 and F-16 fighters in ten countries throughout the world. It incorporates the proven F100 core module (high-pressure compressor, combustor, and high pressure turbine), gearbox, fuel pump, and forward ducts without change as well as the F100 digital electronic engine control with only minor schedule modifications. Unique PW1120 components include a new low-aspect-ratio, wide chord blade design low-pressure compressor, a new single-stage uncooled low-pressure turbine; a simplified, single-stream augmentor; and a lightweight convergent/divergent exhaust nozzle. The unique PW1120 components such as the low-pressure compressor, low-pressure turbine, and augmentor/nozzle are similar to the respective components in the F100 regarding design principles, materials and manufacturing processes. The unique components also incorporate reliability, durability, and safety features based on lessons learned from over two million hours of F100 operational service. Figure 1 illustrates the areas of commonality between the PW1120 and the F100.

III F-4/PW1120 – Initial Feasibility Study

A. Issues. Three fundamental issues required investigation initially in the F-4/PW1120 project:

1 Will the PW1120 significantly improve F-4 survivability into the next century?

Contributed by the Gas Turbine Division of THE AMERICAN SOCIETY OF MECHANICAL ENGINEERS and presented at the 30th International Gas Turbine Conference and Exhibit, Houston, Texas, March 18-21, 1985. Manuscript received at ASME Headquarters, December 21, 1984. Paper No. 85-GT-69.

Copyright © 1985 by ASME
Downloaded 01 Jun 2010 to 171.66.16.71. Redistribution subject to ASME license or copyright; see http://www.asme.org/terms/Terms_Use.cfm

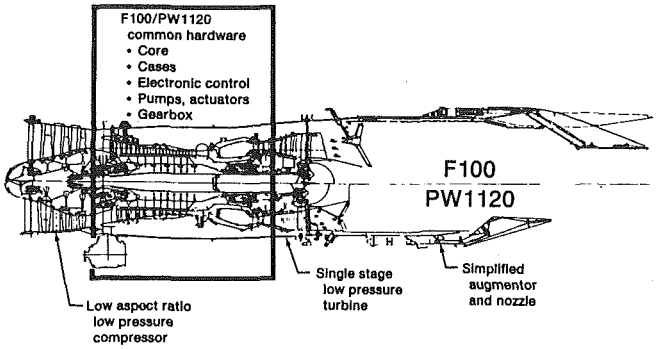


Fig. 1 PW1120 commonality with F100-PW-100 engine

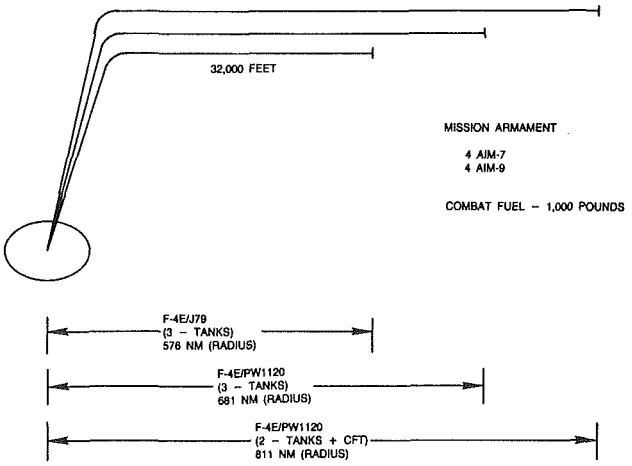


Fig. 2 Modernized F-4 range enhancement

2 Will the re-engined F-4 be a cost-effective modification?

3 Is the PW1120 physically compatible with the F-4? Will re-engining the F-4 solve known deficiencies in the system?

Only with affirmative answers to these questions could F-4 re-engining be considered a viable enough project to warrant the expenditure required for a full-flight demonstration.

1 Survivability. Improved survivability of the re-engined F-4 can be measured in terms of the performance of the modernized aircraft relative to threat aircraft over the proposed life of the system. Thrust and weight differences between the PW1120 and the J79-17 suggest a potentially substantial performance increase, made possible by the years of technological advancement enjoyed by the PW1120. Table 1 illustrates an uninstalled performance comparison between the PW1120 and the J79-17 and shows the superior performance offered by the PW1120.

As can be seen in Table 1, the PW1120 offers 15% thrust improvement, and coupled with the 25% weight decrease produces a 51% improvement in thrust-to-weight ratio. At the same time, the PW1120 promises a 5% to 6% improvement in TSFC, thereby offering greater fuel efficiency with the increased performance.

Re-engining the F-4 will improve penetration speed, ordnance carrying capability, turn rate, acceleration time, and rate of climb for the air-to-air and air-to-ground missions. Range/loiter for reconnaissance and air defense missions will also be improved. When evaluated with the Boeing 1100 gal conformal fuel tank (CFT), which decreases aircraft drag relative to the present 600 gal centerline tank, there is a further improvement in the range/loiter time. Figure 2 illustrates the increase in air-to-air combat radius. This enhances early interception of incoming threats and allows

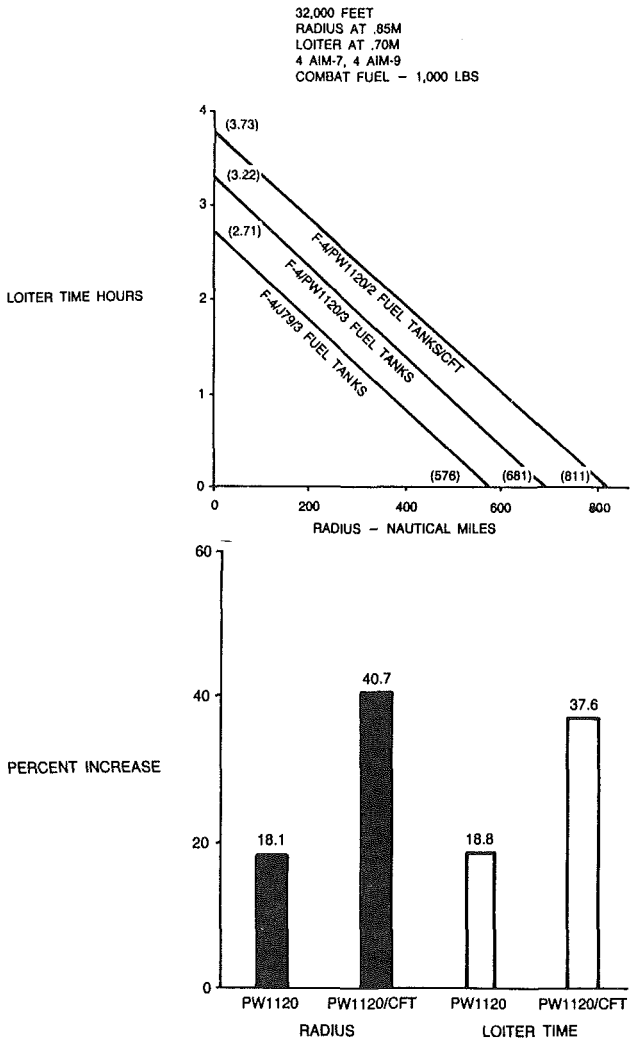


Fig. 3 Modernized F-4 range loiter benefits

Table 1 Uninstalled SLS J79-17 and PW1120 engine comparison

	J79-17	PW1120	Percent improvement
Thrust (lb)			
Maximum	17,900	20,600	15%
Intermediate (dry)	11,870	13,550	14%
Weight (lb)	3,835	2,848	26%
Thrust/weight	4.7	7.3	51%
TSFC lb/hr/lbf			
Maximum power	1.97	1.86	5.6%
Intermediate power	0.84	0.80	5.0%
Corrected airflow (lb/s)	171	178	
Engine size			
Length (in.)	209	162	
Inlet flowpath dia.	30.35	30.5	
Maximum diameter (in.)	39.1	38.5	

one airplane greater potential for engaging more targets prior to enemy weapons release.

The modernized F-4 also allows increased time on station for shorter missions as illustrated in Fig. 3.

Thrust-to-weight ratio is particularly important for determining air combat performance. Figure 4 shows the superior T/W ratio of the F-4/PW1120 relative to the F-4/J79 and the airplanes which comprise the major enemy threat.

A comparison of the F-4/PW1120, the F-4E, and more modern fighter aircraft is shown in Fig. 5. Again, this figure

Downloaded 01 Jun 2010 to 171.66.16.71. Redistribution subject to ASME license or copyright; see http://www.asme.org/terms/Terms_Use.cfm

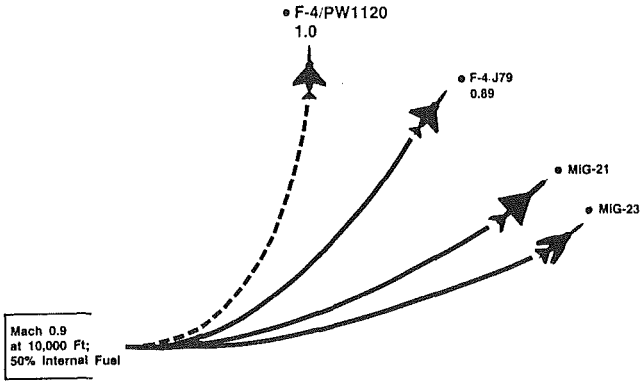
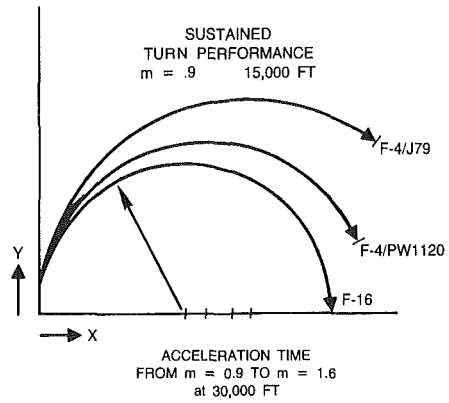


Fig. 4 F-4/PW1120 has superior thrust-to-weight



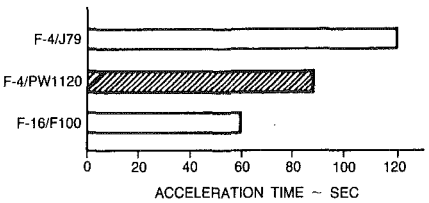
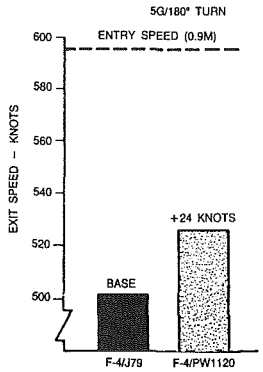


Fig. 5 Improvements in turn and acceleration performance



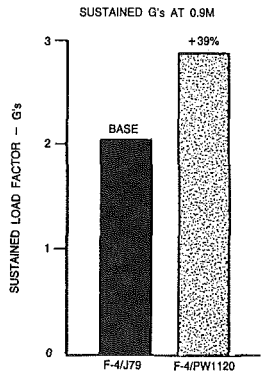


Fig. 6 F-4/PW1120 enhanced maneuverability in air-to-ground mission

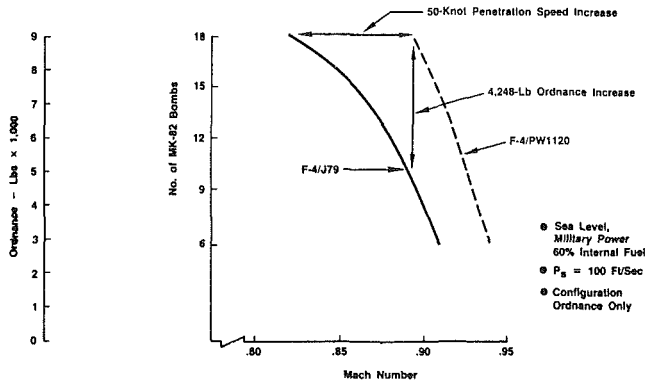


Fig. 7 F-4/PW1120 increased speed/load capabilities

illustrates the magnitude of performance enhancement available in the F-4/PW1120.

The air-to-air benefits of the re-engined F-4 are, as shown above, significant.

Aircraft survivability and effectiveness are similarly enhanced in the air-to-ground mission. A comparison of maneuverability when loaded with air-to-ground munitions, Fig. 6, shows the modernized airplane has less speed bleed-off and a 39% greater load factor (sustained G capability) than the F-4E. Additionally, the reduced weight and increased thrust of the new engines can result in speed and/or payload benefits. Figure 7 indicates considerable improvements for both parameters.

The performance enhancements available in the F-4/PW1120 clearly upgrade the F-4 into a present/future threat competitive aircraft as illustrated. The re-engined aircraft also solves other aircraft deficiencies. The F-4E exceeds takeoff gross weight in certain mission configurations, so fuel is off-loaded, permitting a full ordnance load but reducing range. The projected 1600 pound weight reduction with PW1120 engines allows both full ordnance and a full fuel load, recouping lost range. Another benefit of the PW1120 is that it is smokeless, thus reducing the F-4 visibility and increasing aircraft survivability.

2 Cost Effectiveness. The cost of a fully modernized F-4 Super Phantom, including conformal tank, new digital avionics suite, and 2 PW1120 engines is estimated to be under $10 million. As was illustrated in the earlier section, the modernized F-4/PW1120 approaches the performance of the newest state-of-the-art fighter aircraft, but at less than half of the cost. Additionally the PW1120 powered F-4 will realize the benefits of 70% commonality with the F100 engine. Present F100 users who elect to upgrade their F-4 fleet will have substantial assets in place, such as aerospace ground-support equipment and engine spares, and will realize substantial savings in logistics and support costs. These factors will yield a 15 year payback in which the cost of modernization will be offset by the reduction in operating costs in a peace time scenario. A dramatic reduction in the payback period can be seen in a wartime scenario due to a reduction in attrition rate and the number of aircraft required to accomplish a given mission as noted in Fig. 8. On an effectiveness basis with an equal number of targets killed, the relative number of aircraft required for a mission is reduced by one-half and the exchange ratio of targets killed per air-

Downloaded 01 Jun 2010 to 171.66.16.71. Redistribution subject to ASME license or copyright; see http://www.asme.org/terms/Terms_Use.cfm

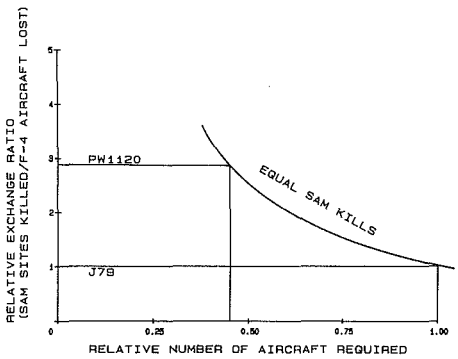


Fig. 8 F-4/PW1120 reduces aircraft requirements in air-to-ground mission

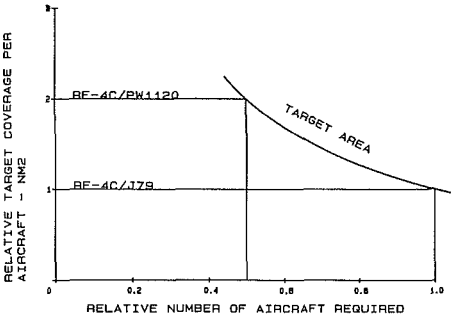


Fig. 9 F-4/PW1120 reduces aircraft requirements in recce mission

craft lost is doubled. This improvement is due to the improved maneuverability of the aircraft when re-engined.

Another measure of effectiveness can be seen in the standard F-4 reconnaissance mission. Figure 9 shows the same trend as the previous chart in that the relative number of aircraft required to perform a mission is one-half with nearly twice the photo area coverage realized on a per-aircraft basis.

3 Installation

A Inlet/Airflow Compatibility. The present J79 engine installation utilizes a translating ring mounted forward of the engine inlet that regulates the engine airflow and bypass air. When pressures indicate throat Mach number is too low, the bypass is opened, allowing more secondary air to flow around the engine providing adequate inlet buzz margin and reduced inlet spillage drag. This air exits through the exhaust nozzle between the primary and secondary nozzles used in the J79 installation. The J79 requires 50 sq in. of inlet bypass air to cool the engine bay. Holes are drilled into the bypass ring to allow this continuous bypass airflow. The present translating ring diameter-to-length (D/L) ratio is approximately 7, causing frequent jamming during engine installation and removal. It is difficult to free and rerig the mechanism once it has jammed.

The design of the J79 bypass ring was dictated by engine length, and nacelle space limitations. The shorter PW1120 allows for a 30 in. inlet extension duct (IED) providing for a D/L ratio of approximately 1. The inlet extension duct mates with the PW1120 low-pressure compressor using a proven design, flexible lip seal. Use of the flexible seal on the IED serves to isolate it from the engine mount loads, allowing for independent mounting on the airframe mount rail. Additionally the IED provides a mounting surface for a remote airframe mounted accessory drive (AMAD) system.

The IED is composed of a sleeve covering a cylinder containing 11 ports yielding 320 sq in. in total bypass area. The sleeve is moved by two hydraulic actuators which are controlled by a servovalve which receives command signals

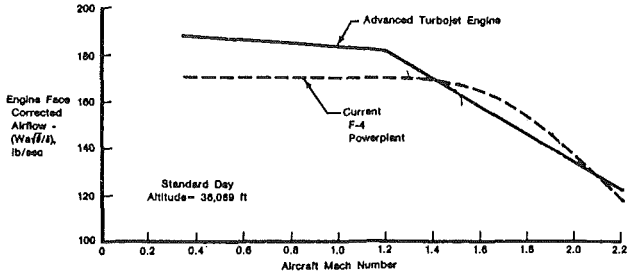


Fig. 10 Engine airflow demand comparison, PW1120 and J79

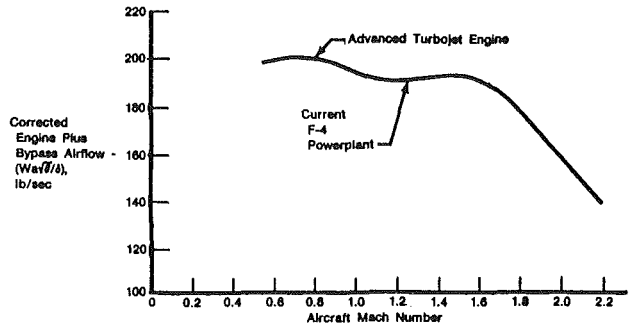


Fig. 11 Engine plus bypass airflow demand for PW1120 and J79

from an electronic propulsion interface unit. In the event of aircraft electrical system malfunction, the system is biased to close the bypass ports to prevent overpressurization in the nacelle in high "Q" flight conditions. The engine/inlet combination has sufficient stability and buzz margin to permit continuous safe engine operation with the bypass fully closed.

Analysis of the F-4 inlet flow characteristics relative to the PW1120 has demonstrated that the F-4 inlet variable ramp control schedules can be retained without modification. The PW1120 engine/inlet airflow matching with this installation design will equal or exceed that of the J79. Figure 10 compares the airflow demands of the J79 and PW1120. Figure 11 illustrates the total airflow demand engine plus bypass air of the two engines.

As can be seen from Fig. 11, total airflow demand of the two installations is the same, so the F-4/PW1120 configuration will not be subject to any increased inlet spillage drag or inlet created distortion. In fact, the inlet extension duct will serve to attenuate inlet distortion, and this, coupled with the superior surge margin built into the PW1120, will yield stall-free operation throughout the flight envelop.

B Accessories. The smaller PW1120 provides sufficient room in the nacelle for more modern and maintainable accessories than can be realized in the J79 installation. The inlet duct extension design allows inclusion of the airframe mounted accessory drive (AMAD) system presently in use in the F100 powered F-16 with only minor modification or adaptations. The power drive input on the AMAD gearbox does not align directly with the power takeoff (PTO) pad on the PW1120. An offset adapter will be added to the AMAD to realign the input and output pads on the AMAD and engine respectively. Also, the power takeoff drive shaft will be adapted from the F-16 AMAD/F100 system to provide for a proven flightworthy accessory drive system.

The inclusion of the AMAD and its associated hydraulic, electrical and oil systems will serve to improve aircraft maintainability. The AMAD components can remain in the aircraft independent of the requirement to remove an engine for maintenance. These improvements are projected to reduce the engine-related maintenance from 3.2 maintenance

Downloaded 01 Jun 2010 to 171.66.16.71. Redistribution subject to ASME license or copyright; see http://www.asme.org/terms/Terms_Use.cfm

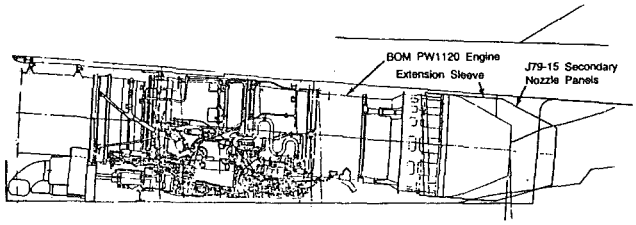


Fig. 12 Proposed F-4/1120 installation with secondary nozzle

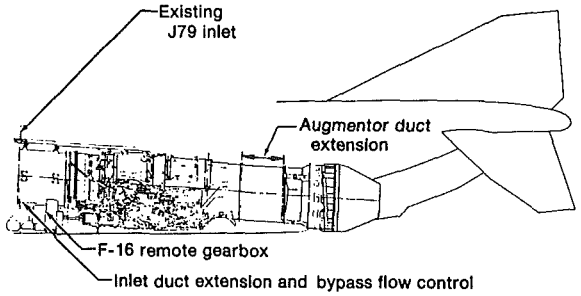


Fig. 13 Selected F-4/PW1120 installation

manhours per engine flight hour with the J79 to 1.9 MMH/EFH with the PW1120.

Another feature of the PW1120 installation in the F-4 is in the area of engine starting. The customer will have the option of retaining the present air turbine starting system or choosing a jet fuel starter which would further expand the airstart envelope, and eliminate the requirement for ground starting carts.

The present F-4 engine starting system employs two modes of operation. The primary system depends on an air supply from a ground power source to feed an air turbine starter. The secondary system uses an engine starter cartridge in a breech on the air turbine starter and is used for emergency starts. Ground service carts must be available to wherever F-4's are deployed.

The alternative to a system requiring ground carts for starting the F-4 is an engine-starting system employing a jet-fuel starter (JFS) to drive the engine compressor through a clutch system in the AMAD. The JFS configuration proposed for the F-4 is similar to the present system in the F-16. That system includes a hydraulic accumulator which drives a small hydraulic motor which in turn starts the JFS. The accumulator is recharged by the aircraft hydraulic system after each engine start. The JFS is mounted on the AMAD and has an insulated exhaust duct that directs hot exhaust gases outboard and downward through the wall of the engine compartment. The intake port in the IED has a shutoff valve to prevent air leakage through the JFS. Fuel is supplied to the JFS from a bypass line in the main engine fuel supply line. The incorporation of a JFS would give the F-4 self-contained start capability from any airfield worldwide, not just current F-4 operational bases.

The PW1120 has two bleed ports, at the 7th and 13th compressor stages. The environmental control system in the F-4 will remain compatible with the PW1120 engine through use of a pressure-regulation system similar to that in use on the F-16 and Boeing 757. A selector valve is controlled by pressures and temperatures to automatically switch between the 7th and 13th stage bleeds on the PW1120 according to aircraft environmental system requirements. This bleed system allows the present F-4 environmental control and pneumatic systems to be retained without change.

Other modifications to the F-4 are minimal. The existing fuel boost pumps must be reoperated to allow for greater pumping capacity, due to the increase in fuel required for

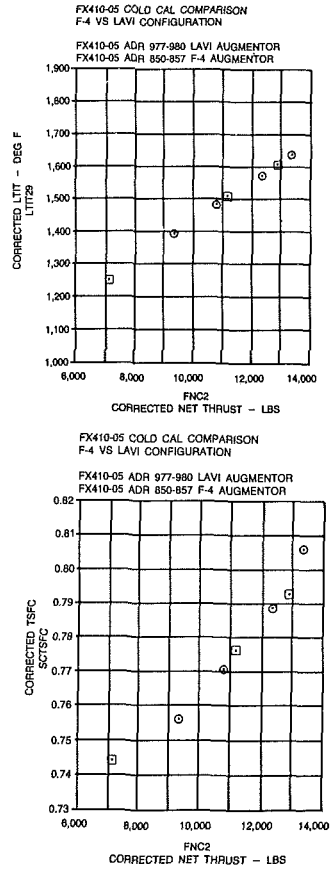


Fig. 14 PW1120/F-4 nonaugmented performance

maximum afterburning operation with the PW1120. Minor modification to the mechanical throttle linkage will be required to accommodate the PW1120 angle of rotation of the throttle lever with the existing cockpit power lever.

C Engine Nozzle/Airframe Integration. Particular attention was paid to optimizing the location of the PW1120 exhaust nozzle exit plane to minimize aircraft base drag and to remain within the aircraft allowable aft fuselage skin temperature. The PW1120 engine produces a higher exhaust gas temperature and has greater exhaust plume expansion than the current J79 engine.

Four installations were studied in order to arrive at a satisfactory engineering solution in the nozzle airframe integration area. The first configuration examined was the current 161″ long bill of material (BOM) engine mounted in the nacelle with the IED described previously. The advantage to this installation is that no engine configuration changes from the current PW1120 bill of material were required. However, the resultant PW1120 nozzle exhaust plane was situated so as to cause high boattail drag and an aft fuselage overtemperature condition. For that reason it was rejected.

A second installation concept once again retained the BOM PW1120 configuration, but included a refaired aft fuselage. Modification to the aircraft's primary structure was viewed as very costly and therefore undesirable. Fuselage rework was limited to the aft engine bay door on the aircraft structure and the lower outboard 120 degrees of the engine exhaust nozzle area. Analysis of this configuration indicated a slight reduction in base drag. The problem associated with aft fuselage overtemperature and possible plume attachment to the empennage still remained a concern with this installation and the concept was therefore rejected.

The third proposed configuration is similar to the present J79 installation, utilizing both the primary engine exhaust

Downloaded 01 Jun 2010 to 171.66.16.71. Redistribution subject to ASME license or copyright; see http://www.asme.org/terms/Terms_Use.cfm

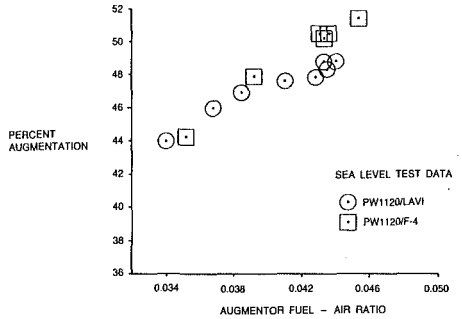


Fig. 15 PW1120/F-4 augmented performance

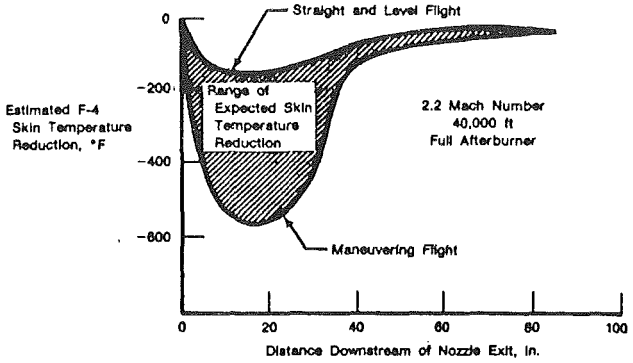


Fig. 16 Reduced F-4 afterbody skin temperatures with the PW1120/F-4

nozzle and an associated secondary nozzle, as illustrated in Fig. 12.

The secondary nozzle would be attached to the airframe and could be modulated in flight by a set of actuators independent of the engine nozzle actuators. Consequently, secondary nozzle loads would be transferred to the airframe rather than the engine.

This configuration gave external boattail drag coefficients similar to the J79 configuration, and required no engine modifications from the bill of material PW1120. This installation required a heavy secondary nozzle and negated much of the weight advantage of the PW1120 engine installation. Therefore associated performance improvements would be reduced and system complexity increased causing rejection of this design concept.

The fourth installation configuration, depicted in Fig. 13, involves a modification of the BOM PW1120 configuration.

In this configuration a 25.2 in. augmentor extension is introduced at the engine augmentor nozzle flange. Although the requirement to maintain the BOM engine configuration was waived, the mechanical modification to the engine in this configuration is straightforward and therefore warranted investigation. Sea-level testing of the PW1120 configured with the 25 in. extension began in late 1984. Figure 14 shows a comparison of the nonafterburning performance of the BOM PW1120 and the F-4 configuration.

There was no measurable nonaugmented performance difference with the extended and BOM nozzle configurations. Augmented performance testing has been equally successful. In the F-4 configuration, the PW1120 has demonstrated sea-level augmentation levels in excess of 51%. Figure 15 compares the levels of augmentation obtained with the extended and BOM nozzle configuration.

Development testing of the PW1120/F-4 is continuing to optimize liner and nozzle cooling-flow distributions in order to maintain durability commensurate with the BOM design. Altitude testing of various augmentor liner and sprayring configurations is scheduled to continue at the P&W altitude facility in 1985.

Inclusion of the 25.2 in. augmentor spool piece places the PW1120 nozzle exit plane 5 in. aft of the J79 secondary nozzle exit plane. P&W studies indicate that with this configuration the exhaust nozzle plume will not impinge on the aircraft afterbody. In fact, the aft fuselage and stabilizer temperatures downstream of the nozzle exit are projected to be lower with the PW1120 than with the present installation. Figure 16 shows the anticipated reduction in aft fuselage temperatures with the installation.

With this PW1120 installation, boattail drag is estimated to be lower than with the present J79 installation. On the basis of this reduction in drag and aircraft skin temperature, and considering the relatively simple nature of the engine modifications, the extended augmentor configuration was chosen for the F-4 installation.

The changes to the aircraft to accommodate the PW1120 are minimal. The aft engine mount is within 5″ of the current aft J79 mount. A bridging between two major structural bulkheads of the F-4 is all that is required to accommodate the PW1120. The forward engine mount will pick up the existing J79 mount rail which will be extended by some 30 inches. Positioning of the engine with the 30″ IED and 25″ augmentor extension requires recontouring in the aircraft engine removal doors, the dropout link and a panel on the outboard side of the engine bay. This will eliminate minor interferences caused by the packaging of the engine accessories on the bottom of the PW1120 engine. The door changes are limited to the forward nonstructural door, and will result in a design that allows for simpler installation and removal of the PW1120 over the existing J79.

Conclusion

The fundamental issues that demanded investigation in the F-4 modernization feasibility study – performance enhancement, cost effectiveness, and physical installation compatibility – were studied and satisfactorily answered. With new PW1120 engines the F-4 becomes a fighter with a thrust-to-weight ratio exceeding 1 to 1, and an airplane that can be a combat survivable viable fighter through the 1990's. Further, the cost benefits realized by the system are substantial: performance approaching that of the newest fighters at less than half of the cost. Finally, the PW1120 fits well into the F-4 with few aircraft or engine modifications required.

On the basis of the feasibility study, the F-4 modernization program is continuing. Engine design installation work is nearly complete. A mockup of PW1120 has been installed in an F-4, and a first flight is scheduled for late 1985.

Downloaded 01 Jun 2010 to 171.66.16.71. Redistribution subject to ASME license or copyright; see http://www.asme.org/terms/Terms_Use.cfm

Impingement Starting and Power Boosting of Small Gas Turbines

C. Rodgers
Chief Analytical Engineer,
Turbomach Division of Solar Turbines, Inc.,
San Diego, Calif. 92123

The technology of high-pressure air or hot-gas impingement from stationary shroud supplementary nozzles onto radial outflow compressors and radial inflow turbines to permit rapid gas turbine starting or power boosting is discussed. Data are presented on the equivalent turbine component performance for convergent/divergent shroud impingement nozzles, which reveal the sensitivity of nozzle velocity coefficient with Mach number and turbine efficiency with impingement nozzle admission arc. Compressor and turbine matching is addressed in the transient turbine start mode with the possibility of operating these components in braking or reverse flow regimes when impingement flow rates exceed design.

Introduction[1]

An appealing, yet apparently simple, gas turbine start system involves the impingement of high-pressure air or hot-gas products from stationary shroud supplementary nozzles directly upon the rotor(s) of the rotating assembly. Normally, the impingement point is in the vicinity of the high-pressure turbine stage requiring penetration of the hot-end casing. Impingement can also be upon the compressor rotor, providing the impingement gas temperature is below approximately 811 K (1460 R).

Low-cost turbojets and turbofans for drone aircraft and cruise missiles invariably use impingement start systems to ensure minimum installed weight and volume. Compressed air is commonly supplied on the ground through an umbilical line, or monopropellant cartridges are used.

The basic advantage of the impingement system is that it can directly apply large amounts of starting energy where it is most effective, at the rotating assembly, avoiding parasitic friction losses through a starter gear train. As a result, extremely fast starts can be demonstrated, limited only by the combustion and ignition system of the gas turbine. Start times of three seconds to idle were demonstrated for a tank application gas turbine in [1].

Relative to the more conventional gas turbine start systems, the major disadvantages of the impingement system are energy storage and logistics limitations, together with limited restart capability.

Until the advent of the large thrust turbofan, impingement cartridge starters were cost effective. The increased starting energy requirements for turbofans, however, and environmental considerations motivated a change to air turbine start systems using compressed air from either on-board or ground cart gas turbine auxiliary power units (APUs).

Advancements in propulsion technology, with increased sophistication, particularly higher bypass ratio turbofans and fly-by-wire aircraft, continue to pace the design and optimization of secondary aircraft power systems to the point where an in-flight aircraft power outage of even a few seconds can no longer be tolerated. This requires either an air-breathing APU with high altitude rapid start capability and/or stored energy emergency power units (EPUs) with monopropellant or bipropellant fuel supplies. These needs have led to the Super Integrated Power Unit (SIPU), which is a single aircraft power unit capable of supplying all secondary power and main engine start power needs throughout the entire aircraft operating envelope [2].

The development of the SIPU and other APU rapid start systems at the author's company has led to an improved understanding of impingement start systems for radial inflow compressors and radial airflow turbines. The generic development path by which this understanding was achieved is described in this paper.

Impingement Turbine Theory

Rapid gas turbine starts are accomplished with high energy impingement nozzles. Overall nozzle expansion ratios may be as high as 30:1. Consequently, the design and performance of the nozzle is of primary importance.

Extensive research was conducted on small, low-specific-speed, supersonic, axial impulse turbines in [3]. Turbine

[1] Units of Measurement

The following English units of measurement were used in the evaluation of the impingement turbine performance. Equivalent metric conversions are given.

Item	English	Metric	
A	sq in.	1 m^2	= 1549 sq. in.
D,S	in.	1 mm	= 0.0394 in.
H	ft	1 m	= 0.305 ft
N	rpm	rpm	
P	psia, psig	1 kg/m^2	= 1422 psia, psig
Q	ft^3/s	1 m^3/s	= 35.2 ft^3/s
T	R	K	= R/1.8
U,V_o	fps	1 m/s	= 3.281 fps
W	pps	1 kg/s	= 2.205 pps

Contributed by the Gas Turbine Division of THE AMERICAN SOCIETY OF MECHANICAL ENGINEERS and presented at the 29th International Gas Turbine Conference and Exhibit, Amsterdam, The Netherlands, June 4-7, 1984. Manuscript received at ASME Headquarters January 12, 1984. Paper No. 84-GT-188.

Copyright © 1985 by ASME
Downloaded 01 Jun 2010 to 171.66.16.71. Redistribution subject to ASME license or copyright; see http://www.asme.org/terms/Terms_Use.cfm

performance was concluded to be dependent on many factors, including nozzle and rotor performance, leakage, Reynolds number effects, and parasitic losses.

Basically, turbine performance depends on the momentum change across the rotor, which is described by the turbine hydraulic efficiency equation. This equation reflects the basic turbine efficiency from which leakage, Reynolds number effects, and parasitic losses detract. The effects of nozzle and rotor performance are included in the hydraulic efficiency equation for an axial impulse turbine with symmetrical blading

$$\eta_h = 2(U/V_o)\,(1+\Psi_r)\,[(\Psi_n \cos\alpha_n) - (U/V_o)] \qquad (1)$$

Equation (1) defines the maximum attainable turbine efficiency with zero parasitic losses or leakage. Since the turbine hydraulic efficiency is a strong function of U/V_o, maximum efficiency is obtained when the turbine is operating at optimum U/V_o. The optimum U/V_o is obtained by differentiating equation (1) with respect to U/V_o and solving for U/V_o when the differential is equated to zero

$$(U/V_o)_{\text{opt}} = (\Psi_n \cos\alpha_n)/2 \qquad (2)$$

Solving equation (2) yields optimum values of U/V_o from 0.4 to 0.5 for typical values of Ψ_n and α_n.

A torque coefficient can also be defined as

$$\pi = \frac{12g\ \text{Torque}}{WV_o(D/2)} = \frac{\eta_h}{2(U/V_o)} \qquad (3)$$

At stall ($U/V_o = 0$), this becomes

$$(\Psi_r)_{\text{stall}} = (\pi/\Psi_n) - 1 \qquad (4)$$

At a U/V_o of 0.5, turbine hydraulic efficiency changes 2.1 times the percentage change in nozzle coefficient. For example, if the nozzle coefficient is 0.90 instead of 1.0 at a U/V_o of 0.5, the hydraulic efficiency will be reduced by 2.1 × 10 percent = 21 percent. Changes in rotor coefficient, however, effect much smaller changes. For example, a 10 percent change in rotor coefficient changes hydraulic efficiency by only 4 or 5 percent.

In sum, nozzle and rotor velocity coefficients have a large effect on the ultimate obtainable impulse turbine efficiency, with the nozzle coefficient being much more important than the rotor coefficient. When operating a turbine at the design pressure ratio, nozzle coefficients of approximately 0.96 may be realized. However, for pressure ratios greater or less than design, this coefficient decreases rapidly, particularly for nozzles with high area ratios and, hence, high design Mach numbers.

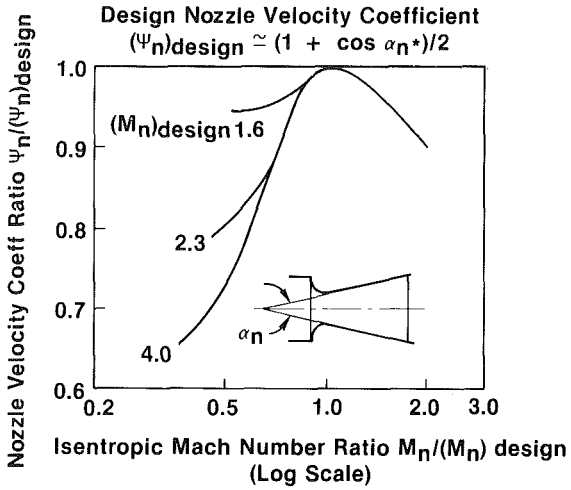


Fig. 1 Normalized supersonic conical convergent/divergent nozzle performance

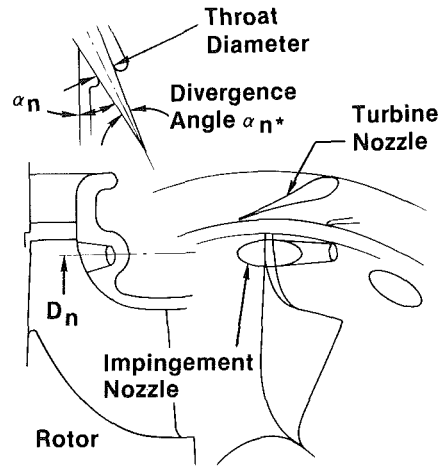


Fig. 2 Impingement nozzle configurations

Correlation of open literature and test performances of conical convergent/divergent nozzles in [3] generally showed the nozzle velocity coefficient near the design point condition to be

Nomenclature

a = admission arc
A_n = nozzle area
APU = auxiliary power unit
D = diameter
D_s = specific diameter = $D(gH)^{0.25}/\sqrt{Q}$
EPU = emergency power unit
g = gravitational constant
H = isentropic head
M_n = nozzle Mach number
N = rotational speed
N_s = dimensionless specific speed = $\omega\sqrt{Q}/(gH)^{0.75}$
P_1 = inlet pressure
Q = volume flow
S = blade pitch
SIPU = super integrated power unit
T_1 = compressor inlet temperature
T_2 = compressor discharge temperature
T.I.T. = turbine inlet temperature
t = time
W = airflow
U = rotor tangential speed
V_o = isentropic spouting velocity = $\sqrt{2gH}$
α_n = nozzle angle (relative to tangential)
α_{n^*} = nozzle included angle
β = blade exit angle (relative to tangential)
π = torque coefficient
η_t = isentropic turbine efficiency
η_h = hydraulic efficiency
Ψ = velocity coefficient (actual velocity/ideal isentropic)
ρ = reaction
ϵ = rotor diameter ratio (inlet/exit)
λ = disk windage constant
ω = angular velocity

Subscripts

a = airflow
h = hydraulic
n = nozzle
o = spouting
opt = optimum
r = rotor
s = specific
t = turbine
w = windage
1 = inlet
2 = compressor discharge
3 = rotor exit

Downloaded 01 Jun 2010 to 171.66.16.71. Redistribution subject to ASME license or copyright; see http://www.asme.org/terms/Terms_Use.cfm

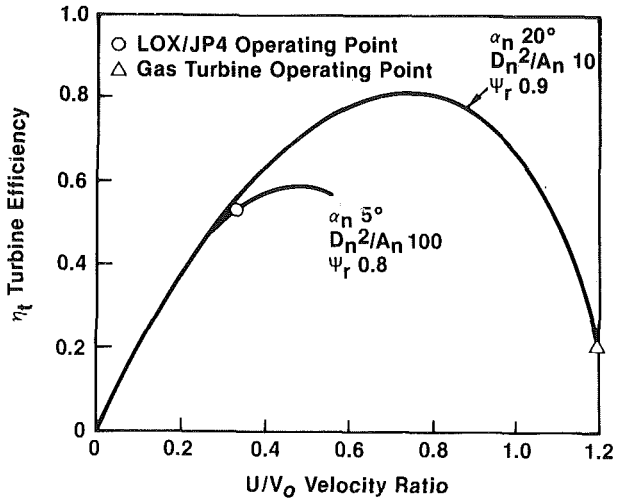


Fig. 3 Predicted turbine efficiency

$$\Psi_{n\,\text{design}} \simeq (1+\cos\alpha_{n^*})/2 \tag{5}$$

At design conditions, the nozzle velocity coefficient can be normalized in terms of $\Psi_n/(\Psi_n)_{\text{design}}$ versus $M_n/(M_n)_{\text{design}}$ as portrayed in Fig. 1.

Test characteristics of the side impingement nozzle for radial turbomachinery similar to that depicted in Fig. 2 indicate that rotor velocity coefficients are quite low, due to large incidence effects and high internal losses. Peak turbine efficiency is almost singularly dependent upon the nozzle velocity coefficient. The hydraulic efficiency of these turbines is

$$\eta_h = 2(U/V_o)[(\Psi_n\cos\alpha_n) - (U/\epsilon^2 V_o)] \tag{6}$$

By differentiation to determine $U/(V_o)_{\text{opt}}$ and substitution, the optimum efficiency for $\epsilon = 1.0$ becomes

$$(\eta_h)_{\text{opt}} = [(\Psi_n\cos\alpha_n)^2]/2 \tag{7}$$

Thus maximum efficiencies of 45 percent are anticipated.

Since disk windage losses may also be significant in low specific speed turbines, turbine efficiency may be expressed as

$$\eta_t = 2(U/V_o)[(\Psi_n\cos\alpha_n) - (U/\epsilon^2 V_o) - [(U/V_o)^2\lambda_w(D_n^2/A_n)]] \tag{8}$$

With a windage coefficient (λw) on the order of 0.003, equation (8) is similar to that of [4] for side admission Terry turbines and can be expressed in terms of specific speed and specific diameter

$$\eta_t = [(\Psi_n\cos\alpha_n) - N_s D_s/(\epsilon^2\sqrt{8}) - (0.5\lambda_w N_s^2 D_s^4)]2^{-0.5}(N_s D_s) \tag{9}$$

Although not as effective as Ψ_n, turbine performance can be improved by reducing rotor incidence and internal losses, such as increasing Ψ_r. At the most, equation (9) indicates that increasing Ψ_r from 0 to 0.8 increases peak turbine efficiency from 45 to 63 percent for full admission. Lower rotor velocity coefficients are expected with partial admission according to the relationship

$$(\Psi_r)_{\text{partial}} = (\Psi_r)_{\text{full}}[1-(S/2a)] \tag{10}$$

Attempts to improve performance of radial inflow turbines under low specific speed, low reaction (near impulse conditions), as described in [5], concluded that only minor improvements are possible beyond that attained by conventional 50 percent reaction designs, operating at low velocity ratio (part load) conditions. Peak efficiencies for radial impulse ratios of 50 to 60 percent were indicated at a velocity ratio of 0.36.

A generalized expression for both axial and radial turbine efficiency in terms of velocity ratio, reaction, nozzle, and rotor velocity coefficients, and windage losses is derived in [4] and can be simplified to

$$\eta_t = [(\Psi_n\cos\alpha_n\sqrt{1-\rho}) + \epsilon^{-1}[(\Psi_r\cos\beta_3\sqrt{A}) - (U/V_o\epsilon)] - [(U/V_o)(2\lambda_w/\rho)(D^2/A_n)]]2(U/V_o) \tag{11}$$

where:

$$A = \rho + \Psi_n^2(1-\rho) - (U/V_o\epsilon)^2 - [2\Psi_n\cos\alpha_n(U/V_o)\sqrt{1-\rho}] \tag{12}$$

Equation (12) is shown plotted in Fig. 3 for two radial turbine flow path geometries that will be discussed later. Note that the rotor velocity coefficient is defined as that being close to the design incidence condition.

Test Performances

Test performances of impingement turbines can be determined in several ways. Due to the transient operation of impingement turbines, a popular testing method is to determine output power from accelerating a flywheel of calibrated moment of inertia.

The impingement turbine test efficiencies described in this paper were determined from transient acceleration/deceleration data. Turbine efficiency was defined as

$$\eta_t = \frac{\text{Acceleration and Braking Power}}{\text{Isentropic Expansion Power}} \tag{13}$$

Data accuracy was essentially governed by measurement uncertainty in the differentials of speed to time, dN/dt, during acceleration and deceleration plus isentopic expansion power. Acceleration uncertainty increases with very rapid start times, whereas the actual expansion process is isentropic only for very short blowdown durations due to thermal and moisture content effects. For these reasons, turbine impingement nozzle tests were conducted with heated air at 500°F and acceleration rates kept to approximately 500 rad/s.

Radial rotors generate an inherent centrifugal static pressure rise and behave essentially as 50 percent reaction turbomachines. Since the static rotor pressure at the impingement diameter determines the downstream back pressure of the nozzle, the higher the rotor speed, the higher the nozzle back pressure.

For the test described herein, the static rotor pressure was measured at the impingement diameter and the expansion ratio was defined as

$$\text{Expansion Ratio} = \frac{\text{Nozzle Inlet Total Pressure}}{\text{Static Rotor Pressure}} \tag{14}$$

Impingement gas flow rate was determined both from choked nozzle calculations and an upstream standard ASME flow measurement orifice. Flow difference during some tests was as high as 10 percent, but the average difference was 4 percent. Expansion power was calculated using the impingement nozzle flows with a discharge coefficient of 0.95.

Turbine Shroud Impingement

Eleven supersonic, convergent/divergent, conical shroud nozzles are shown in Fig. 4 for a 6.5-in. (166-mm) tip dia, radial inflow turbine. Two sets of nozzles are visible: the conventional gas turbine radial inflow nozzles and the side impingement nozzles. Geometric features of the impingement nozzle, which was originally designed for a specific heat ratio of 1.153 and a specific heat of 0.72, are shown in Fig. 5.

Test performance, using air with all 11 impingement nozzles flowing, is shown in Fig. 6 in terms of turbine efficiency and torque coefficient versus velocity ratio with

Downloaded 01 Jun 2010 to 171.66.16.71. Redistribution subject to ASME license or copyright; see http://www.asme.org/terms/Terms_Use.cfm

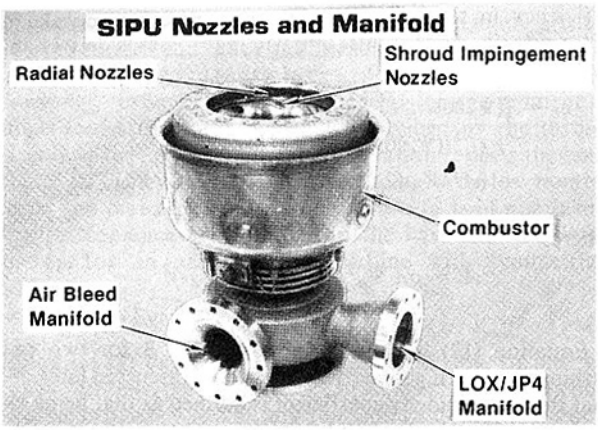


Fig. 4 SIPU nozzle

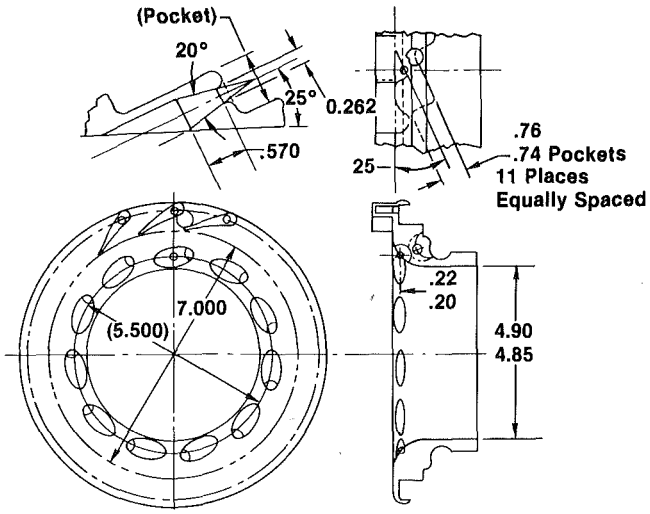


Fig. 5 SIPU nozzle geometry

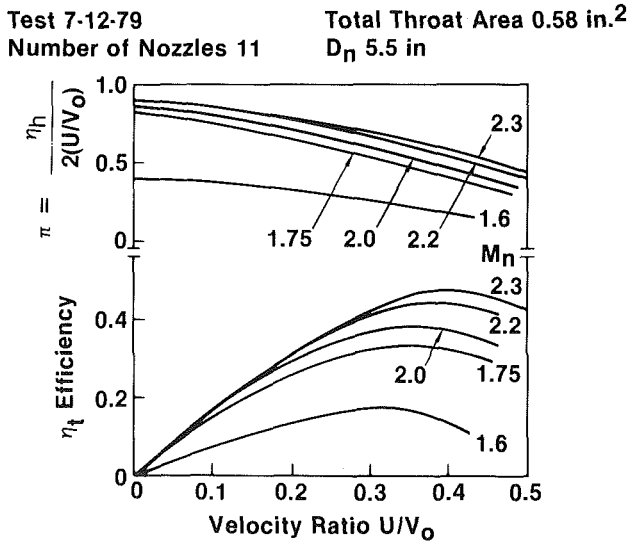


Fig. 6 SIPU impingement turbine efficiency, 11 nozzles

nozzle Mach number as a parameter. Peak turbine isentropic efficiency was 46 percent at a velocity ratio (U/V_o) of 0.42 with a corresponding expansion Mach number of 2.3. Since the nozzle area ratio was 3.2, the air test was not run to the optimum expansion ratio of the nozzle. Thus a slightly higher efficiency level of 47 percent could be projected.

Test results with 4 of the 11 nozzles blocked are plotted in

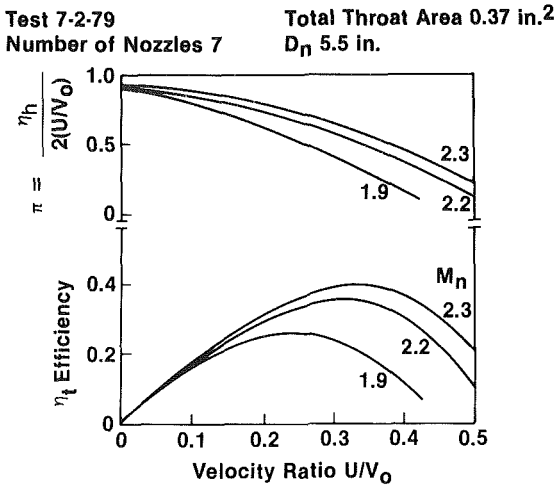


Fig. 7 SIPU impingement turbine efficiency, 7 nozzles

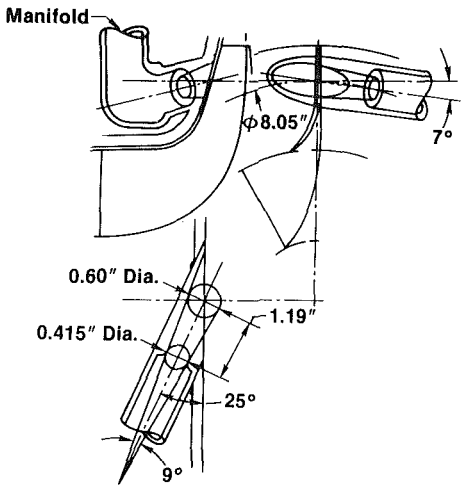


Fig. 8 Compressor shroud impingement nozzle geometry

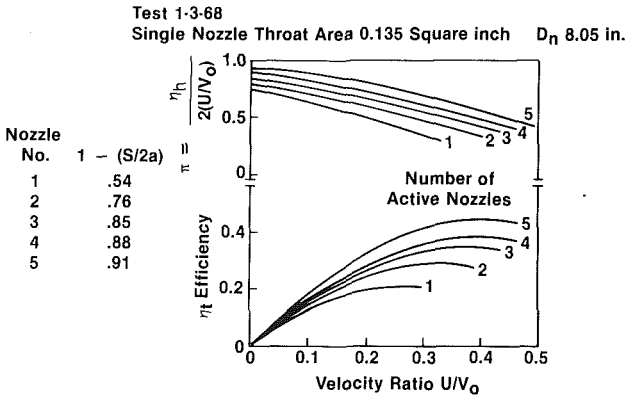


Fig. 9 Compressor shroud impingement turbine efficiency

Fig. 7. Peak efficiency reduced from 46 to 40 percent at a Mach number of 2.3.

Additional tests, not covered in this paper, were conducted on a second nozzle design, where efficiency was determined both from transient techniques and steady-state dynamometer measurements. Efficiency levels calculated by the two techniques were within ±4 percent.

Compressor Shroud Impingement

The geometry of a centrifugal compressor shroud im-

Downloaded 01 Jun 2010 to 171.66.16.71. Redistribution subject to ASME license or copyright; see http://www.asme.org/terms/Terms_Use.cfm

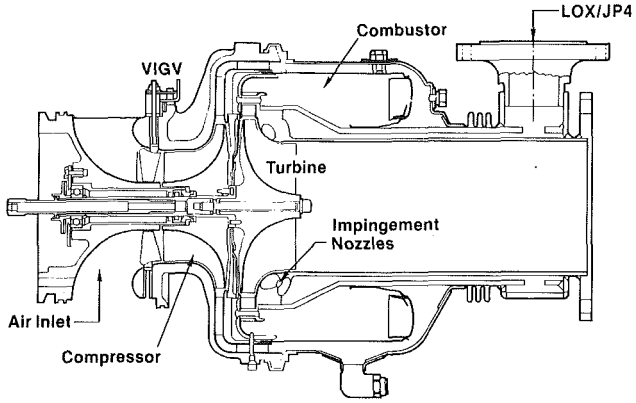


Fig. 10 SIPU cross section

pingement nozzle is shown in Fig. 8. This nozzle was designed for a rapid start system for a 350-hp (260-kW) gas turbine incorporating a 9.7-in. (246-mm) tip dia compressor.

Test performance using air with one to five of these nozzles flowing is shown in Fig. 9 in terms of turbine efficiency and torque coefficient versus velocity ratio with nozzle number as a parameter. With all five nozzles flowing, peak turbine isentropic efficiency was 45 percent at a velocity ratio (U/V_o) of 0.43 and a Mach number of 2.27, which was close to the design Mach number of 2.3. It was possible to reduce the active nozzle arc because the nozzles were individually manifolded with separate valves. Incremental reduction of nozzle number showed that turbine efficiency monotonically decreased to a peak value of 21 percent with only one nozzle flowing.

Using the nozzle velocity coefficient (Ψ_n) at stall and assuming the flow vectors are close to the metal angles, a rotor velocity coefficient at stall can be computed from

$$(\Psi_r)_{\text{stall}} = [(\epsilon\pi/\Psi_n) - (\epsilon\cos\alpha_n)]/\cos\beta_3 \tag{15}$$

However, if the rotor velocity coefficient is close to zero, then

$$\pi_{\text{stall}} = (\Psi_n)_{\text{stall}}(\cos\alpha_n) \tag{16}$$

The stall test data corroborate that the stall torque coefficient is close to the anticipated nozzle velocity coefficient in cases where the operating Mach number approaches the design value and windage losses are small.

Summary of Test Efficiencies

The test efficiencies measured for both radial compressor and turbine shroud impingement nozzles determined from transient acceleration and deceleration traces and system polar moment of inertia reveal the following:

- Expansion efficiencies on the order of only 40 percent are possible based upon nozzle inlet total to shroud impingement diameter static pressure.
- Overall expansion efficiences are even lower if expressed in terms of the overall pressure ratio, nozzle inlet to rotor outlet, as a consequence of the rotor reaction.[2]
- Efficiency decreases with increasing windage losses that are reflected by larger ratios of D^2/A_n.
- Higher efficiencies of up to 60 percent are predicted for conventional radial inflow supplementary impingement nozzles.
- Stall torque coefficients are close to unity near the design nozzle Mach number and, with negligible windage losses, indicate rotor velocity coefficients close to zero.

[2]This was necessary since impingement nozzle performance had to be separated from the radial rotor reaction characteristic to enable nozzle and overall expansion performance prediction with impingement gasses other than air.

Super Integrated Power Unit

An application of impingement nozzles is the Super Integrated Power Unit (SIPU) [2]. Currently at Rockwell International's Rocketdyne Division, sponsored by the Aero Propulsion Laboratory at Wright-Patterson Air Force Base, a demonstration program is underway to design, fabricate, assemble, and test an SIPU capable of supplying secondary power for an advanced tactical fighter aircraft, in several operating modes:

Function	Operating Mode
• Ground power	Air-breathing
• Engine ground start	Air-breathing
• Emergency power	Gas generator and main engine crossbleed air
• Engine in-flight restart	Gas generator

The demonstrator is built around a modified version of Turbomach's T-62T-40-8 single-shaft Titan gas turbine currently used as a jet fuel starter in the F-16 fighter aircraft. JP-4 and oxygen are used as propellants in the gas generator mode because of their universal availability at military air bases.

The T-62T-40-8, a strictly air-breathing device, was modified for gas generator and bleed air modes of operation (Fig. 10). Side admission impingement nozzles were added along with the existing nozzle of the radial in-flow turbine. These nozzles, used to direct both the oxygen/JP-4 gas and crossbleed air onto the turbine, are fed by an annular flow passage connected to an aft-mounted manifold. This manifold has two inlets: one for mounting the gas generator and one for mounting a crossbleed air check valve and a modulating bleed air control valve.

Both side and radial admission impingement nozzles were designed originally. However, the minimum size constraints of the nozzle throat and the extent of the nozzle modifications favored the side admission configuration for exploratory testing.

Variable inlet guide vanes were installed at the compressor entry to minimize the braking drag of the unfired gas turbine and to prevent compressor surge as a consequence of the added gas generator flow. The gas generator impingement flow, which mixes with the radial turbine nozzle flow within the rotor, increases the rotor reaction and reduces the effective turbine nozzle area, moving the operating line closer to compressor surge. Incrementally, increasing the gas generator flow eventually chokes the exducer throat and finally precipitates backflow.

The overall expansion process of the SIPU in the gas generator mode is analogous to two parallel path turbines, where the net effective nozzle area dictating compressor and turbine matching is found to be essentially inversely proportional to[3]

$$1 + (W_n/W_a) \tag{17}$$

Thus equal impingement and airflows reduce the turbine capacity by the order of 50 percent. In the unfired braking mode, the net power produced by expansion of the compressor flow across the turbine approaches zero and can become negative when passing runaway (high velocity ratio) conditions. Most of the braking power is required to drive the compressor, and runaway velocity ratios are approached since

$$(U/V_o)_{\text{unfired}} \simeq (U/V_o)_{\text{design}}\sqrt{(\text{T.I.T.})_{\text{design}}/T_2} \tag{18}$$

The typical four quadrant operation of a centrifugal impeller [6], as shown in Fig. 11, indicates that after passing the runaway and braking modes, the turbine flow eventually

[3]This was essentially the effect even though the impingement nozzles were downstream of the turbine nozzles (Fig. 10).

Downloaded 01 Jun 2010 to 171.66.16.71. Redistribution subject to ASME license or copyright; see http://www.asme.org/terms/Terms_Use.cfm

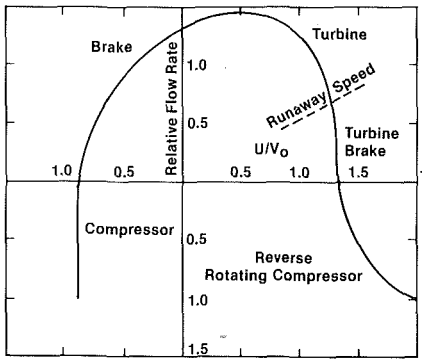


Fig. 11 Four quadrant impeller operation

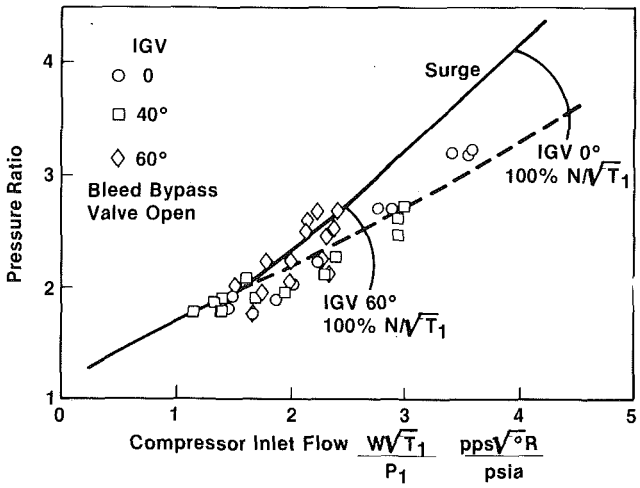


Fig. 12 SIPU compressor operating line

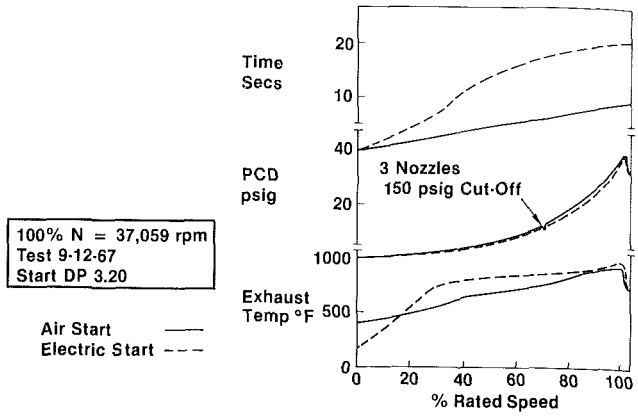


Fig. 13 Gas turbine generator set start trace

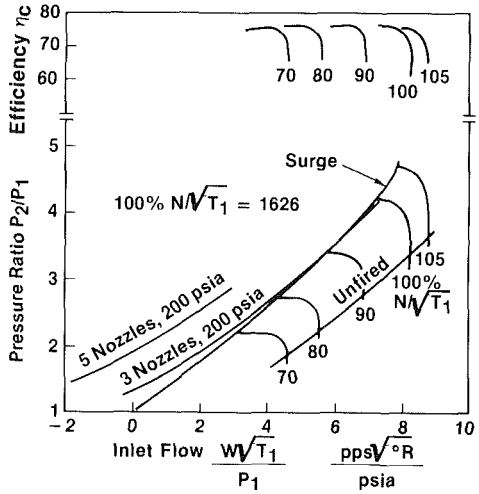


Fig. 14 Generator set compressor operating lines

backflows because the impeller acts as a reverse rotating compressor. Turbine backflow is actually not uncommon in gas turbines with radial compressors and turbines during starting before light-off, particularly if the turbine rotor is more than 10 percent larger than the compressor rotor.

SIPU performance analysis indicates that impingement nozzle efficiency and reduction of turbine braking drag are of paramount importance because they essentially dictate gas generator size and stored energy capacity. Impingement turbine efficiency improvements can be obtained by redesigning the nozzle assembly to direct the impingement nozzle flow complementary with the air breathing nozzles. As such, the expansion can be modeled with two stream channels: the air path working near runaway conditions, and the gas generator path working near stall conditions. Representative operating points for the two stream channels are depicted in Fig. 3.

Such a model was used to predict SIPU performance in all operating modes under ground-based and in-flight conditions. Measurd SIPU demonstrator performance has since corroborated these predictions.

Figure 12 shows the test SIPU operating line superimposed on the turbine compressor map with air impingement. The predicted match line with LOX/JP4 impingement is computed to be slightly to the right, providing more surge margin. During the initial start, the operating line moves instantaneously through surge. However, due to the high acceleration energy, the time to rated speed (61,656 rpm) is only 1 s and the surge recirculating period is less than ½ s.

Generator Set Rapid Start System

A rapid start system was designed for a 350-hp (260-kW) gas turbine generator set [7] using a compressed nitrogen energy source through impingement nozzles onto the compressor shroud as illustrated in Fig. 8. Compressor shroud impingement was selected as the most convenient method of installing the impingement rapid start system nozzles.

Impingement tests were conducted over a range of operating conditions by varying both the nozzle inlet pressure and number of active nozzles in addition to performing both unfired (cold crank) and fired turbine starts.

As previously discussed, impingement turbine performance was determined from the transient acceleration and deceleration traces and system polar moment of inertia. This is shown in Fig. 9 for nozzle Mach numbers close to design. Tests were also conducted at much higher pressures up to 850 psig (0.598 kg/m^2) at $M_n = 3.2$.

Figure 13 shows the results of a fired start with three nozzles at 160 psig (0.112 kg/m^2) compared to a normal electric start. Typical time to 100 percent speed under these conditions, with air supply shut-off at 69 percent speed, was 9.3 s for air start and 20 s for electric start. Compressor discharge pressure remained essentially the same, indicating normal compressor operation.

Start tests at nozzle pressures increasingly higher than design indicated no further reduction in start time, although flow was being expelled from the compressor inlet. This was later corroborated by a theoretical matching analysis for the compressor and turbine performance with a supplementary flow stream entering near the impeller tip.

The actual turbine compressor test performance prior to installation of the impingement nozzles is shown in Fig. 14.

Downloaded 01 Jun 2010 to 171.66.16.71. Redistribution subject to ASME license or copyright; see http://www.asme.org/terms/Terms_Use.cfm

Turbine performance calibrations conducted prior to and after installation of the nozzles indicated that the nozzles reduced compressor efficiency approximately 2 percentage points.

Predicted turbine start operating lines are superimposed on the compressor map for the unfired operating line, as well as starts with three and five nozzles for nitrogen impingement at 200 psia (0.141 kg/m^2). The acceleration match line with three nozzles active initially results in negative compressor flow (backflow) from the impingement source and then switches to positive flows adjacent to and parallel with the surge line above 50 percent speed. The acceleration match line with five nozzles active results in larger backflows and operation in surge. During periods of backflow, the compressor was operating in the braking zone shown in Fig. 11.

This indicates that operating the SIPU and the quick start gas turbine generator set with large impingement flows causes abnormal turbine and compressor operation, which is not advisable for high-speed, highly stressed turbomachinery. Caution must also be exercised in selecting the correct impingement nozzle number to preclude high cycle fatigue blading resonance. The highly concentrated energy of the impingement jet(s) quickly causes high cycle fatigue under resonant conditions.

In addition, shroud-mounted impingement nozzles increase shroud clearance losses because the aft expansion cone pockets allow more blade tip leakage from the blading pressure to suction surfaces for either the compressor or the turbine. As mentioned earlier, compressor shroud nozzles caused a compressor efficiency loss of 2 percent during normal turbine operation. Comparable turbine efficiency loss was also experienced with the SIPU in the air breathing mode.

Conclusions

Test data for supersonic, side admission impingement nozzles mounted on the stationary shrouds of either the compressor or the turbine of a small gas turbine using single-stage radial outflow compressors and radial inflow turbines indicate that expansion efficiencies on the order of only 40 percent are attainable. This is the result of rotor velocity coefficients close to zero with high rotor incidence and internal losses similar to that of the side admission, low specific speed Terry turbine. Overall expansion efficiencies are even lower if expressed in terms of the overall nozzle inlet to rotor outlet pressure as a consequence of the rotor reaction.

Impingement turbine expansion efficiency was found to decrease with larger values of D^2/A_n (lower specific speed), due to the higher windage loss fraction. Analysis of the potential performance of more conventional radial inflow impingement nozzles mounted parallel with, but separate from, the gas turbine nozzles predicted higher impingement turbine efficiencies on the order of 60 percent. These higher levels of impingement turbine efficiency are desirable for such applications as the Super Integrated Power Unit in which stored energy requirements must be minimized.

Compressor shroud impingement nozzles, used to rapid start a gas turbine generator set, typically reduced the standard electric system start time to rated speed from 20 to 9 s. Impingement flows beyond design revealed backflow out of the compressor inlet but with no further reduction in start time.

These data indicate that impingement starting is the most direct method of applying start energy to the rotor system. This is demonstrated by the fact that SIPU start time to the rated speed of 61,565 rpm is 1 s. However, caution must be observed in designing gas turbine impingement start systems to avoid gross mismatching of the turbine components, which can result in compressor surge and/or abnormal braking modes of operation.

Acknowledgments

The author wishes to acknowledge Turbomach Division of Solar Turbines Incorporated, for permission to publish this paper; the Aeropropulsion Laboratory of the United States Air Force, Wright Patterson Air Force Base; and the Turbomach and Rocketdyne Engineering personnel involved in the SIPU and quick start generator programs.

References

1 Hull, L. E., and Santo, H. A., "Development of a Rapid Start System for the Boeing Model 502-2E Gas Turbine Engine," SAE 670, 1961.

2 Williams, J. A., Lucci, H. D., and McFadden, B. L., "Aircraft Super Integrated Power Unit," SAE 821461.

3 Barber, R. E., and Schultheiss, M. T., "Effect of Nozzle Geometry on Off-Design Performance of Partial Admission Impulse Turbines," Sundstrand AER 486, Apr. 1967.

4 Balje, O. E., *Turbomachines*, J. Wiley and Sons, New York.

5 Knoernschild, E. M., "The Radial Turbine for Low Specific Speeds and Low Velocity Factors," ASME JOURNAL OF ENGINEERING FOR POWER, Jan. 1961.

6 Tognola, S., "Further Development of High Head Storage Pumps," *Escher Wyss News*, Vol. 33, 1960.

7 Carlson, P. G., and Pembleton, T. K., "A 300-HP Recuperative Gas Turbine for EFL Energy System Application," ASME Paper No. 63-AHGT-75.

Downloaded 01 Jun 2010 to 171.66.16.71. Redistribution subject to ASME license or copyright; see http://www.asme.org/terms/Terms_Use.cfm

Experimental Evaluation of Heavy Fan-High-Pressure Compressor Interaction in a Three-Shaft Engine: Part 1—Experimental Setup and Results

A. Schäffler
Head of Component Testing,
MTU,
Munich, Germany

D. C. Miatt
Manager Compressors Fleet Engines.
RR,
Bristol, England

Severe aerodynamic interaction between the fan core stream section and the high-pressure compressor of a three-shaft low-bypass-ratio engine is described. At high fan running lines a heavy single-cell rotating stall was found in the fan core stream even at high aerodynamic speeds between 90–98%. The rotating circumferential distortion with 180–200 deg sector angle is swallowed by the intermediate pressure compressor but erodes the high-pressure compressor surge margin by about 22%, leading to steady-state surges. A remotely mounted transducer in a specific arrangement was used successfully for measurements in the hot environment behind intermediate and high-pressure compressor using a so-called "long-line" system with a closed end at the downstream pipe.

Introduction

During an early development phase of the 70 kN thrust RB 199 three-shaft mixed-flow bypass engine, the high-temperature rise capability of the reheat system made it desirable to operate the engine at its maximum permissible fan pressure ratio. This led in the upper speed range of the fan around 90–98% to definite high-pressure compressor surges during fan operating line excursions in fast transient and also steady-state operations with small final nozzle areas 10–14% below the design value.

The fact that the high-pressure compressor surged within the three-shaft compression system despite the fan being throttled closer toward its surge line pointed to an interesting fan-core compressor interaction phenomenon.

Observed Phenomenon and Possible Mechanisms

Perfectly handling engines, capable of very high external power off-take, very fast 2.2 second acceleration from idle to maximum power and stable operation with severe inlet pressure distortions at levels about 0.7 d-c_{120} run into repeatable high-pressure compressor surges when the fan running points were raised closer to the fan surge line. This phenomenon was only experienced in the regime above 90% fan aerodynamic speed. The surge could be triggered by slowly closing the final nozzle or by increasing the reheat setting under quasi-steady-state conditions in fully warmed-up machines as well as in transient operations.

Observation of the pressure pulse signals seen by closely coupled pressure transducers in measuring planes between the compressors and switching of specially built-on bleed valves behind the intermediate or high-pressure compressor, revealed that the high-pressure compressor (HPC) and not the fan or the intermediate pressure compressor (IPC) was the first to break down. The two front compressors reacted with clear pressure spikes against the pressure drop at the end of the compression system.

Performance simulations showed that reduced final nozzle areas moved only the fan working line toward higher pressure ratios, whereas IPC and HPC operating lines remained almost constant.

Figure 1 shows the three-shaft compression system with the nondimensional isolated rig characteristics of the three compressors at the development state when the investigations described in this paper were pursued. The steady-state

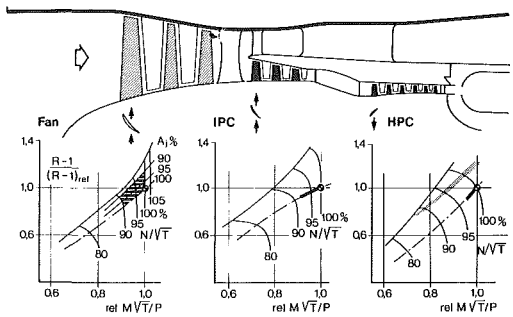


Fig. 1 Three-spool compression system

Contributed by the Gas Turbine Division of THE AMERICAN SOCIETY OF MECHANICAL ENGINEERS and presented at the 30th International Gas Turbine Conference and Exhibit, Houston, Texas, March 18–21, 1985. Manuscript received at ASME Headquarters, January 10, 1985. Paper No. 85-GT-173.

Copyright © 1985 by ASME
Downloaded 01 Jun 2010 to 171.66.16.71. Redistribution subject to ASME license or copyright; see http://www.asme.org/terms/Terms_Use.cfm

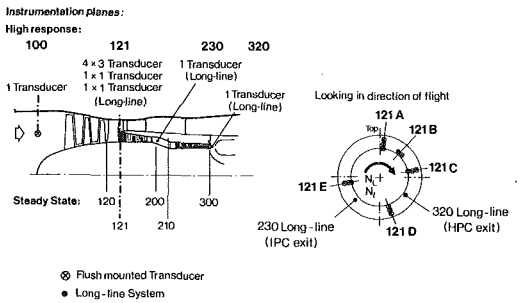


Fig. 2 Measuring planes and instrumentation

working lines are plotted together with the minimum surge line demonstrated by the high-pressure compressor installed in the engine, denoted by a hatched area line. The minimum surge line—which describes the demonstrated margin available without surge with relatively simple means—was evaluated by a test program tailored to as high HPC working line excursions as possible in steady-state and transient operations. The program consisted of extreme external power off-takes of several hundred kilowatts, very fast accelerations from various starting speeds up to the highest settings permitted by the control system, i.e., 2.2 seconds from idle to maximum dry power and combinations of fast accelerations and high power off-take. High-pressure compressor surge margins of at least 15% on the standard NASA definition (see nomenclature) were demonstrated without surge at final nozzle areas around the design value. The 15% minimum surge margin was, however, eroded rapidly to steady-state surges when the fan working line was raised by a reduction of the final nozzle of about 10% in the high fan speed regime.

A very powerful and severe distortion mechanism must therefore have been acting on the HPC. As can be seen from the thick black lines in Fig. 1, in the critical fan speed range between 90 and 100 $N_L/\sqrt{T}$ the HPC operates only over a very small speed band from 97–99% $N_H/\sqrt{T}$, where very large surge margins ought to be expected, based on the rig surge line.

Engine test experience showed that the loss of HPC surge margin appeared to be highly nonlinear with final nozzle area reduction. Satisfactory handling characteristics were still obtained at 95% nozzle area whereas at areas below 90% stability was impaired to steady-state surges.

During diagnostic tests with the standard instrumentation indications of fan exit pressure fluctuations were observed, which increased as the final nozzle area was reduced. This tentative information together with a thorough analysis of all available experience and information led to the assumption that a severe unsteady pressure distortion, orginating in the fan core stream section, caused the HPC surges.

Three possible mechanisms emerged from the analysis:

(*a*) Unsteady flow breakdown in the fan core section over a sufficient circumferential extension, forming a heavy HPC pressure or pressure/temperature inlet distortion of sufficient endurance.

(*b*) Severe form of fan rotating stall, which would essentially lead to a similar inlet distortion as described in (*a*).

(*c*) LPC-generated low-amplitude fluctuations of higher frequency exciting the core engine compressors in a resonance mode, triggering excessive excursions of individual HPC stage working points.

Theoretical work pursued did not confirm this to be a probable case in the two-spool core engine environment.

In order to understand the phenomenon an experimental investigation program was set up with sufficient high response instrumentation along the compression system.

Experimental Investigation

Instrumentation and Data Acquisition System. The instrumentation for the steady-state and the unsteady flow evaluation tests used the normal "highly instrumented engine" bossings. Two additional instrumentation ports for intrascope inspection behind the intermediate and the high-pressure compressor were used for high-response transducers. The main instrumentation planes and the circumferential positions of the high response instrumentation are described in Fig. 2.

Steady State Instrumentation. Multihead rakes for total pressure and temperature were inserted at the fan exit guide vane leading edge and at the fan, IPC and HPC exit planes with 3–12 radially spaced measuring points.

High-Response Instrumentation. For the unsteady flow measurements the instrumentation was kept to the necessary minimum for reasons of cost and time, tailored to the probable effects to be expected. Only one transducer was placed ahead of the fan; heavy instrumentation was concentrated at fan exit in the core flow section with 5 rakes spread over the circumference in order to detect instantaneous distortion patterns and one high-response transducer at IPC and HPC exit in order to resolve the flow direction of low-pressure areas and pressure peaks before and after surges.

Two different types of high-response instrumentation were used. For the low-temperature end, ahead and behind the fan, plain flush-mounted Kulite transducers were built into multihead rakes. In the high-temperature areas behind the IPC and HPC a remote-mounted, calibrated measuring system was used which was developed by Rolls Royce Measuring Department on the basis of the so-called "Boeing Long-Line System." The system allows the temperature-limited transducers to be placed outside the hot environment.

The following instrumentation was inserted during the unsteady flow evaluation tests:

Plane *100* (fan exit):
- 1 probe with one flush-mounted sensor.

Plane *121* (fan exit):
- 4 high-response total pressure probes with 3 radially spaced flush-mounted and one remote-mounted transducer, both placed at midposition for comparison of amplitude ratio and phase shift of the long-line system at position B.

Plane *230* (IPC exit):
- 1 high-response, remote-mounted, calibrated long-line system.

Plane *320* (HPC exit):
- 1 high-response, remote-mounted, calibrated long-line system.

Nomenclature

A_j = nozzle area, m^2
M = mass flow, kg/s
N = rotational speed of distorted compressor, 1/min
P = total pressure, kPa
R = compressor pressure ratio
SM = surge margin, $\frac{R_s}{R_w} \cdot \frac{\phi_w}{\phi_s} - 1$
T = total temperature, K
ϕ = mass flow function, $M\sqrt{T}/P$

Subscripts

L = fan
ref = reference value
rel = related to design value
s = at surge
w = at working line

Downloaded 01 Jun 2010 to 171.66.16.71. Redistribution subject to ASME license or copyright; see http://www.asme.org/terms/Terms_Use.cfm

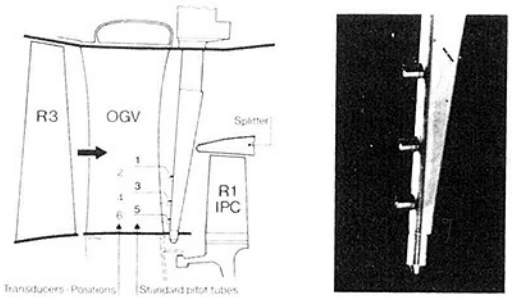


Fig. 3 High-response flush-mounted instrumentation at fan exit

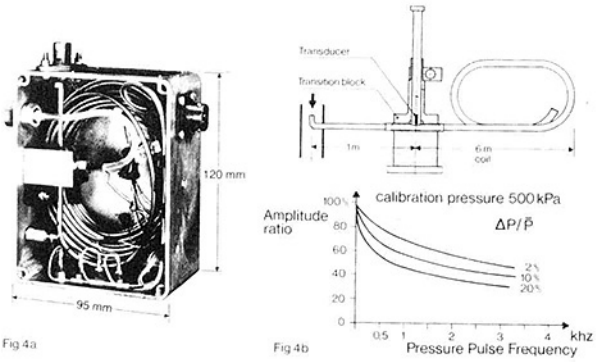


Fig. 4 Remote-mounted "long-line" system for IPC and HPC exit

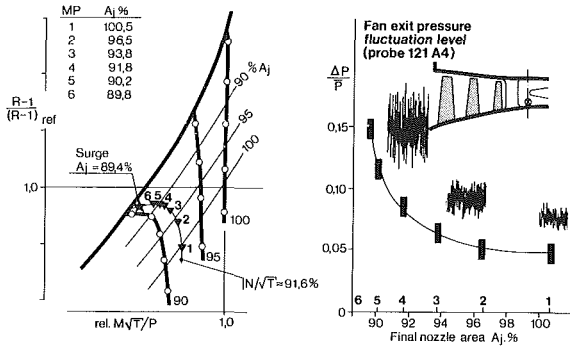


Fig. 5 Fan exit pressure fluctuation level

High-Response Instrumentation Design. Flush-mounted transducers are at fan entry and exit planes. The plane 121 Kulite transducers with a diameter of 2.3 mm and a total length of 7.5 mm were flush mounted in total pressure rakes at three radial positions within the core stream. Each transducer was paired with a normal pitot tube of 0.8 mm i-d for steady-state pressure level calibration. Figure 3 shows a three-head rake used in plane 121. The transducers were calibrated statically up to 275 kPa pressure.

Currently high-response pressure transducers are limited to operating temperatures of about 500K. The remote-mounted long-line system appeared well suited for the high-temperature environment in the high-pressure-ratio compression system for the answers sought, which were primarily concentrated on distortion direction and frequency rather than on quantification of distortion amplitudes behind the IPC and HPC.

The "long-line system" is based on development by Tjonneland and O'Neill of the Boeing Company [1]. As shown in Fig. 4 the long-line system consists of an upstream thin tube of a definite length and inner diameter, a transition block with a thin bore and a high-response transducer of suitable measuring range, sitting flush mounted at right angles to the transition block bore followed by a long downstream tube of 6–18 m length. The downstream tube is blocked at the end and to make the system easy to apply it is rolled up in a box which also contains the transition block with the transducer.

The closed-end long-line measuring system does have the advantage of an aperiodic damping characteristic versus frequency which can be calibrated with a broad-band siren or whistle-type pressure pulse generator. The system is free of the usual acoustic resonances and uncontrolled frequency transfer characteristics normally encountered with remotely applied transducers. The system damps the amplitudes strongly at frequencies above 1 kHz and produces a time phase shift to the real event signal.

The long-line systems used in the tests are described in [2] and shown on Fig. 4. They consisted of a 1 m upstream length tube of 3 mm outer and 2 mm innner diameter and a 6 m downstream section of the same tube dimensions incorporating an additional insert of 1.5 m length with 1.6 mm outer and 1.1 mm inner diameter for consistent aperiodic damping within the relatively short downstream length. The complete system is packed into a box of about 120 mm length, 95 mm width and 55 mm height.

The frequency-amplitude damping characteristics were calibrated at Rolls Royce with a variable frequency whistle at various pressure levels and low amplitudes and at MTU [3] with a siren-type pulse generator at 200 kPa pressure and high amplitudes from 10–30% of the average pressure. Thus, the two main effects, pressure level and modulation ratio, are available. The damping characteristics are shown in Fig. 4(*b*) for a 500 kPa pressure level.

The data acquisition system was built up from two 14 track magnetic tape recording machines which were synchronized by a standard time code (IRIG B) within 0.05 ms accuracy. The fan exit plane signals are all on one magnetic tape.

The signals could either be replayed on-line on oscilloscopes or on ultraviolet films in the time domain or analyzed off-line for power spectral density to recognize periodic contents and auto/cross correlation functions to determine the identity of the signals and their relative time lags.

Experimental Program. The engine test program consisted of three main parts:

(*a*) Thorough steady-state performance calibration using multihead steady-state pressure and temperature rakes along the compression system for the evaluation of the individual compressor performance maps as far as possible.

(*b*) Evaluation of unsteady flow effects. Using the high-response instrumentation described, quasi-steady-state excursions into the fan-core interaction process up to surge were pursued at different speeds by reducing the final nozzle area in small steps at constant fan aerodynamic speed.

(*c*) Comparative testing of different fan variants incorporating modifications in individual blade rows.

Experimental Results. The basic test to understand the high-pressure compressor surge mechanism consisted of an engine run up to 91.6% corrected fan speed in nonreheated mode along a 100.5% nozzle area line. After a 20 min stabilization at this point, the final nozzle area was closed in small steps and the engine rerated in order to keep the fan speed constant. At each point a 2 min stabilization phase was held and continuous data recording pursued.

As can be seen from Fig. 5 six stable points (1–6) were obtained with nozzle areas ranging from 100.5% to 89.8%. Immediately after the last stable point 6 surge occurred at 89.4% nozzle area during the quasi-steady-state nozzle closure. Similar procedures were repeated at various speeds.

Downloaded 01 Jun 2010 to 171.66.16.71. Redistribution subject to ASME license or copyright; see http://www.asme.org/terms/Terms_Use.cfm

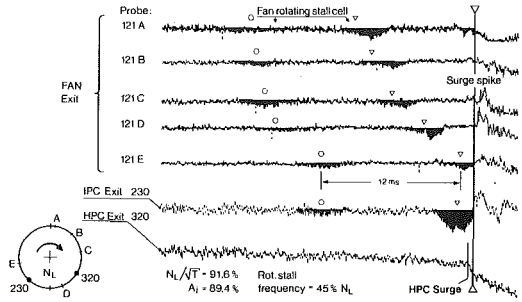


Fig. 6 Pressure signals at fan, IPC, and HPC exit planes before surge

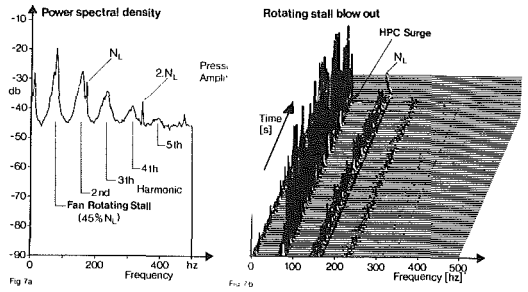


Fig. 7 Power spectral density and rotating-stall blowout event

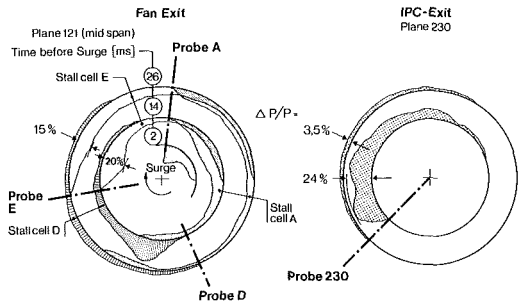


Fig. 8 Rotating stall cell circumferential extension and amplitude distribution during last three revolutions before surge

The data recorded during the first surge at 91.6% fan aerodynamic speed were directly replayed on oscilloscopes and the most interesting phases fixed on ultraviolet-sensitive films for more detailed inspection. These traces revealed four important results without more sophisticated analysis:

(*a*) The fan exit pressure signals measured by the flush-mounted transducers indicated significant fluctuations with rapidly increasing amplitudes as the nozzle area was reduced toward the surge inducing value. Typical fan exit signals are shown in Fig. 5 for three different values over all six stable working points.

(*b*) Figure 6 shows the pressure traces of the five midspan transducers in plane 121 together with the IPC and HPC exit signals. The drop in HPC delivery pressure and the pressure spikes exhibited by the transducers at IPC and fan exit confirm that the high-pressure compressor surges first.

(*c*) About 30–50 milliseconds before surge occurred the fluctuations of the fan and IPC exit signals appeared as a clear structure of two or three periodically emerging deep-pressure troughs with time intervals of 12 ms. The traces of the midposition transducers at fan exit are arranged in Fig. 6 sequentially around the circumference in the direction of fan rotation. The phase shifts of 3.4 ms produced by the long-line systems are eliminated in Fig. 6 for clarity, using the data from cross-correlation functions.

(*d*) The periodicity of the obviously identical deep-pressure trough signal at fan exit represent a single rotating stall cell of large circumferential extension, moving at 45% fan speed in the direction of fan rotation. The amplitudes of the rotating stall cells virtually "explode" within the last 2 or 3 revolutions and lead to HPC surge due to excessive inlet spoiling. From Fig. 6 it can be concluded that the HPC surge pulse hits the fan exit plane at the moment when the stall cell is located between probes *E* and *C*, covering probes *A* and *B*. The stalled fan sector there is naturally unable to produce any over-pressure against the pressure wave flowing upstream.

Analysis of the Rotating Distortion. *Frequency Analysis, Power Spectral Density, and Auto/Cross-Correlations.* The power spectral density of the fan exit data showed a characteristic high-power signal in the frequency domain at 45% fan speed with second, third, fourth, and fifth harmonics, as shown on Fig. 7(*a*). The relatively wide and strong signal is indicative of the modulation occurring in the rotating stall cell circumferential extension and frequency.

In Fig. 7(*b*) a surge event is shown in an amplitude-frequency-time plot. As the HPC surges, the fan rotating stall system is immediately blown out. The signals of the rotating stall cell and its harmonics disappear completely. The cross-correlation functions for the two probes incorporated in probe 121 *B*, of which one was connected to a flush-mounted and one to a long-line system transducer, provided precise data for the phase shifts and enabled the correction for the time axis of the IPC and HPC exit signals.

Shape and Intensity of Distortion. From the amplitude-time traces as shown in Fig. 6 it is possible to evaluate the distortion patterns and their intensity at fan and intermediate pressure compressor exit. As the stall cell passes the probes the time scale can be directly converted into circumferential angular extension, assuming constant average rotational speed. In order to obtain the basic surge inducing low-pressure troughs, the fan exit signals were filtered to eliminate the high-frequency content about 1 kHz. The remaining low-frequency signals revealed that the stall cells extended over 180–200 deg within the last two or three rounds before surge occurred. The stall cells were analyzed for their amplitude and plotted in form of concentric rings on Fig. 8. Each ring represents a 12 ms time interval corresponding to one revolution of the rotating-stall system. The thickness distribution of the cells illustrates the distortion intensity seen at the midspan position transducer in form of the pressure deficit to the undistorted sector pressure. The IPC exit signals measured with the long-line system were reconstructed to their real value by an inverse Laplace transformation. The necessary time constants are obtained by comparison of the data measured by the flush-mounted and long-line system incorporated in probe 121 *B* and the long-line system calibration curves shown in Fig. 4(*b*). The circumferential extent of the distortion cell varies between 150 and 210 deg and the distortion intensity from 4–24% $\Delta P/P$ within the last two rounds. The graphs are plotted in Fig. 8 so that the stall cell rearward end is placed at the respective probe position where it has been seen. The stall cells are alternately drawn to the inner and outer side of the reference circle with the data for probes *B* and *C* omitted for clarity. The considerable modulation already indicated by the power spectral density function can be verified from the essentially triangular to saw-tooth type distortion, which normally has its lowest pressure at the rearward part of the clockwise rotating cell.

In the example selected here for demonstration surge occurs at a time when the deep rotating stall cell has just passed probe 230, so the very deepest distortion leaving the IPC before HPC surge occurs can be seen. The striking change of

Downloaded 01 Jun 2010 to 171.66.16.71. Redistribution subject to ASME license or copyright; see http://www.asme.org/terms/Terms_Use.cfm

shape and distortion intensity within 12 ms is especially pronounced at IPC exit. With the limited calibration data available the accuracy of the reconstructed IPC exit distortion amplitude is within ± 10%.

Conclusions

An experimental analysis of a heavy fan-core interaction in a three-spool low bypass engine revealed the following results:

- A severe single-cell rotating-stall system with 10–20% pressure amplitude was encountered at high fan speeds between 90–98% in the fan core stream section.
- The rotating-stall intensity increases rapidly in the final phase within two to three revolutions leading to high-pressure compressor surge.
- A remote-mounted high-response pressure measuring system based on the Boeing "Long-Line" system was successfully used in the hot section of a three-spool compression system for fan-core compressor interaction analysis.

Acknowledgments

The authors wish to thank NAMMA, MTU, and Rolls Royce for the permission to publish this paper.

References

1 Tjonneland, E., and O'Neill, E. B., "Total Pressure Turbulence in a Sharp Lip Axisymmetric Supersonic Intake Operating in the Flow Field of an Airplane Wing and Flap System in Takeoff Configuration," AIAA Paper No. 68-650, 1968.

2 "Wide Band Dynamic Pressure Measurement Using a "Long-Line" System," RR internal report IDW/GH/16844.

3 "Breitband-Staudruckmessung mit "long-line"-Systemen verschiedener Konfigurationen," MTU-München, EV2-Notiz No. 156/78, MTU internal note.

Downloaded 01 Jun 2010 to 171.66.16.71. Redistribution subject to ASME license or copyright; see http://www.asme.org/terms/Terms_Use.cfm

Integrated Flight/Propulsion Control System Considerations for Future Aircraft Application

R. W. Vizzini
Science & Technology Group,
Advanced Control Systems,
Naval Air Propulsion Center,
Trenton, N.J.

Flight and propulsion controls can effectively be integrated to provide operational benefits to the weapon system which cannot be achieved with either system acting independently. The key factor is the synergistic effect of digital computers and associated high-speed data links, engine condition monitoring, diagnostics, and shared power systems (hydraulic and electrical), thus providing potential improvements in reliability, life cycle cost, weight, and maintenance actions. This technical paper will address the integration concepts required for the airframe and the propulsion control configurations (for consideration in the design stages) to achieve the optimum weapon system configuration by assessing fiber optic and hardwired systems for future applications.

Background

The challenge of high-performance, multimission aircraft has resulted in a progression of gas turbine engine technology from simple aeromechanical systems to sophisticated integration of gas path hardware and engine control systems. Future aircraft will require significant flight propulsion and weapon system control integration to maintain air superiority.

Advanced propulsion configurations will require highly reliable, fault tolerant, Full Authority Digital Electronic Control (FADEC) systems to meet the reliability of flight controls. The propulsion control system should be designed to provide alternate fuel capability, low costs, high reliability, low weight and volume, low maintenance, low mission abort rate, and optimized engine performance. One approach, Fig. 1, is dual FADEC computer, identical and housed separately to enhance reliability and survivability. The computers are interfaced to a redundant fuel and air management system providing fail operational capability, [1].

Electronic control system reliability will be enhanced by internal fault detection and switching logic that will transfer data and control functions between redundant electronic units for fail operational performance. Comprehensive fault detection and corrective features will allow fail operational performance with dual hardware redundancy.

The air management system consists of hydraulic actuations providing high forces for thrust vectoring and reversing systems. Hydraulic systems are very responsive and reliable and operate with redundant hydraulic pumping systems. Future fuel pumping systems based upon centrifugal designs will minimize the number of fuel pumps and valves

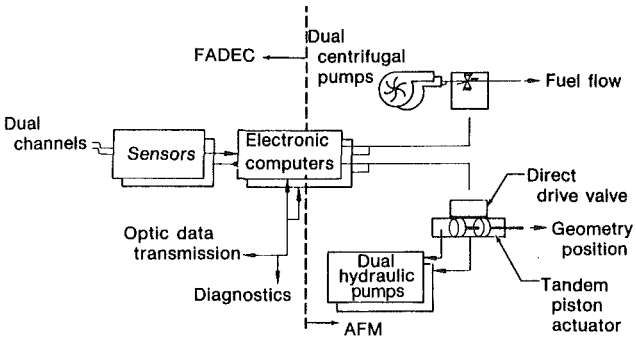


Fig. 1 Fault-tolerant control system architecture

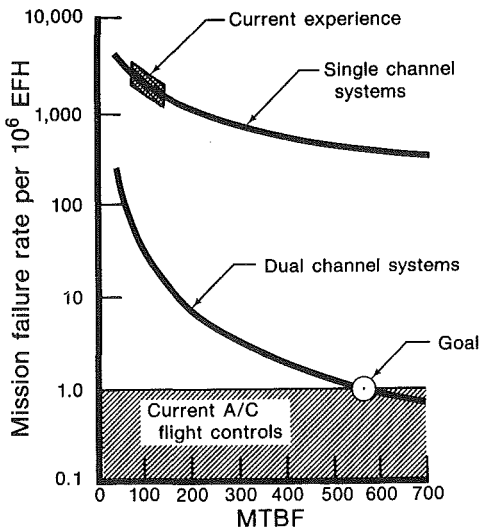


Fig. 2 Dual channel systems improve mission reliability

Contributed by the Gas Turbine Division of THE AMERICAN SOCIETY OF MECHANICAL ENGINEERS and presented at the 29th International Gas Turbine Conference and Exhibit, Amsterdam, The Netherlands, June 4-7, 1984 Manuscript received at ASME Headquarters, January 18, 1984. Paper No. 84-GT-192.

Copyright © 1985 by ASME
Downloaded 01 Jun 2010 to 171.66.16.71. Redistribution subject to ASME license or copyright; see http://www.asme.org/terms/Terms_Use.cfm

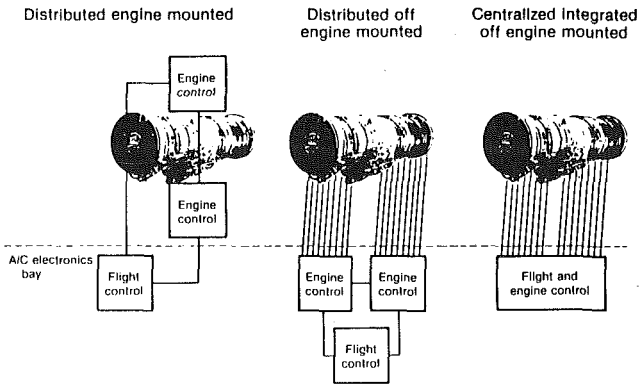


Fig. 3 Integrated airframe-propulsion control

required for advanced engines providing durability when operating with low lubricity fuel, shale, or coal derivative fuels and anti-misting kerosene.

The propulsion electronic control system is designed to achieve the reliability levels currently demonstrated inflight control systems, Fig. 2, and is considered a prime requirement for future engine control systems where, under certain operating conditions, such as control of thrust vectoring and reversing exhaust nozzles, the engine control acts as a part of the flight control system.

This engine-mounted control system is currently being developed under Navy contract (N00019-79-C-0614) to Pratt & Whitney Aircraft for application to advanced propulsion systems and establishes the technology base for near term operational readiness with the capability of airframe-propulsion control integration.

Introduction

This year 2000 will produce integrated fly-by-light (optics) airframe-propulsion control weapon systems consisting of fiber optic data buses for airframe-propulsion control communication and optic sensors and actuator position feedback devices providing inherent electromagnetic immunity and reduced system weight. Also, the use of a total optic system will allow the engine control configuration to be mounted off-engine to a more benign environment either as a distributed or centralized integrated control system. Functional integration of the aircraft electrical power and hydraulic power normally engine-mounted as dedicated subsystems will be aircraft supplied.

This paper will briefly discuss optic and wire systems as applicable. Emphasis is placed on hardware considerations required in the design stages for synergistic aircraft control integration. These are:

- Propulsion control configuration location
- Aircraft control system communication

Identify impact of flight critical and non-critical data transmission

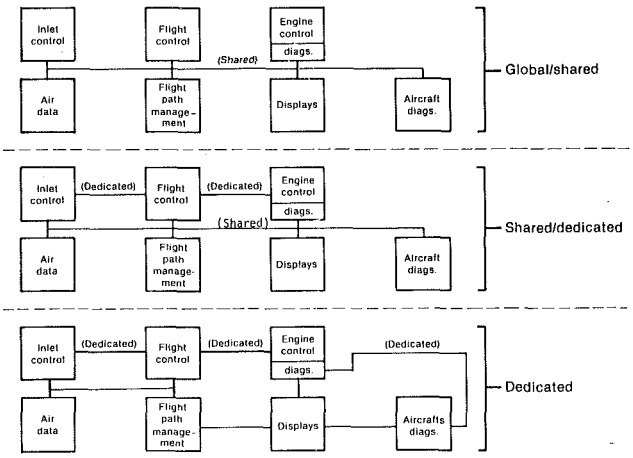


Fig. 4 Data bus architecture

- Engine control monitoring (ECM) and diagnostics
- Exhaust nozzle architecture
- Hydraulic power system design
- Electrical power source

To achieve the optimized system, integrated control modes and hardware implementation must be assessed from aerodynamic aircraft computer models, dynamic engine models, man-in-the-loop simulations, hardware-in-the-loop, and engine testing to flight verification.

Electronic Propulsion Control Location. The introduction of FADEC systems led to Government and industry studies to assess the location of engine controls [2]. The locations considered were the aircraft bay, the nacelle, the boom, and the engine. Each location was evaluated in terms of reliability, weight, maintenance actions, LCC, electromagnetic considerations, and accountability. The engine-mounted location was selected. However, the advances in fiber optic technology projected for future airframe-engine data links, sensor, and actuator will inherently provide Electromagnetic Interference (EMI), Electromagnetic Pulse (EMP), and lightning strike protection with some weight reduction. Figure 3 shows a distributed engine mounted, a distributed off-engine mounted, and a centralized configuration. For hardwired systems, the distributed engine mounted is the most viable. With the advent of fiber optic systems, the control system can be located in a more benign environment as a distributed off-engine system or integrated with the flight control as a centralized system. Distributed or centralized off-engine mounted controls are not practical without the application of fiber optic technology, specifically in the areas of sensors and actuators, and passive optic multiplexers for application to fighter aircraft.

Propulsion/Flight Control Communication. A key element

Nomenclature

AFM = advanced fuel management
A/C = aircraft
cm^2 = square centimeters
CPU = central processor unit
ECMS = engine condition monitoring system
EEPROM = electrically erasable programmable read only memory
EMI = electromagnetic interference
EMP = electromagnetic pulse
FADEC = full authority digital electronic
GEN = generator(s)
kg = kilograms
LCC = life cycle cost
Light = fiber optics
M = million
MHz = megahertz
MIL-STD-1553B = Military Standard, Aircraft Internal Time-Division Command/Response Multiplex Data Bus
MIL-STD-1773 = Military Standard, Fiber Optic Aircraft Internal Time-Division Command/Response Multiplex Data Bus
MTBF = Mean Time Before Failure

Downloaded 01 Jun 2010 to 171.66.16.71. Redistribution subject to ASME license or copyright; see http://www.asme.org/terms/Terms_Use.cfm

Table 1 Integrated control modes and benefits

Control mode	Potential Benefits: Performance	Supersonic persistence	STOL	Survivability	Maneuverability	Range	Weapon delivery
Stall margin control	X	X	X	X	X	X	X
Rapid thrust modulation	X			X	X		X
Combat	X			X	X		X
Thrust reversing/vectoring			X	X	X		X
Flow modulation	X	X				X	
Auto throttle				X		X	X

in the integration of flight and propulsion controls is communication. Communication is achieved via data link, wire or light (optic) as specified by MIL-STD-1553B or MIL-STD-1773, respectively. In contrast, current airframe-engine communication is implemented by means of mechanical links, flexible cables, and a few dedicated sensors.

Future aircraft will operate on an entirely different concept. Almost all communication will be accomplished by means of digital links for aircraft and engine data information exchange. The selection of the data bus architecture depends on the impact of flight critical and noncritical data transmission. Figure 4 shows three types of data bus architecture. The global system is for information only. In actual practice, it would not be used due to data bus loading and an undesirable mix of flight critical and noncritical information. The selection of the data bus architecture is dependent on the criticality of information.

The dedicated system overcomes the drawbacks of the global system providing all data as if it were critical to aircraft status and/or requirements. This system does not take advantage of communication integration and introduces an excess number of hardware interfaces associated with reduced reliability.

For integrated systems, the most viable method appears to be the dedicated/shared communication system since bus loading is no longer a factor and critical information, such as aircraft status/requirements can be transmitted and received via a dedicated bus. Diagnostic information can be obtained by a dedicated or shared bus depending on the designed control system.

Communication between the engine controls and the flight controls can be achieved by light or wire. There are advantages to both systems and these are discussed below.

Hardwired Communication Systems. One of the possible means of communication in future aircraft is by means of the data bus structure defined by MIL-STD-1553B. This link is a command/response multiplex bus, operating at 1 MHz, where an aircraft executive computer acts as the bus controller and the engine electronic control is a remote terminal. Using this system, the aircraft and engine will be able to share all operating information necessary to operate the aircraft as an integrated weapon system. This architecture is typical of those being studied. It could, of course, be modified to incorporate dedicated buses for flight critical information on high speed (10 to 20+MHz) links. The use of a data bus architecture to transmit information has several obvious benefits compared to current systems:

- Simple system – all communication is over twisted shielded pairs of wire
- Reduced cost – mechanical links, dedicated wires, and dedicated displays eliminated.
- Reduced weight – less physical hardware to interconnect the systems.
- Improved maintainability – no complicated mechanical rigging required.
- Increased reliability – reduced parts count and the MIL-STD-1533B data bus is dual.

As important as the above benefits are, the principle benefit of this type system is the potential for overall operational improvement to the aircraft. Using an integrated system of this type, all of the pertinent aircraft and engine operating information can be shared to provide new and/or automated operating modes. A typical list of modes and their benefits is shown in Table 1. As an example of how one of these modes might be implemented let us address the "Min Drag – Max Thrust" mode. This mode could be requested by the pilot when requiring a set airspeed at minimum fuel consumption. The airframe and engine control systems operating synergistically would automatically configure the aircraft and engine to the optimum operating configuration. For instance, when the aircraft flight attitude, inlet airflow distortion, and flight plan are satisfactory, the aircraft control system can signal the engine to take action to reduce stall margin. This reduction in stall margin shifts the engine operating line so that fuel consumption will decrease at constant thrust. This function can be provided with an integrated digital electronic engine control throughout the flight envelope, if it is provided with information available in the flight control system. When the flight attitude is changed or an engine transient is requested by the pilot that would increase inlet distortion, the engine control automatically resets the appropriate stall margin. Response of the electronic controls and the engine allow stall margin to be set before the aircraft can respond to the flight attitude change.

Optical Communication Systems. If a hardwired communication system, such as that presented above, has so many obvious benefits, why investigate the use of a relatively new technology such as optic data links?

The use of fiber optics appears to offer three basic advantages over conventional wired data bus systems: greater band width over larger distances, improved physical characteristics, and increased channel integrity. Historically, aircraft have not required much signal bandwidth as high data rates can be accommodated by conventional wire over the short distances required by aircraft. Thus, bandwidth alone does not justify the use of fiber optics on aircraft, [3].

The physical properties inherent to fiber optic data links offer significant benefits for aircraft application:

- Reduced weight for a *total* optic system.
- EMI/EMP immunity.
- Improved channel integrity.
- Reduced susceptibility to intermittents.

A typical aircraft twisted shielded pair weighs approximately 16 kg per 300 meters, more for engine cables where two layers of stainless steel overbraid are routinely used. This may be compared to prototype fiber optic cables which weigh about 2.2 kg per 300 meters. Due to the short length of cables on the engine, this weight penalty does not produce a significant impact to the engine system.

One of the most important characteristics of fiber optics is that they are nonconductive and thus have no potential current paths, do not require any grounding, and cannot result in short circuits. This nonconductivity means that a fiber optic data bus system, which interconnects all of the

Downloaded 01 Jun 2010 to 171.66.16.71. Redistribution subject to ASME license or copyright; see http://www.asme.org/terms/Terms_Use.cfm

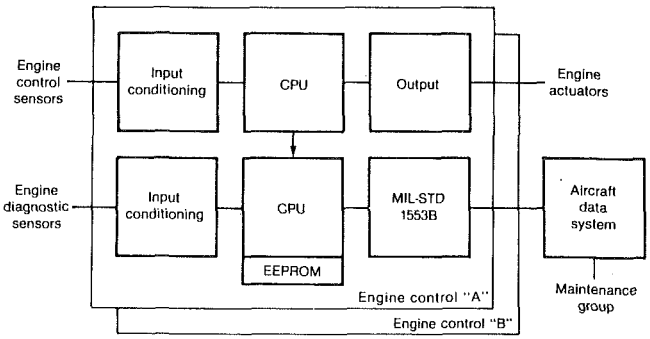


Fig. 5 ECMS and diagnostics integrated for cost effective use of available data

critical aircraft and engine control systems, is not affected by the electromagnetic interference (EMI) produced by power cables, switch and relay closures, and all of the extraneous electrical noise sources prevalent on any aircraft. For military aircraft, the danger of electromagnetic pulse (EMP) and lightening are a major concern. Fiber optic systems are basically immune to these phenomena and do not radiate energy which could cross talk to other cables.

The final benefit of fiber optics is the reduced impact of intermittent electrical connections. When vibrated, electrical connectors are prone to short duration (nanosecond) intermittents which can cause errors on the data bus. Since optical connectors do not require physical contact for transmission, intermittents do not occur.

Engine Condition Monitoring System. The Engine Condition Monitoring System (ECMS) receives information from three separate sources, Fig. 5. The primary source of ECMS information is the engine control processor. All engine speeds, pressures, temperatures, and signals that are used to control and protect the engine, are available to the ECMS. This information is loaded into buffered registers so that it can be accessed without interferring with the engine control. Diagnostic sensors provide supplementary information, not required for control, such as lubrication system data and engine vibration. Access to the ECMS is also through a MIL-STD-1553B or MIL-STD-1773 data bus. This access point is used to write in and read out historical information, such as part numbers and serial numbers which are stored in an Electrically Erasable Programmable Read Only Memory (EEPROM) device.

The ECMS thus has information to diagnose and record engine and control system faults to the line replaceable unit level. Should maintenance action be required, the part number, serial number, and operating time of the failed component would be available to the mechanic. When a failed part is replaced, its history can be updated in EEPOM over the data bus. If the failed component is an electronic control, the replacement unit can be uploaded with historical information from the redundant ECMS in the other engine control, reference [4]. Engine historical data could be used to identify a maintenance program keyed to actual wear and degradation and not fixed to normal maintenance procedures. This would result in the reduction of maintenance manhours on those engines not subjected to unusually severe combat conditions.

Exhaust Nozzle Architecture. Future aircraft may employ thrust vectoring and reversing nozzles to enhance aircraft performance at specific operating conditions. This control component acts with the authority of the flight control surfaces and, therefore, control surfaces and redundancy must be considered.

The three subcomponents of the exhaust nozzle control

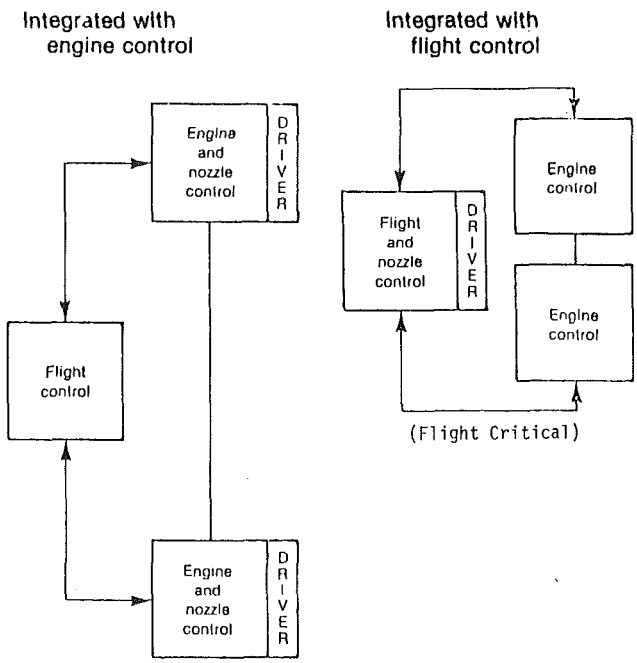


Fig. 6 Exhaust nozzle architecture

(ENC) are computation, command and feedback circuits (drivers), and the actuators. Figure 6 shows two typical ENC configurations, one integrated with the engine control and the other integrated with the flight control. If the nozzle is not flight critical and is used primarily as a trim function or to increase the authority of conventional flight surfaces, the ENC is usually integrated with the electronic engine control. The nozzle now has the same level of fault tolerance as the rest of the engine, fail operational/fail safe. In the event of a second failure in the ENC loop, the nozzle is fixed in a fail-safe operating mode with no impact on aircraft operation.

If the exhaust is flight critical, the level of redundancy of the hardware and software must be compatible with that of the flight control. The ENC system would be triplex or quadruplex. This type of redundancy would provide at least a fail operational/fail operational/fail safe system. However, engine operation, accountability, and development costs should be assessed previous to the development of this system.

Airframe-Propulsion Power System. The source of hydraulic and electrical power is a major consideration for future integrated control systems. Current engine control systems are independent of airframe power. Electric and hydraulic power are provided by dedicated alternators and pumps mounted on the engine gearbox (G/B). Advanced weapon systems will functionally integrate these components with the airframe power source, Figs. 7 and 8.

Hydraulic Power Source. Advanced weapon systems with thrust vectoring nozzle configurations will require high horsepower, high pressure, and fast response actuators to comply to nozzle demands. An aircraft system designed with this nozzle configuration and considered flight critical will require a redundant power supply increasing engine frontal area in a normally constrained area of the nacelle impacting aircraft drag.

One viable design for an integrated hydraulic power system is shown in Fig 7. By relocating the hydraulic pump(s) to a remote G/B, the frontal area is reduced providing improvements in cost and weight of the aircraft system. A comparison of the frontal area, weight and associated LCC for a full duty and remote G/B results in net values of 645

Downloaded 01 Jun 2010 to 171.66.16.71. Redistribution subject to ASME license or copyright; see http://www.asme.org/terms/Terms_Use.cfm

Weight and frontal area consideration favor the remote gearbox (twin engine LCC)

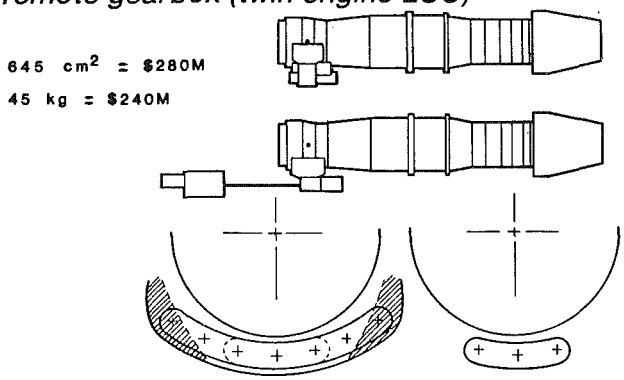
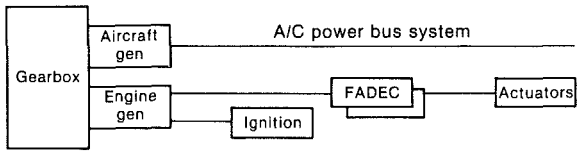


Fig. 7 Full duty gearbox versus remote gearbox

Current system



Integrated system

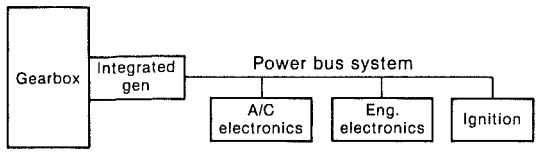


Fig. 8 Integrated aircraft electrical system

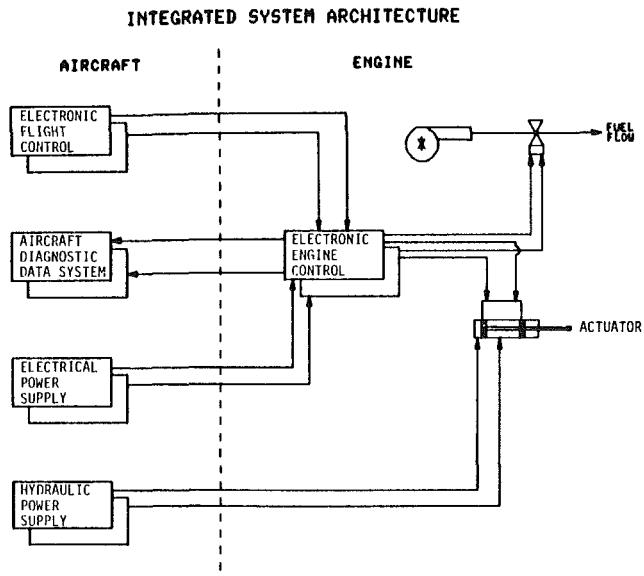


Fig. 9 Functionally integrated airframe-propulsion control system

cm² in frontal area and 45 kg in engine weight allowing for additions to the aircraft system, [7].

Electrical Power Source. The introduction of digital computers in flight and propulsion control systems presents the opportunity to reduce aircraft weight and improve reliability through the elimination of dedicated engine alternators (generators). Redundant electrical power required for computers is available on the aircraft electrical power bus system. The current and projected integrated electrical power architecture is shown in Fig. 8. Current systems provide power to the propulsion control, actuators, and ignition. Advanced systems may employ a common aircraft power source.

The electrical power supply to the actuators is an area which must be considered in the development of future optic engine control systems. When a total optic system is used in the engine control system to protect against the effects of EMI/EMP, a wired connection still exists through the electrical power bus system. Future aircraft, designed with shared aircraft power, still do not get around this common tie point. In fact, shared electrical systems tend to interconnect all of the aircraft control systems. An option proposed to the shared power concept is the use of locally generated power at each actuator [6]. This type of power supply would have a source of electrical power, either a hydraulically driven generator or a piezoelectric stack located on each actuator. Before this type system is implemented, the implications of redundancy and increased weight need to be determined.

Summary

Future aircraft will benefit from the integration of the flight and propulsion control systems, providing trade studies are performed prior to system design to identify the impact of life cycle cost, reliability maintenance, and weight for the integrated system. The integrated system architecture, Fig. 9, summarizes the functional control integration discussed in this paper. Control systems can communicate over hardwire or optic data buses depending upon the application and the available technology. Fiber optic technology will provide the opportunity to locate the engine control configuration to a benign environment as a distributed or centralized integrated control system.

Integrated ECMS and diagnostics will improve the maintainability of the weapon system by providing engine status information, engine health, etc. The common electrical and hydraulic system will provide the same quality of power and level of redundancy to both the airframe and the engine, thus providing reduced weight and drag through reduced G/B frontal area and improved reliability.

A totally integrated fiber optic airframe-propulsion control system will optimize aircraft and engine performance, aircraft persistence, combat effectiveness, mission reliability, and combat aircraft survivability; thus, assuring air superiority for future military aircraft.

Acknowledgments

The author appreciates the support and cooperation of W. W. Wagner, Deputy Director, Science and Technology Group, Naval Air Propulsion Center, Trenton, N.J.

References

1 Davies, W. J., Hoelzer, C. A., and Vizzini, R. W., "F-14 Aircraft and Propulsion Control Integration Evaluation," 83-GT-234, ASME 28th International Gas Turbine Conference and Exhibit, Phoenix, Ariz. Mar. 27-31, 1983.

2 Vizzini, R. W., "The Packaging of Electronic Engine Control Units and Related Subcomponents," AGARD Lecture Series No. 113, "Microcomputer Applications in Power and Propulsion Systems," Apr. 1981.

3 Husbands, C. R., Currier, P., and Portor, D. R., "The Evolution of Fiber Optics in Avionics," SAE BO1145, SAE Aerospace Congress and Exposition, Los Angeles Convention Center, Oct. 13-16, 1980.

4 Vizzini, R. W., "Propulsion-Airframe Control Integration, Status and Possibilities," Purdue University Short Course on Engine-Airframe Integration, 17 Oct. 1983.

5 Emerson, L. C., and Davies, W. J., "Flight/Propulsion Control System Integration," AIAA-83-1238, AIAA/SAE/ASME, 19th Joint Propulsion Conference, Seattle, Wash., June 27-29, 1983.

6 Stern, A. D., and Carlin, C. M., "Study of Integrated Airframe/Propulsion Control System Architecture," NASA Report D180-27657-1, Sept. 1983.

Downloaded 01 Jun 2010 to 171.66.16.71. Redistribution subject to ASME license or copyright; see http://www.asme.org/terms/Terms_Use.cfm

Aircraft Engine Control Mode Analysis

H. Brown
Manager, Engine Dynamics and Control Simulation.

J. A. Elgin
Senior Engineer, Control Mode Analysis.

General Electric Company, Cincinnati, Ohio 45215

This paper describes the control mode analysis procedure that is used to establish closed-loop control requirements for advanced aircraft propulsion systems. The procedure utilizes anticipated variations in engine component performance, engine deterioration, and control tolerances in a statistical analysis to establish corresponding variations in engine output performance and safety parameters. Potential closed-loop control configurations are evaluated by this process, compared, and the best configuration selected for implementation into control law and schedule designs. A byproduct of the analysis is the establishment of engine design and performance margins. The paper will describe typical engine variational models used in this process, the General Electric COMET program designed to automate the analysis, and typical mode study results based on a current augmented turbofan engine.

Introduction

Flight propulsion control systems utilize closed-loop control for setting engine performance and safety parameters such as thrust, stall margin, and high-pressure turbine rotor inlet temperature that cannot be measured directly on the engine. Measurable parameters such as rotor speeds, gas temperatures, or pressures must be sensed and compared with control schedule demands derived from a model of the engine. The effectiveness of the closed-loop control will be dependent on the accuracy of the engine model, the characteristics of the sensors used, and the complexity of the engine and its required control process. Increasing demands on current and advanced propulsion systems for improved fuel economy, in-flight thrust vectoring and reversing, and multiple operating modes are leading to more active internal variable geometry and a more complex propulsion control design problem. Integrated flight and propulsion control will add additional complexity in the form of multiple input commands, multiple engine outputs, and a more complex requirement for protecting the engine from operation beyond its safe limits. Control mode analysis is used by the General Electric Company as the initial step in the propulsion control design process to establish closed-loop control requirements and to identify specific actuators and engine-sensed parameters which should be used in the closed-loop control process.

The control mode analysis uses a linear model of the engine and a series of models of anticipated performance variations due to engine quality, performance deterioration, and control tolerances to establish maximum anticipated variations in the principle engine performance and safety parameters. Potential closed-loop control configurations are evaluated by this process for each engine operating mode and the best configuration selected for implementation into control law and schedule design.

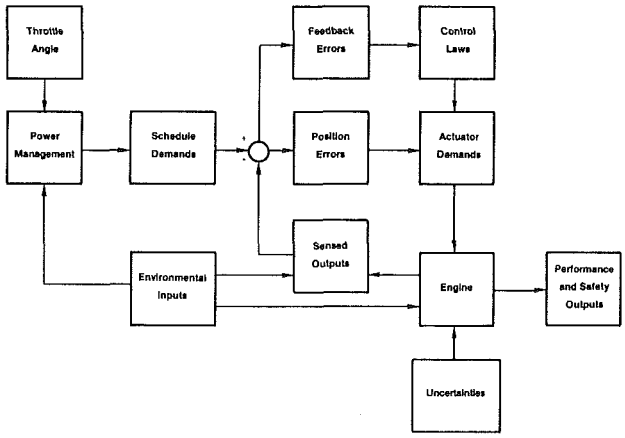


Fig. 1 Engine and control system

This paper will describe typical component variational models that are used as the basis for the variational studies and will show the major elements of an automated control mode analysis procedure. A current augmented turbofan engine will be used to illustrate results that can be obtained by this process.

Discussion

Closed-Loop Control. Figure 1 illustrates the major elements of the propulsion control system. Control schedule demands are derived from the engine power management system which contains schedules for fan rotor speed and the internal geometries as a function of power lever angle, inlet temperature and pressure, and internally sensed variables. The demands are compared with the sensed output signals from the engine, and closed-loop feedback errors are obtained

Contributed by the Gas Turbine Division of THE AMERICAN SOCIETY OF MECHANICAL ENGINEERS and presented at the 29th International Gas Turbine Conference and Exhibit, Amsterdam, The Netherlands, June 4–7, 1984. Manuscript received at ASME Headquarters January 24, 1984. Paper No. 84-GT-262.

Copyright © 1985 by ASME
Downloaded 01 Jun 2010 to 171.66.16.71. Redistribution subject to ASME license or copyright; see http://www.asme.org/terms/Terms_Use.cfm

Table 1 Deviations from nominal

MODEL TYPE	COMPONENT QUALITY			DETERIORATION
PERCENTILE	2.28 (LOW)	50.00 (MED)	97.72 (HIGH)	MAXIMUM
EFFICIENCY				
FAN	- .6	0.0	.4	-1.6
COMPRESSOR	- .24	0.0	.16	-1.3
HP TURBINE	- .3	0.0	.2	- .65
LP TURBINE	- .24	0.0	.16	- .65
FLOW				
FAN	- .3	0.0	.2	- .8
COMPRESSOR	- .12	0.0	.08	- .37
HP TURBINE	- .5	0.0	.5	1.39
LP TURBINE	- .3	0.0	.3	0.0
LEAKAGE (%W25)	0.0	.7	2.1	.7
FAN EFFICIENCY/AIR FLOW CORRELATION				60%
COMPRESSOR EFFICIENCY/AIR FLOW CORRELATION				60%

Table 2 Typical sensor variations

SENSOR	SYMBOL	2σ ERROR % OF POINT
FAN SPEED	N2	.23
CORE SPEED	N25	.25
PRESSURE		
FAN INLET	P2	.74
FAN DISCHARGE	P14	1.18
COMPRESSOR DISCHARGE	PS3	.53
HPT DISCHARGE	P42	.68
LPT DISCHARGE	P5	1.23
BYPASS STATIC	PS14	.55
BYPASS DIFFERENTIAL	P14-PS14	4.43
TEMPERATURE		
FAN INLET	T2	.35
FAN DISCHARGE	T25	.30
HPT DISCHARGE	T42	1.00
LPT DISCHARGE	T5	1.11

from the comparisons. These are input to the control laws for translation into closed-loop actuator demands. Open-loop-actuators are set by direct comparison of the demand schedules and the corresponding actuator position.

Variations in the engine operating characteristics due to initial engine component quality and subsequent in-service deterioration will affect the ability of the selected closed-loop sensed parameters to set the primary performance and engine safety parameters. Closed-loop sensor tolerances and open-loop actuator tolerances will also affect the output accuracy. The control mode analysis represents a statistical analysis of the effects of the foregoing variations or uncertainties on the output characteristics of the engine for the selected closed-loop configurations at particular operating conditions. Potential closed-loop configurations are compared by this process and a design selection made on the basis of minimum variational effects.

Variational Models. The primary inputs to the control mode analysis are defined by the variational models which establish the anticipated variability in the engine component performance characteristics and in the actual values of the sensed engine parameters. Three variational models are used—a Component Quality Model, a Deterioration Model, and a Control Tolerance Model. Each of the models are derived from prior engine operating experience on earlier engine programs and are adjusted to reflect known changes in design concept, materials, and manufacturing and assembly processes.

Component Quality Model. The component quality model represents anticipated variability or uncertainty in the actual engine component performance characteristics relative to the nominal average engine steady-state model used for engine design and performance analysis. The quality model represents new engine performance after installation on the aircraft. Table 1 illustrates a typical component quality model for a modern fighter engine. The model defines a low extreme value (2.28th percentile), a median value (50th percentile), and a high extreme value (97.72th percentile). These values are used to generate a Weibull distribution [1] for each individual component performance parameter. The Weibull distribution can be used to generate a skewed distribution on either side of the median by the choice of low and high extreme values. Symmetrical Weibull inputs around the median will produce a distribution that is essentially a Gaussian (normal) distribution. Note that the low and high extreme values correspond to $\pm$ 2 σ deviations for symmetrical inputs.

The quality model includes distributional data for the major component flow and efficiency parameters and for engine airflow leakage. A strong correlation has been assumed between fan air flow and efficiency and between compressor air flow and efficiency. No correlation has been detected between turbine flow and efficiency and they have

Nomenclature

A = open-loop matrix elements
A/D = analog to digital conversion
B = transformation matrix elements
D/A = digital to analog conversion
DAH8 = exhaust nozzle area
DH = 97.5th percentile variation
DHC = constrained value of DH
DL = 2.5th percentile variation
DLC = constrained value of DL
DM = mean value
DPP = constraint penalty
DPQC14 = fan duct $\Delta P/P$
DWF36 = main engine fuel flow
EPR = engine pressure ratio
FN = net thrust
IRP = intermediate rated power
$N2$ = fan rotor speed
$N25$ = core rotor speed
$N2K$ = fan rotor corrected speed
$PCN2$ = percent fan rotor speed
$PS14$ = fan duct static pressure
$P14$ = fan duct total pressure
$P2$ = engine inlet total pressure
$P48$ = interturbine pressure
$P5$ = turbine discharge pressure
RSS = root-sum-square
SD = standard deviation
SFC = specific fuel consumption
$SM2$ = fan stall margin
$SM25$ = compressor stall margin
$TB41$ = high-pressure turbine blade metal temperature
$T2$ = engine inlet total temperature
$T41$ = high-pressure turbine inlet temperature
$T48$ = low-pressure turbine inlet temperature
$T5$ = turbine discharge temperature
$W25$ = core compressor air flow
$XN2$ = fan rotor speed
$XN25$ = core rotor speed
ΔC = sensed variable variations
$\Delta M1$ = closed-loop manipulated variable variations
$\Delta M2$ = open-loop manipulated variable variations
ΔP = performance parameter variations or differential pressures
$\Delta P/P$ = duct total-static pressure difference/static pressure
ΔQ = engine quality variations
ΔS = engine safety parameter variations
σ = standard deviation

Downloaded 01 Jun 2010 to 171.66.16.71. Redistribution subject to ASME license or copyright; see http://www.asme.org/terms/Terms_Use.cfm

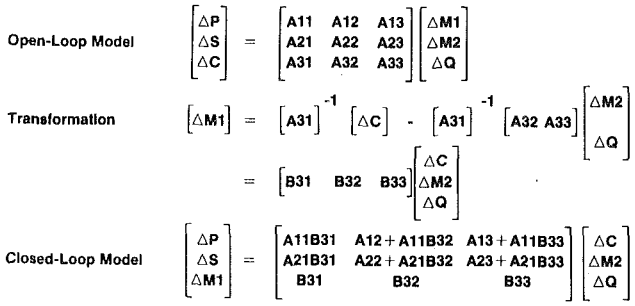


Fig. 2 Open- and closed-loop engine models

been assumed to be uncorrelated. Fan, compressor, and turbine efficiency effects have been assumed to be skewed in the unfavorable direction. The correlation effects produce a similar skewing in the fan and compressor air flow effects. The leakage distribution has been assigned a lower bound of zero leakage, a median value which is poorer than the nominal engine, and a skewed upper value. All other effects have been assumed to be symmetrical about the median.

Deterioration Model. The deterioration model represents anticipated engine component performance deterioration between new engine installations and final removal from service. Deterioration studies [2] indicate that component performance deteriorates at a rate which decays with time and is partially restored after engine cleaning, module replacement, or overhaul. High initial quality engines appear to deteriorate more than low initial quality engines, thereby reducing the spread on old engines. Current data are, however, insufficient to define either a usable variation with time or a statistical distribution around a nominal deterioration model. The current approach, therefore, uses a deterministic deterioration model that represents the maximum deterioration anticipated before retirement from service. A typical fighter engine deterioration model is also shown in Table 1 and is based on prior operating engine experience.

Control Tolerance Model. The control tolerance model represents anticipated errors in the engine and actuator sensors relative to actual parameter values that will effect closed-loop feedback signals and commands. The sensor errors are assumed to be the random residual after calibration has removed all biases. The control tolerance model includes basic sensor noise, acquisition errors (sampling errors in a non-homogeneous gas stream), signal conditioning errors, A/D or D/A conversion errors, transmission line noise, and actuator linkage errors in positioning engine variable geometry. The individual errors are assumed to be normally distributed and can, therefore, be combined by an RSS (root-sum-square) process to obtain a total error estimate for each sensor. Table 2 contains typical data for a selected group of analog sensors which utilize D/A conversion for use in a digital control system. The tabulated data represent two standard deviations for each distribution. Note that errors expressed as a percent of actual value can vary significantly over the total engine operating envelope.

Sensor outputs are generally used in combination to establish corrected parameter closed-loop feedback signals. Typical corrected parameters include the fan corrected speed ($N2/\sqrt{T2}$), engine pressure ratio or EPR ($P5/P2$), and bypass duct $\Delta P/P$ ($(P14-PS14)/PS14$). In such cases, the sensor error effect must be modified by the transfer function between each individual sensor and the final parameter. When the sensor outputs are used to establish a scheduled command, the slope of the associated schedule must be used to establish the final parameter error. Since the individual errors are assumed to be normally distributed, the combined parameter

Table 3 Typical control tolerance model

CONTROL PARAMETER	SYMBOL	2σ ERROR % OF POINT
FAN CORRECTED SPEED	$N2/\sqrt{T2}$	.29
CORE CORRECTED SPEED	$N25/\sqrt{T25}$	.29
INTERTURBINE PRESSURE RATIO	P42/P2	1.00
BYPASS DELTA P/P	$\frac{P14-PS14}{PS14}$	4.46
FAN PRESSURE RATIO	P14/P2	1.43
ENGINE PRESSURE RATIO	P5/P2	1.43

errors will also be normally distributed and can be obtained by an RSS of the products of the individual sensor errors and their corresponding transfer functions. This process is illustrated by the following example:

- Fan corrected speed is defined by

$$N2K = N2/\sqrt{T2} \tag{1}$$

- The log differential of equation (1) produces:

$$\partial N2K/N2K = \partial N2/N2 - 1/2\ \partial T2/T2 \tag{2}$$

- The percent transfer function between $N2$ and $N2K$ will be 1.0 from equation (2). The corresponding transfer function between $T2$ and $N2K$ will be -0.5.
- The corresponding standard deviation of $N2K$ can then be obtained from

$$\sigma^2_{N2K} = (1.0\ \sigma_{N2})^2 + (-0.5\ \sigma_{T2})^2 \tag{3}$$

Table 3 provides a list of typical control tolerances derived by the foregoing process for use in control mode analysis studies. These data have been used as the basis for the studies described in this paper.

Engine performance will be affected directly by the selected control mode (closed-loop control configuration). The actuator sensor errors for actuators that are controlled open-loop will have a direct effect on the engine output. An example of open-loop actuator control on current engines is the compressor variable stator position that is scheduled directly as a function of core compressor corrected speed. Closed-loop actuator control substitutes a feedback signal of some other parameter for the actuator position feedback. An example of closed-loop actuator control is the fuel metering section of the primary fuel control, which sets fuel flow by a fan speed or EPR feedback signal. Under closed-loop control, the engine is affected by the engine sensor errors for the selected feedback parameter but is not affected by actuator positioning errors. The purpose of the control mode study is to determine the closed-loop control configuration that will produce an acceptable effect on the engine output characteristics.

Control Mode Analysis Procedure. The control mode analysis process has been automated in the General Electric COMET (Control Mode Evaluation of Temperature Margin) Program. COMET combines the variational modes with a steady-state linear model of the engine and performs the statistical analyses necessary to evaluate potential multivariable closed-loop control configurations. The following sections describe the major elements of the COMET program.

Linear Engine Model. The linear model defines the effects of component performance variations (derived from the quality, deterioration, and control tolerance models) on the output characteristics of the engine. It represents a matrix of partial derivatives which are obtained from successive perturbations around a selected operating point. The linear

Downloaded 01 Jun 2010 to 171.66.16.71. Redistribution subject to ASME license or copyright; see http://www.asme.org/terms/Terms_Use.cfm

Table 4 Typical performance variations with $N2$, $\Delta P/P$ mode (COMET output)

NO.	NAME	BASE	AGE	SD	DL	DM	DH
1	PCN2	Base Values At SLS/IRP	NEW	1.22464E-03	-2.31016E-03	8.50659E-06	2.31318E-03
1	DPQC14		NEW	2.30686E-02	-4.45040E-02	-6.36508E-04	4.24800E-02
2	FN		NEW	6.99766E-03	-1.57819E-02	-1.10657E-03	1.54745E-02
2	SM2		NEW	3.11209E-02	-6.12045E-02	7.04203E-04	5.75649E-02
3	XN2		NEW	1.22464E-03	-2.31016E-03	8.50955E-06	2.31318E-03
3	XN25		NEW	1.27979E-03	-1.30573E-03	8.83465E-04	3.81544E-03
3	T41		NEW	1.44570E 01	-6.11873E 00	1.84867E 01	4.83627E 01
3	T48		NEW	1.16574E 01	-6.90695E 00	1.42113E 01	3.69041E 01
3	T5		NEW	1.02677E 01	-5.23735E 00	1.26399E 01	3.31554E 01
3	SFC		NEW	6.68646E-03	-5.73617E-04	9.59282E-03	2.34488E-02
3	SM2		NEW	3.11209E-02	-6.12045E-02	7.04203E-04	5.75649E-02
3	SM25		NEW	1.00733E-02	-5.92831E-03	1.27222E-02	3.26129E-02
4	DWF36		NEW	1.08104E-02	-1.41470E-02	8.50753E-03	3.15498E-02
4	DAH8		NEW	4.96684E-03	-9.56546E-03	-3.19958E-04	9.10435E-03
5	DWF36		OLD	1.09772E-02	3.01995E-02	5.34792E-02	7.67163E-02
5	DAH8		OLD	4.92757E-03	-1.84073E-03	7.32500E-03	1.66669E-02
6	PCN2		OLD	1.22464E-03	-2.31016E-03	8.50650E-06	2.31318E-03
6	DPQC14		OLD	2.30686E-02	-4.45040E-02	-6.36508E-04	4.24800E-02
6	FN		OLD	7.21544E-03	-1.28447E-02	2.26277E-03	1.87062E-02
6	SM2		OLD	3.05404E-02	-1.03226E-01	-4.27768E-02	1.35768E-02
6	XN2		OLD	1.22464E-03	-2.31015E-03	8.52087E-06	2.31319E-03
6	XN25		OLD	1.28320E-03	-1.66956E-03	5.64421E-04	3.47772E-03
6	T41		OLD	1.45187E 01	9.15303E 01	1.16579E 02	1.46164E 02
6	T48		OLD	1.17082E 01	8.11270E 01	1.02476E 02	1.24954E 02
6	T5		OLD	1.02984E 01	7.27040E 01	9.08825E 01	1.11442E 02
6	SFC		OLD	6.68334E-03	4.03965E-02	5.11039E-02	6.49026E-02
6	SM2		OLD	3.05404E-02	-1.03226E-01	-4.27768E-02	1.35768E-02
6	SM25		OLD	1.00678E-02	-6.75884E-04	1.79146E-02	3.77842E-02

ΔT in °F and All Others Per Unit

Table 5 Effects of minimum thrust and fan stall margin constraints

NO.	NAME	NEW ENGINE DPP	NEW ENGINE DLC	NEW ENGINE DHC	OLD ENGINE DLC	OLD ENGINE DHC
1	PCN2	7.70852 52E-03	5.3983644E-03	1.00217 05E-02	5.3983644E-03	1.00217 06E-02
1	DPQC14	8.7864371E-02	4.33604 08E-02	1.30344 34E-01	4.33604 08E-02	1.30344 34E-01
2	FN	1.5781852E-02	0.	3.1256313E-02	2.9371949E-03	3.44880 49E-02
2	SM2	1.03226 10E-01	4.20215 90E-02	1.60791 02E-01	1.8626451E-09	1.16800 94E-01
3	XN2	7.7085269E-03	5.3983691E-03	1.00217 10E-02	5.3983787E-03	1.00021722E-02
3	XN25	2.06998 88E-03	7.64263 07E-04	5.88543 09E-03	4.00042767E-04	5.54771 06E-03
3	T41	1.2748458E 01	6.6297233E 00	6.1111119E 01	1.04278 79E 02	1.58912 50E 02
3	T48	9.5139341E 00	2.60698 42E 00	4.6417995E 01	9.06400 968E 01	1.3446831E 02
3	T5	3.82699 06E 00	-1.41036 08E 00	3.6982435E 01	7.65310 16E 01	1.1526937E 02
3	SFC	-1.1324557E-03	-1.70607 27E-03	2.2316359E-02	3.97640 08E-02	6.37701 08E-02
3	SM2	1.03226 10E-01	4.20215 90E-02	1.60791 02E-01	1.8626451E-09	1.16800 94E-01
3	SM25	-5.7173739E-03	-1.1645687E-02	2.6895477E-02	-6.3932579E-03	3.20668 61E-02

engine model has been derived from a steady-state, nonlinear engine model with engine fuel flow and internal variable geometries set to their steady-state operating schedules.

Potential closed-loop control configurations can be defined in terms of specific sensed parameters (from the list of measurable outputs) that will be used to control a corresponding number of manipulated variables that will define actuator positions. The initial phase of the COMET procedure transforms the open-loop linear model to a closed-loop model corresponding to the specified closed-loop control configuration. This process is illustrated in Fig. 2. A transformation matrix is obtained from the open-loop model, which expresses the selected closed-loop manipulated variables [$\Delta M1$] as a function of the closed-loop sensed parameters [ΔC], the remaining open-loop manipulated variables [$\Delta M2$], and the quality variables from the variational model [ΔQ]. The resulting transformation matrix is then combined with the open-loop model to produce the corresponding closed-loop model.

Engine performance [ΔP] and safety [ΔS] parameter variations will be dependent upon the engine quality variations, control tolerances associated with the selected closed-loop sensed parameters and open-loop manipulated variables, and the engine model. Since the engine model is dependent on engine operating condition (altitude, Mach number, and power setting), the control-mode analysis should be repeated at a number of critical engine operating conditions. The analysis should be conducted at maximum power setting at sea level static, maximum flight Mach number, and at any other conditions which might be expected to operate in a significantly different manner. Engines with multiple operating modes—such as variable cycle engines or V/STOL engines—should be analyzed for each mode. An open-loop linear engine model will be required for each individual condition/operating mode to be evaluated.

Monte Carlo Analysis. Each potential closed-loop control mode is evaluated by a Monte Carlo analysis to develop statistical data on the effects of the engine quality and control tolerances on the output characteristics of the engine. A random number generator is used to assign a deviation from the nominal engine to each element of the quality and control tolerance models. Engine output characteristics are obtained from the closed-loop engine model and the results are stored as new engine data. Deterioration effects are then added and stored as old engine data. The foregoing random generation process must be repeated for a series of additional engines in order to develop statistical data on the variational characteristics of the engine output performance and safety parameters. Prior studies of the effects of engine sample size have indicated that approximately 300–320 engines are required to obtain statistical data that will not change significantly with increased sample size.

Table 4 illustrates the initial part of a typical COMET output. It describes the statistical variation of each of the selected engine output parameters for the new and the old engine populations. Temperatures are shown as an absolute difference (in °F) from the nominal engine model and all other parameters are shown as a per unit difference from the nominal engine. The following data are provided by the COMET output:

Downloaded 01 Jun 2010 to 171.66.16.71. Redistribution subject to ASME license or copyright; see http://www.asme.org/terms/Terms_Use.cfm

Table 6 Steady-state design margins

MARGIN		QUALITY	DETERIORATION	THRUST	TOTAL
THRUST	%	-1.58	0	1.58	0
FAN STALL MARGIN	%	-6.1	-4.2	10.3	0
FAN SPEED	%	.23	0	.77	1.00
CORE SPEED	%	.38	0	.21	.59
HPT INLET TEMPERATURE	°C	26.9	54.3	7.1	88.3
LPT INLET TEMPERATURE	°C	20.5	48.9	5.3	74.7
LPT DISCHARGE TEMPERATURE	°C	18.4	43.4	2.1	63.9
SPECIFIC FUEL CONSUMPTION	%	2.34	4.15	-.11	6.38
CORE STALL MARGIN	%	-.6	0	-.6	-1.2

Table 7 Control mode selection study

MODE	21	22	23	24	25	26
SENSED VARIABLES	TB41 N2	N25 N2	N25 ΔP/P	P5/P2 ΔP/P	P48/P2 ΔP/P	N2 ΔP/P
CONSTRAINTS						
MIN. FN	0	0	0	0	0	0
MIN. SM2	0	0	0	0	0	0
MAX. VALUE						
THRUST (%)	19.8	6.1	5.2	4.8	2.9	3.4
T41 (°C)	110	99	95	96	91	88
T48 (°C)	92	84	81	82	77	74
T5 (°C)	63	69	68	68	64	64
SFC (%)	4.9	6.5	6.4	6.6	6.4	6.4
N2 (%)	5.4	2.0	1.6	1.6	1.2	1.0
N25 (%)	2.6	.8	.6	.7	.5	.6

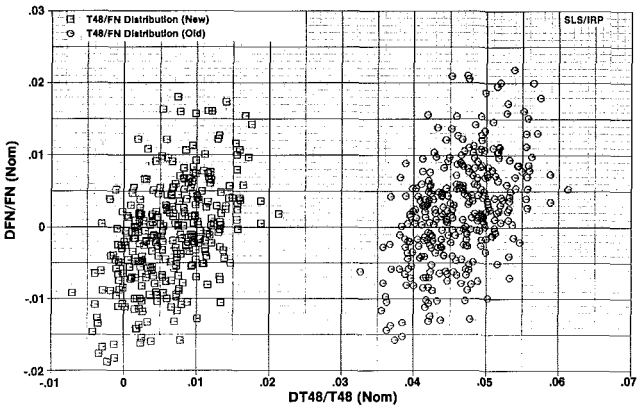


Fig. 3 Thrust temperature distribution for *N2/ΔP/P* control

• SD represents the standard deviation of the engine population.

• DL represents the 2.5th percentile engine. It establishes the minimum anticipated value after discarding the lowest 2.5 percent of the population.

• DM represents the population mean value.

• DH represents the 97.5th percentile engine and establishes the corresponding maximum anticipated value after discarding the highest 2.5 percent of the population.

The data of Table 4 have been obtained from a linear engine model at sea level static, Intermediate Rated Power. These data are based upon an actual augmented turbofan control mode using fan speed (PCN2) and bypass duct $\Delta P/P$ (DPQC14) or duct Mach number as closed-loop sensed parameters. These data indicate the following:

• The assumption of a skewed component quality model will shift the means in the unfavorable direction by 18.5°F (10.3°C) on *T*41, 12.6°F (7.0°C) on *T*5, and 1 percent on SFC.

• The minimum thrust engine is down 1.6 percent from nominal and the maximum temperature engine (*T*41) is 48.4°F (26.9°C) from nominal. The maximum SFC engine is up 2.3 percent from nominal.

• Deterioration has the same effect on all engines and results in mean shifts of a 0.3 percent increase in thrust, 98°F (54.4°C) increase in temperature (*T*41), and an additional 4.2 percent in SFC.

The bivariate distribution of any two selected parameters can be plotted for the total engine population. Figure 3 contains a typical plot which shows the thrust variation against *T*48 (low-pressure turbine inlet temperature). These data represent deviations from the nominal engine representation due to the combined effects of component quality, deterioration, control tolerances, and the selected closed-loop control mode. This type of plot illustrates the degree of correlation between the two variables in that perfect correlation would collapse the array to a single line for all new engines and a second line for old engines. The plot could be useful in identifying sensed parameters that could be used for closed-loop control of unmeasurable output parameters such as thrust or stall margin.

The computed distributions shown in Table 4 are used to provide guidance in assuring that at least 97.5 percent of the production engine population will meet or exceed performance commitments and minimum safety requirements over the useful operating life of the engine. These data indicate that the minimum thrust engine will produce 1.6 percent less thrust than the nominal engine. The following options are available for adjusting either the engine or its performance commitments:

• The thrust quote can be derated by 1.6 percent. This makes the minimum thrust engine meet quoted thrust.

• The fan speed control can be biased to overspeed all engines by an amount which will increase thrust by 1.6 percent. This approach also produces quoted thrust on the minimum thrust engine.

For either case, engine speed and temperature margins must be based on the maximum requirements for achieving the quoted thrust. General Electric tends to use the thrust derate approach on military engines and the control bias approach on commercial engines. The control bias approach results in engine design penalties in the form of higher speeds, temperatures, and pressures required to meet minimum thrust

Downloaded 01 Jun 2010 to 171.66.16.71. Redistribution subject to ASME license or copyright; see http://www.asme.org/terms/Terms_Use.cfm

and any other specified constraints on a minimum engine. The COMET program is used to compute these penalties for one or more of such constraints. The number of potential constraints is limited only by the number of control schedules available for biasing.

Table 5 contains COMET output based upon the data of Table 4 for a minimum thrust constraint of 0 percent and a minimum fan stall margin constraint of 0 percent. The COMET output contains the following data:

- DPP is the penalty associated with meeting the selected constraints.
- DLC is the low (2.5th percentile) value after applying the constraints.
- DHC is the high (97.5th percentile) value after applying the constraints.

Minimum and maximum values are summarized for both new and old engines.

The constraining process simplifies the control mode selection process by putting all candidate modes on a common basis with respect to minimum thrust and other constrained parameters. The foregoing constraint penalty results in an increase in maximum *T*41 requirements by 12.7°F (7.1°C), a corresponding increase of 0.8 percent in fan speed, and a core speed increase of 0.2 percent. These parameters would normally be the primary parameters to be compared in the control mode selection process.

Steady-State Design Margins. Table 6 contains typical steady-state engine design margins that can be obtained from the data of Tables 4 and 5. These data are derived from the most severe new or old engine data. The individual design margins have been based on the following:

- Quality Margin—Component quality and control tolerance effects
- Deterioration Margin—Deterioration effects
- Thrust Margin—Constraint penalty
- Total Margin—Algebraic sum of the foregoing margins

Actual engine steady-state design margins include additional margin requirements for the effects of inlet humidity and fuel heating value variations. Total engine design margins include transient margins for acceleration and long-term overshoot. These additional factors are beyond the scope of the current paper.

The thrust margin requirements on engine performance parameters—such as thrust and specific fuel consumption—should be used to develop performance derates to be applied to the nominal steady-state engine cycle model for establishing performance commitments. The margin requirements for fan and compressor stall margin represent an input to the stability stack-up used to assess the adequacy of the design. The remaining design margins on rotor speeds and temperatures must be added to the nominal engine data to establish engine mechanical design criteria to be used in the engine design process.

Control Mode Studies. The COMET procedure can be used for conducting a variety of studies that explore the effects of component quality, deterioration, and control tolerance variations on the performance of an engine and its associated design requirements. Its primary application is the control mode selection study that will establish the preferred closed-loop control configuration and associated performance derates and design margins. The COMET procedure can also be used to examine control cutback options when operating against one, or more, engine limits. The following sections will describe typical control mode studies for each of the foregoing purposes.

Closed-Loop Control Mode Selection Study. The control mode selection study involves a comparison of potential closed-loop control configurations and would normally include the open-loop mode (no closed-loops), one or more potential single-loop configurations, one or more two-loop configurations, etc. The maximum number of closed-loops is limited by the number of operable engine actuators at the operating condition to be examined. The control tolerance model must include an estimate for the tolerances for each potential closed-loop sensor and should reflect the sensor technology level to be used as the basis for the selection process.

Table 7 summarizes the results of a control mode selection study based on sea level static Intermediate Rated Power (IRP) of the study engine and on the variational models of Tables 1 and 3. Zero and single-loop modes were omitted from the study, since the actual baseline engine control system contains a two-loop control at IRP. All modes have been constrained to a minimum thrust constraint (relative to the nominal engine) of 0 percent and to a minimum fan stall margin constraint of 0 percent.

The first mode, mode 21, is based on fan speed (*N*2) for setting thrust and high-pressure turbine inlet temperature (*T*41) for protecting the core from overtemperature. It requires an SFC derate of 4.9 percent, which is about 1.5 percent better than any of the other two-loop modes investigated. It requires the control temperature to be set to meet thrust on a low thrust deteriorated engine and would overboost a high thrust new engine by almost 20 percent. Design margins on temperature and rotor speeds are high and

Table 8 Temperature-limiting mode

MODE	CONSTANT $\Delta P/P$		CONSTANT N2	
VARIATION	MIN.	MAX.	MIN.	MAX.
THRUST - %	-24.5	-15.0	-26.8	-15.6
T41 - °C	-46.3	-11.1	-46.9	-11.4
T48 - °C	-29.4	- 0.5	-33.1	- 3.0
T5 - °C	-16.2	7.1	-46.7	-13.9
FAN SPEED - %	- 6.0	- 3.7	- .25	.25
SFC - %	1.48	3.64	- 1.82	- .36
SM2 - %	-1.8	9.6	101	172

Table 9 Effect of temperature-limiting mode on design margins

	QUALITY VARIATION			TEMPERATURE	
	NOMINAL MODE	TEMPERATURE LIMITING MODE	THRUST CORRECTION	LIMITING MODE MARGIN	TOTAL DESIGN MARGIN
THRUST - %	-1.58	-6.38	4.80	0	0
FAN STALL MARGIN - %	-6.1	-4.7	-1.79	-.4	-.4
FAN SPEED - %	.23	.73	1.15	1.65	2.65
CORE SPEED - %	.38	.45	.60	.67	1.26
T41 - °C	26.9	19.7	22.2	15.1	103
T48 - °C	20.5	16.5	17.2	13.2	88
T5 - °C	18.4	14.2	13.2	8.9	73
SFC - %	2.34	1.92	.62	.2	6.6
CORE STALL MARGIN - %	-.6	-1.0	-1.75	-1.2	-2.4

Downloaded 01 Jun 2010 to 171.66.16.71. Redistribution subject to ASME license or copyright; see http://www.asme.org/terms/Terms_Use.cfm

would result in a substantial engine weight penalty. These characteristics are typical of most control modes using temperature as a primary control variable. Temperature can, however, be used as an override on the primary thrust setting parameter in order to limit deterioration at rated thrust. This approach will be discussed in more detail in the next section.

Mode 22 retains fan speed and uses core speed ($N25$) for core overspeed protection. It also provides effective protection for core overtemperature. It uses only speed sensors and represents the least expensive sensor set. It reduces the temperature margin contribution by 11°C to 99°C and significantly reduces the fan and core speed margins. This approach is affected strongly by core stator variability, which results in a significant variation in the core air flow at speed.

Mode 23 retains the core speed and substitutes fan duct $\Delta P/P$ (or duct Mach number) for fan speed. This mode uses core speed as the primary thrust setting parameter and $\Delta P/P$ for protecting the engine from fan stall. This mode represents a slight improvement over Mode 22 but also suffers from core stator variability.

Modes 24 and 25 use engine pressure ratio (EPR) as the primary thrust setting parameter and duct $\Delta P/P$ for fan stall margin protection. Turbine discharge EPR ($P5/P2$) is used for Mode 24 and interturbine EPR ($P48/P2$) for Mode 25. The Mode 24 results do not differ significantly from those of Mode 23. Mode 25, however, shows a further reduction in temperature margin contribution to 91°C. It also has the smallest thrust variation (2.9 percent) of all the modes investigated. Turbine discharge EPR should be the best parameter for setting thrust and $\Delta P/P$ the best parameter for controlling fan stall margin. EPR controls are, however, strongly affected by sensor accuracy. The smaller percent error associated with the $P48/P2$ tolerance would account for its improved performance relative to the $P5/P2$ EPR.

The final mode (mode 26) substitutes fan speed for EPR and retains $\Delta P/P$. It represents the actual baseline control mode. It is slightly better than mode 25 on fan speed and temperature margin and somewhat poorer on core speed and maximum thrust variation. The two modes are essentially a stand-off and a mode selection decision would probably involve other considerations such as sensor cost, reliability, previous practice, etc.

Temperature-Limiting Mode. A constant thrust rating can be maintained over a significant range of cold to hot day temperatures by the use of a corrected fan speed ($N2K$) schedule instead of physical fan speed. Turbine temperature will increase with increasing ambient temperature. Military engine controls generally include a control temperature limit to provide positive temperature protection for the engine. The temperature limit should permit maximum rated power on a sea level hot day with nominal component quality variations, deterioration, control tolerances, and bleed and power extraction. The limit will override one of the nominal control demands (fan speed or $\Delta P/P$) when any combination of high engine inlet temperature, poor engine quality, deterioration, and bleed and power extraction would produce an overtemperature at the nominal set point. The temperature-limiting mode could, therefore, be based on temperature, $\Delta P/P$, temperature-fan speed, or some combination of both.

Table 8 summarizes the results of a temperature-limiting mode study that compares the above options. The study has been based on deteriorated engine operation at a constant blade metal temperature ($TB41$) which is 50°F (28°C) below the nominal set point. The constant $\Delta P/P$ mode involves reduced fan speed for meeting the temperature constraint and the constant fan speed mode uses an opened exhaust nozzle and reduced $\Delta P/P$. The $\Delta P/P$ mode has relatively little effect on fan stall margin and results in a 4–6 percent fan speed reduction, a 1.5–4 percent increase in specific fuel consumption, and a 15–25 percent thrust reduction relative to the nominal set point. The constant fan speed mode significantly increases fan stall margin and results in a larger thrust loss, lower low pressure turbine temperatures, and an improvement of 0.4–1.8 percent in SFC. The fan speed mode holds fan air flow, which would generally produce better inlet performance, but the lower fan operating line corresponding to the fan stall margin increase would result in poorer augmentor performance. This type of study should be repeated at several flight conditions in order to assess the relative effects of inlet and augmentor performance shifts so that a mode selection can be made.

The selected temperature-limiting mode will have quality variations, which are generally different from those of the nominal control mode. These differences must be converted into corresponding performance margin requirements, which must be added to the margin requirements of the nominal mode. This process is illustrated in Table 9 and is based on the constant $\Delta P/P$ temperature-limiting mode. The first two columns contain the quality variations (engine component quality and control tolerance effects) for the nominal and temperature-limiting modes. These data represent maximum adverse variations from the nominal engine. The temperature-limiting mode reduces the individual temperature variations but results in a substantial increase in thrust variation. A thrust correction is, therefore, necessary to adjust the minimum thrust engine in temperature-limiting mode to the same thrust as the minimum engine in the nominal mode. The resulting temperature-limiting mode margin is the sum of the thrust correction and the difference between the temperature-limiting and nominal mode quality variations. The final column represents total design margin requirements for the nominal and temperature-limiting modes and is obtained by adding the temperature-limiting margin to the design margin in Table 6. The resulting margins must be adjusted by the humidity, fuel heating value, and transient effects omitted from this paper and the resulting margins used to establish engine design criteria, performance commitments, and qualification and acceptance testing criteria.

Summary

Control mode analysis is used to identify closed-loop control configurations that will minimize the variations of engine performance and safety parameters that cannot be measured directly on the engine. The analysis is based on projected variational models that define anticipated variations in component quality, deterioration, and control tolerances. A statistical analysis is used to establish the maximum variations anticipated by 97.5 percent of the production engine population, and these variations are used to establish engine design and performance margins for the selected control mode. The design and performance margins will include a quality margin for the effects of component quality and control tolerance variations, a deterioration margin for component deterioration over the operating life of the engine, and a thrust margin requirement for meeting rated thrust on a minimum engine. The use of a temperature-limiting mode will add additional margin requirements for meeting rated thrust on a minimum engine during temperature-limiting operation. The resulting engine design and performance margins must be used to establish component design criteria, performance commitments, and qualifications and acceptance test criteria.

References

1 Weibull, W., "A Statistical Distribution Function of Wide Applicability," ASME *Journal of Applied Mechanics*, Vol. 18, No. 3, 1951, pp. 293–297.

2 Wulf, R. H., "CF6-50 Engine Performance Deterioration," NASA CR-159867, Nov. 1980.

Downloaded 01 Jun 2010 to 171.66.16.71. Redistribution subject to ASME license or copyright; see http://www.asme.org/terms/Terms_Use.cfm

Design of Noninteracting Multivariable Feedback Control Systems Without Decoupling Filters

D. A. Baker[1]
Graduate Student.

C. J. Maday
Associate Professor.

Mechanical and Aerospace Engineering Department,
North Carolina State University,
Raleigh, N.C. 27695-7910

The design of multivariable control systems for modern applications is an important challenge to the control system engineer. Active control of metal machining operations, control of gas turbine operations, and chemical process control are current areas of interest. In precision machining operations where tolerances of a few microinches are required, in-process control with several servos will be required. These servos could control spindle axis location and tool position about several axes, thus forming a multi-input/multi-output system. Modern gas turbines, required to operate over more extended regimes, are provided with multiple controls, e.g., nozzle settings and fuel flows which must be implemented in some rational manner. In the chemical process industries, there are many examples of multivariable systems with several control variables and several desired or controlled outputs. One control approach considers a separate system for each of the controlled variables, so that a change in one input will produce an interaction effect that must be managed by another separate system. This approach is attractive and straightforward to implement, but current practice shows significant coupling effects. In order to reduce or eliminate interaction, a control algorithm, with strong integral compensation, for a sixth-order, two-input, two-output linear plant with dynamic coupling is proposed. Decoupling filters are not used. The primary goal is to realize a substantial reduction in the coupling effects when a step input is used for a single variable. A secondary goal is to achieve deadbeat response for the controlled variable to the step input. Moreover, these goals are to be attained in the presence of significant changes in the system parameters or in the presence of arbitrary external disturbances, i.e., robustness is required. The control strategy uses cascaded integral error compensation that permits conceptual division of the network so that two single-input/single-output systems result. Coupling effects are treated as arbitrary disturbances. Poles for each loop are placed on the real axis in the left-half plane. Numerical solutions to the system equations show that this approach produces a system that achieves effective decoupling and robustness simultaneously. It is significantly superior to Proportional-Integral-Derivative controllers which also are considered in detail.

Introduction

Precision machining operations, automatic control of gas turbines, and in-process control of chemical processes are representatives of important classes of feedback control systems that are characterized by more than one input and more than one output, i.e., multivariable systems with multi-inputs and multi-outputs. Such systems are the subject of many recent and current investigations [1–11]. Often there are difficulties with the accessibility of the output states, and these problems must be addressed effectively with observers to realize a satisfactory feedback control system. Even where it is possible to observe all of the state variables there remains the problem of selecting feedback gains to achieve some desired performance level. An immediate question centers about the nature of the desired time response. In multivariable systems with significant coupling, such as gas turbines, one performance criterion is the lack of interaction among the output variables when it is required to change only one of them. For example, in gas turbine applications it may be required to change shaft speed while maintaining certain

[1]Present address: University of California at Davis, Davis, CA.

Contributed by the Gas Turbine Division of THE AMERICAN SOCIETY OF MECHANICAL ENGINEERS and presented at the 29th International Gas Turbine Conference and Exhibit, Amsterdam, The Netherlands, June 4–7, 1984. Manuscript received at ASME Headquarters January 11, 1984. Paper No. 84-GT-157.

Copyright © 1985 by ASME
Downloaded 01 Jun 2010 to 171.66.16.71. Redistribution subject to ASME license or copyright; see http://www.asme.org/terms/Terms_Use.cfm

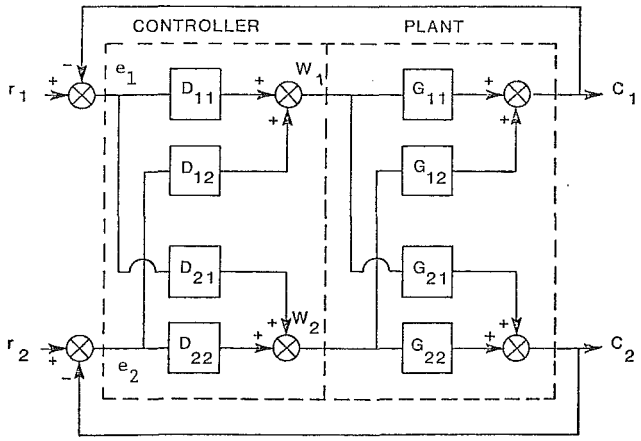


Fig. 1 Two-input/two-output plant and controller with coupling

pressures and temperatures within specified limits. Moreover, it is usually desirable to keep these limits very small. One approach to eliminate interaction is to diagonalize the plant transfer function matrix with a decoupling filter and then use a Proportional-Integral-Derivative controller. A second approach, superior to the first one, uses complete state feedback with integral compensation of the errors but without a decoupling filter. It is referred to as Integral Error plus State Feedback and is an extension or generalization of the Pseudo-Derivative Feedback controller [12].

A comparison is made of the performance of these two feedback control strategies (Proportional-Integral-Derivative versus Integral Error plus State Feedback) for use with multivariable systems to reduce interaction or coupling effects. Comparisons are made for the Proportional-Integral-Derivative controller with and without decoupling filters. Advantages of decoupling are the ability to control one output with one input, and the ability to apply the standard analytical techniques that are available for the study of single-input/single-output systems. Disadvantages of decoupling include: (*i*) the requirement of knowing the plant parameters accurately, since incomplete decoupling may occur and this could reduce disturbance attenuation [13]; (*ii*) possible loss of controllability due to pole cancellation; (*iii*) possible physical unrealizability of the decoupling filter [11].

We consider a specific 2×2 (two inputs, two outputs) plant with dynamic coupling that results in a sixth-order system. It is simulated numerically with CSMP (Continuous Systems Modeling Package) [14] to determine the time response to a step input. While the two control strategies are substantially different, every effort is made to compare them equitably. Feedback gains for the Proportional-Integral-Derivative controller are determined with the aid of the Ziegler-Nichols rules [15] and also through the use of the Integral of Absolute value of Error (IAE) criterion. Feedback gains for the Integral Error plus State Feedback method followed from pole assignment at $s=-25$. Time domain performance characteristics for the controllers are obtained.

The robustness of the two strategies is investigated by changing system time constants 25 percent and, where appropriate, leaving unchanged the decoupling filter to produce a worst-case scenario. The performance of the Integral Error plus State Feedback controller, without a decoupling filter, is found to be significantly superior to the Proportional-Integral-Derivative controller, with or without the decoupling filter, in reducing or eliminating interaction.

Decoupling Filters With Proportional-Integral-Derivative Control

A two-input/two-output multivariable system can be represented in block diagram form as shown in Fig. 1.

In matrix notation, the plant is represented as

$$\{\mathbf{c}\}_{2\times1}=[G]_{2\times2}\{\mathbf{w}\}_{2\times1} \tag{1}$$

and the controller as

$$\{\mathbf{w}\}_{2\times1}=[D]_{2\times2}\{\mathbf{e}\}_{2\times1} \tag{2}$$

where

$$\{\mathbf{e}\}=\{\mathbf{r}\}-\{\mathbf{c}\} \tag{3}$$

Combining the foregoing equations and using unity feedback, the overall transfer function becomes [11]

$$[TF]=[I+[G][D]]^{-1}[G][D] \tag{4}$$

and

$$\{\mathbf{c}\}=[TF]\{\mathbf{r}\} \tag{5}$$

The forward transfer function of the control and plant together is

$$\{\mathbf{c}\}=[G][D]\{e\} \tag{6}$$

When the system is decoupled, the matrix

$$[G][D]=\begin{bmatrix} G_{11}D_{11}+G_{12}D_{21} & G_{11}D_{12}+G_{12}D_{22} \\ G_{21}D_{11}+G_{22}D_{21} & G_{21}D_{12}+G_{22}D_{22} \end{bmatrix} \tag{7}$$

will be diagonal. Thus, by setting the off-diagonal terms equal to zero [13]

$$D_{21}=-\frac{G_{21}D_{11}}{G_{22}} \tag{8}$$

and

$$D_{12}=-\frac{G_{12}D_{22}}{G_{11}} \tag{9}$$

Substituting these into the main diagonal terms of equation (7) yields

$$[G][D]=\begin{bmatrix} \dfrac{[G]D_{11}}{G_{22}} & 0 \\ 0 & \dfrac{[G]D_{22}}{G_{11}} \end{bmatrix} \tag{10}$$

which represents two single-input/single-output forward

Nomenclature

c = plant output
D = control matrix
D_{ij} = element ij of control matrix
e = error signal; $r-c$
G = plant matrix
G_{ij} = element ij of plant matrix
I = identity matrix
K,K_C,K_D = gains
r = control input signal
s = Laplace operator
T_D = rate (derivative) gain
T_I = reset (integration) gain
TF = transfer function
w = control output signal; plant input
{ } = a column vector
[ ]nxn = nxn matrix
| | = the absolute value of a number, or determinant of a matrix
PID = Proportional-Integral-Derivative
IESF = Integral Error plus State Feedback

Downloaded 01 Jun 2010 to 171.66.16.71. Redistribution subject to ASME license or copyright; see http://www.asme.org/terms/Terms_Use.cfm

transfer functions. Each of these resulting transfer functions can be treated separately at this point. One approach to feedback control is the use of Proportional-Integral-Derivative compensation such as shown in Fig. 2. The transfer function of the complete system is

$$\frac{c}{r} = \frac{K_c(1+T_I s+T_I T_D s^2)Gp(s)}{T_1 s+K_c(1+T_I s+T_I T_D s^2)Gp(s)} \tag{11}$$

We note that this control introduces zeros in the transfer function. This contributes to fast response but also may increase the oscillatory behavior of the system and also may increase the settling time. The three gains are selected with the aid of the Ziegler-Nichols rules

$$K_c = \frac{1.2}{RL} \quad T_I = 2\mathrm{L} \quad T_D = 0.5L \tag{12}$$

where R is the maximum slope of a tangent drawn to the unit-step input response of the plant to be controlled, and L is the time at which the tangent intersects the time axis.

Feedback gains are selected also to minimize the Integrated Absolute value of the Error (IAE) to provide another measure of system performance. In general, the gains required to minimize this criterion gave better system performance than those obtained from the Ziegler-Nichols rules.

Integral Error Plus State Feedback Control

The Integral Error plus State Feedback controller is shown in Fig. 3 for a Single Input/Single Output system [12]. The gain $K_D(s)$ may contain derivatives of the output depending upon the order of $G_p(s)$ so that

$$K_D(s) = K_{D1} + K_{D2}s + \ldots\ldots + K_{Dn}s^{n-1} \tag{13}$$

where n is the order of the plant $G_p(s)$. For an nth-order plant there are more than n viable versions of the Integral Error plus State Feedback that permit pole assignment. One version with a single integration is shown in Fig. 3. We note that a similar system could use complete state variable feedback rather than successive derivatives of the output. This would be the preferred approach, because it eliminates the computational problems associated with determining derivatives. A variation of this system, without the integrator but with complete state feedback, gives the optimal linear regulator or servomechanism. Other versions, also referred to as subvariable control [16], include cascaded integrators such as shown in Fig. 4. As more integrators are added, the feedback gains generally must be increased to maintain system response. Sufficiently high gains virtually necessitate the use of Direct Digital Controllers rather than analog devices for satisfactory performance. On the other hand, these cascaded integrators provide robustness, i.e., insensitivity to external disturbances or parameter changes and, most importantly, insensitivity to coupling or interaction effects. The transform of the response for the system in Fig. 3 is

$$c(s) = \frac{KG_p(s)}{s+(D+sK_D(s))G_p(s)}\, r(s) \tag{14}$$

We note that the Integral Error plus State Feedback compensator does not add any zeros to the transfer function. Moreover, this compensator, in its various forms, provides complete pole assignment capability.

Comparison Procedure

The comparison of the control strategies for a multivariable system is based upon a plant transfer function given by Niederlinski [17]

$$[G(s)] = \frac{1}{(1+.1s)(1+.2s)^2} \begin{bmatrix} 1. & \dfrac{2.4}{1+.5s} \\ \dfrac{.5}{1+.1s} & 1. \end{bmatrix} \tag{15}$$

This example was selected because the Ziegler-Nichols rules were used for selecting the Proportional-Integral-Derivative feedback gains for a multivariable system [15].

Comparisons are made for (*i*) Integral Error plus State Feedback control with three cascaded integrators and six

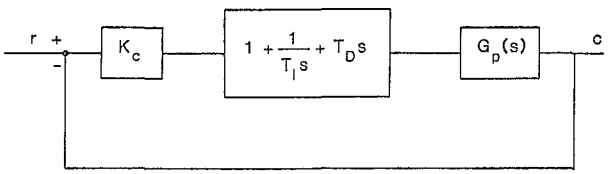


Fig. 2 Single-input/single-output plant with PID (Proportional-Integral-Derivative) control

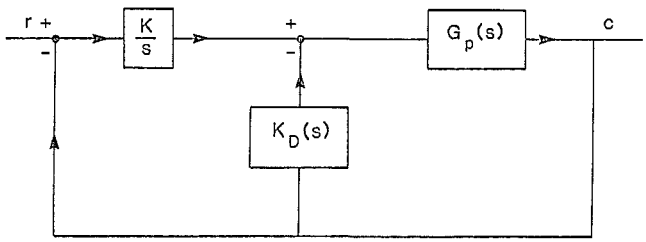


Fig. 3 Single-input/single-output plant with IESF (Integral Error plus State Feedback) control

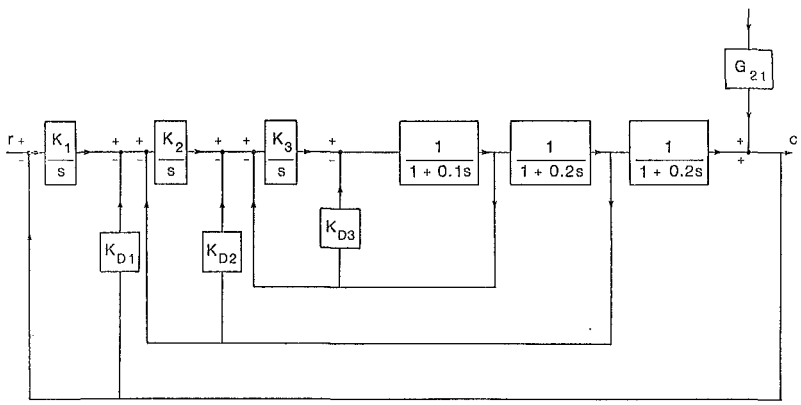


Fig. 4 Three-pole plant with IESF (Integral Error plus State Feedback) control

Downloaded 01 Jun 2010 to 171.66.16.71. Redistribution subject to ASME license or copyright; see http://www.asme.org/terms/Terms_Use.cfm

Table 1 Performance criteria for PID and IESF controllers. Off-design results are for time-constant changes of 25 percent.

Control type	Off-design	Decoupling filter	Gains K_c	T_I	I_D	Rise time	Settling time	Peak overshoot %	IAE r_2/c_1	IAE r_2/c_2
PID Z-N	N	N	6.4	0.364	0.091	0.24	1.36	47	0.211	0.351
	Y	N				0.28	4.25	65	0.675	0.773
	N	Y	6.4	0.364	0.091	0.22	0.76	51	0.0	0.303
	Y	Y				0.26	2.86	75	0.232	0.684
PID Min IAE	N	N	6.4	2.0	0.11	0.28	0.56	7	0.314	0.210
	Y	N				0.32	0.94	16	0.317	0.288
	N	Y	6.4	2.0	0.11	0.26	0.55	10	0.0	0.205
	Y	Y				0.30	1.01	24	0.043	0.299
IESF			$K_1 = 10.82$		$K_{D1} = 1.6$					
	N	N				0.38	0.43	0	3.E-4	0.240
			$K_2 = 112.5$		$K_{D2} = 5.77$					
	Y	N				0.38	0.40	4	3.5E-4	0.260
			$K_3 = 795.0$		$K_{D3} = 13.0$					

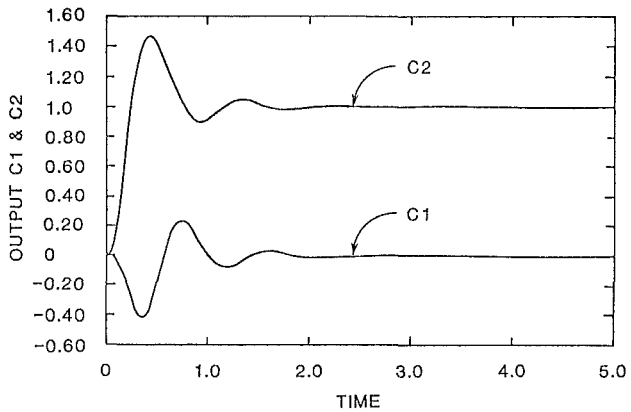


Fig. 5 Response of interacting system with PID (Proportional-Integral-Derivative) control, Ziegler-Nichols gains: unit step input at r_2

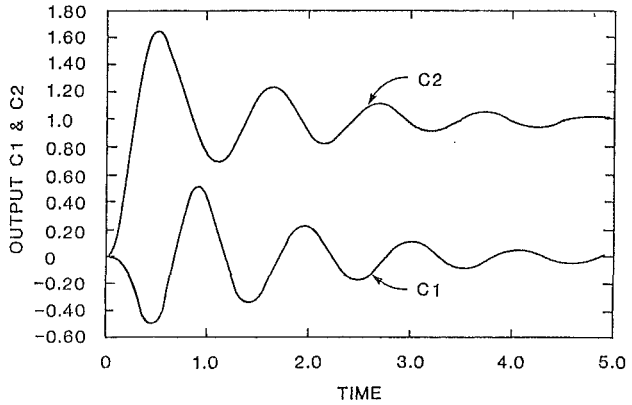


Fig. 7 Response of interacting system with PID (Proportional-Integral Derivative) control, Ziegler-Nichols gains. Plant time constants changed 25 percent. Unit step input at r_2.

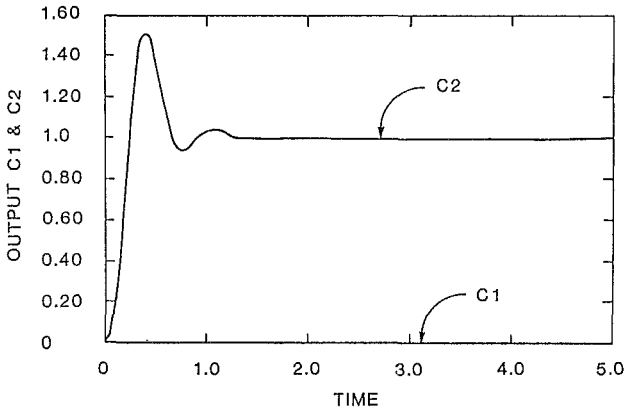


Fig. 6 Response of decoupled system with PID (Proportional-Integral-Derivative) control, Ziegler-Nichols gains: unit step input at r_2

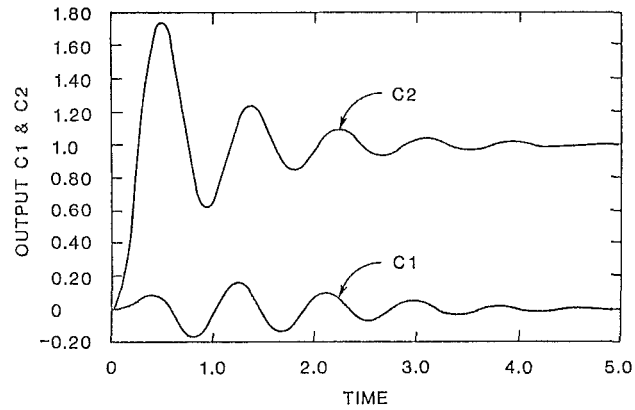


Fig. 8 Response of decoupled system with PID control, Ziegler-Nichols gains. Plant time constants changed 25 percent. Unit step input at r_2.

repeated roots at $s = -25$, (*ii*) Proportional-Integral-Derivative control with Ziegler-Nichols gains, and (*iii*) Proportional-Integral-Derivative control with Integral Absolute value of the Error optimum gains. For cases (*ii*) and (*iii*), comparisons are made also for the system with a decoupling filter and without a decoupling filter. For the first case, decoupling filters are not used because the system performed with almost no interaction without the decoupling filter. Further comparisons are made to determine the effects of changing the plant time constants 25 percent while leaving unchanged the feedback gains and the decoupling gains. This is one way to take into account uncertainties about the plant parameters, modeling inaccuracies, and changes in materials properties due to temperature and aging. This provides an estimate of system robustness. The form of coupling between the two inputs and the two outputs did not permit a direct application of Integral Error plus State Feedback compensation. It was decided therefore to consider the coupling "inputs" as disturbances to two single-input/single-output systems and then use Integral Error plus State Feedback compensation with three cascaded integrators as shown in Fig. 4. The cascaded integrators with complete state variable feedback allows for pole assignment. Response to a unit step input was simulated using the CSMP program [14]. A step input at r_2 was found to be the more severe case and was used in the simulations.

Downloaded 01 Jun 2010 to 171.66.16.71. Redistribution subject to ASME license or copyright; see http://www.asme.org/terms/Terms_Use.cfm

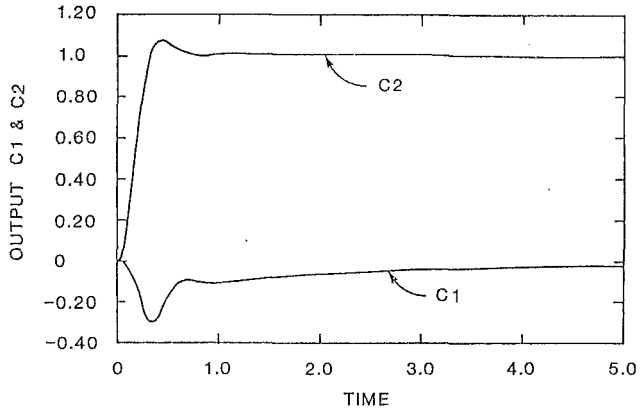


Fig. 9 Response of interacting system with PID control, minimum IAE gains. Unit step input at r_2.

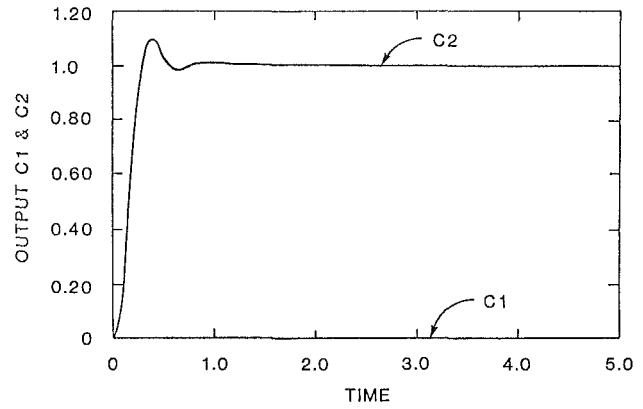


Fig. 10 Response of decoupled system with PID control, minimum IAE gains. Unit step input at r_2.

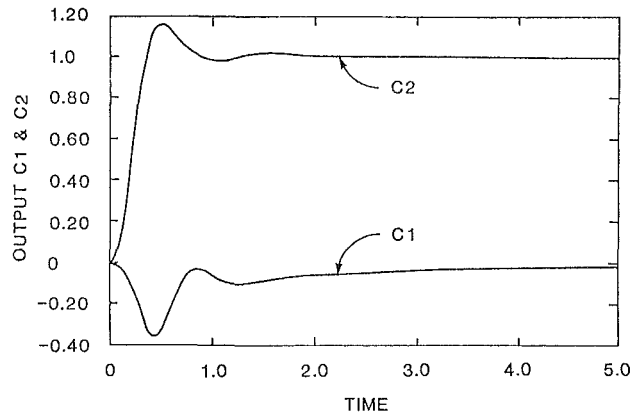


Fig. 11 Response of interacting system with PID control, minimum IAE gains. Plant time constants changed 25 percent. Unit step input at r_2.

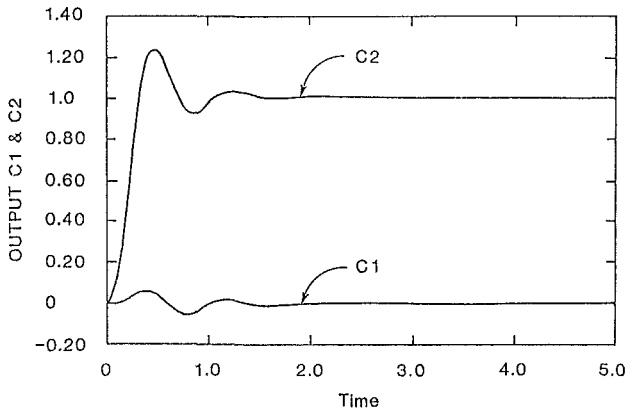


Fig. 12 Response of decoupled system with PID control, minimum IAE gains. Plant time constants changed 25 percent. Unit step input at r_2.

Results

Table 1 contains common measurements of control performance for interacting systems and for decoupled systems with Integral Error plus State Feedback or Proportional-Integral-Derivative compensation. Time-response curves for these cases are presented also.

Proportional-Integral-Derivative Control With Ziegler-Nichols Gains. The gains K_C, T_I, and T_D were determined in [17] for the interacting system. The r_1 and r_2 controllers use the same values. When the decoupling filter is added, two single-input/single-output systems result and the control gains are recalculated. It was found that the new values were only little different from the original ones, but they did not result in better response. We decided to use the original values (interacting control) for both cases. Time response for the interacting case, Fig. 5, shows considerable interaction through c_1 and substantial overshoot for c_2. The addition of the decoupling filter completely decouples c_1 but still allows about the same overshoot for c_2, as shown in Fig. 6. Time constant changes of 25 percent produced significant changes in the time response as shown in Fig. 7 and Fig. 8. In particular the decoupling filter did little to reduce interaction effects. Certainly, the filter was designed for one plant and could not handle changes in the plant. This illustrates one of the difficulties associated with decoupling filters.

Proportional-Integral-Derivative Control for Minimum Integrated Absolute Value of the Error. The Integral of the Absolute value of the Error criterion is

$$\text{IAE} = \int_0^\infty |r - c| \, dt$$

Just as was found with the Ziegler-Nichols case, there was not much difference between optimum gain values of the interacting systems or the decoupled systems. Hence the decoupled optimum values were used with the interacting case.

It should be pointed out that if the Integrated Absolute Value of the Error were used for the disturbance r_1 to c_2 or r_2 to c_1, different optimum values would have resulted. Also there are other integrals [11] such as Integrated Square of Error or Integral of Time multiplied by Absolute Value of Error. We selected the Integral of the Absolute Value of the Error criterion and used it for the Proportional-Integral-Derivative controller. Also, we made IAE calculations for all runs to establish another comparative measure of performance.

Figures 9 and 10 show the time response without and with the decoupling filter, respectively. We note considerable improvement over the cases that used the Ziegler-Nichols gains. Similarly, the interaction and overshoot are changed less for the plant parameter changes as shown in Figs. 11 and 12.

Integral Error Plus State Feedback Control. All state variables are considered to be available for feedback. They are the output of each first-order pole. The gains are selected by assuming two single-input/single-output systems where the original coupling is considered to be a disturbance. The six gains were selected to assign the six poles on the real axis at $s = -25$. Decoupling filters are not used. Time responses, Figs. 13 and 14, show that interaction is virtually nonexistent

Downloaded 01 Jun 2010 to 171.66.16.71. Redistribution subject to ASME license or copyright; see http://www.asme.org/terms/Terms_Use.cfm

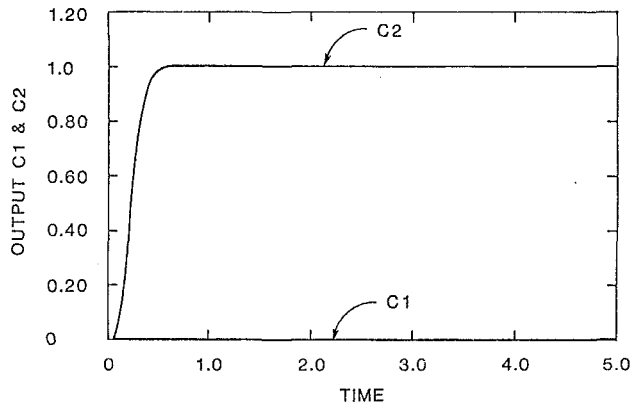


Fig. 13 Response of coupled system with IESF control. Unit step input at r_2.

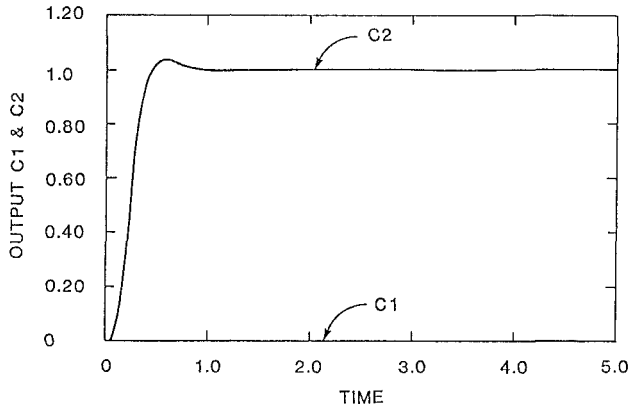


Fig. 14 Response of coupled system with IESF control. Plant time constants changed 25 percent. Unit step input at r_2.

and off-design performance was little changed from the original case. We have achieved noninteracting response through the use of cascaded integrators and state variable feedback and without the use of decoupling filters.

Discussion

A control algorithm based on state variable feedback and cascaded integrators has been shown to eliminate or substantially reduce interaction in multivariable systems with significant coupling. Decoupling filters are not required. Moreover, the system performs well even when the plant time constants are changed 25 percent. Numerical simulations show the superiority of this approach over the Proportional-Integral-Derivative controller.

The algorithm permits complete freedom in pole assignment. For low-order systems, this is a straightforward exercise, but as the order increases beyond eight or ten, the algebraic operations, e.g., determinant expansion, become burdensome. Much of this tedious activity can be eliminated, however, with one of the algebraic manipulation languages. The author has found REDUCE (University of Utah) to be very useful. SCRATCHPAD (IBM) and MACSYMA (Symbolics, Inc.) are also available with additional features.

In an earlier paper [18], the author has shown that this control algorithm permits state variable and control variable inequality constraints to be realized through error signal compensation. Moreover, this is achieved within a linear framework with gain scheduling.

Acknowledgment

This work, based upon the first author's M.S. thesis, was supported in part by ONR Grant N00014-83-K-0064.

References

1 Anderson, B. D. O., and Moore, J. B., *Linear Optimal Control*, Prentice-Hall, Englewood Cliffs, N.J., 1971.

2 Athans, M., Dertouzos, M. L., Spann, R. N., and Mason, S. J., *Systems, Networks, and Computation: Multivariable Methods*, McGraw-Hill, New York, 1974.

3 Callier, F. M., and Desoer, C. A., *Multivariable Feedback Systems*, Springer-Verlag, New York, 1982.

4 Chen, C. T., *Introduction to Linear System Theory*, Holt, Rinehart, and Winston, New York, 1970.

5 Foss, A. M., "Multivariable Limit Control With Application to Gas Turbines," Ph.D. thesis, London University, 1981.

6 Fossard, A. J., *Multivariable System Control*, North Holland Publishing Company, Amsterdam, 1977.

7 Hung, Y. S., and MacFarlane, A. G. J., *Multivariable Feedback, A Quasi-Classical Approach*, Springer-Verlag, Berlin, 1982.

8 Owens, D. H., *Multivariable and Optimal Systems*, Academic Press, London, 1981.

9 Patel, R. V., and Munro, N., *Multivariable System Theory and Design*, International Series on System and Control, Vol. 4, Pergamon Press, Oxford, 1982.

10 Safonov, M. G., *Stability and Robustness of Multivariable Feedback Systems*, MIT Press, Cambridge, Mass., 1980.

11 Takahaski, Y., Rabins, M. J., and Auslander, D. M., *Control and Dynamic Systems*, Addison-Wesley, Reading, Mass., 1970.

12 Phelan, R. M., *Automatic Control Systems*, Cornell University Press, Ithaca, N.Y., 1977.

13 Niederlinski, A., "Two-Variable Distillation Control: Decouple or Not Decouple," *AI Ch E Journal*, Vol. 17, No. 5, 1971, pp. 1261-1263.

14 "Continuous Systems Modeling Program (CSMP)," Program No. 5734-X59, IBM.

15 Ziegler, J. G., and Nichols, N. B., "Optimum Settings for Automatic Controllers," ASME *Transactions*, Vol. 64, 1942, pp. 759-768.

16 Phelan, R. M., *Subvariable Control*, copyright 1981.

17 Niederlinski, A., "A Heuristic Approach to the Design of Linear Multivariable Interacting Control Systems," *Automatica*, Vol. 7, 1971, pp. 691-701.

18 Maday, C. J., "Synthesis and Design of Feedback Control Systems for Time Response I," presented at the 1984 American Control Conference, San Diego, CA, June 6-8, 1984.

Downloaded 01 Jun 2010 to 171.66.16.71. Redistribution subject to ASME license or copyright; see http://www.asme.org/terms/Terms_Use.cfm

Fiber Optics for Propulsion Control Systems

R. J. Baumbick
National Aeronautics and Space Administration, Lewis Research Center, Cleveland, Ohio 44135

The term "fiber optics" means the use of dielectric waveguides to transfer information. In aircraft systems with digital controls, fiber optics has advantages over wire systems because of its inherent immunity to electromagnetic noise (EMI) and electromagnetic pulses (EMP). It also offers a weight benefit when metallic conductors are replaced by optical fibers. To take full advantage of the benefits of optical waveguides, passive optical sensors are also being developed to eliminate the need for electrical power to the sensor. Fiber optics may also be used for controlling actuators on engine and airframe. In this application, the optical fibers, connectors, etc., will be subjected to high temperatures and vibrations. This paper discusses the use of fiber optics in aircraft propulsion systems, together with the optical sensors and optically controlled actuators being developed to take full advantage of the benefits which fiber optics offers. The requirements for sensors and actuators in advanced propulsion systems are identified. The benefits of using fiber optics in place of conventional wire systems are discussed as well as the environmental conditions under which the optical components must operate. Work being done under contract to NASA Lewis on optical and optically activated actuators sensors for propulsion control systems is presented.

Introduction

Fiber optics offers potential improvements in reliability over conventional wire systems in aircraft applications. The term fiber optics as used herein means the use of dielectric waveguides to transfer optical signals from one point to another. The complete optical circuit consists of a light source, photodetector, optical connectors, optical waveguide and a device that either modulates the optical signal or uses it to accomplish some other task such as activation of an actuator.

This paper discusses the requirements of sensors and actuators needed on future propulsion control systems. The requirements for optical components are also included in this discussion. The benefits of using fiber optics over conventional wire systems are listed and the work sponsored by NASA Lewis Research Center to develop fiber optics and optical sensors for use in propulsion control systems is discussed.

Requirements

Figure 1 illustrates sensors and actuators that might be required for a supersonic propulsion system. In general, the sensor and actuator requirements will depend on the type of propulsion system being considered. For example, commercial propulsion systems will be different than military systems and supersonic operation will result in different requirements than subsonic operation. Parameters that might be measured in the inlet are pressures to determine terminal shock position and position measurements to identify spike position and bypass door position. For the engine, pressures are measured to control engine steady-state operation. Speed measurements and rate of change of engine speed are needed to control engine acceleration. Speed and turbine inlet temperatures are measured to guard against overspeed and overtemperature. Inlet conditions at the compressor are required measurements to optimize engine geometry. Position measurements are required to monitor and control the variable geometry of the compressor and turbines in order to insure optimum engine operation. Also, in some instances, tip clearance measurements and control may be required to improve engine operating efficiency.

The following discussion describes current design practice for electronic control systems. Pressure sensors are usually located in the electronics box to minimize the temperature effects on the pressure measurements. Pressure from the engine is brought to these sensors via pneumatic tubes. Temperature sensors are usually thermocouples located on the engine. Electrical wires connect the sensors to the computer module. Position measurements are made with linear variable displacement transducers which require electrical excitation at the transducers. Electrical signals are received from these position sensors and processed in the computer module. Speed measurements are usually made with a magnetic pickup and the resultant frequency signals are transmitted to the control via electrical conductors. The actuators are driven by two-stage electrohydraulic servovalves. The first stage of the servovalve is a torque motor which receives electrical energy

Contributed by the Gas Turbine Division of THE AMERICAN SOCIETY OF MECHANICAL ENGINEERS and presented at the 29th International Gas Turbine Conference and Exhibit, Amsterdam, The Netherlands, June 4–7, 1984. Manuscript received at ASME Headquarters January 9, 1984. Paper No. 84-GT-97.

Copyright © 1985 by ASME
Downloaded 01 Jun 2010 to 171.66.16.71. Redistribution subject to ASME license or copyright; see http://www.asme.org/terms/Terms_Use.cfm

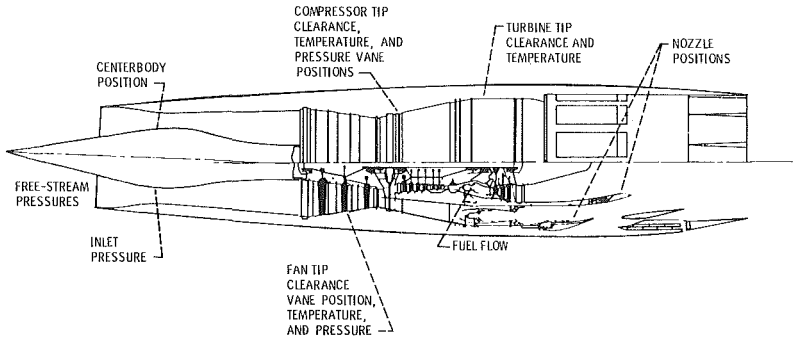


Fig. 1 Inlet/engine measurements for control and monitoring

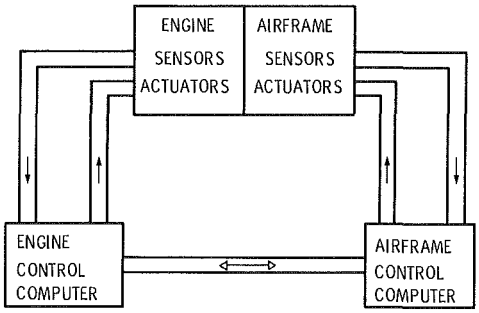


Fig. 2 Optical circuits in aircraft systems

from the computer. The torque motor drives a higher power hydraulic stage which in turn operates the actuator.

Current configurations use FET switches located in the electronic control to control current to actuator torque motors. As the number of servovalve interfaces increase on future engines, heat dissipation in the electronic control poses a potential problem. Moving the drive switches outside the electronic box reduces the heat dissipation requirements. To withstand the high temperatures, gallium arsenide is used as the active material in the switch circuit components.

The use of fiber optics in place of electrical components offers potential improvement in reliability because of optic's inherent immunity to EMI, EMP, and lightning. Fiber optics eliminates the threat of fires on aircraft because of electrical insulation failures as well as the threat of short circuits which can cause inadvertent actuation of critical control components. Two additional advantages of fiber optics are weight reduction, when fiber optics replaces metallic conductors, and easily implementable redundant circuits.

Since future aircraft materials are likely to be mostly composite, rather than metallic, isolation of the electronic computer from lightning effects and other EMI sources will depend on the type of cables used to transfer signals between the computer, sensors, and actuators. With conventional wire systems, electrical transmission lines must be well shielded and surge quenching circuits must be provided to protect the computer from the effects of lightning. Electrical insulation deteriorates due to weather extremes and contact with fuel, cleaning solvents, and in certain cases, salt spray. The insulation cracks, frays, and is embrittled. This breakdown of the insulation can cause fires and short circuits. Fiber-optic cables can eliminate these problems.

Figure 2 illustrates the different optical circuits that could be used in aircraft applications. Fiber-optic waveguides can link the computer of the airframe and propulsion system with their respective optical sensors and actuators which are to be controlled with optical signals. For integrated control of airframe and propulsion system the two computers can be linked via fiber optics.

Since most initial applications involving fiber optics were for land communication lines operational reliability in severe engine environments was not of concern. More work is required to strengthen the resistance to heat of both sources and detectors so that they can operate in a higher temperature environment. Temperatures in the electronics box are usually maintained at 100°C or less. Rugged optical connectors that can be disconnected and reconnected repeatedly need to be developed and evaluated.

Sensors

The number of concepts for measuring physical parameters, such as pressure, temperature, and vibration using optics has increased dramatically in the past few years because of advances made by the communication industry in the area of fiber optics, integrated optical circuits, sources and detectors. Optical parameters such as phase, intensity, wavelength, and polarization are used to measure physical parameters such as pressure, temperature, position, magnetic fields, and electrical current. Many concepts have been demonstrated in the laboratory and some prototypes have been built and tested. Optical sensors to measure acoustic pressure and magnetic fields using phase modulation are well documented as are amplitude modulating sensors for measuring temperature. Various schemes are compared in [1] and [2].

The technology of optical encoders and tachometers is a mature technology compared to the other types of optical sensors, although significant developments are needed to integrate these components into engine control systems. A passive optical encoder and optical tachometer were the first sensors built for Lewis and tested on an engine in an altitude facility. These sensors were not packaged for mounting on a flight engine but rather represented prototypes which demonstrated remote operation of these sensors [3].

When compressor and turbine blade tip clearances are excessive, component performance and efficiency are adversely affected. To decrease this loss, closed-loop or open-loop tip clearance control can be used. Tip clearance measurements are required for closed-loop control or for monitoring purposes.

An optical sensing scheme for measuring tip clearances, shown in Fig. 3, was built and tested in the laboratory by General Electric under contract to NASA Lewis. Fiber-optic bundles direct light to the sensor and carry the modulated signal to the detectors. Light from the input bundle is directed across the gap between the engine case and blade tips and is imaged onto a coherent output bundle which transmits the signal to the detector array. As the blade intercepts part of the light beam directed between the source and detector fibers, light that normally would fall on the detector bundle is blocked. Blade clearance is determined by the position of the boundary between light and dark areas on the detector array. The laboratory tests on the tip clearance sensor were con-

Downloaded 01 Jun 2010 to 171.66.16.71. Redistribution subject to ASME license or copyright; see http://www.asme.org/terms/Terms_Use.cfm

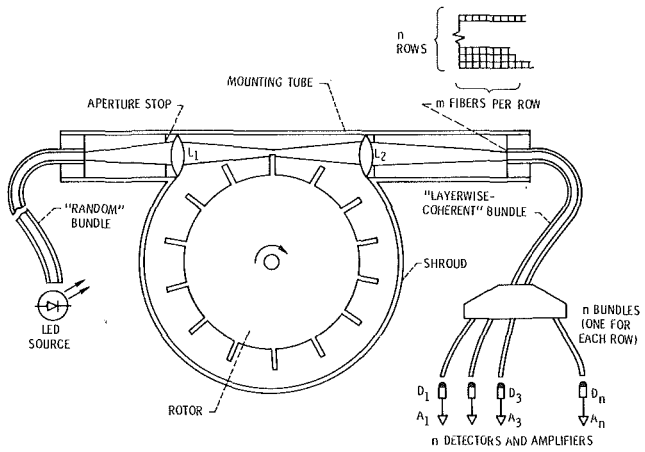


Fig. 3 Optical tip clearance sensor

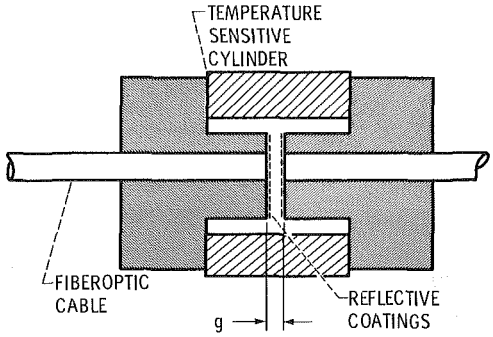


Fig. 4 Temperature sensitive gap for use in Fabry-Perot temperature sensor

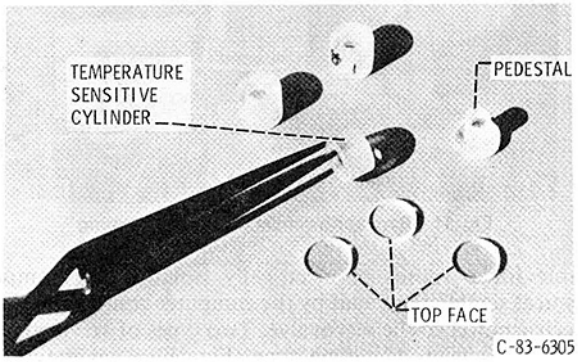


Fig. 5 Temperature sensitive Fabry-Perot sensor

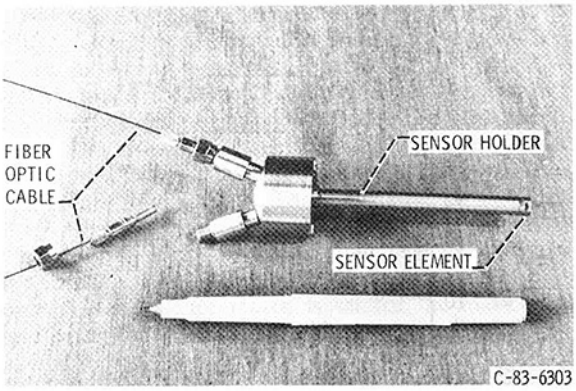


Fig. 6 Assembled Fabry-Perot temperature sensor

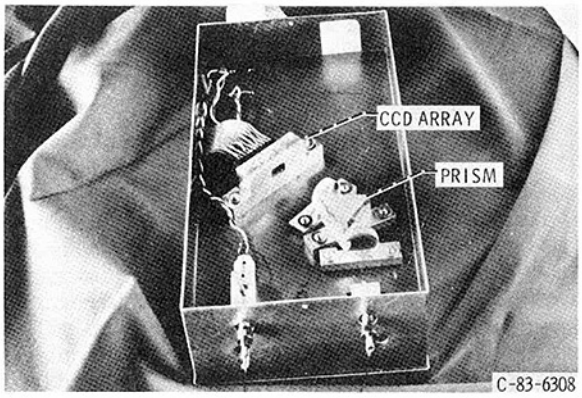


Fig. 7 Electro-optics for Fabry-Perot

ducted with a compressor rotor stage driven by an electric motor [4].

One concept for measuring engine gas temperature using optical techniques is the Fabry-Perot interferometer. The Fabry-Perot sensor produces spectral amplitude modulation using multiple interference of a broad band input spectrum. The modulation is related to the resonator thickness, which in turn is a function of temperature. A temperature sensitive cylinder controls the spacing between two parallel mirrored surfaces whose faces are partially transmitting and partially reflecting as shown in Fig. 4. The Fabry-Perot principle provides for multiple reflections between mirrored surfaces. The maximum transmitted intensities occur at wavelengths for which the resonator gap ($g = N\lambda/2$), where N is the order of interference.

Figure 5 is a photograph of the Fabry-Perot sensing element. The pedestal is constructed of ultra-low expansion silica material. The temperature-sensitive expansion element is made of silica as is the end cap. In this prototype model, the Fabry-Perot element is held in the sensor holder by a spring. The input and output fibers are shown installed in the Fabry-Perot element. Ceramic cement is used to hold the fibers in the sensing element. The assembled sensor is shown in Fig. 6.

Figure 7 shows the electro-optics box. The electronics are located on the bottom side of the box. Shown in the figure are the light source (on left) and the receiver fiber on the right side. In the current prototype model and incandescent bulb (similar to one used in medical applications) is used to produce a broad band light source. The modulated signal returns on the right hand fiber, is collimated by the first lens and directed through a prism, where the wavelengths are spread out and focused on the CCD element by the second lens. The dispersed spectrum is focused on the face of a 128-element linear CCD array. The output from the CCD array is converted to 128, 8-bit digital words and fed into a microprocessor. Algorithms are then used to determine the maximum intensity wavelengths, which are then correlated to resonator gap thickness and hence temperature. This sensor was built by OPCOA, Inc. (Anaheim, Calif.) under contract to NASA Lewis. This sensor has been tested up to 1000° C.

Another sensor measures temperature by measuring the change in light intensity as it passes through a rare-earth material. This sensor was developed by United Technologies Research Center under contract to NASA Lewis. Rare-earth materials were chosen for the sensor because they have numerous absorption lines in the visible and near IR spectrum. Absorption lines result from optical transitions originating in the electronic ground state of the ion and from low-lying excited states. The population distribution of ions is a function of temperature. The strength of the absorption is proportional to the populations of ions in the state from which the absorbing transition originates.

Figure 8 shows some of the energy levels of europium. Absorption peaks arise from the transition from the low-lying states to the 5_{d0} and 5_{d1} states. The expected distribution of ions in the lower states as a function of temperature is shown in Fig. 9. The population of the ground state N_0 decreases

Downloaded 01 Jun 2010 to 171.66.16.71. Redistribution subject to ASME license or copyright; see http://www.asme.org/terms/Terms_Use.cfm

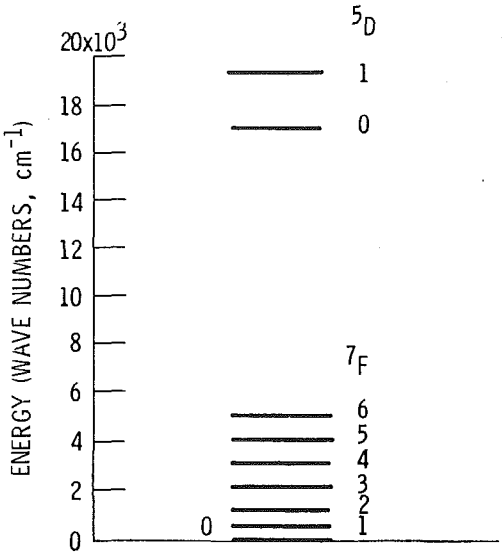


Fig. 8 Energy level diagram for europium in glass

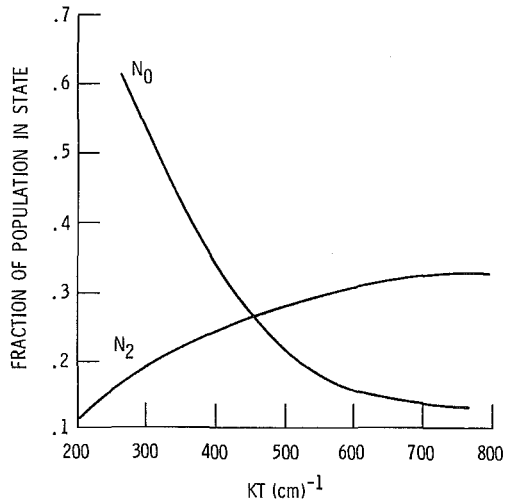


Fig. 9 Population of ground states of Eu^{3+}

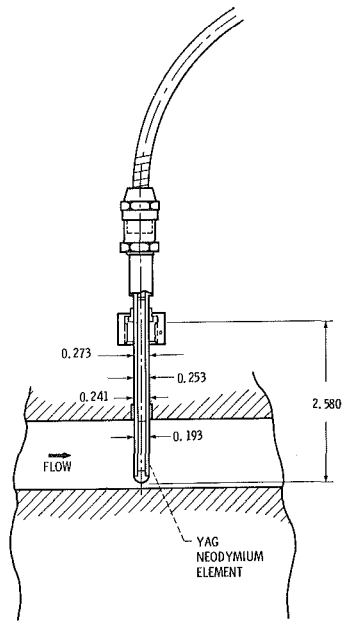


Fig. 10 Rare-earth temperature probe

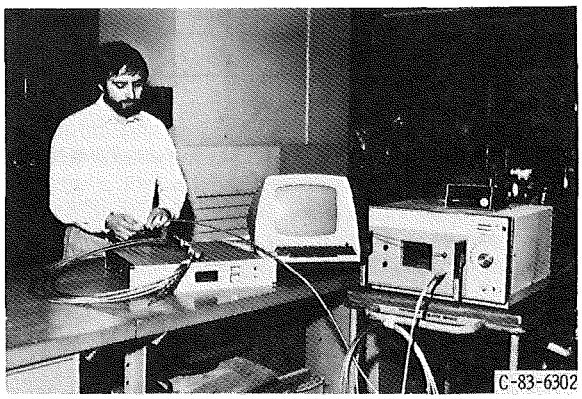


Fig. 11 Rare-earth sensor acceptance testing

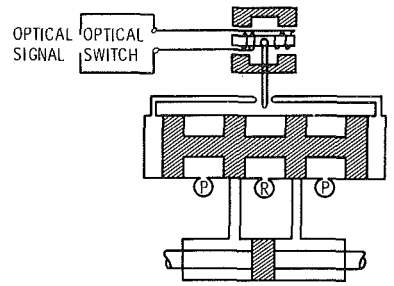
with temperature. The 7_{F2} state (N_2) shows a population that increases with temperature. Absorption lines that originate in this state would increase in strength as temperature increases. The physical configuration of this rare-earth sensor is shown in Fig. 10. This configuration uses aluminosilicate glass doped with neodymium as the sensing element. A sensor using this configuration has been designed for testing in a turboshaft engine between the gas generator turbine and power turbine. To separate the temperature-dependent absorption from cable and connector losses, a second wavelength, at which the change in intensity is temperature-independent, is used to factor out the losses in the cable/connectors. The sensor to be installed in the engine is shown in Fig. 11 undergoing acceptance tests in the laboratory. The optical cable is enclosed in a braided metal tube to protect it during engine installation.

Pressure sensing using fiber optics is also being investigated. Concepts that are being considered for use in measuring pressure are microbending and photo elastic effect. Both of these sensors are intensity measuring sensors. These sensors must be relatively temperature insensitive. A material study is also being conducted to minimize temperature effects on the force transmitting member of the pressure sensor.

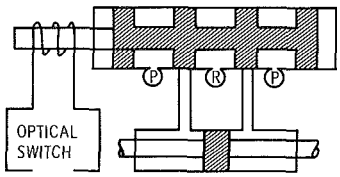
Actuators

Actuators will be connected to the computer by fiber-optic cable for purposes of electrically isolating the computer. Optical signals generated by the computer control the flow of electric power to the servovalve. Two types of servovalves are considered (Fig. 12). One type (Fig. 12(*a*)) is a two-stage servovalve which has a low-power torque motor (60 mw) which drives a higher-power spool valve. The spool valve controls the flow of hydraulic power to the actuator. The second type (Fig. 12(*b*)) is a direct-drive valve which has no low-power stage. The spool valve is driven directly by a torque motor. This configuration requires much more power (50 W) to operate than does the two-stage valve. The direct-drive valve eliminates the low-power stage with its potential for plugging because of contaminants in the fluid. There were two configurations considered for the optical circuit in a program done at UTRC for NASA Lewis (Fig. 13). In one, an optical link would be used to control the flow of electrical energy to the torque motor. The electrical power supply is connected to the torque motor through a JFET power transistor. The gate of the power JFET is connected to the circuit containing the phototransistor. When an optical signal is applied to the phototransistor the JFET turns on, allowing current to flow to the torque motor. This concept can be applied to either the two-stage or direct-drive servovalve. The configuration illustrated in Fig. 13(*a*) was built and tested over the temperature range −55 to 260° C. The switch was designed to switch 100 ma with an off state voltage of +20 V. For the direct drive valve, the switched current would be considerably

Downloaded 01 Jun 2010 to 171.66.16.71. Redistribution subject to ASME license or copyright; see http://www.asme.org/terms/Terms_Use.cfm

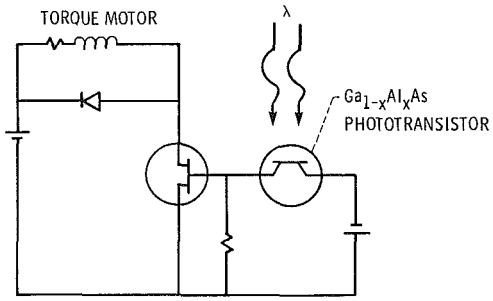


(a) Fly by light two stage servovalve.

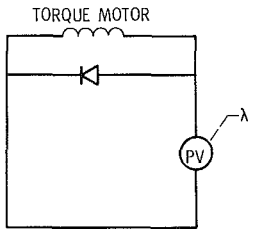


(b) Fly by light direct drive valve.

Fig. 12 Optical actuation of servovalves



(a) Light on, power switch off.



(b) Power by light.

Fig. 13 Optical circuit configurations for actuators

higher (1 amp). In either case the electrical energy is developed locally, at the point of use. Various schemes to generate this electrical power have been proposed. Included in these concepts are the use of piezolectric stacks, photovoltaic cells, photomechanical techniques, and hydraulically driven electric driven generators. The hydraulic electric generator contains a small hydraulic motor that can be operated from the aircraft hydraulic power supply. This latter concept can develop relatively large amounts of electrical power, enough to operate the direct drive valve.

The second configuration is illustrated in Fig. 13(*b*) and is called power-by-light, because whatever power is required to operate the torque motor is converted directly from optical power. This scheme does not require locally generated power. The power conversion can be accomplished a number of ways. One scheme uses photovoltaic cells to convert the optical energy directly to electrical energy. Since the power requirements are considerably larger for the direct-drive valve, the power by light system was considered only for use with the two-stage servovalve. If system efficiency is to be optimized for the photovoltaic case an active impedance matching device between the torque-motor load and photovoltaic cells must be provided which will compensate for temperature induced impedance changes. The system would be too complex, and the impedance matching technique wasn't pursued any further. The alternative to impedance matching over the range of operating temperatures (55 to 260°C) is to consider impedance matching of the torque motor and photovoltaic cell only at one temperature. In this approach the impedance match is set for the highest temperature since the power output of the photovoltaic cells is lowest at the high temperature. Because of the high temperature requirement, a number of photovoltaic cells are required for impedance matching. If the highest temperature is reduced to approximately 150°C instead of 260°C, the number of photovoltaic cells needed for an impedance match are reduced by a factor of 1/2. However, the overall system efficiencies for the photovoltaic system are extremely poor with today's technology.

Cable and Connectors

The development of rugged, reliable optical cables and connectors for aircraft installation is needed before fiber optics can be considered as a replacement for electrical wires. An optical cable made of glass core and cladding usually has a buffer material applied to the cladding to protect the optical fiber. The buffer material commonly used breaks down at temperatures above 125°C. To accommodate temperatures that will be encountered in an aircraft environment the buffer material will have to operate over −55 to 260° C. Current research on buffer material indicates that polyimides or silcone with teflon jackets have potential for a durable buffer coating on cables.

Discussion

Fiber optics in aircraft systems has potential for improving the reliability of the overall electronic control system because of its immunity to EMI, EMP, and lightning effects. In addition, fiber optic waveguides eliminate the potential of fire and short circuits caused by corrosion of the electrical insulation.

To fully utilize the benefits of fiber optics, research into passive optical sensors and optically activated actuators was initiated by NASA Lewis. This would completely eliminate the need for electrical wires and thereby divorce the engine control computer from any sources of disturbances due to EMI, EMP or lightning.

Before fiber optics can fully replace wire systems in aircraft, reliability of all components from light sources and detectors to optical connectors and fiber optic wave guides must be assured. The optical cables and connectors will have to operate reliably over a −55 to 260°C temperature range. In addition, engine test experience must be obtained and optical system integration, including packaging, must be fully addressed.

References

1 Giallorenzi, T. G., et al., "Optical Fiber Sensor Technology," *IEEE Journal of Quantum Electronics*, Vol. QE-18, No. 4, Apr. 1982, pp. 626–665.

2 Harmer, A. L., "Optical Fibre Sensors and Instrumentation: a Review," *Advances in Electronic Components and Systems, Proceedings of the 11th Seminex '82 Conference, London, England*, Benn Electronics Publications, Luton, Beds., England, 1982, pp. 229–244.

3 Baumbick, R. J., "Fiber Optic Sensors for Measuring Angular Position and Rotational Speed-Air Breathing Engines," NASA TM-81454, 1980.

4 Poppel, G. L., Marple, D. T. F., and Baumbick, R. M., "Optical Tip Clearance Sensor for Aircraft Engine Controls," AIAA Paper No. 82-1131, June 1982.

Downloaded 01 Jun 2010 to 171.66.16.71. Redistribution subject to ASME license or copyright; see http://www.asme.org/terms/Terms_Use.cfm

Cool Water Coal Gasification—a Progress Report

D. R. Plumley
Gas Turbine Division,
General Electric Company,
Schenectady, NY

On May 20, synthetic gas made by gasifying coal was burned in a commercial size gas turbine in Daggett, CA and the electricity produced from that coal flowed into the Southern California Edison system. This event marked the initial operational phase of the Cool Water Coal Gasification Program that expects to demonstrate that the integrated coal gasification combined cycle (IGCC) power plant can burn coal in an environmentally superior manner while also meeting a utility system's operational and reliability requirements.

Background

In the mid to late 1970s, a number of studies concluded that the integration of the world's most efficient power plant—the combined cycle—and an environmentally superior process for removing sulfur from coal before combustion promised a very attractive option for utility and industrial power generation. Even though a number of privately and publicly funded studies had reached this conclusion, it was also clear that unless and until such a plant operated successfully at commercial scale, there was little likelihood of ever realizing the advantages of these two systems (Fig. 1). It is fortunate, then, that in 1979 the Southern California Edison Company (SCE) and Texaco, Inc., initiated the Cool Water Coal Gasification Program (CWCGP) because their program objectives (Fig. 2) were exactly those needed to prove the concept of coal gasification. These two original partners in the program were joined by the Electric Power Research Institute (EPRI), the Bechtel Corporation, the General Electric Company, a consortium of Japanese companies (Tokyo Electric Power Company, Ishikawagima Harima, Toshiba and CREIPI), and two contributors, ESSERCO and Sohio.

Detailed engineering began in February 1980 (Fig. 3) with on-site construction beginning in January 1982 after the completion of final program funding in December 1981. Because of the decline in world oil prices and the subsequent impact on operating revenues which were tied to Southern California Edison's costs for producing the power elsewhere on their system (avoided costs), the program sought and obtained a price support agreement from the Synthetic Fuel Corporation (SFC) in July 1983. This agreement, the first awarded by the SFC, will provide price support up to a maximum of $120 million for the production of synthetic gas during the first five years of operation.

Construction ended on April 1, 1984, and the first gas was generated on May 7, a full 25 days ahead of the schedule established in December 1981. From June 13 to June 26, the plant operated continuously for almost 13 days. The 10-day SFC acceptance test was completed at 0948 hours on June 23, 1984 and the program is now in its operational phase.

Cycle Configuration

The arrangement of the major plant components is shown in Fig. 4. Unit trains deliver coal to the plant, where it is unloaded from each hopper car and conveyed to storage. The coal is then crushed and ground to the required size, slurried with water, and fed to the refractory-lined gasifier. At a

- EQUIVALENT INSTALLED COSTS
- AT LEAST 10% BETTER EFFICIENCY
- HIGHER CAPACITY FACTORS: 5-10 POINTS
- LOWER RESERVE MARGIN REQUIREMENTS
- LOW NO_x, 99% SULFUR REMOVAL, BENIGN WASTE
- 30% LESS WATER, 50% LESS LAND REQUIRED
- PART LOAD HEAT RATES MUCH BETTER
- SHORTER CONSTRUCTION CYCLES/PHASED INSTALLATION

RESULT - LOWER COST OF ELECTRICITY

Fig. 1 Advantages of IGCC

- CONFIRM COMMERCIAL SCALE OPERATION WITH A VARIETY OF GOALS
- DEMONSTRATE OPERATING COMPATIBILITY WITH UTILITY SYSTEMS
- ASSESS SYSTEM RELIABILITY AND AVAILABILITY
- DEVELOP OPERATING AND MAINTENANCE PROCEDURES
- ESTABLISH ECONOMIC BASE FOR FUTURE COMMERCIAL PLANTS

Fig. 2 Cool Water Program objectives

• ENGINEERING STARTED	FEBRUARY 1980
• PROGRAM FUNDING COMPLETE	DECEMBER 1981
• CONSTRUCTION BEGUN	JANUARY 1982
• COMBINED CYCLE SHIPPED	NOV./DEC. 1982
• $120M SFC PRICE SUPPORT	JULY 1983
• GASIFIER/SYNGAS COOLERS SHIPPED	SEPTEMBER 1983
• FIRST GAS MADE	MAY 7, 1984
• GAS TURBINE ON SYNGAS	MAY 20, 1984 (5 h)
• COMBINED CYCLE ON SYNGAS	MAY 31 - JUNE 3 (95 h)
• SFC ACCEPTANCE TEST COMPLETED	JUNE 13 - JUNE 26 (13 DAYS)

Fig. 3 Cool Water Program

Contributed by the Gas Turbine Division of THE AMERICAN SOCIETY OF MECHANICAL ENGINEERS and presented at the 30th International Gas Turbine Conference and Exhibit, Houston, Texas, March 18–21, 1985. Manuscript received at ASME Headquarters, December 21, 1984. Paper No. 85-GT-55.

Copyright © 1985 by ASME
Downloaded 01 Jun 2010 to 171.66.16.71. Redistribution subject to ASME license or copyright; see http://www.asme.org/terms/Terms_Use.cfm

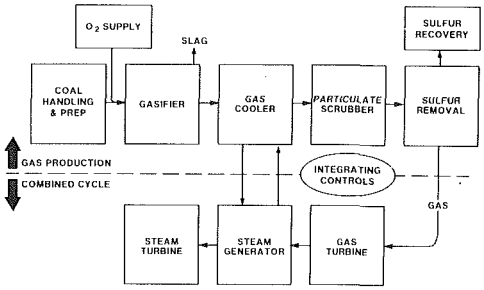


Fig. 4 The Cool Water plant configuration

	UNTREATED GAS MOL. %*	CLEAN GAS MOL. %*
CO	41.34	43.53
H_2	36.38	38.33
CO_2	21.42	17.39
CH_4	0.10	0.11
Ar	0.16	0.17
N_2	0.44	0.47
H_2S	0.15	15 PPM
COS	0.01	55 PPM
HEATING VALUE (Btu, SCF)		265.2

* DRY BASIS

Fig. 5 Gas analysis for Cool Water Program coal

POWER PLANT EMISSIONS
lb/10^6 Btu OF COAL INPUT

	COOL WATER DESIGN CAPABILITY	SITE LIMITS	CONVENTIONAL STEAM-NSPS
SO_2	0.35	0.2	0.35
NO_X	< 0.14	0.14	0.6
PARTICULATE	< 0.01	0.01	0.03

BASED ON 0.7% S COAL

Fig. 6 Cool Water environmental impact

pressure of 600 psig (4,136,854.2 Pa) and at temperatures between 2300°F (1200°C) and 2800°F (1500°C) in the gasifier, the coal and water are reacted with oxygen, producing a raw synthesis gas (syngas). This syngas, consisting primarily of hydrogen (H_2), carbon monoxide (CO), carbon dioxide (CO_2), and steam, has a heating value of 260–280 Btu-scf (9700–10,400 kJ/m^3). During gasification the coal ash is melted into slag, quenched with water, and removed through a pressurized lockhopper system. The syngas produced is cooled in the radiant and convection gas coolers to produce saturated steam [which will be superheated in the combined cycle unit heat recovery steam generator (HRSG)], thus recovering and utilizing much of the process waste heat.

The syngas passes through the particulate scrubber to remove particulates and is then cooled to near ambient temperature prior to sulfur removal. Sulfur compounds, consisting primarily of hydrogen sulfide (H_2S), are removed in a Selexol physical solvent sulfur removal system. The sulfur recovery system receives the H_2 stream from the sulfur removal unit and converts it to elemental sulfur, which is sold. The clean syngas leaving the sulfur removal system is delivered to the General Electric Combined Cycle after saturation with water for NO_x suppression.

The combined cycle generating system includes a gas turbine generating unit of approximately 65 MW capacity. The gas turbine was designed to operate primarily on the coal gas although provisions are made for firing diesel fuel oil during startup. The 55-MW steam turbine is operated on superheated steam (1350 psia, 950°F) produced in the heat recovery steam generator utilizing the hot exhaust gas from the gas turbine, thereby increasing the overall efficiency of the integrated gasification-electric generation system.

Gas Composition

Figure 5 indicates typical fuel-gas composition. The syngas produced from this oxygen-blown, high-temperature gasification process is a very good gas turbine fuel. It exhibits a broad flammability and turndown range due to the high hydrogen content of over 30%. The gas heating values range between 260–280 Btu (9700 and 10,400 kJ/m^3) and do not represent a technical obstacle for use in the combustion systems of General Electric gas turbines.

The absence of alkali metals or other corrosive containments offers not only longer component life, but the potential for the continued development of higher temperature turbine technology without the design and fouling constraints imposed when operating with low-quality fuels such as residual and heavy oils.

The flame temperatures experienced with this fuel are somewhat higher than those for natural gas or oil and they aid in ensuring complete combustion of the large carbon monoxide constituent. The resulting higher levels of thermal NO_x can be readily controlled by several known and proven techniques.

Environmental Implications

Extensive testing of the Texaco coal gasification process has shown that the various effluent gas, liquid, and solid waste streams have a low environmental impact, requiring a minimum of subsequent treatment before disposal. The raw gas contains no detectable heavy hydrocarbons and there are very low nitrogen-bound fuel components in the cleaned gas. The Cool Water Plant site emission requirements, design capability emissions, and current Federal New Source Performance Standards (NSPS) for the program coal are shown in Fig. 6.

The plant sulfur system is designed for 97% sulfur removal on a continuous basis. The sulfur produced is of commercial grade and is being sold for use in various industrial applications. The very low SO_2 emission level designed into the plant (1/10 of current NSPS standards) will be particularly advantageous for applications in nonattainment areas or other locations requiring very low sulfur emission levels.

The Cool Water site NO_x requirement of 0.14 lb/10^6 Btu (0.06 kg/10^6 kJ) is the lowest level in the United States. Use of low-temperature process heat for introducing fuel gas moisture into the gas turbine controls NO_x levels while improving overall plant efficiency and increasing specific power output. Further optimization of this system offers potential for reduction of NO_x below the Cool Water site requirements.

The particulate emission levels at Cool Water are projected to be very low. The fuel gas particulate is now anticipated to be on the order of 0.003 to 0.005 lb/10^6 Btu (0.012 to 0.002 kg/10^6 kJ), well below the 0.01 lb/10^6 Btu (0.004 kg/10^6 kJ) site limit.

Other environmental advantages include solid and liquid waste characteristics. The vitrified ash contains virtually no leachable constituents and will be stored temporarily at the site. Water from the particulate scrubbing sections is clarified and reused in the process and in the slurry-preparation section. Water vapor condensed from the cooled raw gas is also recycled in the process. The use of low-quality recycled water for the slurry and the subsequent decomposition of a fraction of this water in the gasifier afford an opportunity for the reduction of effluent wastewater streams. Wastewater from bleed streams, which concentrates contaminants, is degassed

Downloaded 01 Jun 2010 to 171.66.16.71. Redistribution subject to ASME license or copyright; see http://www.asme.org/terms/Terms_Use.cfm



Fig. 7 Cool Water Coal Gasification Combined Cycle Plant

in a closed system and then sent to a lined evaporation pond at the site.

Plant Layout

Figure 7 is a picture of the Cool Water Plant layout. The control room has a central location with the gasification, coal-handling, and cleanup system to the left, and the gas turbine, HRSG, and steam turbine equipment on the right. The oxygen is supplied from the facility at the lower left. The plant layout has been configured to accommodate easy access to the various subsystems with generous spacing for equipment monitoring, change-out, and storage. This configuration facilitates demonstration of various plant features and equipment designs. However, commercial plant layouts incorporating multiple gasification and combined cycle power trains can interface the fuel and combined cycle steam and feedwater sources in a much more compact arrangement to minimize space requirements. Recent studies show that 0.5 acre/MW (0.2 ha/MW) is required for a 600-MW plant.

Startup and Operating Experience

As stated previously, Btu's were first generated on May 7, 1984, and the SFC acceptance test was completed 47 days later—an outstanding achievement. Between and subsequent to those two runs, there have been several other runs, as can be expected during startup of a prototype plant. A brief description of these runs follows (Fig. 8):

Run 1 Started at 1813 hours on May 7, 1984, and shut down automatically after 1 h and 24 min. The run was initially very unstable because of control valve tuning characteristics. Also a number of valves did not work correctly in the automatic mode. During this run the pressure control system through the scrubber was lined out and many of the problems in the water-handling system were identified. The unit shutdown on the low radiant cooler sump level was caused by opening the bypass around the radiant sump blowdown flow controller while the lockhopper sump blowdown flow control valve was open for instrument work. Before the operator could take corrective action, the combined flow from these valves drew the radiant sump level below the shutdown point.

Run 2 Started at 1355 hours on May 8 and ran less than one minute when the unit shut down automatically on low slurry flow. The slurry pump pulsation dampers were adjusted and the automatic shutdown system was further tuned.

RUN NO.	DATE	DURATION h min	SHUTDOWN CAUSE/COMMENT
1	5/7	1 - 24	GASIFIER SUMP VALVE
3	5/9	2 - 41	GASIFIER PIPING
4	5/15	7 - 14	SULFUR CLEAN UP INCINERATOR
5	5/20	16 - 3	STEAM RECIRC. VALVE/GT 32 MW
6	5/25	6 - 26	O_2 PRESSURE INTERRUPTION
7	5/30-6/3	95 - 16	COAL HANDLING, GT - 50 MW ST - 45 MW
9	6/10 - 6/12	32 - 51	SPURIOUS N_2 PURGE
10	6/13 - 6/26	306-52	S.F.C. ACCEPTANCE TEST C.C. - 117 MW INTENTIONAL SHUTDOWN

Fig. 8 Cool Water startup history

Run 3 Started up at 1518 hours on May 9 and ran 2 h and 41 min until manually shut down at 1759 hours. During this run, the water system was stabilized. The shutdown was required when the 1/4 in. pipe taps and valves began breaking off the main grey water lines because of excessive vibration on the reciprocating hp grey water return pumps.

Run 4 Started at 1121 hours on May 15 and ran 7 h and 14 min before manual shutdown at 1835 hours, when the incinerator backfired on a relight. During this run, the downstream equipment was pressurized and leak-checked with syngas through the Selexol absorber to the combustion turbine. Fine turning of the grey water system continued.

Run 5 Started at 1117 hours on May 20 and ran 16 h and 3 min until automatically shut down at 0320 hours on May 21, by the low syngas cooler (SGC) to gasifier pressure trip. The low syngas cooler pressure occurred because of a valve positioner failure that caused the valve to open and depressure the syngas cooler to the condenser. During this run, dry (unsaturated) syngas was fed to the combustion turbine for the first electrical production from syngas. The switch from diesel fuel to syngas went very smoothly. Total electrical production from syngas was 132 MWh. The gas turbine ran very smoothly on syngas.

Run 6 Started at 1503 hours on May 25 and ran 6 h and 26 min until automatically shut down at 2129 hours, by what appeared to be low oxygen flow to the gasifier burner although there were no indications of any trouble with the oxygen system either at AIRCO or our plant. The trouble was later traced to a spurious signal that actuated the gasifier burner nitrogen purge system. The unit was lined out and preparing for the first time to send saturated, superheated syngas to the combustion turbine when the trip occurred.

Run 7 Started at 1520 hours on May 30 and was terminated manually at 1436 hours on June 3, after running 95 h and 16 min. The run was terminated when:

1 The coal-grinding system plugging problems from wet, fine coal reduced slurry inventory to the minimal level.
2 The slag-handling system sheared pins and could not be repaired immediately.

Shutdown was initiated by reducing the oxygen flow to below the safety system set point to test the first-out system. The first-out system functioned correctly. A number of significant firsts were acheived during Run 7:

1 Full operation of the combined cycle on saturated syngas.
2 Steam from syngas coolers commingled successfully with steam produced in the heat recovery steam generator.
3 Established good circulation of Selexol to Selexol absorber.

Downloaded 01 Jun 2010 to 171.66.16.71. Redistribution subject to ASME license or copyright; see http://www.asme.org/terms/Terms_Use.cfm

Table 1 Major process parameters: heat and material balance period

6/18/84 – 8:00 – 16:00

	Actual	Design
Process Plant (Gasification)		
Carbon Conversion (%)	99.0	95.0
Atomic O/C Ratio	1.04	0.99
Slurry Concentration (wt% solids)	57.8	60.0
Slurry Heat Content (Btu/lb)	7 290.0	6 620.0
(kJ/kg)	16 920.0	15 365.0
Specific Oxygen Consumption*	418.0	421.0
Cold Gas Efficiency**	72.1	71.1
Overall Plant		
Gross Output (ex. O_2 & Aux.) (MW)	115.5	117.1
Gross Heat Rate (Btu/kWh) (HHV)	8 940.0	9 010.0
(kJ/kWh) (HHV)	9 432.0	9 507.0
Net Output (incl.O_2 & Aux.) (MW)	90.1	91.9
Net Heat Rate (Btu/kWh) (HHV)	11 460.0	11 480.0
(kJ/kWh) (HHV)	12 090.0	12 112.0

*SCF O_2/100 SCF (CO & H_2)
**HHV Clean Syngas /HHV Coal

4 Commissioned absorber No. 1 in the Scot unit.
5 Lockhopper emergency dump facilities utilized successfully.

Run 8 Commenced at 0951 hours on June 10 and shut down automatically 53 min later on low slurry flow. The problem appeared to be associated with the failure of the slurry charge pump to deliver adequate slurry flow due to a check valve problem.

Run 9 Commenced at 2231 hours on June 10 and shut down automatically on low oxygen flow at 0722 hours on June 12, after 32 h and 51 min of operation. At the time of the shutdown, there were no apparent problems with the CWCGP oxygen system or the AIRCO plant. Investigation revealed that a momentary faulty signal from one of the two safety shutdown monitors caused initiation of a burner purge. The burner purge consists of a momentary blast of high-pressure nitrogen designed to rapidly clear the burner of any oxygen and slurry at shutdown. When the purge was initiated during operation, the high-pressure nitrogen pressured up the oxygen line to the burner, thereby causing a reduction of the oxygen flow below the automatic safety system shutdown point.

Run 10 Started at 0938 hours on June 13 and was shut down manually at 0430 hours on June 26, 1984 after 306 h and 52 min of operation. The run was shut down because of a significant HRSG leak and to allow a number of repairs and modifications to various systems to improve plant operability. AIRCO also needed a shutdown to determine their unit.

Major accomplishments during Run 10 include:

1 Completion of the 10-day SFC Acceptance Test and initiation of the Production Commencement Date.
2 Gross electrical production reached 117 MW during various portions of the run.
3 Claus and Scot units commissioned and sulfur production started.
4 SCE's Unit 1 (60-MW Steam Boiler) commissioned on syngas.
5 Produced first "Eligible Product" (as defined by the Price Guarantee Commitment) acceptable for SFC support.
6 Successfully tested various optional modes of operation (combustion turbine lead, gasifier lead).

The two problems which plagued earlier runs, plugging of the coal grinding system and failure of the slag-handling system to operate smoothly, were not major concerns during this run.

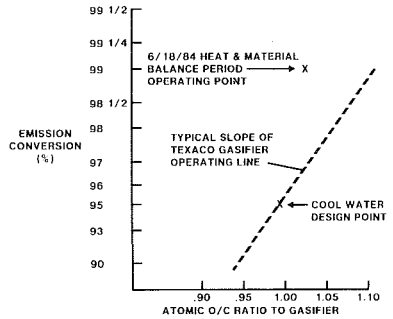


Fig. 9 Gasifier operating line

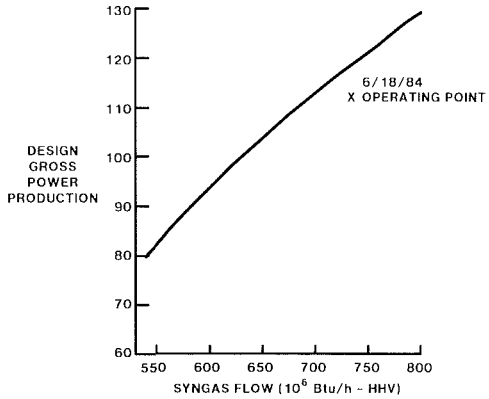


Fig. 10 Power plant operating curve

Plant Performance

The major plant performance parameters during the heat and material balance period are summarized in Table 1. The overall Cool Water complex (including AIRCO) operated at the design heat rate of about 11,500 Btu/kWh (12,133 kJ/kWh) during the balance period.

The gasification plant performed better than design, having somewhat lower specific oxygen consumption and higher cold gas efficiency than expected. Figure 9 is a graph of the primary gasification operating parameters: carbon conversion versus the atomic O/C ratio in the gasifier feed. The operating point of the Cool Water gasifier is definitely above the design curve, i.e., the Cool Water gasifier provides higher carbon conversion that does the design at a given O/C ratio. Possible reasons are:

1 The Sufco coal used in the run had a higher heating value than that in the design case (12,600 Btu/lb or 29,245 kJ/kg).
2 Carbon recycle was not practiced during the run, which resulted in a slurry with a greater higher heating value than design (7920 Btu/lb (16,920 kJ/kg) versus 6620 Btu/lb (15,365 kJ/kg)), despite the fact that the slurry was slightly weaker during the test (57.8% versus 60% solids).
3 The burner may operate at higher efficiency than design. High-performance burners such as the one used at Cool Water were just being developed and tested on a small scale when Cool Water's design calculations were done. The projected performance may have been conservative.

The power plant produced 3.3% (4 MW) less electricity than design at the syngas rates achieved during the test (Fig. 10). This discrepancy is probably due to a combination of three factors, none of which is related to the power plant itself:

Downloaded 01 Jun 2010 to 171.66.16.71. Redistribution subject to ASME license or copyright; see http://www.asme.org/terms/Terms_Use.cfm

1 The syngas saturator was out of service due to a control problem. Consequently, the syngas fed to the gas turbine was dry instead of containing 23% water vapor per design. This lack of vapor reduced the "free" high-pressure mass flow to the turbine, reducing the output by about 2.7 MW as a result.
2 Because the saturator was out of service, some boiler feed-water streams were rerouted. This rerouting prevented efficient operation of the syngas cooler economizer which reduced steam turbine power production by about 0.7 MW.
3 Two significant syngas leaks to the flare were reported downstream of the syngas flow measurement point. It was estimated that these leaks cost 1 to 2 MW.

Considering these three factors, the power plant equipment (gas turbine, steam turbine, and HRSG) was performing at or above design efficiency.

Summary

At this point the Cool Water Coal Gasification Program has been extraordinarily successful. Plant engineering and construction costs are expected to show about a 10% underrun and the first gas made at the plant was 25 days ahead of the June 1, 1984, scheduled date. Both of these facts represent a remarkable achievement given the prototypical nature of the project. Additionally, plant performance is very satisfying because it is essentially better than design in most areas, with correctable situations accounting for the 3.3% shortfall in total plant output.

Over the next five years the plant will provide valuable operating experience on several coals and confirmation that this technology does provide a viable option for burning coal in power generation that is economically and environmentally attractive.

References

1 Spencer, D. F., et al., "The Cool Water Coal Gasification Combined Cycle Project," *Proceedings of the American Power Conference*, Vol. 43, Apr. 1981.
2 O'Shea, T. P., Holt, N. A., and Alpert, S. B., "The Cool Water Project—Demonstration of Coal to Electric Power via the GCC Route," *AIChE Winter National Meeting*, Orlando, FL, Mar. 1982.

Downloaded 01 Jun 2010 to 171.66.16.71. Redistribution subject to ASME license or copyright; see http://www.asme.org/terms/Terms_Use.cfm

A Cost-Effective Indirect Coal-Fired Gas Turbine Power and Water-From-Air Cycle

P. R. Trumpler
Life Fellow, ASME.
President.
Trumpler Associates, Inc.,
West Chester, PA
Director.
Exton Center for Advanced Studies,
West Chester, PA

An ideal open gas turbine cycle with multiple-stage intercooled compression and multiple-stage reheat expansion theoretically approaches Carnot thermal efficiency. A proposed practicable process to utilize this cycle with indirect firing of coal as fuel, with an air heater in place of the boiler, a turbine inlet temperature of 1700°F (927°C) and top pressure of 788 psia (53.6 atm) gives promise of lowering power plant station heat rates (HHV) from 8970 Btu/kWh currently realized by the best scrubber-equipped coal fired steam plants to 7460, a reduction of 16.8% in fuel consumption and consequently the cost of flue gas scrubbers. In addition, a 316 MW plant delivers at rated output 130,000 gal per day water stripped from atmospheric air. Primarily because of an expensive air heater and regenerator the gas turbine plant is penalized by an estimated increase in initial cost from $1000/kW for a steam plant to $1433/kW. With coal priced at $3/million Btu, water selling at 2¢/gal, money at 8% interest, inflation at 5%, and an 81% plant capacity factor, the payback period is 17 years.

Introduction

The purpose of this paper is primarily to discuss the relative merits of two power plant cycles, namely: (1) an open high-pressure gas turbine cycle with intercooling, reheating, and regeneration and (2) the critical pressure steam cycle with reheat stages and feed-water heating. Because of their special problems nuclear plants will not be included in this discussion. Important as nuclear power may be and certainly will become, it is assumed that for some time to come and at various locations around the world, for various reasons, the desired fuel will be of fossil origin, whether oil, gas, or coal from underground, or from synfuels derived from coal. Since nature's oil and gas are likely to be depleted within perhaps 50 years while coal should last 200–400 years (these estimates arguable), oil and gas are likely to become soon, if they are not now, expensive as energy sources compared with coal. This paper is concerned primarily with plants firing coal as the fuel of choice.

In recent years the combined cycle [1, 2, 4] has received considerable attention. In this cycle, an industrial-type open cycle gas turbine direct-fired by oil or gas has been used as a topping unit, with the hot turbine exhaust serving as heat source for the steam boiler of a standard steam cycle. Direct firing the gas turbine poses two problems: As a practical matter, only oil and gas, not coal, can be fired; the combustion products impinging on turbine blades, particularly at the high inlet temperatures proposed by some, are corrosive to the extent of seriously limiting blade life. Coal can indeed be converted to fuel gas in an auxiliary plant [4], but this is an expensive complication destroying the simplicity of current combined-cycle plants. When we couple these problems to the inherent thermodynamic deficiencies of the steam cycle and the thermodynamic losses from heat transfer across necessarily large temperature differences between steam and gas turbine exhaust in the boiler, we must take a hard look at the basic concept of the combined cycle and ask, why not eliminate the steam entirely and concentrate on the gas turbine alone? The objections to a fully gas turbine cycle are well known:

1 If we discard direct firing for reasons just stated, indirect firing requires an expensive air heater in place of the steam boiler.

2 The normal cycle is inefficient unless high turbine inlet temperature, perhaps 2200°F (1204°C), can be achieved, and then there are serious problems to design stressed parts for long life. With indirect firing such high inlet temperatures require at best very expensive heater tube materials only now in the development stage [9].

3 If the gas turbine is operated in a non-normal cycle with compression intercooling, expansion interheating, and regeneration, the efficiency indeed can be high but the required heat transfer equipment is too expensive.

4 Even with high cycle efficiency the net work output per unit mass flow of working fluid is low, thus requiring much expensive equipment to generate the desired power.

Any proponent of a fully gas turbine cycle must address these objections. The author will attempt to show that an indirect fired high-pressure ratio (54:1) gas turbine with inlet temperature a modest 1700°F (927°C), using multiple in-

Contributed by the Gas Turbine Division of THE AMERICAN SOCIETY OF MECHANICAL ENGINEERS and presented at the 30th International Gas Turbine Conference and Exhibit, Houston, Texas, March 18–21, 1985. Manuscript received at ASME Headquarters, December 21, 1984. Paper No. 85-GT-54.

Copyright © 1985 by ASME
Downloaded 01 Jun 2010 to 171.66.16.71. Redistribution subject to ASME license or copyright; see http://www.asme.org/terms/Terms_Use.cfm

tercooling and multiple reheating will result in a cycle efficiency increased to such an extent that fuel savings should justify the additional installed cost of equipment.

Burton [3] points out the direction in which the gas turbine must go to meet the challenge of the 1980s. It is of particular interest to note that his design goal with respect to efficiency of a "cogeneration combined cycle" is "electric-power-generation efficiency potential (coal pile to bus bar) greater than mature coal steam plants that are environmentally acceptable (≅ 35% HHV) without credit for salable thermal energy." The gas turbine plant proposed in this paper predicts a corresponding efficiency of 45.8%. But high efficiency by itself is meaningless unless increased plant and operating costs are justified by the fuel savings. Burton's other goals concerning plant operating availability and forced outage rate cannot, of course, be convincingly addressed until a plant is actually built and operated.

No attempt is made to discuss closed-cycle gas turbine power plants, although a number have apparently proved themselves in operation, primarily in Europe. The closed-cycle plant, like the steam plant, has an advantage over the open cycle in continually reprocessing a clean, treated working fluid, without danger of accumulating trace impurities from the large mass of air drawn from and rejected to the environment. The proposed 316 MW output gas turbine plant processes about one million cu ft/min of atmospheric air.

Water From Air

The study of power-plant cycles was begun by the author some time ago in the context of the water problem. In many arid or semiarid regions of this country, and indeed around the earth, can water be efficiently stripped from the surrounding atmospheric air? The current interest in synfuels plant development in our western areas where cheap coal is plentiful has raised serious concerns about water availability in many locations. From the initial study of the problem it appeared that the best prospect for efficient water removal from the atmosphere was in conjunction with a power generation cycle using gas turbines.

In an arid region, is there enough water in the air to do us any good? We think of the desert atmosphere as dry. But we know that large-scale movements and massive circulation patterns characterize the atmosphere. How can the mixing which clearly occurs support a large gradient in water vapor content? Does the desert exist because the air above it is without water or because certain environmental factors (topography, vegetation, earth temperature patterns, for example) are not conducive to removal by rainfall of the water in the air?

A visit to the Caribbean islands suggests the answer. A lush tropical forest with rainfall every day on one island (Puerto Rico) is about 400 miles from a desert island (Aruba). Is it conceivable that the atmosphere above the two islands can be that much different in water-vapor content?

Measurements with a sling psychrometer by the author during his travels verified that substantial water vapor is in the atmosphere even in arid regions. Two representative humidity measurements and results are as follows:

Location and date	Temperature, °F wet bulb	Temperature, °F dry bulb	Relative humidity, %	Abs. humidity, lb vapor/lb dry air
Ovando, Montana July 1962	60	79	30	0.0068
Yazd, Iran (desert) May 1969	63	88	23	0.0070

The water content of 0.0070 lb vapor per lb dry air is less than the value 0.01105 used for the cycle calculations of the study, and thus the water recovery would be somewhat less for the tabulated humidities.

We tentatively conclude that there is a substantial amount of water vapor in the air everywhere.

The evolution of power-plant design with respect to water usage is interesting. Fifty years ago large power plants were located on rivers, lakes, or oceans to supply large quantities of condenser cooling water. Then came evaporative cooling of circulating water in cooling towers, using the atmosphere in place of large bodies of water as a heat sink but still requiring substantial water for evaporation makeup. Recent power plants (Gillete, WY for one) have eliminated the need for almost all water by using air-cooled surface condensers. Now the power plant can supply water. For atmospheric air with 0.01105 lb vapor per lb dry air (dew point of 60°F) the proposed gas turbine cycle will strip 93% of the moisture from the air which for a 316 MW plant becomes a water output of 130,000 gal/day.

It should be understood that a price is paid (in increased fuel fired) for stripping water out of the process air, since compressing the water vapor requires power not recovered by expansion in the turbines. If the atmosphere were perfectly dry, calculations show a station rate savings of 51 Btu/kWh, which if fully charged to water output assuming a fuel cost of $3/million Btu results in a water cost of 0.89¢/gal. This shows that if cheaper water is available[1] the power plant should be operated by reinjecting the water into the downstream high-temperature air, thus improving station heat rate to approximately 7405 Btu/kWh.

In our discussion of plant economics we shall assume that the plant is located in an area where all the produced water can be sold "at the gate" for 2¢/gal. Even at this high selling price the income from water is small compared to the fuel saving. At an 81% capacity factor the fuel saving per day of the proposed 316 MW gas turbine plant (7460 Btu/kWh) over the best steam plant (8970 Btu/kWh) of the same output is $27,800 whereas the income from water at 2¢/gal is $2100.

Ideal Power Plant Cycles

The focus of this paper is on the question of steam versus air as a working fluid. As a first step, it is instructive to consider ideal heat-power cycles: The two of primary interest are here shown in the temperature–entropy diagrams of Figs. 1 and 2. The former represents what might be considered the highest thermal efficiency cycle that deserves consideration by the designer of the future steam power plant. The pressures are in line with current practice. The top temperature of 1200°F (649°C) is being approached. But three reheats are only now being proposed and reheat temperatures do not now reach maximum cycle temperature. Nine extraction points were selected at indicated locations. The mass flow of steam extracted at each point, shown on the figure as a percentage of boiler flow, was taken as the maximum that could be used for heating the feedwater from the exit of the lower-temperature extraction stage. For the ideal cycle the temperature "pinch point" in the heaters was taken as zero. The temperature at *c* (Fig. 1) of the vapor-water leaving the last feedwater heater,

[1] In Philadelphia water is sold at retail for 0.22¢/gal. Production cost is much less. Other communities are not so fortunate in their water supply.

Downloaded 01 Jun 2010 to 171.66.16.71. Redistribution subject to ASME license or copyright; see http://www.asme.org/terms/Terms_Use.cfm

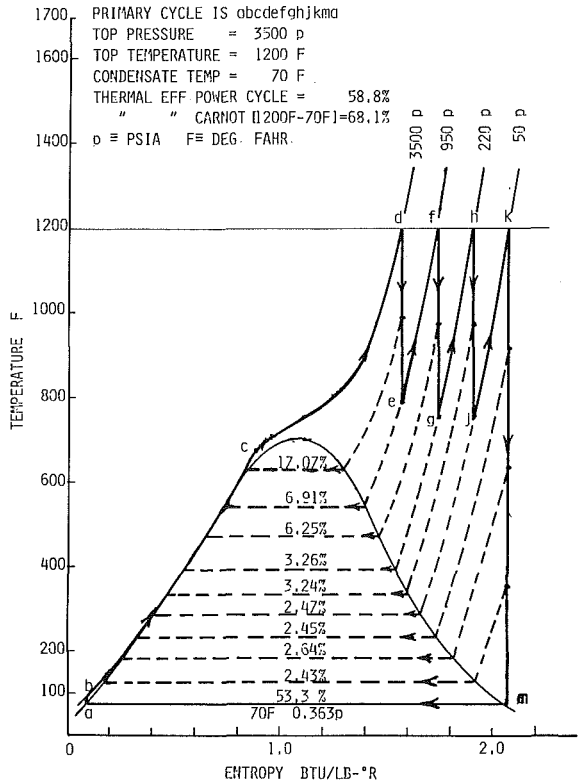


Fig. 1 Ideal steam cycle with three reheats and nine feedwater heaters

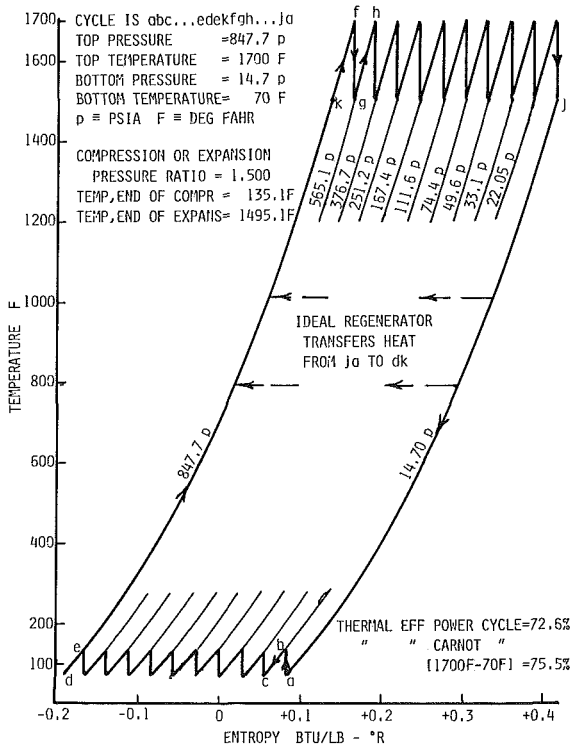


Fig. 2 Ideal air power cycle with intercooling and reheating

that is, entering the boiler, is 665°F (352°C). The calculations, made with the aid of standard tables [6], are well understood and will not be detailed here. The thermal efficiency of the cycle is 58.8%. The cycle is identified as No. 7 in Table 1 summarizing the ideal cycle calculations. That table also lists the output shaft work per pound of working fluid traversing the cycle, and an index not previously seen by the author, namely, the output shaft work divided by the maximum

Table 1 Thermal performance of ideal cycles

Cycle No.	Source Temp °F	Sink Temp °F	Description	Thermal Efficiency = Shaft work out / Heat in %	Shaft work out / Lb working fluid Btu/lb	Shaft work out / Max Ft³ workg fluid Btu/ft³
1	1700	70	Carnot	75.5		
2	1700	70	Gas Turbine: 848 p to 14.7 p, 10 stage intercooled compr., 9 reheats	72.6	414	8.42
3	1700	70	Gas Turbine: 848 p to 14.7 p, 10 stage intercooled compr., 3 reheats	70.5	372	8.80
4	1200	70	Carnot	68.1		
5	1200	70	Gas Turbine: 848 p to 14.7 p, 10 stage intercooled compr., 9 reheats	64.3	282	7.49
6	1200	70	Gas Turbine: 848 p to 14.7 p, 10 stage intercooled compr., 3 reheats	61.7	252	7.85
7	1200	70	Steam: 3500 p to 0.363 p, 9 feedwater heaters, 3 reheats	58.8	798	1.72
8	1200	70	Steam: 3500 p to 0.363 p, no feedwater heaters, 3 reheats	52.6	1179	1.36
9	1700	70	Combined Cycles 3 and 7 GT exhaust 1220 F to steam boiler and steam reheaters. $\frac{\text{Mass flow air}}{\text{Mass flow steam}} = 9.91$	68.1		

Notes: Symbol p following a number stands for psia, pressure in pounds per square inch absolute. For pressure in atm, divide p by 14.70

70F = 21.1C ; 1200F = 648.9C ; 1700F = 926.7C

volume of the working fluid anywhere in the expansion process through the turbines. The intent of the new index is to give a simple measure, admittedly very imperfect, of the size and therefore cost of equipment, supplementing the well-known work-per-pound index.

The gas turbine cycle used for comparative purposes is shown in ideal form in Fig. 2. Haywood [5] identifies this cycle, shows that indeed Carnot efficiency is achieved with an infinite number of intercooling and interheating steps, and judges such a cycle with many such steps (presumably more than one or two at each temperature level) as "impracticable." Calculations of ideal cycle performance using standard low-pressure air and gas data [7] are summarized in Table 1 for 70°F (21°C) atmospheric air (sink) temperature, and turbine inlet (source) temperatures of 1700°F (927°C) and, for comparison with the steam cycle, of 1200°F (649°C). All cycles have nine stages of intercooling. Cycles 2 and 5 have nine stages of interheating; cycles 3 and 6, three stages of interheating.

The selection of 1700°F (927°C) and 848 psia (57.7 atm) for the gas turbine cycles was not entirely arbitrary, although no attempt was made to find the economic optimum values. Today's best materials for tubular heaters (for example, Inconel 617) operate at their upper limit of 1800°F (982°C) with a design stress near 1500 psi. With this material a heater can be designed to raise air to 1700°F (927°C) with a tube wall not over 1800°F (982°C).

The top pressure of 848 psia (57.7 atm) was selected by an intuitive compromise among three considerations, namely, (1) high pressure with many intercooling and interheating steps yields high work output per pound working fluid, that is, each mass of working fluid is made to "work hard" each cycle by being reheated and re-expanded many times; (2) high pressure permits a high proportion of water to be stripped from the air in the intercoolers and aftercooler; and (3) the low allowable working stress of the metals to heat air to 1700°F (927°C) calls for low pressure if excessive equipment cost is to be avoided.

Downloaded 01 Jun 2010 to 171.66.16.71. Redistribution subject to ASME license or copyright; see http://www.asme.org/terms/Terms_Use.cfm

Cycle 9 represents an attempt to evaluate the best conceivable ideal combined cycle. Since the turbine exhaust in Cycle 3 (3 reheats) is at 1220°F (660°C) and the steam plants have a top temperature of 1200°F (649°C) the slight loss of 20°F (11°C) from the ideal is ignored and Cycle 3 was joined to Cycle 7. The ratio of gas turbine exhaust flow to boiler steam flow was set by permitting zero temperature difference between air and water at the 665°F (352°C) boiler feed temperature. Even so, the large variation of specific heat of the water-steam passing through the boiler produced a maximum temperature gap of 205°F (114°C) between air and steam. For this cycle the mass flow of air was 9.91 times the mass flow of boiler steam. If the mass flow ratio were lower the increased temperature gap between air and steam in the boiler would reduce the cycle thermal efficiency.

From Table 1 we may develop certain thought orientations, not conclusions, since the latter must be based on economic realities which are yet to be discussed:

1 No matter what basis of comparison one may use, the gas turbine cycle shows superior thermal performance to the steam cycle. This is the consequence of unavoidable[2] low-temperature expansion of the steam, since constant-temperature condensation and specific heat differences make it impossible to use more than about half the steam to heat the boiler feed. In the gas turbine cycle, since the specific heat of air at atmospheric pressure is close to that at 848 psia (57.7 atm) at any given temperature, the entire flow of air exhausting at high temperature from the low-pressure turbine can be used to preheat the air going to the air heater. As a result, all the exhaust heat in the process *ja* of Fig. 2 may be used to preheat the stream in process *dek*. The fuel-fired furnace begins heating air only at *k*, supplying heat only from 1495°F (813°C) to 1700°F (927°C). As Haywood says, "For [the limiting Carnot efficiency to be achieved] all internal processes must be reversible, while all heat reception must occur at the highest temperature [points *f*, *h*, . . .], and all heat rejection at the lowest temperature [points *a*, *c*, . . .*d*]." In the steam cycle the internal heat-transfer processes at the feedwater heaters cannot approach reversibility even with a zero temperature "pinch point" because of the necessarily significant temperature spread between hot and cold fluids on each side of the "pinch point"; and heat reception in the boiler after feedwater heating occurs not at a temperature close to 1200°F (649°C) but at 665°F (352°C). In the gas turbine cycle of Fig. 2, the internal process *ja* transferring heat to process *dek* can be made to approach zero temperature spread between the high and low pressure streams, and zero pressure loss in both streams, thus approaching reversibility, if the heat exchanger (regenerator) is made large enough; and all heat reception (or rejection) occurs close to the highest (lowest) temperature if there are many reheat (intercooling) steps. The reason for the proposed large number of reheat and intercooling steps is now clear. The gas turbine cycle of Fig. 2 actually achieves Carnot efficiency if one takes the highest temperature as the average of the temperatures at *f* and *g*, and the lowest temperature as the average of temperatures at *a* and *b*.

2 While the thermal efficiency of the combined Cycle 9 (Cycle 3 plus Cycle 7) appears to be a high 68.1%, the "good" performance is illusory. Cycle 3 alone does better. Attaching the best steam cycle to that of the gas turbine by the most efficient connection (boiler) simply pulls down the performance of the gas turbine cycle alone. While the gas turbine topping unit might be a desirable addition to an existing steam plant, perhaps to increase its peak output with small capital expenditure if direct fired with oil or gas, there would appear to be no conceivable argument in favor of the combined cycle with coal firing.

3 Concerning work output per unit throughflow as set forth in the two right-hand columns of Table 1, it appears that neither index alone, and probably not both together, is very helpful in estimating relative equipment costs. The mass-flow index of the middle column shows that it requires two to three pounds of air in the gas turbine cycle to do the work that one pound of steam does in the steam cycle. Because steam must be expanded to low pressure to achieve a low sink temperature, however, its volume is large at turbine exhaust, which produces a low volume-related index (last column). Gas turbine exhaust is at atmospheric pressure although at high temperature. Comparing Cycles 2 and 7, we find the maximum steam volume in the turbine to be 4.9 times the air volume in the comparable gas turbine. This suggests that for a given maximum flow passage size the gas turbine plant produces more work by a factor of almost five. On the contrary, the mass-flow index suggests that the gas turbine plant produces an output of only 414/798 = 0.52 that of the steam plant for the same size equipment. A little reflection will show that neither index is more than a very limited indication of economic realities. In fact, the only reason for mentioning the indexes here is that the mass-flow index (middle column) is a commonly used economic measure.

4 Another popular but fallacious argument favoring steam as a working fluid is that water requires low work of compression (process *ab* in Fig. 1) compared to that of air or any gas. In the narrow perspective this is true, but when it is recognized that the thermodynamic properties of water-steam with which one must then work make it impossible even to approach top cycle efficiency, the price of saving compression work is a high one indeed!

The Operational Cycle

Of the cycles listed in Table 1, as the fuel becomes relatively more expensive Cycle 2 with its near Carnot efficiency becomes more attractive and we ask if an economically viable process cannot be developed to approximate Cycle 2. In this and following sections on equipment design and economics, only one of many possible operational cycle variants will be examined. Clearly, the optimum variant is a function of costs which are different for each plant location and change with the years. The object in selecting the variant here discussed is not to solve everyone's problem on how to design a power plant, but to suggest that there exists at least one variant which may prove in many cases to be superior to the best steam process. For the setting of practical process specifications a knowledge of equipment design is crucial. The author's extensive industrial experience in turbomachinery and heat exchanger design suggests that the numbers specified for equipment performance are not unreasonable and will be met by the designs outlined in the next section.

In Fig. 3 the hydraulic (also known as polytropic or stage) efficiency of the turbocompressors is taken as 88%. Axial compressors currently achieve this at favorable operating conditions, and radial (centrifugal) single-stage compressors in gas pipeline service do almost as well. It is probable that axials will be used in the low-pressure stages and centrifugals in the high-pressure stages. While the process diagram shows all compressors and turbines on one shaft, this is only for convenience in representation. It would be expected that two or three shafts, each with its own generator and group of

[2] Haywood [5] shows an "ideal superregenerative" cycle credited to Field that does achieve Carnot efficiency, but he correctly labels it "highly impracticable."

Downloaded 01 Jun 2010 to 171.66.16.71. Redistribution subject to ASME license or copyright; see http://www.asme.org/terms/Terms_Use.cfm

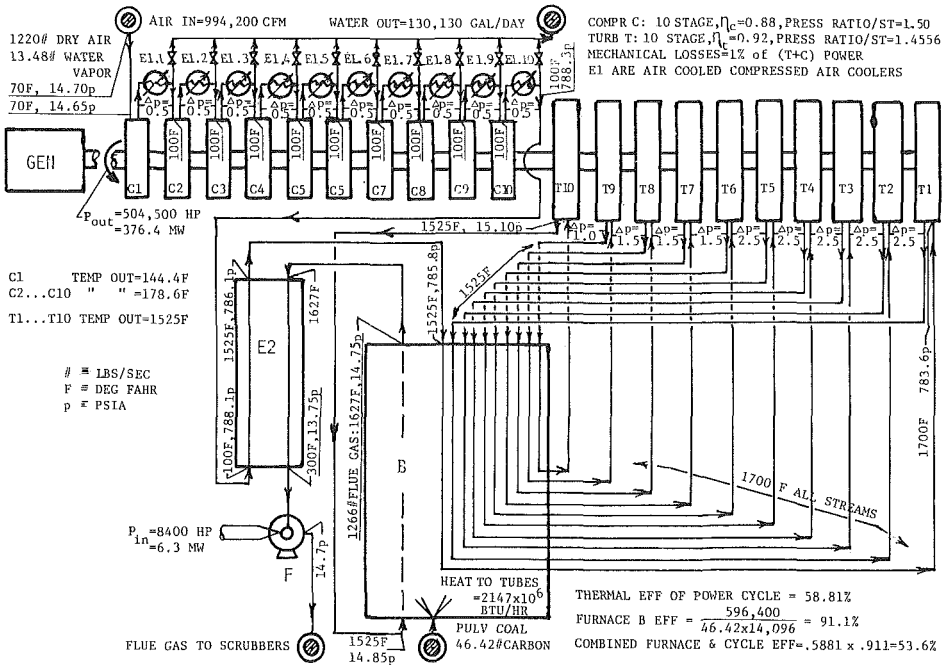


Fig. 3 Process diagram for high efficiency gas turbine power and water-from-air cycle

compressor and turbine stages, would be employed. The intercoolers E1.1 . . . E1.9 and aftercooler E1.10 are radiators, rejecting heat of compression to the atmosphere at 70°F (21.1°C) and condensing water as compression takes place. If air with a water-vapor content of 0.01105 lb per lb dry air (dew point 60°F) is drawn into the first compressor, 93% of the vapor will be drawn off as water by the end of compression and aftercooling. It should be noted that the cycle is charged with the power to compress the vapor. With dry air only, the cycle has a thermal efficiency of 59.22% in place of the 58.81% noted.

The turbine hydraulic efficiency is taken as 92%. Air enters at 1700°F (926.7°C) and leaves each stage at 1525°F (829.4°C). To calculate net shaft power from turbine output and compressor input, 1% of the total compressor and turbine power is subtracted for shaft-bearing losses. The cycle is charged with the power required for induced draft fan F. Power for other auxiliaries such as oil pumps, radiator cooling fans, coal pulverizers, antipollution scrubbers, and station utilities, is included under the heading of general station auxiliaries and taken into account separately.

The air-heating furnace B fired with air from the exhaust of turbine T10 takes the place of the boiler in a steam plant. Combustion is easily maintained with the 100% excess air supplied. This arrangement for gas turbine operation with pulverized coal as fuel also favors long turbine life because combustion gases do not enter the turbine. The flue gas discharges from preheater E2 to the scrubbers at 300°F (148.9°C), high enough to avoid corrosion from condensation on preheater surfaces.

The pressure losses for flow through heat exchangers and piping may appear to some to be unacceptably low; possibly increased losses at one or more sections may indeed be cost effective. With care in design the indicated figures can be achieved. When we consider the high cost of carefully designing and fabricating turbomachinery passages to gain just a percent or two of efficiency, nullifying such a gain by crude design of piping or heat exchanger passages would seem to make little sense.

It should be noted that the process air leaving aftercooler E1.10 has a low moisture content of about 0.0008 lb per lb dry air. As we examine air against steam as a working fluid, air, particularly when it is this dry, should be better with respect to corrosion. Stress corrosion from fluids at high temperature and high pressure can be an important problem, resulting in cracking and failure of stressed metals. It is too simplistic to say only that oxygen and nitrogen molecules do not break down as readily as steam molecules, that is, that air is more stable. The corrosion mechanism is complex and not well understood. It is probable that steam and oxygen originally dissolved in water, in contact with metal at high temperature cause free hydrogen in the presence of oxygen to react destructively with the metal. Apparently very small amounts of impurities, chlorine for example, accelerate stress corrosion. Such impurities are often unintentionally introduced when an operational upset occurs in a steam plant. Residual stresses in the metal appear to accelerate stress corrosion in steam service. With air having a moisture content so low that it is considered chemically to be reacting as dry air, there would be negligible hydrogen attack and stress corrosion should be practically eliminated.

In air heating furnace B, however, corrosion problems of a different nature may be more serious with the air cycle. Tube wall temperatures will be as high as 1800°F (982°C), certainly hundreds of degrees higher than the tube wall temperatures in a steam plant. Since the fly ash softens above 1800°F (982°C) the formation of slag on tubes should not be too serious. However, the corrosion of external tube surfaces from sulfur and other coal impurities could be greater at the higher temperatures. This problem was not explored.

Gas heating furnaces operating close to conditions here specified are not unique in petrochemical processing. The author is informed of a cracking furnace heating ethane with many impurities, at a pressure of about 1000 psi (68 atm), where the tube metal temperature is at 1700°F (927°C). While petrochemical plant design probably tolerates a shorter equipment life than power plant design, the cracking furnace service would appear to be more severe than that of the proposed dry air cycle.

Whether or not the proposed air cycle with 788 psia (53.6 atm) top pressure and 1700°F (927°C) top temperature is near the upper limit of current technical feasibility, in a situation

Downloaded 01 Jun 2010 to 171.66.16.71. Redistribution subject to ASME license or copyright; see http://www.asme.org/terms/Terms_Use.cfm

Table 2 Design of air stream heat paths, furnace B

Air Stream No.	Stream Pressure, psia In	Out	ΔP	Pressure Diff. Across Tube Wall psi	Tube Wall Thickness inch	Tube I.D. inch	Tube Length feet	No. Tubes in Parallel	Film Coef., h Btu/hr-ft²-F	Active Tube Weight for Stream lbs.
1	785.8	784.1	1.7	771	0.6875	2.625	50	446	140	541,800
2	537.8	536.3	1.5	523	0.5156	2.969	58	455	105	505,800
3	367.6	366.1	1.5	353	0.375	3.250	60	443	94	385,500
4	250.7	249.2	1.5	236	0.266	3.469	63	478	78	319,100
5	170.3	168.8	1.5	156	0.1875	3.625	65	538	65	266,700
6	115.2	113.7	1.5	100	0.125	3.750	63	616	56	200,500
7	77.3	76.6	0.75	63	0.125	3.750	57	1036	37	305,200
8	52.0	51.3	0.75	37	0.125	3.750	53	1246	33	341,300
9	34.6	33.8	0.75	20	0.125	3.750	52	1583	26.5	425,400
10	22.73	22.23	0.50	8	0.125	3.750	48	2390	19	592,800
								Total Weight =		3,884,100

For each stream:

Temperature of air in = 1525F — Air Flow = 1220lbs/sec

Temperature of air out = 1700F — Air Duty = 48.80 Btu/lb = 59,536 Btu/sec

Tube O.D. = 4.00 inches — Design stress = 1500 psi

Temperature difference, air stream to tube wall = 100F

Table 3 Design of regenerator (air preheater) heat paths, exchanger E2

Section No.	1	2a	2b	2c	3	4
Flue gas temp in, F	1627	1575.8	1473.4	1287.1	1091.5	789
Flue gas temp out, F	1575.8	1473.4	1287.1	1091.5	789	300
HP air temp in, F	1470	1360	1160	950	625	100
HP air temp out, F	1525	1470	1360	1160	950	625
Material (Cost,$/lb)	(20)[1]	[Car Tech RA 330 TX(10)]			(5)[2]	(0.60)[3]
Tube wall thickness, inch	0.325	0.375	0.250	0.125	0.125	0.125
Tube wall stress, psi	3980	3350	5400	11,600	11,600	11,600
LP film coef h_o, Btu/hr-ft²-F	13.6	13.35	12.8	12.1	11.2	9.7
HP film coef h_i, Btu/hr-ft²-F	63	63	54	46	44	41
HT film coef U_o, 4" dia "	10.8	10.6	10.1	9.45	18.5[4]	16.6[4]
Mean temp difference, F	103.9	109.6	120.2	134.3	152.8	182
Active stream length, ft	80	160	240	280	160	280
No. rows deep (70 tubes/row)	20	40	60	70	40	70
ΔP, HP stream, psi	0.36	0.82	0.74	0.54	0.23	0.25
ΔP, Flue gas stream, psi	← Total = 0.80 →					
Weight active tubes, lbx10⁻⁶	0.714	1.624	1.680	1.013	0.868	1.519
Cost active tubes, $ x10⁻⁶	14.27	16.24	16.80	10.13	4.34	0.91

LP flue gas flow = 1266 lb/sec

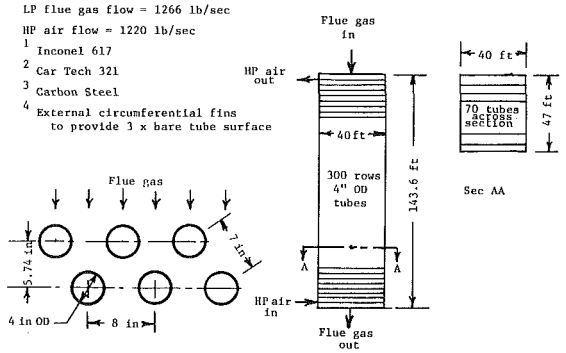
HP air flow = 1220 lb/sec

1 Inconel 617

2 Car Tech 321

3 Carbon Steel

4 External circumferential fins to provide 3 x bare tube surface



comparable to that of the steam cycle with a top pressure of 3500 psia (238 atm) and a top temperature of 1200°F (649°C), cannot be convincingly argued until we have detailed design studies, and probably operating data on an air plant.

Figure 3 indicates a gas turbine shaft output of 504,500 hp or 376.4 MW, resulting in a combined furnace and power cycle efficiency of 53.6%. For net station electrical output and heat rate (coal pile to bus bar) these figures must be corrected by station losses which may be estimated from steam plant experience. Taking generator efficiency as 98%, auxiliary losses as 5%, flue gas scrubber and control air losses as 8%, and taking separate account of the fan F power requirement of 6.3 MW, we calculate the electrical output at the station bus bars as

$$376.4 \times 0.98 \times (1-0.05) \times (1-0.08) - 6.3 = 316 \text{ MW}$$

The station overall thermal efficiency is

$$\frac{316{,}000 \times 3412}{46.42 \times 14{,}096 \times 3600} = 0.458$$

This efficiency is commonly expressed in the form of station heat rate

$$\frac{46.42 \times 14{,}096 \times 3600}{316{,}000} = 7455 \text{ Btu/kWh}$$

To simplify furnace heat calculations, coal was taken as pure carbon fired completely to carbon dioxide with a heat of combustion of 14,096 Btu/lb. The resulting mixture of oxygen, nitrogen, and carbon dioxide was taken into account in proper proportion in the heat calculations of preheater E2.

Equipment Design

The initial-cost penalty chargeable to the air plant is predominantly the result of replacing the boiler, air preheater, and feedwater heater group of the steam plant by the air heating units B and E2, Fig. 3. The basic boiler group (excluding flue gas cleanup) costs about $200/kW, which for a 316 MW installation comes to $63.2 × 10⁶. It will be shown that B and E2 together may be expected to cost about $210.6 × 10⁶. With respect to the heat rejection exchangers, the ten after and intercoolers E1.1-E1.10 may cost a total of perhaps $8 × 10⁶, which is greater than that of the condenser in a steam plant (unless cooling water supply is charged to it); the penalty on the air plant is considered too small for more than brief attention.

The air heating furnace B raises the temperature of each of ten air streams at various pressure levels from 1525°F (829°C) to 1700°F (927°C). While B is shown in Fig. 3 as one furnace, practical design will almost surely divide it into a number of smaller furnaces. For our design approach each of the ten air streams is treated as a heat transfer problem in which the temperature drop between air and inner tube wall is taken as 100°F (55.6°C) in order that the tube wall does not exceed 1800°F (982°C), and the air stream pressure loss is taken substantially less than the specified drop from turbine to turbine shown in Fig. 3, to allow for pressure drop in the external piping. Tubes are fabricated of seamless cold-finished Inconel 617, 4 in. o.d. of variable wall thickness designed for working stress not exceeding 1500 psi. Table 2 summarizes the calculations for all ten streams. The design of B involves important problems not mentioned here. For a good overview see [8].

Total active tube weight comes to 3.884 × 10⁶ lb. Since this tube material is quoted at a price of $20/lb in quantity, the active tubes will cost $77.68 × 10⁶. A rough figure for the entire furnace cost is taken without detailed check as 50% above the price of the active tubes, which comes to $116.5 × 10⁶.

The regenerator or air preheater E2 is estimated to cost almost as much as the furnace B. The design of the active elements, summarized in Table 3, envisions a counterflow exchanger having the shape of a box 143.5 ft (43.74 m) long with an internal cross section 47 ft (14.33 m) by 40 ft (12.19 m). The flue gas flows the length of the exchanger in cross flow over 300 rows of staggered 4-in. (10.16 cm) o.d. tubes each 40 ft (12.19 m) long. There are 70 tubes in each row. Seven hundred tubes, or ten rows, are manifolded in parallel. The tube material and the wall thicknesses are selected to withstand the stress to meet normal creep standards at operating wall temperature for 100,000 hours. The materials range in cost from $20/lb (Inconel 617) to 60¢/lb for carbon steel in the form of finned tubes. Note that the tubes in low-temperature sections 3 and 4 are specified with circumferential fins rolled from the base metal which are assumed to triple the external tube surface and increase tube weight by 50% over the unfinned tube of the same wall thickness.

Downloaded 01 Jun 2010 to 171.66.16.71. Redistribution subject to ASME license or copyright; see http://www.asme.org/terms/Terms_Use.cfm

The proposed arrangement of E2 heat transfer surface represents a conventional approach and would be recommended for the first plants. However, the return bends or manifolding for the many passes of the high-pressure stream, and possibly also the solving of the relative thermal expansion problem, are likely to be expensive. For future plants both problems should be considerably simplified by a radical design: winding 700 4-in. (10.16 cm) o.d. tubes each 1200 ft (366 m) long helically in layers over a central closed cylindrical core tube.[3] The tubes are manifolded (in parallel) only at the ends; the coil geometry inherently permits a certain degree of freedom for thermal expansion different for each tube. However, the fabrication, transport, and handling of a tube bundle with support structure perhaps 49 ft (14.9 m) in diameter, 150 ft (45.7 m) long weighing 5000 tons (4.55×10^6 kg) are awesome to contemplate and surely require major setup expenditures for facilities, equipment, and special tools. Such expenditures could probably be justified only by production of a number of these exchangers.

Whatever basic form of design is chosen, it is clear that E2 is so large that the problems of how to fabricate, transport, and assemble the various parts that together constitute the exchanger will be critical considerations in the design. These problems are not discussed here. They should not in any event pose difficulties unfamiliar to the designer of convection sections in large modern power plant steam generators.

We return to the proposed design. As with furnace B, to price E2 a factor of 1.5 is applied to the cost of all active tubes. Since the total of tube costs for all sections in Table 3 comes to $\$62.69 \times 10^6$, the estimated cost of the entire exchanger E2 is $\$94.04 \times 10^6$.

Concerning the air coolers E1.1–E1.10 only a rough design calculation will be presented to show that costs will be low compared to costs of B and E2. For these E1 low-temperature air-to-air exchangers it is clearly advisable to use extended surface on both sides. A standard form of circumferential fin on the outside of tubes, to increase base tube surface by a factor of approximately 10, is specified for the atmospheric air side. Film coefficient is taken as 15 Btu/h-ft^2-°F (85 W/m^2-K). Internal extended surface is more of a problem. The author, however, has worked some years ago with edge-wound ribbon packed tubes in dual annular spaces inside 3¼ in. (8.3 cm) o.d. copper tubes. With such tubes a ratio of inside surface to base tube (o.d.) surface of 15 is taken, and a film coefficient of 20 Btu/h-ft^2-°F (114 W/m^2-K) is assumed. Such tubes with added outer circumferential fins are estimated to weigh 12.5 lb/ft (17.3 kg/m) and cost \$3/lb (\$6.61/kg). The duty of an exchanger cooling 1227 lb/s (556.6 kg/s) compressed air from 178.6°F (81.4°C) to 100°F (37.8°C) is 83.8×10^6 Btu/h (24.56 W). If atmospheric cooling air rises from 70°F (21.1°C) to 75°F (23.9°C), the mean temperature difference between the two air streams is 58°F (32°C). The overall heat transfer coefficient U for the 3¼ in. (8.3 cm) o.d. base surface is 100 Btu/h-ft^2-°F (568 W/m^2-K). Thus a base surface of 14,450 ft^2 (1342 m^2) is required, which implies an active tube length of 17,000 ft (5182 m), and an active tube weight of 212,500 lb (96,390 kg) costing \$637,500. With casing structure and manifolding, the exchanger cost should come to about \$800,000. The total price of the ten E1 exchangers should be roughly $\$8 \times 10^6$.

Of the ten compressor bodies shown in Fig. 3, the low-pressure units will probably be axial machines to handle high-volume flows. For high-pressure low-volume stages the centrifugal compressor of the single-stage volute diffuser design would appear to be the choice. Pipeline applications have shown such machines to operate efficiently, and the radial flow orientation makes for an axially compact suction and discharge arrangement. It is a natural development to combine a number of such single stages into a single casing with multiple suction and discharge connections. Such multiple connection machines are now available but not with the efficient volute diffusers.

The turbine problem offers no unusual challenge to the gas turbine designer, unless it is to make an axially compact multiple inlet-discharge train of many stages. Since the hot gas temperature drop from inlet to discharge is only 175°F (97.2°C) the thermal strain and stress problems in the casing will be much less than the designer usually encounters.

What can one say about the comparative cost of the gas turbine and steam turbine machinery? The installed power per unit output power for the gas turbine train is 2.32, whereas with the steam cycle it is 1.03 (considering pump work). Against this considerable penalty the gas turbine train benefits from operation at low top-cycle pressure and at low gas volume at the end of expansion. But gas turbine temperatures are higher. No attempt is made here to judge the net effect, which is almost certainly not great enough to be decisive in the economic evaluation since the steam turbine alone (without generator) is estimated to cost only about 8% of the plant investment or $\$25 \times 10^6$ for our 316 MW plant at \$1000/kW. Even a substantial percentage increase in drive machinery cost for the gas turbine plant implies a small penalty compared to the penalty paid for the heat exchangers.

Economic Analysis

In [11] are found data on the performance of our best current steam plants. The heat rates were taken for 1981; they represent annual averages and thus include startup, hot standby, and part-load operation. At the top of the list as best performers are units without environmental cleanup (flue gas scrubbers), which is generally accepted as costing about 2% in heat rate. Thus the top performer (Marshall 4 of Duke Power) listed at a heat rate of 8792 Btu/kWh corrected for 2% scrubber loss rises to 8970 Btu/kWh, which is close to the values of the fourth and fifth best performers.

The value of 8970 Btu/kWh will be taken as the best scrubber-equipped steam station performance. For the proposed gas turbine plant the corresponding value has been estimated to be 7455 Btu/kWh. To establish cost effectiveness it is necessary to show that the additional investment, operating and maintenance costs are justified by the anticipated saving in fuel plus the small income from water.

First, consider the additional investment costs.[4] In the proposed GT plant the estimated cost of furnace B is $\$116.5 \times 10^6$ and of exchanger E2 is $\$94.1 \times 10^6$. The basic steam boiler which B and E2 replace costs about \$200/kW, which for a 316 MW plant comes to $\$63.2 \times 10^6$. The flue gas precipitators and scrubbers for the steam plant are estimated to cost about the same as the steam boiler, namely $\$63.2 \times 10^6$. The fuel saving of (8970 – 7455)/8970 or 16.9% implies a corresponding saving in this cleanup equipment, resulting in a credit of $\$10.7 \times 10^6$. For this economic study it will be assumed that the investment in intercoolers E1 is balanced against that of the steam condenser, and that the turbine-generator machinery trains of both plants will also cost roughly equal amounts. The *investment penalty* charged to the gas turbine plant is thus estimated at

$$\$(116.5 + 94.1 - 63.2 - 10.7) \times 10^6 = \$136.7 \times 10^6$$

Since the investment cost of the 316 MW steam plant at \$1000/kW is $\$316 \times 10^6$, the gas turbine plant's cost of $\$452.7 \times 10^6$ is 43.3% higher.

[3] This is a simplified form of the Hampson exchanger used in certain cryogenic (air separation) plants. For reference see Ruhemann, *The Separation of Gases*, Oxford University Press, 1940, pp. 166–167.

[4] All figures in this paper are based on the 1982 dollar.

Downloaded 01 Jun 2010 to 171.66.16.71. Redistribution subject to ASME license or copyright; see http://www.asme.org/terms/Terms_Use.cfm

What can be said about maintenance and operating costs? Gas turbines operated with an inlet air temperature of 1700°F (927°C) with air uncontaminated by moisture or combustion gas should have long maintenance-free life. On the other hand, the coal-fired furnace B with tube metal at 1800°F (982°C) will probably encounter greater flue-gas side fouling and corrosion problems. It appears impossible to make even a rough evaluation of these and numerous other possible differences between the two plants. For the purposes of this study it will be assumed that differences in maintenance and operating costs are not large enough to be economically significant.

The cost of coal varies substantially but the figure of $3/million Btu from [4] is generally accepted as a fair average and will be used in this study. Water is assumed to sell for 2¢/gal. If the plant operates at an average capacity of 81% [4] the fuel saving per year is

$$(8970-7456)\times 315{,}700\times 8760\times 0.81\times 3\times 10^{-6}=\$10.17\times 10^{6}$$

Income from water is

$$130{,}130\times 365\times 0.81\times 0.02=\$0.77\times 10^{6}$$

Thus the yearly income gain of the gas turbine plant over the steam plant is $\$10.94 \times 10^6$. Will this support the additional capital expenditure of $\$136.7 \times 10^6$?

The answer is indicated in Fig. 4, primarily on the basis of the solid line identified as "cash assets GT plant over steam plant – constant dollars." To understand what this line means, consider two competing companies each building and operating a 316 MW coal-fired electric power plant in the same area. In each company the management has been allocated $\$316 \times 10^6$ for capital investment. Company A builds a conventional steam plant. Company B borrows an additional $\$136.7 \times 10^6$ to build the proposed GT plant, paying 8% interest yearly on the unpaid balance of the loan. Revenue and costs for both plants increase each year by the 5% inflation rate. Interest and inflation rates are assumed constant for the full life of the plants. The yearly income gain of B over A, namely $\$10.94 \times 10^6$ the first year (increased by 5% each subsequent year), is applied first to pay the interest on the balance of the loan and then with what remains to repay principal. (By coincidence the first year interest payment of 8% on $\$136.7 \times 10^6$ is $\$10.94 \times 10^6$, the full increased income of the GT plant. If the interest is greater than increased income the deficiency will be added to the principal of the loan. Note that even if such a deficiency occurs in the earlier years of the loan, this does not necessarily mean unprofitable long-term operation.) After the loan has been fully repaid the surplus income is invested at the 8% interest rate in what may be termed a surplus or "cash asset" account. If this account is generalized to reflect a negative asset in the form of loan principal at any time, beginning with [−] $\$136.7 \times 10^6$ at year zero, we calculate the dashed line (inflated dollars) or the solid line which is corrected for the 5% yearly compounded inflation, reflecting constant first-year dollars.

If the life of both plants is taken as 20 years, we see that at the end of 16-2/3 years Company B has paid off the $\$136.7 \times 10^6$ loan and at 20 years is $\$37.6 \times 10^6$ (constant first-year dollars) richer than Company A.

If, however, we assume a scenario which is commonly favored today, we shall come to an even better result for Company B. Take the life of both plants as 40, not 20, years, but rebuild the plants in the 21st year of life, to replace worn-out elements such as turbine rotors, boiler tubes, and high-temperature heat exchanger tubes. Assume the rebuilding cost to be half the initial full equipment purchase price, which results in a penalty charge to the GT plant of $\$136.7 \times 10^6/2$ in first-year dollars or $\$68.35 \times 10^6 \times 2.6533 = \$181.35 \times 10^6$ in the 21st-year dollars. Also, rebuilding is assumed to interrupt operations in the 21st year so that each plant runs the equivalent of only one-half year, with a consequent 50% loss in GT savings. Finally, it is assumed that after 20 years both plants being old are no longer used for base-load service with a maximum service factor, but for peak-load service at 70% of that factor. The consequences of these assumptions on the operational savings of the GT plant are shown in the upper solid line of Fig. 4.

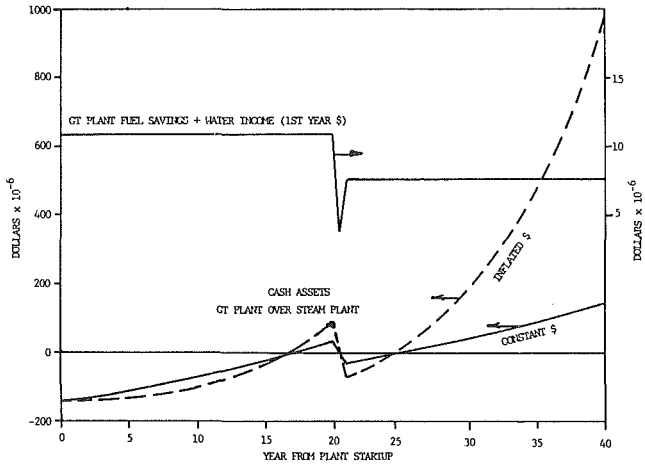


Fig. 4 Cost-benefit of 316 MW GT power plant over steam plant

During the 21st year Company B must borrow additional funds to pay for its rebuilding, but this loan is paid off by the 25th year. At the end of 40 years Company B is ahead of Company A by $\$145.4 \times 10^6$ (constant dollars).

It is of interest to note that the break-even extra initial investment (that is, the borrowed amount that makes the gain of Company B zero at the end of 40 years) is $\$172 \times 10^6$. This figure is 1.26 times the $\$136.7 \times 10^6$ predicted investment penalty for the GT plant. The 1.26 will be seen as an economic safety factor.

It should also be noted that a commonly used annual charge of 18% [4] on initial investment would require the proposed GT plant to save $0.18 \times \$136.7 \times 10^6 = \$24.6 \times 10^6$ each year. Such savings clearly cannot be anticipated. The origin of the 18% figure has not been established and therefore its application to our economic model cannot be discussed.

Conclusions

Technical and economic arguments are presented in favor of serious consideration of an air cycle in place of a steam cycle for a coal-fired electric power plant. The air cycle with ten-stage intercooled compression and nine reheat stage expansion is shown to be not only very efficient in ideal cycle calculations, but when adapted to a process using practical equipment it shows operating savings (mainly fuel) which justify the 43.3% increased initial investment.

Since the assumptions on which the above conclusion is based will vary widely for different situations, it is expected that major variations in process (for example, less reheat and intercooling steps, a less efficient air preheater) will be economically justifiable; or the steam plant will be the economic choice. Much depends on the economic outlook. The objective of this study is to show that for certain assumptions which are reasonable in many situations, the air-cycle plant should be given serious consideration. The more efficient use of fuel is justified not only by the economic factors discussed in this study but by an important factor whose economic benefits are difficult to quantify, namely, the improvement of air quality resulting simply from the firing of less fuel for a given electric output.

Downloaded 01 Jun 2010 to 171.66.16.71. Redistribution subject to ASME license or copyright; see http://www.asme.org/terms/Terms_Use.cfm

So we now answer the objections to a fully gas turbine cycle listed in the introduction:

1 Indeed the air heater (B and E2) is expensive, but the operating savings may justify the expense.
2 High temperature (by gas turbine standards) is not required. The proposed cycle has a top temperature of 1700°F (927°C) primarily because alloy steels are now available that can sustain a low but sufficient design stress at 1800°F (982°C). The preheater or regenerator calls for a metal temperature of only 1600°F (871°C). The tube materials are indeed expensive, but again the savings may justify the expense.
3 It is indeed essential for a proponent of the air cycle to show that the high cost of heat transfer equipment is justified.
4 The net work output per unit mass flow of working fluid may be low, but this is a poor standard with which to make economic judgments. The question again is whether or not the extra equipment cost is justified. It is the purpose of this study to show that the answer may well be affirmative.

From a purely technological point of view the conclusions may be summarized as follows. A coal-fired electric power plant using air as the working fluid is proposed which has a thermal efficiency (coal pile to bus bar) near 45.8%, as compared to the best steam plants having an efficiency of 38.0%. The initial plant investment is estimated to increase by 43.3%, which is shown to be cost effective. For an air-cycle power plant delivering 316 MW the required atmospheric air flow is about one million cu ft/min, from which at an atmospheric dew point of 60°F (15.6°C) water is removed at a rate of 130,000 gal per day, which at 40 gal per day per person supplies a community of 3250 persons.

Acknowledgments

During the course of this study the writer received constructive suggestions and expert evaluation from professional associates, particularly William E. Trumpler, Robert H. Cherry, and Edmund G. Filetti, for which sincere gratitude is expressed. Of major importance have been the comments and critical reviews of two friends of long standing: Peter B. Corson, Principal Engineer, Fossil Plant Engineering and Construction Department, Carolina Power and Light Company; and William H. Jackson, retired Vice President of the Power Generation Division, Babcock and Wilcox Company. In fairness to the individuals whose names I note in appreciation of help received, neither they nor the organizations with which they are associated should necessarily be considered in favor of the views expressed in the paper. Responsibility for these views is mine alone.

References

1 Rice, I. G., "The Reheat-Gas-Turbine Combined Cycle," *Mechanical Engineering*, Vol. 104, No. 4, Apr. 1982, pp. 46-57.
2 Rice, I. G., and Jenkins, P. E., "Comparison of the HTTT Reheat-Gas-Turbine Combined Cycle with the HTTT Nonreheat Gas-Turbine Combined Cycle," ASME JOURNAL OF ENGINEERING FOR POWER, Vol. 104, No. 1, Jan. 1982, pp. 129-142.
3 Burton, D. C., "Combustion Turbines at the Crossroads," *Mechanical Engineering*, Vol. 104, No. 4, Apr. 1982, pp. 79-85.
4 Foster-Pegg, R. W., "Combined Cycles Have Potential for Cleaner, More Economical Use of Coal," *Power Engineering*, Apr. 1982, p. 80-84.
5 Haywood, R. W., *Analysis of Engineering Cycles*, Pergamon Press, 1980.
6 Meyer, C. A., McClintock, R. B., Silvestri, G. J., and Spencer, R. C., Jr., *Thermodynamic and Transport Properties of Steam*, ASME, New York, 1967.
7 Keenan, J. H., and Kaye, J., *Gas Tables*, Wiley, New York, 1948.
8 Anson, D., Hazard, H. R., and Flanigan, L. J., "Indirect Pulverized-Coal Fired Air Heaters for Gas Turbine Service," ASME Paper No. 82-GT-172.
9 Ward, M. E., Metcalf, A. G., and Dapkunas, S. J., "Ceramic Tube Heat Exchanger Technology Development for Indirect-Fired Gas Turbine Cycle," ASME JOURNAL OF ENGINEERING FOR POWER, Vol. 105, No. 2, Apr. 1983, pp. 310-316.
10 McAdams, W. H., *Heat Transmission*, Third Edition, McGraw-Hill, New York, 1954.
11 "Top 20 Generating Units—by Heat Rate" (Table 4), *Electric Light and Power*, Vol. 60, No. 8, Aug. 1982, pp. 12-13.

Downloaded 01 Jun 2010 to 171.66.16.71. Redistribution subject to ASME license or copyright; see http://www.asme.org/terms/Terms_Use.cfm

So we now answer the objections to a fully gas turbine cycle listed in the introduction:

1 Indeed the air heater (B and E2) is expensive, but the operating savings may justify the expense.
2 High temperature (by gas turbine standards) is not required. The proposed cycle has a top temperature of 1700°F (927°C) primarily because alloy steels are now available that can sustain a low but sufficient design stress at 1800°F (982°C). The preheater or regenerator calls for a metal temperature of only 1600°F (871°C). The tube materials are indeed expensive, but again the savings may justify the expense.
3 It is indeed essential for a proponent of the air cycle to show that the high cost of heat transfer equipment is justified.
4 The net work output per unit mass flow of working fluid may be low, but this is a poor standard with which to make economic judgments. The question again is whether or not the extra equipment cost is justified. It is the purpose of this study to show that the answer may well be affirmative.

From a purely technological point of view the conclusions may be summarized as follows. A coal-fired electric power plant using air as the working fluid is proposed which has a thermal efficiency (coal pile to bus bar) near 45.8%, as compared to the best steam plants having an efficiency of 38.0%. The initial plant investment is estimated to increase by 43.3%, which is shown to be cost effective. For an air-cycle power plant delivering 316 MW the required atmospheric air flow is about one million cu ft/min, from which at an atmospheric dew point of 60°F (15.6°C) water is removed at a rate of 130,000 gal per day, which at 40 gal per day per person supplies a community of 3250 persons.

Acknowledgments

During the course of this study the writer received constructive suggestions and expert evaluation from professional associates, particularly William E. Trumpler, Robert H. Cherry, and Edmund G. Filetti, for which sincere gratitude is expressed. Of major importance have been the comments and critical reviews of two friends of long standing: Peter B. Corson, Principal Engineer, Fossil Plant Engineering and Construction Department, Carolina Power and Light Company; and William H. Jackson, retired Vice President of the Power Generation Division, Babcock and Wilcox Company. In fairness to the individuals whose names I note in appreciation of help received, neither they nor the organizations with which they are associated should necessarily be considered in favor of the views expressed in the paper. Responsibility for these views is mine alone.

References

1 Rice, I. G., "The Reheat-Gas-Turbine Combined Cycle," *Mechanical Engineering*, Vol. 104, No. 4, Apr. 1982, pp. 46-57.
2 Rice, I. G., and Jenkins, P. E., "Comparison of the HTTT Reheat-Gas-Turbine Combined Cycle with the HTTT Nonreheat Gas-Turbine Combined Cycle," ASME JOURNAL OF ENGINEERING FOR POWER, Vol. 104, No. 1, Jan. 1982, pp. 129-142.
3 Burton, D. C., "Combustion Turbines at the Crossroads," *Mechanical Engineering*, Vol. 104, No. 4, Apr. 1982, pp. 79-85.
4 Foster-Pegg, R. W., "Combined Cycles Have Potential for Cleaner, More Economical Use of Coal," *Power Engineering*, Apr. 1982, p. 80-84.
5 Haywood, R. W., *Analysis of Engineering Cycles*, Pergamon Press, 1980.
6 Meyer, C. A., McClintock, R. B., Silvestri, G. J., and Spencer, R. C., Jr., *Thermodynamic and Transport Properties of Steam*, ASME, New York, 1967.
7 Keenan, J. H., and Kaye, J., *Gas Tables*, Wiley, New York, 1948.
8 Anson, D., Hazard, H. R., and Flanigan, L. J., "Indirect Pulverized-Coal Fired Air Heaters for Gas Turbine Service," ASME Paper No. 82-GT-172.
9 Ward, M. E., Metcalf, A. G., and Dapkunas, S. J., "Ceramic Tube Heat Exchanger Technology Development for Indirect-Fired Gas Turbine Cycle," ASME JOURNAL OF ENGINEERING FOR POWER, Vol. 105, No. 2, Apr. 1983, pp. 310-316.
10 McAdams, W. H., *Heat Transmission*, Third Edition, McGraw-Hill, New York, 1954.
11 "Top 20 Generating Units—by Heat Rate" (Table 4), *Electric Light and Power*, Vol. 60, No. 8, Aug. 1982, pp. 12-13.

DISCUSSION

G. J. Silvestri, Jr.[5]

The author has proposed a thought-provoking, interesting concept. The use of intercooling coupled with a high-pressure-ratio gas turbine that produces water, even in arid or semiarid regions, is intriguing. Moreover, the design heat rate, 7450 Btu/kWh, is impressive. However, the large number of stages of reheat and intercooling, plus regeneration, raise concerns related to parasitic losses.

While it appears that the low compression power of a steam cycle is purchased at a heavy price (last paragraph in the section "Ideal Power Plant Cycles") because of large deviations from Carnot's principle, there is a major distinction that should be recognized. Since the compression power is low in a steam plant, deviations in compression efficiency or pressure losses that increase compression power have minimal effect. For example, the compression power is about 4 percent of net turbine output in a 3500 psig steam plant. If the compression power is actually 10 percent higher (because of high pressure drops in the feedwater heaters, boiler and main steam piping and/or lower pump efficiency), the plant efficiency would decrease by less than 0.5 percent. In the case of the gas turbine cycle, if parasitic losses increased the compression power, 252 MW, by 10 percent, the net plant output would decrease by about 25 MW or 8 percent. Because the cycle is intercooled, the increased compression power would not change the cycle heat added and the heat rate would increase by 8 percent. The intercooler surface area and cost would also increase.

If parasitic losses decreased the gross turbine output, 629 MW, by 10 percent, the net plant output would decrease by 63 MW or 20 percent. In this instance, the increased parasitic losses associated with the turbine-reheater system would reduce the heat added in the reheaters so that the heat rate would increase by less than 20 percent. Nevertheless, the penalty is substantial.

The estimated efficiencies for the gas turbine components, 89 percent for the compressor and 92 percent for the turbine, are reasonable. However, the estimates for pressure losses are extremely optimistic in this observer's judgment. For example, the first reheat stage pressure loss is only 0.4 percent with the loss increasing in successive stages, being 1.7 percent on the last stage. Each stage of reheat (total of nine) will result in an exit loss from the preceding turbine stage (total and possibly static pressure loss), pressure loss in the piping or ducting connecting the turbine sections and the reheaters, pressure loss in the reheater and an inlet loss of the next turbine section. It is no simple feat to transport a high-pressure gas at 1525°F to 1700°F. The cost of such ducting and the required expansion joints is high. Moreover, the pressure losses in the regenerator and the intercoolers also seem overly optimistic.

About 15 years ago the Westinghouse R&D Center investigated a novel gas turbine cycle designated CYCLE IV.

[5]Advisory Engineer, Westinghouse Electric Corporation, Power Generation Division, Orlando, FL 32817

Copyright © 1985 by ASME
Downloaded 01 Jun 2010 to 171.66.16.71. Redistribution subject to ASME license or copyright; see http://www.asme.org/terms/Terms_Use.cfm

The cycle had intercooling and one stage of reheating. The initial results were very encouraging. However, the pressure losses and costs (particularly of high-temperature ducting and expansion joints) were found to be considerably higher in subsequent investigations than had been originally estimated. To bring some perspective to the pressure loss question, it should be noted that the transport of steam from the IP to the LP element of a steam turbine at modest pressures and temperatures typically results in a 2 percent pressure loss plus an exit loss in the IP element.

If large pipes are used to reduce the pressure losses (lower velocities), the piping system becomes more rigid and bends or expansion joints must be incorporated to achieve sufficient flexibility. Crossover piping between the moisture separator outlet and the LP turbine inlet of a nuclear unit requires the inclusion of a number of elbows and piping bends to provide sufficient flexibility to transport the 500°F, 150 to 200 psia steam. In the proposed cycle the temperatures are much higher, 1525°F to 1700°F, with pressures up to 540 psia, so the flexibility requirements are greater. Typically, methods to achieve flexibility result in increased cost and pressure loss.

Since the compressor power is so large, 376.4 MW, starting considerations may require that the compressor train be separated from the turbine train. Because the volume of fluid is large in the reheaters and in the piping to and from the reheaters, overspeed during a trip is a concern. This would require the incorporation of interceptor valves at several locations in the turbine train, which would increase the pressure losses and cost. The use of large pipes and heat exchangers to reduce pressure losses aggravates the overspeed.

The sizable cost associated with the heat exchangers and unknowns regarding operation and fabrication introduce a large uncertainty in the gas turbine plant capital cost. Heat exchanger and ducting costs and pressure losses eliminated CYCLE IV as a viable concept.

The 8 percent interest expense is atypical. A value of 17 percent would be more appropriate. This would substantially increase the payback period of the gas turbine cycle even if the heat rate were achievable.

Finally, the gas turbine cycle is more sensitive to changes in ambient temperature. At 90°F ambient dry bulb temperature it would incur a larger capability penalty than the steam plant, requiring the addition of simple gas turbine peaking units. This would increase the equivalent capital and energy costs.

There are other lesser important items that were noted, such as fuel composition, which helps the gas turbine cycle and penalizes the steam plant (moisture in the flue gas). The heat rate for the reference steam plant (Marshall Station) is an annual one reflecting seasonal and off-design operation. Consequently, a more realistic comparison would be between the design heat rates of the two plants as the annual heat rates are typically 2 to 5 percent higher than the design heat rates. A recent study of an advanced steam plant (4500 psig, 1100°F with two reheats to 1050°F and a scrubber) had an annual design heat rate of 8335 Btu/kWh [12].

References

12 *Engineering Assessment of an Advanced Pulverized-Coal Power Plant*, CS-2223, prepared for the Electric Power Research Institute by Westinghouse Electric Corp., Combustion Engineering, Inc. and Gilbert Associates, Inc., Jan. 1982.

Author's Closure

It is gratifying that a person who is as competent and familiar with the power generation field as Mr. George Silvestri presents important points, a discussion of which should add greatly to the value of the paper.

The "high price" of low compression work in the steam cycle is intended to refer only to ideal cycle comparisons. Mr. Silvestri is correct in pointing out that the efficiency of an operational cycle is much less sensitive to feedwater pump efficiency (steam) than it is to compressor efficiency (air). Holding compressor efficiency high, with whatever this implies in maintenance and operation, has always been recognized as particularly important to gas turbine performance. Similarly, the air turbine T must be maintained and operated to keep losses low, although losses here are not as sensitive to cycle efficiency as they are for the compressor.

Conventional power plant practice indeed suggests that my indicated pressure losses are unrealistically low. However, my background in chemical plant heat exchanger design, particularly in cryogenic processes where gas-to-gas exchangers play a major role, indicates that such pressure drops are standard practice. Of course, they result in big exchangers and large piping. The question is one of economics, and so it is essential to design the equipment to specifications, including pressure drop, and estimate the cost. This I have done to the degree of accuracy I think appropriate at this time. I conclude that the low pressure drops (and the low temperature differences particularly in heater B) are cost effective in the overall picture. It is indeed possible, in fact probable, that a more detailed study will show that higher pressure drops (or many other possible changes) will improve the economics, but such a result could only make the gas turbine plant look even better than I now suggest it is.

With respect to pressure losses in piping or ducting, I have the feeling that these must be taken as appropriately low with respect to equipment pressure losses. Yes, the piping will be expensive, but can it possibly represent an item large with respect to the cost of the equipment to which the piping is connected? I am at this point not prepared to give firm figures, but my associates also share my question as to why expansion joints, of which there are indeed a considerable number, should necessarily be so expensive, although of course everyone recognizes that they will not be cheap. I should note that air pressure at equipment entrance and exit are considered in the calculations as total pressure taken at the inlet or outlet flange connection; the piping is not charged with inlet or exit losses.

There are indeed unknowns and uncertainties in any new plant design. Yet what is worse than facing these with courage may be seeing others succeed and our having to follow. I am not acquainted with CYCLE IV, which I assume is proprietary. I look forward to learning about the proposed Westinghouse advanced steam plant.

The matter of interest rates and inflation over the next 40 years is a guessing game I would like to stay out of, but I may not. As of August 1984 Mr. Silvestri was correct about current interest near 17 percent, but that figure has dropped substantially in the past year. Historically, the prime rate has been mostly 2 to 3 percent above the inflation rate. Utilities should be able to borrow at the prime rate. I predicate my calculation on a 3 percent difference between prime and inflation. On that presupposition, the higher the inflation rate, the easier it is to justify an initial investment expenditure. If I take a 17 percent prime, and consequently a 14 percent inflation, the initial plant investment will be paid back in short order. I was conservative in assuming an 8 percent prime and 5 percent inflation.

Mr. Silvestri is correct in stating that change in ambient temperature will have more of an effect on the air cycle than it does on the steam cycle. This assumes that steam condensers are not air cooled. But I have not calculated the numbers to check the magnitude of the ambient temperature effect. If water is used to cool the steam condenser, however, the cost of locating near a large body of water and piping the water to the condenser must be included in the economics. In my study you will note that the possible saving in plant investment by not locating the plant near a large water source has never been credited to the gas turbine plant.

Downloaded 01 Jun 2010 to 171.66.16.71. Redistribution subject to ASME license or copyright; see http://www.asme.org/terms/Terms_Use.cfm

Is the heat rate of 8970 Btu/kWh for the best conventional steam plant comparable to the 7456 Btu/kWh predicted for the gas turbine plant? I have tried to make it so by selecting large loss factors for the gas turbine plant performance estimates. Auxiliary losses of 5 percent, and flue gas scrubber and control air losses of 8 percent, the latter including presumably startup and off-design operation, are on the high end of the ranges suggested to me as "reasonable." But I admit that even what I consider high loss factors are still guesses.

Perhaps the most serious problem with the proposed gas turbine cycle, which I began to look into after the paper was written, concerns the pulverized coal fired air heater *B*, with a maximum tube wall temperature of 1800°F. The steam plant with steam leaving the boiler at 1200°F has a maximum tube wall temperature of perhaps 1300 to 1400°F, substantially below that of the air heater. At the higher surface temperature the fly ash may stick to the tubes more readily and corrode the metal more severely. If this problem is serious we may have to redesign the standard furnace to separate the fly ash from the combustion gas before the ash gets to the tubes, perhaps by directing the hot combustion gas into a kind of cyclone built of firebrick which forces the swirling gas to deposit molten ash on the cyclone wall. The ash that remains in the stream may not do much harm.

Downloaded 01 Jun 2010 to 171.66.16.71. Redistribution subject to ASME license or copyright; see http://www.asme.org/terms/Terms_Use.cfm

Evaluation of Polytropic Calculation Methods for Turbomachinery Performance

R. A. Huntington
Senior Engineer.
Exxon Research and Engineering Company,
Florham Park, NJ 07932

Performance calculations for centrifugal compressors have been based on polytropic analysis for many years. The basic polytropic equation, in which head is found from gas pressure, temperature, and compressibility factor at the end points of compression, is applied by virtually all engineers involved with turbomachinery design, selection, or operation. The problems and errors associated with this simple calculation method when applied to nonideal gases have long been recognized. Schultz [1] proposed a correction factor to the head equation to compensate for the errors. This "polytropic head factor" correction is required by the ASME Power Test Code 10 [2] for the evaluation of compressor performance. Recently, the accuracy of even the corrected head equation has been questioned for the compression of gases to high pressures and an alternative calculation method has been proposed by Mallen and Saville [3]. Although differences were found between their method and the Schultz method of up to three percent, they did not show which method was more accurate. This paper evaluates the accuracy of these previous calculation methods and shows that both have errors for some compression calculations. In addition, a new polytropic calculation method is described and is shown to be substantially more accurate than the methods of both [1] and [3], thus allowing more precise evaluations of compressor performance.

Introduction

Centrifugal compressor thermodynamic performance calculations are generally based on the assumption that the gas compression follows a simple polytropic path from inlet to discharge conditions. This assumption takes the usual form of:

$$PV^n = \text{constant} \tag{1}$$

along the thermodynamic path of compression. Furthermore, equation (1) is limited to a constant value of n that is determined from the endpoints of the compression path. Next, equation (1) is combined with the definition of polytropic head:

$$H = \int_1^2 VdP \tag{2}$$

to yield the familiar head equation:

$$H = \left(\frac{n}{n-1}\right)[P_2V_2 - P_1V_1] \tag{3a}$$

or

$$H = Z_1RT_1\left(\frac{n}{n-1}\right)[(P_2/P_1)^{\frac{n-1}{n}} - 1] \tag{3b}$$

While this equation has been derived using equation (1), which is only exact for perfect gases, equation (3) is used routinely for all gases – without regard for and often without knowledge of this limitation.

In contrast to the relative simplicity of equation (1), the general definition of the polytropic path for a real gas is a path on which "the ratio of the reversible work input to the enthalpy rise is constant" [2] and is given by the differential equation [1]:

$$edh = VdP \tag{4}$$

where the polytropic efficiency, e, is constant along the path. This general definition of the polytropic path, however, cannot help us solve equation (2) but it does provide efficiency when combined with equation (2):

$$e\int_1^2 dh = \int_1^2 VdP$$

or

$$e = H/(h_2 - h_1) \tag{5}$$

Recognizing the potential inaccuracies associated with the assumptions of equation (1), Schultz, in his classic paper [1], formulated a correction factor for the polytropic head calculated by equation (3). This factor, known as the polytropic head factor, is derived from the assumption that the errors associated with equation (3) remain constant as the polytropic path ($PV^n = C$) deviates from an isentropic path ($dh = VdP$). With this correction factor, the polytropic head equation becomes:

Contributed by the Gas Turbine Division of THE AMERICAN SOCIETY OF MECHANICAL ENGINEERS and presented at the 30th International Gas Turbine Conference and Exhibit, Houston, Texas, March 18-21, 1985. Manuscript received at ASME Headquarters, December 17, 1984. Paper No. 85-GT-13.

Copyright © 1985 by ASME
Downloaded 01 Jun 2010 to 171.66.16.71. Redistribution subject to ASME license or copyright; see http://www.asme.org/terms/Terms_Use.cfm

$$H = f\left(\frac{n}{n-1}\right)[P_2 V_2 - P_1 V_1] \tag{6}$$

where

$$f = (h_{2s} - h_1)/\left\{\left(\frac{n_s}{n_s - 1}\right)[P_2 V_{2s} - P_1 V_1]\right\} \tag{7}$$

It can be seen by inspection that equations (6) and (7) satisfy the requirement that $H = (h_2 - h_1)$ for an isentropic compression path ($e = 1$, $n = n_s$), but the accuracy of the polytropic head factor is open to question for any polytropic efficiency other than 100%.

Regardless of this potential question and because it was recognized as the best available method at that time, Schultz's polytropic head factor was incorporated into the 1965 revision of the ASME Power Test Code 10 [2] for the evaluation of compressor head and efficiencies from test data. This method has continued in use for the many years since 1965. However, more recently the accuracy of equation (6) has been seriously questioned for the compression of gases to high pressure [3]. In [3], Mallen and Saville have proposed an alternate method for the calculation of polytropic head and efficiency, and have compared their results with those of the Schultz method for several cases. Maximum deviations of 3% of head were found between the methods.

The Mallen and Saville calculation method is based on the assumption that along the compression path:

$$T\frac{dS}{dT} = \text{constant} \tag{8a}$$

or

$$dS = C\frac{dT}{T} \tag{8b}$$

Equation (8*b*) leads to a simple equation for head by combining it with one of the Maxwell relations [4]:

$$dh = TdS + VdP \tag{9}$$

to yield:

$$H = (h_2 - h_1) - (S_2 - S_1)\frac{T_2 - T_1}{\ln(T_2/T_1)} \tag{10}$$

Efficiency is then calculated using equation (5).

This method is somewhat easier to use than Schultz's method since isentropic discharge conditions need not be calculated. However, by substituting equation (8*b*) into the general entropy derivative given by [4]:

$$dS = C_p\frac{dT}{T} - \left(\frac{\partial V}{\partial T}\right)_p dP \tag{11}$$

and eliminating the dS term, it may be shown that this method requires that the specific heat of the compressed gas satisfy the following relation along the polytropic path:

$$C_p = \frac{(1 + eX)(S_2 - S_1)}{(1 - e)\ln(T_2/T_1)} \tag{12}$$

where X is the Schultz compressibility function [1, 2].

This relationship is only satisfied exactly by perfect gases, where $X = 0$ and C_p is constant. In general, these restrictions are not met by real gases encountered in industry and therefore the accuracy of equation (10) is diminished.

The potential errors introduced by the two methods described above are strictly computational; that is, the errors in the formulations of equations (6) and (10) are caused solely by simplifying assumptions necessary to allow head and efficiency calculations based only on the endpoints of compression. As stated before, [3] gives several examples where the results of their method differ from those of Schultz's method by as much as 3%. However, these authors do not determine which of these two methods is more accurate. In the following sections, we will describe a "reference" calculation method that will then be applied to demonstrate the accuracy of each of the above methods. In addition, in the latter sections, we will develop a new method to calculate polytropic head and efficiency from the endpoints of the compression path, and show that this new method is substantially more accurate than both the Schultz and the Mallen and Saville methods.

"Reference" Polytropic Calculation Method

As stated before, the errors in the two previous polytropic calculation methods are caused by the simplifying assumptions made in formulating the equations. Therefore, in order to check these calculations, a "reference" must be found that does not rely on simplifying assumptions. One such method would calculate polytropic head by the direct integration of VdP along the polytropic path defined by equation (4). This integration cannot be done in closed form but can be accomplished numerically to a very high precision.

The numerical integration requires breaking the polytropic compression path between two pressure levels into a large series of short subpaths, each of which contributes only a small pressure rise. If the compression path is divided sufficiently, equations (2) and (4) can be linearized without significant error and for the i-th subpath are given by:

$$H_i = V_{\text{avg}}\Delta P_i \tag{13a}$$

$$H_i = e\Delta h_i \tag{13b}$$

V_{avg} is the average specific volume over the subpath and e is the constant efficiency throughout the compression path. Alternately, equation (3) could replace equation (13*a*) for each subpath with similar or better accuracy.

Head calculations for each subpath require that equation (13*a*) be solved by trial and error where the initial pressure and temperature (and thus the specific volume) are known but only the final pressure of the subpath is known. Therefore, an estimate of subpath final temperature must be made, H_i calculated by equation (13*a*) and then checked with equation (13*b*). The subpath final temperature is adjusted until equations (13*a*) and (13*b*) agree to the required precision.

For the complete compression path, the total polytropic head is simply the sum of the subpath heads:

$$H = \Sigma H_i \tag{14}$$

By carefully programming the above equations and procedure on a computer, polytropic heads may be calculated very accurately. On the other hand, computational precision

Nomenclature

a,b,c = constants for compressibility function
e = polytropic efficiency
f = polytropic head factor
h = enthalpy, kJ/kg
n = polytropic volume exponent
C_p = specific heat at constant pressure, kJ/kg•K
H = polytropic head, kJ/kg
P = pressure, kPa
R = gas constant, kJ/kg•K
S = entropy, kJ/kg•K
T = temperature, K
V = specific volume, m^3/kg
Z = compressibility factor

Subscripts

1 = inlet
2 = discharge
3 = intermediate
s = isentropic
i = i-th subpath of numerical integration
avg = average over subpath

Downloaded 01 Jun 2010 to 171.66.16.71. Redistribution subject to ASME license or copyright; see http://www.asme.org/terms/Terms_Use.cfm

Table 1 Sample cases for polytropic compression calculations

Description	Case number 1	2	3	4
Gas	R-12	Ethylene	Ethylene	CO_2
Inlet pressure (kPa)	68.9	2500	2500	7585
Inlet temperature (K)	250	310	310	310
Discharge pressure (kPa)	896.3	50,000	30,000	41,370
Discharge temperature (K)	372	570	535	460

Notes: • Case 1 is from [1];
• Case 2 is from [3];
• Case 3 is similar to an example from [3].

Table 1A Sample cases for polytropic compression calculations (English units)

Description	Case number 1	2	3	4
Gas	R-12	Ethylene	Ethylene	CO_2
Inlet pressure (psia)	10.0	362.5	362.5	1100.1
Inlet temperature (°F)	−10.0	98.3	98.3	98.3
Discharge pressure (psia)	130.0	7250.	4351.2	6000.3
Discharge temperature (°F)	210.0	566.3	503.3	368.3

Notes: • Case 1 is from [1];
• Case 2 is from [3];
• Case 3 is similar to an example from [3].

Table 2 Results of polytropic calculations

Results	Case number 1	2	3	4
Reference method				
Head (kJ/kg)	51.58	356.77	273.57	80.56
Efficiency (%)	75.24	80.99	74.99	64.51
Schultz's method				
Polytropic head factor	1.0151	0.8992	0.9433	0.9586
Head (kJ/kg)	51.67	350.66	269.33	79.55
Efficiency (%)	75.38	79.60	73.83	63.70
Mallen and Saville's method				
Head (kJ/kg)	51.62	359.61	275.49	81.45
Efficiency (%)	75.30	81.63	75.52	65.22

Notes: All calculations of real gas properties were made with the Lee–Kesler equation of state [5, 6].

Table 2A Results of polytropic calculations (English units)

Results	Case number 1	2	3	4
Reference method				
Head (ft-lb/lbm)	17,255.	119,357.	91,525.	26,953.
Efficiency (%)	75.24	80.99	74.99	64.51
Schultz's method				
Polytropic head factor	1.0151	0.8992	0.9433	0.9586
Head (ft-lb/lbm)	17,288.	117,313.	90,104.	26,614.
Efficiency (%)	75.38	79.60	73.83	63.70
Mallen and Saville's method				
Head (ft-lb/lbm)	17,268.	120,309.	92,167.	27,249.
Efficiency (%)	75.30	81.63	75.52	65.22

Notes: All calculations of real gas properties were made with the Lee–Kesler equation of state [5, 6].

Table 3 Errors in polytropic head calculations

Calculation method	Case number 1	2	3	4
Schultz (PTC-10)	+0.19%	−1.71%	−1.55%	−1.26%
Mallen and Saville	+0.08%	+0.80%	+0.70%	+1.10%
Reference method*	0.0011%	0.015%	0.004%	0.001%
Entropy change**	0.0004%	−0.0036%	−0.0013%	−0.0005%

*Potential error in reference polytropic head based on observed error in numerically integrated entropy.
**Difference between entropy increase found via numerical integration of equations (16) and (17) and actual entropy change per the equation of state for the gas.

and roundoff errors may also cause significant errors that may preclude this method's use as a reference polytropic calculation method. To prove the accuracy of the numerical integration outlined above, we will use its results to calculate the entropy change along each subpath. Then by summing along the entire compression path, the total entropy change may be found. Finally, we will compare this total entropy change to the known value calculated from the equation of state for the gas.

This numerical entropy integration along the polytropic path is done by combining equation (9) with the path equation (equation (4)) to yield:

$$TdS = \left(\frac{1-e}{e}\right) VdP \tag{15}$$

Downloaded 01 Jun 2010 to 171.66.16.71. Redistribution subject to ASME license or copyright; see http://www.asme.org/terms/Terms_Use.cfm

and converting it to a difference equation, as before, for the i-th subpath:

$$\Delta S_i = \left(\frac{1-e}{e}\right) H_i / T_{\text{avg}} \tag{16}$$

where H_i is calculated using equation (13a) and T_{avg} is the average temperature along the subpath. As with equation (14), the total entropy change along the compression path is given by:

$$\Delta S = \Sigma \Delta S_i \tag{17}$$

Since the average temperature along each subpath is known very accurately, differences found between equation (17) and the entropy change calculated from the equation of state will be directly proportional to errors in the reference polytropic head. In the example cases that will be discussed in the following sections, step sizes for the numerical integration and computational precision were chosen to always maintain errors in ΔS of less than 0.004%. This maximum error in the entropy change implies a potential error in the reference polytropic head and efficiency of roughly 0.015%. This potential error is sufficiently small to use our reference values as the basis for comparison by other polytropic calculation methods.

Evaluation of Polytropic Calculation Methods

The accuracy of the Schultz method or the Mallen and Saville method can be evaluated by comparing their results to those obtained with the reference method described in the preceding section. For these comparisons, four example cases were selected; three of these are identical or similar to examples presented in [1 and 3]. These cases are described in Table 1 and the results of the polytropic calculations for each case are listed in Table 2. Finally, a tabulation of the errors found with the Schultz and the Mallen and Saville methods is given in Table 3.

The deviations shown in Table 3 reflect the accuracy of the calculation methods evaluated relative to the very precise reference method. The effect of gas property data on the relative errors has been virtually eliminated by the use of a common and accurate source of gas data for all of the methods presented in this paper. All of the gas properties were evaluated with the Lee–Kesler equation of state [5, 6] which is recommended over the pressure and temperature ranges of the four examples [5].

Review of Table 3 shows that errors (in head and efficiency) of up to 1.7% were found with the Schultz method and up to 1.1% with that of Mallen and Saville in comparison to the reference method. In addition, this table shows that the Schultz method generally calculates lower values of head than the reference method, while the Mallen and Saville method calculates higher values. This accounts for the large discrepancies between these methods reported in [3]. Finally, the magnitude of potential inaccuracy of the reference head and efficiency values are listed in Table 3. These range from only 0.001% to 0.015% and are proportional to the actual deviations (also listed) of the numerically integrated entropy change from the exact values calculated via the equation of state for the gas.

When one considers that serious disputes have been raised between turbomachinery vendors and customers over less than one half point of efficiency (one half or so of the above deviations), the errors associated with the two calculation methods evaluated are significant and unacceptably large. Also, one must remember that these calculation inaccuracies are in addition to any errors associated with the evaluation of gas composition and properties and the errors in pressure and temperature readings taken during a performance test. These latter sources of error are often difficult to reduce below certain levels. However, significant inaccuracies in the calculation of head and efficiency can be avoided by the proper formulation of the polytropic equations.

New Polytropic Calculation Method Developed

The previous section demonstrated that the Schultz and the Mallen and Saville methods produce significant errors for some compression calculations. These errors are caused by the simplifying assumptions used to formulate the equations. To improve the accuracy of the polytropic calculations, a new calculation method is formulated with the following distinctions:

1 The polytropic path equation (equation (4)) is directly incorporated into its derivation; and
2 a general relationship of the compressibility factor and pressure is assumed along the polytropic path of compression.

With these bases, we begin the derivation by combining the path equation (equation (4)) and the Maxwell relation (equation (9)) to give the general relationship of the entropy derivative along the polytropic path:

$$dS = \left(\frac{1-e}{e}\right) \frac{V}{T} dP \tag{18}$$

Next, we replace (V/T) by (ZR/P) per the general equation of state $PV = ZRT$. This now becomes:

$$dS = R\left(\frac{1-e}{e}\right) Z \frac{dP}{P} \tag{19}$$

Since this equation is defined along a reversible path, the compressibility factor can be expressed as a function of one state property of the gas. Therefore, we may choose to express Z as a general function of pressure and directly integrate equation (19) to yield a relationship between polytropic efficiency and the pressure and entropy at the endpoints of the compression path.

Several functional forms for $Z(P)$ along the path were considered before a final selection was made. Initially, a linear relationship was tried but this was found to yield only slightly better results for polytropic head and efficiency than the calculation methods of [1 and 3]. The best relationship found that is still reasonably simple to use is:

$$Z = a + b(P/P_1) + c \ln(P/P_1) \tag{20}$$

With this relation for Z, equation (19) may be integrated to become:

$$S_2 - S_1 = R\left(\frac{1-e}{e}\right)\left\{a \ln(P_2/P_1) + b[(P_2/P_1) - 1] + \frac{c}{2}[\ln(P_2/P_1)]^2\right\} \tag{21}$$

This equation is then rearranged to solve for polytropic efficiency:

$$\frac{1}{e} = 1 + \frac{(S_2 - S_1)/R}{a \ln(P_2/P_1) + b[(P_2/P_1) - 1] + \frac{c}{2}[\ln(P_2/P_1)]^2} \tag{22}$$

Polytropic head is calculated by the relationship defined by equation (5).

The constants a, b, and c are evaluated from the compressibility factors found at the endpoints of the compression path and at one intermediate pressure along the path. To simplify the calculation of a, b, and c, the intermediate pressure, P_3, is:

$$P_3 = \sqrt{P_1 \times P_2} \tag{23}$$

With this choice, the constants are calculated by:

Downloaded 01 Jun 2010 to 171.66.16.71. Redistribution subject to ASME license or copyright; see http://www.asme.org/terms/Terms_Use.cfm

Table 4 Results of this paper's polytropic calculation method

Results	Case number 1	2	3	4
Head (kJ/kg)	51.58	356.60	273.55	80.56
Efficiency (%)	75.24	80.95	74.99	64.51
Error in comparison to reference method	–	−0.05%	−0.01%	–

Notes: All calculations of real gas properties were made with the Lee-Kesler equation of state [5, 6]

Table 4A Results of this paper's polytropic calculation method (English units)

Results	Case number 1	2	3	4
Head (ft-lb/lbm)	17,255.	119,300.	91,518.	26,953.
Efficiency (%)	75.24	80.95	74.99	64.51
Error in comparison to reference method	–	−0.05%	−0.01%	–

Notes: All calculations of real gas properties were made with the Lee-Kesler equation of state [5, 6]

$$a = Z_1 - b \tag{24a}$$

$$b = (Z_1 + Z_2 - 2Z_3)/[(P_2/P_1)^{0.5} - 1]^2 \tag{24b}$$

$$c = [Z_2 - a - b(P_2/P_1)]/\ln(P_2/P_1) \tag{24c}$$

The only problem remaining is to determine the intermediate temperature, T_3, so that Z_3 may be calculated. As a first estimate we will use:

$$T_3 \sim \sqrt{T_1 \times T_2} \tag{25}$$

based on the perfect gas relationship between temperature and pressure rise along a polytropic path.

Using this approximation and equation (22) for the four example cases, polytropic heads and efficiencies may be calculated with one half or less error than with the better of the Schultz and the Mallen and Saville methods. However, this error may be reduced much further by improving the T_3 estimate as follows:

$$T_3' = T_3 \exp[(S_3' - S_3)/C_p] \tag{26}$$

where T_3' = improved estimate for T_3

T_3 = initial estimate

S_3 = entropy at $P = P_3$, $T = T_3$

$$S_3' = S_1 + (S_2 - S_1) \times \left\{ \frac{\frac{a}{2}\ln(P_2/P_1) + b[(P_2/P_1)^{0.5} - 1] + \frac{c}{8}[\ln(P_2/P_1)]^2}{a\ln(P_2/P_1) + b[(P_2/P_1) - 1] + \frac{c}{2}[\ln(P_2/P_1)]^2} \right\} \tag{27}$$

(a, b, c are calculated per equation (24) with the previous T_3 estimate).

Recursive calculations with equations (26) and (27) converge to a precise value for T_3. However, one iteration has been found to be sufficient to reduce the T_3 variation to less than 0.1 K and produce good results.

Calculations of polytropic head and efficiency using the method just described are presented in Table 4 for each of the example cases cited previously. As shown by Table 4, the errors found with the Schultz and the Mallen and Saville methods have been virtually eliminated with this new method. While these previous calculation methods had a maximum error of 1.7% and 1.1% respectively for the example cases, the new method has a maximum error of only 0.05% and duplicates the reference head and efficiency for both example cases 1 and 4. From these four examples, it is clear that this new method produces much more accurate results than either of the previous calculation methods.

Conclusions and Recommendations

With the examples cited in this paper, the accuracies of the Schultz and the Mallen and Saville methods for polytropic head and efficiency calculations have been demonstrated. Errors in the Schultz method of 0.2 to 1.7% were found while the Mallen and Saville method had errors of 0.08 to 1.1%. These errors result from the simplifications made in the formulations of the equations and can be avoided with improved calculation methods. Also, differences of up to 2.5% were found between these methods thus raising a large potential uncertainty in the head and efficiency of a compressor when using these methods.

A new method to calculate polytropic head and efficiency from compressor inlet and discharge conditions has been described and shown to virtually eliminate the calculation errors found with the other methods. A maximum error of 0.05% was found for the example cases and the reference values were duplicated for two of these four cases. As a result of these findings, we recommend that the ASME Power Test Code 10 for Compressors and Exhaustors be amended to allow polytropic head and efficiency calculations by the method described in this paper. Furthermore, this method should be required whenever the calculated polytropic head factor (per the Schultz calculation) is beyond the range of roughly 0.995 to 1.005.

Acknowledgments

The author wishes to gratefully acknowledge the support of the Machinery and Project Services Division and Exxon Research and Engineering Company for permission to publish this paper. I would also like to thank Mr. John W. Fulton of ER&E for his help and criticism and especially for his encouragement to write this paper.

References

1 Schultz, J. M., "The Polytropic Analysis of Centrifugal Compressors," ASME JOURNAL OF ENGINEERING FOR POWER, Jan. 1962, pp. 69–82.

2 ASME Power Test Code 10 - 1965 for Compressors and Exhausters, ASME, New York, 1965.

3 Mallen, M., and Saville, G., "Polytropic Processes in the Performance Prediction of Centrifugal Compressors," Institute of Mechanical Engineers, Paper No. C183/77, pp. 89–96.

4 Van Wylen, G. J., and Sontag, R. E., *Fundamentals of Classical Thermodynamics*, Second Edition, Wiley, New York, 1973.

5 Reid, R. C., Prausnitz, J. M., and Sherwood, T. K., *The Properties of Gases and Liquids*, Third Edition, McGraw-Hill, New York, 1977.

6 Lee, B. I., and Kesler, M. G., "A Generalized Thermodynamic Correlation Based on Three-Parameter Corresponding States," *American Institute of Chemical Engineering Journal*, Vol. 21, May 1975, pp. 510–527.

Downloaded 01 Jun 2010 to 171.66.16.71. Redistribution subject to ASME license or copyright; see http://www.asme.org/terms/Terms_Use.cfm

T. E. Blehar[1]

1 Based on previously conducted gas property method comparison studies, it has been my experience that work factors that deviate from 1.0 by more than 1.5 percent are indicative of erroneous or inconsistent gas properties or equations of state in that particular region. That is, by utilizing multiple gas property methods, it often becomes apparent that the gas method that yielded a 0.89 or 0.94 work factor (as in Mr. Huntington's examples) was, in fact, inconsistent with other more applicable gas methods. The more accurate gas property methods resulted in work factors nearer 1.0, and in fact values of polytropic head and efficiency nearer the design and expected values. The differences in these results, then, were functions of the different gas property methods and not the Schultz equations. For this reason, it would appear to be more beneficial to select examples with gas property methods that resulted in work factors nearer 1.0 for Mr. Huntington's comparisons. This may yield a more valid comparison.

2 The work factor deviations occur most frequently over large compression paths. As Mr. Huntington has subdivided the compression path into shorter polytropic paths (which, in fact, more closely approach the isentropic path in the extreme), a more valid comparison would be to evaluate the Schultz method over these same smaller intervals, and sum the results. In this manner the work factor should approach 1.00 for each of the shorter paths and yield more accurate results or minimally a more valid comparison.

3 The area of application and gas property evaluation relative to the "dome" or critical point has a significant effect on the long path of compression versus the short path evaluation due to large variations in gas properties in that region. Therefore, the area of application and range of gas property accuracies for that area would be of value in assessing the significance of the differences in calculation methods. That is, if the gas properties are highly inaccurate in the area of evaluation, then a 1.0 percent difference in calculation methods may not be a significant value.

In conclusion, I would like to compliment Mr. Huntington on his efforts to identify a more accurate method to evaluate centrifugal compressor performance. The range of pressure, temperature, and gas mixture applications and required accuracies has changed considerably since the original Schultz publication. It is a credit to Mr. Huntington that he has devoted considerable time and effort to question, investigate and improve those methods. As a final note, if further comparisons are conducted relative to my above comments, I would be interested in discussing those results with Mr. Huntington.

Author's Closure

Mr. Blehar's comments generally deal with two areas of concern: firstly, the question of the use of appropriate gas property methods and data and secondly, the large deviations of the Schultz polytropic head factors from 1.0. While Mr. Blehar is correct in stating that the use of inaccurate gas properties may result in significant errors in the f-factor, it is not clear that deviations in f from 1.0 are alone sufficient to condemn a gas property method as inaccurate. If this were true, our thermodynamicist colleagues would have a simple and efficient method to evaluate equations of state. In addition, they would always conclude that the perfect gas equations were best since they are quaranteed to give f-factors equal to 1.0. Realistically, one must accept that some compression services, especially high-pressure services where compressibility factor changes may be 30 percent or more between inlet and discharge, may have f-factors that deviate significantly from 1.0. These deviations are simply an indication of the nonideality of the compressed gas for the given conditions.

The scope of the paper has been limited to a comparison of the three simple (i.e., hand calculable) polytropic head/efficiency calculation methods versus the precise reference (numerical integration) method and did not include an evaluation of the effects of various gas property evaluation methods. In fact, the use of a single accurate source for gas properties for all of the methods was intended to eliminate gas property deviations as a source of comparative error between the methods evaluated and the reference method. However, preliminary studies to this work were carried out using equations of state (Redlich-Kwong and Redlich-Kwong-Soave) that are considered to be less accurate than the Lee-Kesler equation of state that was finally used. These preliminary studies showed similar relative comparisons among the methods as those given in the paper. This validated the use of a single gas property source to eliminate gas property deviations as a source of relative error between the methods.

Regarding the specific source of gas data for the examples cited in the paper, each calculation method demonstrated (and this includes the reference method) used an identical equation of state with identical basic gas data (critical pressure, tem-

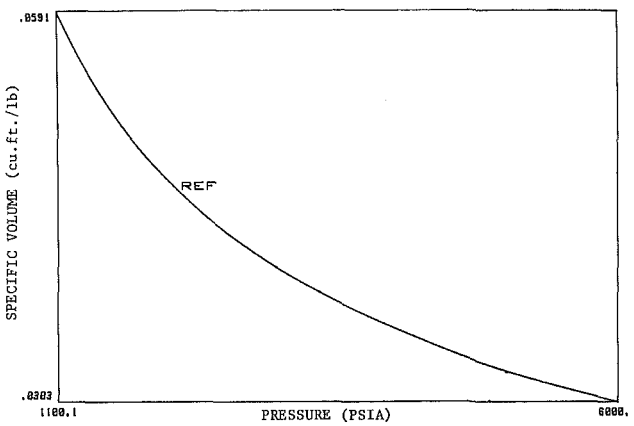


Fig. 1 Specific volume versus pressure along the constant efficiency polytropic path calculated by the reference method for case 4

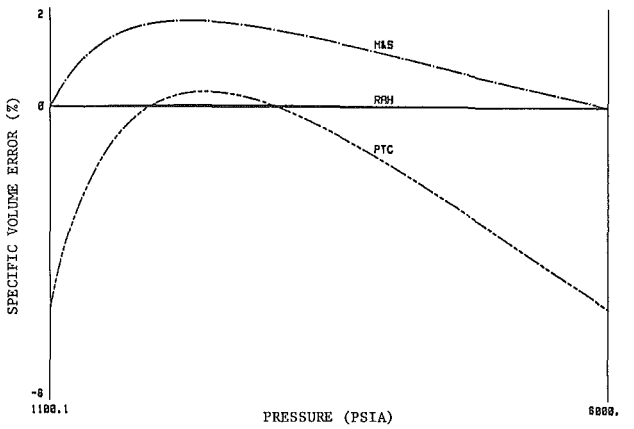


Fig. 2 Percentage deviation from the reference of the specific volume versus pressure paths predicted by the three simple methods

[1]Senior Engineer, Compressor Design and Development, General Electric Company, Fitchburg, MA 01420.

Copyright © 1985 by ASME
Downloaded 01 Jun 2010 to 171.66.16.71. Redistribution subject to ASME license or copyright; see http://www.asme.org/terms/Terms_Use.cfm

perature, specific heat function, etc.) for its calculations. The equation of state used was the Lee-Kesler equation cited in the paper and recommended by the Reid, Sherwood, and Prausnitz text also cited. The source of basic gas data for Refrigerant-12 was from Dupont literature on Freon while the other basic gas data for carbon dioxide and ethylene were taken from the Exxon proprietary gas data library which has been used and refined over the many years of Exxon's gas handling experience. Finally, the equation of state and basic data were coded into a single gas property computer subprogram to provide functionally continuous gas property evaluations for each of the methods.

Mr. Blehar also states his belief that the comparison of the Schultz method to the reference method is perhaps not valid since the reference subdivides the polytropic path into many short paths while the Schultz method is asked to negotiate the entire path in one step. It is clear that subdividing the polytropic path significantly reduces the gas property variation along each subpath and makes calculation of polytropic head much more accurate. This is precisely the idea behind the reference calculation method. What is not clear is how Mr. Blehar would use this subdivision technique to improve the Schultz method without completely duplicating the calculation procedures used by the reference method. Therefore, since this "subdivided" Schultz method and the reference method would be essentially identical, comparisons between them would be pointless.

Since it is clear from the discussion above that Mr. Blehar agrees (at least in concept) with the reference method, his comments do not address the major focus of the paper which is simply the order-of-magnitude accuracy improvement possible with the new polytropic calculation method (equation (22)) developed in the paper over the previous "simple" methods in comparisons to the very precise reference. To understand the reasons for the better accuracy of the new method, it is best to look at the definition of polytropic head given by equation (2). This equation simply represents the area under the curve of specific volume versus pressure along the polytropic path. This functional curve as produced by the reference method for example case 4 is shown in Fig. 1. The area under this curve is the reference head. The simple polytropic methods, through their assumptions and basic equations, either explicitly or implicitly approximate this curve in order to calculate head. Deviations between these approximate curves and the true curve may lead to errors in polytropic head and efficiency. Figure 2 is a plot of these percentage deviations for all three of the simple methods presented in the paper for example case 4. As can be easily seen, the Schultz and the Mallen and Saville curves (labeled as PTC and M&S) deviate significantly from the reference curve (Fig. 1) in both bounded area and curve shape. In contrast, the new method (labeled as RAH) is barely discernible from the zero-error axis and thus shows that it best matches the true polytropic path and will produce the most accurate results with consistency.

A. A. Fozi[2]

I would like to congratulate the author for his contribution to better understanding of the polytropic analysis. The method described in the paper as the "reference method" does in fact yield the most accurate evaluation of the polytropic values as defined by the equation

$$edh = VdP \ (e = \text{const})$$

John Schultz, in his original paper, showed an approximate integration method by use of auxiliary polytropic constants m and n. Mr. Huntington proposes to do the same by numerical methods utilizing computers for achieving very high accuracies. In this discussion I would like to point out that such accuracies may not be necessary in view of the inherent simplifying assumptions of the application of the polytropic analysis to the evaluation of gas compressor test results.

Volume flow through a compressor is continually changing (decreasing) and, therefore, the inlet stage of a multistage compressor is larger (higher specific speed) than the exit stage. This means that some stages having optimum specific speed will be more efficient than other stages. Depending on where these efficient stages are located, the actual path of compression will lie to the left (often) or to the right (seldom) of the hypothetical polytropic path.

A good example is the ethylene compressor case number 3 of Mr. Huntington's paper. In this case a typical compressor with six stages may perform, on a per-stage basis, as follows:

	Pressure (psia)	*Temperature (°F)*	*Polytropic efficiency*
1st stage	362.5- 609.2	98.3-171.7	0.8098
2nd stage	609.2- 980.3	171.7-245.2	0.7593
3rd stage	980.3-1515.4	245.2-317.3	0.7159
4th stage	1515.4-2357.4	317.3-390.6	0.7309
5th stage	2357.4-3262.6	390.6-449.9	0.6402
6th stage	3262.6-4351.2	449.9-503.3	0.6368

Using an equation of state[3] the total polytropic head is equal to 88,367 (ft-lb/lbm) compared to the value of 91,525 obtained by Mr. Huntington.

Another compressor having a different number of stages, different diameter, or of a different manufacture will have another interstage characteristic and, therefore, a different polytropic head and efficiency for the same inlet and discharge conditions.

This result should not be surprising since the path of compression lies to the left of the constant efficiency path (i.e., reference method) when plotted on a Mollier chart.

The significance of the foregoing is that a mathematically accurate polytropic analysis is no nearer to reality than the calculations based on the extra assumption of a polytropic compression constant (i.e., J. Schultz' method). Again, this is so because the typical gas compressor does not follow a constant polytropic efficiency path. Once a simplifying assumption such as constant e has been introduced, the accuracy of calculations will be limited and may not be arbitrarily increased.

Any argument as to interpretation of test results may be settled early if the parties involved agree between themselves which method of polytropic analysis is acceptable to both. In such a case, the "reference" method is only as valid as any other method. It should be noted that the isentropic analysis

[2]Senior Engineer, Gas Compressor and Systems Dynamics, Solar Turbines Incorporated, San Diego, CA 92138-5376.

[3]The equation of state used was a modified Soave-RK. The difference in head calculation is due largely to the "assumed" versus "actual" compression path rather than the choice for the equation of state.

Downloaded 01 Jun 2010 to 171.66.16.71. Redistribution subject to ASME license or copyright; see http://www.asme.org/terms/Terms_Use.cfm

(not to be confused by the isentropic perfect gas relations) is superior to the polytropic analysis since it is not a path function and is not ambiguous. The special utility of the polytropic analysis is the correlation between test and field measurements and is another issue.

There are other factors in the PTC-10 code which introduce a higher percentage of errors in the calculations than the method of polytropic analysis; for example, the accuracy of test measurements, the accuracy of gas property evaluation, and the method for performance correction due to Reynolds number effects. With respect to revising the PTC-10 code, we believe that the method of Reynolds number correction introduces largest errors, and thus is in greater need of revision.

I would like to conclude these remarks by, again, acknowledging the analytical achievements in Mr. Huntington's paper.

Author's Closure

Mr. Fozi's comments raise several important issues concerning the evaluation and use of PTC-10 test results. He correctly points out that compressors generally do not exhibit a constant efficiency throughout the gas compression and therefore the PTC-10 assumption of a constant efficiency is a simplification. However, this assumption is valid because the PTC-10 performance test is used as a flange-to-flange evaluation and seeks to find an average efficiency that represents the compressor as a whole. It is not concerned with individual stage performances but only their cumulative operation both on the test stand and in the field.

The advantages of the two methods introduced in the paper are that they accurately and consistently represent the true (i.e., constant efficiency) polytropic compression path that is basic to PTC-10 and will provide a precise correlation of test stand and field results for all gases. The other calculation methods discussed, including the Schultz method, deviate from the true polytropic path for nonperfect gases and therefore cannot provide as good a correlation.

Mr. Fozi also suggests through his hypothetical stage-by-stage analysis of Case No. 3 that major differences (roughly 3.5 percent) in calculated head may be attributed to the nonconstant nature of the actual compression path efficiency and not to gas property evaluation errors. I must disagree with this and state that the bulk of this calculated head difference is due to gas property errors. Using Mr. Fozi's pressure and temperature breakpoints for each stage and the identical gas property evaluation method used in the paper, the following stage performances are found:

	Polytropic head (ft)	Polytropic efficiency (percent)
1st stage	14584	81.08
2nd stage	14872	76.88
3rd stage	15149	73.67
4th stage	17279	77.02
5th stage	14405	68.87
6th stage	14439	69.42
Net	90728	74.34
Table 2A Results (Ref)	91525	74.99

This shows a 0.9 percent difference in head and average efficiency due to the nonconstant efficiency but a 2.6 percent difference due to the different gas property evaluation methods.

In this example, the differences in calculated head due to changing versus constant efficiency are not unexpected or of any concern because of the intended use of the PTC-10 results as discussed above. However, it is a major concern that such large discrepancies in gas property evaluations are possible as these may have a serious impact on the design and successful field operation of a compressor.

Finally, I would like to gratefully thank both Mr. Blehar and Mr. Fozi for their excellent and thought-provoking discussions. Both have pointed out significant areas of concern in the evaluation of compressor performance tests. It is clear that all major areas of concern should be addressed by future PTC-10 revisions including the polytropic calculation method as discussed in this paper, Reynolds number effects, and updated gas property evaluation methods and data.

Downloaded 01 Jun 2010 to 171.66.16.71. Redistribution subject to ASME license or copyright; see http://www.asme.org/terms/Terms_Use.cfm

On Thermodynamics of Gas-Turbine Cycles: Part 1—Second Law Analysis of Combined Cycles

M. A. El-Masri
Associate Professor of Mechanical Engineering.
Massachusetts Institute of Technology, Cambridge, MA 02139

The energy-balance approach to cycle analysis has inherent limitations. These arise from the fact that the first law of thermodynamics contains no distinction between heat and work and no provision for quantifying the "quality" of heat. Thus, while producing the correct final result, energy-balance analysis is incapable on its own of locating sources of losses. Identifying and quantifying those sources can be a useful design tool, especially in developing new, more complex systems. The second law of thermodynamics, applied in the form of entropy and availability balances for components and processes, can locate and quantify the irreversibilities which cause loss of work and efficiency. Perhaps one reason that such analysis has not gained widespread engineering use may be the additional complication of having to deal with the combustion irreversibility, which introduces an added dimension to the analysis. A method of cycle analysis, believed to circumvent this added difficulty for combustion cycles, is proposed and applied to complex combined cycles with intercooling and reheat. The fuel is treated as a source of heat, which supplies potentially available work to the cycle depending on the peak temperature constraint on work extraction. The availability is then traced as it cascades through the cycle, portions of it being wasted by the various components and processes, and the balance emerging as shaft work. Linkage with the traditional first-law efficiency is thus preserved, while establishing the location, cause, and magnitude of losses. Analysis and results for combined cycles with component irreversibilities are presented. The air-standard approximation with constant properties is used for simplicity. The turbine is treated as adiabatic since the cooling losses depend on the type of technology applied, particularly at higher temperatures. A model for quantifying those losses is presented in Part 2 of this paper.

1 Introduction

The combined gas/steam turbine cycle has long been recognized as an efficient power system. For base-load generation where high efficiency is vital, it has been shown that the simple gas-turbine cycle in its present form may not be optimum. This is obvious since achieving turbine exit temperatures adequate for the steam cycle requires either excessive turbine inlet temperatures or low pressure ratio. The reheated gas turbine has been recognized as a promising solution [1, 2]. Such a cycle with single reheat and compressor intercooling is under construction [3]. Although much new technology has yet to be developed and proven, it is the author's view that the trend toward more efficient and more complex cycles will continue. Thermodynamic and economic optimization of a combined cycle with a simple cycle gas turbine is a complicated process. When compressor intercooling and turbine reheat are included, the large variety of cycle configurations makes it extremely difficult.

A reasonable configuration may be reached by a large number of runs of computer programs that simulate the plant's energy balance. Such a "brute force" approach, however, can fail to provide insight as to why one configuration is superior to another. This is because the first law of thermodynamics does not distinguish between heat and work, and thus cannot be used on its own to identify the sources of loss in a cycle. For instance, the energy balance of a typical steam plant says that about half the heat from the fuel is rejected at the condenser. It does not, and cannot, say why this happens. The energy balance analysis is incapable of pinpointing the location of the components or processes which cause the loss. Moreover, it is misleading to the point of indicating the highest efficiency for processes (like combustion and heat transfer) which cause a major proportion of the loss of work. Applications of the second law in the form of work and availability balances for the processes constituting the cycle enable the loss incurred and the true effectiveness of each process to be determined.

In this paper a thermodynamic methodology for analyzing combustion power cycles is presented. It is developed specifically for gas-turbine combined cycles but may readily be extended to other systems. While using the second law to

Contributed by the Gas Turbine Division of THE AMERICAN SOCIETY OF MECHANICAL ENGINEERS and presented at the 30th International Gas Turbine Conference and Exhibit, Houston, Texas, March 18-21, 1985. Manuscript received at ASME Headquarters, January 7, 1985. Paper No. 85-GT-129.

Copyright © 1985 by ASME
Downloaded 01 Jun 2010 to 171.66.16.71. Redistribution subject to ASME license or copyright; see http://www.asme.org/terms/Terms_Use.cfm

define process and component efficiencies, linkage with traditional first-law energy-balance analysis is preserved (at the expense of thermodynamic rigor) by treating the fuel as a source of heat rather than availability.

This heat contains a certain amount of "potentially available" work, depending on the peak cycle temperature. Each component and the overall cycle is then analyzed using a work-balance approach, based on the combination of actual work and thermodynamically available work. Unlike the first law energy balance, which says that energy is conserved, the work balance includes the destruction of work due to process and component irreversibility.

Closed form solutions are obtained for the gas-turbine cycle with constant properties. A simplified correlation is developed relating steam bottoming cycle output to available work in gas turbine exhaust. Based on those models, results for the performance of combined cycles are presented.

2 Thermodynamic Methodology

The first-law definition of cycle thermal efficiency is

$$\eta_1 = W/\Delta H_r \tag{1}$$

where ΔH_r is the enthalpy of reaction of the fuel at standard conditions. The more rigorous second-law definition is

$$E = W/\Omega_{\text{fuel}} \tag{2}$$

where Ω_{fuel} is the available work (free energy) of reversibly reacting the fuel at standard conditions. For most fuels the enthalpy of reaction is slightly larger than the fuel availability, so E is slightly larger than first-law efficiency. The difference between them varies from one fuel to another. In comparing energy conversion processes in general, definition (2) is the more appropriate measure. However, in combustion cycles where the peak temperature of work extraction is significantly below that for equilibrium between reactants and products, the irreversibility of the combustion process cannot be influenced and the fuel can be simply treated as a source of thermal energy Q. The work that could have been extracted from reversible reaction at standard conditions loses relevance and definition (1) becomes more appropriate. Normally the equivalent heat source Q differs from ΔH_r by a small amount dependent on fuel and combustion conditions. For most hydrocarbon fuels the dependence of this difference on cycle pressure and temperature as well as fuel composition is very slight.[1] Therefore, to the extent that this difference may be neglected, a sound basis for comparing performance of different cycles can be obtained by rewriting equation (1) as the classical thermal efficiency definition of

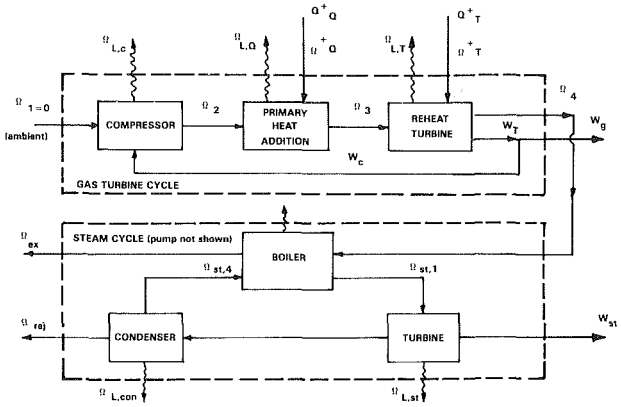


Fig. 1 Work and availability flow in combined cycle

$$\eta_1 = W/Q^+ \tag{3}$$

The technology constraint on practical equipment is the peak temperature at which work can be extracted. If this is θ times ambient, then the potentially available work from the heat source Q is

$$\Omega_Q^+ = \eta_{\text{carnot}} \cdot Q^+ = \left(1 - \frac{1}{\theta}\right) Q^+ \tag{4}$$

and this quantity may be treated as the available work supplied to the real cycle.[2] Due to the irreversibility of the processes in the real cycle, entropy is generated and available work destroyed with the net result that the real work output is less than the potentially available work. This process is illustrated for a gas-turbine reheat cycle by the availability flow chart of Fig. 1 and the following availability balances:

$$W_c = (\Omega_2 - \Omega_1) + \Omega_{L,c} \tag{5}$$

[1] It is this difference that makes gas turbines exhibit a higher apparent efficiency with fuels of high hydrogen-to-carbon ratio such as natural gas over fuels with lower hydrogen-to-carbon ratio such as residual oil.

[2] This assumes that combustion permits supplying this availability, a valid assumption in many practical cases.

Nomenclature

c_p = specific heat at constant pressure
E = effectiveness (or second-law efficiency)
e = polytropic efficiency
h = enthalpy
ΔH_r = enthalpy of reaction at standard conditions
L = loss coefficient, defined as ratio of availability lost to cycle heat added
ln = natural logarithm
n = number of compression or expansion stages
p = stagnation pressure
δp = stagnation-pressure loss ($<<p$)
Q = heat per unit mass of gas
q = dimensionless heat $= Q/c_p T_0$
R = gas constant
r_p = pressure ratio
r = isentropic temperature ratio $= r_p^{\left(\frac{\gamma-1}{\gamma}\right)}$
s = specific entropy
T = absolute temperature (stagnation)
W = work per unit mass of gas
w = dimensionless work $= W/c_p T_0$
γ = specific heat ratio
η_1 = first-law efficiency
η_2 = total efficiency, defined in equation (10)
θ = peak cycle dimensionless temperature $= T_3/T_0$
τ = dimensionless temperature $= T/T_0$
Ω = availability per unit mass of gas $= h - T_0 s$
ω = dimensionless availability $= \Omega/c_p T_0$

Subscripts and Superscripts

ad = adiabatic
c = compressor
comb = combined cycle
g = gas turbine cycle
gen = generated
iso = isothermal
L = lost
Q = main combustor
s = isentropic
st = steam, steam cycle
T = turbine
$+$ = added
$\sim$ = dimensionless
0 = ambient
1 = compressor inlet
2 = compressor delivery
3 = turbine inlet
4 = turbine exit
ex = boiler exhaust
1,st = turbine inlet
sat = saturated

Downloaded 01 Jun 2010 to 171.66.16.71. Redistribution subject to ASME license or copyright; see http://www.asme.org/terms/Terms_Use.cfm

$$\Omega_Q^+ = (\Omega_3 - \Omega_2) + \Omega_{L,Q} \tag{6}$$

$$\Omega_T^+ = (\Omega_4 - \Omega_3) + W_T + \Omega_{L,T}. \tag{7}$$

The net work output of the gas turbine is

$$W_g = W_T - W_c \tag{8}$$

and the total thermodynamic output is $(W_g + \Omega_4 + \Omega_{ic})$, where Ω_4 and Ω_{ic} are the available work in the exiting gas stream and intercooler cooling water (if used). The latter is generally too small and will be considered lost and included in $\Omega_{L,c}$. Adding equations (5–7), and using (8) we get

$$W_g + \Omega_4 = (\Omega_Q^+ + \Omega_T^+) - (\Omega_{L,c} + \Omega_{L,Q} + \Omega_{L,T}) \tag{9}$$

and the thermodynamic efficiency of the gas-turbine cycle may be defined as its total work output (shaft plus available work in gas) divided by heat, added,

$$\eta_2 = (W_g + \Omega_4)/Q^+ \tag{10}$$

using equation (9) and substituting for $(\Omega_Q^+ + \Omega_T^+)$ from (4) gives

$$\eta_2 = \eta_{\text{carnot}} - \Sigma L_i \tag{11}$$

where L_i denotes the ratio of availability lost in a process to the total heat added to the cycle. It is interesting to note that the first-law efficiency of the gas-turbine cycle alone is

$$\eta_1 = \eta_{\text{carnot}} - \Sigma L_i - \Omega_4/Q^+. \tag{12}$$

The gas stream leaving the turbine at state 4 enters the stream cycle where a fraction E_{st} of its availability is recovered as shaft work and the remaining availability destroyed by irreversibility or rejected,

$$W_{st} = E_{st}\Omega_4 \tag{13}$$

and the combined cycle efficiency is

$$\eta_{\text{comb}} = \frac{W_{\text{comb}}}{Q^+} = \eta_2 - (1 - E_{st})\frac{\Omega_4}{Q+}. \tag{14}$$

In the following section the availability losses in the various components will be determined and the dependence of steam cycle effectiveness on turbine exhaust temperature will be established.

3 Process and Component Efficiency for the Gas-Turbine Cycle

3.1 Compression. The second-law efficiency of a compression process (1-2) is the ratio of increased availability to work input. Following Keenan [4], we shall call this effectiveness E to distinguish it from the commonly used isentropic efficiency, thus

$$E_c = (\Omega_2 - \Omega_1)/W_c. \tag{15}$$

For frictionless reversible compressions, adiabatic or isothermal, no entropy is generated or availability destroyed and $E_c = 1$. In a real compressor of polytropic efficiency e_c[3], for an infinitesimal adiabatic increase in pressure dp the temperature increase dT is greater than the isentropic value dT_s,

$$dT = dT_s/e \tag{16}$$

using the isentropic relation for a perfect gas

$$\frac{dT_s}{T} = \frac{\gamma - 1}{\gamma}\frac{dp}{p} \tag{17}$$

and the property relation

$$ds = C_p\frac{dT}{T} - R\frac{dp}{P} \tag{18}$$

yields the entropy generated

[3] The subscript for polytropic efficiency will be dropped from the equations for brevity.

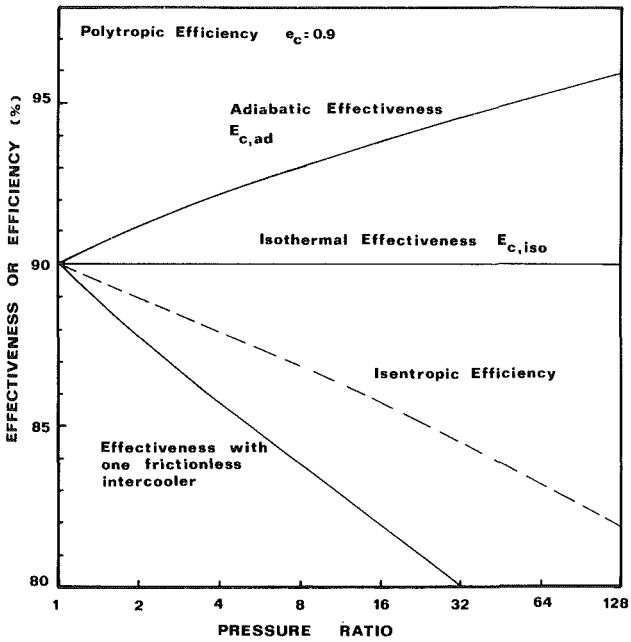


Fig. 2 Compressor efficiency and effectiveness

$$ds_{\text{gen}} = \left(\frac{1-e}{e}\right)R\frac{dp}{p} \tag{19}$$

and the availability destroyed $T_0\ ds_{\text{gen}}$ is obtained by multiplying (19) by T_0 and integrating. After nondimensionalizing this gives

$$\omega_{L,c} = \frac{1-e}{e}\ln r. \tag{20}$$

Since equation (19) is independent of temperature, the result (20) holds for adiabatic compression as well as any number of adiabatic stages separated by frictionless intercoolers. In the latter case, however, it accounts only for available work destroyed within the machine and does not account for available work rejected or destroyed in intercooler heat transfer. The compressor work for the infinitesimal adiabatic stage is $C_p dT$, so that the compressor work in dimensionless form is

$$w_c = \frac{\gamma - 1}{\gamma e}\int_1^2 \frac{T}{T_0}\frac{dp}{p} \tag{21}$$

Unlike the availability destroyed this depends on local temperature, and the compression works for adiabatic compression starting from T_0 and perfectly intercooled isothermal compression at T_0 are

$$w_{c,\text{ad}} = r^{1/e} - 1 \tag{22}$$

$$w_{c,\text{iso}} = \frac{1}{e}\ln r \tag{23}$$

respectively.

Applying the availability balance (5) and the definition (15) gives the corresponding effectiveness as

$$E_{c,\text{ad}} = 1 - \left(\frac{1-e}{e}\right)\frac{\ln r}{r^{1/e} - 1} \tag{24}$$

$$E_{c,\text{iso}} = e. \tag{25}$$

Equations (24) and (25) are plotted in Fig. 2 versus pressure ratio. Although the absolute value of availability destroyed equation (20) is identical, the adiabatic compressor exhibits greater effectiveness since the absolute values of work input and availability increase are both larger. Plotted also on Fig. 2 is the classical isentropic efficiency of adiabatic compression. It falls with pressure ratio whereas effectiveness increases. The isentropic efficiency considers only the work dissipated

Downloaded 01 Jun 2010 to 171.66.16.71. Redistribution subject to ASME license or copyright; see http://www.asme.org/terms/Terms_Use.cfm

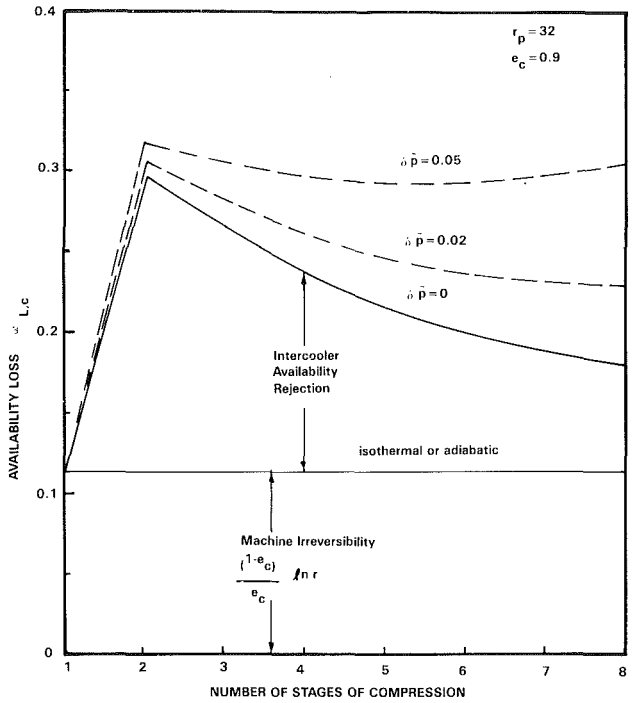


Fig. 3 Availability losses in compression

but fails to reflect the fact that work dissipated at increasing temperatures contains an ever-increasing recoverable fraction which may be recouped elsewhere in the cycle. Thus, isentropic efficiency is a poor measure of compressor performance, particularly in cycles which present the opportunity for rejecting entropy at ambient temperature such as combined cycles. In cycles where we are constrained to reject entropy at ambient pressure, regardless of temperature, such as open-cycle gas turbines, this is not always correct.

In a compressor with a finite number of intercoolers where pressure drops occur and/or the intercooler heat cannot be utilized reversibly, the availability loss will always be greater than for adiabatic compression. Consider the case of n adiabatic stages of equal pressure ratio separated by $(n-1)$ intercoolers that restore air temperature to ambient while incurring a dimensionless pressure drop $\delta\tilde{p}_c << 1$. The work input may be shown to be

$$w_c = n(r^{1/ne} - 1) + \frac{(\gamma-1)(n-1)}{\gamma e}\delta\tilde{p}_c r^{1/ne} \tag{26}$$

and if intercooler available work is lost, then the total availability lost is

$$\omega_{L,c} = (n-1)(r^{1/ne} - 1) + \frac{(\gamma-1)(n-1)}{\gamma ne}\delta\tilde{p}_c[(n - 1)r^{1/ne} + 1] + \left(\frac{1}{ne} - 1\right)\ln r \tag{27}$$

and the effectiveness may be found from applying equations (5) and (15). An illustration of the decrease in effectiveness with a single frictionless intercooler is shown in Fig. 2. An example of the breakdown of the total availability loss in an intercooled compression and its dependence on number of stages is illustrated by Fig. 3.

An absolute conclusion concerning the impact of intercooling on cycle performance cannot be drawn without considering its impact on the availability loss in the subsequent process of primary heat addition as well as on the total amount of heat added to the cycle, this in view of equation (11). This conclusion is drawn at the end of the next section.

3.2 Primary Heat Addition. Consider the primary heat addition process (2–3) which raises temperature from T_2 to T_3 and incurs a small pressure drop $\delta\tilde{p}_Q << 1$. The heat added

$$q_Q^+ = \theta - \tau_2 \tag{28}$$

contains potentially available work ω_Q^+, which by equation (4) is

$$\omega_Q^+ = (\theta - 1)(\theta - \tau_2)/\theta \tag{29}$$

The increase in availability is

$$\omega_3 - \omega_2 = (\theta - \tau_2) - \ln\frac{\theta}{\tau_2} - \frac{\gamma-1}{\gamma}\delta\tilde{p}_Q \tag{30}$$

The available work lost is found by using equation (6)

$$\omega_{L,Q} = \frac{\tau_2}{\theta} + \ln\frac{\theta}{\tau_2} - 1 + \frac{\gamma-1}{\gamma}\delta\tilde{p}_Q \tag{31}$$

and the effectiveness may be defined as

$$E_Q = (\omega_3 - \omega_2)/\omega_Q^+ \tag{32}$$

which depends on compressor delivery temperature, a function of pressure ratio and number of intercoolers, as well as peak temperature.

We are now in a position to draw the definite conclusion regarding impact of intercooling on cycle efficiency η_2, as defined by equations (10) and (11). For a given pressure ratio and peak temperature, intercooling the compressor would always result in a net decrease of η_2 if the sum

$$L_c + L_Q = (\omega_{L,c} + \omega_{L,Q})/q^+_{\text{total}}$$

were increased. The perfectly intercooled isothermal compressor provides the least $\omega_{L,c}$ and most q_Q^+. It can be shown to be the best of all intercooled compressors. Intercooling always results in a loss of efficiency if $(L_c + L_Q)_{\text{iso}} > (L_c + L_Q)_{\text{ad}}$. It may be shown that if this inequality is satisfied in a nonreheat turbine cycle it will always be satisfied with reheat also. Thus if

$$\left\{\frac{\omega_{L,c} + \omega_{L,Q}}{q_Q^+}\right\}_{\text{iso}} > \left\{\frac{\omega_{L,c} + \omega_{L,Q}}{q_Q^+}\right\}_{\text{ad}} \tag{33}$$

intercooling always produces lower cycle efficiency. Applying equations (20), (28), and (31) to this inequality allows solution for the breakeven condition when this inequality is just satisfied. It is plotted in Fig. 4 on r_p versus θ coordinates. For a given θ intercooling always produces a decrease in η_2 if r_p is below the breakeven line. For pressure ratios above this line, intercooling may or may not produce an efficiency increase depending on the number of intercoolers, their pressure drop, number of turbine reheats, etc.

3.3 Expansion. Consider an expansion process (3–4) producing work at the expense of a drop in availability of the gas. If the expansion is reheated by an amount possessing potentially available work Ω_T^+ then availability balance (7) can be solved for work lost $\Omega_{L,T}$. The effectiveness of this process may be defined as ratio of work to availability consumed,

$$E_T = W_T/(\Omega_T^+ + \Omega_3 - \Omega_4) \tag{34}$$

An equally rational definition, differing only in magnitude but not in sense is the ratio of work plus potential work output to availability supplied, i.e.

$$E'_T = (W_T + \Omega_4)/(\Omega_T^+ + \Omega_3) \tag{35}$$

Since definition (34) is more consistent with the manner in which heat addition effectiveness was defined in equation (32), it will be adopted.

For an infinitesimal adiabatic expansion in a turbine with polytropic efficiency e_t[4], the temperature drop dT for a pressure drop dp is smaller than the corresponding isentropic value dT_s,

[4] The subscript is dropped from the equations.

Downloaded 01 Jun 2010 to 171.66.16.71. Redistribution subject to ASME license or copyright; see http://www.asme.org/terms/Terms_Use.cfm

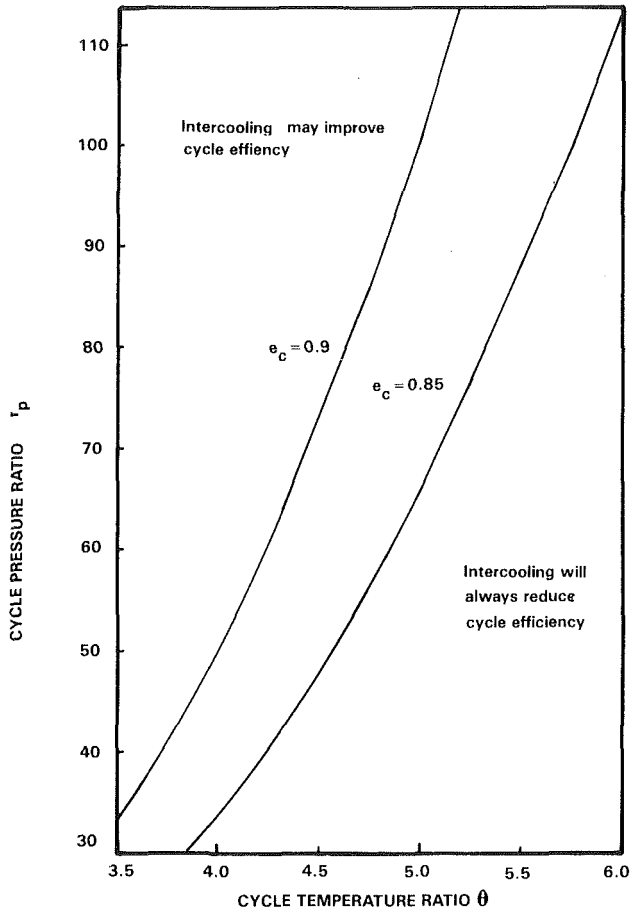


Fig. 4 Breakeven condition for intercooling

$$dT = e dT_s \tag{36}$$

Using equations (18) and (19) we see that the entropy generated in the infinitesimal adiabatic stage is

$$ds_{\text{gen}} = (1-e)R\frac{dp}{p} \tag{37}$$

Multiplying by T_0 and integrating gives the available work destroyed as

$$\omega_{L,T} = (1-e)\ln r \tag{38}$$

Just as for the compressor, this is independent of temperature and is the same whether the turbine is adiabatic or consists of any number of reheat stages. In the latter case, of course, it accounts only for availability destroyed within the machine but not for reheat pressure losses or heat transfer losses. The expansion work is

$$w_T = -e\frac{\gamma-1}{\gamma}\int_3^4 \frac{T}{T_0}\frac{dp}{p} \tag{39}$$

and depends on the pressure-temperature path. For adiabatic expansion starting at T_3 and an infinitely reheated isothermal expansion at T_3 this is, respectively,

$$w_{T,\text{ad}} = \theta(1-r^{-e}) \tag{40}$$

$$w_{T,\text{iso}} = \theta e \ln r. \tag{41}$$

The corresponding effectivenesses are

$$E_{T,\text{ad}} = \left[1 + \frac{(1-e)r\ln r}{\theta(1-r^{-e})}\right]^{-1} \tag{42}$$

$$E_{T,\text{iso}} = \theta e/(\theta e - e + 1). \tag{43}$$

Note that as $\theta \to 1$, $E_{T,\text{iso}} \to e$, similar to the isothermal compressor at ambient temperature. Turbine effectiveness increases with θ since a greater proportion of work dissipated at higher temperature may be recovered. For the same reason the isothermal expansion has a higher effectiveness than the adiabatic. The availability lost is the same for both by equation (38) but the isothermal case provides larger work and allows a larger availability input.

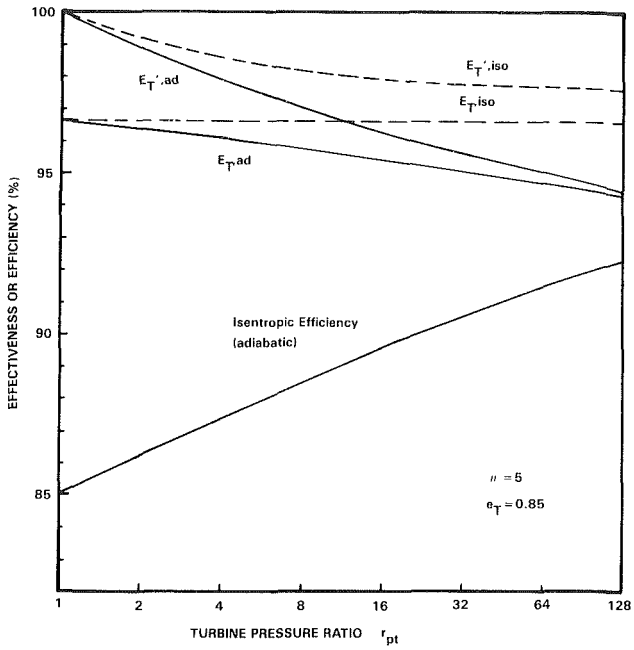


Fig. 5 Turbine efficiency and effectiveness

An example of variation of the effectiveness with pressure ratio for $e_T = 0.85$, $\theta = 5$ is plotted in Fig. 5. Also shown is the classical isentropic efficiency which exhibits a misleading trend of increased efficiency at increased pressure ratio for an adiabatic turbine. This reflects the fact that while the ratio of work to isentropic work increases with pressure ratio, the difference between them, representing dissipated work, becomes increasingly unrecoverable with declining temperatures.

Now consider the turbine consisting of n adiabatic stages of equal pressure ratio separated by $(n-1)$ reheaters that restore the temperature to T_3 while incurring a dimensionless pressure drop $\delta\tilde{p}_T << 1$. Applying energy, entropy, and availability balances to this turbine gives the following expressions for turbine work output, reheater heat supplied, potentially available work supplied, and availability destroyed, respectively,

$$w_T = \theta\{(n-1)(1-1/x') + (1-1/x)\} \tag{44}$$

$$q_T^+ = \theta(n-1)(1-1/x') \tag{45}$$

$$\omega_T^+ = (\theta-1)(n-1)(1-1/x') \tag{46}$$

$$\omega_{L,T} = \ln\left(\frac{r}{x}\right) - (n-1)(1-1/x') \tag{47}$$

where x' is the temperature ratio across all stages except the last whose temperature ratio is x, those quantities are

$$x = r^{e/n} \tag{48}$$

$$x' = r^{e/n}\left(1 - \frac{\gamma-1}{\gamma}e\delta\tilde{p}_T\right). \tag{49}$$

An illustration of the losses in a reheated expansion is provided in Fig. 6 which shows an example of the availability destroyed and its breakdown due to the mechanisms outlined above as a function of number of turbine stages.

4 Effectiveness of Steam Bottoming Cycles

Relation Between Effectiveness and Efficiency. The traditional first-law efficiency of a steam cycle is

Downloaded 01 Jun 2010 to 171.66.16.71. Redistribution subject to ASME license or copyright; see http://www.asme.org/terms/Terms_Use.cfm

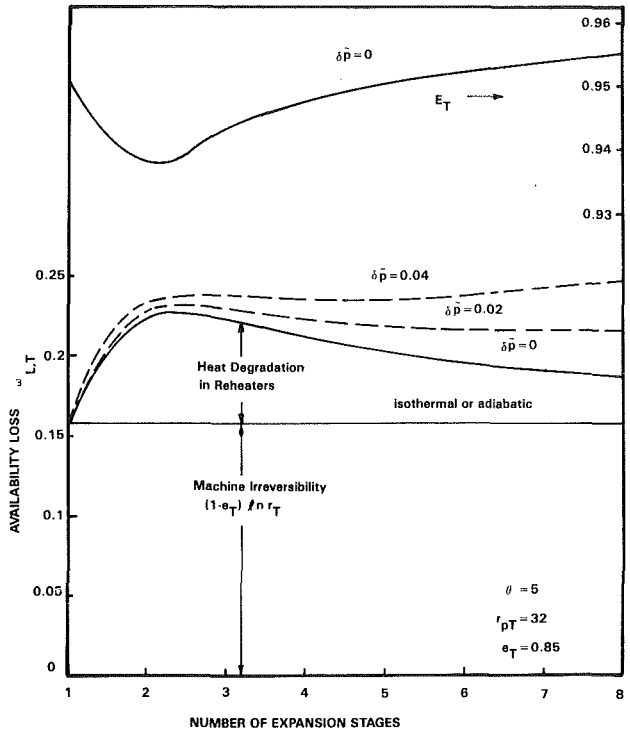


Fig. 6 Availability losses in reheated expansion

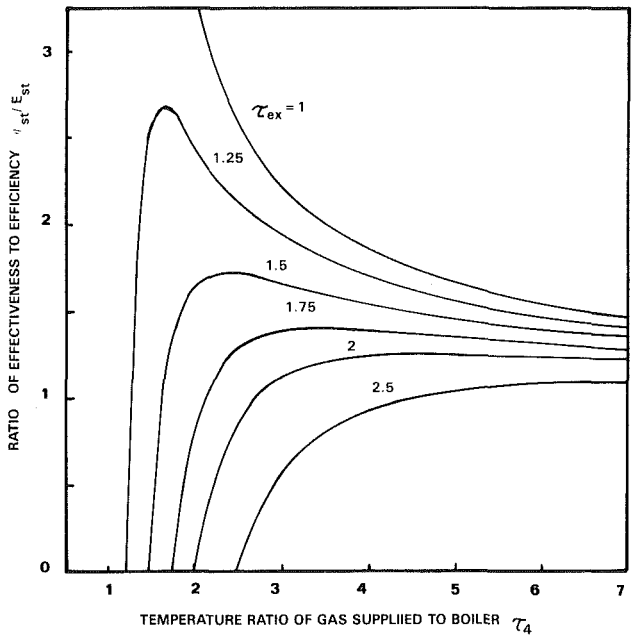


Fig. 7 Relation between effectiveness and efficiency for steam bottoming cycles

$$\eta_{st} = W_{st}/Q_{st}. \tag{50}$$

Its effectiveness has been defined by equation (13). Thus the ratio of its effectiveness to its efficiency is just the ratio of heat supplied to the boiler per unit mass of hot gas to specific availability of hot gas entering the boiler. If the gas has constant specific heat, enters the boiler at T_4 and leaves at T_{ex} with negligible pressure drop then

$$\frac{E_{st}}{\eta_{st}} = \frac{\tau_4 - \tau_{ex}}{\tau_4 - 1 - \ln\tau_4} \tag{51}$$

This is plotted in Fig. 7 versus τ_4 with τ_{ex} as parameter. The effectiveness is larger than the efficiency so long as $\tau_{ex} < 1 + \ln\tau_4$, a condition satisfied in any practical bottoming cycle. Most practical conditions will be to the right of the peaks of the curves of Fig. 7, showing that the effectiveness of

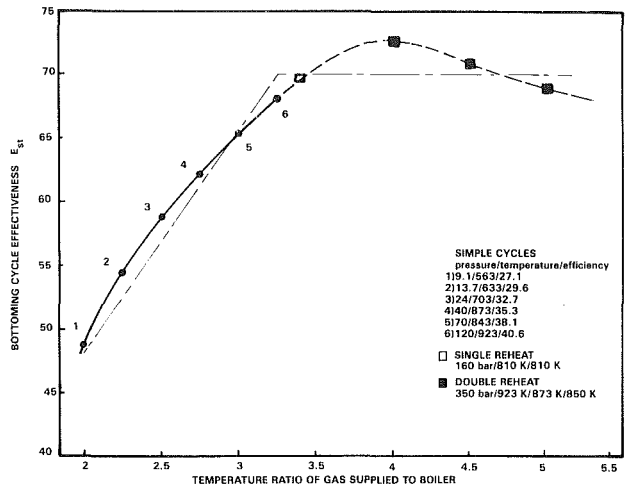


Fig. 8 Effectiveness correlation for bottoming cycles

a *given* steam cycle declines with increasing gas temperatures above the minimum that can operate this cycle. This minimum gas temperature is constrained by the required steam superheat and/or the "pinch point" on the heat exchanger.

Correlation of Steam-Cycle Effectiveness. For a simple steam cycle without reheat or regeneration, such as one might use at moderate gas temperatures, one may expect the maximum possible effectiveness to correlate with gas temperature T_4 for a fixed exhaust temperature. That is because steam cycles of increasing pressure and superheat and thus higher efficiency may be used at higher temperatures. Moreover, a larger percentage of the exhaust gas energy can be used.

To find this correlation, calculations were done for several gas temperatures T_4; in each case, the steam cycle pressure and peak temperature $T_{1,st}$ were first determined by setting pinch point (saturation) and maximum steam temperatures at 5K and about 20K respectively below the corresponding gas temperature profile. Thus, the percentage of gas and steam enthalpies above the pinch point must be the same giving

$$\frac{T_4 - (T_{sat} + 5°)}{T_4 - T_{ex}} = \frac{h_{1,st} - h_{sat\ liq}}{h_{1,st} - h_{feedwater}} \tag{52}$$

which may be solved iteratively for steam-cycle pressure.

In the following calculations, the assumptions are:

1 Ambient temperature $T_0 = 290$K
2 Exhaust temperature $T_{ex} = 420$K
3 Condenser pressure = 0.045 bar (304K)
4 Steam turbine and feedwater pump have 90% and 70% isentropic efficiency respectively.

For each T_4 these assumptions were applied, the pressure was found using equation (52), and the effectiveness was computed. The results are shown in Fig. 8, which also shows the steam conditions and efficiency computed for each point. Availability balances for those cycles are shown in Fig. 9.

For $\tau_4 > 3.25$ the peak steam temperature of an optimized simple cycle exceeds current practice but opportunities for steam reheating and regenerative feedwater heating arise. Detailed analysis for the optimum steam cycle configuration at the higher temperatures becomes quite complicated and has not been performed. However, for the purpose of extending the correlation, calculations were performed for two cycles: 160 bar 810K/810K single reheat and 350 bar 923K/873K/850K double reheat. The former represents steam conditions in widespread use and the latter close to the highest attempted in the United States [5]. No regenerative feedwater heating was assumed. The point representing the former cycle, and the leftmost point representing the latter on Fig. 8

Downloaded 01 Jun 2010 to 171.66.16.71. Redistribution subject to ASME license or copyright; see http://www.asme.org/terms/Terms_Use.cfm

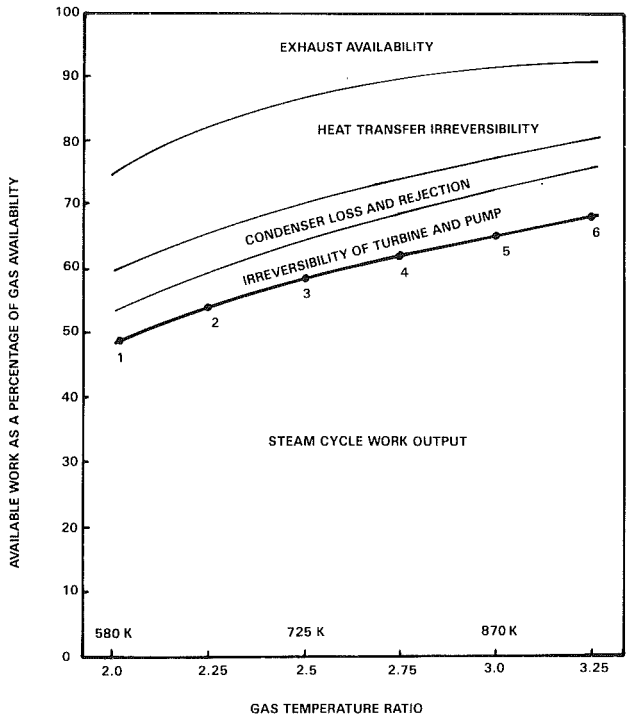


Fig. 9 Availability balances for simple steam bottoming cycles

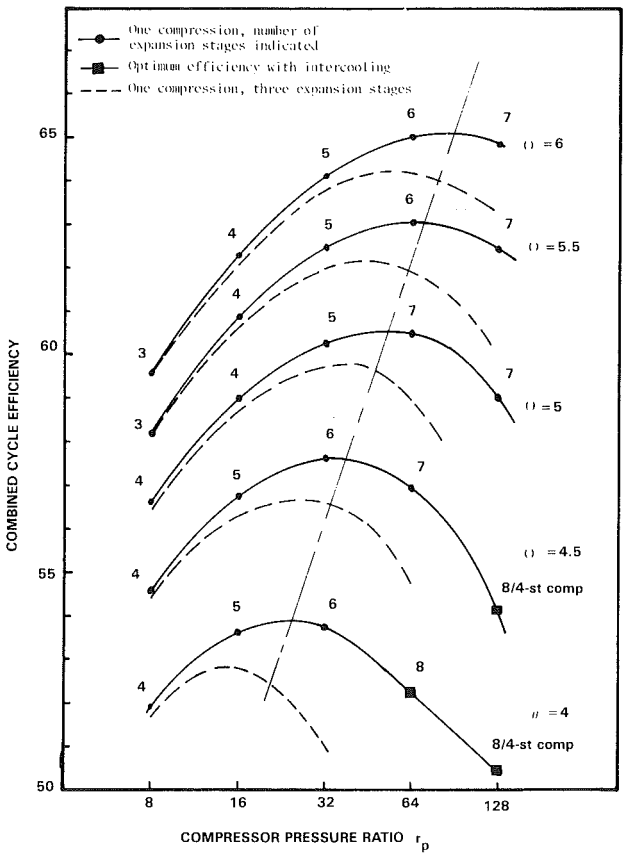


Fig. 10 Combined cycle efficiency at optimum configuration

are at the lowest value of τ_4 consistent with clearing the pinch point on the heating curve. For the purpose of the combined cycle computations presented in the next section, the effectiveness of steam-bottoming cycles was assumed to follow the dashed lines on Fig. 8, namely zero for $\tau_4 < 2$ where the bottoming cycle was judged impractical, linearly increasing from 48% at $\tau_4 = 2$ to 70% at $\tau_4 = 3.25$, and constant at 70% for $5 > \tau_4 > 3.25$. For gas temperatures higher than that, the

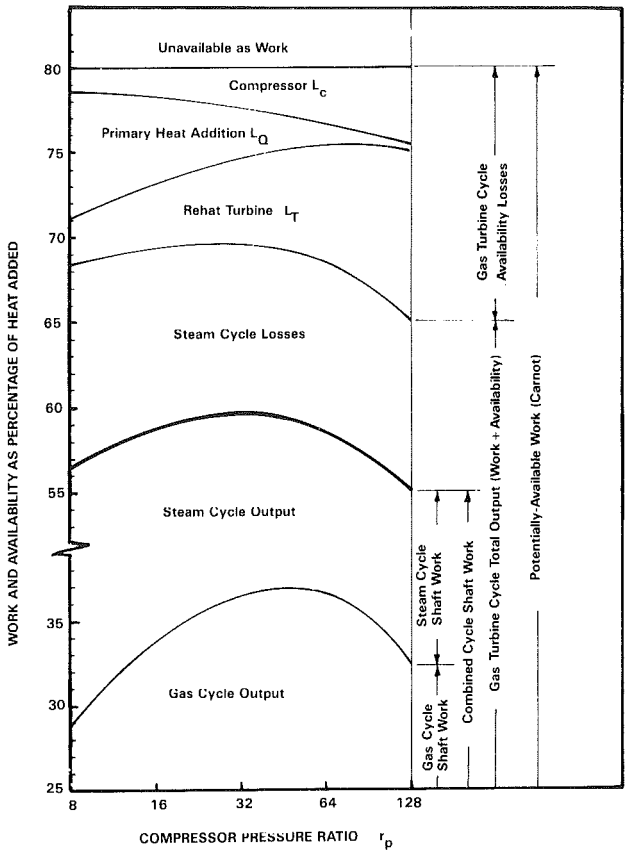


Fig. 11 Availability and work balance

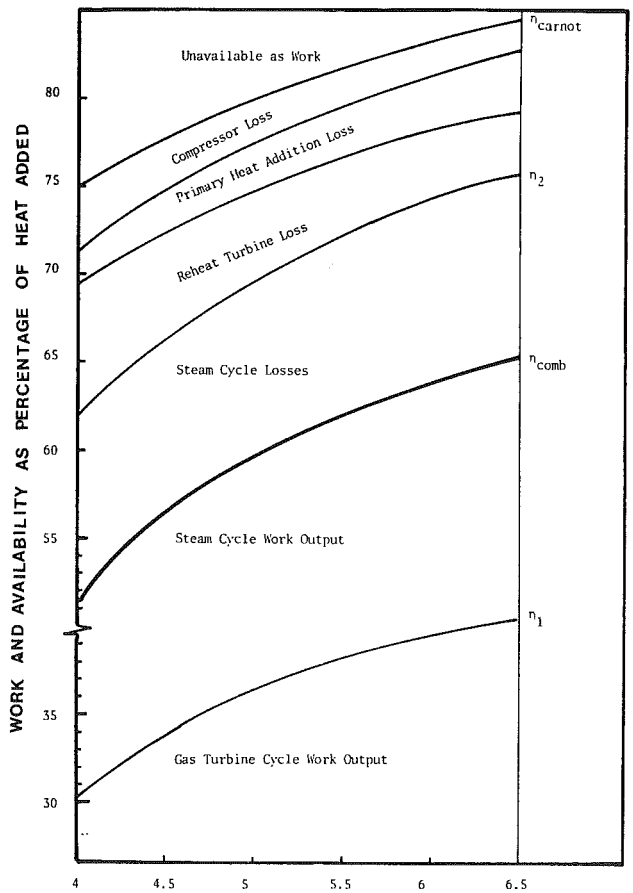


Fig. 12

Downloaded 01 Jun 2010 to 171.66.16.71. Redistribution subject to ASME license or copyright; see http://www.asme.org/terms/Terms_Use.cfm

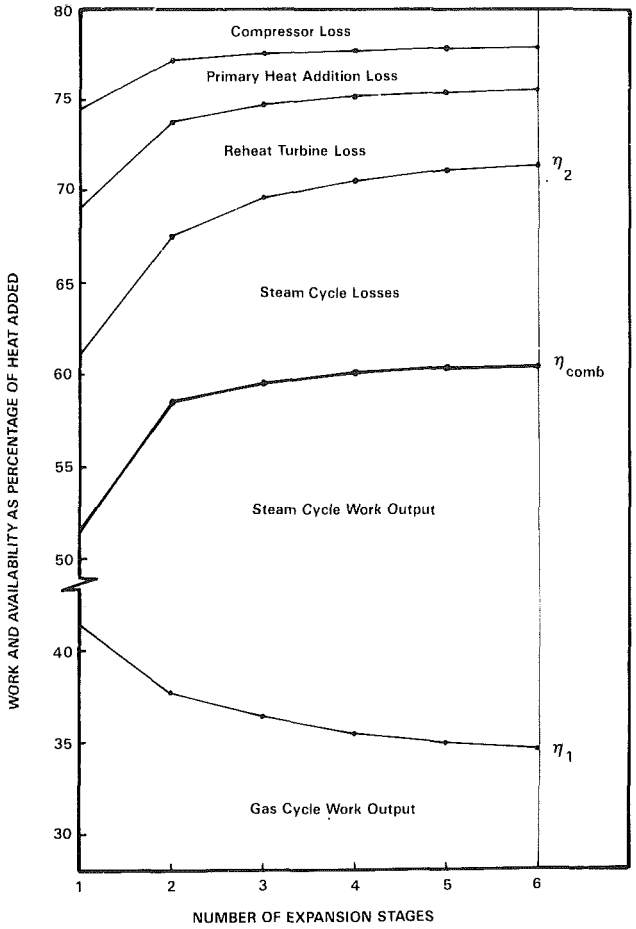


Fig. 13

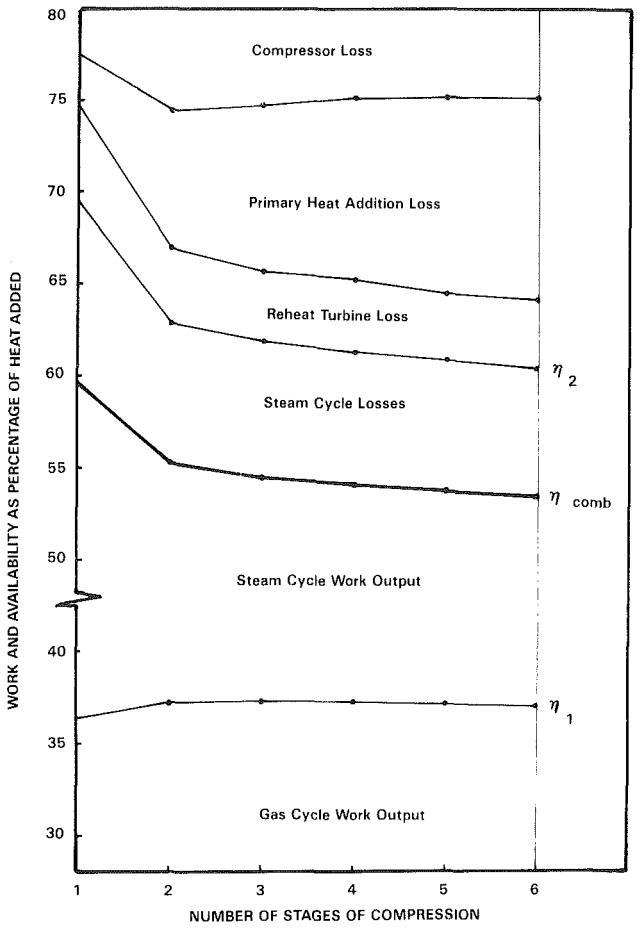


Fig. 14

gas is simply treated as a heat source driving a steam cycle at 45% thermal efficiency, resulting in a falling effectiveness as Fig. 7 indicates.

5 Results for Combined Cycles

Based upon the methodology and equations presented, a computer program was constructed to solve for combined cycle efficiency as well as effectiveness of each process involved in the cycle. Work and availability balances enable the location of all losses to be identified.

Examples of the results are shown in Figs. 10–18. In those examples polytropic efficiencies of compressor and turbine are 0.9 and 0.85 respectively. Pressure drops in each intercooler, the primary combustor, and each reheat combustor are 5%, 3%, and 2% respectively. The gas is assumed to have constant properties with $\gamma = 1.4$, $R = 287$ J/kg K.

Figure 10 shows computed combined cycle efficiency versus pressure ratio at various peak temperatures. Each point represents the maximum efficiency configuration of single-stage compressor and reheat turbine. The optimum number of turbine stages is indicated at each point. The only exceptions are the points for $\theta = 4$ and $\theta = 5$ with $r_p = 128$ which optimize with intercooled compressors. It is worth noting that if we were to restrict the maximum number of reheat stages to three, say, the cycle with $\theta = 4$, $r_p = 64$ would also optimize with compressor intercooling. This is consistent with the conclusions of section 3.2 depicted in Fig. 4. Those points are marked with squares on Fig. 10.

Due to design constraints, it would be difficult to construct a machine with more than three stages (two reheats). To investigate the effect of this restriction the dashed curves for a configuration of single compressor/3 turbines are plotted in Fig. 10. They fall below the solid curve for optimum efficiency by an amount that increases at higher pressures and lower temperatures.

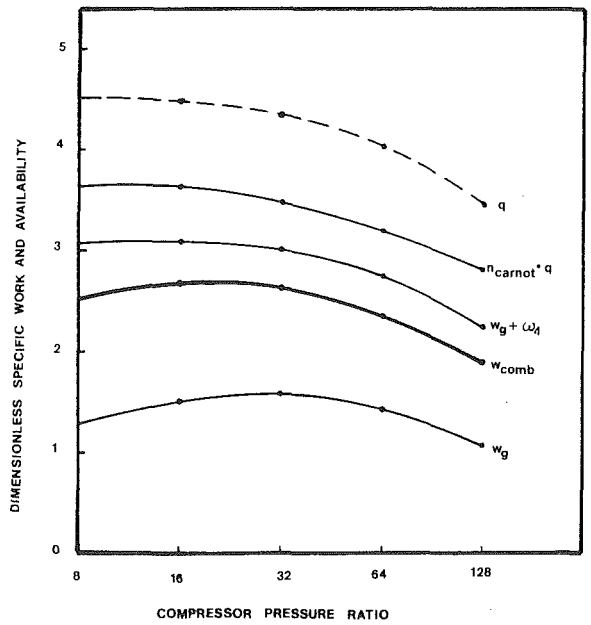


Fig. 15 Balance of specific work and availability as a function of pressure ratio

To illustrate how pressure ratio, peak temperature, number of expansion stages, and number of compression stages affect cycle efficiency and specific work output Figs. 11–18 were prepared. For the purpose of this illustration, a central point

Downloaded 01 Jun 2010 to 171.66.16.71. Redistribution subject to ASME license or copyright; see http://www.asme.org/terms/Terms_Use.cfm

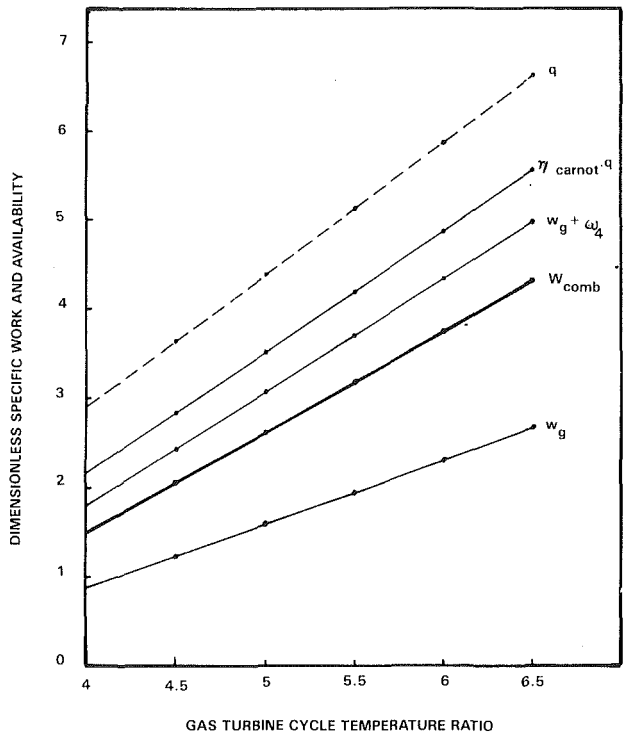


Fig. 16 Balance of specific work and availability as a function of temperature ratio

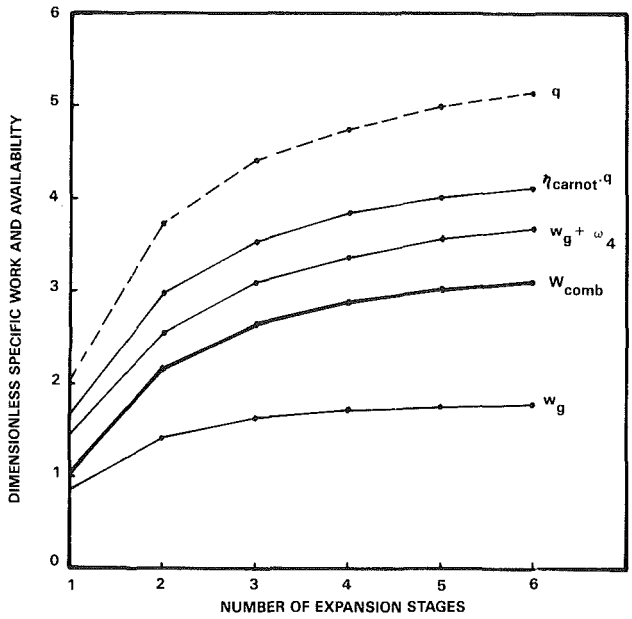


Fig. 17 Balance of specific work and availability as a function of number of expansion stages

was selected at a pressure ratio of 32, temperature ratio $\theta = 5$, three-stage turbine and single-stage compressor.

Those variables were changed one at a time and the work and availability balances constructed. In Figs. 11–14 those are expressed as percentages of heat added. Thus, the total work output represents combined cycle efficiency. This is indicated by the heavy line. Also shown on those figures are the gas-turbine cycle simple efficiency η_1 and total efficiency η_2. The breakdown of the work balance is explained on Fig. 11. It may be regarded as a graphic representation of the availability flow chart of Fig. 1. Figures 15–18 represent the work balances per unit mass of compressor air in absolute magnitude nondimensionalized by the absolute specific enthalpy of air at ambient conditions $C_p T_0$. Thus, the cycle output represents the total power per unit air mass flow rate; this is shown as the heavy line. Also indicated are the specific power output of the gas and steam cycles individually. Heat added per unit mass of air is indicated by the dashed lines.[5]

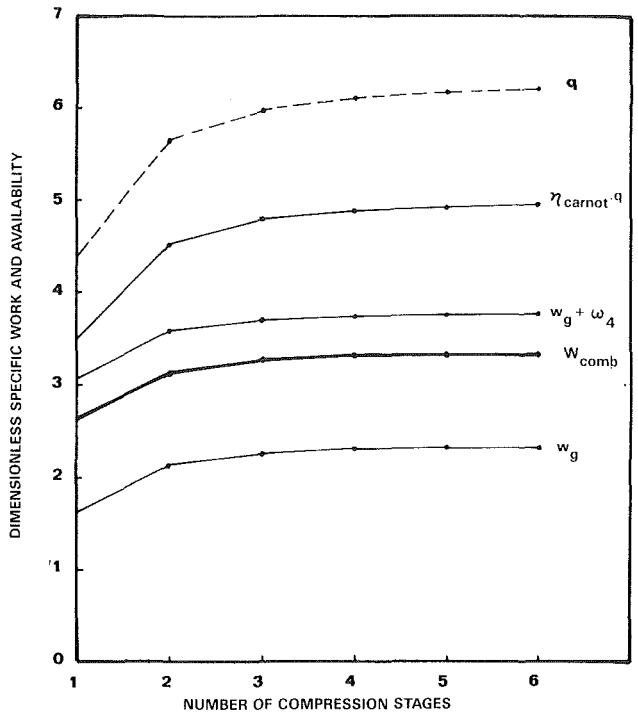


Fig. 18 Balance of specific work and availability as a function of number of compression stages

The effect of changing the pressure ratio is illustrated in Figs. 11 and 15. If it is too low, the gas-turbine efficiency and specific work drop, whereas the steam cycle work increases due to the higher gas temperature T_4. In the limit as the pressure ratio approaches unity, the gas turbine becomes simply a burner for the steam cycle, the overall efficiency falls to that of the steam cycle alone and we lose the thermodynamic advantages of work extraction at the higher temperature. At intermediate pressure ratios both efficiency and specific power peak, the latter occurring first. If the pressure ratio is too high, the compressor and turbine work both increase but their difference, the net gas-turbine power output, drops. This is due to the decline in heat added between them. The absolute magnitude of the availability destroyed in both compressor and turbine increases (as the logarithm of pressure ratio). The availability loss in heat addition in the turbine reheats also increases due to the lower mean temperature of reheat. Those effects expressed as a fraction of head added, which decreases, amplify the loss factors L_c and especially L_T as seen in Fig. 11. Steam-cycle output also suffers with the lower gas temperature.

As would be expected, raising the peak temperature would improve both efficiency and specific power as seen in Figs. 12 and 16. If turbine and component cooling losses were included, the performance would decline at some temperature, depending on the type of cooling technology applied. This matter is addressed in the next part of this paper.

The impact of number of turbine stages is illustrated by Figs. 13 and 17. Although gas-cycle efficiency drops, its net output increases. Both efficiency and specific power increase for the steam cycle which benefits from the higher gas temperature. The combined cycle efficiency and specific output

[5] For typical hydrocarbon fuels combusted in air, the stoichiometric limit on q is approximately nine.

Downloaded 01 Jun 2010 to 171.66.16.71. Redistribution subject to ASME license or copyright; see http://www.asme.org/terms/Terms_Use.cfm

increase sharply in going from one to three stages and more slowly thereafter. It is interesting to note from Fig. 17 that specific power (per unit gas flow) increases by a factor of 2.6 for the two reheats in this example. This may well justify the additional capital cost of the reheated machine.

Finally, Figs. 14 and 18 show that for this example, intercooling provides a modest increase in specific output but a significant drop in combined efficiency. Partial utilization of intercooler availability in the feedwater would reduce this decline.

6 Conclusions

1 The second-law approach of work-balance analysis presented facilities design and optimization of complex cycles by pinpointing and quantifying the losses. Linkage with traditional first-law definitions is preserved to ensure engineering usefulness.

2 Applications to combined cycles show that:

(a) Steam bottoming cycle effectiveness correlates with gas temperature in a simple and compact form.

(b) While some increase in specific output can be obtained by compressor intercooling, this is likely to be at some cost to efficiency. The condition for efficiency decrease with intercooling is derived.

(c) Reheating the expansion improves both specific output and efficiency. The gains are substantial for one and two reheats but progressively smaller for subsequent stages.

References

1 Rice, I. G., "The Reheat Gas Turbine Combined Cycle," *Mechanical Engineering*, Vol. 104, No. 4, Apr. 1982, pp. 46–57.

2 Rice, I. G., and Jenkins, P. E., "Comparison of the HTTT Reheat Gas Turbine Combined Cycle with the HTTT Non-Reheat Gas Turbine Cycle," ASME JOURNAL OF ENGINEERING FOR POWER, Vol. 104, No. 1, Jan. 1982, pp. 121–142.

3 Hori, A., and Takeya, K., "Outline of Plan for Advanced Research Gas Turbine," ASME JOURNAL OF ENGINEERING FOR POWER, Vol. 103, No. 4, Oct. 1981.

4 Keenan, J. H., *Thermodynamics*, Wiley, New York, 1941.

5 Nesbit, W., "Advancing Pulverized Coal," *EPRI Journal*, Vol. 6, No. 7, Sept. 1981, pp. 17–23.

Downloaded 01 Jun 2010 to 171.66.16.71. Redistribution subject to ASME license or copyright; see http://www.asme.org/terms/Terms_Use.cfm

Development of Operating Heat Rate Functions for Cyclically Loaded Coal-Fired Power Plants Without In-Plant Computer Systems

T. F. Talty, P. E.
System Performance Engineer.
Gulf Power Company,
Pensacola, FL 32520

Accurate heat rate functions for cyclically loaded coal-fired power plants are extremely difficult to obtain without the aid of plant computer systems which most older U.S. plants do not have. Special tests or theoretical heat balances generally are not the best means for developing these functions for reasons discussed. An easily applicable, but sufficient, regression-based method of determining the normal operating heat rate equation under these circumstances is presented. Along with the model used, actual results of application of the methodology to several plants are shown and discussed. Special emphasis is given to use for performance monitoring and incremental heat rate development.

Background and Information

General. Heat rate functions which represent the actual running condition of a steam power plant are pivotal for economic dispatch, the optimal selection of generation from each of several alternative sources, and performance monitoring and evaluation. For cyclically loaded coal-fired power plants, the difficulty of developing typical running heat rate equations is magnified because of effects associated with continuous load changes, varying fuel parameters, varying weather conditions, and critical measurement difficulties.

If in-plant computers which can continuously monitor, store, and analyze plant cycle parameters are not available, as is the case with most U.S. plants, the problem is further compounded. Fortunately, most, if not all, plants are tied into computerized power broker systems that store individual plant generation figures which can be used along with daily fuel consumption figures, taken manually from plant fuel scales, to arrive at multiple regression based running heat rate functions suitable for unit dispatch and performance monitoring.

Because of age or additional reserves created by decline in the growth rate for electricity, there are a number of coal-fired plants which are cyclically rather than base loaded. These units normally follow the daily load requirements of their system and/or may be used for system regulation. As more and more oil-fired units are converted to coal or retired, more coal-fired units can be expected to begin this type of operation.

At the present time, heat rate functions for these units are usually estimated based on the results of periodic heat rate tests, computer-based thermodynamic cycle simulations, original vendor design data, or some combination of the above. It is the author's experience that all of these methods have serious drawbacks which, for the subject units, usually lead to average heat rate functions that are not representative at certain MW loads as well as to incremental heat rate functions which may be significantly in error.

Figure 1 illustrates the vendor design average gross heat rate curve for a 500 MW coal-fired subcritical unit. Also, several heat rate curves are plotted for this unit assuming the

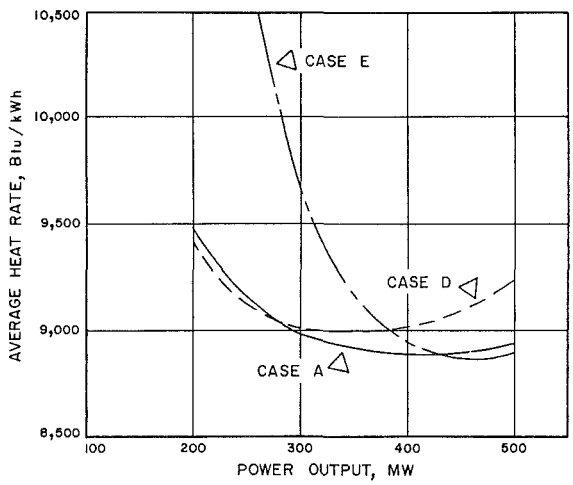


Fig. 1 Potential average heat rate curves corresponding to conditions of Table 1

Contributed by the Power Division for publication in the JOURNAL OF ENGINEERING FOR GAS TURBINES AND POWER. Manuscript received by the Power Division October 1983.

Copyright © 1985 by ASME
Downloaded 01 Jun 2010 to 171.66.16.71. Redistribution subject to ASME license or copyright; see http://www.asme.org/terms/Terms_Use.cfm

Table 1 Sample illustration for a 500 MW plant of effects of differing cycle conditions on heat rate function constants*

		Quadratic form energy input/output function coefficients*		
Case	Description	A	B	C
A	Design conditions	461.0	6.606	0.002817
B	High turbine back pressure	442.3	7.023	0.002758
C	Boiler efficiency impaired at low MW output	382.2	7.701	0.001029
D	Boiler efficiency impaired at high MW output	479.8	6.142	0.004219
E	Boiler efficiency degraded at low MW output	2166.8	−0.735	0.010598

* Please see equation (1)

various scenarios of either boiler or turbine cycle degradation shown in Table 1.

Table 2 Some typical occurrences which alter heat rate function formulations from design

1 Post design plant modification
2 Equipment out of or at reduced service
3 Instrumentation off of calibration
4 Turbine seal leakage
5 Operation of dump drains
6 Valve leakage
7 System regulation
8 Wet coal
9 Use of other than design coal
10 Pulverizer settings
11 Feedwater heaters out of service
12 Heat exchanger tube pluggage
13 Soot blowing
14 Single valve operation
15 Off valve point operation
16 Vacuum leaks
17 Boiler tube leaks
18 Restricted damper control
19 Other control restrictions
20 Spray water

These scenarios are just some of the many operating situations found in actual day-to-day operations which cause generating unit performance to differ markedly from design. Table 2 more explicitly lists everyday occurrences which affect unit performance.

Many of these problems may not be remedied. In some

Nomenclature

A = constant term in rate of energy input equation, MBtu/h
ABS = absolute value of
B = population value of P coefficient constant in rate of energy input equation, MBtu/MWh
C = population value of P^2 coefficient constant in rate of energy input equation, MBtu/MW^{2}h
E = amount of thermal input energy consumed in a subperiod, MBtu
EBR = rate of thermal energy input to plant, MBtu/h
EBR′ = average rate of energy input during the subperiod, MBtu/h
EBR_i = average rate of energy input during subinterval period i, MBtu/h
HV_i = heating value of fuel consumed during subperiod i, Btu/Lbm
K = constant of $24 * 10^6$
L_i = fuel mass flow rate for subperiod i, Lbm/h
LIM = limit value for removing observations from the data base based on $\delta p'$, MW
LSRF = variable representing the magnitude and duration of load fluctuations during the subperiod, MW^2
n = number of subintervals in the subperiod
n_1 = sample size from population 1
n_2 = sample size from population 2
P = instantaneous plant gross electrical power output, MW
P' = average power output during the subperiod, MW
P_i = average power output during subinterval i, MW
R^2 = multiple coefficient of determination
T_i = subinterval period time span, h
TSP_i = total time of subperiod i, h
X = model independent variable, $\delta\text{LSRF}/\delta P'$, MW
$\bar{X}$ = mean value of the independent variable, MW
Y = model dependent variable, $\delta\text{EBR}'/\delta P'$, MBtu/MWh
$\bar{Y}$ = estimate of the mean value of the dependent variable for a given value of the independent variable, MBtu/MWh
Y_i = observed value of the dependent variable, MBtu/MWh
$\delta\text{EBR}'$ = difference between EBR′ for the current subperiod and EBR′ for the immediately preceding subperiod, MBtu/h
$\delta P'$ = difference between P' for the current subperiod and P' for the immediately preceding subperiod, MW
δLSRF = difference between LSRF for the current subperiod and LSRF for the immediately preceding subperiod, MW^2
ΔP_i = difference between power output for subinterval i and the subperiod average
ϵ, ϵ_i = error terms
σ_c = standard error of the C regression constant, MBtu/MW^{2}h
σ_{HV} = standard error of the difference between measured and actual fuel heating value, Btu/Lbm
σ_L = standard error of the measured fuel flow rate, Lbm/h, for given HV_i, P', and LSRF
σ_{TSP} = standard error of the difference between measured and actual subperiod time length, h
σ_{yx} = standard error of the model dependent variable for a given value of the independent variable, MBtu/MWh
$\sigma_{\delta p'}$ = standard error of the difference between measured and actual difference in P' between sequential subperiods
σ_{ϵ_i} = standard deviation of the error in measuring P'
μ_y = population value of Y conditional on value of X
Σ = summation from i equals 1 to n

Superscripts

$\hat{}$ = estimated value of

Downloaded 01 Jun 2010 to 171.66.16.71. Redistribution subject to ASME license or copyright; see http://www.asme.org/terms/Terms_Use.cfm

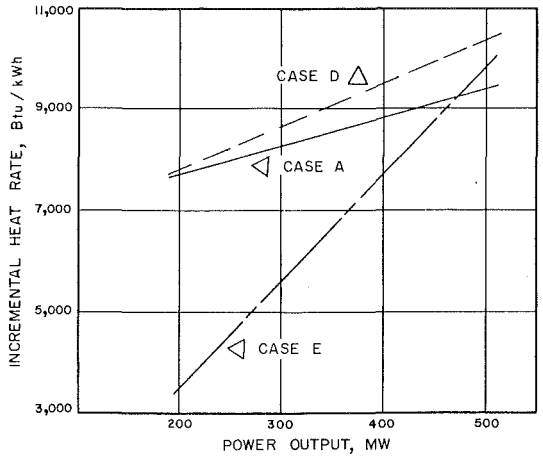


Fig. 2 Potential incremental heat rate curves corresponding to conditions of Table 1

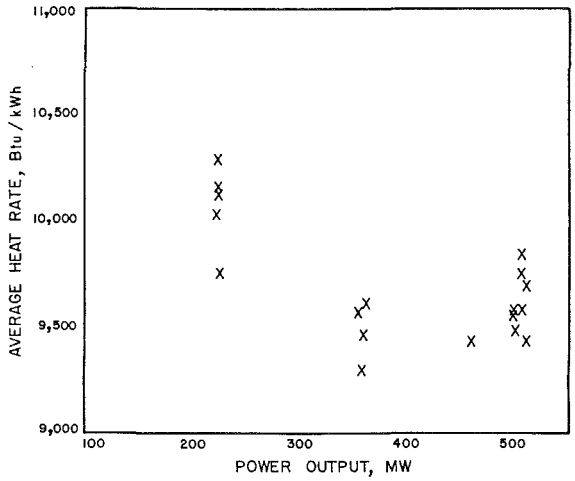


Fig. 3 Test heat rates for 500 MW plant

cases, a remedy may not exist at the present time, or funds may not be available for construction or replacement equipment. Some problems may involve parameters for which it is not economical to continuously maintain design conditions, or involve actions taken for reasons of unit safety, control, or optimization of performance in a restricted load range. Some of the reasons for off-design performance are not likely to be known to even the most astute plant operator. An example of this would be operator reliance on out-of-calibration station instrumentation.

Inadequacy of Vendor Heat Balance Based Functions. The result of such routine occurrences is that vendor supplied design heat rate data cannot be expected to represent typical operating conditions. If equations are curve fit to design heat rate data, and these functions are used for economic dispatch, the incremental heat rates upon which the cheapest increment of MW generation is selected may differ by 20 percent from the actual incremental heat rate and, therefore, incremental cost may be under or overstated by 20 percent. Figure 2 shows incremental heat rate curves corresponding to the average heat rate curves in Fig. 1 and several of the cases of Table 1.

Inadequacy of Test-Based Heat Rate Functions. Many utilities use periodic heat rate tests as the basis for developing heat rate functions. Usually this involves a procedure whereby a generating unit is brought to a desired MW output and stabilized at that load for a period of hours so that the fuel input is measured over a test period of a few hours. During the test, fuel to the coal pulverizers is sampled periodically so that it can later be aggregated and an average as fired heating value of coal determined for the test period. Having determined the energy input rate per hour and the electrical output, simple division provides the average heat rate for the unit. By accumulating a number of test points in this manner, sufficient data can be obtained to develop heat rate functions using well-known statistical regression techniques.

For cyclically loaded coal-fired units, the drawbacks to heat rate functions developed in this manner are as troubling as those associated with design based functions.

First, such tests can be expensive. Additional fuel expenses are incurred when operating the test unit at loads other than those mandated on a strictly economic dispatch basis. Their costs may be as high as $4800 per test, depending on the severity of mismatch between test and optimum load called for by economic dispatch, the relative cost of the alternative energy, and length of test.

Second, because of errors associated with accurately measuring coal flow, as well as those associated with measuring the heating value content of the coal consumed, considerable random scatter is introduced into the heat rate data. Typical results of round robin testing in which a homogeneous coal sample is divided and sent to a number of laboratories that independently determine its constituents and heating value have shown that heating value differences of 0.7 percent are not uncommon.

It has been the author's experience that coal weighing devices, whether batch, feeder, or belt type, while touted to obtain ± 0.5 percent accuracy or better, rarely if ever attain this level on a continuing basis in the plant environment. Whether because of less than necessary maintenance or the effect of the corrosive and vibratory environment, or modifications made to ease maintenance of the indirect effects of freeing objects from the coal path, it is believed that sustainable accuracy of ± 2.0 percent is more representative.

Third, additional scatter and bias are built into the heat rate results because of what may be called "test mentality." This is the natural human reaction of the plant manager and his personnel to want to perform well on a test and gain recognition from their supervisors for doing well. The effect of this reaction is a tendency to operate the unit during the test in as nearly a flawless condition as possible and in a manner which only represents the special situation of running a test and not normal operation. In some cases, the pressure for efficiency may be so intense that test results are screened and only the most favorable submitted to the requesting engineers.

Figure 3 shows heat rate test data taken by this method for a 500 MW cyclically loaded coal-fired power plant.

Inadequacy of Cycle Computer Design Codes. Some utilities are experimenting with the use of plant cycle computer design codes for heat rate function determination. Several of these codes have become available in recent years. In essence, these codes are duplicates of the computer codes used by vendors to produce original design heat balances. Therefore, these design codes are restricted regarding development of heat rate functions similar to those based on vendor design heat balances because of lack of knowledge as to what the time distribution of the input data should be.

To attempt to achieve representative results from these programs, numerous computer simulations would be required to represent a large number of possible cycle configurations and conditions which occur from time to time in normal operation. Resulting heat rates at each MW output level would subsequently need to be weighted by the percentage of time the unit would be expected to operate in each condition. Clearly, this process would require many computer runs based on numerous hypothetical cycle conditions combined with uncertain prognostications.

Downloaded 01 Jun 2010 to 171.66.16.71. Redistribution subject to ASME license or copyright; see http://www.asme.org/terms/Terms_Use.cfm

What Is Required. What is needed is a method of determining what a power plant's average and incremental operating heat rates can be expected to be at a given MW output level within some estimable plus or minus amount based on actual typical operating data. Actual operating data will contain all of the typical operating effects sought in approximately their true relative weighted strengths if the sample is large enough. While the application of such a methodology presents a number of problems, such an approach is warranted in the interest of production of energy at its lowest cost.

The Statistical Model

Statistical regression methods are commonly used to best fit mathematical functional relationships to actual data observations. The first step is to develop a model of the function expected to best explain or fit the observed actual data. Because cyclically loaded coal-fired plants are subject to uncertainties regarding fuel measurement, as mentioned earlier, because of the continuously changing load of these units, and because of the lack of short interval fuel flow data, the model developed will need to be specially structured to overcome these problems if actual operating data are to be used and the attributes of normal operation captured.

Both average and incremental heat rate functions for a power plant are derived from the thermal energy input rate as a function of MW output. The general form of this function, equation (1), and its derivatives are widely used in the industry, and the author has found this form to provide nearly perfect fits of design data for many generating units and acceptable fits over a wide range of off-design conditions.

$$\text{EBR} = A + B*P + C*P^2 \tag{1}$$

Taking the derivative of the energy input rate in equation (1) with respect to power output would yield the accompanying form of the incremental heat rate equation, equation (2) [1].

$$\frac{d\ \text{EBR}}{dp} = B + 2*C*P \tag{2}$$

However, if both sides of equation (1) are divided by the MW output level, the result is the accompanying form of the average heat rate equation

$$\frac{\text{EBR}}{P} = \frac{A}{P} + B + C*P \tag{3}$$

The heat rate function of equation (2) is used for economic dispatch and the function of equation (3) is useful for performance monitoring. The objective of the statistical model, therefore, is to provide the best unbiased estimates of the constants A, B, and C, which will enable equations (2) and (3) to be defined.

The average energy input rate, Btu/h, over a period of time during which a unit operates at various MW output levels can be closely approximated by combining equation (1) written for small subintervals of time comprising the desired period as follows:

Subinterval period

1 $\quad \text{EBR}_1 * T_1 = (A + B*P_1 + C*P_1^2)T_1$

2 $\quad \text{EBR}_2 * T_2 = (A + B*P_2 + C*P_2^2)T_2$

$\vdots$

$n \quad \text{EBR}_n * T_n = (A + B*P_n + C*P_n^2)T_n$

Summing the total energy consumed in each subinterval:

$$E = \Sigma \text{EBR}_i * T_i$$

$$E = A*\Sigma T_i + B*\Sigma(P_i * T_i) + C*\Sigma(P_i^2 * T_i) \tag{4}$$

Dividing equation (4) by the total time of the period:

$$\frac{E}{\Sigma T_i} = A + B*\frac{\Sigma(P_i * T_i)}{\Sigma T_i} + C*\frac{\Sigma(P_i^2 * T_i)}{\Sigma T_i} \tag{5}$$

Recognizing in equation (5) that the average MW output for the period P' equals the B term coefficient, and substituting the variable LSRF for the C term coefficient, the formula for the average energy input rate per hour for the total period can be restated as:

$$\text{EBR}' = A + B*P' + C*\text{LSRF} \tag{6}$$

where P' is the average load for the period, and the term LSRF, which is to be referred to as the load square range factor, equals:

$$\text{LSRF} = \frac{\Sigma(P_i^2 * T_i)}{\Sigma T_i} \tag{7}$$

If actual unit operating data in terms of the energy consumed per day, average daily MW output level P', and variable LSRF can all be obtained with sufficient numbers of observations, a statistical regression can be attempted for the A, B, and C constants of equation (6), which are the same constants needed to determine equations (2) and (3). These functions could then be considered for heat rate monitoring and unit dispatch. However, there are additional complications with coal-fired units other than continuous load changes which the model must overcome and which will require further modification before application. These steps will be discussed after a brief discussion of the variables of equation (6).

The LSRF term of equation (7) is a measure of load variability. It can be seen from equation (7) that, if a power plant operated at steady-state output, that is constant MW load, LSRF would simply be the MW load squared, and equation (5) would be just like equation (1). If each load change during the period P_i is viewed as a change from the average MW output P' for the period, the LSRF equation (7) can be expanded, then simplified to:

$$\text{LSRF} = P'^2 + \frac{\Sigma(\Delta P_i^2 * T_i)}{\Sigma T_i} \tag{8}$$

The A and B constants of equation (6) are the most easily estimable by regression. The C constant often proves difficult because of its sensitivity. Accurate estimation of the C coefficient is very important, however, in determining incremental heat rates and costs, as will be demonstrated later.

Model Reformulations Directed at Coping With Poor Data. Because coal flow measurement is typically not very accurate on a percentage basis relative to the percentage change in heat rate from minimum to full load, a special measure must be taken if we hope to obtain estimates of the C coefficient from equation (6).

Accurate weighing of fuel in transit within a power plant is not easy. It can be likened to weighing oneself while attempting to walk over a bathroom scale. The problem is further compounded by the fact that coal scales, like all instruments, begin to move away from calibration immediately after being reset, that fuel counter and other weighing system components occasionally do not function properly, and that, in some cases, fuel may even be bypassed around malfunctioning weighing systems. As a result, it can be expected that a very substantial number of observations would not be suitable for inclusion in the regression data base.

To combat these problems, two steps are necessary: (1) The model should be adjusted to mitigate the effects of calibration creep in order to preserve the greatest number of observations and eliminate the serial effect of a scale going out of calibration, and (2) observations based on substantially incorrect measured fuel input data must be removed from the

Downloaded 01 Jun 2010 to 171.66.16.71. Redistribution subject to ASME license or copyright; see http://www.asme.org/terms/Terms_Use.cfm

Table 3 Illustration of relative reduction of dependent variable error terms with equation (9) model form

Case 1. Assume: One generating plant with fuel scales calibrated at the beginning of the month and moving continuously and linearly out of calibration during the month until they are overreading 6 percent at the end of the month. Each day of the month the unit is cycled exactly as for all other days of the month, and each day an observation of the dependent variable is collected.

Model equation	Dependent variable	Day 1	Day 31	Average error in dependent variable
(6)	EBR′	0.0 percent	6.0 percent	3.0 percent
(9)	δEBR′	0.0 percent	6.0 percent	0.2 percent

The error for the equation (9) model is much smaller, since the rate of change of measurement error between successive days is 0.2 percent.

Case 2. Assume: Same situation as Case 1, except that the fuel scales are not moving continuously out of calibration during the month, but are instead in absolute error, reading 3 percent too high constantly.

Equation	Variable	Day 1	Day 31	Dependent variable
(6)	EBR′	3.0 percent	3.0 percent	3.0 percent
(9)	δEBR′	3.0 percent	3.0 percent	0.0 percent

The error for the equation (9) is much smaller since the rate of change of measurement error between successive days is 0.0 percent.

regression data base. The first step will be discussed now and the second under the Data Reduction section.

By writing equation (6) for the average energy consumption rate in two sequential periods of equal length, and subtracting these equations, the following relationship results:

$$\delta\text{EBR}' = B * \delta P' + C * \delta\text{LSRF} \tag{9}$$

The model described in equation (9) has an important advantage over that described in equation (6) in that coal flow measurements which are changing due to calibration creep can still be utilized to provide reliable dependent variable observations, and even absolute scale errors are usually tolerable as long as period 1 and period 2 are sequential and of small, equal time spans.

This reduces the amount of data which must be culled as "bad" data and reduces the extent of problems associated with determining which observations are unusual and signal a model deficiency, from those which are due to poor measurement. Table 3 illustrates with two simple examples the relative reduction in error of the dependent variable of equation (9) versus that of equation (6) for two situations common in cyclically loaded coal-fired power plants. Because plants such as these are often operated at different ends of their MW output range from one day to the next, it should be noted that fuel measurement errors of the magnitude of those in the Table 3 examples will not be obvious to the plant operators. Regression for the constants A, B, and C in equation (6) using data with fuel measurement percentage errors such as those shown is one of two major reasons why reliable estimates of the C coefficient are not normally obtainable with this model form.

Application of model equations (6) or (9) using a standard linear regression technique often yields impressive R^2 statistics. However, R^2 statistics can be illusory in that, the greater the size of the observed dependent variable values, the greater the tendency for R^2 results to be high. Furthermore, high R^2 values are not the model's goal so much as a confident estimation of the true normal operating B and C regression constants. Poor estimates of the B and C constants, while achieving high R^2 statistics, are common with regressions performed using either equation (6) or (9).

Model Adjustment for Intercorrelated Independent Variables. While model equation (9) has a number of attributes, it has a serious drawback. Referring to equation (8), it is clear that the LSRF variable is a function of the average

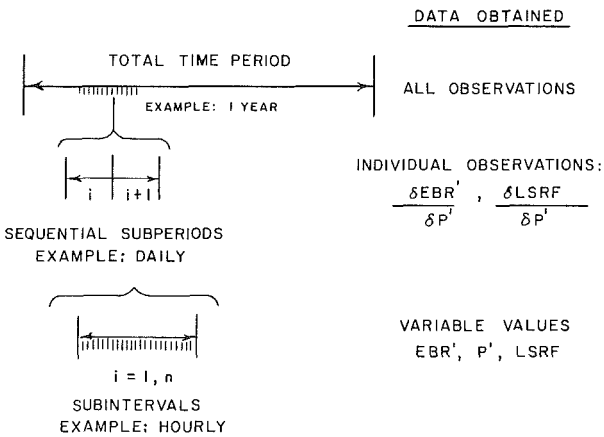


Fig. 4 Diagram of relationship between data development time periods

MW output variable P', and that these two variables are intercorrelated. That is, if the value of one increases or falls, the other will follow similarly. The effect of intercorrelation of these two independent variables is that the regression estimates of the sought-after B and C constants may not be unbiased estimates of their true values [2].

To eliminate concern over potential bias, one or the other of the intercorrelated dependent variables must be removed from the model. This is accomplished by dividing both sides of equation (9) by the variable $\delta P'$ yielding:

$$\frac{\delta\text{EBR}'}{\delta P'} = B + C * \frac{\delta\text{LSRF}}{\delta P'} \tag{10}$$

Equation (10) is the final form of the statistical model for use in determining estimates of the B and C constants which form the desired heat rate functions of equations (2) and (3), and equation (1) when the A constant is also known.

Earlier in the development of the model, the A constant was deleted from the model equation when equations written for adjacent periods were differenced. Equation (6), which is not predicated on a specific time period, may be used as shown below to determine the A constant if the B and C coefficients have been estimated, and the values of the variables EBR′ P', and LSRF for the period are known.

$$A = \text{EBR}' - B * P' - C * \text{LSRF} \tag{11}$$

Downloaded 01 Jun 2010 to 171.66.16.71. Redistribution subject to ASME license or copyright; see http://www.asme.org/terms/Terms_Use.cfm

Data Gathering

For best results in estimating the A, B, and C regression constants when using the model, it is desirable to obtain as many data observations as possible, as long as all observations are taken from a total period of time in which there is no reason to suspect that the typical operating heat rate relationship changed significantly during the period. Annual periods, periods between major equipment modifications or overhauls, seasonal periods, or periods established by suspected heat rate degradation or improvement are examples of suitable total time periods from which to extract data observations, provided a sufficient number of observations can be obtained. The choice of total time period is also governed by the purpose to which the results will be applied.

Conversely, in contrast to the total period of time from which all observations are taken, the sequential subperiods between which differences are taken for values of δEBR′, $\delta P'$, and δLSRF should be short, and the subintervals which comprise each of these periods as small as practical.[1] Figure 4 shows a diagram illustrating the relationship between the several time periods discussed and observation data development. Unless stated otherwise, heat rate function results presented here were based on annual total periods, daily subperiods, and hourly subintervals. Text references to these specific times are used interchangeably with the more general terms of total period, subperiod, and subinterval.

As mentioned previously, most U.S. utilities operate in power broker systems, whereby energy purchases and sales are made between utilities. To operate effectively in these systems, electrical output from each generating station is measured frequently, analyzed, and usually stored in computer storage for later use in reconciling who owes whom what for energy exchanged, among other uses. This polling of electrical output usually is quite rapid, every few minutes or less. With the aid of a simple computer program, these stored data can be retrieved from the computer's files and both the value of the LSRF variable and the average MW output P' computed for any desired subperiod.

Most U.S. coal-fired power plants also have coal weighing devices, belt, batch, or feeder type, which can provide a measure of daily (subperiod) coal consumption, and other means of measuring supplementary fuels such as daily lighter oil consumption. With daily sampling of the coal input and as needed sampling, depending on variability, of any supplementary fuels for the heating value per consumption unit of each fuel, e.g., Btu/Lbm for coal, the actual total plant energy consumption per day can be determined.

With daily values of EBR′, P', and LSRF, for every two successive days, a single observation of each variable in the regression model, equation (10), can be calculated. For a total period of N operating days, $N-1$ observations are potentially available for the regression.

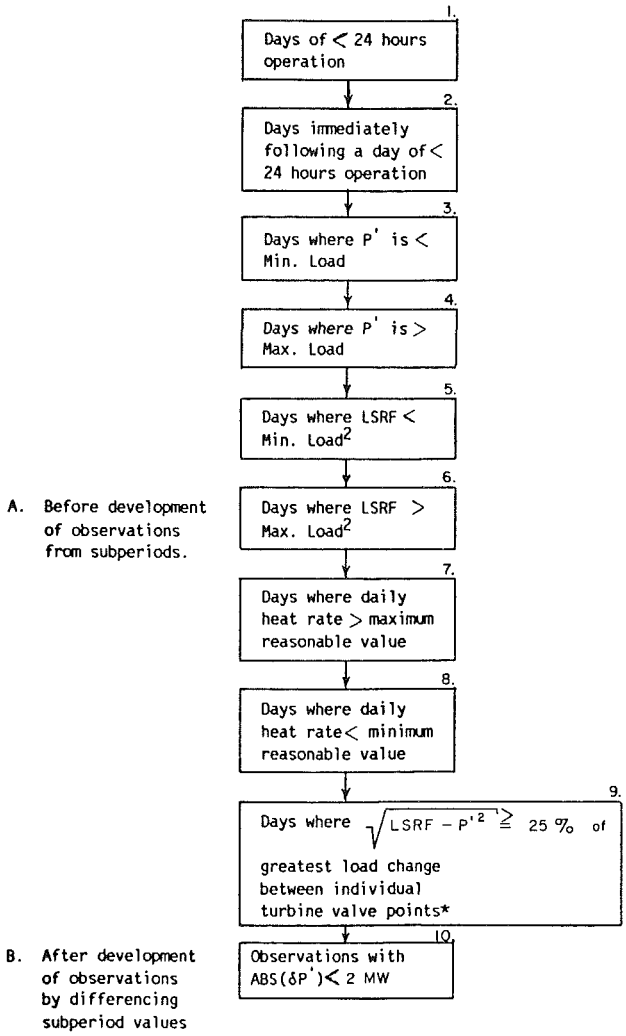
Data Reduction and the Regression Analysis Process

In developing the statistical model, it was implicitly assumed that (1) a power plant's fundamental heat rate characteristics, A, B, and C constants, were not significantly altered from one day to the next due to changes in the rate of MW loading and unloading, and that (2) significant infrequent changes in the mode of operation and/or (3) significant equipment changes did not occur during the period from which observations were selected. Because of these considerations, along with the inability to accurately measure heat input to the cycle, the sensitivity of the model's variables to errors in measuring $\delta P'$ and keypunch and other errors which may make data observations unacceptable, it is extremely important that all observations be screened prior to inclusion in the model's regression data base. It is also equally important that residual values and residual patterns be reviewed after regression.

[1] Previously in this paper subperiods have been referred to as periods.

Table 4 Example block diagram for removal of bad data and data not conforming to model assumptions

Data meeting the following tests are removed from the regression data base prior to attempting initial regression:



*Suggested for use only in cases where the number of observations is limited and the plant is valve point loaded occasionally.

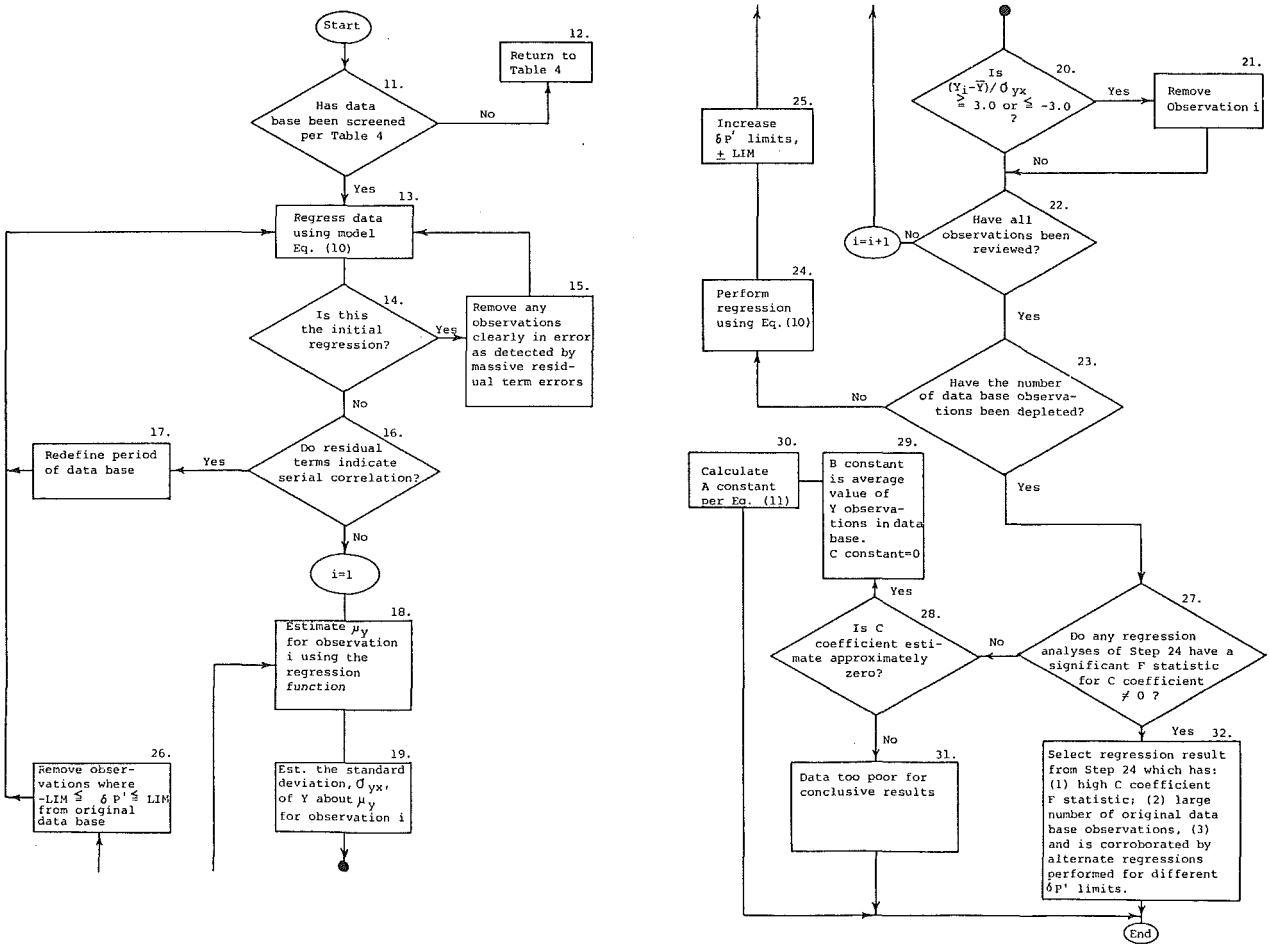
Initial Screening of the Data Base. There are a number of automatic screening steps the author employs to "purify" observation data. These steps can be categorized into those performed prior to regression analysis and those which are contingent upon initial regression function estimates. Table 4 is a block diagram of those measures falling into the first category. Those steps in the second category are included in the process diagram of Table 5 and will be discussed in the next section.

Steps 1 and 2 of Table 4 are employed so that model assumption (1), above, is not violated. Costs associated with unit startups and shutdowns are important considerations in economic dispatch; however, the underlying fuel consumption is appropriately handled outside of the running heat rate function.

Steps 3 through 8 remove data which are outside of possible or reasonable limits and, therefore, are known to be incorrect. Steps 7 and 8, in effect, check the total subperiod heat input rate, EBR′ for gross error. Very liberal limits, such as the

Downloaded 01 Jun 2010 to 171.66.16.71. Redistribution subject to ASME license or copyright; see http://www.asme.org/terms/Terms_Use.cfm

Table 5 Block diagram of analysis methodology



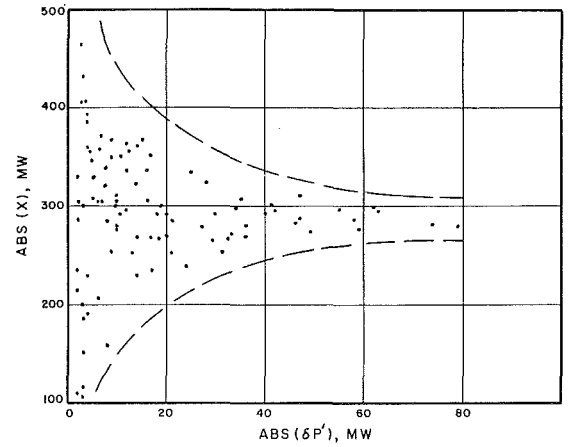


Fig. 5 Sample plot of model independent variable (δLSRF/$\delta P'$) observations versus absolute value of $\delta P'$ for an example 200 MW plant

annual average heat rate plus 60 percent and minus 30 percent, are used since, as discussed earlier, the model's differencing technique greatly reduces the effects of systematic fuel measurement errors.

Step 9, if used, ensures that observations selected are based on subperiods during which the power plant has been exercised, that is operated at several MW output levels during the day.

There are two reasons for desiring *not* to use Step 9: It does reduce the number of available observations; and, for cycling units which are occasionally base loaded, it removes the influence of these periods from the regression equation.

Utilization of this qualifier may be appropriate when observations are limited, and the possibility exists that a few observations will be outliers as a result of steady-state operation near a turbine valve point during one or both of their constituent subperiods, and that unless removed, these observations will have an undue influence on the estimated regression line. This can occur because of incremental heat rate discontinuities which occur around valve points. However, where there are enough observations of this sort, as well as those without valve point effects, so that the proportion of one type to the other can be expected to be near the population proportion, Step 9 should be omitted.

Step 10, in the author's system, is normally the greatest remover of observations from the regression data base. Step 10 must be used in order to effectively eliminate an upward bias of the C regression coefficient due to the effects of random measurement error of the variable $\delta P'$. Because $\delta P'$ is used in the denominator to determine actual observations of the dependent model variable, normally distributed plus and minus errors of equal magnitude do not provide offsetting values of the dependent variable.

It is possible to correct for this bias by adjusting each observation, adjusting the resultant regression equation, or by limiting observations in the data base to those having $\delta P'$ observations at or above some minimum value selected to minimize the bias. The first two of these options are laborious. The third option, restricting the data base based on $\delta P'$, can be easily applied.

It is desirable to establish an absolute value of $\delta P'$ boundary at as low a value as will effectively eliminate the bias. This will allow retention of the greatest number of

Downloaded 01 Jun 2010 to 171.66.16.71. Redistribution subject to ASME license or copyright; see http://www.asme.org/terms/Terms_Use.cfm

Table 6 Example of method used to estimate variance of dependent variable observations about the regression line for a known value of the model independent variable

BY DEFINITION: $$Y = \frac{\delta EBR'}{\delta P'} = \frac{(L_2 * TSP_2 * HV_2 - L_1 * TSP_1 * HV_1)}{K * \delta P'} \quad (16)$$

BASED ON THE UNCERTAINTY ANALYSIS METHOD OF KLINE AND McCLINTOCK (REFERENCE 4.)

$$\sigma_{y,x} = \left[\left(\frac{\partial Y}{\partial L_2} * \sigma_{L_2}\right)^2 + \left(\frac{\partial Y}{\partial TSP_2} * \sigma_{TSP_2}\right)^2 + \left(\frac{\partial Y}{\partial HV_2} * \sigma_{HV_2}\right)^2 + \left(\frac{\partial Y}{\partial L_1} * \sigma_{L_1}\right)^2 + \left(\frac{\partial Y}{\partial TSP_1} * \sigma_{TSP_1}\right)^2 + \left(\frac{\partial Y}{\partial HV_1} * \sigma_{HV_1}\right)^2 + \left(\frac{\partial Y}{\partial \delta P'} * \sigma_{\delta P'}\right)^2\right]^{1/2} \quad (17)$$

THEN APPLYING EQ. (17) TO EQ. (16) AND ASSUMING $\sigma_{TSP} = \sigma_{TSP_1} = \sigma_{TSP_2}$ AND $\sigma_{HV} = \sigma_{HV_1} = \sigma_{HV_2}$ AND $HV_1 = HV_2$, $TSP_1 = TSP_2$

$$\hat{\sigma}_{y,x} \cong \left[\frac{(TSP * HV)^2(\sigma_{L_1}^2 + \sigma_{L_2}^2) + (HV * \sigma_{TSP})^2(L_1^2 + L_2^2) + (TSP * \sigma_{HV})^2(L_1^2 + L_2^2) + (L_2 - L_1)^2(TSP * HV * \sigma_{\delta P'})^2}{(K * \delta P')^2}\right]^{1/2} \quad (18)$$

THE VARIOUS STANDARD DEVIATIONS OF EQ. (18) ARE ESTIMATED FROM FIELD OBSERVATIONS.

EX: $\sigma_{TSP} \cong 0.15$ h

$\sigma_{HV} \cong 49.9$ Btu/h

$\sigma_{L_i} \cong 0.025 * L_i/1.64$ Lbm/h

$\sigma_{\delta P'} \cong 0.096$ MW (FROM EVALUATION OF EQ. (12))

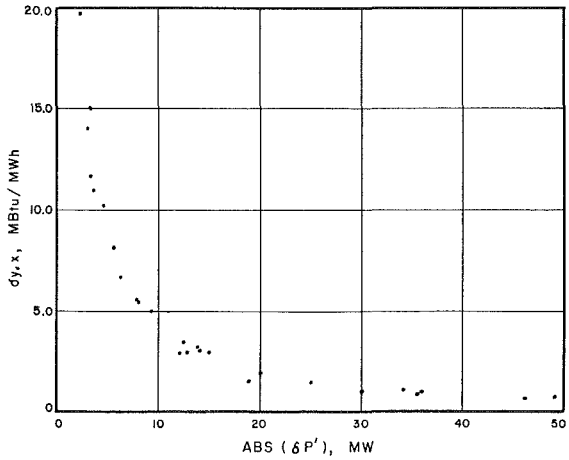


Fig. 6 Sample plot of anticipated values of the standard deviation of the model dependent variable about the regression line for various values of $\delta P'$ for an example 200 MW plant

observations, and particularly of those with the largest values of the independent model variable, as Fig. 5 indicates.

The minimum $\delta P'$ value of 2 MW, shown in Step 10, Table 4, was determined based on the random error associated with $\delta P'$ data from the particular power broker system employed by the author's company. From this system, hourly plant power output data to the nearest 0.5 MW can be retrieved. With sequential subperiods of 24 hours each, the standard deviation of the error in measuring $\delta P'$ can be determined from the formula for the standard deviation of the difference between two sampling distributions of the mean, equation (12) [3]

$$\sigma_{\delta P'} = \sqrt{\frac{\sigma_{\epsilon 1}^2}{n_1} + \frac{\sigma_{\epsilon 2}^2}{n_2}} \quad (12)$$

Using $\sigma_{\delta P'}$ and given an absolute value of $\delta P'$ minimum value, the expected value of the error in the model dependent variable can be determined and, for a particular plant, this error can be translated into a range of C constant error. However, in all cases studied, an absolute value of $\delta P'$ limit of 2 MW virtually eliminated expected bias of the C regression constant.

Additional steps beyond those of Table 4 may be required, depending on any special circumstances regarding the accuracy or validity of raw data values. In devising any additional steps necessary, the user is advised to look at all possible influences which could affect the measurement and handling of the raw data.

Addditional Data Reduction Using Preliminary Regression Analysis. Table 4 describes the process in which incorrect or biasing data should be removed from the regression data base prior to analysis with the model. It is also important to have guidelines for the removal of "obviously" bad data exposed by initial estimates of the regression equation if the best estimates of the A, B, and C constants are to be obtained. Table 5 is a continuation of the methodology employed by the author to arrive at the final estimate of the heat rate function constants. Included in the block diagram of the process are three additional measures to remove questionable data observations.

The first two of these additional measures, dealing with serial correlation and dramatically flawed data, as described by Table 5, blocks 15, 16, and 17, are self-explanatory and standard regression analysis practice. The third measure, comprised of blocks 18 through 22, serves to remove those actual observations from the data base which lie so far from the estimated regression line that there is very little probability that they are legitimate elements of the distribution of the model dependent variable at a given value of the independent variable. This step, which is an adaptation of Chauvenet's criterion for rejecting a data reading [4] is, in effect, a further refinement of the step taken in block 15. It should be noted that the decision described in blocks 18 through 22 to accept or remove an observation is based on the estimated number of standard deviations each observation lies from the initial regression line from block 13, and that this data review is applied only once to each regression data base. Application of this measure should remove only a few percent or less of available observations.

Table 6 illustrates the method of computation for the estimated value of σ_{yx} used. Assumptions underlying this calculation regarding component standard deviations should be on the conservative side and preferably based on field observation.

Application of the Regression Model to Data Base Subsets. Each actual observation of the model dependent variable can be expressed as:

Downloaded 01 Jun 2010 to 171.66.16.71. Redistribution subject to ASME license or copyright; see http://www.asme.org/terms/Terms_Use.cfm

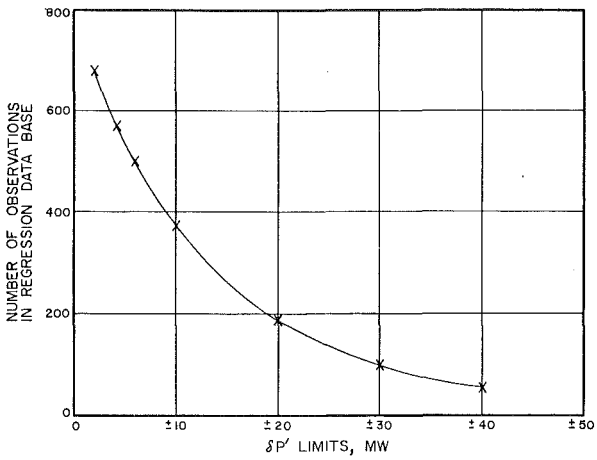


Fig. 7 Example of decline in available data base observations as $\delta P'$ limits are increased for an example 200 MW plant

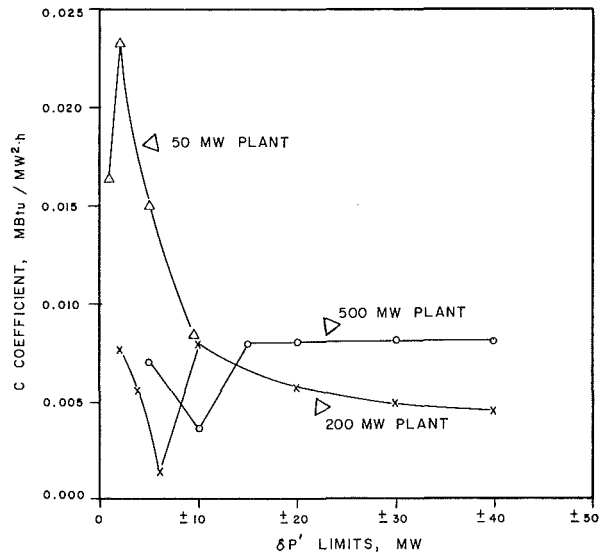


Fig. 8 Results showing variation of estimated regression coefficient C for various data base $\delta P'$ limits for several sizes of plants

$$\frac{\delta \mathrm{EBR}'}{\delta P'} = \frac{\delta \mathrm{EBR}'_B}{\delta P'} + \frac{\delta \mathrm{EBR}'_C}{\delta P'} \pm \frac{\epsilon}{\delta P'} \tag{13}$$

where the following components are defined as:

$$\frac{\delta \mathrm{EBR}'_B}{\delta P'} = B \text{ Population regression constant} \tag{14}$$

$$\frac{\delta \mathrm{EBR}'_C}{\delta P'} = C \text{ Population regression constant}$$

$$* \frac{\delta \mathrm{LSRF}}{\delta P'} \tag{15}$$

Equation (14) dictates that increasing the value of $\delta P'$ will not change the value of $\delta \mathrm{EBR}'_B/\delta P'$. In addition, it can be seen from the typical curve of Fig. 5, the shape of which is a consequence of the definition of δLSRF, and equation (15) that increasing the value of $\delta P'$ rapidly leads to a near constant range of $\delta \mathrm{EBR}'_C/\delta P'$ values also. Referring back to equation (13) with these observations, it is apparent that increasing $\delta P'$ very likely reduces the percentage random error contained in individual observations, and reduces the possibility that a few observations with large error terms will overshadow the relatively small values of $\delta \mathrm{EBR}'_C/\delta P'$ and "pull" the estimated regression line or erroneously indicate

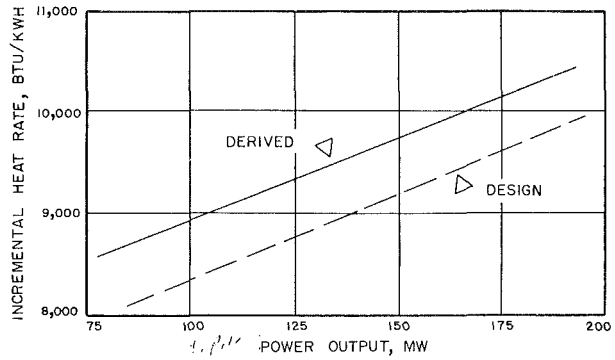


Fig. 9 Regression-derived incremental heat rate versus load curve for 200 MW plant example

no correlation between model variables. This finding is consistent with Fig. 6, which shows the typical relationship between standard deviation of the dependent variable about the regression line, as estimated by equation (18), and $\delta P'$.

Therefore, if observations with absolute value of $\delta P'$ less than or equal to some limit are removed from the data base, the resulting subset data base may provide a better regression function estimate than the original data base. Furthermore, additional subsets might be formed, each one reducing the error term influence by increasing the absolute value of $\delta P'$ limit.

Unfortunately, there are two offsetting costs associated with this process. Obviously, removal of data in this fashion reduces the number of observations available, as shown in Fig. 7, which reduces the accuracy of the regression estimates. Second, observations with the highest values of the independent variable, which would be associated with high values of $\delta \mathrm{EBR}'_C/\delta P'$, are among those chiefly removed. Also, in order to ascribe the results of regression estimates from a population represented by the data base subset to the population represented by the original data base, the assumption must be made that, as the base is reduced, the population regression line of the subset data base and that of the original data base remain the same. However, since there is wide support for the incremental heat rate being a function of power output P, equation (2), and since $\delta P'$ is not strongly correlated with P, this assumption should not be unreasonable unless the data base is severely reduced.

Because of the effects of poor quality data as reflected by the standard deviation σ_{yx} at low values of $\delta P'$, the author develops different data base subsets based on increasing absolute value of $\delta P'$ limits, performs regression analysis on each subset and then reviews the results from each to determine which estimates of the B and C constants most likely best represent the population values. Because of the tradeoffs mentioned, one analysis is likely to stand out as best. It is desirable to select that regression which has (1) a very high, if not the highest, F statistic associated with testing a null hypothesis that the estimated C constant is zero, (2) a large number of the original observations remaining in the data base subset, and (3) least important but reassuring an estimated C constant that is corroborated by regressions on higher $\delta P'$ data base subsets.

Where the results from all regressions provide none with a significant C coefficient F statistic, and the estimated value of C is near zero, it should be taken to be zero.

Table 5 presents the flow chart for application of the process methodology.

Expected Results. If a plot of C coefficient estimates versus the absolute value of the $\delta P'$ limit for each subset regression is constructed, what should be expected? If C is greater than zero, the estimate of C for the $\delta P'$ minimum

Downloaded 01 Jun 2010 to 171.66.16.71. Redistribution subject to ASME license or copyright; see http://www.asme.org/terms/Terms_Use.cfm

Table 7 Summary of regression data for 200 MW plant example

$\delta P'$ limits	No. of observations	Est. B constant, MBtu/MW^{2}h	Est. C constant, MBtu/MW^{2}h	Std. error of C, MBtu/MW^{2}h	C constant F statistic	R^2, percent	Durbin-Watson d statistic	Standard error of estimate
±2	685	7.261	0.007658	0.0016	22.8	3.2	1.83	3.126
±4	574	8.017	0.005693	0.0015	15.3	2.6	1.96	1.881
±6	506	8.779	0.001500	0.0015	4.7	0.9	1.97	1.513
±10*	374	7.371	0.007965	0.0014	31.6	7.8	1.95	1.016
±20	192	7.980	0.005756	0.0017	11.5	5.7	2.16	0.619
±30	111	8.231	0.004971	0.0023	4.5	4.0	2.09	0.484
±40	60	8.332	0.004503	0.0023	3.8	6.2	1.92	0.306

*Selected regression results

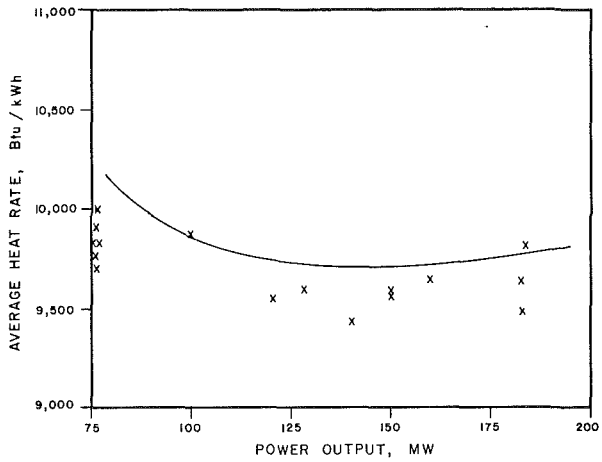


Fig. 10 Regression-derived average heat rate curve compared to steady-state heat rate tests for a 200 MW plant

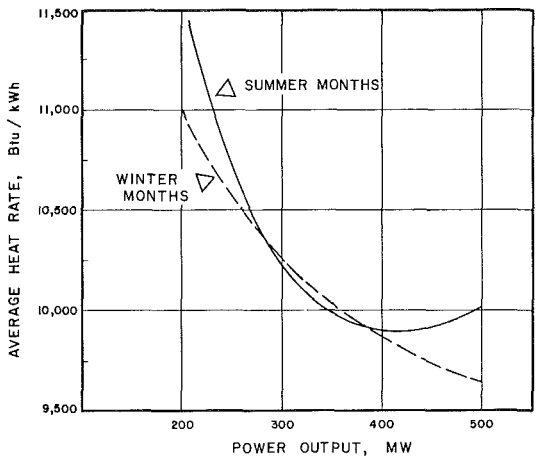


Fig. 11 Regression-derived average heat rate versus load for summer and winter periods for a 500 MW plant

limit of 2 MW may possibly be relatively high, perhaps near the final estimate of the true value of C, due to the presence of observations with large $\delta\text{LSRF}/\delta P'$ values. As the $\delta P'$ limits are increased, the estimated value of C may be expected to fall as high $\delta\text{LSRF}/\delta P'$ observations are removed and the total number of observations decreases. As $\delta P'$ limits are further increased, the estimated value of C will probably rise again to its best estimate of true C as the influence of the error term in equation (13) is greatly reduced. Finally, as the $\delta P'$ limit is increased further, the estimated value of C should remain at its peak or trend downward as the number of observations is greatly diminished.

Example Results

General. Figure 8 shows results of employing the process

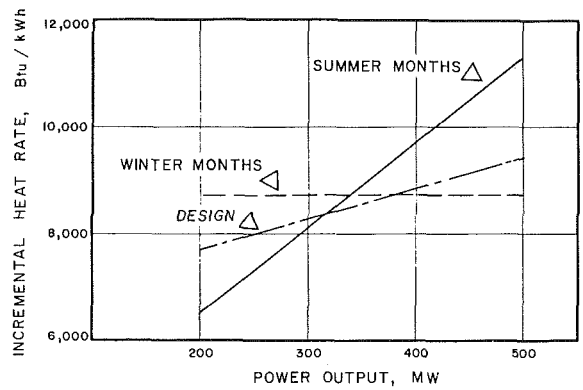


Fig. 12 Regression-derived incremental heat rate versus load for summer and winter periods compared to design for a 500 MW plant

of Tables 4 and 5 to 50, 200, and 500 MW coal-fired cyclically loaded power plants. It should be noted that, in the case of the 50 MW plant, because of its size, increasing the $\delta P'$ limit a small amount will reduce observations much more rapidly than with the larger plants.

Table 7 is a summary of regression data for each data base subset for the 200 MW plant example. Figure 9 shows the estimated incremental heat rate curve for the selected regression, $\delta P'$ limits of ±10, versus the original (pre-environmental equipment modification) design curve for this plant.

From Table 7 it can be seen that the standard error of the C constant is relatively small in spite of the low R^2 values. (The author has experienced regression results with R^2 values ranging from low values such as these to 60 percent for the 500 MW plant case.)

R^2 values of results from using the model are sometimes very low for two reasons. First, the impact of the true C term of equation (10) may be low in comparison to the effects on the dependent variable of some of the typical operating occurrences such as those listed in Table 2. Second, because variables are used in the model which represent changes in quantities from one period to the next, the effects of measurement errors will be exacerbated. However, small R^2 results, while indicating poor data fit, do not mean that the standard error of the regression coefficient C or the standard error of the regression constant B will be large. If the number of observations in the regression data base is sufficiently large, good estimates of the true values of the B and C constants will be obtained in spite of low R^2 values [2].

The effect of sample size n can be seen from the equation for the standard error of the C coefficient

$$\sigma_c = \sqrt{\frac{\sigma_{yx}^2}{\Sigma(x-\bar{x})^2}} \tag{19}$$

Figure 10 shows the resultant average heat rate curve, equation (3), with the estimated regression constants from Table 7, for the 200 MW plant example along with numerous

Downloaded 01 Jun 2010 to 171.66.16.71. Redistribution subject to ASME license or copyright; see http://www.asme.org/terms/Terms_Use.cfm

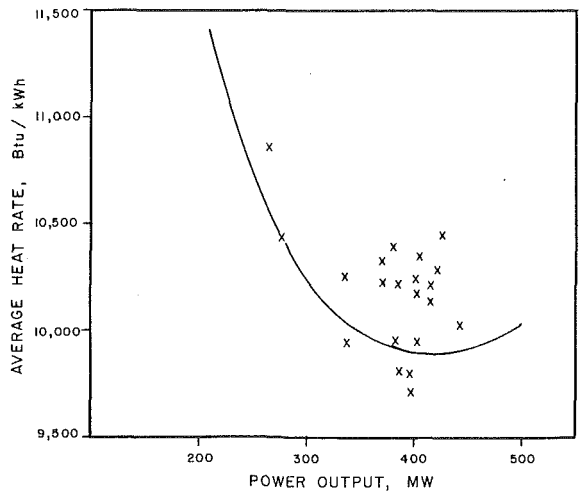


Fig. 13 Sample of daily heat rates for 500 MW plant plotted against average daily load and compared to regression-based function

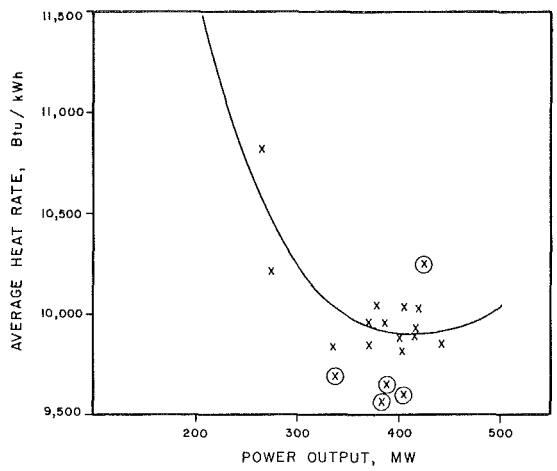


Fig. 14 Sample of daily heat rates for 500 MW plant adjusted for cyclic loading and compared to regression-based function (heat rates needing investigation are circled)

heat rate test points. In general, the heat rate test points fall below the curve, which represents typical operations at steady state, as would be expected. Also, while too scattered to be of use in regressing an estimate of the C constant, the test points tend to corroborate the shape of the regression model derived curve.

In the case of the 500 MW plant example, it was suspected that this plant, which is served by a cooling tower, might actually have quite different heat rate functions in the summer and in the winter because of climatological differences. Accordingly, the data base was divided between the two periods and the process described in Tables 4 and 5 applied to each. Figures 11 and 12 plot the model derived results.

Serial Correlation. As implied by the Durbin-Watson d statistic [5] presented in the example of Table 7, serial correlation has not been found in tests at the 2 percent level of significance (two-tail) in studies made thus far.

Homoscedasticity. Violation of an assumption of equal variance along the regression line will not bias estimates of the model's B and C constants [2, 6]. However, lack of homoscedasticity may affect confidence interval estimation around these constants. Although Figs. 5 and 6 would lead to a priori speculation that equal variance will not exist with the model, F tests of the null hypothesis of equal variance between data base groups formed by evenly dividing the regression data base according to values of the independent variable have usually shown the hypothesis to be accepted at the 2 percent level of significance (two-tail). Rejection cases were borderline at the 2 percent level.

In summary, lack of homoscedasticity was not found to pose a problem with C constant confidence interval estimates; however, the F test described is performed to ascertain whether the interval estimates should be considered rough estimates.

Use of Model Results for Performance Monitoring

Figure 13 shows the regression derived summer average heat rate curve for the 500 MW plant example. Plotted against this curve is a sample of actual daily heat rates for the plant. In each of these days, the unit was loaded according to economic dispatch principles. Some days it was cycled more and some less as required. The curve shown is plotted on the basis of steady-state conditions, i.e., LSRF = P^2, for reference purposes, and is not directly comparable to the plotted points. However, by adjusting each actual heat rate for the extent of cyclic loading according to equation (20), the daily heat rates can be made comparable as shown in Fig. 14.

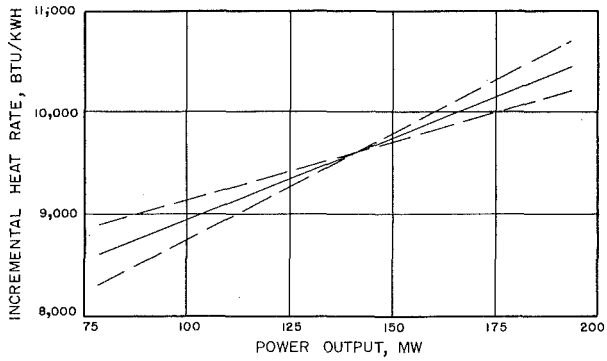


Fig. 15 Approximate boundaries of true incremental heat rate curve for 90 percent C coefficient confidence interval for 200 MW plant example

Adjusted average heat rate = unadjusted heat rate

$$-C*\left(\frac{\text{LSRF}}{P'}-P'\right) \tag{20}$$

At Gulf Power Company, the daily average heat rate of each operating plant is compared to the typical heat rate expected in this manner. When outlying points are detected (circled in Fig. 14), plant personnel report on the underlying cause. Where the underlying cause is not apparent, appropriate testing and calibration steps are undertaken by plant personnel and company engineers. Of the five points circled in Fig. 14, the four at the bottom are often indicative of fuel scale error.

The monitoring technique shown in Fig. 14 is not restricted to daily heat rates but is applicable to any length period. Monthly and annual heat rates are also used to check long term performance.

In addition to the above, before and after results from the regression model may also be used to evaluate performance effects of events such as boiler or turbine inspections.

Use of Model Results for Economic Dispatch

From Figs. 9 and 12, which compare model derived operating and vendor based original design incremental heat rate curves, it is apparent that operating incremental heat rates can also differ significantly from their design counterparts. From Fig. 10 it is apparent that operating incremental heat rates can also differ significantly from test based counterparts, if the latter functions can be estimated. For a large power plant, the extra fuel expense of loading the

Downloaded 01 Jun 2010 to 171.66.16.71. Redistribution subject to ASME license or copyright; see http://www.asme.org/terms/Terms_Use.cfm

wrong plant because of a nonrepresentative incremental heat rate function can easily be large, 4.5 million dollars per year and up. Similarly, not selling power to adjacent utilities because of nonrepresentative incremental heat rate functions can both be inefficient and have large lost opportunity costs, fuel clause adjustments notwithstanding. For many cyclically loaded coal-fired plants, derived incremental heat rate functions based on typical operating conditions can be determined with enough support that they should be used for economic dispatch. Such support can be achieved both by statistical evaluation of results for the current period as well as by emotional confidence builders such as consistently finding similar results for previous periods.

Figure 15 is a plot of the model derived best estimate of the incremental heat rate function for the 200 MW plant example. Also shown are dashed incremental curves representing the approximate boundaries expected to contain the true incremental heat rate function (based on a C constant 90 percent confidence interval). The author recommends that such limits be evaluated when considering what minimum price differential is appropriate for a "split the savings" type interchange between utilities. Not recommended, however, is the use of confidence interval estimates of individual incremental heat rates instead of conditional mean values, since the resultant energy price would be so high in order to ensure the generating party covered its costs that in nearly all cases interchange would be precluded.

It should be noted that the incremental functions presented in the figures are based on gross electrical output, and that these functions in actual dispatch use should be based on net electrical output. Since the relationship between plant station service and net MW output is very nearly linear and easily measured, it is a simple task to convert all regression model results from a gross to a net MW basis.

Conclusion

Estimates of normal operating heat rate functions from actual plant data are needed for both proper economic dispatch and performance monitoring purposes. Although the model and methodology presented are not without fault, reliable estimates can often be achieved with it for cyclically loaded coal-fired plants in spite of poor field data.

With sufficient data and slight modification to the regression model for additional independent variables, heat rate functions for more than one power plant which all use a single fuel measuring source are estimable.

Combined analysis using operating results from the methodology presented along with cycle computer design codes may be able to provide valuable diagnostic information. Also, such codes may be useful for adjusting regression derived operating heat rate functions in order to best estimate what they will be after some forthcoming alteration. Investigations in these areas are encouraged.

References

1 Sullivan, R. L., "Generation System Cost Analysis," *Power System Planning*, McGraw-Hill, 1977, pp. 110–111.

2 Yamane, T., *Statistics: An Introductory Analysis*, Harper & Row, 1973, pp. 428–430, 800, 905, 969, 982, 999, 1009–1014.

3 Hamburg, M., *Statistical Analysis for Decision Making*, Harcourt, Brace & World, 1970, p. 332.

3 Holman, J. P., *Experimental Methods for Engineers*, McGraw-Hill, 1966, pp. 37–40, 53–55.

4 Durbin, J. S., and Watson, G. S., "Testing for Serial Correlation in Least Squares Regression (II)," *Biometrika*, Vol. 38, 1951, pp. 159–178.

5 Braverman, J. D., and Stewart, W. C., *Statistics for Business and Economics*, Ronald Press Co., 1973, pp. 240–242.

APPENDIX

Listing of Conversion Factors for Units Appearing in Text

	Quantity	Value in SI units
Energy	1 MBtu	1055.056 MJ
Power	1 MBtu/h	293.071 kJ/s
Heat rates	1 MBtu/MWh	0.293 kJ/kWs
	1 MBtu/kWh	293.071 kJ/kWs
Mass	1 Lbm	0.454 kg
Heating value	1 Btu/Lbm	2.326 kJ/kg

Downloaded 01 Jun 2010 to 171.66.16.71. Redistribution subject to ASME license or copyright; see http://www.asme.org/terms/Terms_Use.cfm

A Theoretical Approach to the Combustion of Fuel-Alcohol Blends

G. Cau

M. P. Pelagagge
Research Engineers,
Department of Energetics,
University of L'Aquila, Italy

This paper is concerned with the results of a theoretical investigation on combustion of traditional fuel and alcohol blends. An analytical procedure has been developed which examines three different hypotheses for introducing the alcohol: constant mass of primary fuel, constant total energy of fuel, and constant total mass of fuel. The procedure has been applied to combustion at constant volume varying over a wide range of air-fuel ratios, percentage of alcohol, and combustion temperature. The results obtained, of particular interest for reciprocating internal combustion engines, indicate that as far as energy and emissions are concerned, the effects of alcohol on combustion depend strongly on the hypothesis adopted for fueling the alcohol.

Introduction

The production of fuel from agricultural and biological waste using proved techniques has made available alternative energy sources, in some aspects renewable, of growing interest in a variety of fields. In particular biogas and alcohols (methanol, ethanol, etc.) are effective alternatives for producing thermal and mechanical energy [1-3] especially for local requirements in areas of prevalently agricultural economy.

In this regard, particular attention is nowadays focused on the use of alcohols – alone or in blends with traditional fuels – in reciprocating internal combustion engines since this practice can also improve performance. In fact, it is well known, for instance, that appropriate fueling (dual fueling with alternative fuels premixed with air, mixed fuel injection, dual fueling with two injectors, etc.) leads to a marked smoke reduction in compression ignition engines and sometimes enhanced thermal efficiency and a reduction in nitrogen oxide and carbon monoxide emissions [4-6].

Technical data published in recent years [7-15] are not always easy to interpret above all because of the complex phenomena underlying the combustion process, and also due to the fact that experimental investigations are conducted with a variety of apparatus, and operating conditions are not always comparable. So, to facilitate the interpretation of the experimental results the combustion model should not take into account the construction and operating characteristics of the engine.

With a view to contributing to the scarce and fragmentary theoretical data currently available, an analytical procedure has been developed for assessing the effect of alcohol on combustion suitable, at least from a qualitative point of view, for comparisons with the experimental results.

In order to account for the different methods of alcohol fueling in actual configurations, for a number of primary fuel-alcohol blends, and for a given mass of air, three possible hypotheses have been adopted:

(*a*) constant mass of primary fuel
(*b* constant total energy of fuel (primary fuel + alcohol)
(*c*) constant total mass of fuel

The analytical model is remarkably flexible since it can be applied over a wide range of combustion temperatures and air-fuel ratios with any percentage and type of alcohol (fueled in the liquid or vapor phase) and/or primary fuel, also taking into account the nitrogen oxide formation kinetics.

In this paper, after a brief description of the model, the results obtained in the simulation of a variety of conditions are illustrated.

Formulation of the Analytical Model

The model assumes that combustion takes place in an isolated system, giving rise to a homogeneous mixture in thermodynamic equilibrium, except for the nitrogen oxide. The composition of the products and their volume, referred to 1 kg of fuel, are determined for predesignated values of the equivalence ratio, combustion temperature, and pressure, in the absence of alcohol. Regardless of the method adopted for fueling, volume and initial air mass are then kept constant, varying the addition of alcohol in the liquid or vapor phase.

As mentioned, three different hypotheses are adopted for the simulation of a wide variety of alcohol fueling methods, i.e., constant mass of primary fuel, constant total energy of fuel, and constant total mass of fuel. The first and third can obviously be considered as borderline cases.

The fuel mass – however intended – in excess of 1 kg can be written

$$\gamma = W_{pf}(1+\delta) - 1 \qquad (1)$$

where δ is the percentage of alcohol referred to 1 kg of primary fuel. Hence

Contributed by the Fuels Division for publication in the JOURNAL OF ENGINEERING FOR GAS TURBINES AND POWER. Manuscript received by the Fuels Division March 1985.

Copyright © 1985 by ASME
Downloaded 01 Jun 2010 to 171.66.16.71. Redistribution subject to ASME license or copyright; see http://www.asme.org/terms/Terms_Use.cfm

$$W_{pf} = \frac{1+\gamma}{1+\delta} \tag{2}$$

Equations (1) and (2) hold in the general case: For the case where primary fuel mass is constant $\gamma = \delta$, hence $W_{pf} = 1$, whereas with constant total fuel mass $\gamma = 0$ and as a result $W_{pf} = 1/(1+\delta)$. It should be noted moreover that with regards to the constant total energy hypothesis (2) can also be written

$$W_{pf} = \frac{1}{1+\delta \bullet \epsilon} \tag{3}$$

where ϵ is the ratio between the lower heating value of the alcohol and the primary fuel. This case is also characterized by constant total mass of fuel if $\epsilon = 1$ and by constant mass of primary fuel if $\epsilon = 0$[1].

Under the previous assumptions the air–fuel ratio is defined by

$$\alpha_{alc} = \frac{\alpha}{1+\gamma} \tag{4}$$

Combustion conditions in the presence of alcohol (in particular pressure, temperature and composition) are determined – from those calculated in the absence of alcohol – by means of the total internal energy balance. In fact, for 1 kg of primary fuel one has

$$\frac{E_{pf}}{M_{pf}} + \sum_{i=1}^{s} n_i^r \left[E_i + \int_{T_0}^{T_r} (Cp_i - R)dT \right]$$

$$= \sum_{i=1}^{s} n_i^p \left[E_i + \int_{T_0}^{T_p} (Cp_i - R)dT \right] \tag{5}$$

where E_{pf} and M_{pf} are the internal formation energy and molecular mass of the primary fuel, s the maximum number of chemical components in the comburent (reagents) and the burnt gases (products), n_i^r and n_i^p the number of kmoles of the reagents and products per 1 kg of primary fuel; E_i and Cp_i internal molar formation energy and heat at constant pressure of the ith species; R the universal gas constant, and finally T_r, T_p, and T_0 temperature of the reagents, of the products, and the reference temperature for sensible internal energy respectively.

Introducing the heating value H_{pf} at the reference temperature T_0, equation (5) gives

$$\sum_{i=1}^{s} n_i^r \int_{T_0}^{T_r} (Cp_i - R)dT + \sum_{i=1}^{s} (n_i^r - n_{0i}^r)E_i$$

$$= \sum_{i=1}^{s} n_i^p \int_{T_0}^{T_p} (Cp_i - R)dT + \sum_{i=1}^{s} (n_i^p - n_{0i}^p)E_i - H_{pf} \tag{6}$$

where n_{0i}^r and n_{0i}^p, analogously to n^r and n^p, are the kmoles of chemical reagents and products at temperature T_0.

The left-hand side of equation (6), relative to the comburent alone and hence to conditions prior to combustion, is first determined for a given combustion temperature T_p in the absence of alcohol. Then this value is kept constant, for each equivalence ratio ϕ, varying the alcohol addition.

Substituting H_{pf} with

$$H_{tot} = (1 + \delta \bullet \epsilon) W_{pf} H_{pf} \tag{7}$$

which, regardless of the fueling hypothesis adopted, represents the energy of total fuel added [2], actual combustion conditions can be determined by means of equation (6).

The composition at combustion equilibrium with or without alcohol addition is determined by the method of equilibrium constants using the calculation procedure described in [17], whereby the mixture of burnt gases is assumed to contain 14 chemical components, namely, CO, CO_2, H_2O, H_2, OH, O_2, O, H, N_2, NO, N, N_2O, NO_2, Ar. Moreover, with this procedure any type of comburent, provided it has at the most these 14 components, and any type of fuel, with composition defined by the atomic species C, H, O, N, can be used.

As already mentioned, the effect of the presence of alcohol in the fuel on the NO formation kinetics has also been evaluated. For the mechanism underlying NO formation, the classic extended Zeldovich formulation

$$\begin{aligned} N_2 + O &\rightleftharpoons NO + N \\ N + O_2 &\rightleftharpoons NO + O \\ N + OH &\rightleftharpoons NO + H \end{aligned} \tag{8}$$

is assumed, where only the NO concentration is considered variable with time. In fact, as already pointed out in [16], this scheme can be considered the most valid of those commonly found in the literature.

Discussion of Results

The three different alcohol fueling hypotheses were investigated using a primary fuel with C/H ratio of 6.35 and $H_{pf} = 43.06$ MJ/kg (commercially known as "Diesel 1") and as additional fuel liquid methyl alcohol ($H_{alc} = 21.13$ MJ/kg).

[1] In the simulation of fuel addition with zero heating value, this condition allows to assess the effects of inert substances such as water, for instance, [16].

[2] Obviously, for the constant total energy model $H_{tot} = H_{pf}$ by virtue of equation (3).

Nomenclature

e = sensible internal energy
n = number of kmoles
s = maximum number of chemical components in the comburent and in the burned gas mixture
C_p = molar heat capacity at constant pressure
H_{pf}, H_{alc} = heating value of primary fuel and alcohol
E = formation internal energy
M_{pf} = molecular mass of primary fuel
R = universal gas constant
T = absolute temperature
W_{pf} = actual mass of primary fuel
X_{NO}, X_{CO} = mole fraction of NO and CO
α = air–fuel mass ratio
γ = actual fuel excess with respect to 1 kg
δ = mass of alcohol per kg of primary fuel
ϵ = primary fuel-to-alcohol heating value ratio
ϕ = equivalence ratio (α_{stoich}/α)
τ = time

Subscripts

alc = denotes conditions in presence of alcohol
e = thermodynamical equilibrium
i = ith component
pf = primary fuel
stoich = stoichiometric conditions

Superscripts

p = products
r = reagents

Downloaded 01 Jun 2010 to 171.66.16.71. Redistribution subject to ASME license or copyright; see http://www.asme.org/terms/Terms_Use.cfm

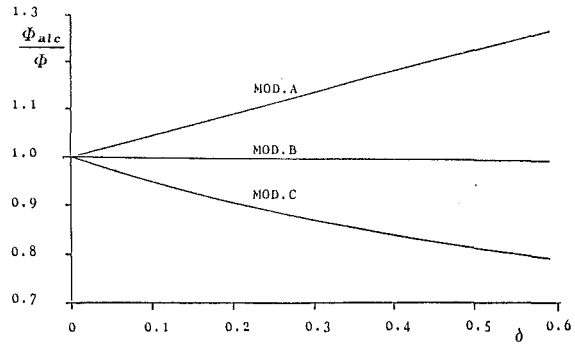


Fig. 1

The analysis was carried out for a combustion pressure (in the reference case in absence of alcohol) of 5 MPa, at three different temperatures (again in absence of alcohol) 2000, 2500 and 3000 K, varying the alcohol additions from 0 to 60 percent[3] and the equivalence ratio (in absence of alcohol) from 0.4 to 1.4.

In the formulation of equations (5) and (6) the thermodynamic data reported in [18] were used assuming the products mixture as an ideal gas.

In the following sections the most salient aspects of the results of the analysis are discussed.

Effect of Alcohol on Equivalence Ratio. The actual equivalence ratio (in presence of alcohol) can easily be correlated to the reference ratio (in absence of alcohol) using equation (4). That is

$$\phi_{alc} = (1+\gamma)\frac{\alpha_{alc,stoich}}{\alpha_{stoich}} \cdot \phi \tag{9}$$

Neither $(1+\gamma)$ nor $(\alpha_{alc,stoich})$ depends on ϕ. Moreover, the latter is not affected by the method of alcohol fueling adopted but only by the percentage of alcohol over primary fuel. Hence, for a given value of δ, ϕ_{alc} is proportional to ϕ. In Fig. 1 the variation of the ϕ_{alc}/ϕ ratio versus δ is plotted for the three hypotheses examined. The different behavior is easily justified insofar as $(1+\gamma)$ is always greater than or equal to 1 while $(\alpha_{alc,stoich}/\alpha_{stoich})$ is always less than 1[4]. Thus, as regards the model with constant mass of primary fuel (Model A), alcohol addition results in an increase in ϕ_{alc} compared to ϕ. Conversely, with constant total mass of fuel (Model C) ϕ_{alc} can only diminish with respect to ϕ as $\gamma=0$. Finally for the constant total energy of fuel model (Model B), it is interesting to note that the two terms compensate each other and consequently the variations in ϕ are of little bearing.

Effects on Temperature and Pressure. Figures 2(*a,b,c*) show for alcohol addition of 40 percent, the variations in combustion temperature at the three reference temperatures examined, versus equivalence ratio. It is clear that the three fueling hypotheses investigated exhibit extremely different characteristics.

With reference to the two borderline cases identified by Model A (constant mass of primary fuel) and Model C (constant total mass of fuel), it can be observed that for lean mixtures, i.e., $\phi<0.8$–0.9, in the former case there is an increase in temperature due to the larger amount of energy introduced, whereas in the latter the reverse occurs due to the smaller amount of energy introduced. These effects however become negligible at higher temperatures (Fig. 2*c*). As was to

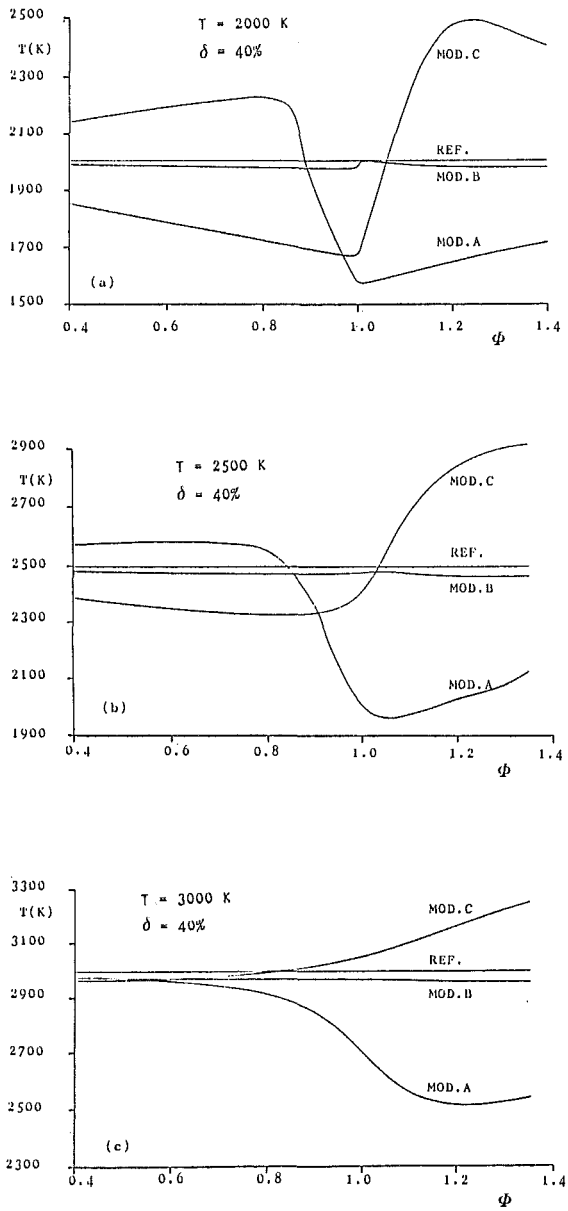


Fig. 2

be expected, in both models the temperature exhibits asymptotic behavior toward the reference temperature (in the absence of alcohol), owing to the increasingly smaller percentage of fuel added, compared to the comburent. By contrast, for stoichiometric and rich blends, Model A leads to a drop in temperature due to the joint effect of the reduction in the amount of air available with respect to total fuel (as already shown in Fig. 1) and the addition of alcohol having a lower heating value than the primary fuel.

Conversely, under the same conditions Model C leads to a rise in temperature brought about by the change in fuel composition. In fact the increased availability of oxygen produced indirectly by the alcohol through the -OH group in conjunction with a reduction in the C/H ratio causes a shift in the thermodynamic equilibria toward higher reaction heats, despite the lower heating value of the total fuel compared to the primary fuel.

Finally, as far as hypothesis B is concerned, a slight drop in temperature can be observed compared to the case where alcohol is absent. This phenomenon can be ascribed exclusively to the different combustion composition, even though the effective air/fuel ratio α_{alc}, derived from equation

[3] It should be recalled that the percentage of alcohol is intended as relating not to the total fuel but to the primary fuel alone.

[4] In fact, although mixing of alcohol with primary fuel entails a reduction in the C/H ratio of the total fuel, the oxygen present in the -OH group of the alcohol brings about a reduction in the stoichiometric air-fuel mass ratio compared to the reference condition.

Downloaded 01 Jun 2010 to 171.66.16.71. Redistribution subject to ASME license or copyright; see http://www.asme.org/terms/Terms_Use.cfm

(4) decreases with alcohol addition. Moreover, the abovementioned drop in temperature is less marked near stoichiometric conditions, especially at lower combustion temperatures.

Figure 3 shows the behavior of combustion pressure versus ϕ at the reference temperature 2500 K and for 40 percent alcohol addition. The pressure variations compared to the reference value exhibit the same trends as those observed in the temperature. However, they are more pronounced percentagewise for Models A and B, owing to the larger number of product moles as compared to combustion in the absence of alcohol.

Effects on Emissions. With a view to assessing the effect of alcohol on the production of pollutants such as nitrogen oxide and carbon monoxide, a detailed analysis was performed over a wide range of temperature, equivalence ratio, and alcohol percentages, for the three fueling hypotheses investigated. The results obtained indicate that in general increased alcohol percentages lead to a reduction in NO, often consistent with lean mixtures. For rich blends, while a marked increase in NO is observed for Model C, only slight variations are encountered for Models A and B. However, this is of a certain significance since the greater quantities of NO are obtained from burning in excess of air.

As far as CO is concerned, alcohol addition brings about an increase in concentration with Model A, while the reverse happens with Models B and C. Such variations are particularly noticeable in combustion in default of air where considerable amounts of unburnts are present.

Figures 4(a,b,c) and 5(a,b,c) show the results obtained for three models A, B, and C at the reference temperature $T = 2500$ K.

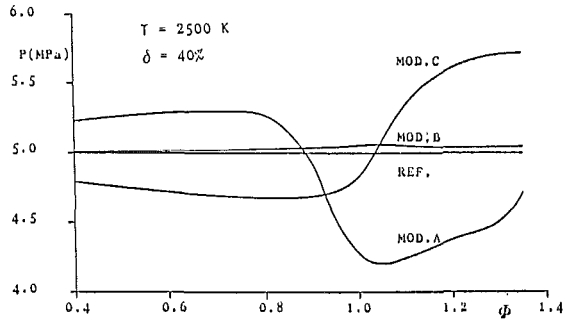


Fig. 3

Effects on NO Formation Kinetics. A detailed analysis was conducted by examining a variety of conditions, for the purpose of evaluating the effects of alcohol addition on NO formation kinetics. The results obtained indicate, as was to be expected, that the effects of alcohol on temperature directly influence the rates of chemical reaction governing NO formation. This is of particular importance, especially for Models A and C where, as already mentioned, conspicuous drops in temperature are observed with rich and lean blends respectively.

In Figs. 6(a,b,c) as an example, the ratio K between the actual NO concentration and equilibrium concentration after 5 ms reaction is plotted.

Effects on Sensible Internal Energy. Alcohol addition can also have a significant effect on the work potentially producible by the system and this was assessed by determining the variation in sensible internal energy with respect to the reference conditions, using the expression

$$\Delta e\% = \left[\frac{\sum_{i=1}^{14} n_{\text{alc}_i}^{p} \int_{T_0}^{T_{\text{alc}}^{p}} (Cp_i - R)dT}{\sum_{i=1}^{14} n_i^{p} \int_{T_0}^{T_p} (Cp_i - R)dT} - 1 \right] \cdot 100 \qquad (10)$$

The results obtained, plotted in Figs. 7(a,b,c), show that in general the introduction of alcohol can bring about an increase or reduction – often not negligible – in sensible internal energy of the system, which did not emerge immediately from the analysis of the previous results. For example, in some certain instances the variations in energy exhibit the opposite trend to temperature variations. This obviously depends not only on the different composition of the products but also – as in the case of Models A and B – on the greater mass of the system.

Effects on Different Kinds of Alcohol. Finally the investigation was extended to other types of alcohol such as ethyl, propyl, and butyl. In qualitative terms, the considerations concerning the effects of methyl alcohol also hold for these substances.

As an example, in Fig. 8(a,b,c), analogously to Fig. 2(a), the effect of the type of alcohol on combustion temperature is shown.

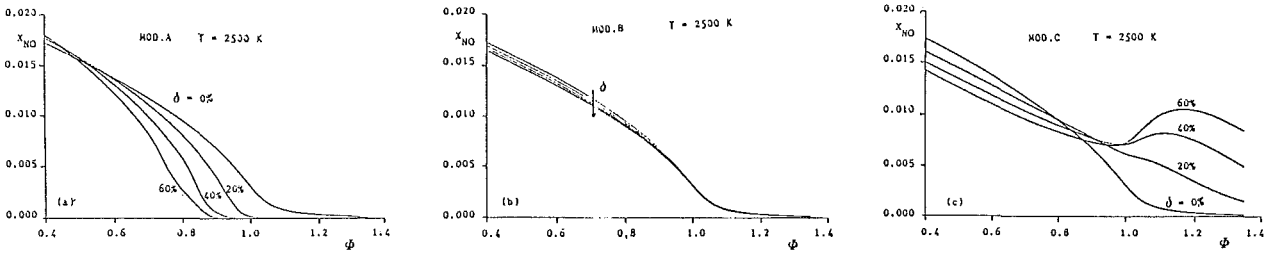


Fig. 4

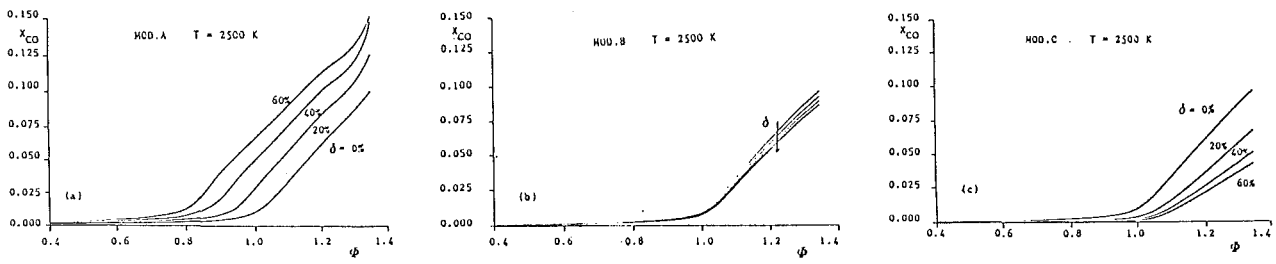
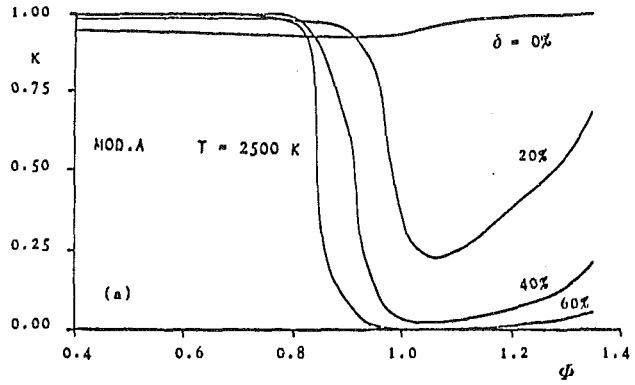
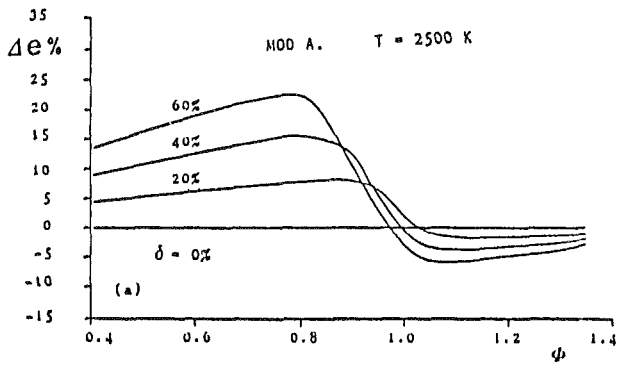
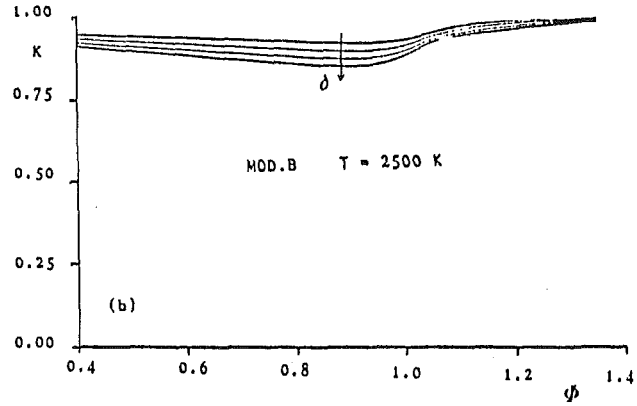


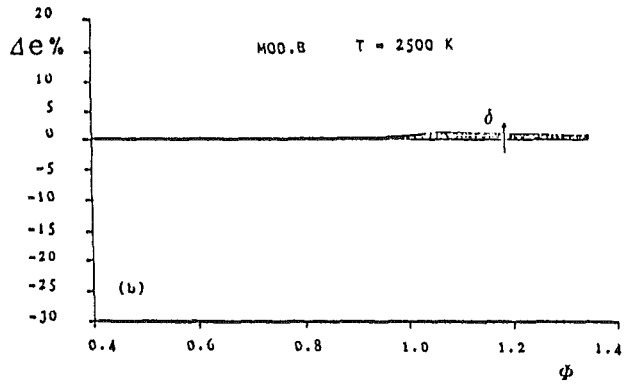
Fig. 5

Downloaded 01 Jun 2010 to 171.66.16.71. Redistribution subject to ASME license or copyright; see http://www.asme.org/terms/Terms_Use.cfm









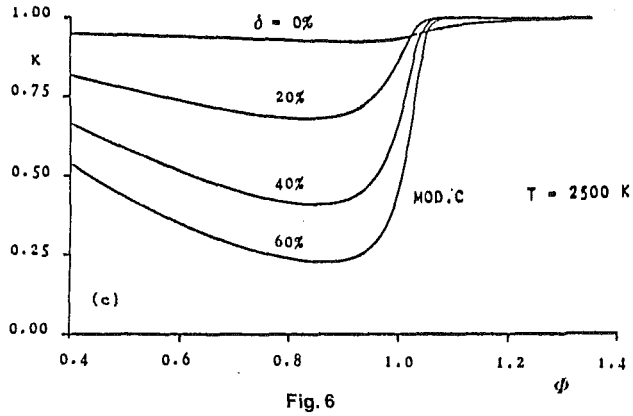


Fig. 6

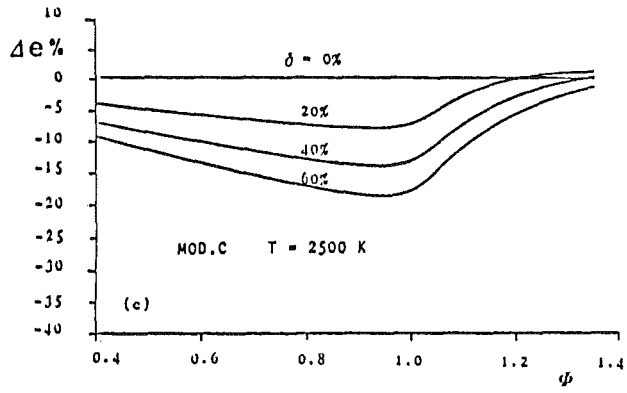


Fig. 7

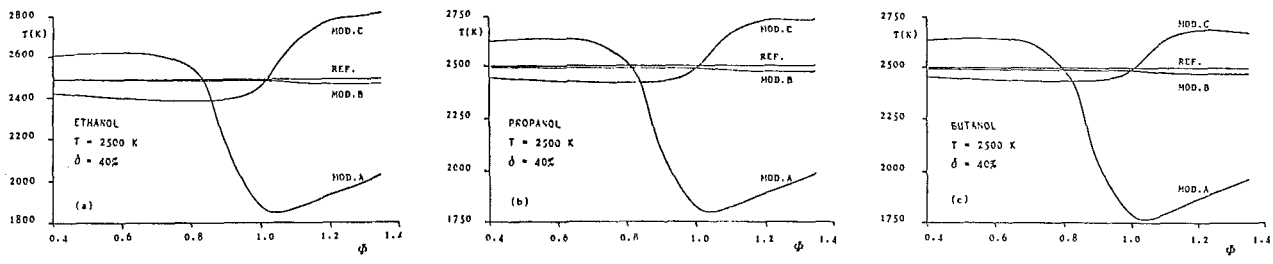


Fig. 8

Conclusions

The findings of a theoretical investigation on the combustion of traditional fuel/alcohol blends point to the importance, often not sufficiently stressed in the literature, of the different fueling methods commonly employed in practical applications.

With particular reference to combustion at constant volume, typical of reciprocating internal combustion engines, three different alcohol fueling hypotheses have been examined, namely: constant mass of primary fuel, constant total energy of fuel, and constant total mass of fuel.

The main operating parameters (combustion temperature,

Downloaded 01 Jun 2010 to 171.66.16.71. Redistribution subject to ASME license or copyright; see http://www.asme.org/terms/Terms_Use.cfm

internal sensible energy, nitrogen oxide and carbon monoxide concentrations) were found to differ substantially with varying equivalence ratio and alcohol percentage with respect to the primary fuel.

Consequently, trends have emerged which were not immediately predictable but which are in any case of considerable interest in the setting up of experimental studies and in the interpretation of the results.

Acknowledgments

This work was carried out in the framework of a theoretical-experimental research program on the use of alcohols in internal combustion engines, with the financial support of the "Provincia di L'Aquila."

References

1 Bardon, M. F., "Modified Brayton Cycles Utilizing Alcohol Fuels," *Eng. Pow.*, Vol. 104, 1982, pp. 341-348.

2 Pullman, J. B., "Methanol, Ethanol and Jet Fuel Emissions Comparison From a Small Gas Turbine," SAE Paper No. 781013, Nov. 1978.

3 Klapaich, R. D., "Gas Turbine Emissions and Performance on Methanol Fuel," ASME-IEE Joint Power Generation Conference, Portland, Sept. 28-Oct. 1, 1975.

4 Adelman, H. G., "Alcohols in Diesel Engines. A Review," SAE Paper No. 790956, 1979.

5 Chen, J., et al., "Ethanol Fumigation of a Turbocharged Diesel Engine," SAE Paper No. 810680, 1981.

6 Lawson, A., et al., "Heavy-Duty Truck Diesel Engine Operation on Unstabilized Methanol/Diesel Fuel Emulsions," SAE Paper No. 810346, 1981.

7 Brinkman, N. D., "Ethanol Fuel—A Single-Cylinder Engine Study of Efficiency and Exhaust Emissions," SAE Paper No. 810345, 1981.

8 Hashimoto, I., et al., "Diesel-Ethanol Fuel Blends for Heavy Duty Diesel Engines. A Study of Performance and Durability," SAE Paper No. 820497, 1982.

9 Hadenberg, H. O., and Schaefer, A. J., "The Use of Ethanol as a Fuel for Compression Ignition Engines," SAE Paper No. 811211, 1981.

10 Heisey, J. B., and Lestz, S. S., "Aqueous Alcohol Fumigation of a Single-Cylinder DI Diesel Engine," SAE Paper No. 811208, 1981.

11 Houser, K. R., Lestz, S. S., Dunovich, M., and Yasbin, R. E., "Methanol Fumigation of a Light Duty Automotive Diesel Engine," SAE Paper No. 801379, 1980.

12 Broukhiyan, E. M. H., and Lestz, S. S., "Ethanol Fumigation of a Light Duty Automotive Diesel Engine," SAE Paper No. 811209, 1981.

13 Khan, N., and Gollahalli, S. R., "Performance and Emission Characteristics of a Diesel Engine Burning Unstabilized Emulsions of Diesel Fuel with Water, Methanol and Ethanol," SAE Paper No. 811210, 1981.

14 "A Technical Assessment of Alcohol Fuels," SAE Paper No. 820261, 1982.

15 Chiv, C. P., and Hong, L. H., "The Effects of Methanol Injection on Emission and Performance in a Carburated SI Engine," SAE Paper No. 700054, 1979.

16 Bignardi, L., Cau, G., and Pelagagge, P. M., "Products of Combustion of Water-in-Fuel Emulsions," 14th International Congress on Combustion Engines (CIMAC), Helsinki, June 7-15, 1981.

17 Cau, G., "Equilibrio di gas di combustione: un procedimento di calcolo," Istituto di Meccanica e Macchine, Università di L'Aquila, Int. Pub. No. 58, May 1982.

18 Stull, D. R., and Prophet, M., *JANAF Thermochemical Tables*, 2nd ed., HSRDS-NBS, 37, Washington DC 20234, 1971.

Downloaded 01 Jun 2010 to 171.66.16.71. Redistribution subject to ASME license or copyright; see http://www.asme.org/terms/Terms_Use.cfm

Comparison of Burning Rates in a Natural-Gas-Fueled Spark Ignition Engine

A. L. Jones
Research Engineer.

R. L. Evans
Associate Professor.

Department of Mechanical Engineering,
University of British Columbia,
Vancouver, B.C., Canada V6T 1W5

A series of tests was conducted on a Toyota, four-cylinder, spark ignition engine which was modified to run on either gasoline or natural gas. The aim of the experiment was to investigate the performance and combustion behavior of natural gas, with particular emphasis on its low burning velocity. A pressure transducer installed in the cylinder head was used to obtain pressure versus crank angle curves from which mass burn rates and burning velocities were calculated, using a heat release analysis program. Results indicate that the low laminar burning velocity of natural gas extends its ignition delay period (time to 1 percent burned) by up to 100 percent compared with gasoline. This contrasts with the remainder of the combustion period which is dominated by turbulence effects that produce very similar burning velocities for the two fuels.

Introduction

A number of comparative studies have been made of the performance of spark ignition engines operating on gasoline and natural gas [1–5]. These studies have provided considerable information concerning the relative power levels, efficiencies, and exhaust emissions of the two fuels. However none of them have included measurements of engine cylinder pressure records for burning rate analysis.

The objective of this study was, therefore, to investigate the combustion behavior of natural gas compared with gasoline in a modern spark ignition engine by the analysis of cylinder pressure records.

The recent paper by Evans et al. [5] confirmed the earlier studies [1–4] by measuring a power loss of approximately 15 percent, and an efficiency loss of up to 5 percent when changing from gasoline to natural gas fuel. These results were obtained on the same four-cylinder Toyota engine that was used in this study. Most of the power loss (10 of the 15 percentage points) occurs as a result of the gaseous fuel occupying nearly 10 percent of the intake charge volume. The remaining 5 percentage points of the power loss, and most of the efficiency loss, result from the low burning velocity of natural gas compared with gasoline. The low burning velocity increases the combustion duration (resulting in the need for greater spark advance) which increases the timing loss and hence reduces power and efficiency by equal amounts as shown by Taylor [6].

The laminar burning velocities of natural gas and methane (the natural gas used in this study consists of 94 percent methane) have been measured by a number of investigators, three of whom have derived empirical formulae for the variation of laminar burning velocity as a function of unburned gas pressure and temperature.

Contributed by the Diesel and Gas Engine Power Division and presented at the Energy-Sources and Technology Conference and Exhibition, Dallas, Texas, February 17–21, 1985. Manuscript received at ASME Headquarters November 1, 1984. Paper No. 85-DGP-2.

The most quoted work is that of Andrews and Bradley [7] who proposed separate formulae for the dependence of methane laminar burning velocity on unburned gas pressure P_u and temperature T_u

$$S_l = 43\ P_u^{-0.5} \quad \text{(at constant } T_u\text{)} \quad (1)$$

$$S_l = (10 + 0.000371\ T_u^2) \quad \text{(at constant } P_u\text{)} \quad (2)$$

where S_l is in cm/s and P_u is in bar.

In order to apply these formulae to enginelike conditions where both the pressure and the temperature are varying simultaneously, they have been combined to obtain

$$S_l = (10 + 0.000371\ T_u^2)\ P_u^{-0.5} \quad (3)$$

Combining the equations in this way is justified by Sharma et al. [8] who show that the rate of increase of burning velocity with temperature does not vary with increasing pressure.

Ryan and Lestz [9] also obtained a formula for the variation of methane laminar burning velocity with pressure and temperature using the constant-volume-bomb method to obtain

$$S_l = 9656\ P_u^{-0.623} \exp(-2145/T_u) \quad (4)$$

over the range T_u = 450-600 K, P_u = 4-18 bar.

The only paper found which deals with the laminar burning velocity of natural gas was that of Sharma et al. [8] who obtained the following formulae

$$S_l = C_4 (T_u/300)^{1.68}/\sqrt{\phi} \text{ for } \phi < 1.0 \quad (5a)$$

and

$$S_l = C_4 (T_u/300)^{1.68}\ \sqrt{\phi} \text{ for } \phi > 1.0 \quad (5b)$$

where

$$C_4 = -418 + 1287/\phi - 1196/\phi^2 + 360/\phi^3 - 15\phi\ (\log P_u)$$

Values of laminar burning velocity obtained from equations (3), (4), and (5) are plotted in Fig. 1 versus un-

Copyright © 1985 by ASME
Downloaded 01 Jun 2010 to 171.66.16.71. Redistribution subject to ASME license or copyright; see http://www.asme.org/terms/Terms_Use.cfm

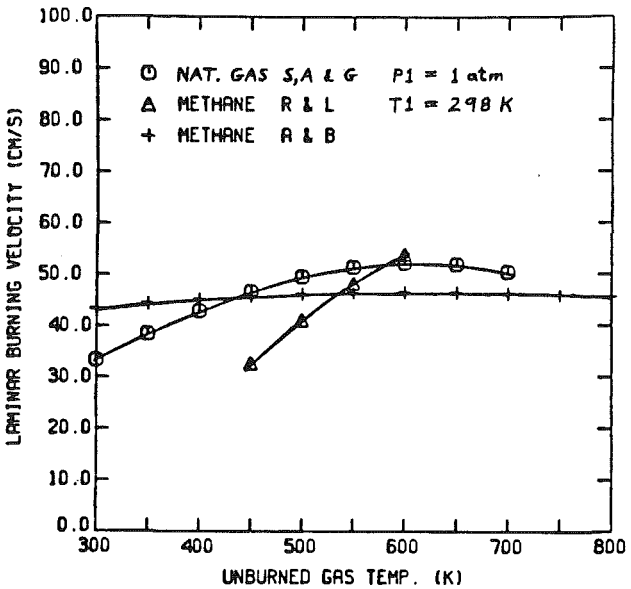


Fig. 1 Comparison of published equations for laminar burning velocities of natural gas and methane, calculated along an unburned gas isentrope (S, A & G = Sharma, Agrawal, and Gupta, R & L = Ryan and Lestz, A & B = Andrew and Bradley)

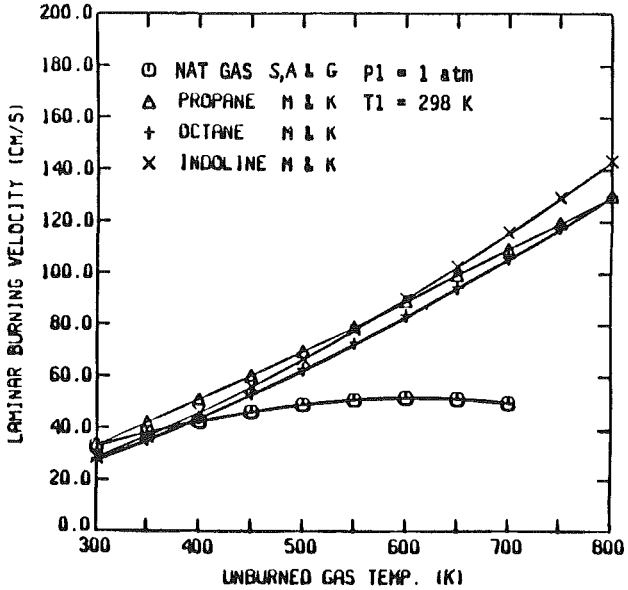


Fig. 2 Comparison of published equations for laminar burning velocities of natural gas, propane, octane, and indoline, calculated along an unburned gas isentrope (S, A & G = Sharma, Agrawal, and Gupta, M & K = Metghalchi and Keck)

burned gas temperature. The pressure at each temperature was calculated by assuming isentropic compression from the initial conditions of 1 atmosphere and 298 K.

It can be seen that the curve obtained using Ryan and Lestz's equation is much steeper than the other two and similar curves drawn from Ryan and Lestz's results for other fuels also show this steep rise from a low initial value, varying considerably from the velocities published by other authors.

The curve obtained from the results of Andrews and Bradley indicates that the increase in laminar burning velocity with temperature is strongly offset by the large negative pressure coefficient, resulting in an almost constant laminar burning velocity under enginelike conditions of isentropic compression.

The curve drawn from the Sharma et al. equations (5*a*) and (5*b*) for natural gas also shows an almost constant laminar burning velocity when temperature and pressure are increased according to isentropic compression. Beyond 450 K (approximately 5 bar) the velocity of natural gas is indicated to be greater than methane which could be a result of the additional components of the natural gas mixture causing a faster reaction rate. The divergence of the two curves below 450 K or 5 bar pressure is to be expected from the large spread of results in this region obtained from various authors and plotted in the paper of Andrews and Bradley.

As a result of the general agreement between equations (3) and (5), and the fact that equation (5) represents natural gas rather than methane, it was decided to use these equations of Sharma et al. in this study.

Figure 2 shows a comparison of the laminar burning velocities of propane, octane, and indoline with natural gas, again plotted along isentropes of unburned gas temperatures and pressures. The values for propane, octane and indoline were obtained using Metghalchi and Keck's [10] equations of the form

$$S_l = S_{l_0} (T_u/T_0)^{\alpha} (P_u/P_0)^{\beta} \tag{6}$$

where P_0, T_0, and S_{l_0} represent values at 298 K and 1 atm, and α and β are constants determined for each fuel.

Figure 2 clearly shows that propane, octane, and indoline have very similar values of laminar burning velocity under enginelike conditions and that all three rise to much higher values than natural gas with increasing temperature and pressure. For this work it was assumed that the equation for indoline provides the closest approximation to the laminar burning velocity of the gasoline used in the engine experiments. For indoline S_{l_0} = 25.2 cm/s, α = 2.19, and β = −0.13 in equation (6). It can be seen that the temperature exponent is greater than that for natural gas or methane and that the pressure exponent has a much smaller negative value.

Nomenclature

A_w = surface area exposed to heat transfer, m^2
a = multiplying constant for heat transfer
b = Reynolds number index
D = engine bore, m^2
E = energy of cylinder contents, kJ
e = specific energy, kJ/kg
$\bar{h}_f$ = enthalpy of formation, kJ/kmol
$\bar{h}$ = specific enthalpy, kJ/kmol
k = thermal conductivity, kW/mK
M = molecular weight, kg/kmol
m = mass, kg
N = number of moles
P = pressure, kPa
Q = heat lost from combustion chamber, kJ
$\bar{R}$ = gas constant, kJ/kmol•K
Re = Reynolds number
r = radius of flame, m
S_l = laminar burning velocity, m/s
S_T = turbulent burning velocity, m/s
T = temperature, K
u_T = turbulence intensity
V = volume of combustion chamber, m^3
v = specific volume, m^3/kg
x = mass fraction burned

Subscripts

u = unburned gas
b = burned gas
i = unburned gas constituent
j = burned gas constituent
g = gas
w = wall
f = flame
1 = previous calculation step
2 = current calculation step

Downloaded 01 Jun 2010 to 171.66.16.71. Redistribution subject to ASME license or copyright; see http://www.asme.org/terms/Terms_Use.cfm

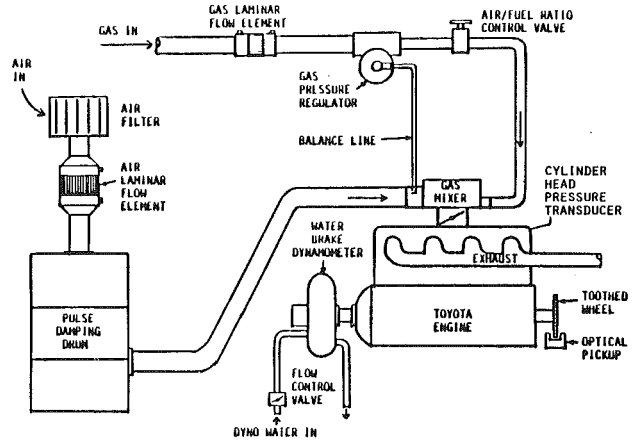


Fig. 3 Experimental apparatus

It is concluded from these comparisons that the laminar burning velocity of natural gas can be less than half that of gasoline under similar enginelike conditions of temperature and pressure. The rest of this paper shows how this affects the various stages of combustion in a natural-gas-fueled engine.

Experimental Apparatus

A schematic drawing of the experimental apparatus is given in Fig. 3. The engine used was a four-cylinder Toyota Corolla, model 3TC, mounted on a dynamometer stand in a test cell of the Alternative Fuels Laboratory at the University of British Columbia. The specifications of the engine are as follows:

Bore	85.0 mm
Stroke	78.1 mm
Swept volume	1772 cc
Comp. ratio	9:1

The engine was coupled to a Go-Power, model DA316D, water brake dynamometer. In this type of installation the power of the engine is absorbed by rotating vanes passing through water, which transmits the torque to stationary vanes inside the dynamometer housing. The housing is prevented from rotating by a strain gage load cell assembly which measures the torque. The load applied to the engine is a function of the water level in the dynamometer and this was controlled by an electropneumatically operated intake valve linked to a load setting dial in the control room. To provide a steady water supply pressure a constant head tank and electric pump were installed, which eliminated the fluctuations in engine speed with building water supply pressure.

Engine cooling was provided by a water column which mixed cold, fresh water with the water circulating through the engine when the temperature rose above a given preset value (80°C for all engine tests).

The standard electronic ignition fitted to the engine was augmented by external circuits which allowed the spark timing to be adjusted remotely from the control room while the engine was running. A pair of optical sensors and a toothed wheel mounted on the engine crank shaft were used to generate electrical pulses at every 2 deg of crank angle revolution together with top and bottom dead center pulses. Electronic circuity then controlled the ignition system to give the spark advance as set on the control panel.

Air flow rate was measured with a Meriam Laminar Flow Element, model 50MC2-4F, mounted on top of a pulse damping drum. The pressure drop across the element was read in inches of water gage on an inclined manometer in the control room, and translated to volume flowrate using the calibration chart provided.

Natural gas was obtained from the building supply and its flow rate was also measured using a Meriam Laminar Flow Element, model 50MWV-1.5, connected to a second inclined manometer. The element was supplied with a calibration chart for air, so corrections were made for the different viscosity of natural gas. Air–fuel ratio was controlled using a flow control valve in the natural gas line leading to the engine, and the gas mixer used was an Impco model 300 positive displacement mixer mounted above the standard gasoline carburetor.

Gasoline flow rate was measured using a Floscan turbine meter and displayed on a digital voltmeter. Thermocouple temperature sensors were installed at the air and gas laminar flow elements, and in the inlet and exhaust manifolds, while inlet and exhaust pressures were measured using mercury manometers.

Measurements of cylinder pressure were obtained by installing an AVL 8QP500C water cooled, piezo-electric pressure transducer passing through the cylinder head water jacket and into the number one cylinder head. The transducer was recessed one passage diameter, as recommended by Benson and Pick [11] to eliminate the effects of thermal shock. The signal from the transducer was transmitted by low noise cable to a Kistler model 504 charge amplifier and then to a data acquisition system. This system consisted of a NEFF System 620 analog to digital converter which was connected to a PDP 11/34 minicomputer.

A program was written to sample the pressure signal at intervals of one degree crank angle synchronized with the signals from the optical sensors mounted on the toothed wheel at the front of the engine. The pressure signal was ensemble averaged by the program over fifty cycles to reduce the effects of cycle-to-cycle variation. The averaged pressure records were then transmitted to the main university computer system as inputs to the mass burning rate analysis program.

Burning Rate Analysis Program

The burning rate analysis program was written to obtain values of mass fraction burned and turbulent burning velocity versus engine rotation in degrees crank angle.

The major assumptions made in the program are the same as those made by Keck [12] and Lavoie [13], namely: (*i*) The combustion chamber is divided into two zones by a thin, spherically expanding flame front separating the burned gas fraction (x) from the unburned gas fraction ($1-x$); (*ii*) both the burned and unburned gases have varying specific heats and obey the ideal gas law; (*iii*) the unburned gas is isentropically compressed by the expanding burned gases; (*iv*) the pressure is uniform throughout the combustion chamber.

The assumption of a spherically expanding flame front is supported by Kozuka et al. [14] who present combustion photographs taken inside an engine having a combustion chamber of the same shape as the Toyota used in this study. Assumptions (*i*) to (*iv*) allow the following procedure to be used in which calculations are performed at each degree crank angle.

The total mass of fuel–air mixture contained in the cylinder is obtained from measured air and fuel flow rates, with the initial mixture composition calculations allowing for exhaust gas residual fraction. At each step of the combustion process the values of energy, temperature, and volume are known for both the burned and unburned gases at the previous calculation step (subscript 1) and these are used as the starting point for calculating values for the current step (subscript 2).

From the assumption of isentropic compression of the unburned gases

$$v_{u_2} = v_{u_1} (P_1/P_2)^{1/k} \tag{7}$$

Assuming ideal gas behavior

$$T_{u_2} = P_2 v_{u_2} / M_u \bar{R} \tag{8}$$

which allows the specific energy of the unburned gas to be calculated

Downloaded 01 Jun 2010 to 171.66.16.71. Redistribution subject to ASME license or copyright; see http://www.asme.org/terms/Terms_Use.cfm

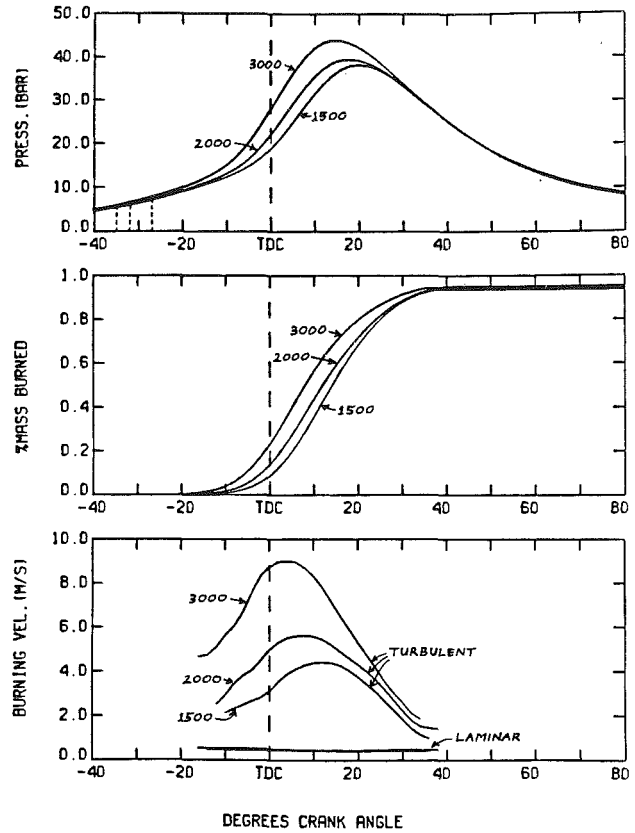


Fig. 4 Comparison of cylinder pressure, percentage mass burned, and burning velocity curves for natural gas, λ = 1, MBT timing at 1500, 2000, and 3000 rpm

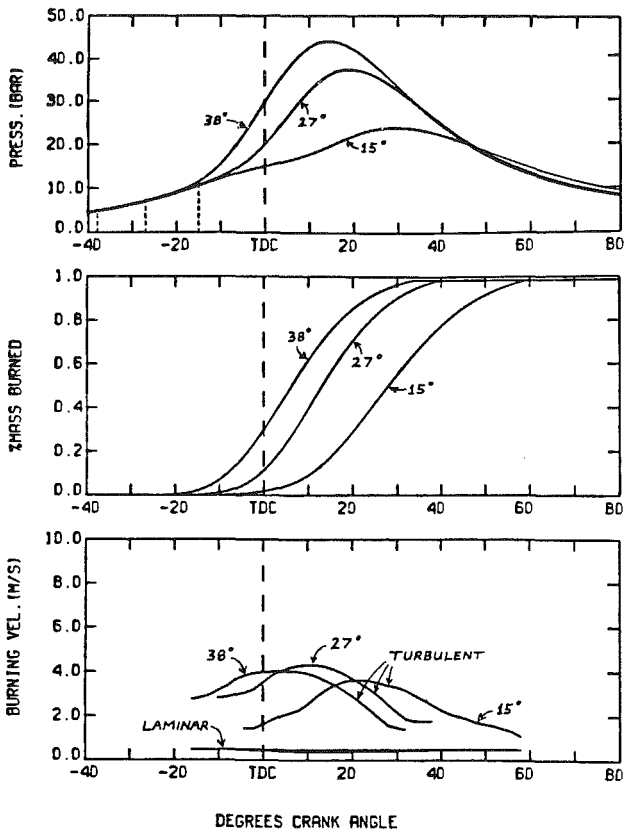


Fig. 5 Comparison of cylinder pressure, percentage mass burned, and burning velocity curves for natural gas, λ = 1, 1500 rpm, spark advance = 15, 27, 38 deg

$$e_{u_2} = \Sigma N_i (h_{fi} + (h_{iTu} - h_{i0}) - \bar{R} T_u) \tag{9}$$

where the values for h_{iTu} are obtained from formulae representing curve fits to published enthalpy data for each constituent.

The new combustion chamber volume V_2 is obtained from the volume/crank angle relationship for the engine, and the new total energy of the control mass contained in the combustion chamber is given by the first law

$$E_2 = E_1 - \int P \cdot dV + dQ \tag{10}$$

The $\int P \cdot dV$ term is approximated by $(P_1 + P_2)/2 \cdot (V_2 - V_1)$ and dQ is obtained using the heat transfer equation proposed by Annand [15]

$$dQ = A_w a (k/D) (\mathrm{Re})^b (T_g - T_w) dT \tag{11}$$

Since the unburned gases are compressed isentropically, heat is only lost from the burned gases, hence $T_g = T_{b_1}$ and A_w equals the area of the combustion chamber in contact with the burned gases calculated in the previous step. T_w is taken to be 450 K, $a = 0.8$, and $b = 0.7$.

From the conservation of mass and energy

$$V_2/m = x_2 v_{b_2} + (1 - x_2) v_{u_2} \tag{12}$$

$$E_2/m = x_2 e_{b_2} + (1 - x_2) e_{u_2} \tag{13}$$

The values of x_2, v_{b_2}, and e_{b_2} are unknown at this point. However, $v_{b_2} = f(T_{b_2}, P_2)$ and $e_{b_2} = f(T_{b_2}, P_2)$ according to the following relationships

$$v_{b_2} = M_{b_2} \bar{R} T_{b_2} / P_2 \tag{14}$$

and

$$e_{b_2} = \Sigma N_j (h_{fj} + (h_{jTb_2} - h_{j0}) - R T_{b_2}) \tag{15}$$

Four dissociation reactions are used to calculate the species concentrations. The program, therefore, proceeds by iterating the burned gas temperature T_{b_2} until the values of e_{b_2} and v_{b_2} calculated by equations (14) and (15) satisfy equations (12) and (13). At this point the mass fraction burned x_2 is obtained.

The burning velocity S_T is calculated using the following relationship

$$S_T = m\dot{x} v_u / A_f \tag{16}$$

The value of A_f is obtained from a geometry subroutine which takes v_b and the distance of the piston from TDC as inputs and calculates r_f and A_w based on the assumption of spherical flame propagation centered at the spark plug.

The above procedure is repeated at each degree crank angle until either the mass fraction burned becomes equal to 1, or $x_2 - x_1$ becomes less than a predefined limit. For comparison purposes laminar burning velocities are calculated at each step using equations (5*a*) and (5*b*) for natural gas and equation (6) for gasoline.

Results

Figure 4 shows the results obtained by running the burning rate analysis program with pressure data obtained from engine operation on natural gas at speeds of 1500, 2000, and 3000 rpm. The final mass burned value achieved in all three cases is about 94 percent. The fact that 100 percent burning is not attained could be the result of a number of factors including: blowby which was not accounted for in the calculations, incomplete combustion, unequal distribution of the fuel between the four cylinders of the engine, and possible errors in the heat transfer calculations. Since 100 percent mass burned was not achieved in any of the calculations, combustion duration $\Delta\theta_i$ is defined to be the time in crank-angle degrees between 1 percent and 90 percent of the charge being burned. The time between the spark occurring and 1 percent of the charge mass being burned is defined here to be the ignition delay period $\Delta\theta_{ig}$.

Downloaded 01 Jun 2010 to 171.66.16.71. Redistribution subject to ASME license or copyright; see http://www.asme.org/terms/Terms_Use.cfm

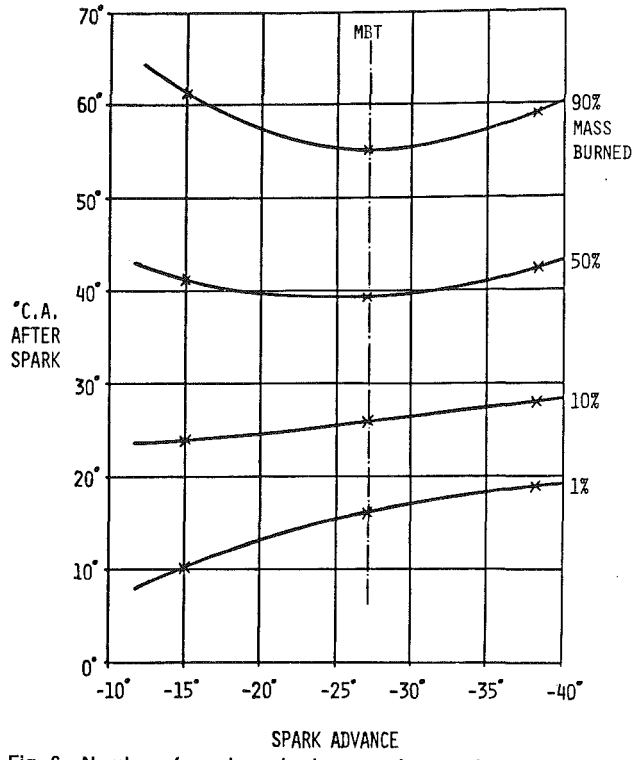


Fig. 6 Number of crank angle degrees after spark to various mass burned fractions versus spark advance for natural gas, $\lambda = 1$, at 1500 and 3000 rpm

Figure 4 also shows the variation of calculated turbulent burning velocity with engine rotation for the three engine speeds. The almost straight line beneath these curves indicates the laminar burning velocity, and it can be seen that the maximum flame speed ratios S_T/S_l are 10, 12.5, and 18.5 at 1500, 2000, and 3000 rpm, respectively, scaling almost linearly with engine speed.

Figure 5 shows the mass burning rates and burning velocities of natural gas at 1500 rpm and varying spark advance. It can be seen that the slope of the mass burned curve is steepest at 27 deg which corresponds to MBT timing. The turbulent burning velocity is also greatest at MBT timing.

Figure 6 shows the results of Fig. 5 replotted in terms of degrees crank angle after spark to various mass burned fractions, as a function of spark advance. It is apparent that the total combustion duration to 90 percent burned is a minimum at MBT timing, however the increasing duration at either side of MBT is a result of different regions of the combustion being extended. When the spark is advanced beyond MBT, the ignition delay period $\Delta\theta_{ig}$ increases but the main combustion period $\Delta\theta_c$ remains almost constant. In contrast, when the spark is retarded closer to TDC, $\Delta\theta_{ig}$ is reduced significantly and $\Delta\theta_c$ is extended.

Figure 7 shows a comparison of the mass burning rates and burning velocities of natural gas with gasoline at 3000 rpm. MBT timing was used for the natural gas, and the gasoline spark advance was knock limited but close to MBT. It is clear from the pressure curves that although the two fuels give approximately the same peak pressure, the natural gas curve is closer to TDC and a significantly greater portion of the pressure rise occurs before TDC than in the gasoline curve. The pressure rise before TDC results in negative work and is part of the cause of the power and efficiency loss experienced when switching from gasoline to natural gas as found by Evans et al. [5]. It can be seen that the total combustion duration is considerably greater for natural gas than for gasoline since both end their combustion at the same time, but the natural gas is ignited 14 deg earlier than gasoline.

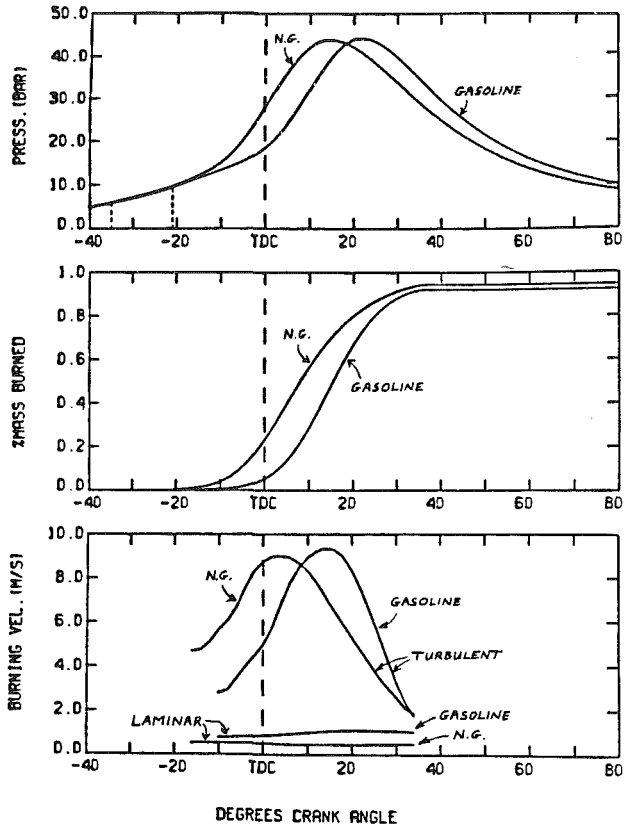


Fig. 7 Comparison of cylinder pressure, percentage mass burned and burning velocity curves for natural gas and gasoline at $\lambda = 1$, MBT timing and 3000 rpm

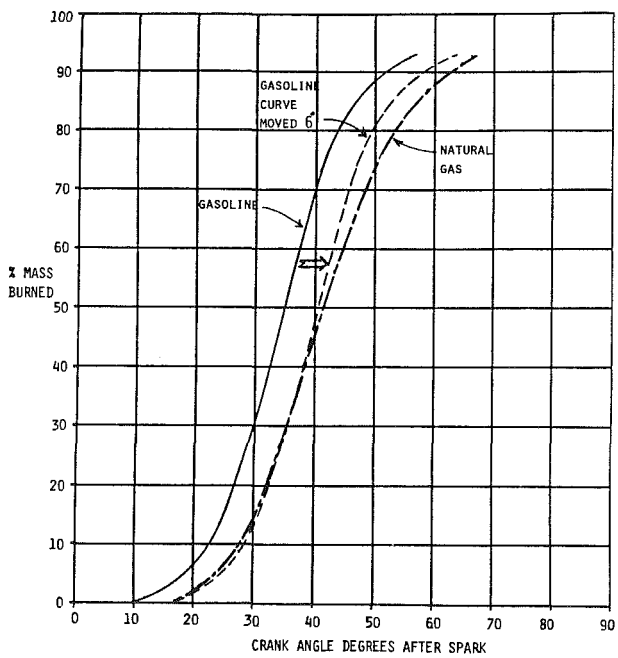


Fig. 8 Percentage mass burned versus crank angle degrees after spark for natural gas and gasoline at $\lambda = 1$, MBT timing, and 3000 rpm

The mass burn rate curves of Fig. 7 have been redrawn in Fig. 8 in terms of percent mass burned versus crank angle degrees after spark. It is clear that the ignition delay period is much greater for natural gas, $\Delta\theta_{ig}$ (gasoline) = 12 deg c.a., and $\Delta\theta_{ig}$ (natural gas) = 18 deg c.a., which is a 50 percent increase. The increase at 1500 rpm was found to be even greater, approaching 100 percent. Some of this increase,

Downloaded 01 Jun 2010 to 171.66.16.71. Redistribution subject to ASME license or copyright; see http://www.asme.org/terms/Terms_Use.cfm

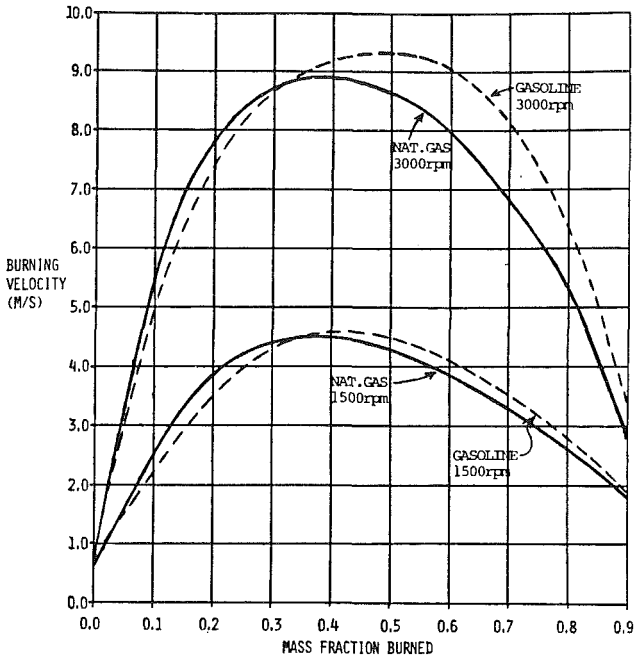


Fig. 9 Turbulent burning velocity versus mass fraction burned for natural gas and gasoline at λ = 1, 1500 and 3000 rpm

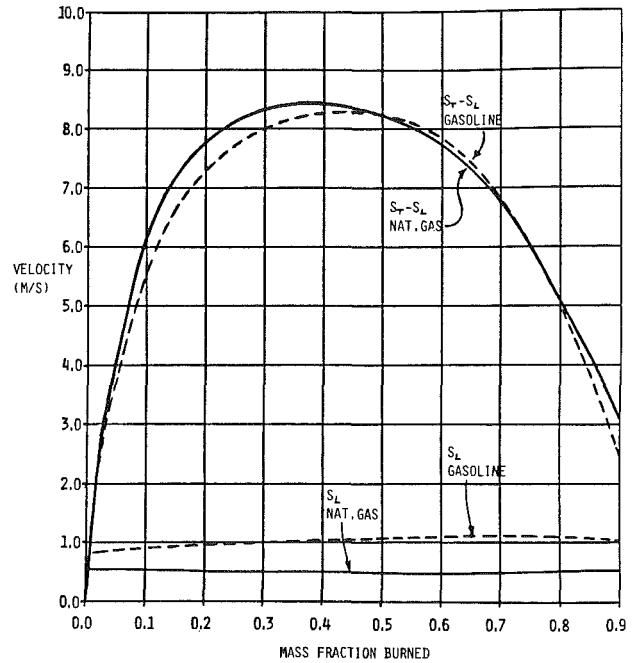


Fig. 10 Laminar burning velocity and (turbulent-laminar) burning velocity versus mass fraction burned for natural gas and gasoline at λ = 1, MBT timing, and 3000 rpm

however, can be accounted for by the fact that the natural gas is ignited at a greater spark advance than the gasoline, and therefore under less favorable conditions of temperature and pressure.

Figure 8 also shows the gasoline mass burned curve displaced to the same ignition delay as the natural gas curve. The displaced gasoline curve is 6 deg to the right of the true gasoline curve and at 90 percent mass burned the natural gas curve is another 4 deg beyond this, indicating that the combustion duration $\Delta\theta_c$ is 4 deg longer for natural gas, an increase of only about 10 percent. These results indicate that the low laminar burning velocity of natural gas has its greatest influence during the earliest stages of combustion up to 1-10 percent burned, and that it plays a less significant role during the main combustion period.

Figure 9 shows the burning velocities of natural gas and gasoline at 1500 and 3000 rpm replotted as a function of mass fraction burned. It shows that the two fuels have very similar turbulent burning velocities and when the laminar burning velocities for each fuel are subtracted from the measured turbulent burning velocities, the curves of Fig. 10 are obtained for natural gas and gasoline at 3000 rpm. These curves are very similar and seem to conform with the equation

$$S_T = S_l + C u_T \tag{19}$$

used by Mattavi [16] where C is a constant for a given engine and u_T is the turbulence intensity which increases approximately linearly with engine speed, as shown by a number of authors including Lancaster and Krieger [17]. Rearranging equation (19) gives

$$S_T - S_l = C u_T \tag{20}$$

where $C u_T$ is a constant for a given engine at a given speed, and it can be seen that Fig. 10 confirms this relationship.

Conclusions

The following conclusions can be drawn from this work:

(*i*) The laminar burning velocity of natural gas is approximately 50 to 60 percent less than gasoline under enginelike conditions.

(*ii*) This low burning velocity has its greatest influence during the ignition delay period, up to 1 percent mass burned, and it can cause increases in ignition delay of up to 100 percent relative to gasoline.

(*iii*) The low laminar burning velocity of natural gas also affects the main combustion period but to a much lesser extent, increasing it by up to 10 percent relative to gasoline.

References

1 Moore, N. P. W., and Roy, M. B. N., "Comparative Studies of Methane and Propane as Engine Fuels," *Proc. I. Mech. E.*, Vol. 170, 1956.

2 Karim, G. A., and Ali, I. A., "The Effects of Low Ambient Temperatures on the Combustion of Natural Gas in a Single Cylinder Spark Ignition Engine," SAE 730084.

3 Genslak, S. L., "Evaluation of Gaseous Fuels for Automobiles," SAE 720125.

4 Fleming, R. D., and Allsup, J. R., "Emission Characteristics of Natural Gas as an Automobile Fuel," SAE 710833.

5 Evans, R. L., Goharian, F., and Hill, P. G., "The Performance of a Spark Ignition Engine Fuelled With Natural Gas and Gasoline," SAE 840234.

6 Taylow, C. F., *The Internal Combustion Engine in Theory and Practice*, Vol. 1, The M.I.T. Press, p. 31.

7 Andrews, G. E., and Bradley, D., "The Burning Velocity of Methane Air Mixtures," *Combustion and Flame*, Vol. 19, 1972, pp. 275-288.

8 Sharma, S. P., Agrawal, D. D., and Gupta, C. P., "The Pressure and Temperature Dependence of Burning Velocity in a Spherical Combustion Bomb," *The Combustion Institute*, 1981, pp. 493-501.

9 Ryan, T. W., and Lestz, S. S., 'The Laminar Burning Velocity of Isooctane, N-Heptane, Methanol, Methane and Propane at Elevated Temperature and Pressures in the Presence of a Dilutent," SAE 800103.

10 Metghalchi, M., and Keck, J. C., "Burning Velocities of Mixtures of Air With Methanol, Isooctane and Indoline at High Pressure and Temperature," *Combustion and Flame*, Vol. 48, 1982.

11 Benson, R. S., and Pick, R., "Recent Advances in Internal Combustion Engine Instrumentation With Particular Reference to High Speed Data Acquisition and Automated Test Bed," SAE 740695.

12 Keck, J. C., "Turbulent Flame Structure and Speed in Spark Ignition Engines," *Nineteenth Symposium (International) on Combustion*, The Combustion Institute, 1982, pp. 1451-1466.

13 Lavoie, G., Heywood, J. B., and Keck, J. C., "Experimental and Theoretical Study of Nitric Oxide Formation in Internal Combustion Engines," *Combustion, Science and Technology*, Vol. 1. 1970, p. 313.

14 Kozuka, K., Saito, A., Otsuka, M., and Kawamura, K., "Television System for Viewing Engine Combustion Processes and the Image Analysis," SAE 810753.

15 Hires, S. D., Tabaczynski, R. J., and Novak, J. M., "The Prediction of Ignition Delay and Combustion Intervals for a Homogeneous Charge, Spark Ignition Engine," SAE 780232.

16 Mattavi, J. N., Groff, E. G., Lienesch, J. H., Matekunas, F. A., and Noyes, R. N., "Engine Improvements Through Combustion Modelling," *Combustion Modelling in Reciprocating Engines*, Plenum Press, 1980.

17 Lancaster, D. R., and Krieger, R. B., "Effects of Turbulence on Spark Ignition Engine Combustion," SAE 760160.

Downloaded 01 Jun 2010 to 171.66.16.71. Redistribution subject to ASME license or copyright; see http://www.asme.org/terms/Terms_Use.cfm

Dual-Fueling of a Prechamber Diesel Engine With Natural Gas

S. Song

P. G. Hill

Department of Mechanical Engineering,
University of British Columbia,
Vancouver, B.C. V6T 1T2, Canada

The feasibility of dual-fuel operation with natural gas in a prechamber diesel engine was studied with special emphasis on fuel consumption and cylinder pressure development. The effects of air restriction, pilot diesel flow rate, and injection timing were also investigated. Near full load the fuel energy consumption rate was close to that of straight diesel operation though at part load (in the absence of air restriction) the fuel energy consumption rate was relatively high. In the absence of injection timing adjustment the maximum power output of dual-fuel operation was severely limited by the maximum cylinder pressure. Retarding the injection timing is effective in reducing the maximum cylinder pressure to a safe level. The analysis of apparent energy release indicates the differences in combustion mechanism between auto-ignition of diesel fuel in straight diesel operation and propagation of flame fronts in dual-fuel operation.

Introduction

Dual-fuel diesel engines are here defined as those which burn either gaseous fuels or diesel, or both at the same time. The mode of operation is defined as straight diesel if only diesel fuel is used, and dual-fuel if two fuels are used at the same time. In dual-fuel operation the gaseous fuel is mixed with air at lean gas-air ratios and the mixture is then compressed during the compression stroke. Near the end of the compression stroke, diesel fuel is injected and auto-ignites, initiating the combustion of the gas-air mixture. Because of its function to initiate the combustion the diesel in dual-fuel operation is often referred to as pilot diesel. The changeover of the mode of operation, either from dual-fuel to straight diesel or straight diesel to dual-fuel, can take place while the engine operates.

Combustion characteristics of dual-fuel operation differ from those of straight diesel operation. In diesel operation the combustion is generally controlled by mixing. As a stream of diesel fuel is injected into the cylinder, it disintegrates rapidly into fine droplets which in turn vaporize and auto-ignite after mixing with high-temperature compressed air. Combustion in dual-fuel operation, in contrast, tends to be controlled by flame propagation. During the intake stroke, a nearly uniform mixture of gas and air is drawn into the cylinder, then compressed by piston movement to high temperature and pressure but not high enough to elicit auto-ignition. A small amount of diesel fuel is injected into the homogeneous gas-air mixture near the end of the compression stroke. The injected pilot diesel initiates flame fronts which propagate through the gas-air mixture.

A prechamber diesel engine is an indirect-injection engine consisting of two chambers, prechamber and main chamber. The main objective of the prechamber design is to burn a small fraction of the injected fuel in the prechamber so that the resulting pressure rise will drive the mixture of partially burned and unburned fuel into the main chamber as a high-speed jet with turbulence sufficient to promote rapid and complete combustion. The type of diesel engine used in dual-fuel operation with natural gas has been almost exclusively direct-injection, so that the behavior of a prechamber diesel engine with dual-fueling over a range of load appears not to have been previously investigated.

Literature Review

The importance of gas-air mixture strength in dual-fuel operation was studied by Elliott and Davis [1]. Their experiments with a CFR diesel engine showed that when the gas-air mixture strength was below a certain limit, the proportion of gas reacting increased with diesel fuel-air ratio and gas-air mixture strength. If the concentration of gas is below the lower limit of flammability (which is commonly defined as the concentration of gaseous fuel in the intake air at which the minimum liquid fuel-air ratio yields consistent and close-to-complete combustion) the gas does not react completely with oxygen unless it is in, or immediately adjacent to, an inflamed or high-temperature region. The lower limit of flammability of natural gas in air under conditions existing at the end of compression was found to be approximately 4 to 5 percent by volume.

The experiments by Lewis [2] on sludge gas (86.6 percent methane, 5.45 percent carbon dioxide, 4.5 percent nitrogen by volume) in a single-cylinder direct-injection engine with compression ratio of 14.7:1 indicated a lower limit of flammability of about 6.2 percent by volume. These tests also showed that intake air restriction and preheating of the intake air could increase the amount of gas reacted.

Simonson [3] used methane in a direct-injection single-cylinder engine with intake charge temperatures ranging from 241 to 325°C and gas-air mixture strength ranging from 0 to 5 percent by volume. Exhaust gas analysis during constant-

Contributed by the Diesel and Gas Engine Power Division and presented at the Energy-Sources and Technology Conference and Exhibition, Dallas, Texas, February 17-21, 1985. Manuscript received at ASME Headquarters November 1, 1984. Paper No. 85-DGP-3.

Copyright © 1985 by ASME
Downloaded 01 Jun 2010 to 171.66.16.71. Redistribution subject to ASME license or copyright; see http://www.asme.org/terms/Terms_Use.cfm

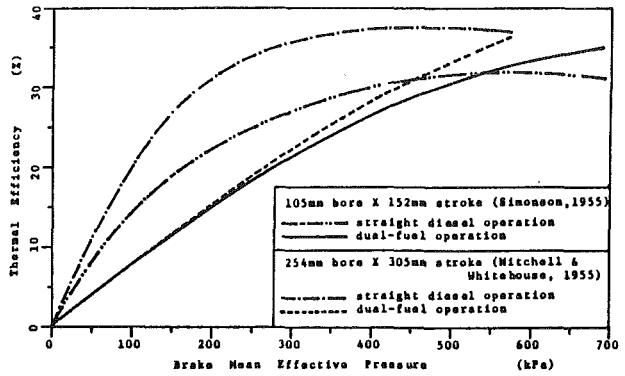


Fig. 1 Typical thermal efficiencies of dual-fuel and straight diesel operations

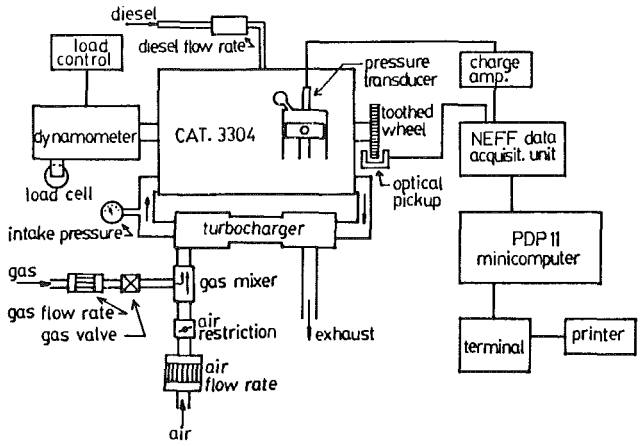


Fig. 2 Apparatus and Instrumentation

speed motored tests revealed that increase in intake charge temperature results in more favorable conditions for flame propagation. Simonson [4] studied the effects of air restriction, and changes in pilot diesel rate and injection timing on operation of a direct-injection engine with methane. Preheating of the intake charge, advancing injection timing, intake air restriction, and increase in pilot diesel rate all gave significant improvements in fuel consumption. Rapid rates of pressure rise were reported to set a limit to the extent to which improved performance can be obtained by advancing the injection timing.

Moore and Mitchell [5] used sludge gas in a single-cylinder direct-injection engine to test the effects of air restriction, intake charge preheating, and advancing injection timing. As much as 20 percent improvement in fuel consumption rate was reported in each separate test of the above methods. In reviewing past work they concluded that raising the intake temperature is the only practical way of extending the lower limit of flammability.

Work on a large engine was described by Mitchell and Whitehouse [6]. A four-cylinder direct-injection engine of 10 in. (254 mm) bore and 12 in. (305 mm) stroke with compression ratio of 13.5:1 was fueled with sludge gas (87.9 percent methane, 5.5 percent carbon dioxide, 4.4 percent nitrogen). Tests on the effect of air restriction showed a considerable improvement in fuel consumption.

Experiments made by Felt and Steele [7] showed that knock-limited maximum power is directly related to the antiknock quality of the primary fuel. Lead alkyl antiknock compounds were found to be quite effective in enhancing the maximum power of dual-fuel operation with natural gas. The knock was described as "audible high-frequency combustion loss," which was visible on the pressure-time trace. The knock was described from the observation of the shape of the pressure-time trace as "end-gas knock": the knock arising from the auto-ignition of the end-gas ahead of the flame front. It is the type of knock which may occur in spark-ignition engines.

The influences of fuel-air mixture strength, pilot diesel rate, and intake air temperature on knock-limited power were studied in detail by Karim et al. [8] with a single-cylinder direct injection engine with compression ratio of 14.2:1 and 97.8 percent methane as the gaseous fuel. The knock was observed to be associated with a sharp change in the running regime of the engine and accompanied by loudly audible sound. It occurred only in a certain range of mixture strength on the lean side of stoichiometric. The effect of the cetane number of the pilot diesel on the onset of knock was found to be small.

In summary, the literature reveals that considerable research has been done on dual-fuel operation with the direct-injection type of diesel engine. At low loads, combustion suffers from excessively lean fuel-air ratio and unburned gas escapes with the exhaust. Figure 1 shows thermal efficiencies typical of dual-fuel operation with direct-injection diesel engines. Restricting or preheating the intake air, increasing the pilot diesel flow rate, and advancing the injection timing have been shown to be effective for improving the fuel consumption at low loads. Maximum power output is limited by the occurrence of knock, which appears to be of the same kind as in spark-ignition engines. Adding lead alkyl antiknock compounds or cooling the intake air were shown to be effective in improving knock-limited maximum power. The literature, however, seems silent on dual-fuel diesel operation with the prechamber type of diesel engine.

Objectives

The primary objective of this study was to determine the feasibility of dual-fuel operation with natural gas in a prechamber diesel engine. Observations were made of fuel consumption and cylinder pressure development, and how these are affected by pilot diesel flow rate and injection timing, and gas-air mixture strength. Computer analysis of apparent energy release was employed to study the combustion characteristics, first for straight diesel operation and then with regard to the above three operating variables.

Apparatus and Instrumentation

A Caterpillar 3304 four-cylinder prechamber engine coupled to an electromagnetic dynamometer was operated at 1600 rpm with variable load and diesel-to-gas flow rates. Full load at 1600 rpm is rated by the manufacturer as 124 psi (856 kPa) in brake mean effective pressure. The engine is turbocharged. Its bore and stroke are 4.75 in. (12.1 cm) and 6.0 in. (15.2 cm), respectively, and its compression ratio is 17.5.

The arrangement of apparatus and instruments is shown in Fig. 2. The torque applied by the engine shaft to the dynamometer was measured by a strain gage load cell. The No. 1 cylinder was instrumented with an AVL piezo-electric pressure transducer, cooled with water and mounted in a steel sleeve through the cylinder head. The signal from the transducer was transmitted by a low-noise cable to a charge amplifier and then to a data acquisition system. The system consisted of a NEFF System 620 analog-to-digital converter which was connected to a PDP-11/34 minicomputer. Pressure signals were sampled at intervals of one degree crank angle, along with a bottom dead center signal, drawn from an optical sensor mounted on the toothed wheel at the front of the engine. Ensemble-averaged values of pressure were obtained from 30 to 50 cycles for each degree of crank angle. The averaged values were then used to compute indicated mean effective pressure and to analyze apparent energy release. Laminar flow elements were used to measure the flow rates of

Downloaded 01 Jun 2010 to 171.66.16.71. Redistribution subject to ASME license or copyright; see http://www.asme.org/terms/Terms_Use.cfm

Table 1 Typical composition of natural gas

COMPOSITION	RELATIVE VOLUME (%)
methane	94.00
ethane	3.30
propane	1.00
iso-butane	0.15
n-butane	0.20
iso-pentane	0.02
n-pentane	0.02
nitrogen	1.00
carbon dioxide	0.30
hexane	0.01

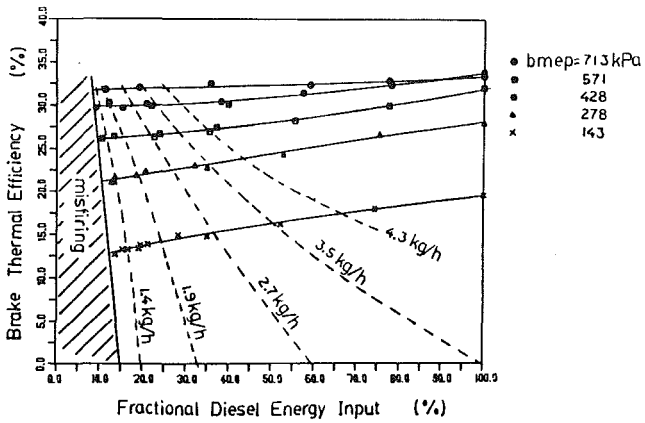


Fig. 3 Effect of pilot diesel flow rate on brake thermal efficiency

air and natural gas. The gas flow was controlled manually. The diesel fuel flow rate was obtained with a stop watch from a positive displacement flow meter which measured accumulated flow. The diesel injection rate of the engine was controlled by two mechanisms: the governor rack setting, which is adjusted manually, and the centrifugal governor flyweights, which respond to any small change in applied load in order to maintain a constant speed. Engine speed was measured by a hand digital tachometer which sends out a continuous light beam and counts the pulses reflected from a piece of reflective tape attached on the engine shaft. Specifications of all instruments and their calibrations have been provided by Song [9]. To prevent turbocharger surge due to excessive air restriction, the air pressure at the compressor inlet was limited (in accordance with manufacturer's specification) to 24 in. of water below atmospheric pressure.

The diesel fuel used throughout the experiments had the following typical properties:

- API gravity – 31
- specific gravity – 0.871
- lower heating value – 45,263 kJ/kg

In the analysis of energy release, and in computation of stoichiometric fuel-air ratio, dodecane ($C_{12}H_{26}$) was assumed to be the representative hydrocarbon for the diesel fuel.

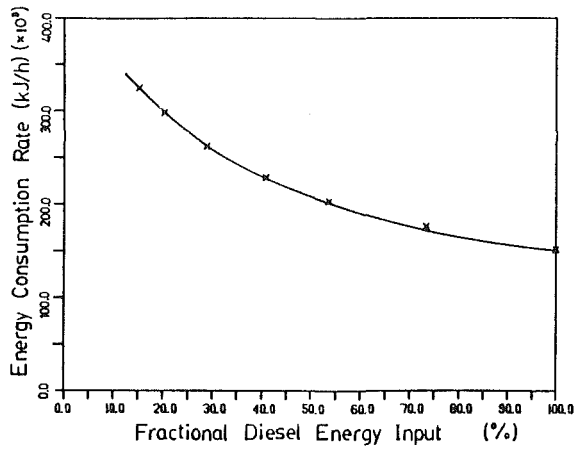


Fig. 4 Fuel consumption at idling operation

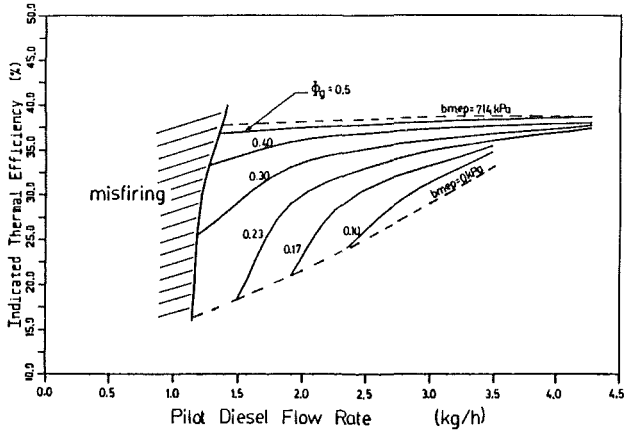


Fig. 5 Effect of pilot diesel flow rate on indicated thermal efficiency

The natural gas used in the experiments had the following properties:

- density – 0.766 kg/m^3 at 101.3 kPa, 25°C
- viscosity – 108.96 micropoise at 21.1°C
- lower heating value – 48,558 kJ/kg

A typical composition of the natural gas used here is given in Table 1.

Experimental Results

1 Fuel Consumption. Tests were carried out to study the change in fuel consumption rate with variation in load and pilot diesel flow rate. Unless otherwise specified the injection timing of the diesel fuel remained constant at 12.3 deg before top dead center.

Figure 3 shows the measured brake thermal efficiencies (based on the lower heating value) as a function of the fractional diesel energy input, i.e., the ratio of the diesel to total energy input. The shaded area on the left corresponds to unstable operation (misfiring) because of insufficient pilot diesel flow rate. The interpolated paths of constant pilot diesel operation are indicated by the dotted lines. As shown the decrease of thermal efficiency due to reduction of pilot diesel flow rate becomes smaller as the load increases. At the brake mean effective pressure of 714 kPa (84 percent of full load), the change in thermal efficiency is less than 1 percent over the range of fractional diesel energy input of 7 to 100 percent. The extent to which the fuel consumption rate depends on the pilot diesel flow rate for idling operation is seen in Fig. 4. The idling operation with a fractional diesel

Downloaded 01 Jun 2010 to 171.66.16.71. Redistribution subject to ASME license or copyright; see http://www.asme.org/terms/Terms_Use.cfm

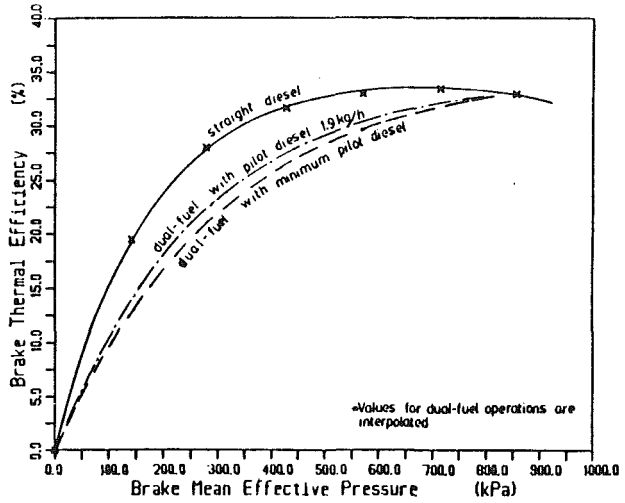


Fig. 6 Comparison of brake thermal efficiencies for dual-fuel and straight diesel operation

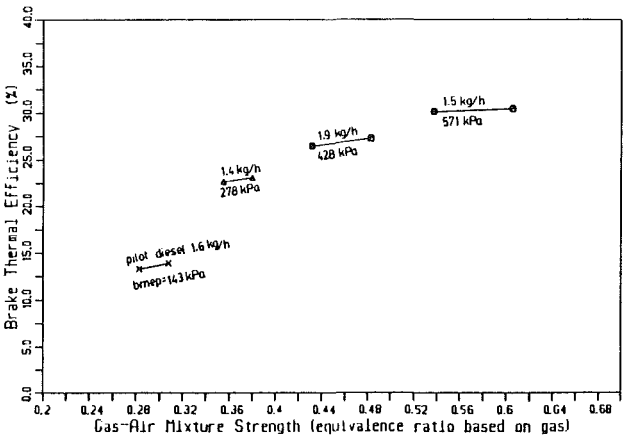


Fig. 7 Effect of intake air restriction on brake thermal efficiency

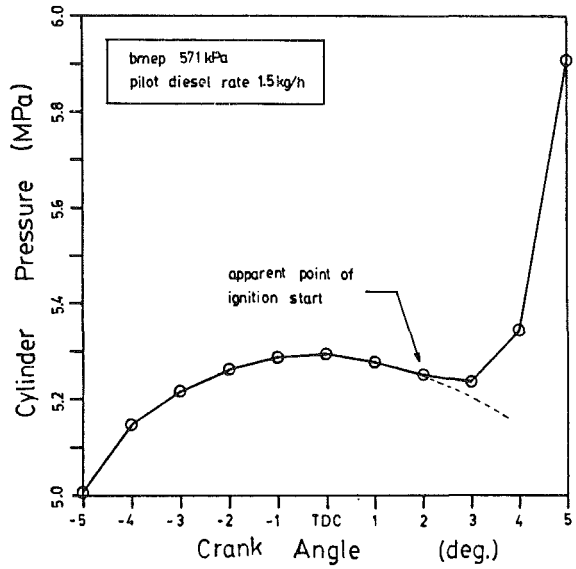


Fig. 8 Typical pressure trace and apparent ignition point

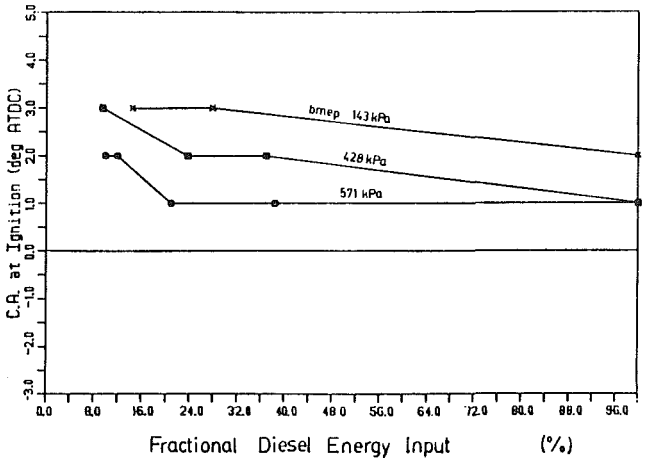


Fig. 9 Apparent point of ignition start at various loads

energy input of 15 percent requires nearly twice as much energy as that of straight diesel operation.

To obtain another picture of the role of pilot diesel flow rate in dual-fuel operation, calculations were made of indicated thermal efficiencies (see Fig. 5) as a function of the flow rate of pilot diesel at constant gas-air mixture strength. The equivalence ratio ϕ_g of the gas was computed as the ratio of the mass of the stoichiometric amount of air required for combustion of the gas alone to the mass of the actual amount of air drawn in, i.e.

$$\phi_g = \frac{\text{stoichiometric air mass flow rate}}{\text{actual air mass flow rate}}$$

It can be seen from Fig. 5 that unless ϕ_g exceeds about 0.5 there will be significant penalties in efficiency with low pilot diesel flow rates.

Figure 6 shows brake thermal efficiency for straight diesel and dual-fuel operations; these curves were obtained from Fig. 3 by interpolation. One of the dual-fuel efficiency curves corresponds to operation with the minimum pilot diesel flow rate needed to assure stable operation without misfiring. The thermal efficiency of the dual-fuel operation at part load is substantially lower than that of straight diesel operation. At the brake mean effective pressure of 850 kPa, which is about the rated full load at 1600 rpm, the thermal efficiencies of both operations are the same.

Tests to determine the effect on thermal efficiency of intake air restriction were performed for several load settings ranging from idling to about 50 percent of full load. For each load setting, the rate of gas flow was controlled so that the flow rate of pilot diesel would remain approximately constant. The air restriction was limited to about 10 percent to prevent surging of the turbocharger. Figure 7 shows the effect of air restriction on brake thermal efficiency at various load settings. The gas-air mixture strength is represented by the equivalence ratio based on the gas alone. The tests for all the load settings exhibit improvements when air restriction is imposed. The increase in brake thermal efficiency however was for all cases less than 1 percent for about 10 percent air reduction.

2 Ignition Delay. The ignition delay of the pilot diesel was studied by observing the averaged cylinder pressure versus crank angle trace. The so-called ignition point was identified from the pressure trace (shown typically in Fig. 8) as the point at which combustion has proceeded far enough to affect the pressure noticeably.

With the injection timing fixed at 12.3 deg BTDC, the change in ignition delay of pilot diesel with addition of gas was investigated at a range of load settings. Figure 9 shows the crank angle at the start of ignition with the pilot diesel rate varying from 10-20 to 100 percent of total energy input. For straight diesel operation at low load, the ignition does not start until 2 deg ATDC. At half-load, the ignition point is

Downloaded 01 Jun 2010 to 171.66.16.71. Redistribution subject to ASME license or copyright; see http://www.asme.org/terms/Terms_Use.cfm

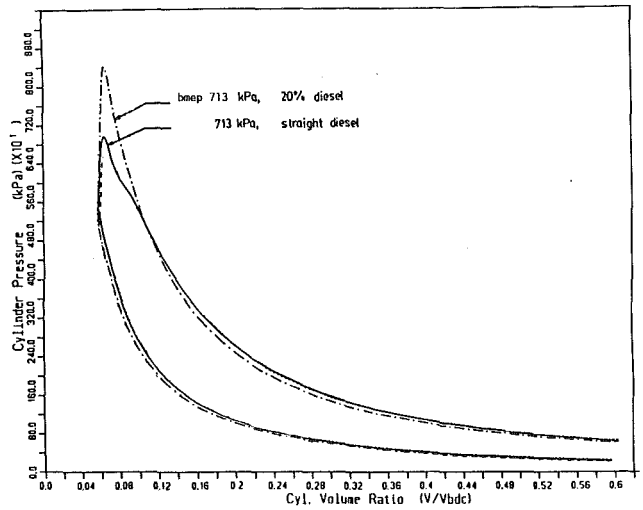


Fig. 10 Comparison of *P-V* diagrams for dual-fuel and straight diesel operation

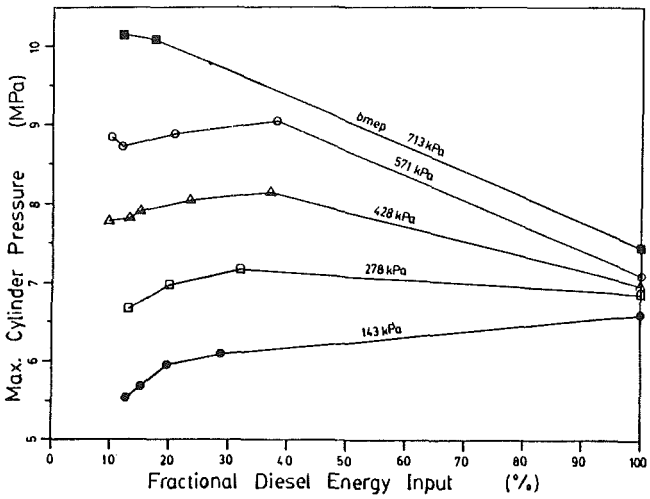


Fig. 12 Comparison of maximum cylinder pressures for dual-fuel and straight diesel operation

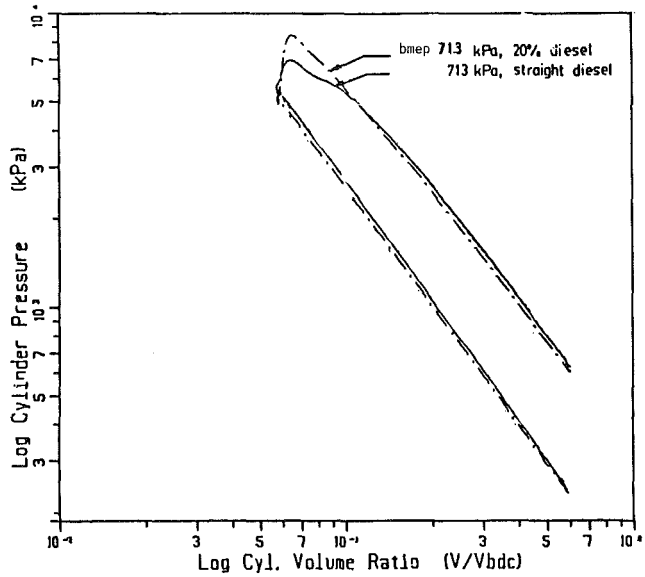


Fig. 11 Comparison of ln *P-V* diagrams for dual-fuel and straight diesel operation

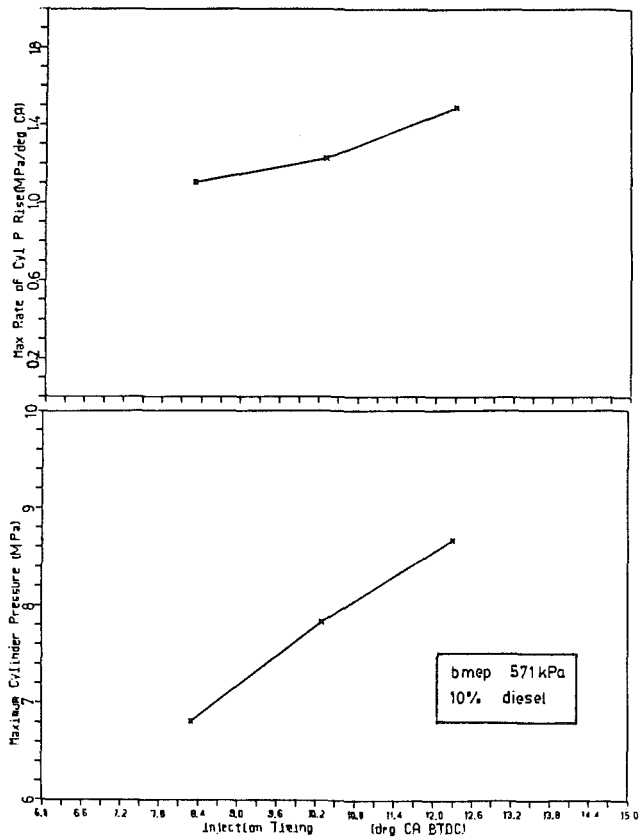


Fig. 13 Effect of varying injection timing on maximum cylinder pressure and rate of pressure rise

advanced by a degree. Addition of gas extends the ignition delay by 1 to 2 deg. The corresponding result obtained by Moore and Mitchell [5] in a direct injection engine was about 2 deg and by Karim [10] also in a direct injection engine, about 1.5 deg. In the absence of air restriction, the point of ignition is no later than 3 deg ATDC for all the loads and pilot diesel flow rates tested.

3 Cylinder Pressures. The cylinder pressures recorded at each crank angle were ensemble-averaged over 30–50 cycles.

Figure 10 compares typical indicator diagrams of dual-fuel and straight diesel operations at comparable loads and pilot diesel flow ratios. With dual-fuel operation and unadjusted injection timing, combustion is faster and peak pressures are substantially higher. The dual-fuel operation exhibits a much slimmer P-V diagram, with much of the combustion taking place within a narrow range of cylinder volume. The corresponding ln (P)-ln (V) diagrams in Fig. 11 (in which compression or expansion without combustion is indicated by an approximately straight line) also show the different combustion characteristics of dual-fuel and straight diesel operations. The ln (P)-ln (V) diagram of dual-fuel operation shows no obvious intermediate expansion period, which is quite distinctively recognized in straight diesel operation at high load; the combustion duration of dual-fuel operation is much shorter than that of straight diesel operation. This would be consistent with rapid propagation of flame fronts in the gas-air mixture, in contrast to the slower combustion in straight diesel operation.

Figure 12 shows maximum cylinder pressure for a wide range of pilot diesel ratios and several loads, all with constant injection timing.

The effect on maximum cylinder pressure of retarding injection timing is shown in Fig. 13 for a brake mean effective pressure of 571 kPa and pilot diesel accounting for 10 percent of total energy input. Retardation of 4 deg reduced the maximum pressure by 1850 kPa. The corresponding change in

Downloaded 01 Jun 2010 to 171.66.16.71. Redistribution subject to ASME license or copyright; see http://www.asme.org/terms/Terms_Use.cfm

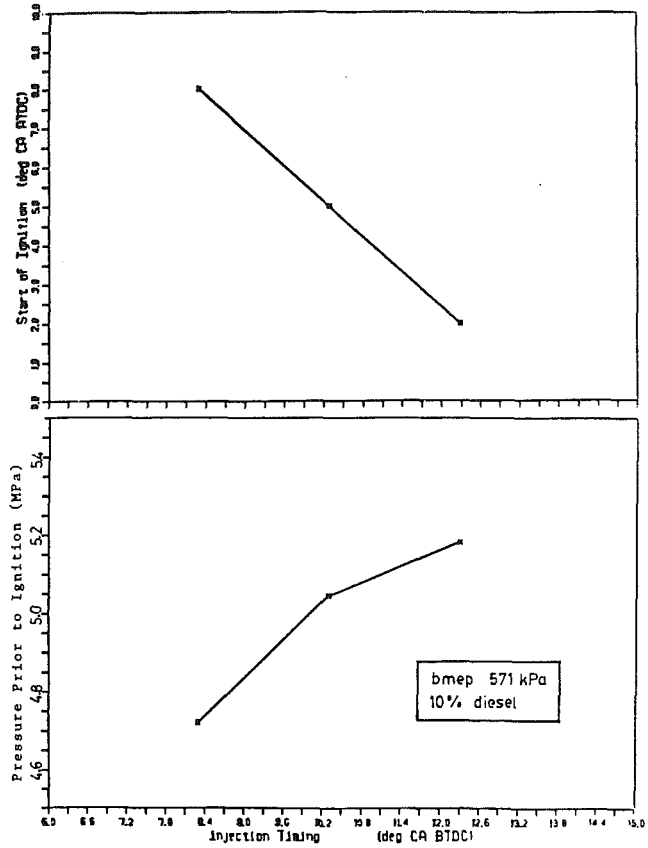


Fig. 14 Effect of varying injection timing on pressure prior to combustion and ignition point

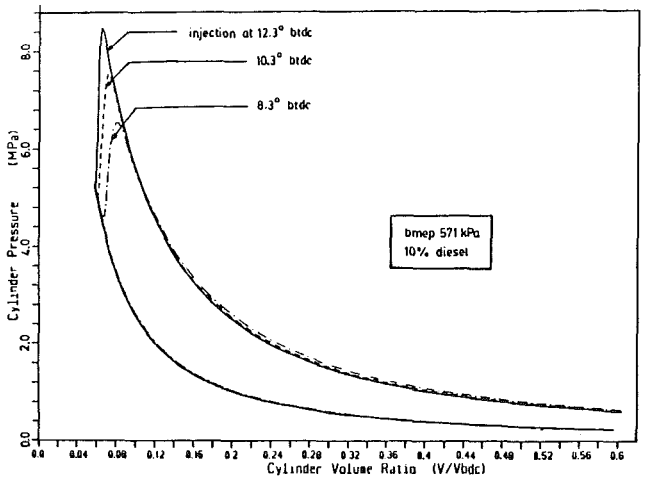


Fig. 15 Effect of varying injection timing on *P-V* diagram

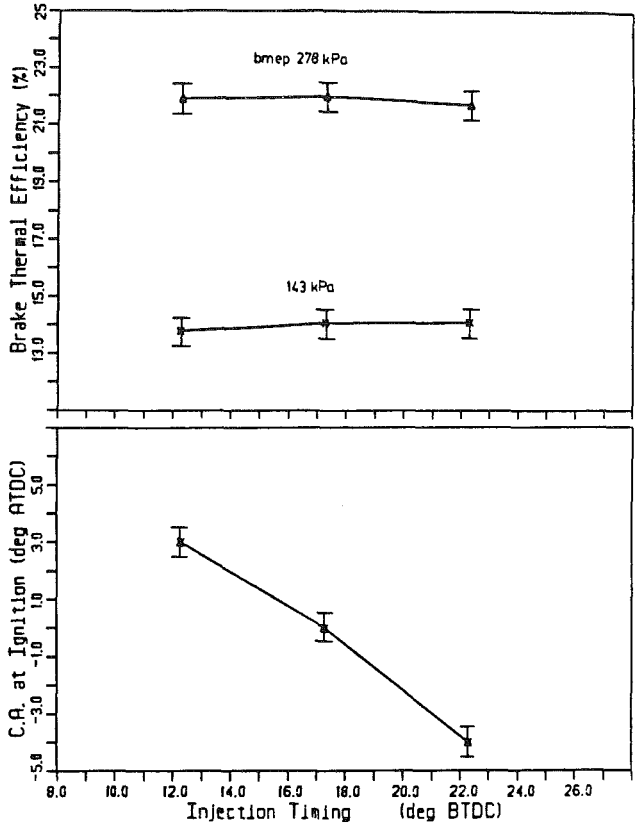


Fig. 16 Effect of injection timing on thermal efficiency and ignition point

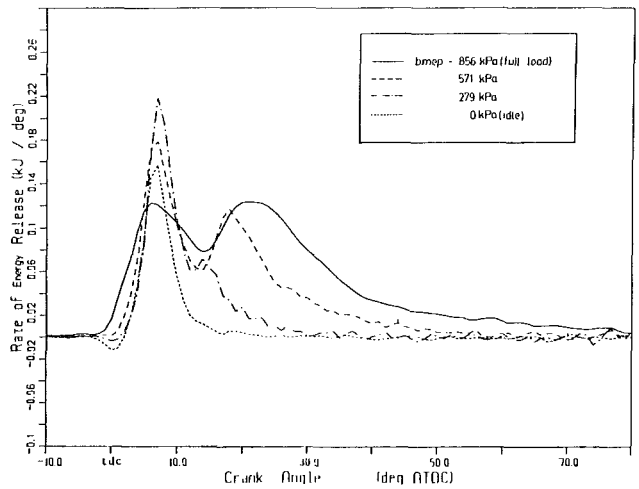


Fig. 17 Rate of energy release of straight diesel operation at various loads

the pressure prior to combustion for the same retardation was 460 kPa as shown in Fig. 14.

Figure 15 shows the *P-V* diagram for different injection timings. As the injection timing is retarded the point of the significant pressure rise is retarded further from the top dead center and the maximum pressure is less. As shown by Fig. 16 the effect on thermal efficiency at low load of even 10 deg change in injection timing was very small. Tests at a brake mean effective pressure of 714 kPa (83 percent of full load), with 10 percent fractional diesel energy input and 4 deg retardation showed reduction of peak pressure from 10.2 to 7.7 MPa. The loss in brake thermal efficiency due to the injection retardation was about 1 percent.

It is estimated that safe full-load dual-fuel operation would require 4 to 6 deg of injection timing retardation and this would result in loss of thermal efficiency of 1 to 2 percent. At loads beyond full load, since it is expected that the thermal efficiency of dual-fuel operation without injection retardation would equal or even surpass that of straight diesel operation, the dual-fuel operation with sufficient injection retardation to assure safe level of peak pressure would still result in thermal efficiency close to that of straight diesel operation. Retarding injection timing seems to be a practical and necessary means of ensuring safe dual-fuel operation at high load.

Apparent Energy Release

Computations of apparent energy release under a range of

Downloaded 01 Jun 2010 to 171.66.16.71. Redistribution subject to ASME license or copyright; see http://www.asme.org/terms/Terms_Use.cfm

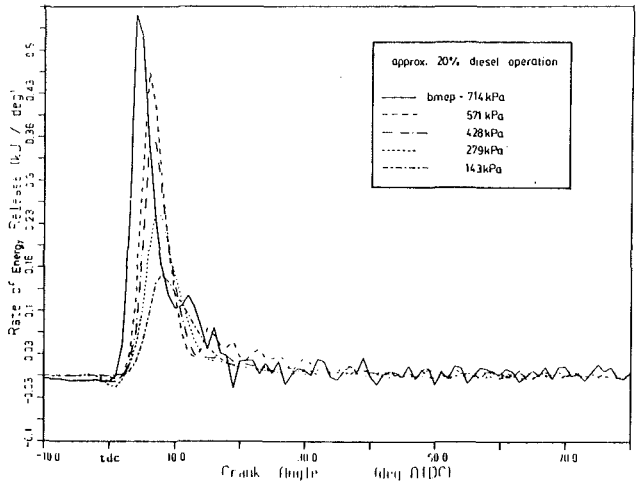


Fig. 18 Rate of energy release of dual-fuel operation at various loads

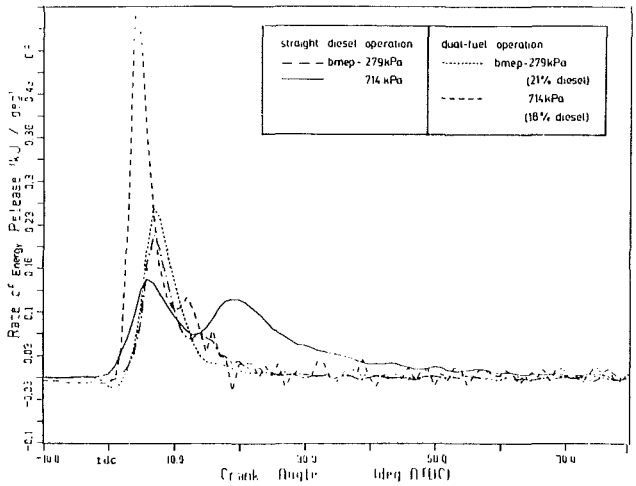


Fig. 19 Comparison of rate of energy release for straight diesel and dual-fuel consumption

test conditions were performed with a computer program whose derivation and description is provided by Song [9]. The effects of heat transfer and dissociation were taken into account and were shown to have relatively small effects on the calculated rate of energy release; these effects are included in the results presented herein. For cases in which there was little unburned fuel in the exhaust (e.g., straight diesel operation) the computed total energy release agreed closely with measured fuel consumption.

The calculated rate of energy release for straight diesel operation with loads ranging from idling to full load is shown in Fig. 17. At full load (bmep = 856 kPa) the rate of energy release reveals two stages of combustion. The first stage lasts until 12 to 14 deg after top dead center. As the load decreases the second stage combustion becomes less distinctive. It seems that the first peak corresponds to combustion in the prechamber and the second to combustion in the main chamber. The maximum rate of energy release is the smallest at full load and increases as the load is decreased. At very low loads the rate of energy release rises very rapidly although the maximum rate of energy release is limited by the total diesel energy input.

Figure 18 shows the rate of energy release with dual-fuel operation in which pilot diesel fuel accounts for about 20 percent of the total energy input, and when no change has been made in diesel injection timing. The most noteworthy feature is the nearly twofold increase in the maximum rate of energy release. It is observed from the figure that the change in combustion duration with varying load is relatively small when compared to that of straight diesel operation. The shapes of the rate of energy release curves exhibit very little of the two-staged combustion characteristic which is observed in straight diesel operation. The rapidity of rise of the rate of energy release increases with the increase in load.

Figures 19 and 20 compare straight diesel and dual-fuel operation (with unadjusted injection timing) at 85 and 33 percent of full load. From Fig. 19 it is seen that for high load operation the combustion duration of the dual-fuel operation is much shorter than that of the straight diesel operation, and the maximum rate of energy release is about 3.7 times higher. The remarkable difference in the shape of the rate of energy release for the two modes of operation is consistent with different mechanisms of combustion. Evidently the combustion in dual-fuel operation is mainly carried out by flame propagation through the premixed gas–air mixture, ignited by the burning diesel spray which penetrates the main chamber as a hot jet. In straight diesel operation, combustion is mixing limited rather than propagating as a turbulent flame.

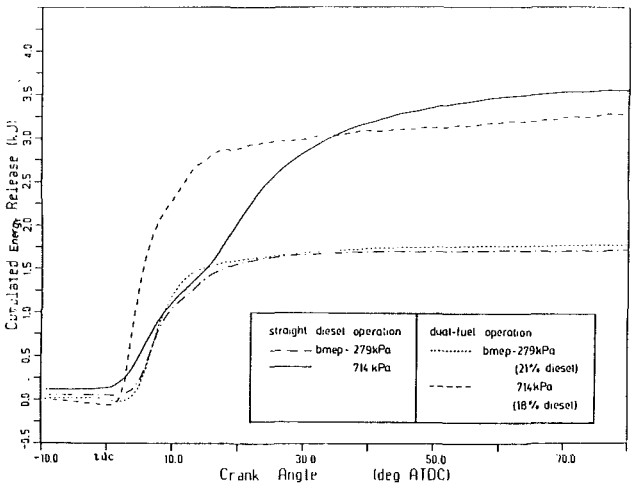


Fig. 20 Comparison of cumulative energy release for straight diesel and dual-fuel operation

Conclusions

Safe operation of a prechamber diesel engine with dual-fueling with natural gas is severely limited by maximum cylinder pressure. Even at half-load the maximum cylinder pressure of dual-fuel operation is as high as that of straight diesel operation at full load. The excessive maximum cylinder pressure is associated with the high rate of energy release by combustion which takes place within a nearly homogeneous gas–air mixture. The maximum cylinder pressure, as well as the rate of cylinder pressure rise, can be reduced to a safe level by retarding the injection timing by about 4 to 6 deg of crank angle. The change in thermal efficiency due to the retardation is small (less than 0.5 percent with 4 deg retardation at 67 percent of full load). Restricting the intake air can reduce also the maximum cylinder pressure, but this results in higher maximum rate of cylinder pressure rise.

Stable dual-fuel operation requires sufficient flow rate of pilot diesel fuel; insufficient amount of pilot diesel fuel results in erratic operation with misfired cycles. The minimum pilot diesel fuel required in order to ensure a stable operation is typically 8 to 15 percent of the total energy input, depending on engine load.

Dual-fuel operation at part load showed generally higher fuel consumption than that of straight diesel operation. The apparent energy release analysis revealed that the higher fuel

Downloaded 01 Jun 2010 to 171.66.16.71. Redistribution subject to ASME license or copyright; see http://www.asme.org/terms/Terms_Use.cfm

consumption rate is mainly due to gas surviving unburned through the combustion chamber. The main cause of this poor combustion is weak gas–air mixture strength. Increase in pilot diesel flow rates reduces the amount of unburned gas and thus improves the fuel consumption rate. The dependence of total fuel consumption rate on pilot diesel flow rate is less with higher gas–air mixture concentration. With restriction on turbocharger inlet pressure (to prevent surge) less than about 10 percent air restriction was possible in the tests conducted; this showed some improvement (perhaps one percent) on fuel consumption rate. Advancing injection timing showed no significant effect on fuel consumption rate.

The fuel consumption rate during dual-fuel operation near full load approached that of straight diesel operation. Extrapolated beyond full load diesel operation, the fuel consumption rate of dual-fuel operation would become lower than that of straight diesel operation.

The combustion characteristics of straight diesel and dual-fuel operation differ in that in the former the combustion consists mainly of auto-ignition of diesel fuel, whereas in the latter the combustion is carried out by the propagation of flame fronts. This distinction was clearly exhibited in the analysis of apparent energy release, where straight diesel operation showed a two-staged combustion and dual-fuel operation a shorter, single-staged combustion.

References

1 Elliott, M. A., and Davis, R. F., "Dual-Fuel Combustion in Diesel Engines," *Ind. and Eng. Chem.*, Vol. 43, No. 12, 1951.

2 Lewis, J. D., "Study of Combustion Processes in the Dual-Fuel Engine by Exhaust Gas Analysis Methods," Ph.D. Thesis, London University, 1954.

3 Simonson, J. R., "Some Combustion Problems of the Duel-Fuel Engine," *Engineering*, Vol. 178, 1954, p. 363.

4 Simonson, J. R., "An Analysis of Dual-Fuel Combustion Processes in Compression Ignition Engine," Ph.D Thesis, London University, 1955.

5 Moore, N. P. W., and Mitchell, R. W. S., "Combustion in Dual-Fuel Engines," *Joint Conf. on Combustion*, ASME/Inst. of Mech. Eng., 1955, p. 300.

6 Mitchell, R. W. S., and Whitehouse, N. D., "The Development and Performance of a Range of Dual-Fuel Engines," *Canadian Mining and Metallurgical Bulletin*, 1955.

7 Felt, A. E., and Steele, A. E., Jr., "Combustion Control in Dual-Fuel Engines," *SAE Trans.*, Vol. 70, 1962, pp. 644–653.

8 Karim, G. A., Klat, S. R., and Moore, N. P. W., "Knock in Dual-Fuel Engines," *Proc. Inst. of Mech. Eng.*, Vol. 181, Pt. 1, No. 20, 1966/67.

9 Song, S., "Performance of a Duel-Fuel Prechamber Diesel Engine with Natural Gas," MASc Thesis, University of British Columbia, 1984.

10 Karim, G. A., "A Review of Combustion Processes in the Dual-Fuel Engine—the Gas Diesel Engine," *Prog. Energy Combust. Sci.*, Vol. 6, pp. 277–285, 1980.

Downloaded 01 Jun 2010 to 171.66.16.71. Redistribution subject to ASME license or copyright; see http://www.asme.org/terms/Terms_Use.cfm

A Procedure for Calculating Fuel Gas Blend Knock Rating for Large-Bore Gas Engines and Predicting Engine Operation

F. S. Schaub
Manager, Research and Development.

R. L. Hubbard
Supervisor, Research and Development.

Energy Services Group of Cooper Industries,
Research and Development Laboratory,
Mount Vernon, OH 43050

This paper describes the procedure developed by Cooper-Bessemer for large-bore gas engines to calculate the knock rating of gas fuel blends and to predict with accuracy the required engine build to use that fuel with optimum detonation margin. Engine prototype test work has included fuel sensitivity tests mapped as a function of compression ratio, fuel air ratio, ignition advance, combustion air temperature, and engine rating. Success in predicting production engine operation for a given application involving a particular fuel blend has been gratifying. The basic reference method blend selected was normal butane in methane. Details are included in the paper to illustrate the problems in making sensitivity correlations between small-bore fuel research engines and large-bore production engines.

Introduction

Large-bore internal combustion engines, utilizing gaseous fuels, require careful matching of the engine to the particular fuel in order to provide good fuel economy while maintaining operating margin for high reliability. This optimization can be done only if there is information available regarding the detonation characteristic of the fuel gas plus information regarding the sensitivity of the engine.

Extensive small-engine data have been accumulated and published [1] which define the detonation characteristics of hundreds of hydrocarbons for a variety of small-engine test conditions. Applicability of these data, however, for the large-bore engines has been found to be very limited. Compression ratio data are mismatched and handling of mixtures is not addressed. The large-engine useful range of fuel sensitivity *starts* at an equivalent small-engine rating of approximately 95 motor octane. Utilization of these internationally accepted ASTM methods is further hampered by the inability of large-engine fuel injection systems to be modified to accept the ASTM scale blending components – isooctane, *n*-heptane, and tetraethyllead.

The sensitivity capability of the large engine is affected by many service variables which include loading requirements, ambient temperature, and installation altitude. Within the past ten years the task had been compounded by exhaust emission requirements and, in some instances, criteria for waste heat recovery. Sometimes floating fuel compositions are involved. Custom engineering by job is a standard practice for most large stationary engines.

Criteria for an acceptable large-engine rating method had to satisfy the following requirements:

1 The method must be directed to the combustion of gaseous fuels in large-bore engines with attendant low and medium crankshaft speeds. It must apply to spark gas, pilot oil, two-cycle, four-cycle, atmospheric, and turbocharged engines.

2 The method must include the capability to handle mixtures of gaseous fuels.

3 The method must be practical and inexpensive to implement to enable complete sensitivity mapping for many types of engines covering a wide range of application conditions.

The knock rating method which evolved is called "normal butane number" (NBN). The reference blend by definition is the volumetric percent (Mol%) of *n*-butane, the proknock ingredient, blended with methane. From a practical standpoint high methane pipeline quality natural gas (>95 percent methane) can be treated as "methane" for base stock blending work.

This paper will discuss the test work which was directed to validation of the NBN method. Engine-to-fuel matching techniques are illustrated.

Data Generated for NBN Procedure Study and Implementation

Table 1 illustrates typical data obtained for each of several type engines. A predetermined matrix of test conditions, including speed, load, spark advance, air rate, and temperature, was selected for each type engine. Each test point was set and stabilized with the engine operating on high methane natural gas, and then *n*-butane was blended in increasing quantity until light detonation was encountered.

Contributed by the Diesel and Gas Engine Power Division and presented at the Energy-Sources and Technology Conference and Exhibition, Dallas, Texas, February 17–21, 1985. Manuscript received at ASME Headquarters November 12, 1984. Paper No. 85-DGP-5.

Copyright © 1985 by ASME
Downloaded 01 Jun 2010 to 171.66.16.71. Redistribution subject to ASME license or copyright; see http://www.asme.org/terms/Terms_Use.cfm

Flow readings for the *n*-butane and natural gas were recorded. Repeat tests were made at the exact engine condition using propane, pentane, hexane, and heptane. Finally, select mixtures of the hydrocarbons were introduced and data recorded.

Table 1 gives specific data for the Cooper GMVA-12 two-cycle blower scavenged engine fitted for 7.2 compression ratio. Lines 6 through 16 give data for the standard 10 deg BTC ignition timing. Note that blends in natural gas of 13.90 percent *n*-butane, 3.50 percent *n*-pentane, 2.37 percent *n*-hexane, or 1.68 percent *n*-heptane all produced light detonation. Lines 8, 9, and 10 show tradeoff of *n*-butane quantities with *n*-pentane quantities. Line 7 shows a mixture which includes four hydrocarbons. Similar data were generated with other ignition timings, combustion air rates, and ambient temperatures. Such matrices were generated for all important large-bore engine groups. By plotting equivalences of *n*-butane in natural gas against other hydrocarbons in natural gas, relationships were established as shown in Figs. 1–5. Some scatter of data is seen as a function of engine type and operating condition, but allowance should be made for cumulative reading errors since the points represent only single readings. Equivalence curves were drawn through the test points in a manner to favor margin when calculating NBN summation equivalences for field fuel blends.

Figure 1 (for ethane) is an example of simple extrapolation from small-bore Waukesha COT-MIL work and from ASTM data [1]. It was not practical to supply ethane in sufficient quantity for full-size engine blending work.

It is interesting to note that all curves are nonlinear. Hydrocarbons with lower weight than *n*-butane show decreasing sensitivity with higher concentration; hydrocarbons with higher weight show increasing sensitivity.

An example for converting a given fuel mixture to a NBN equivalence is shown below:

Compound	*Formula*	*Blend Mol percent*	*Combustion Mol percent*	*NBN*	*Curve*
Methane	CH_4	71.10	73.30	0.00	
Ethane	C_2H_6	14.30	14.74	1.80	1
Propane	C_3H_8	7.50	7.73	2.95	2
n-Butane	C_4H_{10}	2.16	2.23	2.23	–
n-Pentane	C_5H_{12}	0.45	0.46	1.30	3
n-Hexane	C_6H_{14}	0.27	0.28	2.15	4
n-Heptane	C_7H_{16}	1.22	1.26	9.70	5
Nitrogen	N_2	1.60	0.00	0.00	
Carbide					
Dioxide	CO_2	1.40	0.00	0.00	
				19.13 NBN of mixture	

Qualification of Technique Accuracy

Lines 2, 7, and 18 of Table 1 were generated for the study of summing NBN equivalents for multiple hydrocarbon blends. These and additional data are summarized in Table 2. The engine groups identified cover two cycle and four cycle, atmospheric and turbocharged. The data have not been edited.

Identification of Sensitivities for Marketed Engines

Lines 1–6 of Table 2 identify the sensitivities of the Cooper GMVA-12 engine with 7.2 compression ratio. Additional work, dedicated strictly to the task of engine sensitivity identification, results in sufficient data to construct a tabulation, as illustrated by Table 3. Options are presented for fuel sensitivities through a NBN of 28. Tradeoffs for fuel rates and engine rating versus fuel quality are illustrated. Cost of service analyses may dictate fuel stripping since the heavy hydrocarbons that generally contribute to the high NBN also generally have high boiling points. In the mixture-to-NBN conversion example shown above, serious consideration would be given to stripping out *n*-heptane which would reduce the mixture NBN from 19.13 to 9.43, thus allowing standard compression ratio to be used with a significant fuel saving.

Figure 6 is a plot of fuel rate versus NBN for the Cooper 16W330 two-cycle turbocharged engine. A plot of this type provides a useful overview of the total options available for a particular engine model.

1 Note that optimization of compression ratio for a particular NBN requirement is required to provide minimum fuel rate. Excessive spark retard with higher compression ratio results in fuel rate penalty.

2 Spark retard becomes ineffective at lower compression ratios for controlling sensitivity.

3 Excessive compression ratio reduction not only adversely affects fuel consumption, but increases heat rejection requirements for jacket water and lube oil. Correct matching of the engine to the fuel is important.

Test data recorded from Laboratory and Production engines with jet-cell ignition and higher charging pressures (clean-burn mode) exhibit additional NBN capability. Advantage is taken of this by adjusting the compression ratio upward to further lower fuel rate while maintaining commercial operating margin.

Table 3 for the blower scavenged engine represents a relatively simple matrix of adjustment options. Additional options are provided by the turbocharged engines since turbo matching can be used to tailor air flow and charging pressure to particular requirements of ambient temperature and altitude. Still more options are provided by the extended combustion-stable fuel–air ratio of the clean-burn concept.

Combustion flexibility that exists in all Cooper engines produced since 1950 relates to the fact that trapped mixture is regulated to be fuel lean and have 10 to 30 percent excess air.

Nomenclature

amb = ambient temperature, °F
amt = air manifold temperature, °F
$B \times S$ = bore × stroke, in.
bmep = brake mean effective pressure
bsfc = brake specific full consumption, LHV Btu/hp-hr
CR = volumetric compression ratio
F/A = fuel-air ratio
ign = ignition timing, crank degrees before top center
LP = liquefied petroleum
NBN = normal butane number: a measure of fuel sensitivity equal to that of the volumetric percent of *n*-butane blended in methane
% Air = combustion air flow, SCFM, percentage of engine displacement
rpm = revolutions per minute

Downloaded 01 Jun 2010 to 171.66.16.71. Redistribution subject to ASME license or copyright; see http://www.asme.org/terms/Terms_Use.cfm

Table 1 Sensitivity test matrix for GMVA-12

Line	bmep	ign.	amb.	amt	Percent air	Percent C_4	Δ C_4	Percent C_5	Percent C_6	Percent C_7	NBN equivalent from established curves C_5	C_6	C_7	Sum $C_4 + C_5 + C_6 + C_7$
1	79.3	14 deg	100 deg	145 deg	180	11.05								
2						8.14		0.49	0.23	0.18	1.40	1.00	0.80	11.34
3						0.00	11.05	2.63						
4						0.00	11.05		2.24					
5						0.00	11.05			1.23				
6	79.3	10 deg	100 deg	145 deg	180	13.90					2.00	1.50	1.20	13.81
7						9.11		0.68	0.33	0.25				
8						0.00	13.90	3.50						
9						1.35	12.60	2.83						
10						5.14	8.80	1.84						
11						0.00	13.90		2.37					
12						2.40	11.50		2.11					
13						6.73	7.20		1.18					
14						0.00	13.90			1.68				
15						4.05	9.90			1.44				
16						5.76	8.10			0.89				
17	79.3	6 deg	100 deg	145 deg	180	13.95					1.3	0.90	0.70	12.96
18						10.06		0.44	0.21	0.16				
19						0.00	13.95	3.50						
20						0.00	13.95		2.30					
21						0.00	13.95			1.65				

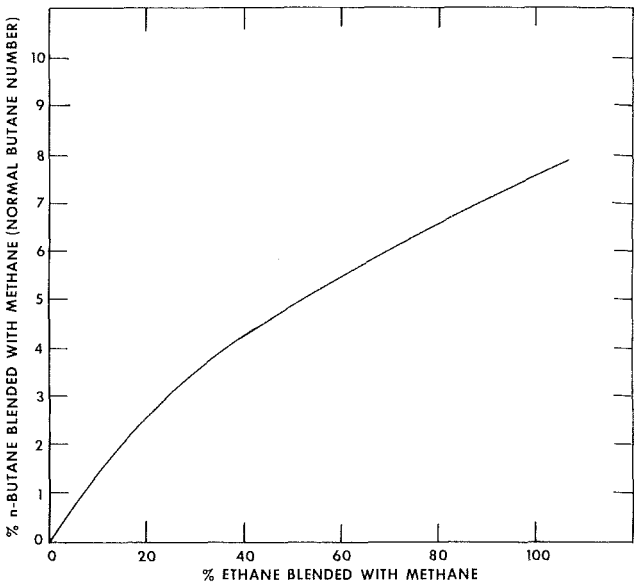


Fig. 1 Ethane NBN equivalent; extrapolated data for C-B engines

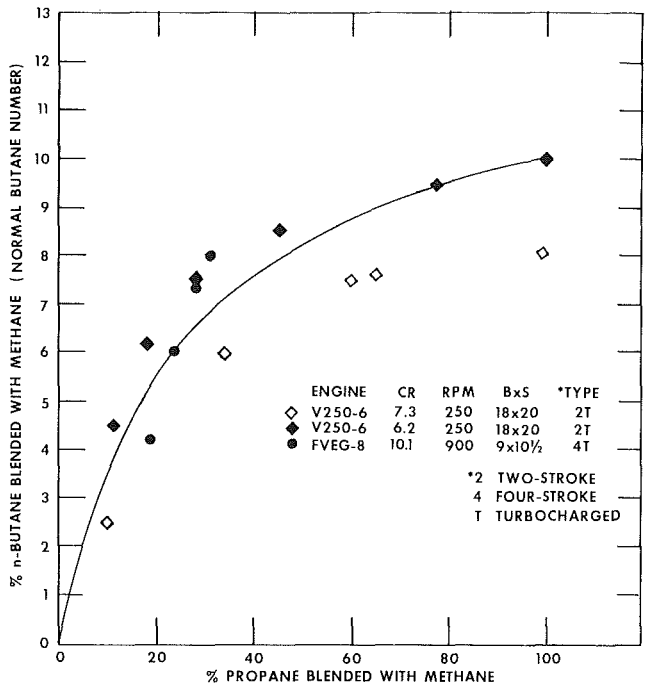


Fig. 2 Propane NBN equivalent; C-B engines

Recent clean-burn techniques have extended this range to 80 percent excess air.

Blending Technique

Normal butane is a convenient "spiker" for sensitivity work. Bulk *n*-butane is stored in a 1000-gal standard LP outside tank and is transported as liquid in standard 23-gal or 46-gal tanks to the laboratory or erection floors. Additional *n*-butane was purchased by our company in June 1984 for 98 cents per gallon with an analysis of 97 percent *n*-butane, 1 percent propane, and 1 percent iso-butane. Precise analyses are obtained and recorded. The *n*-butane is easily metered in liquid phase, vaporized, and blended with natural gas. Its sensitivity level is ideal for large engines since a NBN of 10 approaches the upper sensitivity limit of standard high-compression engines and a NBN of 30 approaches the limit for lowest compression engines. Prototype NBN test work on

Downloaded 01 Jun 2010 to 171.66.16.71. Redistribution subject to ASME license or copyright; see http://www.asme.org/terms/Terms_Use.cfm

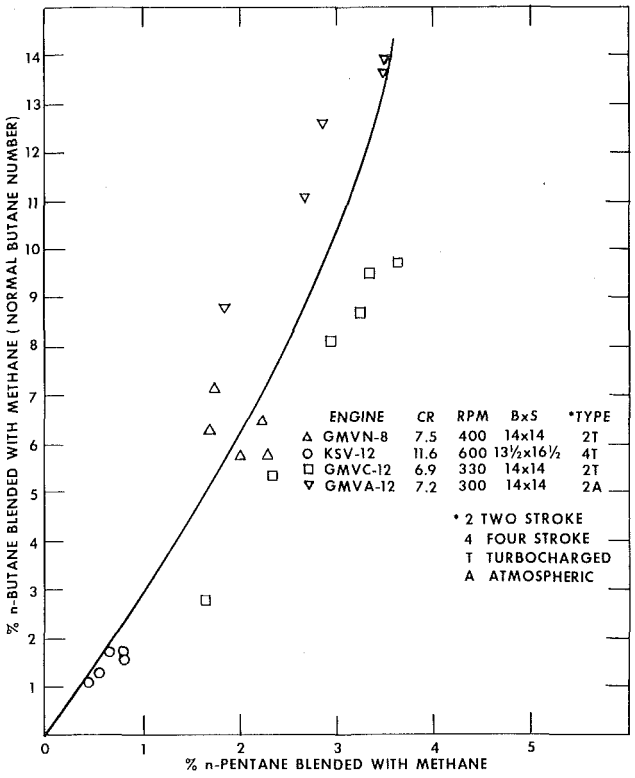


Fig. 3 *n*-Pentane NBN equivalent; C-B engines

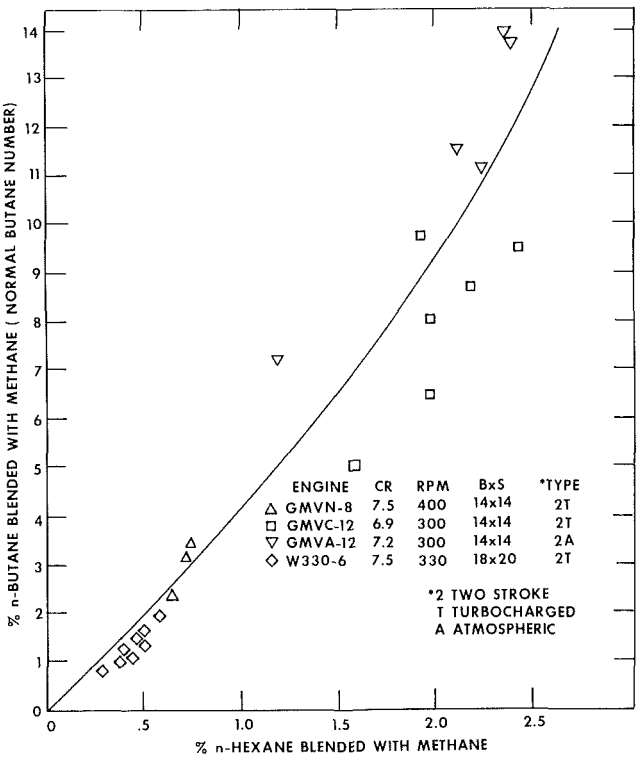


Fig. 4 *n*-Hexane NBN equivalent; C-B engines

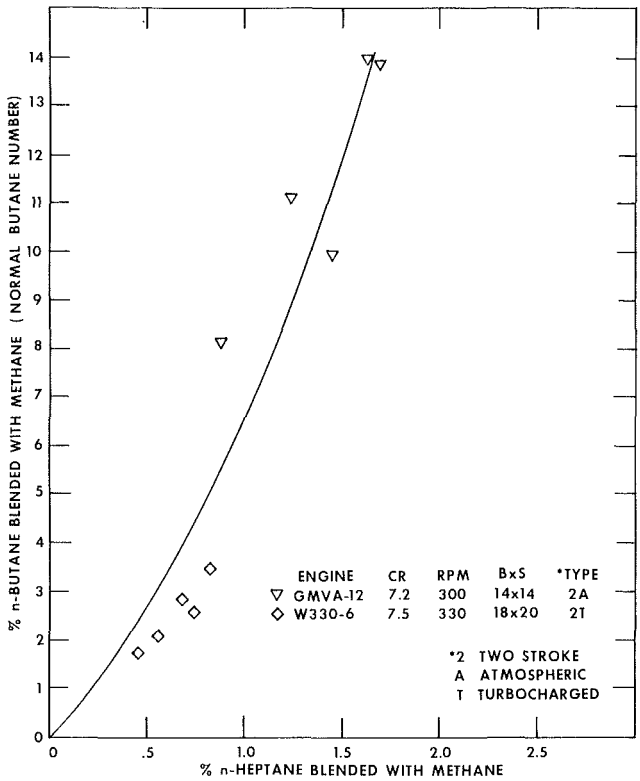


Fig. 5 *n*-Heptane NBN equivalent; C-B engines

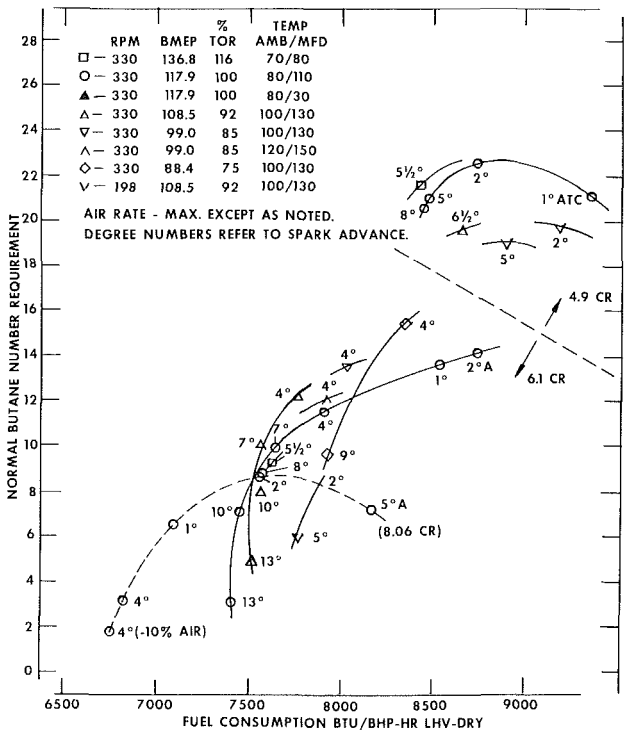


Fig. 6 16 W330 fuel consumption versus NBN requirement

a Cooper 16W330 engine (8000 bhp) would typically require 175 gal of *n*-butane.

Figure 7 is a photograph of a portable two-blend metering system. Liquid is transferred from standard LP tanks using an air-powered gear pump to partially fill the vertical canisters. The canisters and the vertical high-pressure sight glasses are carefully calibrated for liquid capacity with graduate marks scribed for equal increments in liters. During the blending operation nitrogen under pressure is applied to the top of the fluid which displaces the fluid from the bottom of the canister to the vaporizing and blending tank shown in Fig. 8. The blending tank shown is a modified lube oil heat exchanger which has the shell fitted with nine 19.5 gph furnace nozzles. Primary fuel gas is piped to pass through the shell side of the cooler and low-pressure plant steam is passed

Downloaded 01 Jun 2010 to 171.66.16.71. Redistribution subject to ASME license or copyright; see http://www.asme.org/terms/Terms_Use.cfm

Table 2 Study of NBN accuracy using multiple blends

LINE	BMEP	IGN.	AMB.	AMT	% AIR	% C_4	% C_5	% C_6	% C_7	NBN Equiv. from Established Curves C_5	C_6	C_7	Sum $C_4 + C_5 + C_6 + C_7$	Error
GMVA-12 7.2 C.R. 300 RPM 14 x 14 Two Cycle Atmospheric														
1	79.3	14°	100°	145°	180	11.05								
1A	79.3	14°	100°	145°	180	8.14	.49	.23	.18	1.40	1.00	0.80	11.34	+ .29
2	79.3	10°	100°	145°	180	13.90								
2A	79.3	10°	100°	145°	180	9.11	.68	.33	.25	2.00	1.50	1.20	13.81	- .09
3	79.3	6°	100°	145°	180	13.95								
3A	79.3	6°	100°	145°	180	10.06	.44	.21	.16	1.30	0.90	0.70	12.96	- .99
4	79.3	10°	100°	140°	166	11.52								
4A	79.3	10°	100°	140°	166	8.49	.34	.16	.12	1.00	0.60	0.60	10.69	- .83
5	79.3	10°	76°	115°	186	18.90								
5A	79.3	10°	76°	115°	186	12.68	.67	.32	.24	2.00	1.30	1.10	17.08	-1.82
6	79.3	10°	120°	170°	176	9.93								
6A	79.3	10°	120°	170°	176	2.65	.89	.43	.33	2.60	1.90	1.70	8.85	-1.08
GMVH-12 8.8 C.R. 330 RPM 14 x 14 Two Cycle Turbocharged														
7	111.4	5°	55°	81°	199	5.78								
7A	111.4	5°	55°	81°	199	3.65	.23	.11	.08	.60	.50	.40	5.15	- .63
GMVC-12 6.9 C.R. 300 RPM 14 x 14 Two Cycle Turbocharged														
8	102.2	10°	100°	130°	200	8.07								
8A	102.2	10°	100°	130°	200	6.36	.32	.15		1.00	0.70		8.06	- .01
9	102.2	10°	120°	130°	190	6.45								
9A	102.2	10°	120°	130°	190	4.08	.57	.28		1.70	1.10		6.88	+ .43
10	102.2	10°	80°	130°	200	8.72								
10A	102.2	10°	80°	130°	200	5.63	.59	.29		1.80	1.20		8.63	- .09
11	102.2	8°	100°	130°	200	9.54								
11A	102.2	8°	100°	130°	200	4.89	.98	.47		3.00	1.90		9.79	+ .25
12	102.2	6°	100°	130°	200	9.78								
12A	102.2	6°	100°	130°	200	5.98	.68	.33		2.00	1.30		9.28	- .50
13	102.2	10°	100°	130°	181	5.44								
13A	102.2	10°	100°	130°	181	3.42	.52	.25		1.50	1.00		5.92	+ .48
14	86.9	10°	100°	130°	190	8.81								
14A	86.9	10°	100°	130°	190	6.31	.71	.34		2.00	1.40		9.71	+ .90
15	71.5	10°	100°	130°	173	11.65								
15A	71.5	10°	100°	130°	173	8.99	.83	.40		2.50	1.60		13.09	+1.44
KSV-12 11.6 C.R. 600 RPM 13⅛ x 16½ Gas Diesel Four Cycle Turbocharged														
16	200	9°	80°	100°	200	4.37								
16A	200	9°	80°	100°	200	3.54	.20	.09	.07	.60	.30	.30	4.74	+ .37
17	200	9°	80°	86°	200	5.59								
17A	200	9°	80°	86°	200	4.31	.31	.15	.11	.90	.60	.50	6.31	+ .72
18	200	9°	80°	100°	190	3.83								
18A	200	9°	80°	100°	190	2.63	.18	.09	.07	.60	.30	.30	3.83	.00

Table 3 GMVA-12 sensitivity summation

n-Butane sensitivity	bmep	CR*	amb.	amt	Percent air	Ignition timing	bsfc
7.0	82.5	8.4	100 deg	145 deg	180 percent	10 deg	7300
10.0	82.5	8.4	100 deg	150 deg	200 percent	4 deg	7700
11.0	82.5	8.4	80 deg	115 deg	180 percent	10 deg	7300
14.0	82.5	8.4	80 deg	120 deg	200 percent	4 deg	7700
6.0	92.5	8.4	120 deg	170 deg	200 percent	4 deg	7700
8.0	74.3	8.4	120 deg	170 deg	200 percent	4 deg	8200
12.0	74.3	8.4	100 deg	150 deg	200 percent	4 deg	8200
16.0	74.3	8.4	80 deg	115 deg	200 percent	4 deg	8200
11.0	82.5	7.2	100 deg	145 deg	180 percent	13 deg	8100
14.0	82.5	7.2	100 deg	150 deg	200 percent	7 deg	8500
15.0	82.5	7.2	80 deg	115 deg	180 percent	13 deg	8100
18.0	82.5	7.2	80 deg	120 deg	200 percent	7 deg	8500
10.0	82.5	7.2	120 deg	170 deg	200 percent	7 deg	8500
11.0	74.3	7.2	120 deg	170 deg	200 percent	7 deg	8900
15.0	74.3	7.2	100 deg	150 deg	200 percent	7 deg	8900
19.0	74.3	7.2	80 deg	115 deg	200 percent	7 deg	8900
18.0	67.2	5.0	100 deg	150 deg	200 percent	15 deg	9000
22.0	67.2	5.0	100 deg	150 deg	200 percent	9 deg	9500
25.0	67.2	5.0	80 deg	120 deg	200 percent	15 deg	9000
28.0	67.2	5.0	80 deg	120 deg	200 percent	9 deg	9500
15.0	67.2	5.0	120 deg	170 deg	200 percent	9 deg	9500

*Based on cylinder volume above exhaust ports

Downloaded 01 Jun 2010 to 171.66.16.71. Redistribution subject to ASME license or copyright; see http://www.asme.org/terms/Terms_Use.cfm

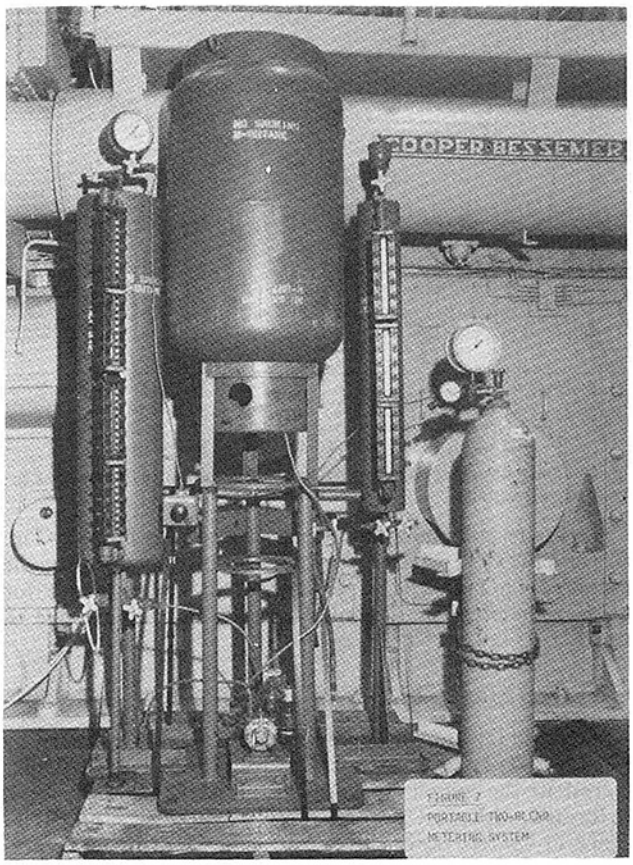


Fig. 7(*a*) Portable two-blend metering system

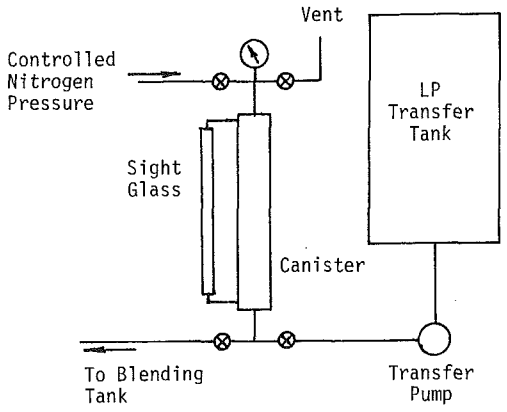


Fig. 7(*b*) Schematic diagram

through the tubes to assure complete vaporization of the butane or other hydrocarbon being injected through the nozzles. Hydrocarbon flow is controlled by a combination of nitrogen pressure adjustment to the canister and selection of active nozzles in the blending tank. Time is recorded for a select liquid level drop.

Prior to doing blending work steam is admitted to the blending tank to stabilize the fuel gas temperature at 160° to 170°F. Actual blending injection periods of 2–3 min allow stable detonation to be established and flows recorded for the blending hydrocarbon and the primary fuel gas. A check on blending flow is provided by comparing the combined energy flow rate during blending to the energy flow of the primary fuel recorded just prior to blending. Multiple hydrocarbons can be introduced by combining select ratios of liquids in one canister and introducing the mix separately or at the same

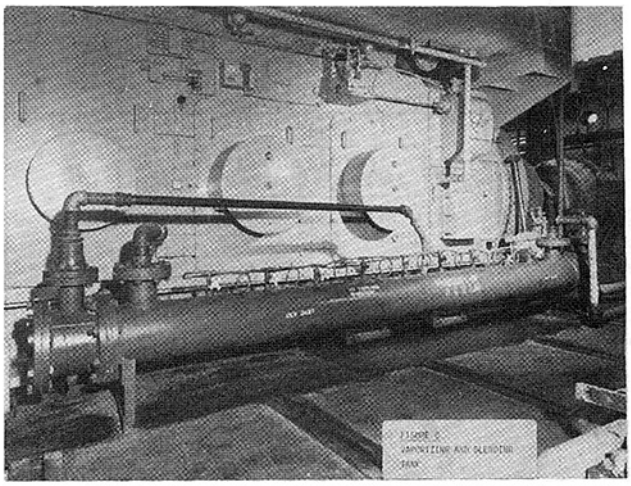


Fig. 8 Vaporizing and blending tank

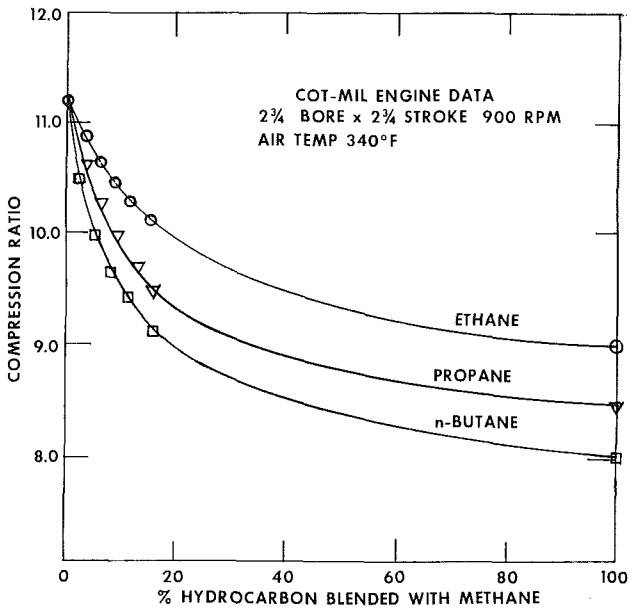


Fig. 9 COT-MIL engine basic sensitivity tests; knock limit CR

time *n*-butane or another hydrocarbon is introduced from the second canister. Good vaporization, and therefore good flow measurement, is generally assured if detonation intensity is readily controlled by the nitrogen pressure and found free of time lag.

Some engine governor control action takes place during the blending transition due to fuel gas enrichment, but operators soon learn to perform the task smoothly. Fuel–air mixture controllers which function from fuel gas header pressure must be set in manual mode due to the reduction in header pressure with blending. Care must be taken to size fuel gas injection valves for fuel enrichment to preclude mixing problems.

COT-MIL Engine Activity

A Waukesha 2-3/4 in. × 2-3/4 in. COT-MIL engine was developed in the mid-1950s for use in Korea by the U.S. Army Quartermaster Corps to qualify available fuels for military use. (A bitter lesson had been learned by the Army in Africa in WW 2 when forced to use fuels with unknown composition.) The basic frame design of this lightweight engine was first produced in the late 1930s for the ASTM Cooperative Oil Test engine (COT). The work by Waukesha in the mid-1950s qualified this engine to duplicate CFR engine

Downloaded 01 Jun 2010 to 171.66.16.71. Redistribution subject to ASME license or copyright; see http://www.asme.org/terms/Terms_Use.cfm

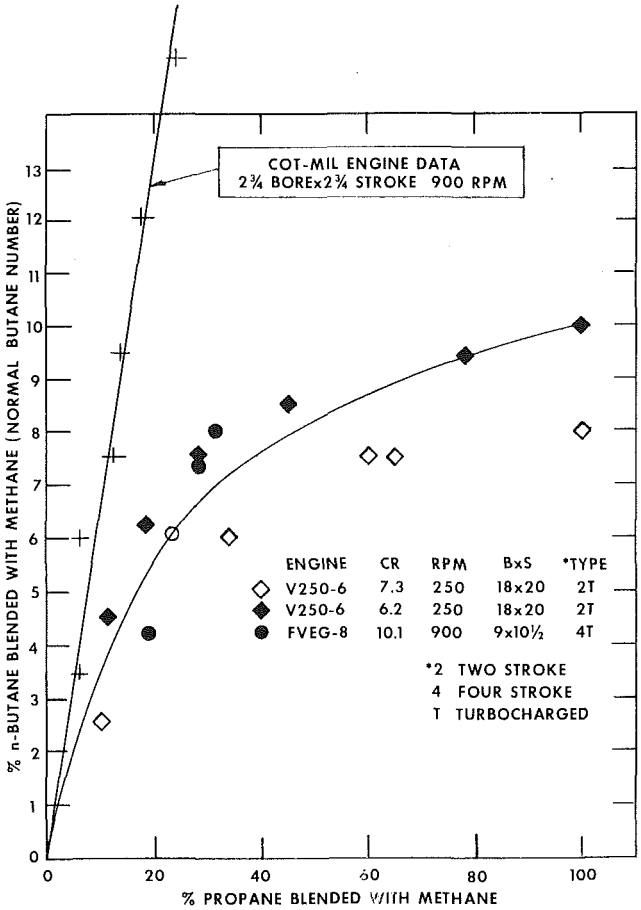


Fig. 10 Propane NBN equivalent; C-B engines versus COT-MIL engine

motor and research method capability. It resulted in a complete package weight of 600 lb as compared to 2750 lb for the CFR engine.

Cooper's interest in a portable fuel test engine was the result of field problems related to poor quality fuel. A correlation had to be established between the knock rating of these field gases and the sensitivity characteristics of the several type engines.

Waukesha agreed to modify a COT-MIL engine to accept either liquid or gaseous fuels and delivery was made to our laboratory in mid-1962. During the following three-year period a considerable volume of gaseous fuel data was generated which included various paraffinic group blending with methane and various correlation studies.

Figure 9 illustrates some of this work. Full-size engine work also continued and engine size effects were studied. Knock limiting compression ratios for a range of fuels are shown below:

Fuel	*Motor method octane*	*Cooper NBN*	*CR Cooper GMVA*	*CR COT-MIL*
100 percent methane	122	0	10.5	11.0
100 percent ethane	101.3	7.5	8.4	8.9
100 percent propane	97.1	10.0	7.2	8.4
18 percent *n*-butane/82 percent methane	116.1*	18.0	5.0	9.1
100 percent *n*-butane	89.5	100.0	Too sensitive	7.8

*Waukesha method for gas octane number (blends)

An attempt is made to partly offset the inherent lack of fuel sensitivity for the small-bore high-speed engine by its high jacket water temperature (212°F) and high air manifold temperature (340°F); however, a significant difference in compression ratio, compared to the large-bore engine, is found for fuels heavier than methane.

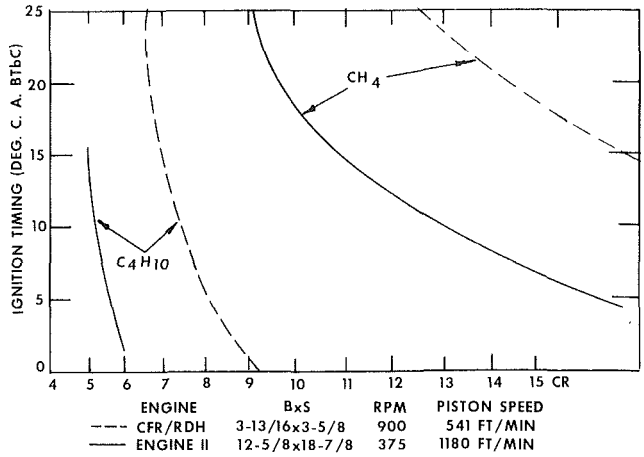


Fig. 11 Data from [2]; comparative knock limit compression ratios for two sizes of engines

The engine size and speed effect are also illustrated by Fig. 10. Here the COT-MIL engine NBN equivalence for propane is plotted on Fig. 2 (Cooper engine NBN equivalence for propane) to illustrate a significant shift in response due to engine size.

Size Effect Studies by Others

Reference [2] summarizes the excellent work performed by AVL and reported at CIMAC in May 1971. Of particular interest are the comparative evaluations of the extensive work performed with fuel gas mixtures using their CFR/RDH engine (3-13/16" bore × 3-5/8" stroke) and the work performed with their Engine II (12-5/8" bore × 18-7/8" stroke). Figure 11 is constructed from data contained in Figs. 1 and 24 from [2]. Figure 11 illustrates the size and speed effect of the above engines in terms of the knock limit compression ratio, including both methane and *n*-butane. It clearly illustrates the greater tolerance of the small-bore high-speed engine. Reference [2] discusses the fact that auto-ignition behavior of fuels in compression apparatuses and engines has been shown by a great number of investigations to be a function of the temperature-time and pressure-time history of the knocking end gas. A small engine/large engine comparison at equal piston speed illustrates that the time ΔT for a given crank angle $\Delta\alpha$ may change by a factor of five. Differences of such magnitude never occur in pressure and temperature.

Data are included in [2] to determine sensitivity levels of propane/methane and *n*-butane/methane blends for both the CFR/RDH and Engine II engines. This was sufficient information to establish the NBN equivalence for propane for each engine and this information is plotted in Fig. 12. Note that the 12-5/8" × 18-7/8" engine data closely follow the Cooper curve and the small CFR/RDH engine parallels the COT-MIL curve.

Taylor [3] provides detail of the work at MIT which was directed to the study of cylinder size and detonation correlation. His conclusions and our results are in agreement.

Downloaded 01 Jun 2010 to 171.66.16.71. Redistribution subject to ASME license or copyright; see http://www.asme.org/terms/Terms_Use.cfm

Table 4 Engine specifications and test conditions for small-bore fuel testing engines

	ASTM	Engine Designation	Method	Application	Size B x S	Speed	Ign. Timing	Air Temp. °F	Jkt. Temp. °F	F/A	C.R.	Mfd. Press.
a)	D2623-83	ASTM-CFR	Motor	LP Gas	3¼ x 4½ (37.4 in³)	900	Var.	300	212	Max. Knock	Var.	ATM
b)	D2699-83	ASTM-CFR	Research	Motor Fuel	3¼ x 4½	600	13°	125	212	Max. Knock	Var.	ATM
c)	D2700-83	ASTM-CFR	Motor	Motor Fuel Aviation Fuel	3¼ x 4½	900	Var.	300	212	Max. Knock	Var.	ATM
d)	D2885-83		Research & Motor	On-Line Analyzers	Provides automatic on-line analysis by either research or motor method conditions of test.							
e)	D2886-83		Distribution Octane No.	Motor Fuel	Provides measure of road antiknock ratings of motor fuels in passenger vehicles at high load, low engine speed. Involves basic D2699 research method with special intake manifold to simulate maldistribution.							
f)	D909-83	ASTM-CFR	Superchg.	Aviation Fuel	3¼ x 4½	1800	45°	225	375	Max. Power	7.0	15" to 110" Hg. ABS.
g)		GM Var. C.R.		Gives critical compression ratio data	3¼ x 4½	600	Max. Power	100	212	Max. Power	Var.	ATM
		"		"	"	600	"	150	350	"	"	"
		"		"	"	2000	"	100	212	"	"	"
		"		"	"	2000	"	150	350	"	"	"
h)		Ethyl 17.6 in³	Superchg.	Supercharged Test Work	17.6 in³	900	20°		300	Max. Knock	5.6	15" to 135" Hg. ABS.
j)		COT-MIL	Research	Portable Military	2-3/4 x 2-3/4	600			212	Max. Knock	Var.	ATM
k)		COT-Mil	Motor	Portable Military	2-3/4 x 2-3/4	900	Var.	340	212	Max. Knock	Var.	ATM
l)		AVL-CFR/RDH		Gas Engines	3-13/16 x 3-5/8	900	15°	68	176	Chem. Correct	Var.	ATM

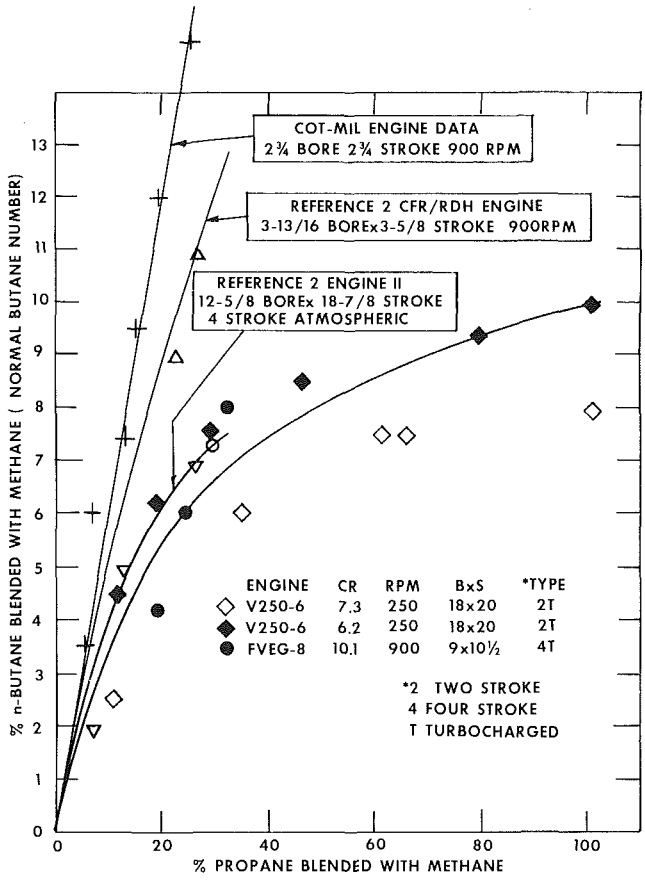


Fig. 12 Propane NBN equivalent; C-B engines; COT-MIL engine; engines from [2]

General Discussion and Conclusions

The NBN procedure, like the established ASTM small-engine procedures or the AVL hydrogen/methane procedure [2], relies entirely on empirical information. Table 4 lists specifications and test conditions for the many types of small fuel research engines for which there are published performance data. The methane number method of [2], like other methods, illustrated the dominant effect of engine bore size. Therefore, meaningful data would necessarily be generated on the large-bore engines. Procurement and handling of sizable quantities of hydrogen present a serious drawback to this method.

Work has been directed by the petroleum and automotive industries to better understand the correlation between fuel molecular structure, chemical reactions, and phenomenon of knock. Reference [1] suggests that progress in this area has been important in directing chemical refining processes. Figure 13 is included from [1] to illustrate the interesting paraffin grouping.

The gaseous fuels commonly used for large-bore engines, unlike liquid fuels, are generally paraffin hydrocarbons with constituents numbering ten or less. Reference [1] concludes that the paraffin hydrocarbons are the best behaved class, exhibiting good correlation between molecular structure and knocking behavior. Paraffins have the least "sensitivity" (ASTM terminology for the difference in knock rating for low-temperature, low-speed research method versus high-temperature, high-speed motor method) and therefore have more predictable performance under different operating requirements. Paraffins are unique in their consistent response to antiknock additives.

During the twenty years of NBN procedure usage *n*-butane equivalence information for hydrocarbons and other combustible gases has been generated in addition to that shown in Figs. 1–5. The work presented in [1], although not specifically applicable, can be used as an aid to relate to untested fuels. Reference [1] was last published in 1958 and copies are available on microfilm through ASTM (Philadelphia, PA).

It is hoped that the information contained in this paper regarding methodology and data may help extend the data base for the large-bore gas engine industry. A commonality of procedures and terminology can serve the same useful purpose for the large-engine manufacturers and users as the existing ASTM procedures have served the small-engine industry.

Downloaded 01 Jun 2010 to 171.66.16.71. Redistribution subject to ASME license or copyright; see http://www.asme.org/terms/Terms_Use.cfm

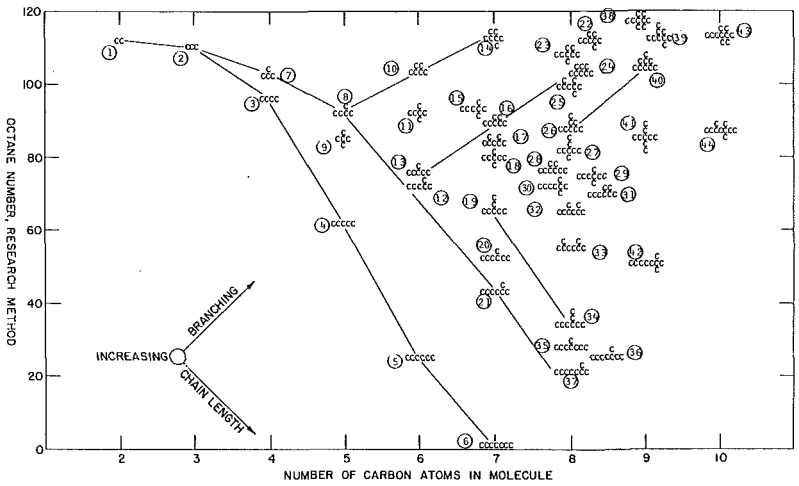


Diagram No.	Common System of Nomenclature	Geneva System of Nomenclature	Formula	Mol. Wt.	Diagram No.	Common System of Nomenclature	Geneva System of Nomenclature	Formula	Mol. Wt.
1	Ethane		C_2H_6	30.07	22	Isooctane	2,2,3-Trimethylpentane	C_8H_{18}	114.22
2	Propane		C_3H_8	44.09	23	Isooctane	2,3,3-Trimethylpentane	"	"
3	n-Butane		C_4H_{10}	58.12	24	Isooctane	2,3,4-Trimethylpentane	"	"
4	n-Pentane		C_5H_{12}	72.15	25	Isooctane	2,2,4-Trimethylpentane	"	"
5	n-Hexane		C_6H_{14}	86.17	26	Isooctane	2-Methyl-3-Ethylpentane	"	"
6	n-Heptane		C_7H_{16}	100.20	27	Isooctane	3- " 3- "	"	"
7	Isobutane		C_4H_{10}	58.12	28	Isooctane	3,4-Dimethylhexane	"	"
8	Isopentane	2-Methylbutane	C_5H_{12}	72.15	29	Isooctane	3,3- "	"	"
9	Neopentane	2,2-Dimethylpropane	C_5H_{12}	72.15	30	Isooctane	2,2- "	"	"
10	Isohexane	2,3-Dimethylbutane	C_6H_{14}	86.17	31	Isooctane	2,3- "	"	"
11	Isohexane	2,2-Dimethylbutane	"	"	32	Isooctane	2,4- "	"	"
12	Isohexane	2,-Methylpentane	"	"	33	Isooctane	2,5- "	"	"
13	Isohexane	3,-Methylpentane	"	"	34	Isooctane	3-Ethylhexane	"	"
14	Isoheptane	2,2,3-Trimethylbutane	C_7H_{16}	100.20	35	Isooctane	4-Methylheptane	"	"
15	Isoheptane	2,2-Dimethylpentane	"	"	36	Isooctane	3- "	"	"
16	Isoheptane	2,3-Dimethylpentane	"	"	37	Isooctane	2- "	"	"
17	Isoheptane	2,4-Dimethylpentane	"	"	38	Isononane	2,2,3,3-Tetramethylpentane	C_9H_{20}	128.25
18	Isoheptane	3,3-Dimethylpentane	"	"	39	Isononane	2,2-Dimethyl-3-Ethylpentane	"	"
19	Isoheptane	3-Ethylpentane	"	"	40	Isononane	2,4- " 3 "	"	"
20	Isoheptane	3-Methyhexane	"	"	41	Isononane	3,3-Diethylpentane	"	"
					42	Isononane	2,2-Dimethylheptane	"	"
					43	Isodecane	2,2,3,3-Tetramethylhexane	$C_{10}H_{22}$	142.27
					44	Isodecane	3,3,5-Trimethylhexane	"	"

Fig. 13 Correlation between fuel molecular structure and research method octane number; diagram taken from [1]

Acknowledgments

The authors would like to thank the management of Cooper-Bessemer Reciprocating Products, Energy Services Group, Cooper Industries, for permission and support to publish this paper. Recognition for contribution should go to the Research and Development Laboratory staff and to Engineering Design personnel.

References

1 *Knocking Characteristics of Pure Hydrocarbons*, ASTM Special Technical Publication 225, American Society for Testing Materials, May 1958.

2 Leiken, M., Christoph, K., Rankl, M., Cantellier, W., and Pfeifer, U., "Evaluation of Antiknocking Property of Gaseous Fuels by Means of Methane Number and Its Practical Application to Gas Engines," ASME Paper No. 72-DGP-4.

3 Taylor, C. F., "The Effects of Cylinder Size on Detonation and Octane Requirement," SAE Paper, presented January, 1961, SAE International Congress and Exposition of Automotive Engineering, Detroit, MI.

4 "Test Methods for Rating Motor, Diesel, Aviation Fuels," 1984 Annual Book of ASTM Standards, Section 5, Vol. 05.04.

5 Baxter, I., "Determination and Significance of Gaseous Fuel Octane Numbers," ASME Paper No. 64-OGP-6.

APPENDIX

Metric Equivalents

Readers more familiar with metric units are asked to use the following information to convert the nonmetric units used in this paper:

Nonmetric	*Multiplied by*	*Yields metric*
Btu	1055	J(W-s)
(°F − 32)	0.5556	°C
hp	745.7	W
in.	0.0254	m
psi	6895	N/m^2
scf	0.0283	m^3
sq in.	6.452×10^4	m^2

Downloaded 01 Jun 2010 to 171.66.16.71. Redistribution subject to ASME license or copyright; see http://www.asme.org/terms/Terms_Use.cfm

The Design, Performance and Analysis of a High Work Capacity Transonic Turbine

J. D. Bryce

M. R. Litchfield

N. P. Leversuch

Procurement Executive, Ministry of Defence, Royal Aircraft Establishment, Pyestock, Farnborough, Hampshire, England

This paper describes the design and testing of a high work capacity single-stage transonic turbine of aerodynamic duty tailored to the requirements of driving the high-pressure core of a low cost turbofan engine. Aerodynamic loading was high for this duty ($\Delta H/\bar{U}^2 = 2.1$) and a major objective in the design was the control of the resulting transonic flow to achieve good turbine performance. Practical and coolable blading was a design requirement. At the design point (pressure ratio = 4.48), a turbine total to total efficiency of 87.0 percent was measured – this being based on measured shaft power and a tip clearance of 1.4 percent of blade height. In addition, the turbine was comprehensively instrumented to allow measurement of aerofoil surface static pressures on both stator and rotor – the latter being expedited via a rotating scanivalve system. Downstream area traverses were also conducted. Analysis of these measurements indicates that the turbine operates at overall reaction levels lower than design but the rotor blade performs efficiently.

Introduction

Compared with its two-stage counterpart, the single-stage high-pressure (HP) turbine offers potential benefits in terms of reduced cost, weight, cooling air and maintenance. The overall commercial competitiveness of an engine is very dependent on the aerodynamic performance of the HP turbine and on the disk and blade lives attainable. For a low-cost, high overall pressure ratio two-shaft turbofan or turboshaft engine, the work duty of a single stage HP turbine is high. If blade speeds are deliberately constrained on the basis of achieving moderate levels of disk and blade stress, then resultant aerodynamic loading is severe ($\Delta H/\bar{U}^2 > 2.0$. The supersonic airflows associated with such a loading pose considerable aerodynamic problems and the question arises as to what level of performance can be achieved from such a turbine with practical blading.

In recognition of these problems research has been conducted at the Propulsion Department, Royal Aircraft Establishment, Pyestock, on a highly loaded turbine of moderate blade speed. This paper describes the aerodynamic design of the turbine and the testing in both cascade and in a cold flow turbine rig using solid blading. Analysis of results and suggestions for further improvement of performance are also described.

Aerodynamic Design

The turbine design point was chosen on the basis of driving the high-pressure core of a low-cost high overall pressure ratio two-shaft turbofan or turboshaft engine. From considerations of the overall engine cycle the turbine has been designed to have a work capacity of $\Delta H/T = 306$ J/kg•K. Turbine blade speed as well as the choice of turbine annulus height have been deliberately constrained by considerations of blade and disk stresses so as to maximize engine life. These constraints lead to a turbine having the following design parameters:

Inlet flow function $\frac{W\sqrt{T}}{P}$	$= 0.709 \times 10^{-3}$ kg•$\sqrt{\text{K}}$•m^2/s•N
Turbine pressure ratio	= 4.48
Work capacity $\Delta H/T$	= 305.6 J/kg•K
Flow factor $\bar{V}a/\bar{U}$	= 0.566
Aerodynamic loading $\Delta H/\bar{U}^2$	= 2.11
Mean blade speed function $\bar{U}/\sqrt{T}$	= 12.0 m/s•$\sqrt{K}$
Rotor hub/tip dia ratio (mean)	= 0.87

Figure 1 shows the turbine design point superimposed on a plot of stage loading, work capacity and mean blade speed function and is compared with other high work capacity research turbines [1, 2, 3].

A meridional view of the annulus evolved in the design is

Contributed by the Gas Turbine Division of THE AMERICAN SOCIETY OF MECHANICAL ENGINEERS and presented at the 30th International Gas Turbine Conference and Exhibit, Houston, Texas, March 18–21, 1985. Manuscript received at ASME Headquarters, December 17, 1984. Paper No. 85-GT-15.

Copyright © 1985 by ASME

Downloaded 01 Jun 2010 to 171.66.16.71. Redistribution subject to ASME license or copyright; see http://www.asme.org/terms/Terms_Use.cfm

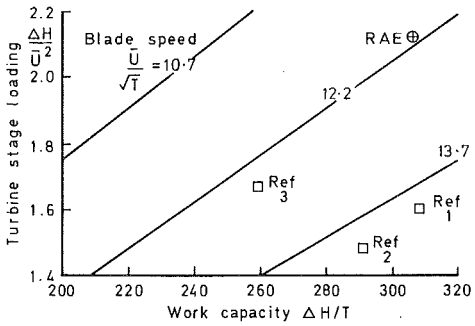


Fig. 1 Single stage HP research turbines

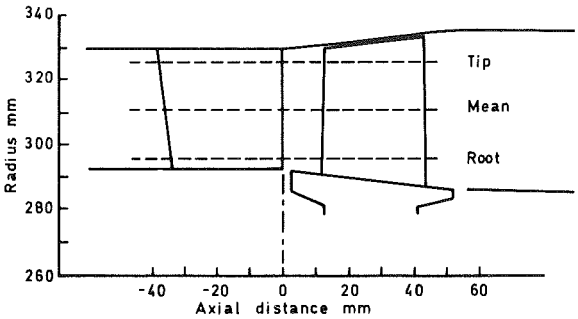


Fig. 2 Turbine annulus

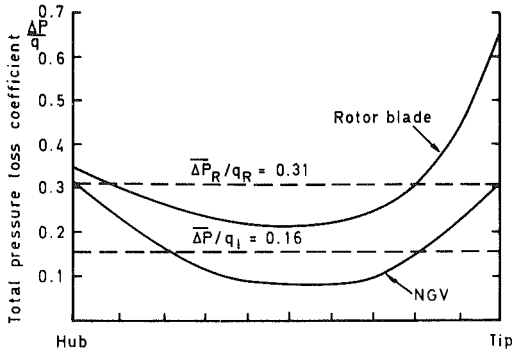


Fig. 3 Turbine losses

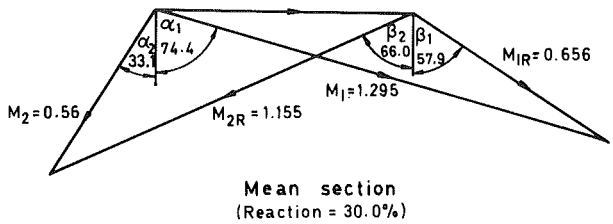


Fig. 4 Mean section vector triangle

shown in Fig. 2. It features cylindrical endwalls on the nozzle guide vane (NGV) and equal and opposite flare of 7.0 deg on the inner and outer walls of the rotor blade which is shroudless.

Estimates of NGV and rotor blade mean losses were based on published correlation methods [4] and cascade data [5] and indicated a mean total pressure loss coefficient of 0.16 and 0.31 for the nozzle and rotor blade respectively – these being based on outlet dynamic head conditions. These mean losses were distributed so as to concentrate the loss in the 30% of blade span nearest the annulus walls and thus take account of the secondary loss in these regions. The rotor blade loss was further loaded on the outer span to allow for the effect of tip clearance. The assumed distributions of loss are shown in Fig. 3.

Having established the losses, streamline curvature throughflow calculations were performed in order to determine the inlet and outlet conditions from the blading and to establish the turbine vector triangles. In selecting gas angles at exit from the NGVs and rotor blades, certain constraints were imposed. On the NGV, for example, the exit angle was kept almost constant from root to tip to minimize twist on the vane and therefore ease cooling in an engine. At the tip of the rotor blade the exit gas angle was reduced substantially, to reflect the lack of turning likely to occur due to tip clearance effects. The resulting Mach number triangle for the mean section is given in Fig. 4. It will be noted that the chosen design employs moderately high supersonic Mach numbers at exit from the NGV. This was a deliberate choice – generating the required high-whirl component at exit from the NGV – in order to limit the swirl and exit Mach number from the rotor blade. However, a result of this decision was that, at the important root section, the Mach number leaving the NGV was $M_1 = 1.32$ and the corresponding relative value on to the rotor blade was high subsonic, $M_{1R} = 0.71$. This raised a challenging factor in the design of the rotor blade. Resulting reaction was 25 and 35% at the root and tip respectively and the ratio of work output to average work was graded across the span – 0.98 at the root, 1.05 (mean), and 0.92 (tip). A total-total adiabatic efficiency of about 87% (excluding windage and bearing losses) was predicted when operating at a tip clearance of about 1% of blade height. This is a gas-path efficiency and the level would be lower if based on shaft output power.

The next stage in the design was that of selecting blade profiles to suit the vector triangles. Blade surface velocity distributions were calculated using the quasi-three-dimensional (Q3D) time-marching computer program developed by Denton [6]. The blading was essentially two dimensional in nature, no three-dimensional features such as blade lean being incorporated in the design. However, the Denton full three-dimensional program has been used in the analysis of results described later.

In the design of the NGV, with its associated supersonic exit Mach number, the initial problem was that of selecting a channel shape to achieve an acceptable velocity distribution. Deich et al. [5] have shown that at exit Mach numbers in excess of about 1.3, a convergent-divergent channel involving internal divergence after the throat and a small degree of suction surface concavity has a lower loss than a purely convergent passage. The former channel has the effect of producing a controlled expansion from the throat to the trailing edge which reduces the intensity of the trailing edge shock system and minimizes boundary layer growth on the

Nomenclature

W = mass flow rate, kg/s
M = Mach number
P = total pressure, N/m^2
T = total temperature, K
H = specific stagnation enthalpy, J/kg
V = velocity, m/s
$\bar{U}$ = mean blade speed, m/s
α = absolute gas angle
β = relative gas angle
q = dynamic head based on exit conditions
η = efficiency based on total conditions

Subscripts

1 = NGV exit
2 = rotor exit
R = relative conditions
a = axial

Downloaded 01 Jun 2010 to 171.66.16.71. Redistribution subject to ASME license or copyright; see http://www.asme.org/terms/Terms_Use.cfm

suction surface. Calculations using the Denton Q3D time-marching program further confirmed a more controlled expansion could be achieved. Zweifel lift coefficient considerations indicated a vane number of 40 and a pitch/true chord ratio of 0.70 – later confirmed by more detailed blade-to-blade calculations. The size of geometric throat was estimated from one-dimensional considerations using a throat discharge coefficient of 0.985 and the suction surface supersonic section was laid out according to the method recommended by Deich. A low trailing-edge wedge angle of approximately 4 deg was incorporated and to avoid an unacceptably thin trailing edge for cooling holes in an engine vane, a trailing-edge thickness of 1.27 mm at model scale was chosen. Gas angle deviation from metal angles was determined from expressions of continuity at the throat and the downstream condition assuming a deviation factor which was a function of NGV loss. The root section profile and the associated design surface Mach number distribution obtained from the Denton program (10 pitchwise × 40 axial grid), is shown in Fig. 5.

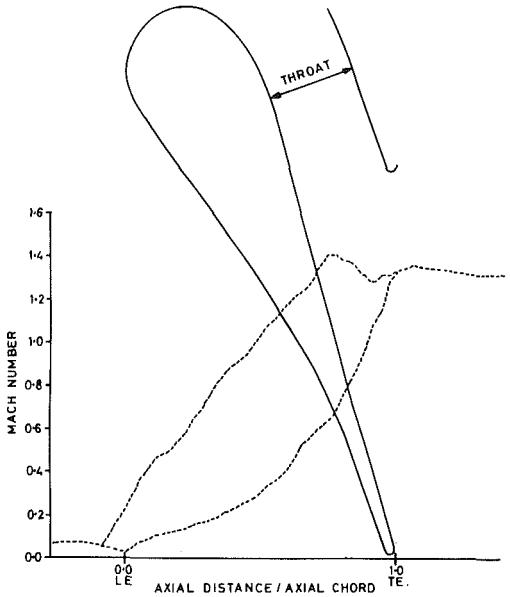


Fig. 5 NGV root design

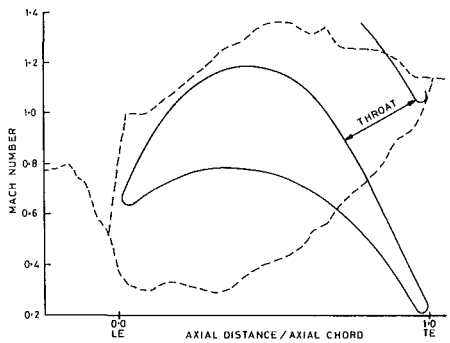


Fig. 6 Rotor blade root design

Time-marching calculations on rotor blade profiles with varying leading edge geometries demonstrated significant sensitivity to such factors as nose radius, wedge angle, and the degree of curvature on the leading suction surface. Firstly, it was found that to achieve the value of required inlet Mach number (allowing some margin for the effect of boundary layer blockage prior to the throat) then a nose radius of 0.762 mm, the minimum considered necessary for satisfactory cooling, was required for the root section. Secondly, curvature on the forward suction surface must be kept to a minimum to obtain acceptable Mach number distributions and again the need for a small nose radius was paramount. In the case of the trailing edge, it was necessary to employ low wedge angles of 4 deg and cooling requirements indicated a trailing-edge thickness of 1.016 mm at model scale. Aerodynamic lift considerations, in association with the aim to keep aspect ratio as high as possible, indicated a rotor blade prime number of 89 – this resulted in a trailing edge/throat blockage of 12% and a pitch/true chord ratio of 0.71. The throat was sized according to one-dimensional continuity and gas-deviation angles were calculated in a similar manner as for the NGV. The resulting time-marching prediction (10 × 40 grid) for the critical root section at zero incidence is shown in Fig. 6. It demonstrates that on the nose suction surface, the flow rapidly accelerates to sonic conditions and after this there is a uniform expansion up to a peak Mach number of about 1.35.

Test Rig

The location of turbine performance instrumentation in the turbine annulus is shown in Fig. 7. Air to the test rig was supplied from plant compressors and the turbine exhausted to atmospheric pressure via an exhaust diffuser system. Measurement of air-mass flow was made via a calibrated venturi-nozzle airmeter located upstream of the turbine. Power from the turbine was absorbed by a high-speed water dynamometer and the primary measurement of shaft torque was by a calibrated torquemeter. Pressure measurement was by transducers via Scanivalves and temperatures were sensed by chromel-constantan thermocouples. All readings were logged by a computer based data acquisition system which determined "on-line" turbine performance from the measurements.

In determining turbine total to total adiabatic efficiency, the most reliable and consistent values of turbine temperature drop were derived from measured shaft speed and torque in association with the measured mass flow. The other important parameter in quantifying the turbine efficiency was turbine pressure ratio. This was determined from the ratio of inlet mean total pressure and the exit total pressure as deduced from continuity considerations involving measured static

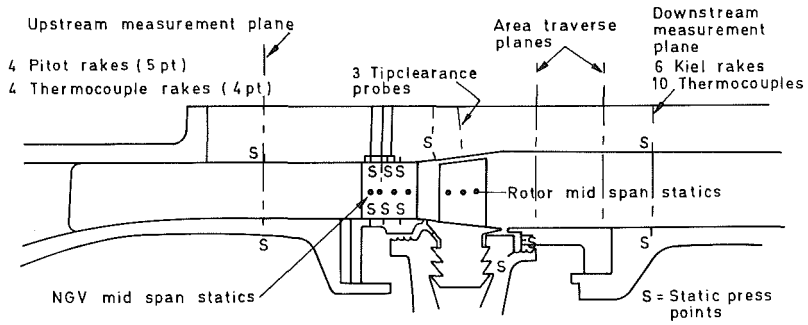


Fig. 7 Turbine test rig and instrumentation

Downloaded 01 Jun 2010 to 171.66.16.71. Redistribution subject to ASME license or copyright; see http://www.asme.org/terms/Terms_Use.cfm

pressure, mean swirl angle across the annulus and mass flow at the mixed-out plane approximately two chord lengths downstream of the rotor blade trailing edge. Comprehensive radial (35 point) traverses – supplemented by area traverses (350 point) – were taken to establish an area meaned value. The absolute level of turbine efficiency derived from these measurements is estimated to be accurate to better than ±1.0 percentage point. Being based on measured shaft power it includes the effects of windage and bearing loss, no attempt being made to measure these in the tests reported here. It is estimated that the gas-path efficiency is 1/2 to 1% higher.

Other important measurements included the facility to do full area traverses of swirl angle and total pressure downstream of the rotor. In addition the NGV was comprehensively instrumented with surface static pressure tappings along the midheight section as well as along the midpassage of the endwalls. Static tappings were incorporated on the outer annulus at NGV exit. The midheight section of the rotor blade was instrumented with ten static pressure tappings (seven on the suction and three on the pressure surface) distributed throughout the 89 rotor blades. Measurements were made via a rotating Scanivalve system with measured corrections applied for centrifugal pumping effect. Running tip clearance was also measured. The most successful method involved a stepping motor device and a probe having a sensing wire which completed an electric circuit when it touched the rotor blade tip. Measurement resolution to ±0.01 mm was achieved.

The turbine rig enabled rotor tip clearance to be altered by changing the axial spacing between the NGV and rotor assemblies. Two builds have been tested as follows:

	Build 1	Build 2
axial spacing, mm	12.0	11.0
static tip clearance, mm	0.880	0.762
running tip clearance at design point, mm	0.710	0.592
% design speed tested	80, 90, 100	80, 90, 100, 110

Build 2 was more comprehensively instrumented and incorporated the rotating Scanivalve assembly and more reliable tip clearance measurement. The importance of Build 1 was that it provided information on the effect of tip clearance, it being assumed that, as its static tip clearance was 0.118 mm greater than Build 2, then a similar difference in running clearance would be measured.

Turbine performance was measured over a range of turbine speed (80-110% design speed) and pressure ratio (2.8-5.2). Test Reynolds numbers based on true chord and blade exit conditions at the design point were 3.0×10^6 for the NGV and 0.9×10^6 for the rotor blade.

Test Results

On account of the nozzle being choked, the values of measured turbine inlet mass flow function were almost constant with turbine pressure ratio and rotational speed. The mean measured value was 1.27% lower than the design value. Considering that the midheight nozzle throat widths were set up before testing to within 1% of design, the measured mass flow function is considered reasonable and reflects well on the value of discharge coefficient assumed in the design. However, as will be seen later, this shortfall in swallowing capacity has a significant effect on the nozzle performance.

Figure 8 shows the variation of turbine efficiency with

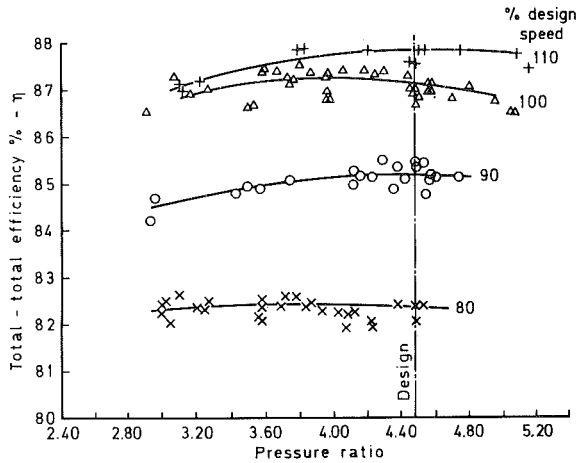


Fig. 8 Variation of efficiency with pressure ratio

pressure ratio for the Build 2 turbine. It will be noted that the general level of efficiency at each speed is relatively constant and each speed characteristic is distinct from the other, there being little overlapping at the relatively high levels of pressure ratio tested. This is because, over the majority of the tested pressure ratio range, the turbine operated with choked nozzle and rotor blade rows; and at a given speed this resulted in nearly constant inlet conditions onto the rotor blade and nearly constant losses. These losses decreased with increasing speed due to reduced incidence and Mach number onto the rotor blade. As there was no appreciable drop in efficiency at high pressure ratio it is concluded that the rotor exit shock losses were not great and the rotor blade was operating below limit load. The measured efficiency at the design point was 87.0% and the following table compares this with the corresponding value for Build 1 together with the relevant tip clearance parameters.

	Build 1	Build 2
$\frac{\text{running clearance}}{\text{mean blade height}}$, %	1.635	1.363
measured design point efficiency, %	86.3	87.0

Assuming a linear variation of efficiency with tip clearance, then the above table indicates an efficiency change of 2.6 percentage points for a 1.0 percentage point change of tip clearance/mean blade height ratio. This rate of exchange is considerably higher than quoted for a moderately loaded turbine by Patel [2] and is in better agreement with results for high reaction tip sections quoted by Haas and Kofskey [7]. It probably reflects the increased tip leakage which is likely to result with a more highly loaded tip section as present on the test turbine. Correcting the measured efficiency level of Build 2 to a tip clearance of 1% of blade height – a value of clearance which one might reasonably expect to achieve in an engine – indicates a total-total efficiency of 87.9%.

NGV Performance. The midheight surface isentropic Mach number distribution at design pressure ratio, determined from measurements of local static pressure on the NGV surface in association with inlet total pressure, is shown in Fig. 9.

It is compared with the 3D time-marching prediction and with measurements made on the midheight section in a linear cascade at Oxford University [8]. It is clear that there is reasonable agreement between prediction and measurement on both surfaces up to approximately the throat position. Downstream of the throat the turbine test measurements

Downloaded 01 Jun 2010 to 171.66.16.71. Redistribution subject to ASME license or copyright; see http://www.asme.org/terms/Terms_Use.cfm

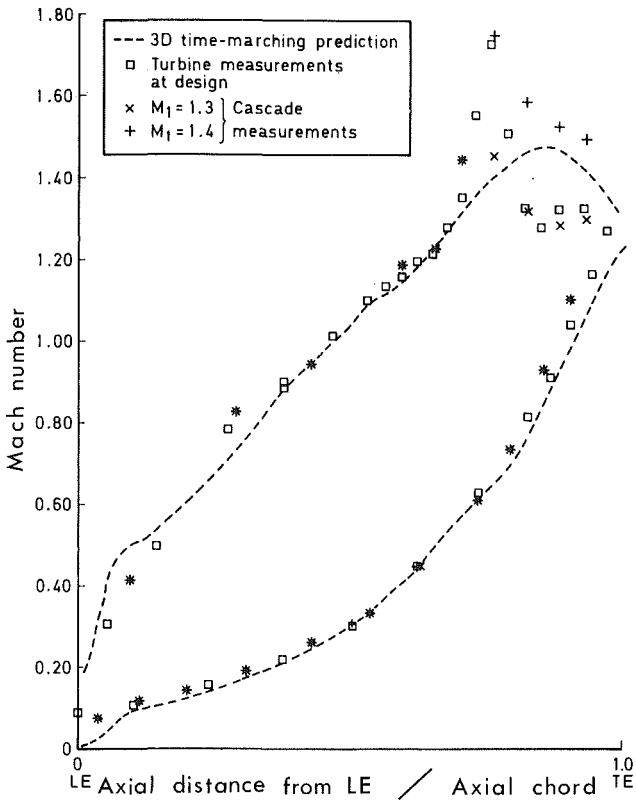


Fig. 9 NGV mean section performance

exhibit significant differences from either prediction or cascade measurements obtained at isentropic exit Mach numbers of 1.3. The turbine measurements show a very much more pronounced peak Mach number of nearly 1.8 and a sharp recompression which was probably caused by an oblique shock system (generated at the trailing edge of the adjacent vane and crossing the passage to impinge on the suction surface) of significantly greater strength than was observed in the cascade test at design conditions. Clearly, this high overexpansion on the NGV suction surface is not conducive to low loss. Throughflow syntheses of the test measurements have been performed which indicate that the effect is caused by the vane operating at significantly higher exit Mach numbers than design: arising from the 1.27% reduced swallowing capacity already mentioned. At the midheight section of the NGV this effect translates to an increase in isentropic exit Mach number from 1.33 as designed to 1.39 at test conditions. This latter condition is close to that tested at elevated exit Mach number in cascade the results of which are superimposed in Fig. 9. It will be noted that there is now better agreement between cascade and turbine test measurements, there being a similar overexpansion to a peak Mach number of about 1.8. The turbine vane does appear to have a greater recompression to lower Mach numbers after the shock which may indicate some thickening and local separation of the boundary layer on the back surface of the vane in the turbine tests.

Further evidence from the NGV midpassage static tappings on the inner annulus wall – not included here – strongly suggests that the hub region of the NGV was operating close to limit load and therefore at a significantly higher exit Mach number than design.

It is apparent that the NGV was not performing as designed and loss of performance was probably resulting from the high peak Mach numbers. An improvement could no doubt be achieved by restoring mass flow to the design value by opening up the nozzle throat. However, the practical difficulty of resetting the internal throats would be significant.

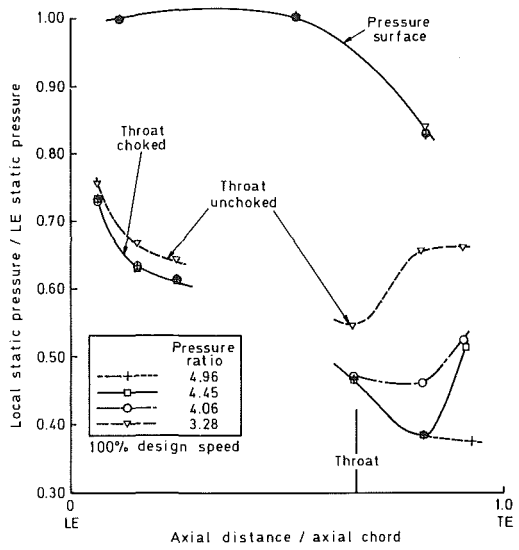


Fig. 10 Rotor blade performance at design speed

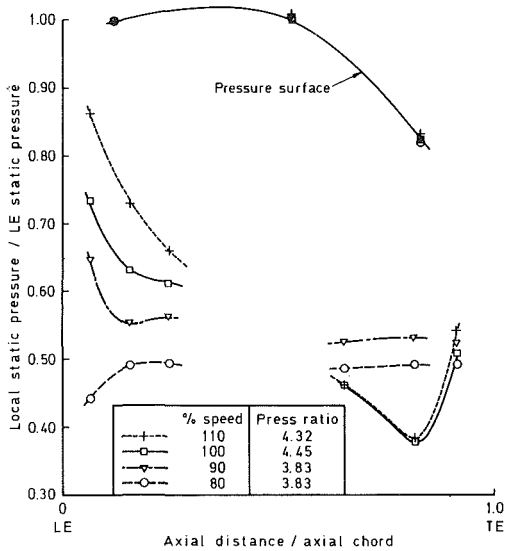


Fig. 11 Rotor blade performance at varying speed

Rotor-Blade Performance. At the lower turbine pressure ratios the rotor blade was still unchoked so that as pressure ratio across the turbine was further increased, the NGV exit Mach numbers, rotor inlet and rotor exit Mach numbers all increased until the rotor choked, at which point all conditions upstream of the rotor trailing edge shock were fixed. Yet further increase in turbine pressure ratio caused the rotor exit Mach numbers to increase supersonically until limit loading on the rotor was reached. This pattern of events is evident on the rotor-blade surface pressure distributions as measured by the rotating Scanivalve (Fig. 10).

Here local static pressure – corrected for centrifugal pumping effect and ratioed with respect to leading edge static pressure (as sensed by the first static hole on the pressure surface) – is shown plotted against tapping position for various turbine pressure ratios at design speed. Unfortunately the tapping situated at the point of maximum curvature on the suction surface gave false readings and is omitted. Clearly, at turbine pressure ratios above 4, the rotor blade choked, reflected by the local static pressure ratios at a given tapping prior to the throat being constant. It will also be noted that the post throat expansion and recompression, and thus the strength of the trailing-edge shock system increases in magnitude and moves downstream, with increase in turbine

Downloaded 01 Jun 2010 to 171.66.16.71. Redistribution subject to ASME license or copyright; see http://www.asme.org/terms/Terms_Use.cfm

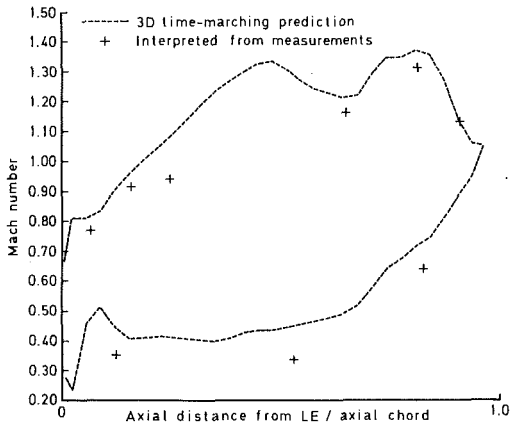


Fig. 12 Rotor blade 3D performance – mean

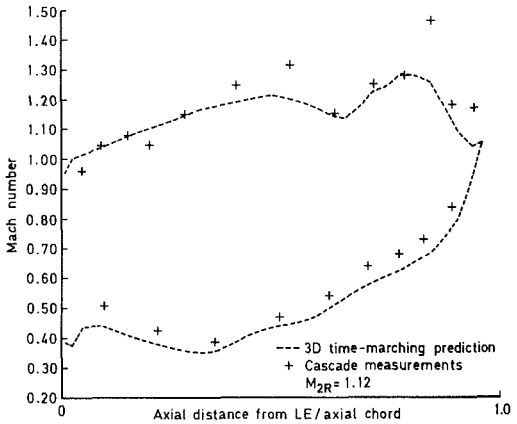


Fig. 13 Rotor blade 3D performance – root

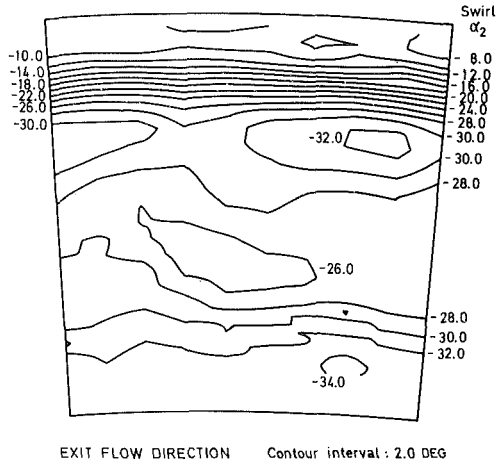


Fig. 14 Turbine exit swirl

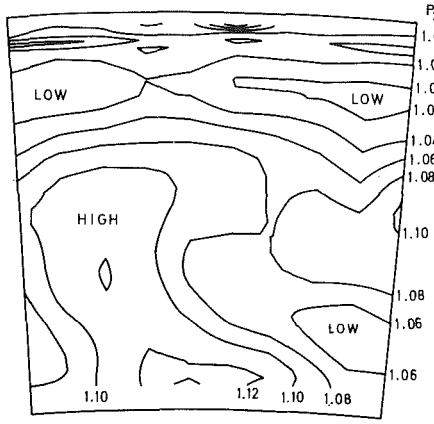


Fig. 15 Turbine exit total pressure

pressure ratio above the choking value. Limit loading has not however been exceeded at the highest turbine pressure ratio of 4.96 because the local pressure ratio of the furthest downstream tapping is still reducing. Figure 11 shows how the local static pressure ratio varies with turbine speed at choked conditions. The pressure surface tappings show no variation but the suction surface upstream pressures indicate, for a reduction in speed, not only reduced level (and thus increased velocities) but also the increasing tendency for the flow to overexpand around the leading edge. This is due to a combination of increased Mach number level and the increased positive incidence at inlet to the rotor blade.

Analysis of the rotor-blade performance is complicated by the fact that very few measurements were made at NGV exit to establish the rotor-blade inlet conditions. Throughflow synthesis of the test measurements at the design point suggests that the rotor blade is operating at inlet Mach numbers higher than design particularly in the hub region. In particular the throughflow studies indicate that at the hub, the relative inlet Mach number to the rotor blade has increased from the design value of 0.71 to 0.75 under turbine test conditions. This reflects the NGV performance where, as already mentioned, there are strong indications that the hub was operating at significantly higher exit Mach numbers than design. Some degree of confidence in the ability of the rotor blade to cope with such a high value of inlet Mach number can be held by reference to the cascade testing of the rotor blade at Oxford University. In this testing the hub section rotor profile was installed in a linear cascade which contained flare on both of the walls of the working section to simulate streamtube thickness increase through the blade row. From this work the relative inlet Mach number was found to be about 0.76 when the blade was choked. This is very similar in level as synthesized from the turbine test measurements and confirms the rotor blade ability to accept an inlet Mach number higher than design. It also reflects the overcautious viscous effect allowance assumed in the design.

The results of the throughflow calculation may be used to establish the rotor inlet conditions across the annulus so that an inviscid three-dimensional time marching calculation (13 $\times$ 61 $\times$ 13 grid) may be performed for the rotor blade. This has been done for the design condition and results of the surface Mach number distribution corresponding to the mid-height section are shown plotted in Fig. 12. Also included are the isentropic Mach numbers indicated by the rotating Scanivalve measurements, where the value of inlet relative total pressure as calculated in the throughflow synthesis has been used in the calculation of local isentropic Mach number. Generally the Mach numbers interpreted from the Scanivalve measurements appear to be less than predicted on both suction and pressure surfaces. However, both distributions are of similar shape up to a peak Mach number of about 1.3 to 1.37. The discrepancy in level of Mach number between measurement and prediction may perhaps be explained by the difficulty in establishing the rotor inlet conditions from hub to tip for the inviscid 3D calculation and also in determining the level of inlet relative total pressure for use with the rotating static pressure measurements. More work needs to be done in this area – perhaps by further analysis of measurements at other speeds and pressure ratios – before a satisfactory modelling of the flow between NGV exit and rotor inlet is achieved. A nonintrusive form of flow measurement in the interblade space, such as laser anemometry, would be very useful in future test work.

The rotor root is a very critical region and it is the good

Downloaded 01 Jun 2010 to 171.66.16.71. Redistribution subject to ASME license or copyright; see http://www.asme.org/terms/Terms_Use.cfm

performance achieved here which is, we believe, the main reason for the satisfactory level of efficiency obtained. Unfortunately, it was not practical to take rotating measurements at the root in the turbine rig but the evidence of the three-dimensional time-marching prediction already described, in association with the linear cascade measurements mentioned earlier, indicates that the blade root should perform well in the turbine. Figure 13 shows a comparison between 3D prediction and cascade which generally are in reasonable agreement, particularly over the forward suction surface. The slight overexpansion and recompression on the top suction surface, measured in cascade, is slightly underpredicted and Schlieren evidence suggests that this could be the result of viscous influence. The overexpansion and recompression downstream of the throat is underpredicted. Over the rotor blade as a whole, the evidence of the rotating Scanivalve, cascade measurements and the 3D prediction is that satisfactory Mach number distributions are achieved, which was one of the major objectives in the design. However, on account of the higher inlet relative Mach numbers to the rotor blade, caused by the turbine swallowing less flow than design, the overall reaction level of the turbine has reduced. Estimates suggest a reduction from 30% to about 25% at midheight. A small restagger of the rotor blades to rematch close to the design condition would probably be beneficial.

Downstream Traverse Measurements. Area traversing was undertaken downstream of the rotor by a series of ten radial traverses separated by 1 deg circumferential intervals equivalent to one complete NGV pitch. Contours of constant exit swirl angle are shown in Fig. 14 which shows clearly the effect of rotor tip clearance upon the flow, the extent of the influence being over the outer 25% span of annulus height. Over the whole span there is little variation of swirl with varying circumferential position which justifies the use of purely radial traversing for measuring the downstream exit flow angle used in the calculation of turbine performance. Over nearly 75% of the annulus height the mean exit swirl angle is close to -30 deg which agrees reasonably with the design value. Contours of total pressure are shown in Fig. 15 and it is clear that there is a wide variation around the annulus. There is a low region at about 15-20% inward from the outer wall and another loss core approximately the same distance from the inner wall. These loss cores are approximately repeated at one nozzle pitch and are probably associated with the NGV secondary loss regions.

Conclusions

A high work capacity, single-stage, shroudless transonic turbine of severe aerodynamic loading $\Delta H/\bar{U}^2 = 2.1$ has been designed and the blading tested in both cascade and in a turbine rig. A design point total–total adiabatic efficiency – based on torquemeter temperature drop – of 87.0% at a running tip clearance of 1.4% of mean rotor blade height has been measured. Detailed measurements indicate that the NGV was operating at higher exit Mach numbers than design, caused by the turbine passing 1% reduced flow. This results in high suction surface peak Mach numbers which could be causing loss of performance. Static pressure measurements on the surface of the rotor blade – expedited via a rotating Scanivalve assembly – indicated that the rotor blade was performing well with smooth blade surface Mach number distributions. Overall the turbine appeared to be operating at reaction levels lower than design and it is anticipated that performance could be improved by a restagger of the blading to restore mass flow to the design value.

References

1 Crow, D. E., Vanco, M. R., Welna, H., and Singer, I. D., "Results from Tests on a High Work Transonic Turbine for an Energy Efficient Engine," ASME Paper No. 80-GT-146, 1980.

2 Patel, K. V., "Research on a High Work Axial Gas Generator Turbine," Society of Automotive Engineers SAE Paper 800618, 1980.

3 Liu, H. C., Booth, T. C., and Tall, W. A., "An Application of 3D Viscous Flow Analysis to the Design of a Low Aspect Ratio Turbine," ASME Paper No. 79-GT-53, 1979.

4 Dunham, J., and Came, P. M., "Improvements to the Ainley-Mathieson Method of Turbine Performance Prediction," JOURNAL OF ENGINEERING FOR POWER, ASME Series A V92 N3, July 1970, pp. 252–256.

5 Deich, M., Fillipov, G., and Lazarev, L., "Atlas of Axial Turbine Blade Cascades," Parts 1 and 2, Central Electricity Generating Board, Translation Nos. 4563 and 4564.

6 Denton, J. D., "A Time Marching Method for Two and Three-Dimensional Blade-to-Blade Flow," Aeronautical Research Council R&M 3775, 1975.

7 Haas, J. E., and Kofskey, M. G., "Effect of Rotor Tip Clearance and Configuration on Overall Performance of a 12.77 Centimetre Tip Diameter Axial Flow Turbine," ASME Paper No. 79-GT-42, 1979.

8 Litchfield, M. R., and Norton, R. J. G., "Heat Transfer Measurements of a Transonic Nozzle Guide Vane," ASME Paper No. 82-GT-247, 1982.

Downloaded 01 Jun 2010 to 171.66.16.71. Redistribution subject to ASME license or copyright; see http://www.asme.org/terms/Terms_Use.cfm

C. H. Liebert

R. Holanda

S. A. Hippensteele

C. A. Andracchio

National Aeronautics and Space Administration, Lewis Research Center, Cleveland, Ohio 44135

High-Temperature Thermocouple and Heat Flux Gauge Using a Unique Thin Film–Hardware Hot Junction

A special thin film–hardware material thermocouple (TC) and heat flux gauge concept for a reasonably high-temperature and high heat flux, flat-plate heat transfer experiment was fabricated and tested to gauge temperatures of 911 K. This unique concept was developed for minimal disturbance of boundary layer temperature and flow over the plates and minimal disturbance of heat flux through the plates. Comparison of special heat flux gauge Stanton number output at steady-state conditions with benchmark literature data was good and agreement was within a calculated uncertainty of the measurement system. Also, good agreement of special TC and standard TC outputs was obtained and the results are encouraging. Oxidation of thin film thermoelements was a primary failure mode after about 5 hr of operation.

Introduction

Experimental verification of analytical predictions for local wall temperature and Stanton number (nondimensional heat transfer coefficient) is very difficult because there is a lack of instrumentation for obtaining accurate measurements at operating conditions [1]. A basic difficulty is that the thermocouple (TC) temperature sensors and heat flux gauges for Stanton number measurement must be very small and nonintrusive. Measurements of metal temperature and Stanton number in zones of airfoil boundary layer separation, laminar-to-turbulent transition, and relaminarization are especially important. The accumulation of reliable measurements at these boundary layer conditions is necessary for the assessment of dependable design tools for high-temperature gas turbine engines.

The use of thin film materials to form TC's is not new. Reference [2] describes the use of thin film TC's for measurement of gun bore surface temperatures. Reference [3] describes early preliminary investigations of techniques for sputtering thin film TC's on turbine blade materials and aerodynamic surfaces. Thin film TC's are advantageous because they will minimally disturb the boundary layer temperature or flow over the blade or heat flux into the blade. Reference [3] demonstrated that thin film TC's could accurately record high steady-state metal temperatures to 1020 K with potential to higher temperatures. References [4–6] describe some recent efforts in the development of thin film surface TC's for measurement of air-cooled turbine blade temperatures.

References [7] and [8] discuss investigations of high-temperature, embedded-wire TC heat flux gauges and embedded Gardon heat flux gauge sensors instrumented with wire TC's. These gauges were designed for use under one-dimensional heat flux conditions through the gauge. The embedded TC heat flux sensors were designed with single conductor swagged wires. Both an alumel and chromel wire were embedded in the cold side of the hardware and an alumel wire was embedded in the hot side. The sensor output was obtained as a differential signal from the alumel wires. The chromel–alumel TC produces a reference temperature. In the Gardon gauge concept, two alumel wires and one chromel wire were installed in sheaths to form small three-conductor cables. These wires were extended from the cable and were fastened in cavities machined into hardware cold-side surfaces. The cavities were filled with ceramic cement. One alumel lead was attached to the bottom center of the cavity; the other alumel and chromel leads were attached to the wall of the cavity near the bottom. Differential signal output was obtained from the alumel wires.

An investigation was initiated to create, fabricate, test, and analytically model a special high-temperature thin film–hardware material measurement system and heat flux gauge concept which is different from those described in [3–8]. This concept incorporates the economical use of only one sputtering operation to form nonintrusive thermoelements. The concept involves sputtering an electrically insulating thin film coating over most of the hardware metal surface exposing only bare metal material at locations where metal temperature measurement is desired. Thin film thermoelement legs (nickel)

Contributed by the Gas Turbine Division of THE AMERICAN SOCIETY OF MECHANICAL ENGINEERS and presented at the 30th International Gas Turbine Conference and Exhibit, Houston, Texas, March 18–21, 1985. Manuscript received at ASME Headquarters, December 17, 1984. Paper No. 85-GT-18.

Copyright © 1985 by ASME

Downloaded 01 Jun 2010 to 171.66.16.71. Redistribution subject to ASME license or copyright; see http://www.asme.org/terms/Terms_Use.cfm

of a metal material different from the hardware material are then sputtered simultaneously onto the bare metal locations, the electrically insulating coating and thin film to leadwire connectors. Sputter deposition of the legs onto the bare-metal (SS316) hardware locations forms the unique TC hot junction. The hardware material serves as the other common thermoelement. Heat flux gauges are formed by placing two thin film–hardware hot junctions opposite each other on the hardware hot and cold surfaces. This concept was created for minimal disturbance of boundary layer temperature and flow or heat flux through the plate.

The investigation was done in several steps. First, an air-cooled control flat plate instrumented with small embedded reference wire TC's and heat flux gauge sensors was designed, built, and tested. This control plate was designed for operation at reasonably high heat flux to give maximum temperature gradients from the hot to cold surfaces and minimum lateral temperature gradients within these surfaces. The control plate was instrumented for measurement of temperature gradients in three dimensions, because it is necessary to know how temperature gradients are related to each other throughout the plate. The accuracy of the reference heat flux gauge sensors was determined by comparing their Stanton number outputs with experimental benchmark quality Stanton number data given in [9] and [10]. In this way, the reference gauge output on the control flat plate was calibrated with the benchmark data.

Secondly, the air-cooled control plate design was utilized on a second and third flat plate instrumented with the special thin film–hardware TC's and heat flux gauges. These special TC's were installed so that both temperature and Stanton number measurements could be made. Film thicknesses of 3 μm and 10 to 12 μm were used on the second and third flat plates, respectively. Ceramic connectors were fabricated for attachment of the thin film thermoelements to lead wire connectors. Embedded reference wire TC's of the same type used for instrumentation of the control plate were installed adjacent to the special TC's only on the hot surface.

The results include data of temperature versus millivolt output of the TC materials used in this study. Comparison of special TC and reference TC steady-state output on plates 2 and 3 are presented. Also, comparisons were made of special heat flux gauge steady-state Stanton number output on plates 2 and 3 with reference gauge output obtained on plate 1 and with benchmark literature data. The comparisons were made at gas-temperature to gas-side plate temperature ratios of 1.3 to 1.4, which corresponds to some cooled turbine engine applications. Thin film fabrication, electrical circuitry and the uncertainties associated with the measurement system are also discussed.

Heat Transfer Analysis

Temperature Distribution. The term one-dimensional is applied to a heat transfer problem when heat flows in only one direction within a heat conducting body. Such a situation rarely exists precisely in real heat transfer problems, but a great number of problems of practical engineering importance may be approximated quite well by assuming a one-dimensional condition. The one-dimensional heat flow equation is

$$q = k\frac{(T_A - T_D)}{L}, \frac{\mathrm{W}}{\mathrm{m}^2} \tag{1}$$

This equation relates the heat flux to the temperature differences, $(T_A - T_D)$ measured differentially through the gauges (plate). Thermal conductivity data of the stainless steel 316 (SS316) flat-plate gauge material used herein as a function of temperature is given in [11] (in table no. 331, curve number 64). A least-square fit through the k versus T curve gives

$$k = 9.25 + 0.015T_m, \frac{\mathrm{W}}{\mathrm{m}\cdot\mathrm{K}} \tag{2}$$

The heat flux value obtained from the gauge is related to the gas-side heat transfer coefficient and driving temperature difference between the hot gas and flat-plate, gas-side surface as

$$q = h(T_g - T_A), \frac{\mathrm{W}}{\mathrm{m}^2} \tag{3}$$

A definition for Stanton number is

$$\mathrm{St} = \frac{h}{(\rho U c_p)} \tag{4}$$

Combining equations (1) and (3) with (4) gives

$$\mathrm{St}_x = \frac{k}{L}\frac{(T_A - T_D)/(T_g - T_A)}{\rho\, U c_p} \tag{5}$$

where c_p was evaluated at the film temperature, T_f. The accuracy of the reference gauges was determined by comparison of values with a turbulent equation of heat transfer

$$\mathrm{St}\ \mathrm{Pr}^{0.4} = 0.0287\ \mathrm{Re}_x^{-0.2} \tag{6}$$

Equation (6) correlated the experimental benchmark Stanton number data given in [9] and [10] for zero pressure gradient airflow over a flat plate and low heat flux through the plate within about 0–10 percent at turbulence levels of 0–6 percent. Values for thermodynamic and transport properties were taken from [12].

Nomenclature

c_p = specific heat of gas, cal/gr•K
f/a = fuel-to-air-ratio
h = heat transfer coefficient, W/m²•K
k = thermal conductivity of heat flux gauge, i.e., flat plate, W/m•K
L = length of gauge, m
p_g = pressure, N/m²
Pr = Prandtl number
q = heat flux, W/m²
R = gas constant, 82.0568 cm³•atm/(gr mole•K)
Re_X = gas Reynolds number based on distance from flat plate leading edge, $\frac{UX\rho}{\mu}$
St = Stanton number
T = temperature, K
T_f = film temperature, $\left(T_f = \frac{T_g + T_A}{2}\right)$, K
T_g = gas temperature, K
T_m = average of gas-side and coolant-side flat plate temperatures, K
t = time, s
U = velocity of gas, m/s
X = distance from the leading edge, m
x = space coordinate, m
ρ = density, kg/m³, p/RT_f
μ = gas viscosity, N•s/m²

Subscripts

A = gas-side surface, upper surface of flat plate or gauge
D = coolant-side surface, lower surface of flat plate or gauge

Downloaded 01 Jun 2010 to 171.66.16.71. Redistribution subject to ASME license or copyright; see http://www.asme.org/terms/Terms_Use.cfm

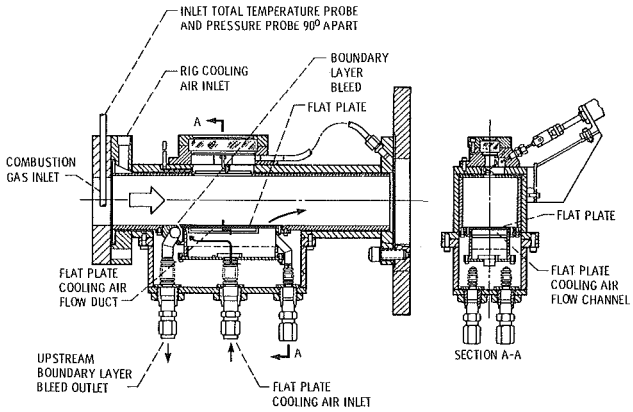


Fig. 1 Air-cooled flat-plate test section

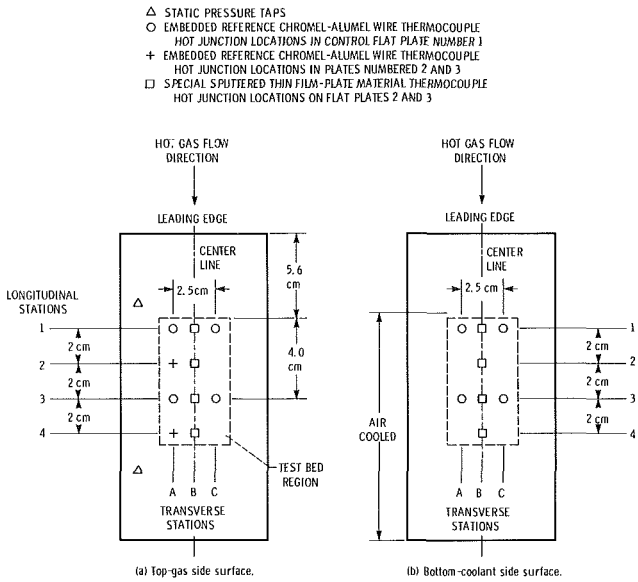


Fig. 2 Hot junction locations on flat plates

Apparatus and Procedure

Test Facility and Flat Plates. A detailed description of the facility is given in [13]. Briefly, the facility (as sketched in Fig. 5 of [13]) is comprised of inlet, combustor, transition, air-cooled test vane, and exit sections. An air-cooled flat plate test section (Fig. 1) was inserted 61 cm behind the air-cooled vane test section and ahead of the exit section shown in [13]. The vanes were removed from the vane test section. Air-cooled flat plates were machined from SS316 material to length and width dimensions of 17.8 and 8.5 cm. Flat-plate, gas-side surfaces were carefully machined and polished. Plate thickness was nominally 0.43 cm. Except at bolt locations, coolant-side surfaces were thermally insulated from the apparatus to which it was bolted. This design aided in reducing heat transfer from the plates to the apparatus, which in turn, aided in maintaining approximately uniform steady-state hot and cold lateral surface temperatures. The high k values of SS316 also aided to give nearly uniform hot and cold lateral surface temperatures. Test section and plates were designed for constant pressure along the gas-side surface in the flow direction. Hot gas was generated by burning either methane fuel in a J-47 gas turbine combustor or by burning Jet-A fuel in a J-58 gas turbine combustor. Hot combustion gas flowed over the leading edge of the plates and along the upper surface of the plates. Cooling air entered a duct fastened to the bottom of the plates and then flowed out into the hot gas stream through a slot machined into the rear of the plates. The cooling air duct dimensions were 0.65 cm high, 5.2 cm wide, and 11.1 cm long. The position of the duct entrance was 1 cm upstream of the longitudinal station 1 (Fig. 2).

The test facility was designed to establish a uniform free-stream gas velocity distribution in front of the leading edge of the plates. Unpublished measurements previously made with a hot-wire probe at gas temperatures of 300 to 400 K verified the establishment of a reasonably uniform velocity distribution in the vicinity of the plate wall at the leading edge. It was assumed that this velocity distribution was also established at gas temperatures up to 1098 K, which was the highest gas temperature generated by the J-58 gas turbine combustor. Inlet total gas temperature and pressure were measured with a movable probe positioned in front of a plate, and measurements could be made over a distance of 1.3 cm from the top of a plate to within 1.3 cm from the top of the wall.

The experiments were performed with three flat plates. The first flat plate was instrumented with chromel-alumel miniature wire thermocouples and a total pressure probe mounted at the rear of the plate. This plate was used to investigate the reliability of obtaining nearly one-dimensional, steady-state temperature gradients and heat fluxes through the plate. This plate was also used as a control to which the outputs from the special TC's and heat flux gauges on the second and third plates were compared.

Figure 2 schematically shows TC hot junction locations on the three flat plates. Longitudinal TC stations were designated by numerals 1, 2, 3, 4, and transverse TC stations were given by letters A, B, C. Two static pressure taps mounted in the top surface of the three plates were used to monitor pressure gradients in the flow direction. A three-dimensional array of wire TC's was formed only on the control flat plate. A minimal amount of wire TC's were used. This reduced inaccuracies due to slots and wire TC assemblies which will interfere with the heat transfer process. Embedded wire TC hot junctions were placed very close to the top surface at a 0.038 cm depth. One-dimensional heat conduction calculations were employed to correct the absolute temperature output to a value corresponding to the surface temperature. The plate thickness was about 11 times the depth of the grooves to cause no serious problems with heat path distortion within the plate.

SS316 was chosen for the flat-plate thermoelement material because it easily oxidizes when heated in the hot combustion gases. Therefore, this is a good material for economically studying effects of oxidation on thermoelectric output over short running times. Structural changes which might indicate damage or deterioration were monitored by testing the resistance of each TC circuit after the rig was shutdown and had cooled off. After all the tests were completed, the plates were removed from the hot gas tunnel and inspected. The inspection consisted of circuit component resistance measurements, visual inspection, and microscopic examination.

Procedure for Determination of Thermoelectric Characteristics. Analytical models for predicting the effects of alloying elements on TC thermoelectric characteristics are ineffective and so it is still necessary to rely on experimental calibration for determination of such properties. Calibrations of millivolt output versus temperature for SS316 versus alumel and for SS316 versus nickel ranging from 273 K to 1273 K were made. The calibrations were based on procedures discussed in [14]. The slope of the SS316 versus alumel calibration curve was used to determine differential temperature measurements on plate 1. The SS316 versus nickel calibrations were needed for determination of absolute and differential temperatures on plates 2 and 3. Calibration data

Downloaded 01 Jun 2010 to 171.66.16.71. Redistribution subject to ASME license or copyright; see http://www.asme.org/terms/Terms_Use.cfm

were obtained on wire materials in 100 K intervals in both ascending and descending temperature modes. The chromel-alumel TC's were not calibrated because their millivolt output versus temperature values are already known to a high degree of accuracy.

Wire TC Assemblies. Miniature chromel-alumel, two-wire sheathed TC assemblies with 0.025 cm o.d. were used. These TC's were commercially available and of standard grade. They passed all TC acceptance tests described in [14]. These tests included inquiries into integrity of the sheath, electrical resistance of the insulation, junction integrity, and tests for spurious emf.

On the top surface only, the assemblies were placed in grooves cut into the plates. The thermoelements of each TC were welded together to form hot junctions and flattened into a thickness of 0.008 cm. Then the hot junctions were laser welded to the bottom of the slots. Sheathed assemblies were laid into the grooves and then the groove voids above the assemblies and hot junctions were filled with nichrome material. Cover plates were spot welded to the plate surface. The cover plates and welds were dressed down to the surface of the plate and polished. On the cold side, the assemblies were strapped to the surface and hot junctions were laser welded in place.

Thin Film Thermoelement Fabrication on the Second and Third Plates. The components of a completely fabricated thin film-plate material temperature and heat flux gage sensor system on a flat plate are shown in Fig. 3. Reference [15] discusses each component of the thin film-plate material system with comments relating to the design and fabrication procedures giving in Table 1. Sputtering parameters are given in Table 2. As discussed in [15], the thin films minimally disturbed the flow and temperature of the boundary layer or heat flux through the boundary layer.

Electrical Circuitry. The electrical circuitry for the thin film-plate material TC's and reference wire TC's is presented in [15].

Test Conditions. The experiments were conducted at the experimental conditions given in Table 3 and a real-time data-acquisition system was used to collect the data. Tests were performed by setting the desired combustion gas temperature and pressure to an exit critical velocity ratio of 0.5 (Mach number = 0.46). Then the cooling air flow rate was varied in a stepwise manner from test-point to test-point to establish a range of plate temperatures. Cooling-air mass flows and temperatures ranged from 1.36×10^{-3} to 1.90×10^{-2} kg/s and 296 to 337 K. All data were taken at steady-state conditions. Measurements were not continued at plate temperatures greater than 911 K, because it was observed after shutdown that the leading edge of the plate was softening. Two fuels were used to cover the temperature range. The first flat plate was operated at lower temperatures with methane fuel and at higher temperatures with Jet A fuel. The second flat plate was operated using only methane fuel, and the third flat plate was run using both methane and Jet A fuel.

Measurement Uncertainty

The discussion in [15] describes statistical analysis used in the comparison and correlation of temperature measurements. The discussion also describes numerical analysis made prior to the tests for determination of the reasons for the dispersion and extent of dispersion (experimental error) expected from the temperature, Stanton number, and Reynolds number data taken on the flat plates. The dispersion was compared in [15] with experimental dispersion obtained herein and in the literature.

Results and Discussion

Thermoelectric Characteristics. The temperature-millivolt outputs of SS316-nickel and SS316-alumel thermoelements are presented in Table 4. The results show that there is adequate millivolt output between the alloys so that meaningful temperature difference measurements in a direction normal to the hot and cold surfaces of plates 1, 2, and 3 can be obtained from an amplified differential electrical

Table 1 Thin film-flat plate fabrication procedure

1. Polish plate surfaces to about 0.15 μm finish.
2. Drill and tap holes for coolant duct and mounting bracket.
3. Drill holes for pressure taps; cut grooves for reference thermocouples; drill holes to pass wires from hot-gas side to cold-gas side of plate; cement insulators in holes to pass bare nickel wires through plate.
4. Grit-blast areas of plate designated for flame-sprayed material.
5. Apply oxygen-acetylene flame-sprayed bond coat of nickel aluminum composite to areas designated for flame-sprayed material.
6. Apply Rokide HiTec HT rod flame-sprayed insulating material base coat to a thickness of about 0.15 mm.
7. Tape lead-wires in place.
8. Apply Rokide flame-sprayed material to leadwire pattern to a thickness of about 0.08 mm.
9. Remove tape and apply Rokide flame-sprayed material to leadwire pattern to a thickness of about 0.03 mm.
10. Install reference thermocouples.
11. Weld pressure taps to plate.
12. Grit-blast surfaces for sputtering with 25 μm aluminum oxide grit at a pressure of 25 psi.
13. Clean surfaces for sputtering with detergent, water, and alcohol.
14. Mask plate and sputter first side of plate with silicon nitride to a thickness of 7.5 μm.
15. Clean and mask plate and sputter second side of plate with silicon nitride to a thickness of 7.5 μm.
16. Clean and mask plate and sputter first side of plate with nickel films to a thickness of 3 μm on plate 2 and 10 to 12 μm on plate 3.
17. Clean and mask plate and sputter second side of plates with nickel films to same thickness.
18. Weld 316 stainless steel wire to plate.

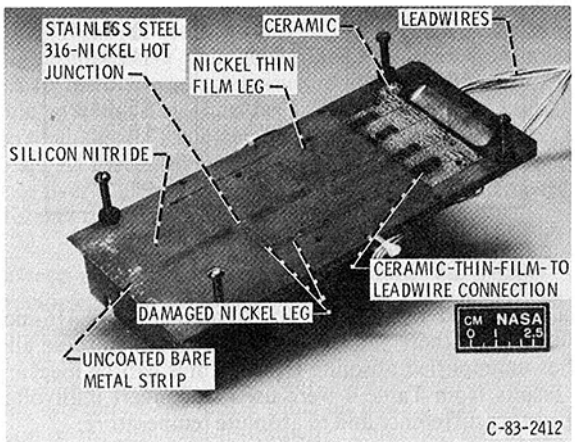


Fig. 3 View of flat plate hot side after tests with 10-12 micrometer thin film-plate material thermocouples

Table 2 Sputtering parameters

Sputtering material	Sputtering gas	Pressure, mtorr	Power, kW	Target-substrate distance, cm	Sputtering rate, μm/hr
Nickel	Argon	10	1.5	7.5	3
Silicon-Nitride	Argon plus Nitrogen	15	1.5	7.5	1.5

Downloaded 01 Jun 2010 to 171.66.16.71. Redistribution subject to ASME license or copyright; see http://www.asme.org/terms/Terms_Use.cfm

Table 3 Experimental conditions for tests of wire thermocouples and nickel thin film/stainless steel 316 flat plate thermocouples

Plate no.	Cooling-air temperature, K	Gas temperature, K	Burner type	Gas pressure, N/m^2	Film thickness	Range of plate temperatures, K		Duration of tests, hr	Plate no./ test no.
						Top	Bottom		
1	311	533	Nat. gas	3.5×10^5	----	424-519	391-517	1.28	1/1 (wire TC)
	329	750		5.7×10^5	----	530-657	475-646	2.67	1/2
	332	811				614-736	569-719	——	——
	337	880				653-789	604-770	——	——
	320	672	ASTM-A-1	5.7×10^5		526-653	470-639	2.35	1/3
	310	1089				765-947	707-892	——	——
	325	922				669-879	586-879	——	——
2	296	533	Nat. gas	3.1×10^5	3 μm	431-495	400-482	2.03	2/1 (thin film-s.s TC)
	302	672		5.7×10^5		541-621	497-608	——	——
	301	672		5.7×10^5		550-577	492-542	2.72	2/2
	307	811				644-739	573-697	——	——
	313	880				694-794	606-685	——	——
3	287	537		3.1×10^5	10-12 μm	448-521	427-518	1.62	3/1 (thin film-s.s TC)
	302	677		5.7×10^5		551-626	500-627	——	——
	308	875		5.7×10^5		682-786	631-769	——	——
	297	677	ASTM-A-1	5.7×10^5		549-580	509-554	2.08	3/2
	298	812				639-683	579-650	——	——
	296	879				651-694	572-658	——	——
	302	924		5.7×10^5		672-724	600-694	3.03	3/3
	302	980				614-777	614-711	——	——
	301	1033				750-822	644-739	——	——
	304	1089				911-753	874-672	——	——

Table 4 Temperature-millivolt characteristics for SS316-nickel and SS316-alumel thermocouples used herein

Temperature, K	Ni-SS316, mV	Al-SS316, mV
273	0	0
323	----	0.88
373	1.94	1.76
423	----	2.55
473	4.15	-----
665	----	3.28
523	----	4.00
573	6.28	4.79
623	----	5.60
673	7.78	6.44
723	----	7.34
773	9.19	8.29
823	----	9.29
873	10.85	10.34
923	----	11.44
973	12.85	12.61
1023	----	13.81
1073	15.16	15.04
1123	----	16.32
1173	17.77	17.64
1273	20.67	-----

signal generated from either SS316-alumel or SS316-nickel circuitry. Also there is adequate output between these alloys so that unamplified absolute temperatures can be measured. The results from Table 4 were used to convert millivolts to temperature difference and to absolute temperature.

Standard Wire TC's and Heat Flux Gages on Control Plate.

One-Dimensional Heat Transfer. Temperature differences measured with differential electrical signals in a direction normal to the hot and cold surfaces of control plate number 1 increased with increasing coolant-air mass flow while temperature differences in the transverse and longitudinal directions, i.e., lateral directions on the top and bottom surfaces remained relatively small. Absolute temperatures and temperature gradients were evaluated during a run at a high gas temperature of 1098 K. During this run the cooling-air mass flow was 8.62×10^{-3} kg/s, gas pressure was 5.7×10^5 N/m^2, exit critical velocity ratio was 0.5, and cooling air temperature was 310 K. These conditions established values of $(T_g - T_A)$ equal to 280 to 305 K. At this experimental condition, temperature gradients measured in a direction normal to the plate hot and cold surfaces were 230 to 283 K/cm, while lateral temperature gradients within the surfaces ranged from only 3.5 to 7.5 K/cm in the longitudinal direction and 0 to 6.4 K/cm in the transverse direction. These lateral temperature gradients (in all plates) were evaluated by subtracting absolute temperature values and are accurate ±3 K/cm. Absolute lateral temperatures measured within the surfaces were small and were within the calculated experimental error discussed in [15]. The heat flux, within experimental error, is highly one-dimensional in a direction normal to the hot and cold surfaces with 97 percent of the heat flux in the normal direction. Heat flux values of 4.8×10^5 to 6.3×10^5 W/m^2 were measured in the normal direction.

Normal and lateral temperature differences in the plate were also evaluated at values of $(T_g - T_A)$ equal to 160 K. Lower values of this temperature difference term were not considered because, as discussed in [15], calculations indicated that Stanton number data scatter would be unacceptably high at $(T_g - T_A)$ values less than 160 K. This large data scatter was also experimentally observed. In the case of $(T_g - T_A) = 160$ K, experimental temperature gradients normal to the plate surfaces were 165 to 230 K/cm and lateral gradients were 0.4 to 3.5 K/cm. Gas temperature was 922 K, cooling-air mass flow was 3.95×10^{-3} kg/s, and cooling-air temperature was 325 K. Heat fluxes in the normal direction of 3.2×10^5 to 3.9×10^5 W/m^2 were measured. Again, it was found that the heat flux is highly one-dimensional in a direction normal to the plate surfaces, with 98 percent of the heat flux in this direction.

Stanton and Reynolds Numbers. Comparison of the control plate Stanton numbers (Fig. 4) and the benchmark data correlated with equation (6) shows acceptable agreement within 6–11 percent. This percent dispersion of the data about values obtained with equation (6) generally corresponds to that obtained in [9] and [10] at all gas conditions with Pr = 0.71 [12]. The reasons for the dispersion of the data are discussed in [15]. The stainless steel 316 plate oxidized during the course of the experiment, but within experimental error, the Stanton numbers were repeatable. Thus, within experimental error, oxidation of the plate had no observable effect on the differential temperature measurement through the SS316-alumel circuit.

Downloaded 01 Jun 2010 to 171.66.16.71. Redistribution subject to ASME license or copyright; see http://www.asme.org/terms/Terms_Use.cfm

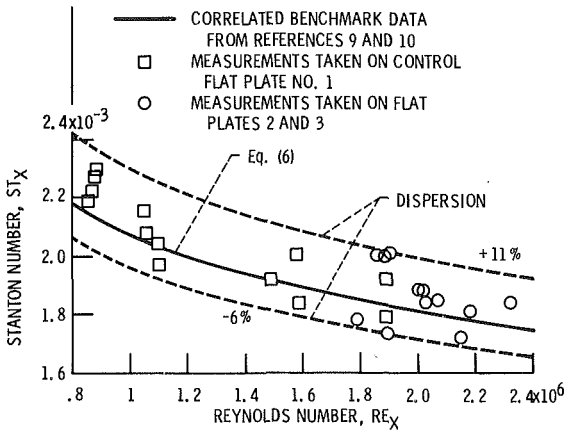


Fig. 4 Heat flux gauge output at $(T_g - T_A)$ values greater than 160K

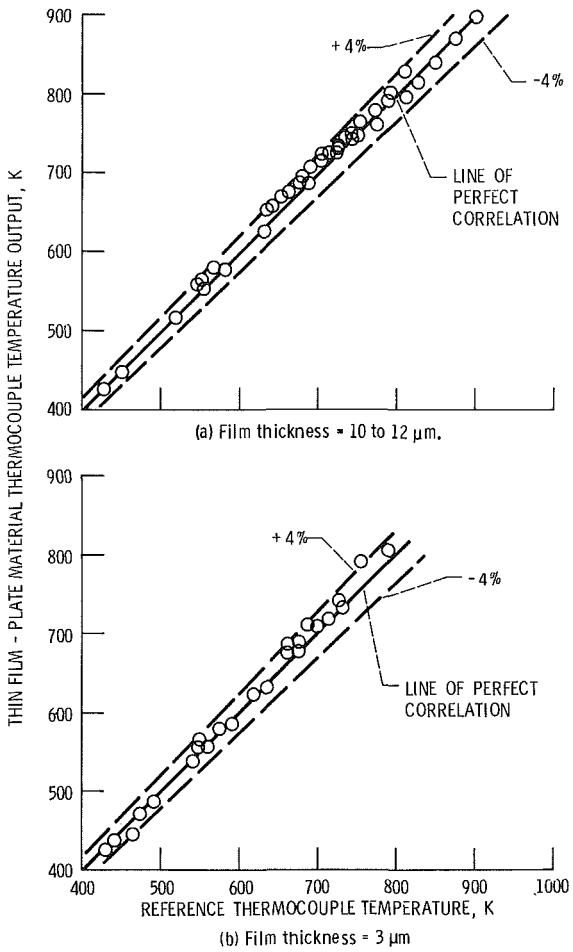


Fig. 5 Comparison of thin film-plate material thermocouple and standard thermocouple outputs at station 4A and 4B

Special Thin Film-Plate Material TC's and Heat Flux Gauges.

Comparison of Special and Standard TC Output. The investigation of the special TC's and heat flux gauges was carried out on plates 2 and 3 at the same test conditions and also at the same temperature differences of $(T_g - T_A)$, and at the same three-dimensional temperature gradient ranges investigated on the control flat plate. At longitudinal station 4 (Fig. 2), metal temperature measurements made with special thin film-plate material TC's agreed well with reference wire TC measurements. This agreement is shown in Fig. 5, which presents a plot of the thin film-plate material TC output at station 4B versus standard wire TC output at station 4A for thin film thermoelement thicknesses of 3 μm and 10 to 12 μm. The deviation of the data points produced by the outputs from these TC's is within 4 percent from a line of perfect correlation. This small deviation corresponds to lower values in the range of uncertainty of 3.29 to 9.20 percent determined from the rms statistical analysis presented in [15], for the uncertainty expected in comparison of wire and special TC outputs. The population linear correlation coefficient calculated from these data for both film thicknesses was a satisfactory 0.995 ± 1 percent based on 99.73 percent of the data falling within the range.

Comparisons of standard and special TC output over the entire gas and plate temperature range could not be made at longitudinal stations 1 to 3 (Fig. 2) because of nickel thermoelement failure after about 5 hr of TC testing on both the thinner and thicker films. However, comparisons could be made at these stations over a smaller temperature range at lower temperatures and at test times less than 5 hr. These comparisons produced values of regression coefficients identical to those obtained at longitudinal station 4.

Comparison of Stanton Number with Standard and Benchmark Data. For comparative purposes, the Stanton number data obtained with the special gauges are plotted in Fig. 4 along with the control plate Stanton number data. The range of Reynolds number (about 1.8×10^6 to 2.3×10^6) over which the Stanton number was determined with the special gauges is smaller than the Reynolds number range corresponding to Stanton number values obtained on the control plate (Re about 0.8×10^5 to 2.3×10^6). The range is smaller because the special gauge measurements were obtained at only one longitudinal location, station 4B, corresponding to $X = 11.6$ cm, whereas the reference data were obtained at longitudinal stations 1A and 1C corresponding to $X = 5.6$ cm and stations 3A and 3C corresponding to $X = 9.6$ cm. Special heat flux gauge measurements obtained with the thin film-plate TC's were consistent with the reference gauge Stanton number data and agreed well with the benchmark data. Also, the agreement was within a calculated uncertainty of the measurement system [15]. This demonstrates that this special gauge concept using nonintrusive thin film-flat plate hardware material TC's to form temperature sensors and heat flux gauges is a viable system. This has been demonstrated at conditions where values of T_A subtracted from T_g values are greater than 160 K. As discussed in [15], this system would probably be viable over a greater range of $(T_g - T_A)$ if this temperature difference quantity could be measured differentially.

Effects of Products of Combustion on Nickel Film Thermoelements. The silicon nitride sputtered onto the surface of the second plate showed no signs of deterioration, but stress cracks were noted at the step formed by the sputtered silicon nitride and the flame-sprayed alumina materials. Some erosion of the nickel films on plate 2 was noted in the region of the thin-film-to-leadwire connection and at the step from the silicon nitride to the ceramic layer. At a plate temperature of 800 K, two circuits failed because of thermal stress cracks and four circuits were inoperable because of nickel film failure. Although temperature measurements were repeatable during the tests, electrical resistance measurements on the films increased during the tests. This suggests that the nickel films were becoming thinner because of oxidation and possibly erosion. These films failed after about 5 hr of testing and also before Stanton number data could be obtained.

The 10 to 12-μm-thick thin film-plate material TC sensor system sputter-deposited onto plate number 3 is shown in Figs. 3 and 6 after removal from the test section. This system

Downloaded 01 Jun 2010 to 171.66.16.71. Redistribution subject to ASME license or copyright; see http://www.asme.org/terms/Terms_Use.cfm

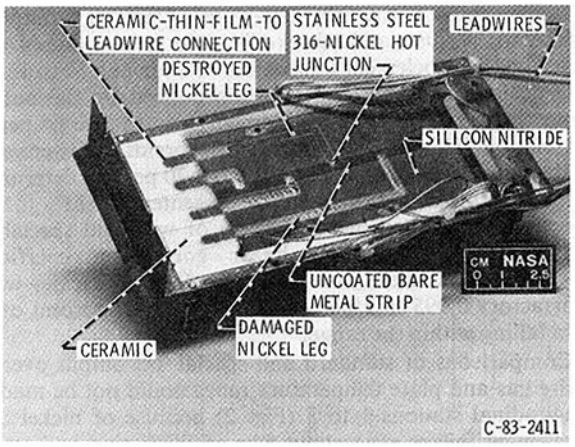


Fig. 6 View of cold side after tests with 10–12 micrometer thin film-plate material thermocouples

was much more durable. The silicon nitride insulating film showed negligible degradation with no significant thermal stress cracking. This suggests that the silicon nitride sputtering process was under better control on the third flat plate. Resistance measurements indicated no significant degradation after TC testing for 4.1 hr. The thicker films successfully withstood two thermal cycles involving two rig start-ups and shutdowns during the 4.1 hr of testing. However, after an additional 0.9 hr of testing at higher gas temperature, five thin film–plate material TC's failed (Figs. 3, 6) at stations 1B, 2B, and 3B (Fig. 2) before Stanton number data at higher ($T_g - T_A$) values could be obtained. The other three TC's continued to operate over the duration of the tests for a total operating time of 6.8 hr. Two of these three TC's were located at station 4 on the top and bottom surfaces. Stanton numbers were determined with these TC's.

It is believed that the life of thin film thermoelements can be extended by increasing their thickness, by use of protective coatings, or by the use of more oxidation-resistant materials.

Conclusions

The most important conclusion obtained from the results of this investigation was that a special thermocouple and one-dimensional heat flux gauge concept using a thin film–hardware material junction is a viable approach for measurement of surface temperature and heat flux. The concept can be used to measure the convective heat transfer between a gas and a wall in a channel-flow situation.

Oxidation of thin film nickel thermoelements was the primary failure mode. Films 10 to 12 μm thick operated for about 7 hr over a temperature range of 391 to 911 K. The life of thin film thermoelements can be extended by increasing their thickness, development of protective coatings or use of more oxidation-resistant materials.

References

1 Liebert, C. H., Gaugler, R. E., and Gladden, H. J., "Measured and Calculated Wall Temperatures on Air-Cooled Turbine Vanes with Boundary Layer Transition," NASA TM 83030, 1983.

2 Bendersky, D., "A Special Thermocouple for Measuring Transient Temperatures," *Journal of Mechanical Engineering*, Vol. 75, No. 2, Feb. 1955, pp. 117–121.

3 Liebert, C. H., Mazaris, G. A., and Brandhorst, H. W., Jr., "Turbine Blade Metal Temperature Measurement with a Sputtered Thin Film Chromel-Alumel Thermocouple," NASA TM-X-71844, 1975.

4 Grant, H. P., and Przybyszewski, J. S., "Thin Film Temperature Sensor," PWA-5526-31, Pratt and Whitney Aircraft, East Hartford, CT, 1980 (NASA CR-159782).

5 Grant, H. P., et al., "Turbine Blade Temperature Measurement Using Thin Film Temperature Sensors," PWA-5604, Pratt and Whitney Aircraft, East Hartford, CT, 1981 (NASA CR-165201).

6 Grant, H. P., et al., "Thin Film Temperature Sensors Phase III," PWA-5708-26, Pratt and Whitney Aircraft, East Hartford, CT, 1982 (NASA CR-165476).

7 Atkinson, W. H., and Strange, R. R., "Development of Advanced High Temperature Heat Flux Sensors," PWA-5723-27, Pratt and Whitney Aircraft, East Hartford, CT, 1982 (NASA CR-165618).

8 Atkinson, W. H., Cyr, M. A., and Strange, R. R., "Turbine Blade and Vane Heat Flux Sensor Development. Phase I," PWA-5914-21, Pratt and Whitney Aircraft, East Hartford, CT, 1984 (NASA CR-168297).

9 Blair, M. F., "Influence of Free Stream Turbulence on Turbulent Boundary Layer Heat Transfer and Mean Profile Development, Part 1-Experimental Data," *Journal of Heat Transfer*, Vol. 105, No. 1, Feb. 1983, pp. 33–40.

10 Kays, W. M., *Convective Heat and Mass Transfer*, Second Edition, McGraw-Hill, New York.

11 Touloukian, Y. S., et al., *Thermophysical Properties of Matter*, Vol. 1, IFI/Plenum, 1970.

12 Poferl, D. J., Svehla, R. A., and Lewandowski, K., "Thermodynamic and Transport Properties of Air and the Combustion Products of Natural Gas and of ASTM-A-1 Fuel with Air," NASA TN D-5452, 1969.

13 Calvert, H. F., et al., "Turbine Cooling Research Facility," NASA TM-X-1927, 1970.

14 Holanda, R., "Analysis of Thermoelectric Properties of High-Temperature Complex Alloys of Nickel-Base, Iron-Base, and Cobalt-Base Groups," NASA TP-2278, 1984.

15 Liebert, C. H., et al., "High Temperature Thermocouple and Heat Flux Gage Using a Unique Thin Film-Hardware Hot Junction," NASA TM-86898, 1984.

Downloaded 01 Jun 2010 to 171.66.16.71. Redistribution subject to ASME license or copyright; see http://www.asme.org/terms/Terms_Use.cfm

M. Koya
Research and Development Department,
Ishikawajima Harima Heavy Industries,
229 Tonogaya, Mizuho,
Tokyo, Japan, 190-12

S. Kotake
Faculty of Engineering,
University of Tokyo,
Tokyo, Japan

Numerical Analysis of Fully Three-Dimensional Periodic Flows Through a Turbine Stage

Fully three-dimensional periodic flows through a turbine stage of stator and rotor are studied numerically by solving time-dependent three-dimensional Euler equations with the finite-volume method. The phase relation of stator and rotor flows and the related blade-row interaction are accounted for in the time-space domain. The established method of numerical calculation makes a practical contribution to predict actual turbine flows through a turbine stage of stator and rotor which have an arbitrary number of blades.

Introduction

In the last five years, the numerical analysis of three-dimensional, transonic turbine flows has made remarkable progress and contributed to the improvement of their aerodynamic performance. The turbine stages comprised of successive blade rows of stator and rotor are always associated with periodically unsteady flows, and these periodic changes of flow variables have a considerable effect on the turbine performance. It is mostly difficult to study the unsteady aerodynamics experimentally by measuring the flow variables in the rotating coordinate system. On the other hand, when the numerical method of computation is established, it is easy to predict the throughflow field in a short time and at relatively inexpensive cost. The latter has further advantages of quick response to the change in the experimental conditions as well as in the geometrical configuration of blades and blade rows.

The boundary layer is thinner in turbine flows than in compressor flows. The exit Mach number in current turbo-fan engines is between 0.9 and 1.0. These result in a fairly small interaction between the boundary layer and shock waves. Considering that the inviscid flow analysis has been successfully applied to the turbine flow, it is also expected to be applicable to unsteady turbine flows. At the present, the viscous flow analysis is beyond practical use from the standpoints of computational time and memory storage.

For three-dimensional and transonic inviscid flows having a radial variation of circulation, it is most straightforward and practical to solve the time-dependent Euler equations with the finite volume method, such as developed by Denton [1], Van Hove [2], Holmes and Tong [3], Hoffmann [4], and Koya and Kotake [5]. Arts [6] reported a numerical calculation of steady, three-dimensional stage-throughflows in which the flow variables were averaged in the pitchwise direction at the connecting surface between stator and rotor rows. Mitchell [7] and Hodson [8] calculated two-dimensional unsteady flows generated by interaction of upstream wake with a moving blade row by imposing a periodically changing wake flow at the upstream boundary of the rotor. Erdos [9] studied the two-dimensional throughflow of fan stages under periodic unsteady conditions.

In the present study, the numerical method for periodic, three-dimensional, transonic flows through turbine stages has been studied. The flows through turbine stage are periodic in time, or have a phase difference in space. In order to solve straightforwardly the fluid-dynamical equations for such a flow, the calculation will be done over multiple blade passages that satisfy the periodic condition. When, as is practical, the number of upstream blades is not an integral multiple of that of downstream blades, it will take extraordinarily huge memory and time for CPU. For practical use, an alternative should be studied to obtain the same periodic unsteady solution. The present method developed needs only one blade passage each for stator and rotor blade rows by replacing the space-phase lag with the time-phase lag. It provides a powerful and practical tool of the turbine stage flow analysis with computing time and memory storage reasonable for current computing machines.

As the numerical study of periodic turbine-stage throughflows, a typical single stage of high-pressure turbine was chosen, and the interaction behavior between the stator and the rotor was studied with a detailed description of the unsteady flow field.

Governing Equations

Equations to be solved are the conservation equations of mass, momentum, and energy for inviscid flows. These are expressed in a cylindrical coordinate system fixed to the blade rotating with a constant angular velocity Ω around the X-axis as follows:

Contributed by the Gas Turbine Division of THE AMERICAN SOCIETY OF MECHANICAL ENGINEERS and presented at the 30th International Gas Turbine Conference and Exhibit, Houston, Texas, March 18-21, 1985. Manuscript received at ASME Headquarters, December 21, 1984. Paper No. 85-GT-57.

Copyright © 1985 by ASME
Downloaded 01 Jun 2010 to 171.66.16.71. Redistribution subject to ASME license or copyright; see http://www.asme.org/terms/Terms_Use.cfm

$$\frac{\partial}{\partial t}\begin{bmatrix}\rho\\ \rho w_x\\ \rho w_r\\ \rho r w_\theta\\ \rho R_r - p\end{bmatrix}+\frac{\partial}{\partial x}\begin{bmatrix}\rho w_x\\ \rho w_x^2+p\\ \rho w_r w_x\\ \rho r w_\theta w_x\\ \rho w_x R_r\end{bmatrix}+\frac{\partial}{r\partial\theta}\begin{bmatrix}\rho w_\theta\\ \rho w_x w_\theta\\ \rho w_r w_\theta\\ \rho r w_\theta^2+r\,p\\ \rho w_\theta R_r\end{bmatrix}$$

$$+\frac{\partial}{r\partial r}\begin{bmatrix}\rho r w_r\\ \rho r w_x w_r\\ \rho r w_r^2+r\,p\\ \rho r^2 w_\theta w_r\\ \rho r w_r R_r\end{bmatrix}-\begin{bmatrix}0\\ 0\\ \{p+\rho(w_\theta+r\Omega)^2\}/r\\ -2\rho r w_r\Omega\\ 0\end{bmatrix}=0 \tag{1}$$

The gas is assumed to be ideal, having the equation of state:

$$p=\rho(\kappa-1)\left(R_r-\frac{p}{\rho}-\frac{w^2}{2}+\frac{r^2\Omega^2}{2}\right), \tag{2}$$

where κ is the ratio of specific heats.

Grid. A simple grid system of finite volume elements is adopted, consisting of one blade passage each for the stator vane row and the rotor blade row with upstream and downstream extensions approximately parallel to the flow direction. The flow passage is divided into unit grid cells by three families of surfaces: axial (x), radial (r), and pitchwise (θ) surfaces. At the interface between the stator vane row and the rotor blade row, one grid cell is overlapped in the axial direction. The finite volume cells consist of these three surfaces. In the case of turbine blades, these surfaces usually have a highly twisted configuration.

Finite Volume Discretization. The governing equations can be expressed in an integral form for a finite time and a finite space volume. The volume integrals of the space derivatives can be replaced by a sum of surface integrals over the six surfaces of the control volume. By assuming constant values of the flow variables over the surfaces, the surface integral is expressed as a product of the constant value and the projected surface area. The surface integrals are then given as follows [5]:

$$\iint\frac{\partial F}{\partial x}\,dvdt=\Delta t\cdot\{F_{i+1,j,k}S_{xxi+1,j,k}-F_{i-1,j,k}S_{xxi-1,j,k}-F_{i,j+1,k}S_{rxi,j+1,k}+F_{i,j-1,k}S_{rxi,j-1,k}-F_{i,j,k+1}S_{txi,j,k+1}+F_{i,j,k-1}S_{txi,j,k-1}\} \tag{3}$$

$$\iint\frac{\partial F}{r\partial\theta}\,dvdt=\Delta t\cdot\{F_{i,j,k+1}S_{tti,j,k+1}\cos(\theta_{i,j,k+1}-\theta_{i,j,k})-F_{i,j,k-1}S_{tti,j,k-1}\cos(\theta_{i,j,k}-\theta_{i,j,k-1})\} \tag{4}$$

$$\begin{aligned}\iint\frac{\partial F}{\partial r}\,dvdt=\Delta t\cdot\{&F_{i,j+1,k}S_{rri,j+1,k}\cos(\theta_{i,j+1,k}-\theta_{i,j,k})\\&-F_{i,j-1,k}S_{rri,j-1,k}\cos(\theta_{i,j,k}-\theta_{i,j-1,k})\\&-F_{i+1,j,k}S_{xri+1,j,k}\cos(\theta_{i+1,j,k}-\theta_{i,j,k})\\&+F_{i-1,j,k}S_{xri-1,j,k}\cos(\theta_{i,j,k}-\theta_{i-1,j,k})\\&-F_{i,j,k+1}S_{tri,j,k+1}\cos(\theta_{i,j,k+1}-\theta_{i,j,k})\\&+F_{i,j,k-1}S_{tri,j,k-1}\cos(\theta_{i,j,k}-\theta_{i,j,k-1})\\&-F_{i,j,k+1}S_{tti,j,k+1}\sin(\theta_{i,j,k+1}-\theta_{i,j,k})\\&-F_{i,j,k-1}S_{tti,j,k-1}\sin(\theta_{i,j,k}-\theta_{i,j,k-1})\}\end{aligned} \tag{5}$$

where S_{rx}, S_{tr}, etc. are the area of the r-surface projected in the x-direction, the area of the θ-surface projected in the r-direction, etc., respectively. These areas should satisfy the condition of a closed surface around the control volume; the terms in brackets in equations (3) to (5) should vanish for constant values of F. Highly three-dimensionally twisted blades result in the grid configuration distorted so significantly that the radial and pitchwise directions of the surfaces differ appreciably within a unit-volume cell. The terms of trigonometric functions in equations (3) to (5) are introduced so as to satisfy the closed-surface condition even for such highly twisted blade configurations.

The time derivative can be approximated by forward discretization. However, from the viewpoint of computational stability, it is preferable to replace the present value at the center point of the control volume by a value averaged over its surrounding points so as to incorporate a numerical viscosity. The finite volume integral of the time derivative is then expressed by [5]:

$$\begin{aligned}\iint\frac{\partial F}{\partial t}\,dtdv=\Delta v_{i,j,k}\Big[&F^{t+\Delta t}_{i,j,k}-(1-\epsilon)F^{t}_{i,j,k}-\epsilon\Big\{F^{t}_{i-1,j,k}\\&+(x_{i,j,k}-x_{i-1,j,k})\cdot\\&\Big(\frac{F^{t}_{i+1,j,k}}{x_{i+1,j,k}-x_{i,j,k}}+\frac{F^{t}_{i,j+1,k}}{r_{i,j+1}-r_{i,j}}+\frac{F^{t}_{i,j-1,k}}{r_{i,j}-r_{i,j-1}}\\&+\frac{F^{t}_{i,j,k+1}}{r_{i,j}(\theta_{i,j,k+1}-\theta_{i,j,k})}+\frac{F^{t}_{i,j,k-1}}{r_{i,j}(\theta_{i,j,k}-\theta_{i,j,k-1})}\Big)\Big\}\Big/\\&\Big(1+\frac{x_{i,j,k}-x_{i-1,j,k}}{x_{i+1,j,k}-x_{i,j,k}}+\frac{x_{i,j,k}-x_{i-1,j,k}}{r_{i,j+1}-r_{i,j}}+\frac{x_{i,j,k}-x_{i-1,j,k}}{r_{i,j}-r_{i,j-1}}\\&+\frac{x_{i,j,k}-x_{i-1,j,k}}{r_{i,j}(\theta_{i,j,k+1}-\theta_{i,j,k})}+\frac{x_{i,j,k}-x_{i-1,j,k}}{r_{i,j}(\theta_{i,j,k}-\theta_{i,j,k-1})}\Big)\Big]\end{aligned}$$

where ϵ is the numerical viscosity coefficient. The introduction of such a numerical viscosity results in favorable convergence but poor accuracy, being associated with a total pressure loss. It has, however, little effect on the continuity and enthalpy conservation. The numerical viscosity coefficient ϵ should thus be given a value as close as possible to

Nomenclature

Ca = axial chord length (m)
e = internal energy
p = pressure (N/m^2)
R = rothalpy
r = radial coordinate
T = temperature (K)
t = time
w = velocity (m/s)
x = axial coordinate
α = radial flow angle at inlet
β = tangential flow angle at inlet
θ = pitchwise angular coordinate
κ = ratio of specific heats
ρ = density (kg/m^3)
Ω = angular velocity
Δt = time step

Subscripts

i = axial coordinate index
j = radial coordinate index
k = tangential coordinate index
o = stagnation condition
t = time
x = axial direction
r = radial direction
θ = tangential direction

Downloaded 01 Jun 2010 to 171.66.16.71. Redistribution subject to ASME license or copyright; see http://www.asme.org/terms/Terms_Use.cfm

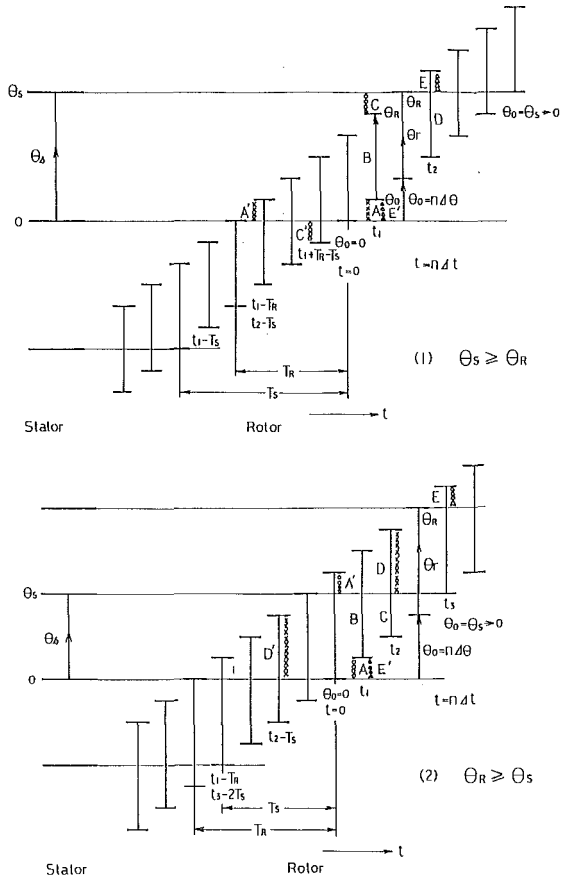


Fig. 1 Boundary conditions at the connecting surface of stator and rotor

zero. In the present calculations, $\epsilon = 0.1$ was adopted after many trial runs. In the case of steady blade-row flows, its lowest value was found to be 0.05.

The time step can be determined by the stability condition

$$\Delta t < \frac{1}{\sqrt{3}} \left(\frac{\Delta x_x}{a + w_x}, \frac{\Delta x_r}{a + w_r}, \frac{\Delta x_\theta}{a + w_\theta} \right)_{\min.}$$

where Δx_x, Δx_r, Δx_θ are the lengths of the control volume in the axial, radial and pitchwise directions respectively, and a is the sound velocity.

Boundary Conditions

Inlet. The total pressure P_o, the total temperature T_o and the two flow angles α, β are to be specified at the inlet boundary. The axial velocity at the inlet is determined with the method of characteristics of wave propagation.

Outlet. It is one of the most crucial conditions to specify the static pressure at the outlet. The static pressure distribution adopted in the present study satisfies the axisymmetric radial equilibrium equation at the design point. The axial velocity at the outlet is also determined with the method of characteristics and the other two velocity components are given by the equations of convective motion.

Blade Surfaces. With the impermeability condition of mass and momentum fluxes, the finite volume integrals of conservation equations are obtained at half and full mesh-size points adjoining the wall surface. The method of characteristics can be adopted to determine the pressure, and the velocity components are given by the convective motion with the zero component of the velocity perpendicular to the wall surface. The boundary conditions at the leading and trailing edges require special consideration since the flow properties

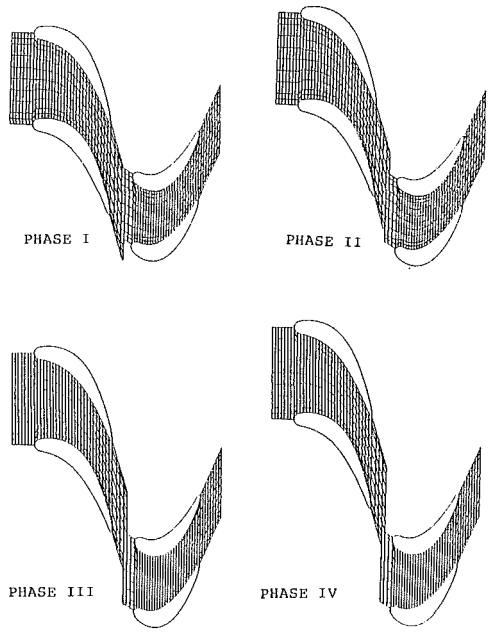


Fig. 2 Grid configuration

are to be changed considerably. To deal with it, the two-value method is employed for the three velocity components at the leading and trailing edges [5]. At the leading edge, two distinct points are defined in order to satisfy that the velocity should be parallel to the blade surface. These two points are the same point and one point is considered as the point on the suction surface and its velocity is along the suction surface. The other point is on the pressure surface and its velocity is along the pressure surface. The density and the pressure at the leading edge are given as the arithmetical averages at these points. At the trailing edge, the boundary conditions are treated in the same way as at the leading edge. This treatment of the boundary conditions at the blade-wall surfaces can reduce greatly the discretization errors associated with highly distorted grid configurations and makes it possible to calculate transonic flows in highly three-dimensional turbine-blade cascades.

Connecting Surface. The stator flow is considered in an absolute coordinate system and the rotor flow is considered in a relative coordinate system fixed to the rotating rotor blade. In an unsteady flow field, flow variables at the connecting surface should be estimated by their convective and wave propagation motions with a method of characteristics. It is not easy to apply such a method in different coordinate systems. This difficulty can be removed by overlapping one volume cell in the axial direction at the connecting surface between the stator and the rotor. The flow variables at the downstream end of the stator are obtained by being equal to those of the rotor located at the same axial position, and the values at the upstream end of the rotor are obtained from those of the stator. Denoting the pitch angle of the stator-vane row, and that of the rotor-blade row as θ_S and θ_R, respectively, the time required for the rows to travel one pitchwise passage is given by $T_S = \theta_S/\Omega$ and $T_R = \theta_R/\Omega$, respectively. Depending on the relative value of θ_S and θ_R, two cases can be considered to connect the flow fields of the stator and rotor as shown in Figs. 1(a) and 1(b).

(a) $\theta_S > \theta_R$. In this case, the pitchwise flow field of the stator is always wider than that of the rotor. The flow variables at the downstream end of the stator should be estimated by the values of the rotor at different times. As

Downloaded 01 Jun 2010 to 171.66.16.71. Redistribution subject to ASME license or copyright; see http://www.asme.org/terms/Terms_Use.cfm

Table 1 Dimensional and flow data of the turbine stage

		Case 1	
		Stator	Rotor
chord (mm)	hub	43.9	33.9
	mean	50.0	34.0
	tip	51.4	35.6
maximum thickness (mm)	hub	6.7	8.4
	mean	7.1	7.7
	tip	8.2	6.4
chord/pitch	hub	1.20	1.22
	mean	1.29	1.13
	tip	1.25	1.11
stagger angle (deg)	hub	53.0	33.5
	mean	54.0	37.8
	tip	49.6	44.0
span height (mm)	inlet	45.0	45.0
	outlet	45.0	45.0
inlet total pressure (N/m^2)		9.36×10^5	
inlet total temperature (K)		1300.0	
inlet mach number	mean	0.21	0.35
inlet tangential flow angle (deg)	hub	0.0	
	mean	0.0	
	tip	0.0	
inlet radial flow angle (deg)	hub	0.0	
	mean	0.0	
	tip	0.0	
outlet static pressure (N/m^2)	hub	4.27×10^5	
	mean	4.06×10^5	
	tip	4.18×10^5	
outlet relative tangential flow angle (deg)	mean	71.0	64.3
outlet relative mach number	mean	1.05	0.82
number of blades		52	68

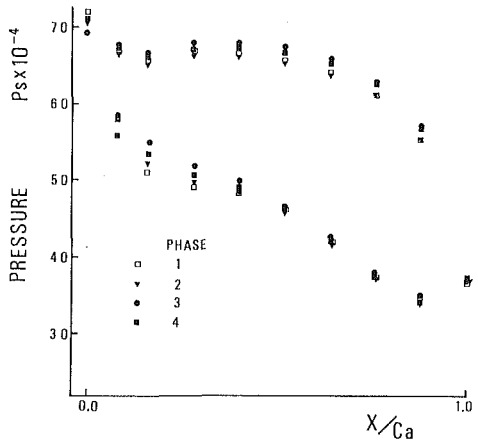


Fig. 3 Periodic pressure distributions on the rotor blade

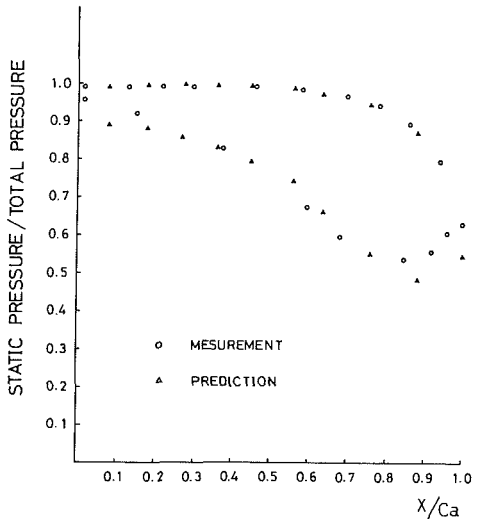


Fig. 4 Comparison of measured and predicted pressure distribution at 50% span height

shown in Fig. 1(*a*), the flow at the upstream end of the rotor is divided into three regions *A*, *B*, and *C* at the time t_1:

$$\text{Region } A: \quad 0 < \theta_s < \theta_o$$

$$\text{Region } B: \quad \theta_o < \theta_s < \theta_o + \theta_R$$

$$\text{Region } C: \quad \theta_o + \theta_R < \theta_s < \theta_S$$

where θ_s is the pitchwise angle in the stator and θ_o is the temporary pitchwise angle of a rotor blade; θ_o is set to zero at $t = 0$. As the rotor goes forward in the pitchwise direction with time, the value of θ_o increases and the temporary rotor positions at $t = t_1$ and $t = t_2$ are shown in Fig. 1(*a*). At the region *B*, the flow variables in the stator vane are obtained directly from those in the rotor blade at the same time $t = t_1$. The flow variables at the downstream end of the stator vane $\phi_S(\theta_s, t)$ should be equal to that of the rotor blade at the upstream end of the rotor $\phi_R(\theta_r, t)$ at $\theta_r = \theta_s - \theta_o$;

$$\phi_S(\theta_s,t) = \phi_R(\theta_s - \theta_o, t) \quad \theta_s \in B$$

At the regions *A* and *C*, the flow variables in the stator and rotor are not directly related to each other at the time $t = t_1$, but with the values at the different time. It is seen from Fig. 1(*a*) that the flow of the region *A* at the time $t = t_1$ corresponds to that of the region *A'* at the time $t = t_1 - T_R$ and the region *C* at the time $t = t_1$ to the region *C'* at the time $t = t_1 - T_S + T_R$;

$$\phi_S(\theta_s,t) = \phi_R(\theta_s - \theta_o + \theta_R, t - T_R) \qquad \theta_s \in A$$

$$\phi_S(\theta_s,t) = \phi_R(\theta_s - \theta_o - \theta_R, t - T_S + T_R) \qquad \theta_s \in C$$

Concerning the flow variables at the upstream end of the rotor blade, the flow region may be divided into the two regions *D* and *E* as shown in Fig. 1(*a*);

$$\text{Region } D: \quad \theta_r < \theta_S - \theta_o$$

$$\text{Region } E: \quad \theta_S - \theta_o < \theta_r$$

where θ_r is the pitchwise angle in the rotor. In the region *D*, the flow values correspond directly to those of the stator vane at the same time $t = t_2$,

$$\phi_R(\theta_r,t) = \phi_S(\theta_r + \theta_o, t) \quad \theta_r \in D$$

In the region *E*, the flow variables correspond to those in the region *E'* with the phase lag in time, $T_S - T_R$, that is, at the time $t = t_2 - T_S + T_R$

$$\phi_R(\theta_r,t) = \phi_S(\theta_r + \theta_o - \theta_S, t - T_S + T_R) \quad \theta_r \in E$$

(*b*) $\theta_R > \theta_S$. In this case, the situation is reversed. The flow field of the rotor is always larger than that of the stator. The flow region at the downstream end of the stator is divided into the two regions *A* and *B* as shown in Fig. 1(*b*).

$$\text{Region } A: \quad 0 < \theta_s < \theta_o$$

$$\text{Region } B: \quad \theta_o < \theta_s$$

With the same consideration as in the preceding case as shown in Fig. 1(*b*), the flow variables at the downstream end of the stator are given by

$$\phi_S(\theta_s,t) = \phi_R(\theta_s - \theta_o + \theta_R, t - T_R + T_S) \qquad \theta_s \in A$$

$$\phi_S(\theta_s,t) = \phi_R(\theta_s - \theta_o, t) \qquad \theta_s \in B$$

The flow region at the upstream end of the rotor is also divided into the three regions *C*, *D*, and *E*.

Downloaded 01 Jun 2010 to 171.66.16.71. Redistribution subject to ASME license or copyright; see http://www.asme.org/terms/Terms_Use.cfm

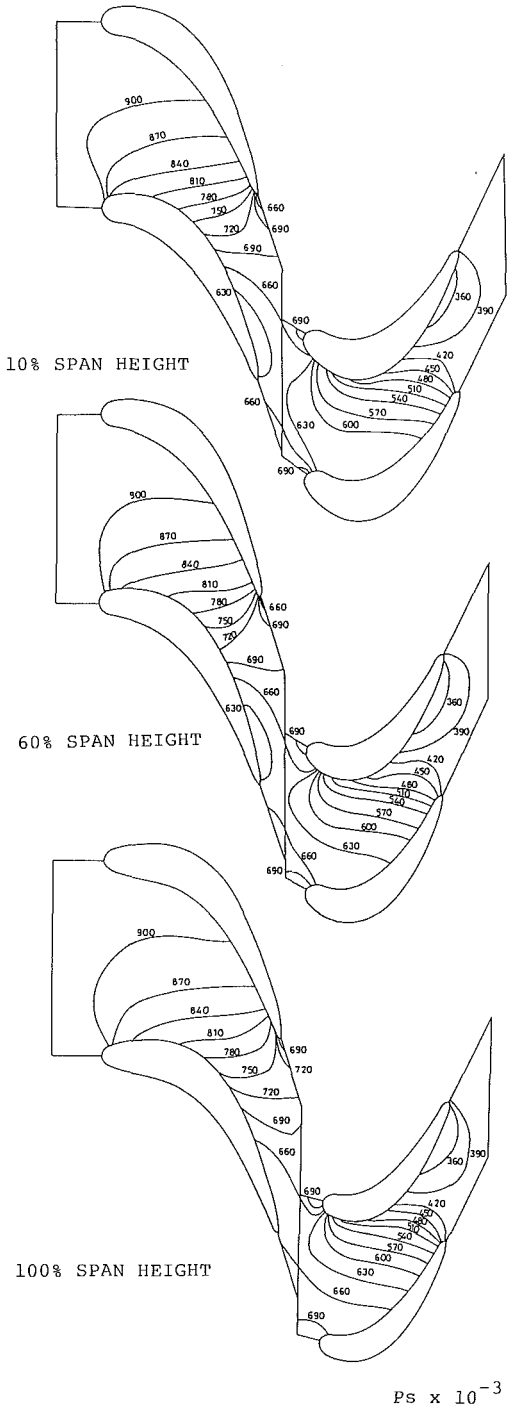


Fig. 5 Pressure contour in the radial surface at Phase II (GAP/*Ca* = 0.25, 7900 rpm)

$$\text{Region } C: \quad 0 < \theta_r < \theta_S - \theta_o$$

$$\text{Region } D: \quad \theta_S - \theta_0 < \theta_r < 2\theta_S - \theta_o$$

$$\text{Region } E: \quad 2\theta_S - \theta_o < \theta_r$$

The flow variables at the upstream end of the rotor are given by

$$\phi_R(\theta_r,t) = \phi_S(\theta_r + \theta_o, t) \qquad \theta_r \in C$$

$$\phi_R(\theta_r,t) = \phi_S(\theta_r + \theta_o - \theta_S, t - T_S) \qquad \theta_r \in D$$

$$\phi_R(\theta_r,t) = \phi_S(\theta_r + \theta_o - 2\,\theta_S, t - 2\,T_S + T_R) \qquad \theta_r \in E$$

For both cases, when θ_o becomes equal to θ_S, t and θ_o are reset to zero.

Free Stream Boundaries. When the stator-blade number is equal to the rotor-blade number, the periodic condition can be imposed at the free stream boundaries. For an arbitrary number of blades, the flow downstream of the stator at $\theta_s = \theta_S$ and $t = t_1$ corresponds to that at $\theta_s = 0$ and $t = t_1 - T_S + T_R$ in the case of $\theta_S > \theta_R$ and to that at $\theta_s = 0$ and $t = t_1 - T_S$ in the case of $\theta_R > \theta_S$:

$$\phi_S(\theta_s,t) = \phi_S(0, t - T_S + T_R) \qquad \theta_S > \theta_R$$

$$\phi_S(\theta_s,t) = \phi_S(0, t - T_S) \qquad \theta_R > \theta_S$$

For the rotor, the flows are related at the time difference $T_S - T_R$ and $2\,T_S - T_R$, respectively:

$$\phi_R(\theta_r,t) = \phi_R(0, t - T_S + T_R) \qquad \theta_S > \theta_R$$

$$\phi_R(\theta_r,t) = \phi_R(0, t - 2\,T_S + T_R) \qquad \theta_R > \theta_S$$

Turbine-Stage Flows

A typical turbine stage is chosen to calculate its periodic, three-dimensional flow field with the above-mentioned numerical scheme. The chosen is a high-pressure turbine stage which is highly three-dimensional with a low aspect ratio. The shape of the stator and rotor blades and the grid configurations used are shown in Fig. 2. The dimensional data of the blades are listed in Table 1 together with the relevant flow data used for the calculation. In Fig. 2, the configuration of the stator and the rotor at the midspan is shown at four different phases in time which are hereafter referred to as Phase I, II, III, and IV, respectively. The grid consisted of 43 $\times$ 8 $\times$ 11 $\times$ 2 calculation points which required 3.0 M bytes of memory storage. The typical CPU time was 4.0 s per time step. About 3000 time steps were required for convergence, although the convergence was dominated largely by the initial values assumed at the start of computation. The convergence of the calculation was examined with respect to the periodicity of the pressure. Figure 3 shows the periodic pressure distributions on the rotor blade. It can be seen from the figure that the convergence is good. At the final convergence, the averaged difference of the tangential flow angle at the stator exit of the same phase was about 0.2 deg. To evaluate the accuracy of this code, the predicted pressure distributions on blade surfaces are compared with an experimental result in Fig. 4. The test was performed by using the stator vane of case 1 in a three-dimensional wind tunnel. The figure shows good agreement between them.

Figure 5 shows the pressure contour at the hub, mean and tip sections in the radial surface at Phase II. The figure characterizes a three-dimensional pressure field both in the stator and the rotor especially close to the connecting plane. The flow through the turbine stage is periodic in time. The magnitudes of these periodic changes in the flow variables are larger as the axial gap between the stator and the rotor is decreased. At first, we consider these periodic changes for a fixed gap of GAP/Ca = 0.25, where GAP is the axial gap and Ca is the axial chord length of the stator. The periodic changes of the flow are observed appreciably in the regions downstream of the stator and upstream of the rotor. Figures 6 and 7 show the contour of the tangential flow angle referred to Phase I in these flow regions. It should be noted that the flow angle changes in the rotor in Fig. 6 are expressed in terms of relative angles. The flow angle in the downstream region of the stator is affected largely by the position of the leading edge of the rotor. The flow that goes into the suction side of the rotor increases the tangential flow angle in the downstream region of the stator, whereas the flow into the pressure side of the rotor decreases the flow angle. The tangential flow angle in the upstream region of the rotor is influenced by its pitchwise distributions at the stator exit which depend on the phase relationship between the stator and the rotor. The periodic changes in the pressure at the stator exit are shown in Fig. 8. The high-pressure regions in the downstream of the

Downloaded 01 Jun 2010 to 171.66.16.71. Redistribution subject to ASME license or copyright; see http://www.asme.org/terms/Terms_Use.cfm

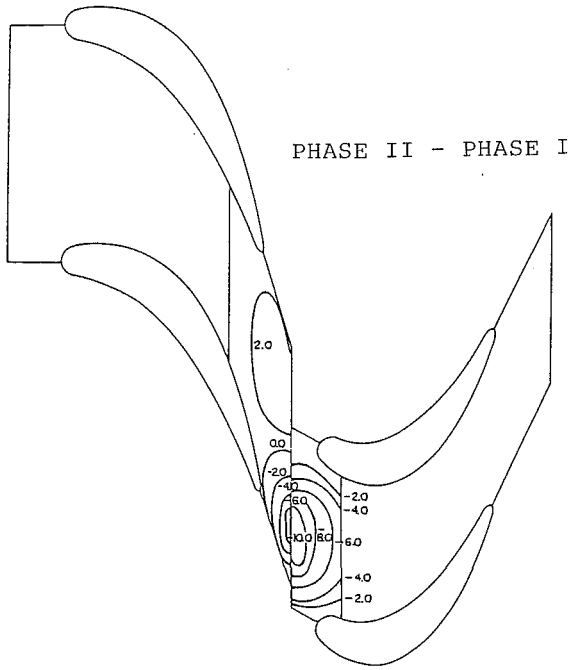


Fig. 6(*a*) Changes in the tangential flow angle (GAP/*Ca* = 0.25, 60% span height, 7900 rpm)

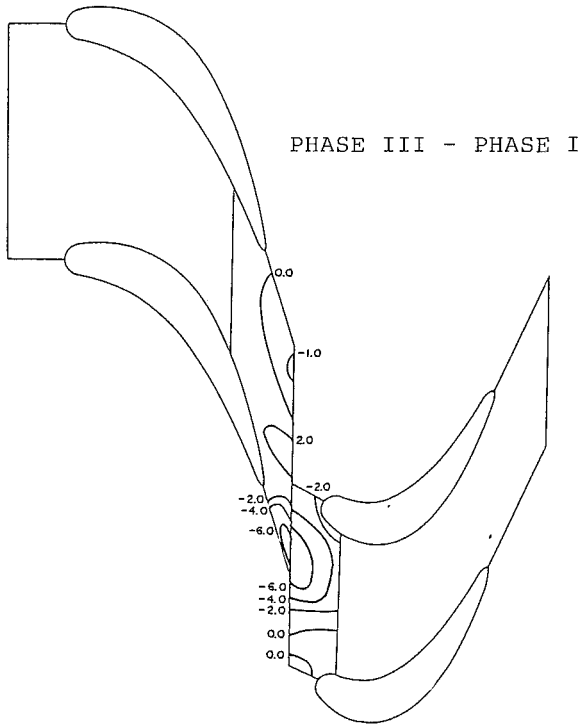


Fig. 6(*b*) Changes in the tangential flow angle (GAP/*Ca* = 0.25, 60% span height, 7900 rpm)

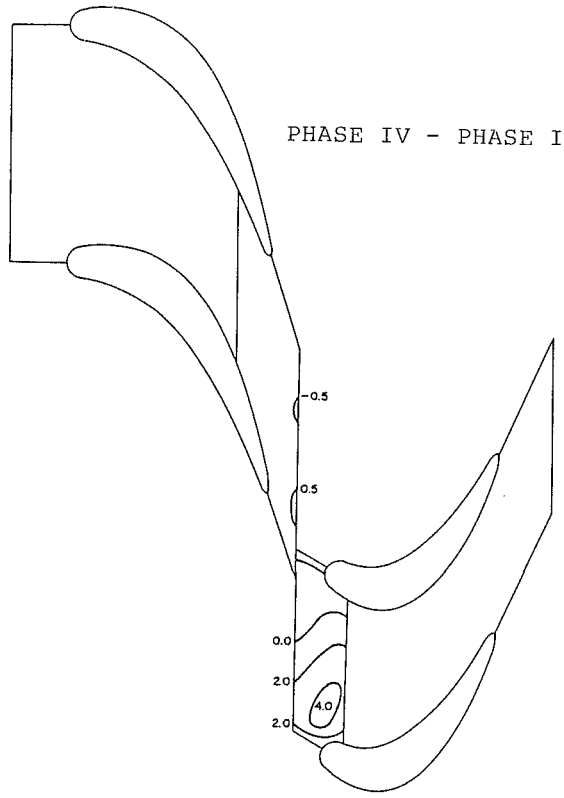


Fig. 6(*c*) Changes in the tangential flow angle (GAP/*Ca* = 0.25, 60% span height, 7900 rpm)

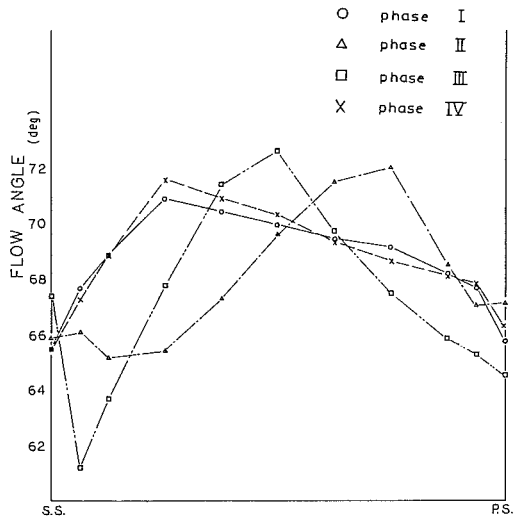


Fig. 7 Periodic changes in the tangential flow angle at the stator exit (GAP/*Ca* = 0.25, 60% span height, 7900 rpm)

stator correspond to the upstream region of the rotor leading edge and may be attributed to its travel in the pitchwise direction with the rotor rotation. The pressure in the upstream region of the rotor is dominated strongly by the pitchwise distribution of the pressure at the stator exit, that is, the pitchwise distributions of the velocity and the total pressure. The total pressure at the connecting surface varies in the pitchwise direction by about 5% in the case of $\epsilon = 0.1$. Although it is the effect of artificial viscosity, the result is likely to simulate the wake flow of the blade row.

Next, we consider the effect of the axial gap between the stator and the rotor on the flow field. Figure 9 shows the contour of the tangential flow angle at Phase II referred to that of Phase I for the case of GAP/*Ca* = 0.45 and is compared with Fig. 6(*a*) for GAP/*Ca* = 0.25. The magnitude of the flow angle variation with GAP/*Ca* = 0.25 is increased about twice that of the case of GAP/*Ca* = 0.45, whereas the phase relationships of pressure distribution are almost similar for both cases. Figure 10 shows the pressure variation with respect to time at the stator exit for the case of GAP/*Ca* = 0.45 to be compared with Fig. 8 for GAP/*Ca* = 0.25. As the gap is decreased, the magnitude of the pressure variation is

Downloaded 01 Jun 2010 to 171.66.16.71. Redistribution subject to ASME license or copyright; see http://www.asme.org/terms/Terms_Use.cfm

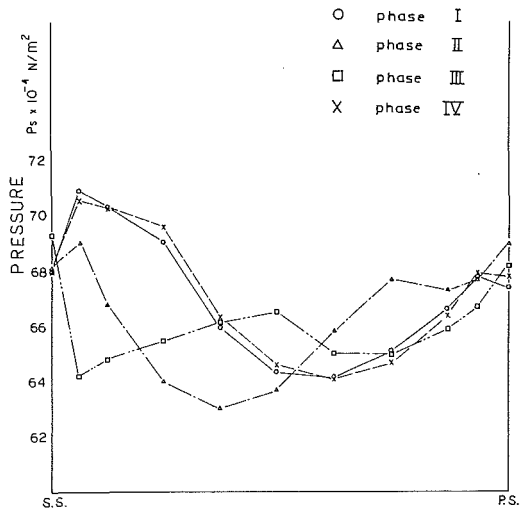


Fig. 8 Pressure distribution at the stator exit (GAP/*Ca* = 0.25, 60% span height, 7900 rpm)

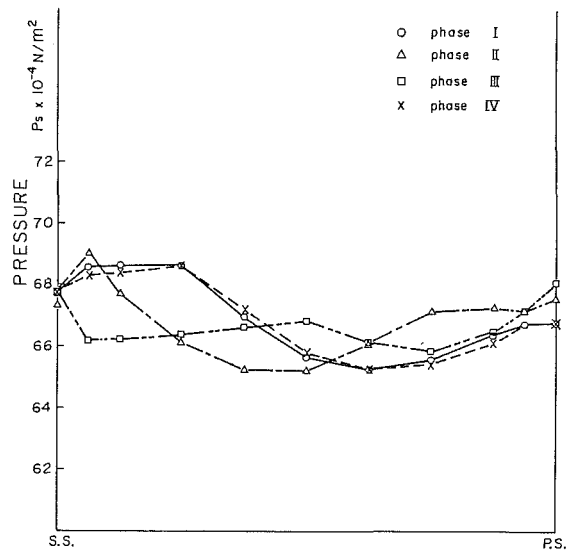


Fig. 10 Pressure distribution at the stator exit (GAP/*Ca* = 0.45, 60% span height, 7900 rpm)

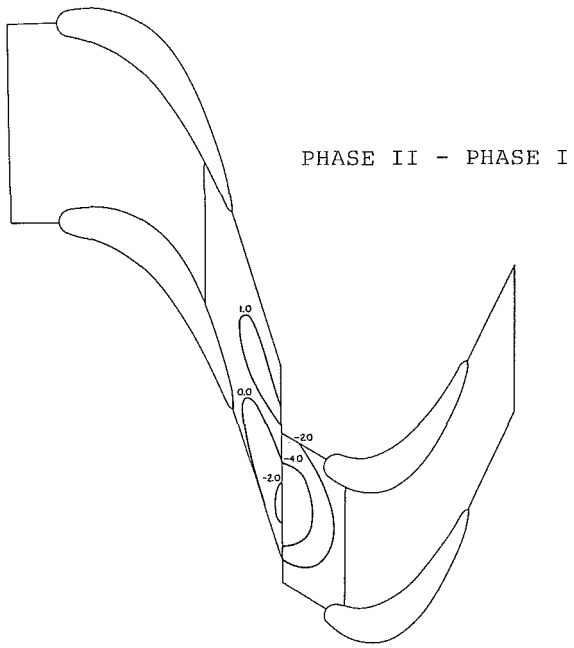


Fig. 9 Changes in the tangential flow angle (GAP/*Ca* = 0.45, 60% span height, 7900 rpm)

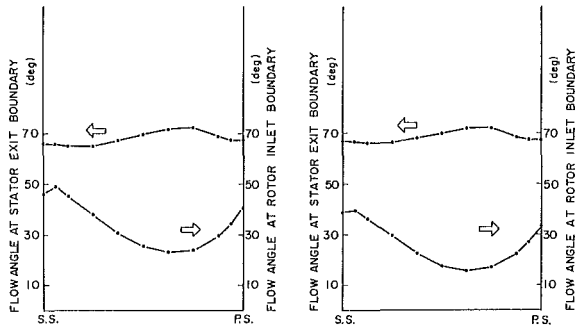


Fig. 11 Effect of the rotor angular velocity on the tangential flow angle (GAP/*Ca* = 0.25, 60% span height)

also increased with keeping the same phase relationships in its pitchwise distribution. These results of the solution of Euler equations should be attributed principally to the inviscid interaction of the fluid motion between the stator and the rotor. The introduction of the numerical viscosity, however, may cause an additional small effect of diffusion on the flow field to account for the results obtained.

At the connecting surface, the relative velocities of the stator and the rotor should satisfy the following relationships.

$$W_{x,\text{stator}} = W_{x,\text{rotor}}$$

$$W_{r,\text{stator}} = W_{r,\text{rotor}}$$

$$W_{\theta,\text{stator}} = W_{\theta,\text{rotor}} + r\Omega$$

Thus, the flow field is also influenced by the angular velocity of the rotor. The pitchwise distributions of the tangential flow angle of the stator and the rotor are shown in Fig. 11 for two cases of the angular velocity, 7900 rpm and 9085 rpm. From the figure, it is seen that the flow angle at the rotor inlet is affected by the angular velocity while the flow angle at the stator exit is little influenced.

Conclusion

In order to calculate periodic, transonic flows in highly three-dimensionally twisted turbine stages, the finite-volume integral method of solving the time-dependent Euler equations is studied. The treatment of boundary conditions at the connecting surface between the stator and the rotor is specially considered to couple the two time-dependent flow fields. Flows in a turbine stage generally have phase differences for each blade passage, but the phase relationships of the stator and rotor flows in the space domain can be related to those in the time domain. The developed scheme makes possible the numerical analysis of periodic unsteady flows through a turbine stage of arbitrary blade numbers in practical CPU time and memory. With the developed method, the flow field through a typical turbine stage was calculated. The periodic behavior in time of the pressure and the flow angles was studied with the obtained results. The effects of the gap between the stator and the rotor and the angular velocity on the stage flow were also discussed.

Downloaded 01 Jun 2010 to 171.66.16.71. Redistribution subject to ASME license or copyright; see http://www.asme.org/terms/Terms_Use.cfm

References

1 Denton, J. D., "An Improved Time Marching Method for Turbomachinery Flow Calculation," ASME JOURNAL OF ENGINEERING FOR POWER, Vol. 105, No. 3, July 1983, pp. 514–524.

2 Van Hove, W., "Calculation of Three-Dimensional, Inviscid, Rotational Flow in Axial Turbine Blade Rows," ASME JOURNAL OF ENGINEERING FOR GAS TURBINES AND POWER, Vol. 106, No. 2, Apr. 1984, pp. 430–436.

3 Holmes, D. G., and Tong, S. S., "A Three-Dimensional Euler Solver for Turbomachinery Blade Rows," ASME JOURNAL OF ENGINEERING FOR GAS TURBINES AND POWER, Vol. 107, No. 2, Apr. 1985, pp. 258–264.

4 Hoffman, W., "Extima-2, Explicit Time Marching Method to Calculate Transonic Turbomachinery Cascade Flow," ASME Paper No. 84-GT-243, 1984.

5 Koya, M., and Kotake, S., "Numerical Flow Analysis of Fully Three-Dimensional Turbine Cascades," ASME Paper No. 84-GT-19, 1984.

6 Arts, T., "Calculation of the Three-Dimensional, Steady, Inviscid Flow in a Transonic Axial Turbine Stage," ASME JOURNAL OF ENGINEERING FOR GAS TURBINES AND POWER, Vol. 107, No. 2, Apr. 1985, pp. 286–292.

7 Mitchell, N. A., "A Time Marching Method for Unsteady Two-Dimensional Flow in a Blade Passage," *Int. J. Heat and Fluid Flow*, Vol. 2, No. 4, 1980.

8 Hodson, H. P., "An Inviscid Blade-to-Blade Prediction of a Wake-Generated Unsteady Flow," ASME JOURNAL OF ENGINEERING FOR GAS TURBINES AND POWER, Vol. 107, No. 2, Apr. 1985, pp. 337–344.

9 Erdos, J. I., "Computation of Unsteady Transonic Flows Through Rotating and Stationary Cascades," NASA CR-2900, 1977.

Downloaded 01 Jun 2010 to 171.66.16.71. Redistribution subject to ASME license or copyright; see http://www.asme.org/terms/Terms_Use.cfm

Local Heat-Transfer Measurements on a Large Scale-Model Turbine Blade Airfoil Using a Composite of a Heater Element and Liquid Crystals

S. A. Hippensteele

L. M. Russell

F. J. Torres

National Aeronautics and Space Administration,
Lewis Research Center,
Cleveland, OH 44135

Local heat-transfer coefficients were experimentally mapped along the midchord of a five-times-size turbine blade airfoil in a static cascade operated at room temperature over a range of Reynolds numbers. The test surface consisted of a composite of commercially available materials: a mylar sheet with a layer of cholesteric liquid crystals, which change color with temperature, and a heater sheet made of a carbon-impregnated paper, which produces uniform heat flux. After the initial selection and calibration of the composite sheet, accurate, quantitative, and continuous heat-transfer coefficients were mapped over the airfoil surface. The local heat-transfer coefficients are presented for Reynolds numbers from 2.8×10^5 to 7.6×10^5. Comparisons are made with analytical values of heat-transfer coefficients obtained from the STAN5 boundary layer code. Also, a leading-edge separation bubble was revealed by thermal and flow visualization.

Introduction

As gas turbine inlet temperatures and pressures increase, the heat loads to the turbine also increase. Consequently, more complex turbine blade cooling configurations are needed to provide acceptable metal temperatures and component life. The attainment of accurate metal-temperature predictions and effectively cooled and durable parts requires accurate knowledge of high-resolution heat-transfer coefficients. A common method used to determine these coefficients consists of finite heater strips with thermocouples [1, 2]. This method, however, only provides average heat-transfer coefficients over intermittent, selected areas and is generally used in one-dimensional idealizations of the problem. As a consequence, methods for measuring high-resolution heat transfer are needed, particularly at near-room-temperature conditions, where the investigation can be conducted at relatively low cost and both turbine flow and heat-transfer dimensionless parameters can be preserved.

The purpose of this study was to demonstrate the method of using a liquid crystal/heater composite sheet for heat-transfer research and to verify accuracy and resolution of the resulting heat-transfer coefficients. The potential of using this method for obtaining heat-transfer measurements was reported in [3]. The present report gives actual quantitative, continuous heat-transfer coefficients on a model turbine blade.

Liquid crystals, by virtue of their property of changing color with temperature, provide a measurement of the continuous temperature and a visualization of thermal patterns. Applying liquid crystals to a uniform heater element and using a heat balance along with the measured electrical input power provides a measure of the local heat-transfer coefficient and its distribution. More information about the nature of liquid crystals and more detail about the uniform heater element are available [3]. Liquid crystals have often been used for indicating temperatures [4]. Liquid crystals have also been used in heat-transfer research [5–8], being sprayed on test surfaces or on carbon-impregnated paper attached to a test surface. The unique features of the composite sheet used for this present report are its simplicity, uniformity, and its use of commercially available materials. This composite was wrapped around the airfoil of the test blade. The test blade was in the center position of a five-blade cascade test section. The test section was part of an atmospheric flow tunnel which was connected to a vacuum exhaust system. The tests were run at room temperature and pressure. The gas-stream Reynolds number varied from 2.8×10^5 to 7.6×10^5 (based on actual chord).

This paper presents quantitative, experimental heat-transfer coefficients around a five-times-size model of a typical high-temperature gas turbine blade airfoil using a liquid crystal/heater composite sheet. In order to lend credence to this method, the results are compared with predicted results obtained using a computer code. Since, in this study, the blade surface was heated and the free stream

Contributed by the Gas Turbine Division of THE AMERICAN SOCIETY OF MECHANICAL ENGINEERS and presented at the 30th International Gas Turbine Conference and Exhibit, Houston, Texas, March 18–21, 1985. Manuscript received at ASME Headquarters, December 21, 1984. Paper No. 85-GT-59.

Copyright © 1985 by ASME
Downloaded 01 Jun 2010 to 171.66.16.71. Redistribution subject to ASME license or copyright; see http://www.asme.org/terms/Terms_Use.cfm

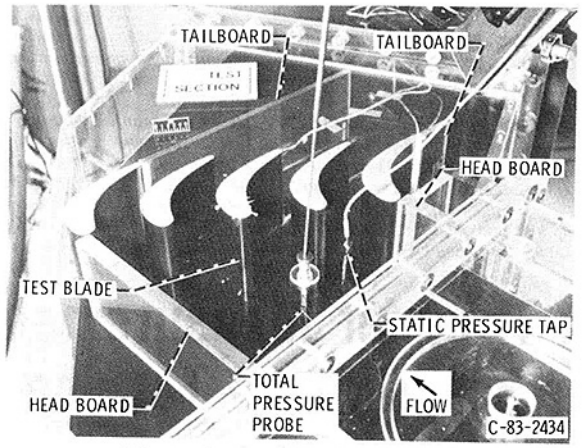


Fig. 1 Close-up view of test section

was at room temperature, the direction of heat transfer is the opposite of what it would be in a real engine with its hot free stream. Areas of high heat transfer in this study resulted in lower surface temperatures. Turbulence measurements and flow visualization results are also presented.

Apparatus

Figure 1 is a photograph of the test section showing the five-blade, two-dimensional cascade which simulates a turbine blade row. The blade profile was five times the size of an existing high-temperature turbine blade. The liquid crystal/heater composite was wrapped completely around the wooden blade and attached to the airfoil surface of the center blade. The free-stream velocity upstream of the blades was measured with the static and total head probes.

Figure 2 is a schematic of the test facility. Room-temperature air was drawn through the tunnel which, except for the inlet and flow straightener sections, was made of clear acrylic plastic and was 15.2 cm (6.0 in.) high. The width was set to 36.8 cm (14.5 in.) by a pair of headboards which extended from the metal inlet section to the blade row leading edge. Tailboards were also used to assure periodicity at the blade row exit. The tunnel is capable of handling up to 4.5 kg/s (10 lb/s) of air with the existing test section installed. The maximum velocity attainable was about 70 m/s (230 ft/s). This velocity produced an inlet Reynolds number (based on actual chord) of 7.6×10^5 which simulates the inlet Reynolds number of typical high-temperature turbines. Typical Mach numbers could not be simulated because of the velocity limitation.

A cross section of the complete liquid crystal/heater composite is shown in Fig. 3. The liquid-crystal sheet was bonded to the heater sheet with a double-coated adhesive material. The same type of adhesive was used to bond the composite sheet to the test blade surface. The total thickness of the composite was 1.17 mm (0.046 in.). The liquid-crystal sheet, purchased commercially, consisted of cholesteric type liquid crystals, which change color with temperature, laid on transparent Mylar covered by a black plastic sealing material.

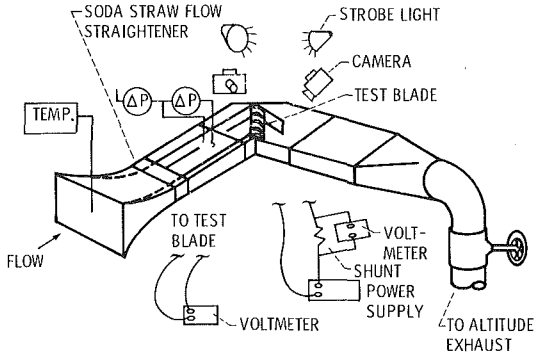


Fig. 2 Schematic of test facility

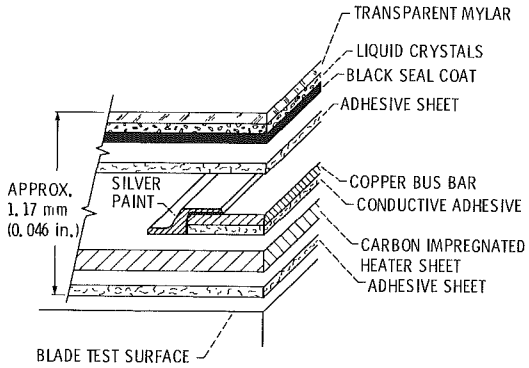


Fig. 3 Cross section of the liquid crystal/heater composite (vertical scale greatly exaggerated)

The overall thickness of the liquid-crystal sheet was 0.20 mm (0.008 in.). The heater element, also commercially purchased, was a carbon-impregnated cardboard-like material with a thickness of 0.76 mm (0.030 in.) and a resistivity of 55 Ω/sq (resistance of any square-shaped area). Copper foil bus bars were attached to the heater sheet at the hub and tip ends of the blade, and a conductive, silver paint was used to ensure good electrical contact. Electrical energy was supplied to copper foil bus bars. The power source was a controllable electric power supply capable of supplying up to 80 V at 25 A.

Procedure

Experimental Heat-Transfer Coefficients. The blade-surface heat-transfer coefficient can be derived from an energy balance on the blade airfoil model:

$$Q_e - Q_l = hA(T_c - T_a) \tag{1}$$

Knowing the measured heat input, Q_e, to the sheet (less heat losses) with heated area, A, and the free-stream air temperature, T_a, the local heat-transfer coefficient, h, can be calculated at the location of the yellow-color band (an isotherm having a uniform heat-transfer coefficient produced by a uniform heat flux). The total heat energy, Q_e, supplied to the heater sheet was calculated from the measured voltage, E, across the heater sheet and the current, I, through a shunt resistor in series with the heater sheet. The heater current was

Nomenclature

a = constant
A = heated area
C,d = constants
E = voltage across heater sheet
h = heat-transfer coefficient
I = current through heater sheet
k = thermal conductivity
L = vertical distance
p = static pressure
P = total pressure
Q = heat flux
Re = inlet Reynolds number based on actual blade chord
S = actual chord length
T = temperature
Δ = difference
δ = uncertainty

Subscripts

a = air
c = liquid crystal at calibrated color temperature
e = electrical power input
H = high value at localized cold spot
L = low value at localized hot spot
l = losses

Downloaded 01 Jun 2010 to 171.66.16.71. Redistribution subject to ASME license or copyright; see http://www.asme.org/terms/Terms_Use.cfm

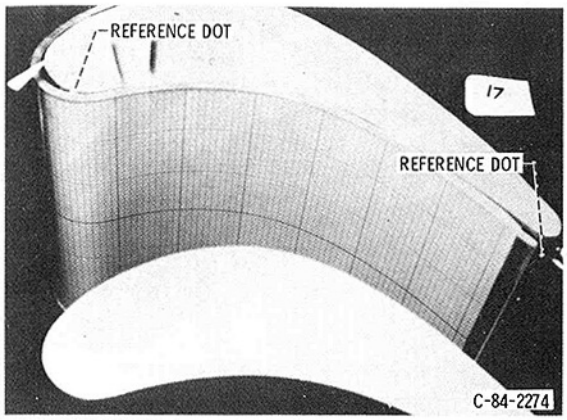


Fig. 4 Location grid, pressure side view

calculated from the measured voltage across the shunt resistor having a known resistance. The heat energy lost, Q_l, is due to conduction through the blade and radiation from the blade. The area, A, is the measured heated area of the heater sheet. The temperature of the yellow-color band, T_c, in the liquid-crystal sheet was determined from a water calibration. The temperature of the upstream, inlet free-stream air, T_a, was measured by the same precision resistance digital thermometer used to calibrate the liquid-crystal yellow-color temperature. Because the technique is new and has little quantitative experience with it, the error analysis is detailed in the Appendix.

Calibration. The liquid-crystal sheet was calibrated for yellow-color-temperature correspondence and uniformity by immersing the sheet in a hot-water bath, and observing and photographing the color changes as the water gradually cooled to room temperature. The water bath was stirred before temperature measurement and photographs were taken. The water temperature was measured by a precision resistance digital thermometer. The blue color corresponded to the highest temperatures with green, yellow, reddish-brown, and black corresponding to decreasing levels of temperature. As discussed in [3], the yellow color occurred over the narrowest temperature band. Therefore, the yellow color was used as the calibration temperature.

The accuracy of the heat-transfer coefficient depends on the uniformity of the heater-element sheet. To measure the uniformity of the heat flux produced by the heater sheet, a temporary composite was made. This temporary composite consisted of a liquid-crystal sheet having a very uniform yellow-color-temperature response and a heater sheet, larger than, but containing the area to be used on the test blade. Electrical power was supplied to this large temporary composite through copper bus bars while it was suspended horizontally in a dead air space. Electrical voltage measurements were made [3] and were used to calculate the local-heat-flux percentage deviation from the overall heater-sheet average heat flux. The area with the most uniform yellow-color distribution (hence, uniform temperature and heat flux) in the large temporary heater sheet was then used on the test blade.

Previous experience with liquid crystals indicates that viewing angle and incident light angle have some effect on the resultant color [3]. Photographs taken showed what effects the camera-viewing and strobe-aiming angles had on the liquid-crystal sheet heated to produce a yellow color. It was found that if the angle between the camera-view and the strobe-aiming was less than 30 deg, then there was no significant color change in the yellow color, regardless of the angle of the liquid-crystal sheet. For angles between the camera-view and the strobe-aiming greater than 30 deg, the color shifted from yellow toward blue, erroneously indicating a temperature greater than that of the calibrated yellow color.

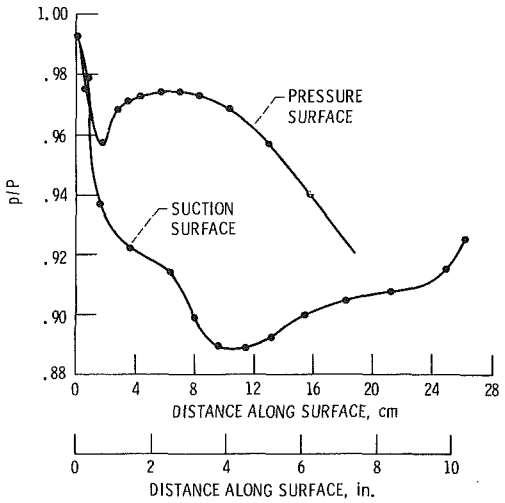


Fig. 5 Measured pressure distribution around blade. Inlet free-stream conditions: velocity, 71.3 m/s (234 ft/s); temperature, 29.5°C (85.1°F); pressure, 91.84 kPa (13.32 psia).

For this reason, the tests for this study were conducted at included angles less than 30 deg.

Testing. Before the turbine-blade tests were performed, the free-stream turbulence intensity level of the tunnel was established. The measurement was made with a hot-wire anemometer at the three free-stream tunnel velocities 24, 37, and 70 m/s (78, 120, and 230 ft/s). The average turbulence intensity was 0.7%. This value is lower than in a typical engine, but it is typical of wind tunnels. Generally, tests were made at three different free-stream inlet velocities 24, 37, and 70 m/s (78, 120, and 230 ft/s). The procedure was to first bring the tunnel to the desired velocity as measured by the total and static pressure probes to produce the proper Reynolds number. Electric power was then supplied to the composite sheet raising its temperature to the point at which the colors began to appear. The power input was "fine tuned" to obtain the desired calibrated yellow color in the locations of interest. The location of the yellow-color band was varied over the airfoil surface by changing the heat input while free-stream velocity remained the same.

Sufficient time had to be given to allow temperatures and the yellow-color band to stabilize. Typically, the first data point in a series of test runs was not taken until about one hour had elapsed at one combination of Reynolds number and electrical power input. Thereafter, data points were taken about 20 to 30 min apart. Data were in the form of color transparency photographs (slides give consistent color balance results) taken with a 35-mm camera to record the yellow-color locations, and the simultaneous documentation of air velocity, power input, air temperature, and pressure. The yellow-color location was established by photographing a grid containing the blade-surface coordinates placed on the blade before the test run. The data pictures showing the yellow-color band and the grid photograph showing the blade surface coordinates were coordinated by the use of two white reference dots located on the blade and in plain view for each picture (see Fig. 4). The coordination process was accomplished by projecting the pictures onto a digitizing table, manually digitizing the locations of the reference dots, grid coordinates, and yellow-color bands, and calculating the yellow-color band locations using a computer.

Analytical Heat-Transfer Coefficients. It is useful to compare the results of any new experimental technique with similar experimental data and analytical results. The primary tools for an analytical simulation were the STAN5 boundary layer code [10, 11] and the measured inlet flow conditions.

Downloaded 01 Jun 2010 to 171.66.16.71. Redistribution subject to ASME license or copyright; see http://www.asme.org/terms/Terms_Use.cfm

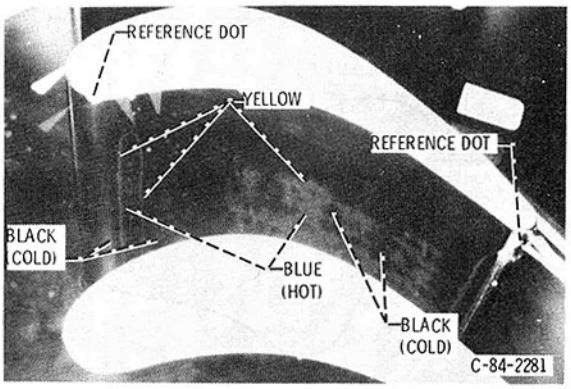


Fig. 6(*a*) Lowest heat flux value, Re = 2.8×10^5

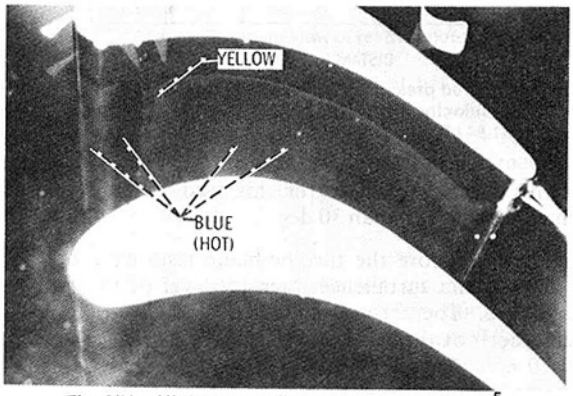


Fig. 6(*b*) Highest heat flux value, Re = 7.6×10^5

Fig. 6 Temperature patterns

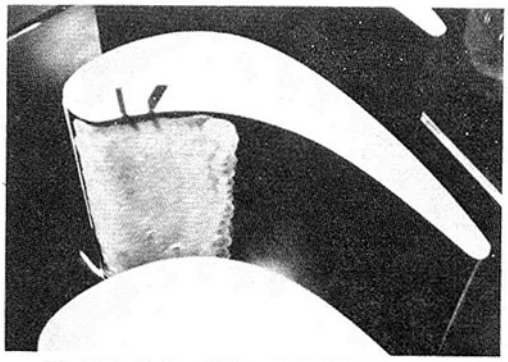


Fig. 7(*a*) Before airflow started, pressure side

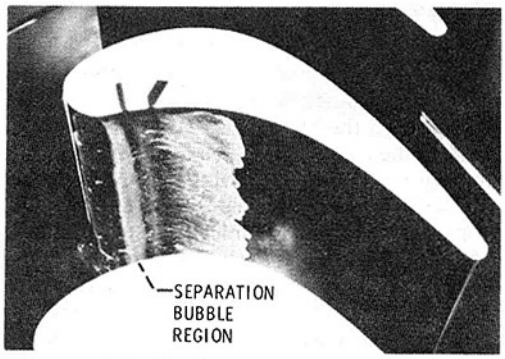


Fig. 7(*b*) After 2 min of airflow, pressure side

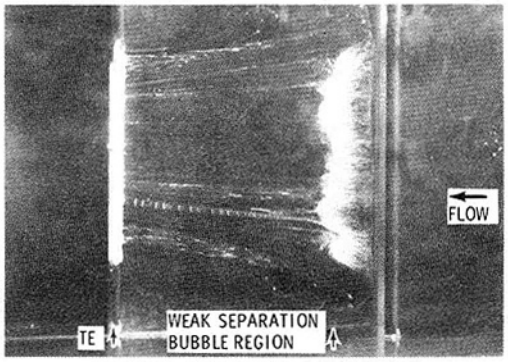


Fig. 7(*c*) After airflow, suction side

Fig. 7 Flow visualization using yellow pigmented oil

The velocity profiles were derived from the measured pressures. There were several models and assumptions available as to the location and type of transition from laminar to turbulent boundary layer flow. The most useful procedure was to choose an instantaneous transition at a momentum thickness Reynolds number of 200 for the first trial. This usually yielded a visible discontinuity in the plotted distributions, marking the general locations of the transition zone. This made possible a second trial, selecting a gradual, smooth transition starting slightly upstream of the discontinuity. By comparing the heat-transfer coefficient distributions obtained with the use of the maximum and minimum heat fluxes, it was possible to determine how much the heat-transfer coefficient varied with the heat flux and whether additional computer simulations were necessary for the intermediate heat fluxes.

Results and Discussion

Pressure Distribution. Measurements were made of the pressure distribution around the midspan of the airfoil surface at the three free-stream velocities. Pressures were measured at 30 locations using a scannivalve system. A plot of the results at maximum velocity is shown in Fig. 5. A large unfavorable pressure gradient on the pressure side near the leading edge is shown in the figure. The calculated critical velocity ratio distribution for this blade profile also indicated a possible flow separation problem just downstream of the leading-edge pressure surface.

Flow Separation. Figure 6(*a*) is a view looking obliquely down at the pressure side of the test blade during a run. At this lowest Reynolds number (based on actual chord) of 2.8×10^5 and the lowest heat-flux input of 1788 W/m^2 (567 Btu/hr ft^2), evidence of a flow separation bubble at a pressure surface distance of about 1.91 cm (0.75 in.) from the leading edge is clearly visible. Since the free-stream air is at room temperature and the test surface is heated, the dark-blue (hot) region just behind the leading edge is an area of low heat transfer indicating that the flow has stagnated in this region. This is where the bubble is presumed to have formed. The black (cool) area just downstream of this region is an area of high heat transfer between the free stream and the surface, probably because of the air reattaching to the surface after it had passed over the bubble. (Of course, in a real engine with its hot free stream, this bubble region would be a relatively cool spot. This would cause surface temperature gradients with their associated potential for damage due to high stresses.) The hot region produced by this separation bubble is still present (see Fig. 6*b*) at the highest Reynolds number of 7.6×10^5 and the highest heat flux input of 5252 W/m^2 (1666 Btu/hr ft^2). Downstream of the hot area, the color pattern appears normal with fairly even temperature until the trailing-edge region. The cool (black) strip along the top edge of the surface is the tip end copper bus bar location. In some cases, for example, near the leading-edge separation bubble region, the yellow band is very narrow. This represents a large chordwise temperature gradient. Where the yellow band

Downloaded 01 Jun 2010 to 171.66.16.71. Redistribution subject to ASME license or copyright; see http://www.asme.org/terms/Terms_Use.cfm

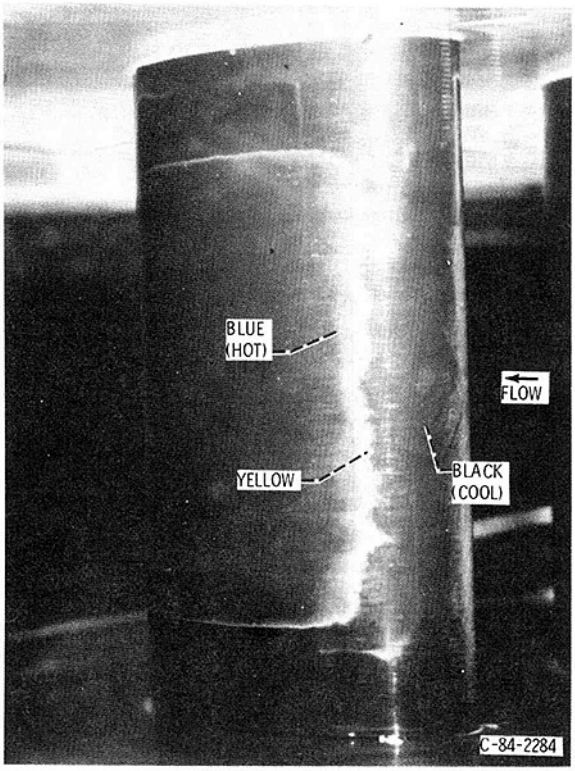


Fig. 8(*a*) Leading edge, Re = 4.2×10^5

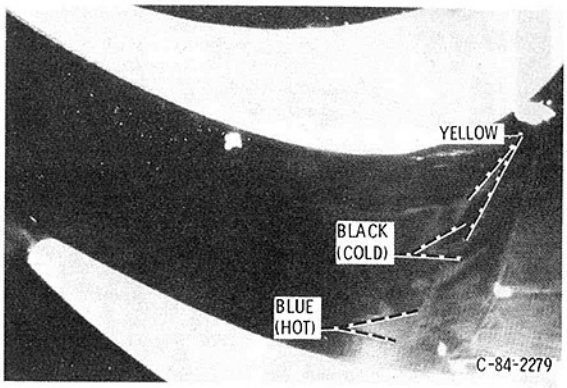


Fig. 8(*b*) Midchord, Re = 4.2×10^5

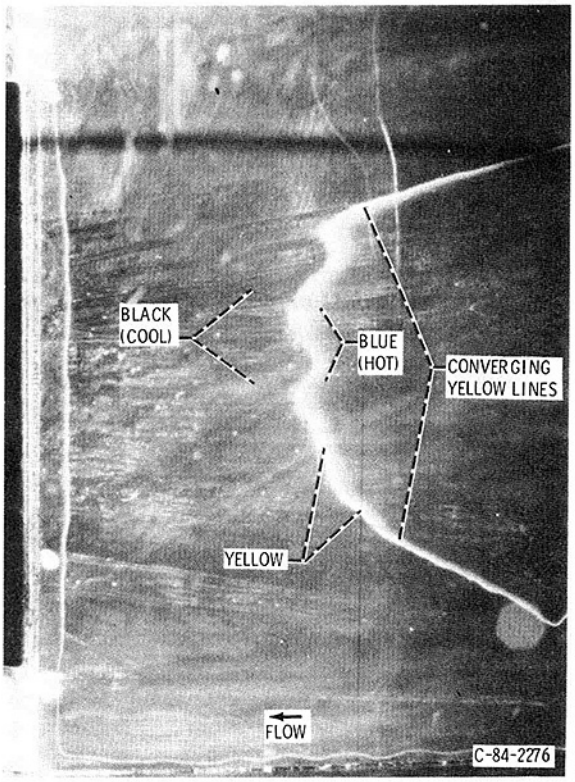


Fig. 8(*c*) Trailing edge, Re = 4.2×10^5

Fig. 8 Suction side temperature pattern

occurs over a wider area, a relatively small temperature gradient exists.

To visualize the flow over the separation bubble, yellow-pigmented oil was used. Figure 7(*a*) shows yellow oil applied over the blade pressure surface before initiation of airflow. Figure 7(*b*) shows the yellow-oil trace after about 2 min of airflow at up to 18 m/s (58 ft/s). The separation bubble is shown where the yellow oil accumulates instead of flowing downstream. A weak separation bubble was also discovered at a surface distance of 12.7 cm (5.0 in.) on the suction side (see Fig. 7*c*).

Experimental Heat Transfer. Figure 8 shows views of the suction side of the blade. Because of surface curvature, three views had to be used to map the local heat-transfer coefficient over the entire suction surface. The electrical power was varied in the three views as needed to show the yellow-color bands over the entire surface at each Reynolds number.

Figure 8(*a*) shows the leading edge region of the blade. An area of high heat transfer is indicated around the leading edge, then a fairly large chordwise temperature gradient (high heat-transfer coefficient gradient) through the yellow area, followed by an even value further downstream. Figures 8(*b*) and 8(*c*) show the midchord and trailing edge regions. Figure 8(*b*) shows a spanwise periodic temperature pattern existing upstream in a small temperature gradient region. Comparative measurements indicate that this pattern is probably caused by the straws in the flow straightener section at the inlet. Further study in this area is recommended. It should be pointed out that this pattern might have gone unnoticed if thermocouples had been used instead of liquid crystals with their high resolution capability. The converging yellow lines in the streamwise direction show increasing cool areas downstream (see Fig. 8*c*) where the endwall passage vortex [9] sweeps across the surface.

The very narrow yellow band (Fig. 8*c*) indicates a very large chordwise temperature gradient (heat-transfer-coefficient gradient) existed. The location of the large gradient was near the minimum passage area (throat area) where the neighboring blade trailing edge was located and the airflow was no longer guided.

Figure 9 shows the suction side trailing edge where another spanwise periodic temperature pattern existed in a small temperature gradient region. This pattern is similar to the one seen upstream (Fig. 8*b*) and is also probably caused by the straw straighteners.

Experimental Heat-Transfer Coefficients. The major objective of the program described here was to obtain a plot of quantitative heat-transfer coefficients with blade surface distance (see Fig. 10). By calibration, the color-temperature correspondence was established for the particular liquid-crystal sheet used. The yellow color for this experiment corresponded to a temperature, T_c, of 40.9°C (105.6°F). The heater-element sheet uniformity produced a heat flux to within 6.0% of the overall heater-sheet average heat-flux value. The calibration and measurement accuracies are presented in the Appendix. Heat-transfer coefficients, h_e (ignoring the small heat losses), were calculated as a function

Downloaded 01 Jun 2010 to 171.66.16.71. Redistribution subject to ASME license or copyright; see http://www.asme.org/terms/Terms_Use.cfm

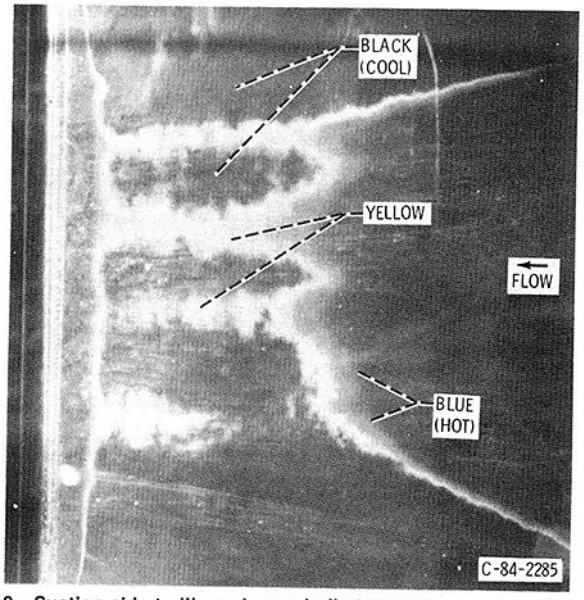


Fig. 9 Suction side trailing-edge periodic temperature pattern, Re = 4.2×10^5

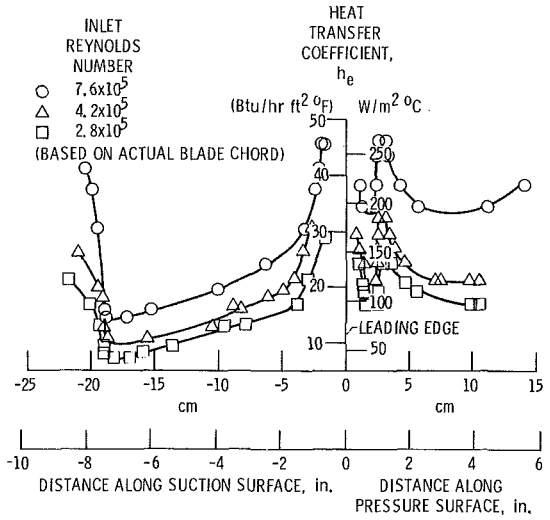


Fig. 10 Heat-transfer coefficient map

of surface distance for three free-stream Reynolds numbers (based on actual chord), 7.6×10^5, 4.2×10^5, and 2.8×10^5.

The heat-transfer coefficient at the leading edge was very high but dropped to a minimum in the pressure surface separation bubble region. After the separation bubble, the coefficient reached a peak as the flow reattached. On the suction surface the heat-transfer coefficient was very high at the leading edge, decreased with surface distance to a minimum at the throat region, and then increased rapidly near the trailing edge where the flow was no longer guided by the neighboring blade.

Analytical Heat-Transfer Coefficients. The analytical results show that on both the pressure and suction sides there was a pronounced dip in the heat-transfer coefficient at a single point per side (see Figs. 11 and 12). On the pressure side, this drop, which also showed up on the friction factor plot (see Fig. 11*b*), coincided with the location of the separation bubble region previously mentioned. This suggested there might be a similar separation on the suction side (see Fig. 12). Indeed, this proved to be the case, as a region of weak separation was later found experimentally by flow visualization using yellow pigmented oil at the same location that the simulation predicted (see Fig. 7*c*). The

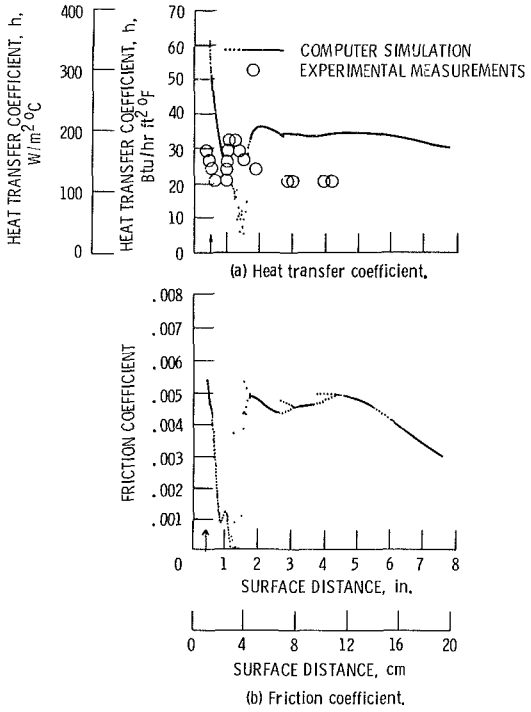


Fig. 11 Pressure side coefficients versus blade surface distance, Re = 7.6×10^5

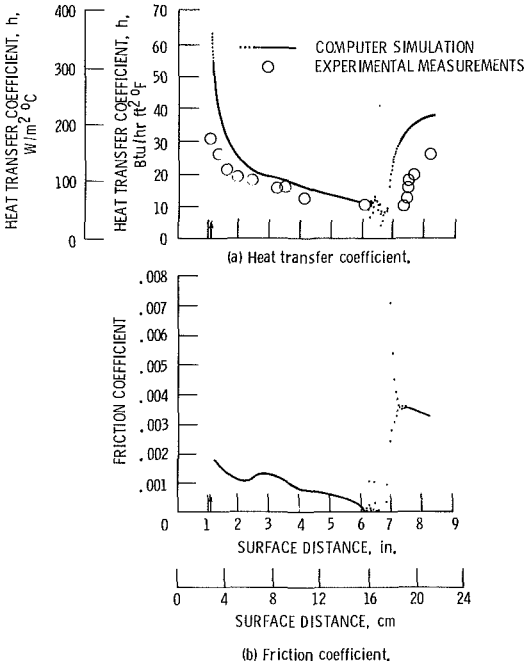


Fig. 12 Suction side coefficients versus blade surface distance, Re = 7.6×10^5

oscillating analytical points were caused by instability calculations in the STAN5 boundary-layer code.

The predicted and measured heat-transfer coefficient plots followed similar curve shapes and had similar values for both the suction and pressure sides, although the calculated curves were displaced slightly in the surface-distance direction. The maximum and minimum heat-flux cases did not differ significantly to require the need for intermediate heat flux computer simulations. Thus, it can be concluded that the experimental technique discussed herein provides good quantitative results and that it was given credence by the computer simulation.

Downloaded 01 Jun 2010 to 171.66.16.71. Redistribution subject to ASME license or copyright; see http://www.asme.org/terms/Terms_Use.cfm

Concluding Remarks

The results indicate that this composite of a liquid-crystal sheet and a heater-element sheet bonded to a model turbine blade provides an accurate, quantitative, and continuous map of heat-transfer coefficients on the blade surface. The effect of a suspected separation bubble on the pressure surface of the blade was clearly revealed in the photographs showing the color-temperature patterns. The maximum error in the experimental heat-transfer coefficients was 6.2% with a maximum heat loss due to blade-chord-plane conduction of 4.94 W/m^2 °C (0.87 Btu/hr ft^2°F), as presented in the Appendix.

The temperature patterns observed and the heat-transfer coefficients found were consistent with pressure distribution measurements and analytical heat-transfer calculations.

References

1 Florschuetz, L. W., et al., "Multiple Jet Impingement Heat Transfer Characteristic: Experimental Investigation of In-Line and Staggered Arrays With Crossflow," NASA CR-3217, 1980.

2 Van Fossen, G. J., et al., "Heat Transfer Distributions Around Nominal Ice Accretion Shapes Formed on a Cylinder in the NASA Lewis Icing Research Tunnel," AIAA Paper 84-0017, Jan. 1984.

3 Hippensteele, S. A., Russell, L. M., and Stepka, F. S., "Evaluation of a Method for Heat Transfer Measurements and Thermal Visualization Using a Composite of a Heater Element and Liquid Crystals," ASME *Journal of Heat Transfer*, Vol. 105, No. 1, Feb. 1983, pp. 184–189.

4 Fergason, J. L., "Liquid Crystals," *Scientific American*, Vol. 211, No. 2, Aug. 1964, pp. 76–85.

5 den Ouden, C., and Hoogendoorn, C. J., "Local Convective-Heat Transfer Coefficients for Jets Impinging on a Plate. Experiments Using a Liquid-Crystal Technique," *Heat Transfer, Proceedings of the Fifth International Heat Transfer Conference*, Vol. V, Japan Society of Mechanical Engineering, Tokyo, Japan, 1974, pp. 293–297.

6 Cooper, T. E., Field, R. J., and Meyer, J. F., "Liquid Crystal Thermography and Its Application to the Study of Convective Heat Transfer," ASME *Journal of Heat Transfer*, Vol. 97, No. 3, Aug. 1975, pp. 442–450.

7 Durao, M. D. C., " Investigation of Heat Transfer in Straight and Curved Rectangular Ducts Using Liquid Crystal Thermography," M.S. Thesis, Naval Postgraduate School, Monterey, CA, June 1977 (AD-A045131).

8 Moody, H. L., and Jechel, K., "Heat Transfer Measurements in Cold Wind Tunnels," AFWAL-TR-81-3176, Wright-Patterson Air Force Base, OH, Sept. 1982.

9 Gaugler, R. E., and Russell, L. M., "Streakline Flow Visualization Study of a Horseshoe Vortex in a Large-Scale, Two-Dimensional Turbine Stator Cascade," ASME Paper 80-GT-4, Mar. 1980.

10 Crawford, M. E., and Kays, W. M., "STAN5: a Program for Numerical Computation of Two-Dimensional Internal and External Boundary Layer Flows," NASA CR-2742, 1976.

11 Gaugler, R. E., "Some Modifications to, and Operational Experiences With, the Two-Dimensional, Finite-Difference, Boundary Layer Code, STAN5," presented at the Gas Turbine Conference and Products Show, ASME Paper 81-GT-89, Mar. 1981.

12 Taylor, J. R., *An Introduction to Error Analysis*, University Science Books, Mill Valley, CA, 1982.

13 Brown, A. I., and Marco, S. M., *Introduction to Heat Transfer*, 3rd ed., McGraw-Hill, New York, 1958.

APPENDIX

Error Analysis

Errors in Measurements. The maximum errors in the experimental measurements are as follows:

Digital voltmeters	±0.1%
Shunt resistor (for measuring current)	±1.0%
Uniformity in heater sheet heat flux	±6.0%
Area of heater sheet	±1.0%
Yellow-color temperature of liquid-crystal sheet	±0.06°C (0.1°F)
Air temperature or	±0.11°C (0.2°F) ±0.04%
Differential pressure transducer	±3.7%
Absolute pressure gauge	±0.5%
Blade chord (actual)	±0.6%

As described in [3], the maximum error in the heat-flux uniformity within a heater sheet is given by:

$$(E_H^2 - E_L^2)/(E_H^2 + E_L^2)$$

This assumes that the average heat flux of the heater sheet equals the median value of the extreme local hot and cold spot heat-flux values.

Error in Heat-Transfer Coefficient, h. The maximum errors in the terms that were used to calculate h_e from equation (1) are as follows:

Heater-sheet heat flux uniformity, $(E_H^2 - E_L^2)/(E_H^2 + E_L^2)$	6%
Heater-sheet heat flux measurement, $\delta Q_e/Q_e$	1%
Heater area, $\delta A/A$	1%
Temperature difference, $\delta(T_c - T_a)/(T_c - T_a)$	1%

A maximum temperature difference at 0.05°C (0.09°F) across the 0.1143 mm (0.0045 in.) thick Mylar sheet (between the liquid-crystal layer and the air stream) was also included along with fluctuation and reading errors in air temperature of 0.12°C (0.21°F). Therefore, as defined in [12], the error in h_e was

$$\frac{\delta h_e}{h_e} = \sqrt{\left(\frac{E_H^2 - E_L^2}{E_H^2 + E_L^2}\right)^2 + \left(\frac{\delta Q_e}{Q_e}\right)^2 + \left(\frac{\delta A}{A}\right)^2 + \left(\frac{\delta(T_c - T_a)}{T_c - T_a}\right)^2}$$

$$= \sqrt{0.06^2 + 0.01^2 + 0.01^2 + 0.01^2} = \pm 6.2\%$$

An additional error in the heat-transfer coefficient existed due to heat losses caused by radiation and conduction.

The maximum loss due to radiation was calculated by assuming an emissivity and configuration factor value of one, and it was found to be negligible. The spanwise component of the conduction heat loss was eliminated by selecting the yellow-color-band locations near the blade midspan where no spanwise heat transfer existed. The only remaining heat loss (conduction through the blade-chord plane) was determined by making a measurement of the total heat input for a no-airflow condition and then subtracting a calculated free convection heat loss.

In [13], the calculated free convection heat-transfer coefficient on a vertical surface with no airflow is given as:

$$h = C\frac{k}{L}(aL^3\Delta T)^d$$

where

C = 0.55
a = 7.374×10^7/m^3 °C (1.160×10^6/ft^3 °F)
d = 1/4
T_c = 40.89°C (105.6°F)
T_a = 15.17°C (59.3°F)
ΔT = 25.72°C (46.3°F)
k = 0.0277 W/m °C (0.016 Btu/hr ft °F)
L = 0.1016 m (0.3333 ft)

from which,

h = 5.62 W/m^2 °C (0.99 Btu/hr ft^2 °F)

Downloaded 01 Jun 2010 to 171.66.16.71. Redistribution subject to ASME license or copyright; see http://www.asme.org/terms/Terms_Use.cfm

The average heat-transfer coefficient determined from measurements made for the no-airflow condition was 10.55 W/m^2 °C (1.86 Btu/hr ft^2 °F). Therefore, the heat-transfer loss expressed in terms of a heat-transfer coefficient, h_l, due to conduction through the blade-chord plane was the difference (for the no-airflow condition) between the total measured value and the free convection value or 4.94 W/m^2 °C (0.87 Btu/hr ft^2 °F). Finally, the maximum error in the experimental heat-transfer coefficient, h_e, was ±6.2% with a maximum heat loss due to blade-chord-plane conduction of 4.94 W/m^2 °C (0.87 Btu/hr ft^2 °F).

The error in the location of the h_e data points (yellow-color bands) was ±1.27 mm (0.05 in.).

Error in Reynolds Number, Re. The maximum errors in the experimental measurements are as follows:

Absolute pressure gauge,	$\frac{\delta P_a}{P_a}$	= 0.5%
Differential pressure transducer: For vel.,	$\frac{\delta \Delta P_a}{\Delta P_a}$	= 8.4%
For straws,	$\frac{\delta \Delta P_a}{\Delta P_a}$	= 7.9%
Blade actual chord,	$\frac{\delta S}{S}$	= 0.6%
Air temperature,	$\frac{\delta T_a}{T_a}$	= 0.04%

Therefore, as defined in [12], the error in Re was

$$\frac{\delta \mathrm{Re}}{\mathrm{Re}} = \sqrt{\left[\frac{1}{2}\sqrt{\left(\frac{\delta P_a}{P_a}\right)^2 + \left(\frac{\delta \Delta P_a}{\Delta P_a}\right)^2}\right]^2 + \left(\frac{\delta T_a}{T_a}\right)^2 + \left[\frac{1}{2}\left(\frac{\delta \Delta P_a}{\Delta P_a}\right)\right]^2 + \left(\frac{\delta S}{S}\right)^2}$$

$$= \sqrt{\left[\frac{1}{2}\sqrt{(0.005)^2 + (0.079)^2}\right]^2 + (0.0004)^2 + \left[\frac{1}{2}(0.084)\right]^2 + (0.006)^2}$$

$$= \pm 5.8\%$$

Downloaded 01 Jun 2010 to 171.66.16.71. Redistribution subject to ASME license or copyright; see http://www.asme.org/terms/Terms_Use.cfm

Secondary Flows and Losses Downstream of a Turbine Cascade

J. Moore

R. Y. Adhye

Mechanical Engineering Dept.,
Virginia Polytechnic Institute and
State University,
Blacksburg, VA 24061

The loss mechanisms and the behavior of secondary flows downstream of a large scale, linear turbine cascade have been investigated experimentally. A five-blade replica of the cascade used by Langston et al. at United Technologies Research Center was used for the present tests. Detailed flow measurements, using five-hole and three-hole probes, were made at four different planes, one just upstream of the trailing edge and the rest downstream. The secondary flow field at each measurement plane was found to be dominated by a single large passage vortex, which decayed in strength because of the mixing occurring in the flow. More than one-third of the losses were found to occur downstream of the trailing edge. This rise in total pressure loss in the present tests was almost entirely explained by a corresponding dissipation of the secondary kinetic energy of the flow. A mixing analysis of the flow was done to predict the additional losses due to "mixing" until the flow became completely uniform.

Introduction

A problem that arises in the design of modern turbines and in the analysis of their performance is the understanding and prediction of the nature and influence of secondary flows and their associated losses. A turbine designer, based on the current state-of-the-art, may well define secondary flows as the "unplanned three-dimensional flow effects in a turbine which lead to unexplained (secondary) losses." A more complete understanding of complex 3-D flows and of losses and their origin would certainly prove helpful in his attempt to make improvements in turbine performance.

In the last ten years, detailed studies of flows in turbine cascades have been undertaken by various investigators [1–11]. Today, it is commonly believed that the flow patterns associated with the secondary losses are adequately understood, but the magnitude of the losses is not [12, 13].

One such area, where the loss mechanism is not at all clearly understood, is the flow region downstream of the trailing edge. There are data in the literature showing loss production downstream of the trailing edge in addition to that occurring within the blade row. For example, Langston et al. [2] show about one-third to one-half of the losses occurring downstream, presumably due to mixing out of a nonuniform flow at the blade exit. Came [14], Marchal and Sieverding [9], and Gregory-Smith and Graves [11] also reported increases in losses behind the trailing edge plane. However, as Sieverding [13] pointed out, "the way in which the losses mix out is entirely unclear. There is not a single test which shows the complete downstream mixing process." Obviously there could be more than one factor, such as the endwall boundary layer, the trailing-edge wake mixing, dissipation of the secondary kinetic energy as well as turbulence kinetic energy, which could collectively result in doubling the losses downstream of the trailing edge. Surprisingly, there are very few attempts in the literature to explain the loss mechanism by considering the abovementioned factors.

Secondary Kinetic Energy. In order to gain a better understanding of turbine flow it is usual to consider an ideal "primary" flow; the difference between this primary flow and the actual flow is then termed "secondary" flow. In the present paper we consider flow downstream of the linear turbine cascade shown in Fig. 1. The primary flow direction is defined in the direction of the mean camber line at the trailing edges of the blades ($\beta_2 = 26$ deg). The velocity component in this direction is termed u and the secondary flow velocity components v and w are thus defined in the cross-sectional

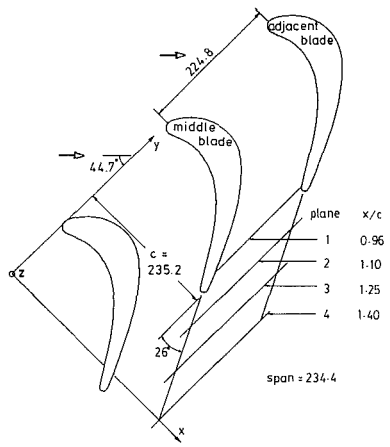


Fig. 1 Cascade geometry and measurement planes (linear dimensions in mm)

Contributed by the Gas Turbine Division of THE AMERICAN SOCIETY OF MECHANICAL ENGINEERS and presented at the 30th International Gas Turbine Conference and Exhibit, Houston, Texas, March 18–21, 1985. Manuscript received at ASME Headquarters, December 21, 1984. Paper No. 85-GT-64.

Copyright © 1985 by ASME
Downloaded 01 Jun 2010 to 171.66.16.71. Redistribution subject to ASME license or copyright; see http://www.asme.org/terms/Terms_Use.cfm

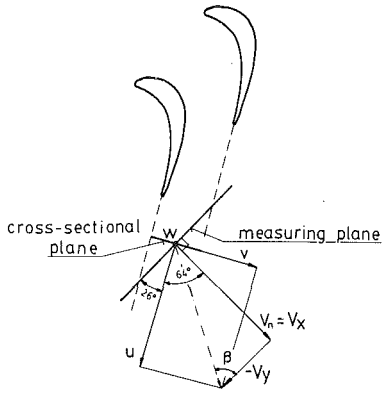


Fig. 2 Velocity components relative to measuring plane

plane as shown in Fig. 2. With these definitions the kinetic energy of the primary flow (per unit mass) is $u^2/2$ and the secondary kinetic energy is $(v^2 + w^2)/2$.

Squire and Winter [15] studied secondary flow in a passage between the turning vanes of a wind tunnel elbow. From the measured secondary flow and from the theoretical distributions they evaluated the ratio of the secondary kinetic energy at the exit of the bend to the inlet kinetic energy. The measured value was about 70% higher than the estimated value. They concluded that "the measured value is of the order of half the profile drag pressure drop coefficient and should be taken into account in estimating corner loss." More recently, Gregory-Smith [16] has included calculations of secondary kinetic energy (based on inviscid secondary flow theory) in a simple approach to the estimation of losses produced by secondary flows near the hub and casing of a turbine. Like Belik [17] and others, Gregory-Smith assumes all the secondary kinetic energy is dissipated as an "extra secondary loss."

Turbulence Kinetic Energy. So far few and rather contradictory data have been published on turbulence measurements. Bailey [18] investigated the flow through a single large turbine-blade passage which had an inlet turbulence level ranging from a rms value of 0.7% at midspan to 10% near the endwall. He found that the turbulent stresses were insignificant in large regions of the passage vortex. On the other hand, Gregory-Smith and Graves [11] found, for an upstream free stream turbulence of 3%, peak turbulence intensities just downstream of the trailing edge to be of the order of 30%. They concluded that some of the total pressure loss through the cascade passage appears as an increase in turbulence kinetic energy, which then gets dissipated by viscous action.

Present Contribution. The present work is intended as a contribution toward improved understanding of secondary flows, mixing and loss production downstream of a turbine cascade. The reaction turbine cascade used is the VPI&SU cascade described in [6–8] and is geometrically similar to the UTRC cascade used in [2–4]. Sufficient measurements have been made to define the primary and secondary flow over the entire exit cross section and over three downstream planes so loss coefficients and secondary kinetic energies can be evaluated. No turbulence measurements are presented as this was beyond the scope of the present investigation, but this does not appear to pose a severe limitation to the present findings.

Experimental Apparatus

VPI&SU Cascade. The geometry and configuration of the middle three blades of the five-blade VPI&SU turbine cascade are shown in Fig. 1. The Reynolds number based on the blade axial chord and an exit velocity of 37.5 m/s is 5.2×10^5.

Measuring Planes. The four measuring planes are also shown in Fig. 1. Plane 1, at $x/c = 0.96$, is at the same location just upstream of the trailing edge as plane 9 of Langston et al. [2]. Plane 4, at $x/c = 1.40$, is the downstream plane used by Moore and Ransmayr [6] and corresponding to plane 12 of Langston et al. Planes 2 and 3 were chosen approximately equally spaced at $x/c = 1.10$ and 1.25, respectively.

Probes were introduced into the flow at these planes through slots in the top endwall.

Measuring Apparatus. The measurements of total pressure, static pressure, and the three velocity components at planes 2, 3 and 4 were carried out with a five-hole probe, manufactured by United Sensor Co., Mass., type DC-125-24-F-22-CD. The probe tip diameter was 3.18 mm and the stem diameter was 6.35 mm. A similar but smaller five-hole probe (type DC-125-12-CD) with a tip and stem diameter of 3.18 mm was used for measurements at plane 1. A three-hole cobra probe (tip thickness 1.12 mm) was used for traversing close to the endwall at each plane and also perpendicular to the blade surfaces at plane 1.

The middle blade and the pressure side of the adjacent blade were instrumented with static pressure tappings. Additional static pressure tappings were fitted in the bottom endwall across planes 1, 2, 3 and 4 and along the mean camber lines. Further details of the apparatus are given in [19].

Experimental Procedure. In order to minimize the blockage effect due to the stem of the probe, the five-hole

Nomenclature

A = area of measuring plane, area of integration
c = blade axial chord
C_{Ps} = static pressure coefficient, $C_{Ps} = (p_s - p_{so}) \Big/ \frac{1}{2}\rho U_o^2$
C_{Pt} = total pressure loss coefficient, $C_{Pt} = (p_{to} - p_t) \Big/ \frac{1}{2}\rho U_o^2$
F_x, F_y = components of blade force in mixing analysis for plane 1, equations (6) and (7)
H_{12} = shape factor δ^*/θ, Table 1
p = pressure
u,v,w = velocity components, Fig. 2
U_o = upstream freestream velocity
V_n = velocity component normal to measuring plane, Fig. 2
x,y,z = Cartesian coordinates, Fig. 1
ΔY = blade pitch
ΔZ = blade span (measured from bottom wall)
β = flow angle, Fig. 2
δ = boundary layer thickness
δ^* = displacement thickness of boundary layer
η = mass flow coefficient
θ = momentum thickness of boundary layer
ρ = density
ϕ = pitch angle, $\tan^{-1}(w/u)$
ψ = yaw angle, $\tan^{-1}(v/u)$

Subscripts

d = downstream
n = normal to measuring plane
o = upstream of cascade
s = static
t = total
u = upstream
x = chordwise direction
y = pitchwise direction

Overbars

$\bar{}$ = average
$\tilde{}$ = mass average

Downloaded 01 Jun 2010 to 171.66.16.71. Redistribution subject to ASME license or copyright; see http://www.asme.org/terms/Terms_Use.cfm

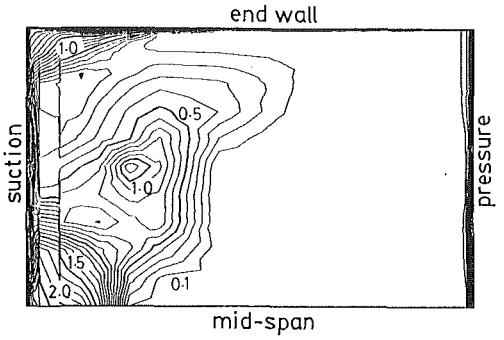


Fig. 3 Contours of total pressure-loss coefficient C_{Pt} at plane 1, $x/c = 0.96$

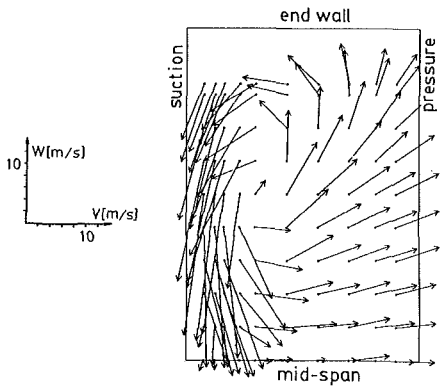


Fig. 4 Secondary flow vectors at plane 1, $x/c = 0.96$, presented in the cross-sectional plane

probe traverses were performed in the top half of each plane. However, because of the slots cut in the top endwall, boundary layer traverses with the three-hole probe were done on the bottom endwall which was fitted with static pressure tappings. This procedure relied on the symmetry of the flow in this linear turbine cascade, which was shown by measurement of the endwall boundary layers upstream of the cascade, by five-hole probe measurements downstream of the cascade, and by flow visualization on the suction surface of the middle blade [20].

At plane 1, the three-hole probe was also used for traversing close to the blade suction and pressure surfaces where the vertical traverses of the five-hole probe could not reach without disturbing the blade boundary layers. These traverses did not exactly lie in plane 1 and so the data obtained were projected onto plane 1 for the purpose of analysis (for each point, constant z and constant distance from the suction surface were maintained).

Scheme of Data Analysis. The results are presented in the form of plots using two planes shown in Fig. 2. The measurement plane is parallel to the plane defined by the trailing edges of the blades. A cross-sectional plane for the projection of secondary velocities is defined to be perpendicular to the direction of the mean camber lines at the trailing edges.

A nominal flow direction is defined in the direction of the mean camber line at the trailing edge. The velocity component in this direction, namely u, is defined to be the primary direction. Thus secondary flow velocities v and w are defined, which lie in the cross-sectional plane. In the analysis of five-hole probe data, apart from the total and static pressures, these three velocity components are calculated along with V_n, the component of velocity normal to the measuring plane (Fig. 2).

The traverses of the three-hole probe in the endwall boundary layer yielded only the total pressure and yaw angle at each location. However, the static pressure was obtained from the wall static tappings and was assumed to be constant in the spanwise direction. Thus, velocity components u, v, and V_n could be calculated with the assumption that the w component of the velocity was zero in the endwall boundary layer.

Results and Discussion of Results

Upstream Boundary Layer Traverses. The inlet endwall boundary layer profile was determined by traversing a total pressure probe 400 mm upstream of the leading edges of the middle and of the adjacent blade ($x/c = -1.2$). The integral parameters of the turbulent boundary layer are presented in Table 1.

These results, together with the freestream velocity $U_o = 23.5 \pm 0.4$ m/s and the freestream turbulence intensity of about 0.24% define the inlet flow conditions at $x/c = -1.20$. The air density and viscosity were 1.12 kg/m^3 and 0.0000188 kg/ms respectively, at the standard test conditions of 95.6 kPa and 298K.

Flow Measurements at Plane 1. *Total Pressure Losses and Secondary Velocities.* The total pressure loss coefficient (C_{Pt}) contour plot for measurements at plane 1 ($x/c = 0.96$) is shown in Fig. 3. Apart from the profile boundary layers on the suction and pressure sides, there are three distinct regions of high losses. There exists a high loss core away from the suction surface, close to the center of the passage vortex. The suction side/endwall corner region and the region at midspan near the suction surface also exhibit high losses. The endwall boundary layer is very thin near the pressure side with a nominal boundary layer thickness of about 1.3 mm, whereas near the suction side it interacts with fluid from the passage vortex and it is difficult to define the edge of the boundary layer.

The secondary velocity vectors obtained in the cross-sectional plane (Fig. 2) are shown in Fig. 4. The flow field appears to be dominated by a single large passage vortex. Near the suction surface, there are strong secondary flows towards midspan. The w component ranges from -20 to -25 m/s in this region, which may be compared with the inlet freestream velocity U_o of 23.5 m/s and an average exit velocity U of 39 m/s at plane 1. The pitch angle ϕ ranges from -30 deg to -40 deg in this region. The secondary velocities on the pressure side of the passage are comparatively smaller (about $+8$ to $+10$ m/s).

Profile Loss. The flow near the pressure surface was found to be essentially two-dimensional. The boundary layer was very thin ($\delta = 1.5$ mm) and was quite uniform along the span, with the pitch angle variation being less than 3 deg. In the total pressure-loss coefficient contour plot (Fig. 3) it looks thicker than the actual size. This is due to the projection of data onto plane 1.

The pitch angle distributions for flow near the suction surface show strong secondary flow down the blade up to 30% of span; here the measured pitch angle was 39 deg compared with a value of 38 deg obtained from surface flow visualization. However, at about 40% of blade height, there is an abrupt change in the pitch-angle profile, which shows a small reversal in direction. This is associated with a three-dimensional flow separation also shown by surface flow visualization at about 34% of blade height; this 3-D flow separation partially explains the high losses observed near midspan in the present tests. The flow visualization studies of Langston et al. [2] and Marchal and Sieverding [9] on the blade suction surface also confirm the presence of a 3-D separation line near midspan.

Static Pressure Contours. The static pressure coefficient

Downloaded 01 Jun 2010 to 171.66.16.71. Redistribution subject to ASME license or copyright; see http://www.asme.org/terms/Terms_Use.cfm

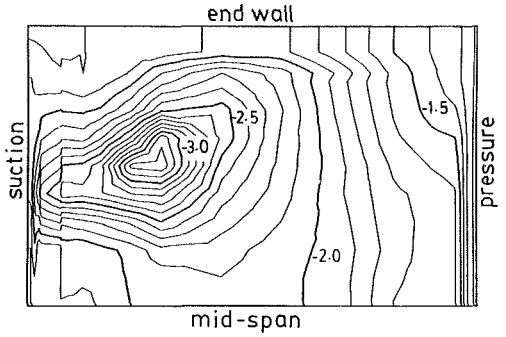


Fig. 5 Contours of static pressure coefficient C_{Ps} at plane 1, $x/c = 0.96$

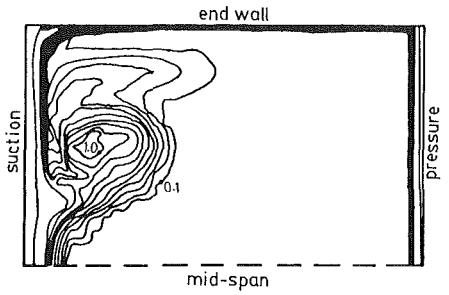


Fig. 6 Reproduction of Langston et al.'s Fig. 7(c) showing contours of total pressure-loss coefficient C_{Pt} at $x/c = 0.96$

(C_{Ps}) contour plot for plane 1 is shown in Fig. 5. The low loss region near the pressure side appears to be a two-dimensional potential flow region with approximately vertical C_{Ps} contours. But the other half of the flow is quite different as evidenced by nearly concentric static pressure contours surrounding the core of the passage vortex. The minimum value of C_{Ps} in the vortex core is -3.2, which may be compared with the nominal exit static pressure coefficient at the blade surface of about -1.8. Static pressure could not be measured near the endwall where three-hole probe traverses were made. The straight contours normal to the endwall represent the static pressures measured at the endwall extrapolated through this region of three-hole probe measurements.

Comparison with Langston et al.'s Data at Plane 1. Figure 6 is a reproduction of Langston et al.'s [2] plot of total pressure loss coefficient contours in a plane at $x/c = 0.96$. It should be noted that the ratio of inlet boundary-layer displacement thickness to blade height for the present tests is larger ($\delta^*/\Delta Z = 0.023$) than that of Langston et al. ($\delta^*/\Delta Z = 0.013$). The principal difference between the two plots is the region of high loss near midspan in the present tests. This is caused by a larger passage vortex located farther from the endwall and closer to midspan, which leads to a different development of the profile boundary layer near midspan on the suction surface as discussed by Sharma and Graziani [5].

Flow Development Downstream of Trailing Edge (Planes 2 to 4). *Total Pressure Losses.* The total pressure loss coefficient (C_{Pt}) contour plots for planes 2 and 4 are shown in Figs. 7 and 8 respectively. The endwall boundary layer grows in size from plane 2 to plane 4 but overall remains relatively thin. Near the suction side, it grows from a thickness of 3-5 mm at plane 2 to 8-10 mm by plane 4. Similarly, on the pressure side it is 2-3 mm thick at plane 2 as compared to its thickness of 5-6 mm at plane 4. Due to the endwall cross flow, fluid near the suction surface/endwall corner region is overturned as it flows downstream of the trailing edge.

Fluid with high total pressure losses in the passage vortex is convected towards the middle of the passage and towards

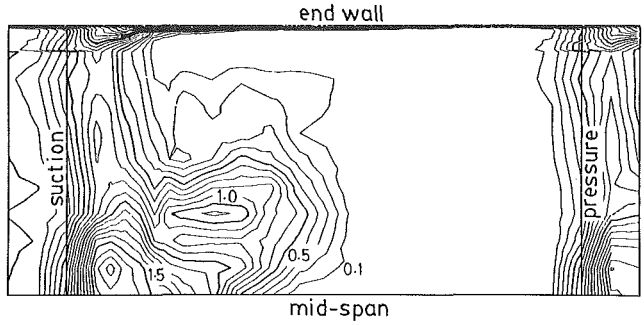


Fig. 7 Contours of total pressure loss coefficient C_{Pt} at plane 2, $x/c = 1.10$. Solid line – projections downstream of blades in direction of mean camber lines at trailing edges; suction – downstream of middle blade; pressure – downstream of adjacent blade.

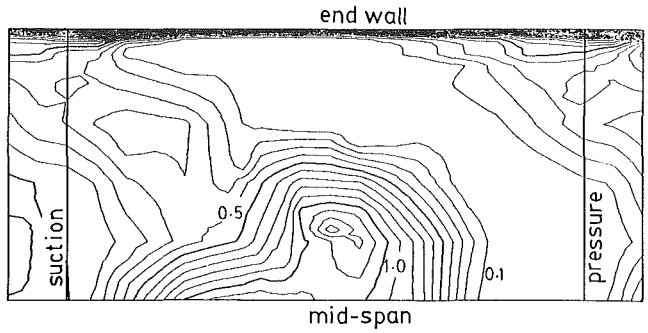


Fig. 8 Contours of total pressure loss coefficient C_{Pt} at plane 4, $x/c = 1.40$

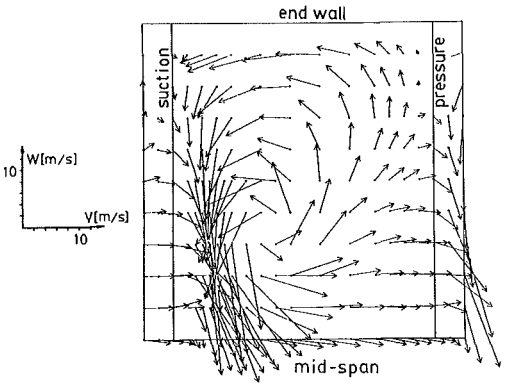


Fig. 9 Secondary flow vectors at plane 2, $x/c = 1.10$, presented in the cross-sectional plane

midspan. The level of the total pressure losses in the core of this fluid changes little between plane 1 ($C_{Pt} \simeq 1.1$) and plane 4 ($C_{Pt} \simeq 1.3$).

Fluid from the high-loss region near midspan appears at plane 2 with a peak value of $C_{Pt} \simeq 1.8$. However, this peak value rapidly diminishes to 1.4 at plane 3 and to 1.1 at plane 4, as this fluid is entrained and mixed with fluid from the passage vortex.

Between this high-loss region and the endwall, in a region essentially downstream of the blade trailing edge, is the blade wake. Fluid in this region does not exhibit very high losses. The local peak value of C_{Pt} decays from about 0.8 at plane 2 to 0.6 at plane 3 and to 0.4 at plane 4.

The low-loss region ($C_{Pt} < 0.1$) which represents nearly two-dimensional flow in the pressure side half of the passage at plane 2 becomes quite skewed by plane 4 as the passage vortex moves towards the pressure side and the low-loss fluid adjacent to the endwall moves toward the suction side. The blade wake is also seen to be skewed by plane 4.

Secondary Velocities. Secondary flow velocities for planes 2 and 4 downstream of the trailing edge are shown in

Downloaded 01 Jun 2010 to 171.66.16.71. Redistribution subject to ASME license or copyright; see http://www.asme.org/terms/Terms_Use.cfm

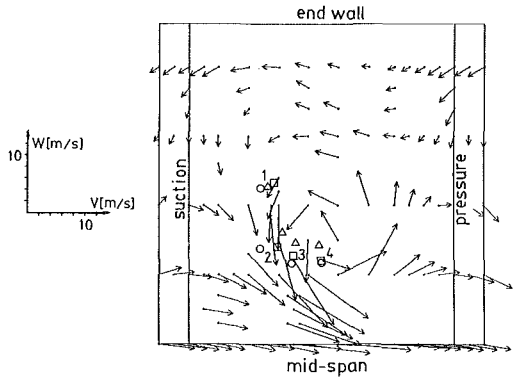


Fig. 10 Secondary flow vectors at plane 4, $x/c = 1.40$. Migration of vortex core downstream of trailing edge; 1,2,3,4 = plane numbers; ○ = maximum C_{Pt}; □ = minimum C_{Ps}; △ = nominal vortex core from secondary velocity vectors

Figs. 9 and 10. The dominance of the passage vortex in each of these figures is clearly seen. Especially at planes 2 and 3, there is an asymmetrical distribution, with large negative w velocities near the suction side; at plane 2, w is of the order of -20 to -25 m/s, whereas at plane 4, the minimum w is about -11 m/s.

The pitchwise variation of w velocity at 30% of blade height at each plane is shown in Fig. 11. The passage vortex has the appearance of a solid body vortex which is about 25 to 30% of the blade pitch in size. In the low loss region (to the right of the passage vortex), the velocity distribution resembles a free vortex structure. The shear layer in the wake decays quite rapidly as the fluid in the blade wake mixes out.

Static Pressure Contours. The extent of the influence of the passage vortex can also be seen in contours of static pressure coefficient (C_{Ps}) at planes 2, 3, and 4. At each plane there exists a low static pressure at the center of nearly concentric static pressure contours. The minimum static pressure coefficient is -2.9 at plane 2, -2.6 at plane 3, and -2.4 at plane 4. This rise in C_{Ps} is associated with the decay of the strength of the passage vortex, shown in Figs. 4, 9, and 10. By plane 4, apart from the vortex core located in the passage near midspan, the static pressure distribution is quite uniform ($C_{Ps} = -1.85 \pm 0.1$).

Migration of Vortex Core. The core of the passage vortex can be located quite closely by any of the following three criteria.

1 Location of maximum C_{Pt} from the contour plots in Figs. 3, 7, and 8.

2 Location of minimum C_{Ps} from contour plots like Fig. 5.

3 Location of nominal center of rotation of the secondary velocity vectors in Figs. 4, 9, and 10.

The results are shown in Fig. 10. The core of the passage vortex is seen to migrate toward midspan and toward the middle of the passage as it flows downstream. The vortex is approximately midway between the endwall and midspan at plane 1. It moves to about 35% of blade height from the endwall at plane 4. This spanwise migration seems to have reached its limiting value, suggesting that further migration of the passage vortex downstream of plane 4 would be toward the pressure side only.

Averaged Flow Properties

Mass and area averaged values of the flow properties – total pressure loss, flow velocity, mean flow angle and kinetic energy of primary and secondary flow – were evaluated from the data obtained at each plane. These averaged quantities and their definitions are given below.

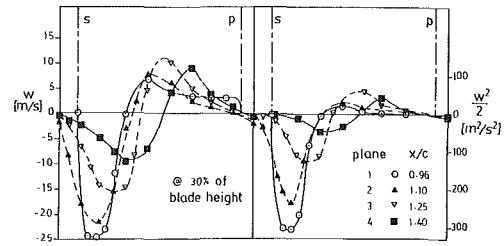


Fig. 11 Distributions of spanwise secondary velocity (w) and spanwise secondary kinetic energy ($w^2/2$) in the blade-to-blade direction at 30% of blade height from the top endwall; s = suction side of blade; p = pressure side of blade

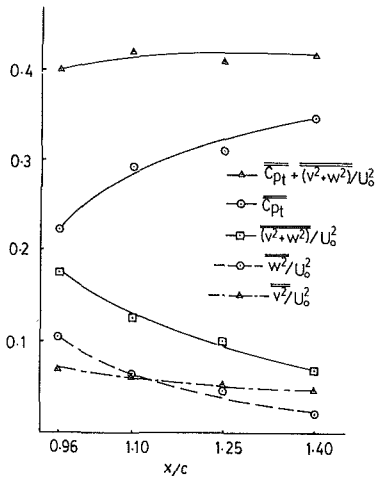


Fig. 12 Variation of mass averaged flow properties downstream of trailing edge

Normal velocity (Fig. 2):

$$\bar{V}_n = \frac{2}{\Delta Y \Delta Z} \int_0^{\Delta Y} \int_{\Delta Z/2}^{\Delta Z} V_n \, dzdy \tag{1}$$

Mass-averaged total pressure loss coefficient:

$$\bar{\bar{C}}_{Pt} = \frac{\int_0^{\Delta Y} \int_{\Delta Z/2}^{\Delta Z} \rho \, V_n C_{Pt} dzdy}{\int_0^{\Delta Y} \int_{\Delta Z/2}^{\Delta Z} \rho \, V_n dzdy} \tag{2}$$

Mass averages of the velocity components V_x, V_y and of the components of the kinetic energy $u^2/2$, $v^2/2$, and $w^2/2$ were obtained similarly.

Flow angle:

$$\bar{\bar{\beta}} = \tan^{-1}[\bar{\bar{V}}_x / (-\bar{\bar{V}}_y)] \tag{3}$$

Mass flow coefficient:

$$\eta = \left. \frac{\int_0^{\Delta Y} \int_{\Delta Z/2}^{\Delta Z} \rho \, V_n dzdy}{\int_0^{\Delta Y} \int_{\Delta Z/2}^{\Delta Z} \rho \, V_n \, dzdy} \right|_{\text{inlet to the cascade}} \tag{4}$$

Increase in Total Pressure Loss. All the averaged flow properties for planes 1 to 4 are given in Table 2. Figure 12 shows the variation of some of these properties downstream of the trailing edge. The mass averaged total pressure loss coefficient ($\bar{\bar{C}}_{Pt}$) at plane 1 is 0.224, which is quite high when compared to the value of 0.13 obtained by Langston et al. [2].

Downloaded 01 Jun 2010 to 171.66.16.71. Redistribution subject to ASME license or copyright; see http://www.asme.org/terms/Terms_Use.cfm

Table 1 Results of boundary layer measurements 400 mm upstream of cascade

	Upstream of middle blade	Upstream of adjacent blade
δ	36.0 mm	41.0 mm
δ^*	5.0 mm	5.9 mm
θ	3.9 mm	4.5 mm
H_{12}	1.28	1.31

Table 2 Averaged flow properties

	Plane 1	2	3	4
$\bar{V}_n$ (m/s)	17.7	16.5	16.9	17.3
η(%)	94.0	104.8	106.8	109.6
$\bar{\bar{C}}_{Pt}$	0.224	0.294	0.310	0.347
$\bar{\bar{V}}_x$(m/s)	19.6	18.3	17.8	18.1
$\bar{\bar{V}}_y$(m/s)	−32.2	−32.8	−32.5	−32.8
$\bar{\bar{\beta}}$(deg)	31.2	29.1	28.7	28.9
$\overline{\overline{u^2}}/U_o^2$	2.58	2.58	2.50	2.55
$\overline{\overline{v^2}}/U_o^2$	0.071	0.062	0.053	0.047
$\overline{\overline{w^2}}/U_o^2$	0.105	0.065	0.046	0.021
$\overline{\overline{v^2+w^2}}/U_o^2$	0.176	0.127	0.099	0.068
$\bar{\bar{C}}_{Pt}+\overline{\overline{(v^2+w^2)}}/U_o^2$	0.400	0.421	0.409	0.415

As mentioned earlier, the ratio of the inlet boundary layer displacement thickness to the blade height for the present tests is larger than that of Langston et al., which could result in stronger secondary flows and a bigger passage vortex, thus possibly explaining the higher losses observed in the present tests at plane 1. There is a large jump in $\bar{\bar{C}}_{Pt}$ from 0.224 at plane 1 to 0.294 at plane 2 ($x/c=1.10$). Thereafter, it further rises to 0.347 at plane 4 ($x/c=1.40$).

Decrease in Secondary Kinetic Energy. In the present tests, this rise in $\bar{\bar{C}}_{Pt}$ is almost entirely explained by a corresponding dissipation of the secondary kinetic energy

$$\frac{1}{2}\overline{\overline{(v^2+w^2)}}.$$

Table 2 shows that the secondary kinetic energy coefficient $\overline{\overline{(v^2+w^2)}}/U_o^2$ was 0.176 at plane 1; it then decreased quite sharply to 0.127 at plane 2 and to 0.068 at plane 4. This decay of secondary kinetic energy is shown in Fig. 12. Here, the decrease in secondary kinetic energy coefficient (0.108) is seen to closely match the rise in the total pressure loss coefficient (0.123) between planes 1 and 4. The sum of the total pressure loss coefficient and the secondary kinetic energy coefficient is seen to remain fairly constant (0.411 ± 0.011) for the present data.

Contributions to Secondary Kinetic Energy. Table 2 also shows the individual contributions of v and w components of the secondary velocity to the secondary kinetic energy at each plane. At plane 1, kinetic energy associated with the w component is approximately 50% larger than that due to the v component, while at plane 4, it is found to be less than 50% of the secondary kinetic energy of the v component. The w component thus contributes more to the increase in the total pressure loss as it is dissipated downstream of the trailing edge. This decay of the spanwise component of secondary kinetic energy ($w^2/2$) is also clearly seen in Fig. 11 at 30% of the blade height. It occurs due to mixing in the blade wake where secondary kinetic energies fall from about 300 m^2/s^2 at plane 1 to about 50 m^2/s^2 by plane 4.

Averaged Normal Velocity. The area averaged normal velocity $\bar{V}_n$ varies from 14.9 to 17.3 m/s, leading to a mass-flow coefficient (η) variation from 94 to 110%. Ideally, η should be 100% at each plane. However, this value was found to be very sensitive to the yaw angle variation. A systematic error of 1 deg in yaw angle measurement results in a 4% change in η. Thus errors of −2.2 deg at plane 1, +1.3 deg at plane 2, +1.8 deg at plane 3, and +2.5 deg at plane 4 could explain the observed discrepancy in η.

Mass Averaged Flow Properties. The mass averaged flow properties, $\bar{\bar{V}}_x$ and $\bar{\bar{V}}_y$ (Fig. 2) for each plane are also given in Table 2. $\bar{\bar{V}}_y$ is found to be 32.5 ± 0.3 m/s, indicating that momentum is conserved in the y direction and suggesting that wall shear stresses are negligible. $\bar{\bar{V}}_x$ changes from plane 1 to plane 2 due to the increased flow area downstream of the trailing edge plane. It would then change if static pressure varied in the x-direction, if there was flow mixing, or if wall shear was significant. However, it is seen to remain at 18.0 ± 0.3 m/s once it changes from its initial value of 19.6 m/s at plane 1.

Mean Flow Angle. A mean flow angle for each plane is given by $\bar{\bar{\beta}}=\tan^{-1}(\bar{\bar{V}}_x/\bar{\bar{V}}_y)$. Due to the change in $\bar{\bar{V}}_x$ between plane 1 and plane 2, $\bar{\bar{\beta}}$ also drops from 31.2 deg to 28.9 deg and then remains fairly constant (28.9 deg ± 0.2 deg) as $\bar{\bar{V}}_x$ and $\bar{\bar{V}}_y$ both remain approximately constant. This value may be compared with the nominal blade exit angle of 26 deg. The alternative (and more common) definition of mean flow angle based on $\bar{V}_n$ is discussed below.

Mixing Analysis

After the flow leaves the blades, mixing takes place and the flow tends to become more uniform. The mass averaged total pressure loss at a downstream plane where the flow is fully mixed out will be higher than the mass averaged total pressure loss obtained at any of the measurement planes in the present tests. By applying the equations of continuity and momentum between a measurement plane and a downstream plane where flow is fully mixed out, it is possible to estimate the additional "mixing loss."

For measurement planes 2–4, downstream of the blades, the control volume used for the mixing analysis is defined by the measurement plane, the downstream plane where the flow conditions are uniform and blade camber lines. The height of the control volume is uniform with only the top half of the span being considered for the analysis. Let us consider forces acting on this control volume. Because of repeating boundary conditions, the forces on the camber lines (planes) balance each other. Thus, if we neglect shear stresses on the endwall and in the upstream measurement plane, the only external forces acting on the upstream and downstream faces of the control volume are the forces due to static pressure at each face.

For a control volume starting upstream of the trailing edge, it is necessary to account for the reduced flow area due to the blade thickness and also to account for the blade forces on the control volume. For the small blade surface areas, in the present analysis for plane 1 ($x/c=0.96$), the blade shear stresses are neglected and the blade forces, F_x and F_y, are calculated simply due to the normal static pressures.

With these assumptions, equations of continuity and momentum for the control volumes may be written as follows:

Continuity:

$$\int_u \rho V_n dA=\rho\bar{V}_{n,u}A_u=\int_d \rho V_n dA=\rho\bar{V}_{n,d}A_d \tag{5}$$

so

$$\bar{V}_{n,d}=\bar{V}_{n,u}\cdot A_u/A_d$$

Downloaded 01 Jun 2010 to 171.66.16.71. Redistribution subject to ASME license or copyright; see http://www.asme.org/terms/Terms_Use.cfm

X-Momentum:

$$F_x + \int_u p_s dA + \int_u \rho V_n V_x dA = \int_d p_s dA + \int_d \rho V_n V_x dA = (p_{s,d} + \rho \bar{V}_{n,d}^2) A_d \tag{6}$$

Y-Momentum:

$$F_y + \int_u \rho V_n V_y dA = \int_d \rho V_n V_y dA = \rho \bar{V}_{n,d} \bar{V}_{y,d} A_d. \tag{7}$$

Also,

$$p_{t,d} = p_{s,d} + \frac{1}{2}\rho(\bar{V}_{n,d}^2 + \bar{V}_{y,d}^2) \tag{8}$$

$$\bar{C}_{Pt,d} = (p_{to} - p_{t,d}) \Big/ \frac{1}{2}\rho U_o^2 \tag{9}$$

$$\bar{C}_{Ps} = (\bar{p}_s - p_o) \Big/ \frac{1}{2}\rho U_o^2 \tag{10}$$

where

$$\bar{p}_s = \frac{1}{A}\int p_s dA. \tag{11}$$

The mixed-out flow properties evaluated from the measured static pressures and velocities at each plane are given in Table 3.

Mixed-Out Total Pressure Loss. The mixed-out total pressure loss $\bar{C}_{Pt,d}$ remains remarkably constant (0.407 ± 0.006) suggesting that neglect of the endwall shear is justified between plane 1 ($x/c = 0.96$) and plane 4 ($x/c = 1.40$) in the present cascade. It is also noteworthy that the mixed-out loss is so close to the sum of $\bar{\bar{C}}_{Pt}$ and $(v^2 + w^2)/U_o^2$ which is 0.411 ± 0.011 (Fig. 12 and Table 2). This closeness could be explained by the following analysis.

Contributions to Additional Mixing Losses. Consider $\bar{\bar{C}}_{Pt} + \overline{\overline{(v^2 + w^2)}}/U_o^2$ at any measurement plane. We have

$$\bar{\bar{C}}_{Pt} + \frac{\overline{\overline{v^2 + w^2}}}{U_o^2} = \frac{p_{to} - \overline{\overline{(p_s + \frac{1}{2}\rho(u^2 + v^2 + w^2))}}}{\frac{1}{2}\rho U_o^2}$$

$$+ \frac{\overline{\overline{\frac{1}{2}\rho(v^2 + w^2)}}}{\frac{1}{2}\rho U_o^2} \tag{12}$$

Therefore,

$$\bar{\bar{C}}_{Pt} + \frac{\overline{\overline{v^2 + w^2}}}{U_o^2} = \frac{p_{to} - \overline{\overline{\left(p_s + \frac{1}{2}\rho u^2\right)}}}{\frac{1}{2}\rho U_o^2} \tag{13}$$

and since $v_d^2 << u_d^2$

$$\bar{C}_{Pt,d} \simeq \frac{p_{to} - \left(p_{s,d} + \frac{1}{2}\rho u_d^2\right)}{\frac{1}{2}\rho U_o^2}. \tag{14}$$

Subtracting (13) from (14) we get

$$\bar{C}_{Pt,d} - \bar{\bar{C}}_{Pt} \simeq \frac{\overline{\overline{v^2 + w^2}}}{U_o^2} - \frac{p_{s,d} - \bar{\bar{p}}_s}{\frac{1}{2}\rho U_o^2} + \frac{\overline{\overline{u^2}} - u_d^2}{U_o^2}, \tag{15}$$

I II III IV

where the numbered terms are

I: Additional loss due to mixing
II: Dissipation of secondary kinetic energy
III: Change in static pressure
IV: Dissipation of primary kinetic energy.

If the net contribution (note opposite signs) of the dissipation of primary kinetic energy and the change in static pressure is small compared to the dissipation of the secondary kinetic energy, then the additional loss due to mixing will simply be due to the dissipation of the secondary kinetic energy; in this case,

$$\bar{C}_{Pt,d} \simeq \bar{\bar{C}}_{Pt} + \frac{\overline{\overline{v^2 + w^2}}}{U_o^2}. \tag{16}$$

Table 4 shows that indeed the net contribution of the dissipation of primary kinetic energy and the rise in static pressure is very small when compared to the dissipation of secondary kinetic energy at each plane. The flow develops downstream of the trailing edge as if the primary flow (in a mass averaged sense) were reversible and only the secondary kinetic energy decays irreversibly. This apparent paradox is seen in Table 4 where the contributions to the increase in total pressure loss ($\bar{C}_{Pt,d} - \bar{\bar{C}}_{Pt}$) due to mixing are shown.

Mixed-Out Flow Angle. The more commonly used method of evaluating the exit flow angle is based on the area averaged velocity $\bar{V}_n$ rather than the mass averaged velocity $\bar{\bar{V}}_x$ of equation (3); then

$$\overline{\overline{\beta'}} = \tan^{-1}(\bar{V}_n / -\bar{\bar{V}}_y). \tag{17}$$

Table 3 Mixed-out flow properties

	Plane 1	2	3	4
$\bar{V}_{x,d}$(m/s)	14.9	16.5	16.9	17.3
$\bar{V}_{y,d}$(m/s)	−32.2	−32.8	−32.5	−32.8
($\bar{\bar{\beta}}$(deg)	31.2	29.1	28.7	28.9)
$\bar{\beta}_d$(deg)	24.8	26.8	27.4	27.8
($\bar{C}_{Ps,u}$	−1.99	−1.95	−1.89	−1.95)
$\bar{C}_{Ps,d}$	−1.68	−1.85	−1.83	−1.90
($\bar{\bar{C}}_{Pt,u}$	0.224	0.294	0.310	0.347)
$\bar{C}_{Pt,d}$	0.401	0.413	0.402	0.403

Table 4 Contributions to mixing losses

Plane No.	$\bar{C}_{Pt,d}$	− $\bar{\bar{C}}_{Pt}$	≃ $\frac{\overline{\overline{v^2 + w^2}}}{U_o^2}$	+ $\frac{\bar{\bar{p}}_s - p_{s,d}}{\frac{1}{2}\rho U_o^2}$	+ $\frac{\overline{\overline{u^2}} - u_d^2}{U_o^2}$
1	0.401	0.224	0.176	−0.296	0.302
2	0.413	0.294	0.127	−0.144	0.138
3	0.402	0.310	0.099	−0.075	0.072
4	0.403	0.347	0.068	−0.071	0.060
				≃0	

Downloaded 01 Jun 2010 to 171.66.16.71. Redistribution subject to ASME license or copyright; see http://www.asme.org/terms/Terms_Use.cfm

For incompressible flow in the constant flow area downstream of a linear cascade, $\bar{V}_n$ is constant; and if endwall shear stresses are negligible, $\bar{\bar{V}}_y$ will also remain constant; thus this definition leads to a downstream flow angle which remains constant independent of downstream distance. To some this is an advantage; the present authors prefer the angle defined in equation (3) because it allows variation due to mixing.

The present mixing analysis with its neglect of endwall shear gives $\bar{V}_{y,d} = \bar{V}_{y,u}$ for planes 2, 3, and 4 downstream of the trailing edge; so for these planes $\bar{\bar{\beta}}' = \bar{\beta}_d$. Table 3 shows the present tests give $\bar{\beta}_d = 27.3 \pm 0.5$ deg, constant to within the accuracy of measurement of the downstream flow angles and quite close to the nominal exit angle of 26 deg.

Conclusions

This test case for downstream mixing losses is an example in the secondary flow limit, dominated by the decay of passage vortices and the dissipation of secondary kinetic energy. The downstream flow is important since more than one-third of the losses for this cascade occur downstream of the trailing edge.

In the region just downstream of the trailing edge, between $x/c = 0.96$ and $x/c = 1.40$:

(*a*) The total pressure loss coefficient $\bar{\bar{C}}_{Pt}$ increases from 0.224 to 0.347.

(*b*) The rise in total pressure loss coefficient (0.123) is almost entirely explained by a corresponding decrease in the secondary kinetic energy coefficient, $\overline{\overline{(v^2 + w^2)}}/U_o{}^2$, (0.108).

(*c*) The spanwise (w) component of secondary velocity contributes more than 75% to the total decrease in the secondary kinetic energy.

(*d*) The sum of $\bar{\bar{C}}_{Pt}$ and $\overline{\overline{(v^2 + w^2)}}/U_o{}^2$ remains almost constant (0.411 ± 0.011).

(*e*) The mixed-out loss (at a plane where mixing is complete and the flow is fully uniform) remains quite constant at $\bar{C}_{Pt,d} = 0.407\ (\pm 0.006)$.

Acknowledgments

The authors wish to thank Rolls-Royce Limited, Aero Division, for supporting this work under a cooperative agreement with Virginia Polytechnic Institute and State University.

References

1 Sjolander, S. A., "The Endwall Boundary Layer in an Annular Cascade of Turbine Nozzle Guide Vanes," M.E. Thesis, Carleton Univ., Ottawa, Ontario, Canada, 1975.

2 Langston, L. S., Nice, M. L., and Hooper, R. M., "Three-Dimensional Flow Within a Turbine Cascade Passage," ASME JOURNAL OF ENGINEERING FOR POWER, Jan. 1977, pp. 21-28.

3 Graziani, R. A., Blair, M. F., Taylor, J. R., and Mayle, R. E., "An Experimental Study of Endwall and Airfoil Surface Heat Transfer in a Large Scale Turbine Blade Cascade," ASME JOURNAL OF ENGINEERING FOR POWER, Vol. 102, Apr. 1980, pp. 257-267.

4 Langston, L. S., "Crossflows in a Turbine Cascade Passage," ASME JOURNAL OF ENGINEERING FOR POWER, Vol. 102, Oct. 1980, pp. 866-874.

5 Sharma, O. P., and Graziani, R. A., "Influence of Endwall Flow on Airfoil Suction Surface Mid-Height Boundary Layer Development in a Turbine Cascade," ASME JOURNAL OF ENGINEERING FOR POWER, Vol. 105, No. 1, Jan. 1983, pp. 147-155.

6 Moore, J., and Ransmayr, A., "Flow in a Turbine Cascade, Part 1: Losses and Leading Edge Effects," ASME JOURNAL OF ENGINEERING FOR GAS TURBINES AND POWER, Vol. 106, Apr. 1984, pp. 400-408.

7 Moore, J., and Smith, B. L., "Flow in a Turbine Cascade. Part 2: Measurement of Flow Trajectories by Ethylene Detection," ASME JOURNAL OF ENGINEERING FOR GAS TURBINES AND POWER, Vol. 106, Apr. 1984, pp. 409-413.

8 Moore, J., "Flow Trajectories, Mixing and Entropy Fluxes in a Turbine Cascade," *AGARD Conference Proceedings No. 351 on Viscous Effects in Turbomachines*, Copenhagen, Denmark, June 1983.

9 Marchal, Ph., and Sieverding, C. H., "Secondary Flows Within Turbomachinery Bladings," *AGARD Conference Proceedings No. 214 on Secondary Flows in Turbomachines*, The Hague, The Netherlands, Mar. 1977.

10 Sieverding, C.H., and Van Den Bosche, P., "The Use of Coloured Smoke to Visualize Secondary Flows in a Turbine-Blade Cascade," *J. of Fluid Mechanics*, Vol. 134, Sept. 1983, pp. 85-89.

11 Gregory-Smith, D. G., and Graves, C. P., "Secondary Flows and Losses in a Turbine Cascade," *AGARD Conference Proceedings No. 351 on Viscous Effects in Turbomachines*, Copenhagen, Denmark, 1983.

12 Dunham, J., "A Review of Cascade Data on Secondary Losses in Turbines," *J. of Mechanical Engineering Science*, Vol. 12, No. 1, 1970, pp. 48-59.

13 Sieverding, C. H., "Recent Progress in the Understanding of Basic Aspects of Secondary Flows in Turbine Blade Passages," ASME JOURNAL OF ENGINEERING FOR GAS TURBINES AND POWER, Vol. 107, No. 2, Apr. 1985, pp. 248-257.

14 Came, P. M., "Secondary Loss Measurements in a Cascade of Turbine Blades," Instn. Mech. Engrs., Conf. Publ. 3, 1973, pp. 75-83.

15 Squire, H. B., and Winter, K. G., "The Secondary Flow Field in a Cascade of Airfoils in a Nonuniform Stream," *J. of Aero. Sci.*, Vol. 18, No. 4, Apr. 1951, pp. 271-277.

16 Gregory-Smith, D. G., "Secondary Flows and Losses in Axial-Flow Turbines," ASME JOURNAL OF ENGINEERING FOR POWER, Vol. 104, Oct. 1982, pp. 819-822.

17 Belik, L., "An Approximate Solution for Kinetic Energy of Secondary Flow in Blade Cascades," *Int. J. Mech. Sci.*, Vol. 10, 1968, pp. 765-782.

18 Bailey, D. A., "Study of Mean- and Turbulent-Velocity Fields in a Large-Scale Turbine-Vane Passage," ASME JOURNAL OF ENGINEERING FOR POWER, Vol. 102, 1980, pp. 88-95.

19 Adhye, R. Y., "Secondary Flows and Losses Downstream of a Turbine Cascade," M.S. Thesis, Virginia Polytechnic Institute and State Univ., Blacksburg, Virginia, April 1984.

20 Moore, J., and Moore, J. G., "Performance Evaluation of Linear Turbine Cascades Using Three-Dimensional Viscous Flow Calculations," ASME JOURNAL OF ENGINEERING FOR GAS TURBINES AND POWER, Vol. 107, No. 4, Oct. 1985, pp. 969-975.

Downloaded 01 Jun 2010 to 171.66.16.71. Redistribution subject to ASME license or copyright; see http://www.asme.org/terms/Terms_Use.cfm

Performance Evaluation of Linear Turbine Cascades Using Three-Dimensional Viscous Flow Calculations

J. Moore

J. G. Moore

Mechanical Engineering Dept.,
Virginia Polytechnic Institute
and State University,
Blacksburg, VA 24061

The overall performance of two geometrically similar linear turbine cascades is calculated using an elliptic flow program. The increase in the mass-averaged total pressure loss is calculated within and downstream of the cascades and the results show good agreement with the measured values. The buildup and decay of the secondary kinetic energy are also shown; measurements are available for one of the cascades near and downstream of the trailing edge and these are in close agreement with the calculated values. Details of the flow development are also compared with measurements. Calculated velocity vectors near the endwall show the overturning revealed by surface flow visualization and similarly near the suction surface the strong spanwise flow is well calculated. Calculated contours of total pressure loss in cross-sectional planes confirm the important interaction of the passage vortex with the profile boundary layer at midspan. Regions of high loss near midspan are calculated downstream of both cascades; this three-dimensional flow development is followed in the calculations.

Introduction

The modern turbine designer increasingly finds himself designing three-dimensional flows. The three-dimensionality arises because of both complex geometry and nonuniform inlet flow. The design objective is certainly to maximize the efficiency but also it is to create a flow downstream of each blade row with a known angle variation and distribution of losses. To aid in this task, three-dimensional viscous flow codes are being developed [1–3] so that designers can determine, for example, the effects of stacking and contouring on work and loss distributions.

The objective of these 3-D flow methods is to allow the calculation of:

- the overall loss production of a blade row;
- the distribution of losses downstream;
- the sources and the rate of buildup of the losses, e.g., due to the increase and decay of secondary kinetic energy; and
- the distributions of velocity and turning angle downstream.

To accomplish this objective the calculations must allow important features of the 3-D flow to develop, such as

- leading edge vortex flow,
- overturning in endwall boundary layers,
- underturning due to passage vortices,
- boundary-layer accumulation, e.g. on suction surfaces, and
- wake and vortex mixing downstream.

It is therefore necessary in evaluating the codes to have data available with detailed measurements of all these flow features and showing the thermodynamic performance of the blade row as well.

UTRC and VPI&SU Turbine Cascades. A blade geometry for which there is a large and growing body of such experimental data is that of the geometrically similar UTRC and VPI&SU turbine cascades [4–11], as shown in Fig. 1. The airfoil section is that of a reaction-turbine rotor with mean camber line angles of $\beta_1 = 43.99$ deg and $\beta_2 = 25.98$ deg giving a nominal turning angle of 110 deg and a velocity ratio of approximately 1.6. The aspect ratios (span/axial chord) of the two cascades are low, 0.989 and 0.997, respectively. But the pitch/axial chord ratio is large, 0.956, giving the Zweifel loading parameter [12] a value of 1.124. Both cascades were tested with the same inlet air angle, $\beta_1 = 44.7$ deg, close to zero incidence. Further details of the two cascades and the inlet flow conditions are given in Table 1.

Present Contribution. The present paper describes some results of 3-D turbulent-flow calculations for these cascades and compares the results with experimental data. It discusses progress made at two levels:

- the modeling of the overall losses, and
- the calculation of fundamental features of the flow.

The calculations are made with an elliptic pressure-correction calculation procedure incorporating a new finite difference formulation of the convection term in the conservation equations [13]. The importance of this method of

Contributed by the Gas Turbine Division of THE AMERICAN SOCIETY OF MECHANICAL ENGINEERS and presented at the 30th International Gas Turbine Conference and Exhibit, Houston, Texas, March 18–21, 1985. Manuscript received at ASME Headquarters, December 21, 1984. Paper No. 85-GT-65.

Copyright © 1985 by ASME
Downloaded 01 Jun 2010 to 171.66.16.71. Redistribution subject to ASME license or copyright; see http://www.asme.org/terms/Terms_Use.cfm

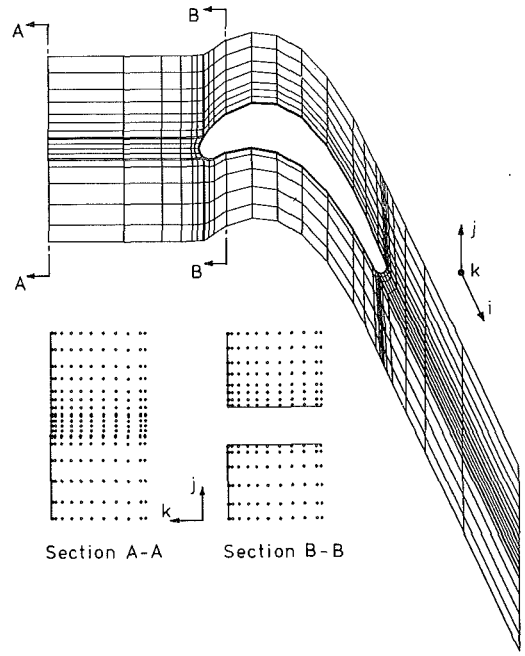


Fig. 1 3-D *i-j-k* grid (28 × 19 × 13) used for turbulent flow calculations

discretization is stressed, in particular the need for consistency in formulating the finite-difference equations.

Computational Method

Governing Equations. The continuity and momentum equations for steady incompressible flow are:

$$\nabla \cdot \rho \underline{u} = 0 \tag{1}$$

$$\rho \underline{u} \cdot \nabla \underline{u} - \nabla \cdot \mu \nabla \underline{u} = -\nabla p + \nabla \cdot \mu \overline{\nabla \underline{u}}^T. \tag{2}$$

The Prandtl mixing-length turbulence model previously used by the authors to calculate flow in boundary layers [14], a rectangular elbow [15], and flow in centrifugal impellers [16] is also employed for the 3-D turbulent flow calculations presented here. Briefly:

$$\mu = \mu_l + \mu_t, \tag{3}$$

where

$$\mu_t = \rho L^2 \left[\left(\frac{\partial u_i}{\partial x_j} + \frac{\partial u_j}{\partial x_i} \right) \frac{\partial u_i}{\partial x_j} \right]^{\frac{1}{2}}. \tag{4}$$

The Prandtl mixing length L is taken to be the smaller of 0.08 times the width of a boundary (or shear) layer and 0.41 times the distance to the nearest wall; and the van Driest correction is applied near walls. Outside boundary layers and shear layers the turbulent viscosity μ_t is set to zero.

Table 1 Geometry of the UTRC and VPI&SU turbine cascades and details of the inlet flows

	UTRC	VPI&SU
Axial chord (mm)	281.3	235.2
Pitch/axial chord	0.956	0.956
Span/axial chord	0.989	0.997
Airfoil mean camber line angles		
β_1(deg)	43.99	43.99
β_2(deg)	25.98	25.98
Inlet flow angle		
β_1(deg)	44.7	44.7
Inlet flow velocity		
U_o(m/s)	33.5	23.5
Endwall boundary layer parameters at inlet		
Distance upstream of leading edge (m)	0.66	0.40
δ_{99}(mm)	33.0	38.
δ^*(mm)	3.76	5.41
θ(mm)	2.79	4.10
H_{12}	1.35	1.32
Exit Reynolds number based on blade axial chord		
Re_c	$10. \times 10^5$	5.2×10^5

Discretization of the Equations. Equations (1) and (2) are not really "solved" by finite difference-calculation procedures. Only discretized forms of these equations are solved. When relatively coarse grids are employed, the numerical accuracy of the calculations is strongly dependent on the choice of discretization, especially for the convection of momentum.

Continuity. The continuity equation is integrated over a control volume with eight grid points as the corners. The velocity is taken to vary linearly between the grid points so that the mass flux for each side is determined from the four-point average of the velocities for that side.

Momentum. The x, y, and z components of the momentum equation are used to obtain the Cartesian velocity components, u_i.

The momentum equation is integrated over upwinded control volumes. The control volumes are formed by dividing the continuity control volume, midway between the grid points in each direction, into eight parts. These one-eighth control volumes are then assigned to the points in such a way that the net effect is to have the momentum control volume on the upstream side of the grid point. This 3-D extension to what is common practice in, for example, 2-D boundary layer calculations is described in [13].

Finite difference forms of the convection and pressure terms are then obtained by assuming the velocity and pressure vary linearly between the grid points. Upwind differencing is not used (and so the associated numerical mixing is not introduced) because the upwinded control volumes eliminate the need to artificially stabilize the finite difference equations. The upwinded control volumes cover the flow domain once

Nomenclature

c = axial chord
C_{pt} = total pressure-loss coefficient, $C_{pt} = (p_{to} - p_t)/\frac{1}{2}\rho U_o^2$
C_{sk} = secondary kinetic energy coefficient, $C_{sk} = (v^2 + w^2)/U_o^2$
H_{12} = shape factor, δ^*/θ
i, j, k = grid-line directions, Fig. 1
L = Prandtl mixing length
p = static pressure
p_t = total pressure
p_{to} = upstream freestream total pressure
$\underline{u}$ = velocity vector
u_i = Cartesian velocity components
U_o = upstream freestream velocity
v, w = secondary velocity components normal to the i-grid direction
x = axial distance from blade leading edge
x_i = Cartesian coordinates
β_1 = angle to the blade-to-blade direction at inlet
β_2 = angle to the blade-to-blade direction at exit
δ_{99} = boundary-layer thickness
δ^* = displacement thickness of boundary layer
θ = moment thickness of boundary layer
μ = effective (total) viscosity
μ_l = laminar viscosity
μ_t = turbulent viscosity
ρ = density
$\underline{\rho}$ = mass average

Downloaded 01 Jun 2010 to 171.66.16.71. Redistribution subject to ASME license or copyright; see http://www.asme.org/terms/Terms_Use.cfm

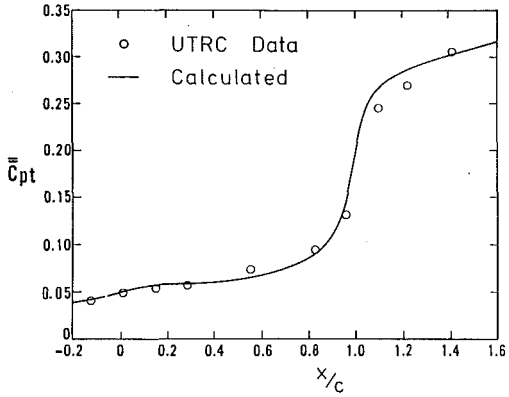


Fig. 2 Mass-averaged total pressure-loss coefficient as a function of axial distance through the UTRC cascade; leading edge: $x/c = 0$; trailing edge: $x/c = 1.0$

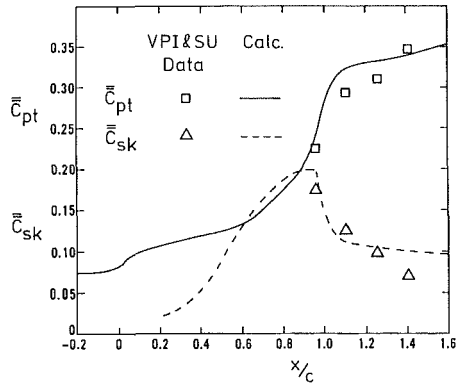


Fig. 3 Mass-averaged total pressure loss and secondary kinetic energy coefficients through the VPI&SU cascade

and only once and so they introduce no inconsistency which could appear as numerical mixing.

Finite difference forms of the viscous terms are also obtained consistent with the linear profile assumption; $\partial u_i/\partial i$, $\partial u_i/\partial j$ and $\partial u_i/\partial k$ have stepwise variations in the i, j, and k grid directions, respectively. To obtain the shear stresses the velocity gradients are multiplied by the viscosity calculated in the center of the continuity control volume consistent with linear profiles and equation (4).

Calculation Grid. A 3-D i-j-k grid is used. The blade is mapped onto a box with four corners near the leading edge and four corners near the trailing edge. Upstream of the blade, the i-direction is chosen to be axial so that grid points are spaced around the suction surface on the leading edge where the pressure and flow velocity vary rapidly. The i-direction downstream of the blade is chosen in the approximate flow direction ($\beta_2 = 26$ deg) allowing the recirculation zone near the trailing edge and the wake mixing downstream to be captured with a relatively fine grid. The j-direction is blade-to-blade, beginning and ending on a repeating boundary midway between the blades. Discontinuities in the i and j grid directions present no difficulties since the equations are expressed in terms of x, y, z velocity components, independent of grid directions. The k-direction is spanwise from midheight in the passage to the endwall. The $28 \times 19 \times 13$ grid used for the present 3-D turbulent flow calculations is shown in Fig. 1.

Pressure-Correction Solution Procedure. The results of any numerical calculation are governed by the discretized equations which are satisfied. The solution procedure determines only the speed at which the solution is obtained. The solution procedure used here is a combination of the pressure-correction methods for elliptic flow described by Patankar [17] and Moore and Moore [2]. The calculations for the UTRC and VPI&SU cascades each required 1 hr of CPU time and 3 Mbytes of memory on an IBM 3081.

Boundary Conditions. *Inlet.* The total pressure distribution at the inlet plane was specified consistent with the inlet boundary layers given in Table 1. The inlet flow angles were fixed and uniform.

Exit. A uniform exit static pressure-boundary condition was employed downstream of the region of interest at $x/c = 1.7$. The level of the pressure was calculated to obtain the specified mass flow rate.

Walls. The velocity was set to zero on the endwall and blade surfaces.

Calculation Results

Overall Losses. The rise in mass-averaged total pressure loss $\bar{C}_{pt}$ through the UTRC cascade is shown in Fig. 2 for the flow conditions given in Table 1. The calculated buildup of loss follows the measurements of Langston et al. [4] quite closely. Both the calculations and the measurements show only a small rise in the first half of the blade passage with an increasing rate of loss production toward the trailing edge. Near the trailing edge and up to about 10% of an axial chord downstream the losses rise very rapidly. Further downstream there is a reduced but significant rate of loss production.

Near the flow inlet at $x/c = -0.2$, the inlet boundary layer gives a total pressure loss $\bar{C}_{pt}$ of about 0.04. At $x/c = 0.96$, just upstream of the trailing edge plane, the loss has risen to about 0.13 in the measurements and to 0.14 in the calculations. In both the calculations and the measurements there is an increase of approximately 0.12 in loss coefficient in the next 10% of axial chord up to $x/c = 1.10$. At the last measurement plane of Langston et al., plane 12 at $x/c = 1.40$, the measured value of loss is $\bar{C}_{pt} \simeq 0.31$ compared with the calculated value of 0.30. The net rise in loss (from $x/c = -0.2$ to $x/c = 1.40$) is $\delta\bar{C}_{pt} \simeq 0.27$.

The corresponding total pressure plot for the VPI&SU cascade is shown in Fig. 3. For these tests the inlet boundary layer was relatively nearly twice as thick (δ^*/span = 0.023) as that for the UTRC cascade (δ^*/span = 0.0135, see Table 1). At $x/c = -0.2$, $\bar{C}_{pt}$ is 0.07 for the VPI&SU cascade compared with $\bar{C}_{pt} \simeq 0.04$ for the UTRC cascade. By $x/c = 0.96$ the measured loss has risen to 0.22 compared with the calculated value of 0.25. There is then an increase of about 0.07 in loss up to $x/c = 1.10$. At $x/c = 1.40$ the measured loss of 0.35 is again slightly higher than the calculated value of 0.34, and the net increase in loss $\delta\bar{C}_{pt} \simeq 0.28$ is surprisingly close to that measured by Langston et al. (0.27).

Comparing the loss development in the two cascades, the major difference is the earlier loss production in the VPI&SU cascade with equivalent levels of loss being produced from 6–20% of an axial chord upstream of their production in the UTRC cascade. The calculations confirm this trend.

Secondary Flow and Secondary Kinetic Energy. A "primary" flow direction is defined as the i-direction of the grid. In the blade passage, the i-grid lines are located at fixed fractions of the blade-to-blade spacing while downstream they are parallel to the blade camber line at the trailing edge (i.e., at 64 deg to the axial direction). The velocity in the i-direction is then termed u and the "secondary flow" velocity components v and w complete an orthogonal set. The velocity component w is taken in the spanwise direction and the v component is taken mutually perpendicular to u and w. With these definitions the kinetic energy of the primary flow (per

Downloaded 01 Jun 2010 to 171.66.16.71. Redistribution subject to ASME license or copyright; see http://www.asme.org/terms/Terms_Use.cfm

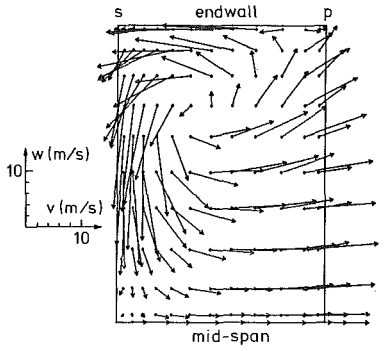


Fig. 4(*a*) Calculated at $x/c = 0.94$

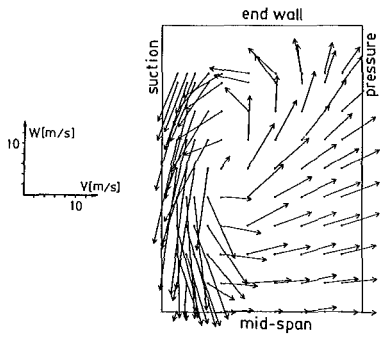


Fig. 4(*b*) Measured at $x/c = 0.96$

Fig. 4 Secondary flow vectors in the VPI&SU cascade viewed looking upstream in the *i*-direction

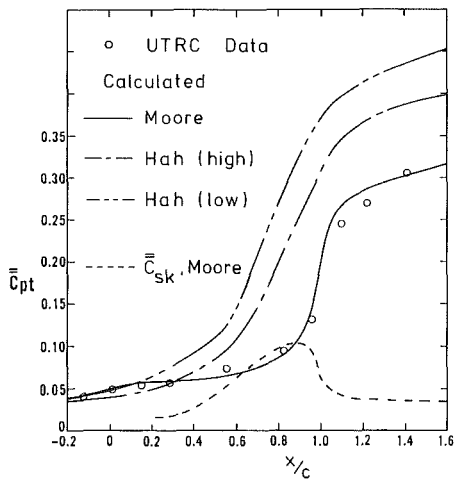


Fig. 5 Mass-averaged total pressure loss and secondary kinetic energy coefficients through the UTRC cascade

unit mass) is $u^2/2$ and the secondary kinetic energy is $(v^2 + w^2)/2$. We then define a mass-averaged secondary kinetic energy coefficient $\bar{\bar{C}}_{sk}$ as

$$\bar{\bar{C}}_{sk} \equiv \overline{\overline{(v^2 + w^2)}}/U_o{}^2. \tag{5}$$

This representation of secondary flow has been used to model flow downstream of the trailing edge of the VPI&SU cascade by Moore et al. [8–11]. They note that the natural way to view the secondary flow is then in the *i*-direction and they plot their secondary flow velocity vectors in a "cross-sectional plane" perpendicular to the *i*-direction. The calculated secondary flow velocities at a plane just upstream of the trailing edge of the VPI&SU cascade ($x/c = 0.94$) and viewed in this way are seen in Fig. 4(*a*); they are in good agreement with the measurements shown in Fig. 4(*b*) [11].

Table 2 Overall losses in UTRC and VPI&SU turbine cascades

	UTRC	VPI&SU
$(\bar{\bar{C}}_{pt})_{x/c=-0.2}$	0.04	0.07
$(\bar{\bar{C}}_{pt})_{x/c=1.40}$(measured)	0.31	0.35
$(\bar{\bar{C}}_{pt})_{x/c=1.40}$(calculated)	0.30	0.34
$(\bar{\bar{C}}_{sk})_{x/c=0.96}$(measured)	–	0.18
$(\bar{\bar{C}}_{sk})_{x/c=0.96}$(peak, calculated)	0.10	0.20
$\delta(\bar{\bar{C}}_{sk})_{x/c=0.96\text{-}1.40}$(measured)	–	0.11
$\delta(\bar{\bar{C}}_{sk})_{x/c=0.96\text{-}1.40}$(calculated)	0.07	0.10

As in the measurements, the calculated secondary velocities show the flow (in the top half of the passage) dominated by a single large passage vortex. There are strong crossflows ($v \sim 13$ m/s, or $0.5\ U_o$) in the endwall boundary layer from the pressure side to the suction side and even higher spanwise velocities ($w \sim 20$ m/s, or $0.9\ U_o$) near the suction surface from the endwall toward midspan. The overturning of the flow near the endwall and the underturning of the flow between the vortex core and midspan are clearly seen together with the flow toward the pressure side due to the blade unloading at this plane.

The buildup and decay of secondary kinetic energy in the calculations for the VPI&SU cascade is shown in Fig. 3. From an initial low level near the blade inlet, it rises steadily to a secondary kinetic-energy coefficient, $\bar{\bar{C}}_{sk}$, of 0.10 at $x/c = 0.5$ and then to a peak value of 0.20 at $x/c = 0.97$. Immediately downstream of the trailing edge the secondary kinetic-energy coefficient decreases rapidly to 0.11 at $x/c = 1.10$ and then falls slowly but steadily to 0.1 at $x/c = 1.40$. The measurements of Moore and Adhye also show the secondary kinetic energy decaying rapidly downstream of the trailing edge. At $x/c = 0.96$ the measured secondary kinetic energy coefficient was 0.18; it then fell quite steadily to 0.13 at $x/c = 1.10$ and to 0.07 at $x/c = 1.40$.

These results for secondary kinetic-energy coefficient show good agreement between the experiment and the computations. The peak values of 0.18 and 0.20 and the reductions from the peak value of 0.11 and 0.10, respectively, are remarkably close. The calculations lend support to the idea that the additional losses downstream of the VPI&SU cascade are largely the result of a dissipation of secondary kinetic energy [11].

It appears that the flow downstream of the VPI&SU cascade is an example in the secondary flow limit – dominated by the decay of passage vortices and the dissipation of secondary kinetic energy. By contrast, the flow in the UTRC cascade has less secondary kinetic energy as shown in Fig. 5. The thinner inlet boundary layer results in a peak value of the secondary kinetic-energy coefficient of only 0.10 and the decay downstream of 0.07 (to 0.03 at $x/c = 1.40$).

Overall Losses in UTRC and VPI&SU Cascades. The measured and calculated values of the overall loss parameters for the UTRC and VPI&SU cascades are summarized in Table 2 (for the flow conditions in Table 1).

Secondary Kinetic Energy and Numerical Mixing. Figure 5 also shows the results of some earlier calculations for the UTRC cascade by Hah [3]. He used a pressure correction method with two different ways of discretizing the finite-difference equations, what he termed a low-order and a high-order scheme. Clearly the results with these schemes are not in agreement with the measured data [4]; but perhaps Fig. 5 shows why. Upstream and downstream, where the secondary kinetic energy (calculated by the present authors) is small, the rates of increase of loss calculated by Hah are close to the measured rates. But as the secondary kinetic energy builds up so the results with the low and high-order schemes rise above the measured losses, until at $x/c = 0.96$ the increases in loss

Downloaded 01 Jun 2010 to 171.66.16.71. Redistribution subject to ASME license or copyright; see http://www.asme.org/terms/Terms_Use.cfm

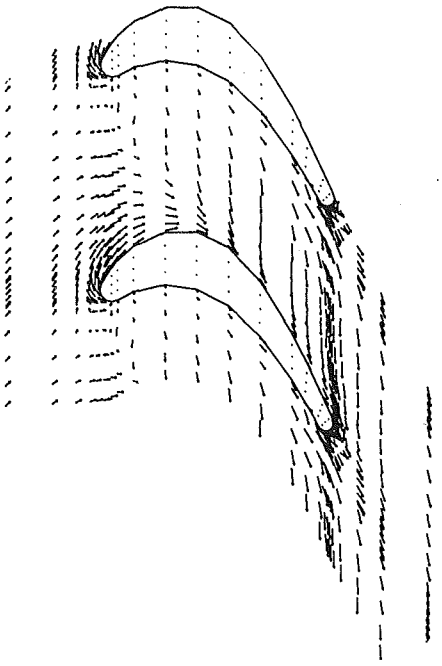


Fig. 6 Calculated velocity vectors near the endwall (0.25% of span) of the VPI&SU cascade

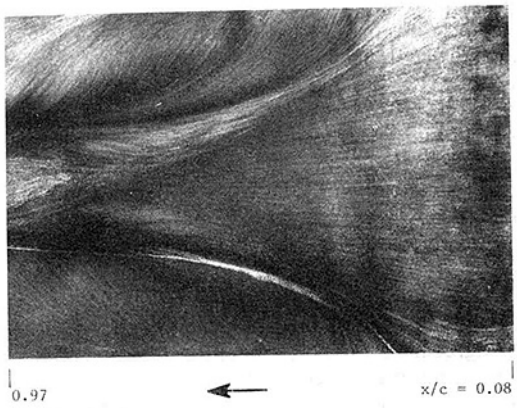


Fig. 7 Experimental visualization of the limiting streamlines on the suction surface of the VPI&SU cascade; flow from right to left; gravity from top to bottom

above the inlet value are about 3.1 and 2.4 times the measured increase, respectively. This high loss production in the Hah results may be connected with high secondary velocities and may be a manifestation of the numerical mixing known to occur with upwinded differencing of the convection term.

By contrast, the discretization technique used for the results in this paper has been tested for inviscid flow [13] and shown to preserve the mass distribution of total pressure as well as the mass-averaged total pressure. Thus, with this new technique the total pressure losses are the result of the viscous terms in the momentum equations as they should be. In brief, Hah's high-order scheme is more complex but less consistent than the discretization technique used for the present calculations.

Flow Near the Endwall. Details of the flow calculated near the endwall for the VPI&SU cascade are shown in Fig. 6. These velocity vectors are at 0.25% of span from the endwall, sufficiently close to the wall to be in the collateral part of the endwall boundary layer and therefore indicating the local direction of the limiting streamlines. These computed flow directions can be compared with the directions of the limiting streamlines in the flow visualization shown in Fig. 2 of [9] and Fig. 11 of [10].

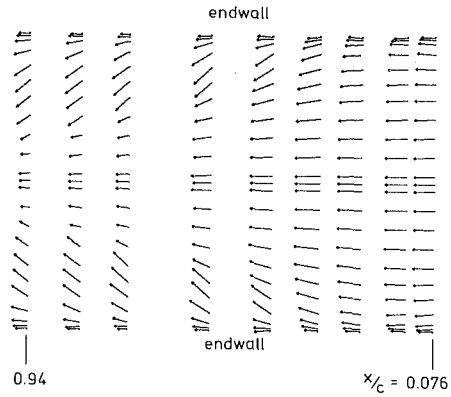


Fig. 8 Calculated velocity vectors near the suction surface (1.0% of the local blade-to-blade distance) of the VPI&SU cascade

Near the leading edges of the blades the endwall boundary layer separates in the well-known saddle-point flow pattern [18]. Many of the calculated flow features here show detail observed in the flow visualization: the backflow between the stagnation point in the pressure side/endwall corner and the saddle point, the strong overturning associated with the three-dimensional flow separation between the saddle point and the suction surface of the next blade at about midchord, the boundary layer converging in the suction side/endwall corner region at about midchord, and the new endwall boundary layer flowing downstream of the separation line from the pressure side toward the suction side.

In the latter half of the passage and just downstream, the calculated endwall flow in the middle of the passage is locally in the blade-to-blade direction with some points even showing backflow; these flow angles are generally in very close agreement (better than 5 deg) with those found on the endwall flow visualization. Near the trailing edges, the endwall crossflow, the recirculating flow and the blade wake merge in a manner quite similar to that observed.

Flow Near the Suction Surface. Figure 7 shows a visualization of the limiting streamlines on the suction surface from $x/c = 0.08$ to $x/c = 0.97$. This starts 1.8 cm downstream of the trip wire on the suction surface and ends 1.5 cm upstream of the beginning of the curvature of the rounded trailing edge. In the spanwise direction the visualization ends about 2% of span from the endwalls.

The dominant features in the flow visualization are the spanwise flows caused by the two symmetrical passage vortices which result in the strongly converging suction side boundary layer near midspan and the two mirror-image 3-D separation lines. The 3-D separation lines appear to start near the endwalls at about $x/c = 0.30$ and by the trailing edge they are at 34% and 66% of span, respectively. Clearly this suction surface flow is dominated by three-dimensional effects.

The corresponding flow vectors close to the suction surface are shown in Fig. 8. The vectors are at a blade-to-blade spacing of 1% from the wall and like those in Fig. 6 they show the calculated directions of the limiting streamlines. Between the passage vortex and the suction surface large spanwise flow angles are found: The visualization shows angles of the order of 55 deg from the horizontal while the calculation gives values as high as 44 deg.

Downloaded 01 Jun 2010 to 171.66.16.71. Redistribution subject to ASME license or copyright; see http://www.asme.org/terms/Terms_Use.cfm

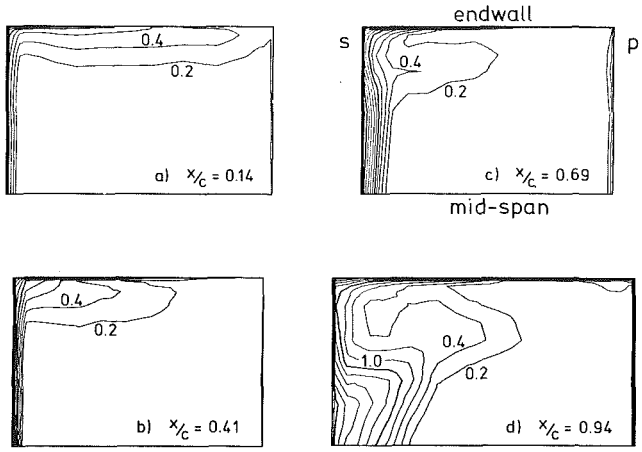


Fig. 9 Contours of total pressure loss coefficient C_{pt}; calculated flow development in the VPI&SU cascade; contour interval = 0.2

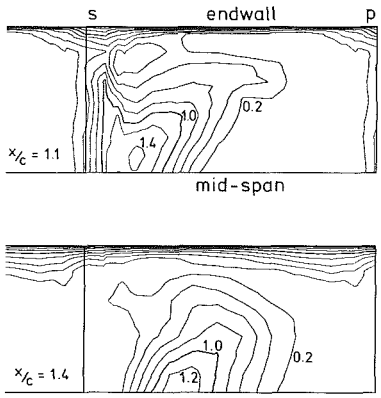


Fig. 10 Contours of total pressure loss coefficient C_{pt}; calculated flow development downstream of the VPI&SU cascade

Overall the calculated flow directions are in remarkably close agreement with the visualized surface pattern and are consistent with the lines of three-dimensional separation shown in Fig. 7.

Contours of Total Pressure Loss. The migration of the inlet boundary layer toward the suction surface of the passage and the subsequent convection of this fluid toward midspan can be followed in Figs. 9 and 10. These show contours of calculated total pressure loss coefficient C_{pt} for the VPI&SU cascade. Figure 9 shows the flow development within the passage at four planes with x/c of 0.14, 0.41, 0.69, and 0.94. Figure 10 shows the downstream development at $x/c = 1.10$ and 1.40.

Between $x/c = 0.14$ and 0.69, the inlet boundary layer is swept from the endwall leaving the very thin boundary layer shown in Fig. 9(*c*). The boundary layer at midspan on the suction surface then grows rapidly between $x/c = 0.69$ and 0.94 as shown by the contours of $C_{pt} = 1.0$ in Figs. 9(*c*) and 9(*d*); this is where the strong spanwise velocities shown in Figs. 7 and 8 sweep the boundary layer toward midspan resulting in three-dimensional flow separation, as suggested by the contours of $C_{pt} = 2.0$ in Figs. 9(*c*) and 9(*d*).

Downstream of the trailing edge, a high-loss core develops near midspan as fluid from the suction side boundary layer and the passage vortex (Fig. 4) continues to be convected away from the endwall and toward the middle of the passage. The peak value of C_{pt} in the high-loss core (~ 1.3) and the location of the core are in close agreement with the experimental results shown in Fig. 3 of [10].

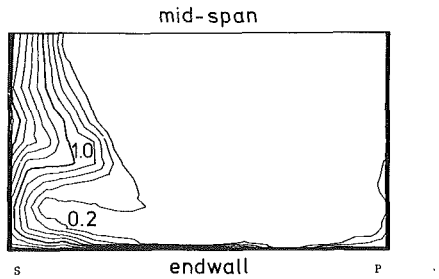


Fig. 11 Contours of total pressure loss coefficient C_{pt} calculated for the UTRC cascade at $x/c = 0.94$

Contours of calculated total pressure loss coefficient for the UTRC cascade at $x/c = 0.94$ are shown in Fig. 11. As expected these show smaller areas of high-loss fluid near the suction surface than the contours of Fig. 9(*d*) because of the thinner inlet boundary layer. They also show less convection toward midspan and consequently a thinner midspan boundary layer. Although the coarse grid does not allow the details of the high-loss core associated with the horseshoe vortex to be resolved, these contours are in reasonable agreement with the measurements of Langston et al. shown in Fig. 7(*c*) of [4].

Conclusions

Progress in modeling three-dimensional turbulent flow in turbine blade rows has been described based on the results of calculations for the UTRC and VPI&SU linear turbine cascades. The calculations were performed with an elliptic pressure-correction procedure incorporating a new finite difference formulation for the convection of momentum. The particular method used here, which is to upwind the control volumes, appears critical to the elimination of numerical mixing and to the calculation of the correct level of overall losses.

The calculations of overall loss including the peak value of secondary kinetic energy and its subsequent level of decay are in good agreement with experimental data. The calculations show that the peak secondary kinetic energy coefficient, $(v^2 + w^2)/U_o^2$, for the UTRC cascade is 0.10, one-half the value for the VPI&SU cascade. They also confirm that the major difference in the loss production of the two cascades is the earlier loss production in the VPI&SU cascade. Further analysis of these results is planned.

Acknowledgments

The authors wish to thank Rolls-Royce Limited, Aero Division, for supporting this work under a cooperative agreement with Virginia Polytechnic Institute and State University.

References

1 Dodge, P. R., "Numerical Method for 2D and 3D Viscous Flows," AIAA Paper No. 76-425, 1976.

2 Moore, J. G., and Moore, J., "Lecture Notes on the Calculation of Three-Dimensional Viscous Flows Using Pressure Correction Methods," *ASME Gas Turbine Division Short Course on 3-D Flows in Turbomachinery Blade Rows*, Phoenix, Arizona, Mar. 1983.

3 Hah, C., "A Navier Stokes Analysis of Three-Dimensional Flow Inside Turbine Blade Rows at Design and Off-Design Conditions," ASME JOURNAL OF ENGINEERING FOR GAS TURBINES AND POWER, Vol. 106, Apr. 1984, pp. 421-429.

4 Langston, L. S., Nice, M. L., and Hooper, R. M., "Three-Dimensional Flow Within a Turbine Cascade Passage," ASME JOURNAL OF ENGINEERING FOR POWER, Jan. 1977, pp. 21-28.

5 Graziani, R. A., Blair, M. F., Taylor, J. R., and Mayle, R. E., "An Ex-

Downloaded 01 Jun 2010 to 171.66.16.71. Redistribution subject to ASME license or copyright; see http://www.asme.org/terms/Terms_Use.cfm

perimental Study of Endwall and Airfoil Surface Heat Transfer in a Large Scale Turbine Blade Cascade," ASME JOURNAL OF ENGINEERING FOR POWER, Vol. 102, 1980, pp. 257–267.

6 Langston, L. S., "Crossflows in a Turbine Cascade Passage," ASME JOURNAL OF ENGINEERING FOR POWER, Vol. 102, Oct. 1980, pp. 866–874.

7 Sharma, O. P., and Graziani, R. A., "Influence of Endwall Flow on Airfoil Suction Surface Mid-Height Boundary Layer Development in a Turbine Cascade," ASME JOURNAL OF ENGINEERING FOR POWER, Vol. 105, No. 1, Jan. 1983, pp. 147–155, ASME Paper No. 82-GT-127.

8 Moore, J., and Ransmayr, A., "Flow in a Turbine Cascade, Part 1: Losses and Leading Edge Effects," ASME JOURNAL OF ENGINEERING FOR GAS TURBINES AND POWER, Vol. 106, Apr. 1984, pp. 400–408.

9 Moore, J., and Smith, B. L., "Flow in a Turbine Cascade, Part 2: Measurement of Flow Trajectories by Ethylene Detection," ASME JOURNAL OF ENGINEERING FOR GAS TURBINES AND POWER, Vol. 106, Apr. 1984, pp. 409–413.

10 Moore, J., "Flow Trajectories, Mixing and Entropy Fluxes in a Turbine Cascade," *AGARD Conference Proceedings No. 351 on Viscous Effects in Turbomachines*, Copenhagen, Denmark, June 1983.

11 Moore, J., and Adhye, R. Y., "Secondary Flows and Losses Downstream of a Turbine Cascade," ASME JOURNAL OF ENGINEERING FOR GAS TURBINES AND POWER, Vol. 107, No. 4, Oct. 1985, pp. 961–968.

12 Horlock, J. H., *Axial Flow Turbines*, Krieger, New York, 1973.

13 Moore, J. G., and Moore, J., "Calculation of Horseshoe Vortex Flow Without Numerical Mixing," ASME Paper No. 84-GT-241.

14 Moore, J., and Moore, J. G., "Calculation of Five Turbulent Flows Using the Moore Cascade Flow Program," *The 1980–81 AFOSR-HTTM-Stanford Conference on Complex Flows: Comparison of Computation and Experiment*, Vol. III, Stanford University, CA, 1981, pp. 1453–1458.

15 Moore, J., and Moore, J. G., "A Calculation Procedure for Three-Dimensional, Viscous, Compressible Duct Flow. Part II—Stagnation Pressure Losses in a Rectangular Elbow," ASME *Journal of Fluids Engineering*, Vol. 101, Dec. 1979, pp. 423–428.

16 Moore, J., Moore, J. G., and Timmis, P. H., "Performance Evaluation of Centrifugal Compressor Impellers Using Three-Dimensional Viscous Flow Calculations," ASME JOURNAL OF ENGINEERING FOR GAS TURBINES AND POWER, Vol. 106, Apr. 1984, pp. 475–481.

17 Patankar, S. V., "Numerical Prediction of Three-Dimensional Flows," *Studies in Convection*, Vol. 1, Ed. B. E. Launder, Academic Press, 1975.

18 Sieverding, C. H., "Recent Progress in the Understanding of Basic Aspects of Secondary Flows in Turbine Blade Passages," ASME JOURNAL OF ENGINEERING FOR GAS TURBINES AND POWER, Vol. 107, No. 2, Apr. 1985, pp. 248–257.

Downloaded 01 Jun 2010 to 171.66.16.71. Redistribution subject to ASME license or copyright; see http://www.asme.org/terms/Terms_Use.cfm

Heat-Transfer Distribution Around a Cylinder in Pulsating Crossflow

C. E. Andraka
Sandia National Laboratories,
Albuquerque, NM 87185

T. E. Diller
Mechanical Engineering Department,
Virginia Polytechnic Institute and
State University,
Blacksburg, VA 24061
Mem. ASME

The effects of sinusoidal flow pulsations on the heat transfer from a cylinder to a crossflow at Re = 50,000 were investigated. A range of different pulsation amplitudes of up to 25% and frequencies both above and below the natural shedding frequency were used. The pulsating flow was clean and well organized. It had greater than 95% of the power at the fundamental frequency with a low turbulence level (less than 0.5%). The time-averaged local heat transfer was experimentally measured for a constant-temperature surface-boundary condition using a small heat flux gage in the cylinder wall. Distributions were obtained by rotating the cylinder through 180 deg. The experiments showed no significant increase of heat transfer due to the flow pulsation in either the wake or attached boundary layer region. Small local increases were found near the separation point.

Introduction

Heat transfer over a circular cylinder in a crossflow is a fundamental problem with many applications, such as tube heat exchangers and the leading edge region of gas turbine blades. The problem is inherently unsteady due to the periodic natural shedding of the flow past the cylinder or the wakes of upstream blades. The flow can also have externally generated random freestream turbulence or organized unsteadiness, which may have an additional effect on the heat-transfer characteristics of the cylinder. The present research reports the effects on the local time-averaged heat transfer of a cylinder when a well-defined single frequency oscillation is added to a low-turbulence crossflow.

Heat transfer from a single cylinder has received much attention in the past [1, 2]. The laminar boundary layer in steady flow is well understood and has been accurately modeled [3, 4]. More recently the unsteady problems associated with heat transfer from a cylinder have received attention. Freestream turbulence effects have been studied experimentally and analytically (e.g., [1, 2, 5–11]), but a complete correlation of the effects on heat transfer has not yet been established. The effects on the heat transfer of different motions of the cylinder relative to the flow have also been experimentally studied [12–14]. Some investigators have measured cylinder heat transfer in a flow with organized disturbances [15–19] and have indicated varying degrees of heat-transfer increases. Little was done in these tests to separate the effects of 3-D turbulence from the 1-D organized disturbance. Also, little detailed experimental work has been done for driving frequencies near the natural shedding frequency of the cylinder.

Analytical work has predicted the phase lag and amplitude of surface heat-transfer fluctuations relative to freestream velocity fluctuation or cylinder motion [4, 20–24]. The effect of oscillation of the flow or body was predicted to have little influence on the time-averaged heat transfer in a stagnation flow [4, 22, 24], unless the amplitudes were large enough to create significant acoustic streaming [23]. This is in contradiction with most of the experimental studies.

Several aspects of this investigation make it significantly different from preceding investigations. Firstly, the effect of 1-D uniform mean flow disturbances on heat transfer from a cylinder with constant wall temperature has been measured independently of the turbulence effects. Secondly, the oscillations consist of a single isolated frequency, with the power in the harmonics less than 5% of the oscillation total power. Thirdly, detailed heat-transfer measurements were performed at driving frequencies below, at, and above the natural shedding frequency. Reduced driving frequencies (fD/U_∞) of 0.0063 to 0.24 were considered, including the case of driving at the natural shedding frequency. The mean crossflow Reynolds number ranged from 35,000 to 164,000. Most of the oscillating flow tests were performed at Re = 50,000, with oscillation amplitudes up to 25% zero-to-peak of the mean flow.

Experimental Apparatus

The experimental investigation was performed using a low-speed pulsating flow wind tunnel constructed primarily for this project. The tunnel design was based on a smaller tunnel designed by Tavakoli [25] and used by Borrell et al. [18]. The blower-type tunnel has a 248-cm-long test section with a 74.1 cm × 52.9 cm cross section. The settling chamber contains a flow straightener consisting of one honeycomb and five screens. The contraction ratio is 6:1. The tunnel is capable of providing up to 33 m/s steady flow. The freestream turbulence was measured with a TSI IFA-100 hot-wire anemometer with output linearizers. For the pulsating flow two separate hot film probes were mounted in the cylinder position with the cylinder removed. A Zonic 5003 digital signal analyzer was used to determine the total power spec-

Contributed by the Gas Turbine Division of THE AMERICAN SOCIETY OF MECHANICAL ENGINEERS and presented at the 30th International Gas Turbine Conference and Exhibit, Houston, Texas, March 18–21, 1985. Manuscript received at ASME Headquarters, December 21, 1984. Paper No. 85-GT-67.

Copyright © 1985 by ASME
Downloaded 01 Jun 2010 to 171.66.16.71. Redistribution subject to ASME license or copyright; see http://www.asme.org/terms/Terms_Use.cfm

Table 1 Flow Conditions Used in This Investigation

f_d(Hz)	f_r	ϵ	Re	Power in the fundamental (%)	Tu(%)
0.0	0.0	0.0	35,000	–	–
0.0	0.0	0.0	50,000	–	.33
0.0	0.0	0.0	56,800	–	–
0.0	0.0	0.0	100,000	–	–
0.0	0.0	0.0	164,000	–	–
0.67	0.0063	0.248	50,000	95.35	–
1.7	0.016	0.098	50,000	98.93	.47
7.0	0.066	0.041	50,000	98.32	.35
18.5	0.174	0.089	50,000	99.16	.50
23.0[1]	0.19	0.089	56,800	99.20	–
23.0	0.216	0.089	50,000	99.20	.55
26.0	0.244	0.067	50,000	98.52	.40

[1] Lock-on frequency

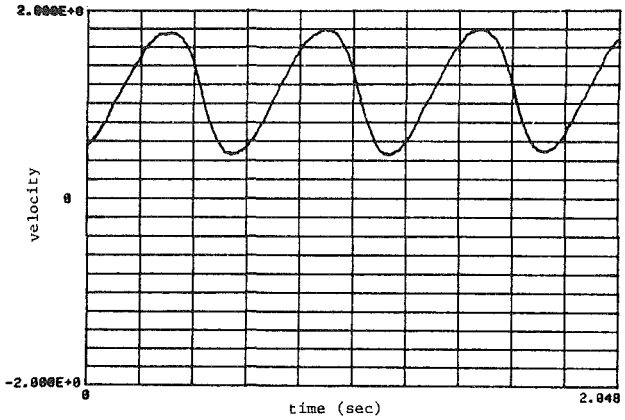
trum and the coherent power spectrum. The coherent spectrum contains the effects of acoustic noise and pulsating flow, so the difference between the spectrums is the random signal or turbulence. Each of the signals is averaged in the frequency domain (autospectrum) from a trigger on the rotating shutters. The measured turbulence in the steady and unsteady flows was between 0.33% and 0.55%, and did not vary significantly with pulsation frequency. The flow was uniform to ±2.1%, neglecting the wall boundary layers.

The flow pulsation is produced by six rotating shutters mounted on parallel shafts in the settling chamber. The vanes are gear driven by a GK Heller 2-hp variable speed d-c electric motor. The waveforms can be controlled by changing the relative orientation of the vanes and by opening hinged panels on the top and bottom to release diffuser pressure spikes [25]. The waveforms used in this experiment were very nearly sinusoidal (Fig. 1) with at least 95% of the wave energy at the fundamental frequency. The wave amplitudes (ϵ) were 4–25% of the mean flow where

$$U = U_\infty(1 + \epsilon \sin 2\pi f t)$$

Table 1 lists the flow conditions used in this investigation, which included frequencies above and below the natural shedding frequency of the test cylinder.

The cylinder model was constructed from a 8.89 cm o.d. aluminum pipe with a wall thickness of 0.76 cm. It was cut in half lengthwise to facilitate assembly. Twenty-eight type T thermocouples were soldered into 0.32 cm o.d. brass plugs, which were press fit into the cylinder wall and sanded smooth with the surface. The thermocouple junctions and solder were positioned close to the cylinder surface to assure an accurate surface-temperature measurement. The thermal conductivity and emissivity of the brass and solder are similar to those of the aluminum cylinder, so that the temperature is not significantly perturbed. The thermocouples were mounted on the surface in a line along the axis at four equally spaced angular positions, providing both lengthwise and angular temperature distributions. A 0.32-cm-diameter Gardon heat flux gage manufactured by Medtherm Corporation was mounted through the cylinder flush with the surface. It was placed near the axial center of the cylinder and 135 deg from



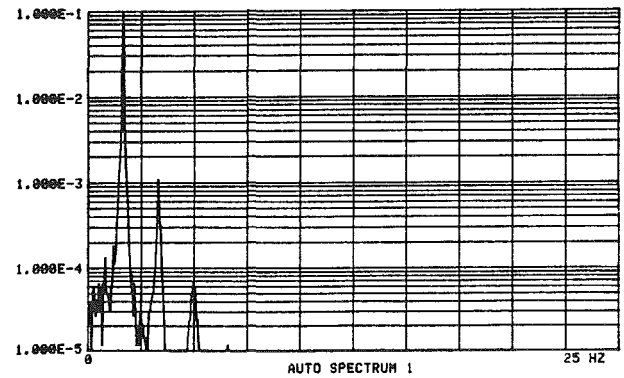


Fig. 1 Sample pulsating waveform (1.7 Hz)

one junction of the cylinder halves. Thermal grease was used to insure good contact with the cylinder. Two separately powered silicon-rubber wire resistance heaters (0.78 W/cm^2) supplied heat to the inside surface of the cylinder. The inside of the cylinder was filled with glass fiber insulation to insulate the back of the heaters and to hold the heaters firmly in place. The cylinder halves were held together with plastic end caps extending 1 cm into the test section. The gap between the cylinder halves was sealed with auto body filler and was wet-sanded smooth. The cylinder was round within 0.38%.

Each heater was powered by a variable voltage a-c power supply. Differences in convection heat transfer from the surface were offset by a high rate of angular conduction heat transfer in the 0.76-cm-thick cylinder walls. The maximum temperature deviation around the cylinder from the point of stagnation to the heat flux gage was less than 1°C, or 5% of the total ΔT for $\theta = 0$ to 135 deg, and 2°C for $\theta > 135$ deg. The temperature measurements along the axial direction were uniform within ± 0.3°C over the main portion of the cylinder. This approximates an isothermal surface for the thermal boundary layer and for the region near the heat-flux gage.

The data were collected by a TRS-80 based data-acquisition

Nomenclature

D = cylinder diameter
f = frequency (Hz)
f_r = reduced frequency, fD/U_∞
h_c = corrected heat-transfer coefficient
h_i = heat-transfer coefficient indicated by gage
k_2 = Seebeck coefficient
Nu = Nusselt number
Re = Reynolds number
t = time
T_a = freestream air temperature
T_c = cylinder surface temperature
T_∞ = temperature of radiation surroundings
Tu = freestream turbulence
U = unsteady upstream velocity
U_∞ = steady upstream velocity
V_A = measured voltage
X = amplification of amplifier
ϵ = pulsation amplitude
ϵ_g = gage emissivity
σ = Stefan–Boltzmann constant
θ = angle from front stagnation point

Downloaded 01 Jun 2010 to 171.66.16.71. Redistribution subject to ASME license or copyright; see http://www.asme.org/terms/Terms_Use.cfm

system. The data-acquisition system read the thermocouples through a Doric 410A thermocouple readout calibrated to 0.1°C. The heat-flux gage output was amplified by two high-gain low-noise amplifiers and sampled by an Analog Devices RTI-1220 12 bit analog-to-digital converter. The output was sampled 5000 times at 1 kHz and then averaged. The cylinder was positioned by a Slosyn stepping motor, geared to 20 steps per deg. For most tests, the gage output was recorded every 10 deg from 0 to 180 deg and every 1 deg from 80 to 90 deg, measured from the forward stagnation point. The cylinder was allowed 250 s to come to steady state at each location based on the experimentally determined thermal time constant of the system of 90 s.

The tests in this investigation were performed on the top half of the cylinder where the cylinder gap did not reach the stagnation point until the gage was at 135 deg. A steady flow test was run to check for symmetry. The results from the bottom side agreed with the top side to within 3% at most all locations even though the cylinder gap reached the stagnation point when the gage was only at 45 deg on the bottom half.

The surface shear was indicated by a flow visualization using a mixture of diesel fuel, titanic oxide, and oleic acid on a thin sheet of black plastic wrapped on the cylinder. The end effects were seen out to about 1/2 diameter from the end walls, which agrees with Sparrow et al. [26]. Otherwise the flow was uniform along the span.

For the heat-transfer tests the computer recorded at each location the gage position, the average and standard deviation of the gage output, five to twenty-eight cylinder temperatures, and the flow and ambient temperatures. The radiation heat transfer was subtracted from the total measured transfer to result in a convective heat-transfer coefficient, using

$$h_i = \frac{V_A/FX - \epsilon_g \sigma (T_c^4 - T_\infty^4)}{T_c - T_a}$$

The cylinder temperature at the gage was taken as the average of the two closest thermocouples (2.5 cm on each side along an axial line) and the surrounding radiative environment was taken as the ambient temperature.

The Gardon thin-foil gage used in this investigation is described in [27, 28]. The 0.32-cm gage has a sensing element 0.16 cm in diameter, which subtends a 2 deg arc on the cylinder. Since the time constant of the gage is ~300 ms only time-averaged data were recorded. The gage was calibrated by Borell and Diller [27] in a stagnation air flow very similar to that experienced by the cylinder. Their results for this gage gave a gage sensitivity of $F = 2.45 \times 10^{-5}$ mV/W/m^2 with a calibration error of less than 2%. Their recommended correction for the nonuniformity of the heat flux across the gage is

$$\frac{h_c}{h_i} = \frac{1}{1 - \dfrac{Fh_i}{k_2}}$$

where the Seebeck coefficient is $k_2 = 0.042$ mV/°C. The size of the correction was kept small (less than 5% for most tests) by using a low-sensitivity gage with a very small temperature difference across the gage and therefore small output signal.

The Nusselt number and Reynolds number,

$$\mathrm{Nu} = \frac{h_c D}{k}, \quad \mathrm{Re} = \frac{U_\infty D}{\nu}$$

were calculated using air properties evaluated at the film temperature as determined at each location,

$$T_f = (T_a + T_c)/2,$$

by linear interpolation of tabulated property values [29]. The mean flow was calculated from the mean pressure differential in the pitot probe, which approximated the mean velocity within the readability of the manometer. The density of air was based on the ideal gas law at the measured room conditions.

The ΔT for most tests was kept at 20°C to minimize variable property effects and the effect of natural convection. For these conditions natural convection effects were estimated as less than 0.2% [1].

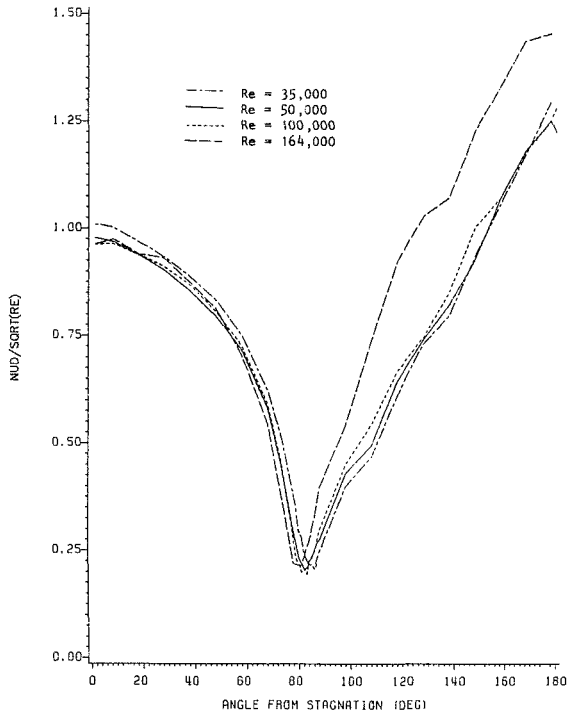


Fig. 2 Steady-flow heat-transfer results

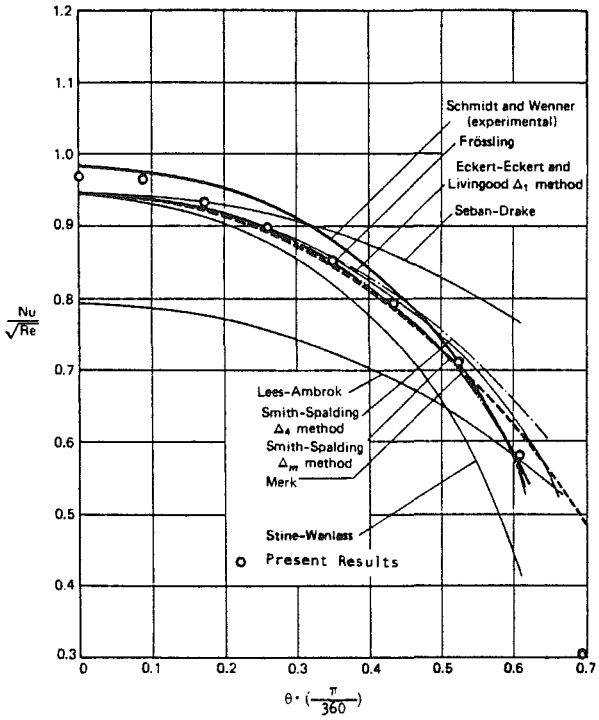


Fig. 3 Comparison of steady-flow experiments at Re = 50,000 with analytical results from [3]

Results

Time-averaged local heat transfer was measured for steady and pulsating flow. The steady flow was investigated at

Downloaded 01 Jun 2010 to 171.66.16.71. Redistribution subject to ASME license or copyright; see http://www.asme.org/terms/Terms_Use.cfm

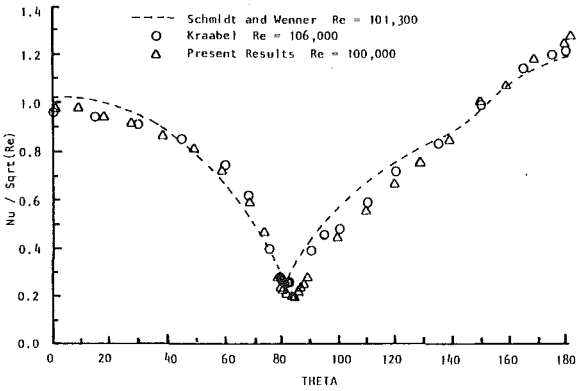


Fig 4 Comparison of steady-flow experimental results

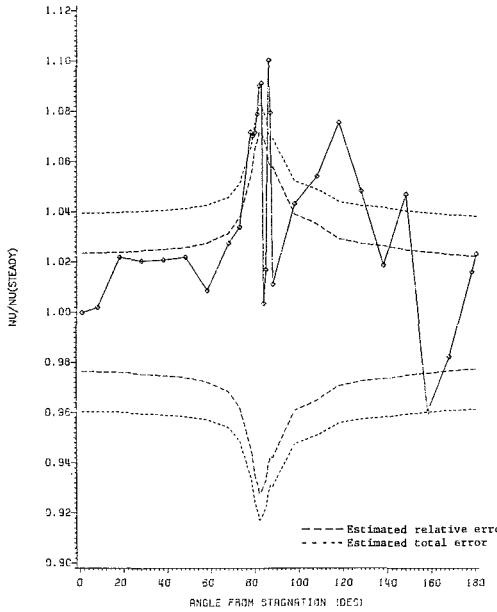


Fig. 5 Results at 0.67 Hz, f_r = 0.0063

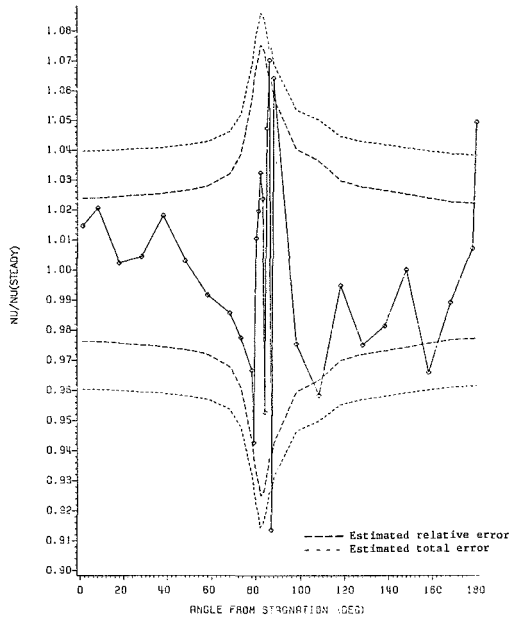


Fig. 6 Results at 1.7 Hz, f_r = 0.016

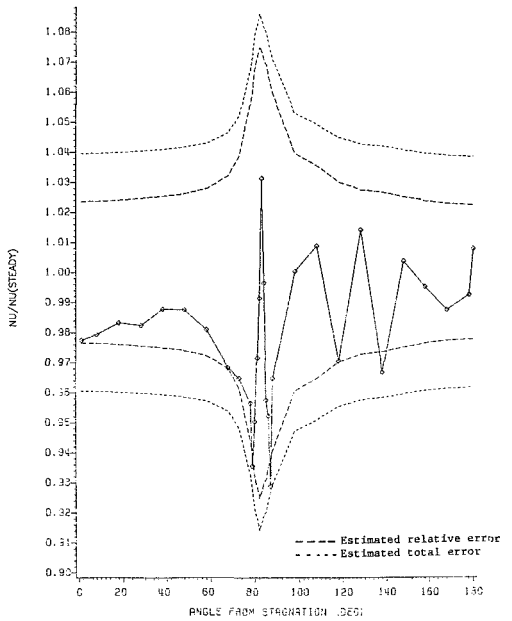


Fig. 7 Results at 7.0 Hz, f_r = 0.066

Reynolds numbers of 35,000 to 164,000. The oscillating flow was primarily at a Reynolds number of 50,000 and frequencies from 0.67 Hz to 26 Hz, or reduced frequencies (fD/U_∞) of 0.0063 to 0.244 (Table 1). To facilitate accurate comparison, each pulsating test was preceded or followed by a steady-flow test at the same Reynolds number. Between those tests, two additional readings were taken at the stagnation point, with both steady flow and oscillating flow, to further insure test-to-test accuracy.

Each set of tests was repeated at least once at different times to provide a check on the data. The estimated absolute error in the readings was less than 2.8% at the stagnation point and 6.0% near separation where the output signal was small. The relative error from test to test, found by neglecting errors in the amplifier gain and the gage calibration, was less than 1.8% at stagnation and 4.5% near separation. Tests of measurement repeatability generally were within these limits except near the separation point. The largest sources of error were due to amplifier zeroing and the gage calibraiton. If the amplifier zero shifted during a test by more than 0.05 volts at the output (1/2% of full scale), the test was rejected.

Numerous steady-flow tests were performed to validate the apparatus and to provide a baseline for the pulsating flow. Figure 2 shows the steady flow Frössling number for a range of Reynolds numbers. Figure 3 compares the attached region heat transfer to various analytical calculations [3]. The analytical models assumed no blockage or turbulence, while the test results are for less than 0.5% turbulence and 16% blockage. Figure 4 compares the steady-flow results of this investigation to those of Kraabel [30] and Schmidt and Wenner [31] at Re = 100,000. Figures 5 through 10 show the change in heat transfer around the cylinder as the ratio of the pulsating over the steady results, Nu/Nu_s, for the same Reynolds number of 50,000. Figure 11 shows the lock-on case where the shedding frequency matches the driving frequency at 23 Hz (f_r = 0.19) with the mean flow increased to Re = 56,800. A frequency plot from the Zonic 5003 of the hot-wire signal in the wake was used to verify the lock-on condition of this test. The estimated absolute and relative errors are displayed on the figures as dashed lines.

Discussion of the Results

The steady-flow results for the attached boundary layer (Fig. 3) agree well with the theoretical predictions. The experimental results are about 2.5% higher than Frössling's

Downloaded 01 Jun 2010 to 171.66.16.71. Redistribution subject to ASME license or copyright; see http://www.asme.org/terms/Terms_Use.cfm

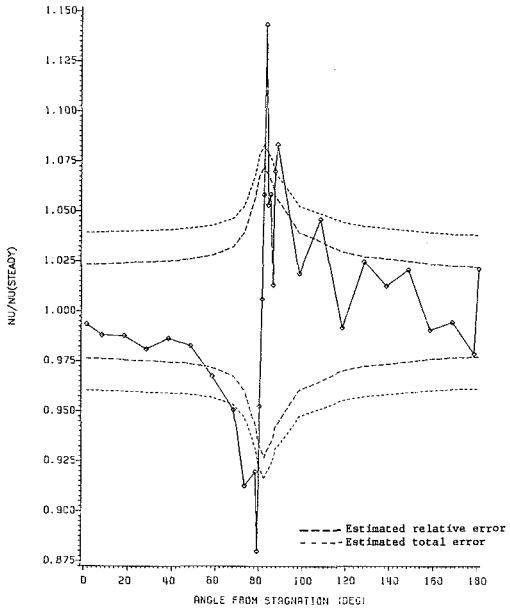


Fig. 8 Results at 18.5 Hz, f_r = 0.174

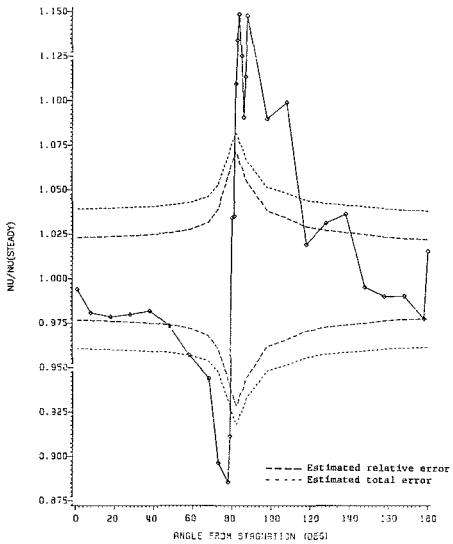


Fig. 9 Results at 23 Hz, f_r = 0.216

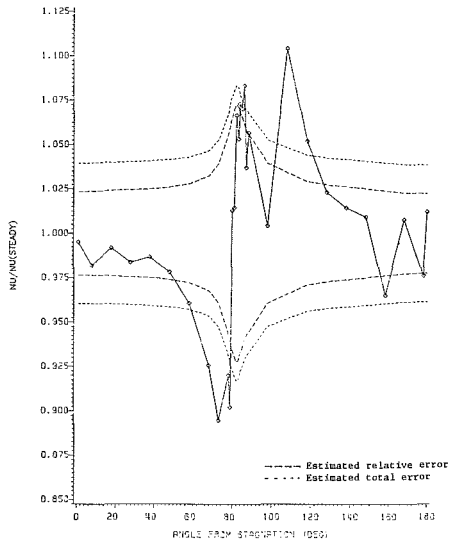


Fig. 10 Results at 26 Hz, f_r = 0.244

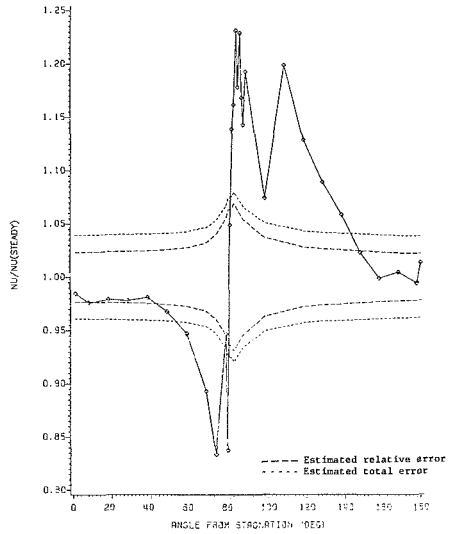


Fig. 11 Results at lock-on, 23 Hz, f_r = 0.19

exact solution at the stagnation point, but they match within experimental error from 20 deg to near separation. The small underprediction of the heat transfer at the stagnation point may be attributed to blockage, flow unsteadiness, and freestream turbulence. Morgan [1] predicts only a 0.7% increase in the overall heat transfer due to the 16% blockage of these experiments. Hiwada et al. [32], however, found that the transfer increase is greatest near the front stagnation point. Their results predict a 1.3% increase in the local Nusselt number at the stagnation point for this blockage. Kim et al. [4] analyzed the effect of the flow oscillation due to the cylinder vortex shedding on the atttached boundary layer heat transfer. They found up to a 2% increase in heat transfer at the stagnation point which went to a slight decrease near the separation point. Although the freestream turbulence levels were low (Tu = 0.004) Boulos and Pei [5] found that the local increase of heat transfer due to turbulence is more pronounced near the stagnation point. Together these effects at the stagnation point should explain the small discrepancy between the experiments and the theoretical solutions.

The dependence of the Frössling number distribution around the cylinder on the Reynolds number is shown in Fig. 2. The attached boundary-layer heat transfer increases as the square root of the Reynolds number, so the Frössling number does not change significantly with Reynolds number for this region. The heat transfer in the separated region, however, increases much faster than the square root of the Reynolds number. Moreover, the point of minimum heat transfer, near the separation point, moves upstream with increasing Reynolds number.

Comparison is shown with data from the literature for Re = 100,000 in Fig. 4. Schmidt and Wenner's [31] data in the attached boundary-layer region are higher, possibly due to freestream turbulence as discussed by Kestin et al. [6]. The present data match Kraabel's results [30] well over the entire cylinder. Schmidt and Wenner's results, however, show more heat transfer from separation to about 140 deg. Schmidt and Wenner also indicate an earlier separation point than the present research or Kraabel. Both Kraabel and Schmidt and Wenner used a large gage so their detail is not as good, particularly around the separation point.

Average heat-transfer coefficients for the whole cylinder were also obtained from the local measurements by numerical integration using the trapezoidal rule. The average Nusselt

Downloaded 01 Jun 2010 to 171.66.16.71. Redistribution subject to ASME license or copyright; see http://www.asme.org/terms/Terms_Use.cfm

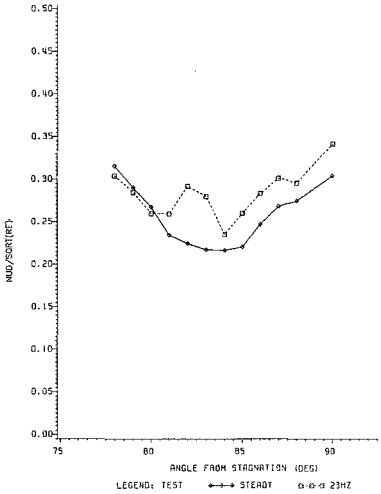


Fig 12 Steady and pulsating flow results near separation for ΔT = 40°C at lock-on

numbers for the steady tests were compared with the correlations by Morgan [1], Zukauskas [2], and Hiwada et al. [32]. At Re = 50,000 and Re = 164,000 the measured average Nusselt number is from 2% to 15% higher than these correlations. The correlations, however, are based on measurements that are usually only accurate to 10% to 15%. The integrated average for the pulsed flow transfer was within 2% of the corresponding steady-flow transfer at all frequencies, which is within the limits of measurement capability.

The pulsed flow results are plotted relative to the steady-flow results in Figs. 5–11. The estimated error bands are indicated for the ratio of these tests. The larger set gives the total error for comparison of the two tests, while the smaller represents only the relative error between tests (no bias error). The pulsating data were all recorded at Re = 50,000 to minimize the number of variables and to avoid any transient turbulence in the boundary layer as experienced at higher velocity when the flow is near the critical Reynolds number. The range of driving frequencies includes data above, below, and at the natural shedding frequency with a range of waveform amplitudes up to $\epsilon = 0.25$. No significant change in the heat-transfer coefficient was found for either the attached boundary-layer region or the wake region. The largest difference between the steady and pulsed flows occurred near separation, although the external error was larger for the smaller heat flux in this region.

For the three series of tests conducted at reduced frequencies well below the natural shedding frequency (Figs. 5–7), the heat transfer in the attached boundary-layer region is essentially unchanged. The heat transfer varies up to 2% in this region, which is within the combined limits of external error. Local variations of up to 10% are apparent around the separation region, but the combined estimated error is as much as 8%. The heat transfer varies as much as 10% between two readings 1 deg apart. A high-temperature test was performed (ΔT = 40°C) around the separation region at f_r = 0.066 (7 Hz) to look at these details for a smaller error band. The results not only show less variance, but they do not correlate with the variations of the heat transfer in the normal tests. Therefore, the effects due to the pulsation are not considered significant for these frequencies.

Three more series of tests were conducted at reduced frequencies above and below the natural shedding frequency of 21 Hz (Figs. 8–10). Although the changes in heat transfer near separation are mostly within the range of error, it is interesting to note that the Nusselt number ratios at all three frequencies first go to a minimum immediately before the point of minimum heat transfer near separation and then go to a maximum immediately afterward. This may indicate that the separation point moves upstream slightly with pulsation, by about 1 deg in these cases.

The case of the driving frequency matching the natural shedding frequency (f_r = 0.19) is shown in Fig. 11. The flow velocity was increased to Re = 57,000 to match frequencies and to take advantage of the high-amplitude fluctuation at 23 Hz. Pulsing the flow at this frequency again had no effect on the attached boundary-layer region. The heat transfer increases almost 25% over a few degrees at separation due to the presence of a local maximum, and about 20% at 120 deg. Once again, the heat transfer decreases just before separation and increases immediately afterward, possibly indicating a forward movement of the separation point. This possible movement of separation and the large local changes in heat transfer are borne out by the high-temperature test (ΔT = 40°C) of the separation region shown in Fig. 12. At 85–86 deg the local heat transfer increases by almost 30%, or eight times the limit of error.

Lebouche and Martin [15] found similar transfer changes near separation for a cylinder in pulsating crossflow. They also found large increases of heat transfer in the wake region, especially at high pulsation amplitudes (ϵ = 0.31). No significant wake region increase is apparent in the present data. Lebouche and Martin, however, performed their experiment at Re = 27,000, and consequently, the pulsation could have caused the separated shear layer to go turbulent before reattachment which could explain the transfer increase. The small increases of local heat transfer (most within the estimated error) reported by Borell et al. [12] at similar frequencies and smaller amplitudes were not apparent in the present data. The presence of greater effects near the separation point and at the natural shedding frequency were, however, also noted by Borell et al. The lack of pulsation effect on heat transfer in the attached boundary-layer region also matches the analytical results of Kim et al. [4]. For a freestream velocity pulsation, ϵ, of 10% at f_r = 0.21 the maximum predicted transfer increase was only 2% at the stagnation point. The effect decreased and even became negative toward the separation point. Such small effects were not measurable with the current equipment.

The range of Reynolds number, reduced frequency, and amplitude of the results presented here were very close to those used by Simoneau et al. [16]. Their results showed up to a 30% increase in average Nusselt number due to simulated rotor disruptions of the flow. Their flow, however, had a high level of turbulence associated with the flow disruption. The influence of turbulence on the effect of unsteady motion was also found by Marziale and Mayle [14] for the stagnation heat transfer on a rotationally oscillating cylinder in a crossflow.

The separation of the pulsation from the freestream turbulence in the present study has important implications in understanding unsteady flow heat transfer. The possible coupling between the effects of pulsation and turbulence forms an area for significant further investigation.

Conclusions

The methods used in this experiment have been shown to be repeatable and accurate for collecting convective heat-transfer data in steady and pulsating flow. The following conclusions can be drawn from the results of this study:

1 There are no significant overall changes in the heat transfer from a cylinder in crossflow due to a well-organized 1-D single-frequency pulsation of the mean flow. Frequencies above, below, and at the shedding frequency were considered, with amplitudes up to 25% at low frequencies and 10% at the higher frequencies.

2 Small local changes in the heat transfer are apparent in the secondary vortex region and near separation for pulsating

Downloaded 01 Jun 2010 to 171.66.16.71. Redistribution subject to ASME license or copyright; see http://www.asme.org/terms/Terms_Use.cfm

flow. Changes in heat transfer are most apparent when the driving and shedding frequencies are matched, including as much as a 30% local increase at separation.

3 The nature of the unsteadiness of the freestream flow apparently has a large effect on the heat transfer from a cylinder.

Acknowledgments

This material is based upon work supported under a National Science Foundation Graduate Fellowship awarded to the first author and supported by the Department of Energy, Grant No. DE-A505-82ER12022. This is a project in the program of Dr. Oscar P. Manley, Division of Engineering and Geosciences of the Office of Basic Energy Sciences.

References

1 Morgan, V. T., "The Overall Convective Heat Transfer from Smooth Circular Cylinders," *Advances in Heat Transfer*, Vol. II, Academic Press, 1975, pp. 199–264.

2 Zukauskas, A., "Heat Transfer from Tubes in Crossflow," *Advances in Heat Transfer*, Vol. 8, 1972, pp. 93–160.

3 Spalding, D. B., and Pun, W. M., "A Review of Methods for Predicting Heat Transfer Coefficients for Laminar Uniform Property Boundary Layer Flows," *Int. Journal of Heat and Mass Transfer*, Vol. 5, 1962, pp. 239–249.

4 Kim, B. K., VandenBrink, D. J., Cramer, M. S., and Telionis, D. P., "Unsteady Heat Convection Over Circular Cylinders," ASME Paper No. 84-HT-100, 1984.

5 Boulos, M. L., and Pei, D. C. T., "Dynamics of Heat Transfer from Cylinders in a Turbulent Air Stream," *Int. Journal of Heat and Mass Transfer*, Vol. 17, 1974.

6 Kestin, J., Maeder, P. F., and Sogin, H. H., "The Influence of Turbulence on the Transfer of Heat to Cylinders Near the Stagnation Point," *Z. Angew. Math. Phys.*, Vol. 12, 1969, pp. 115–132.

7 Mayle, R. E., and Marziale, M.,"Spanwise Mass Transfer Variations on a Cylinder in 'Nominally' Uniform Crossflow," *Proc. Seventh Int. Heat Transfer Conf.*, Vol. 6, Hemisphere Pub. Co., NY, 1982, pp. 135–140.

8 Lowery, C. W., and Vachon, R. I., "The Effect of Turbulence on Heat Transfer from Heated Cylinders," *Int. J. Heat Mass Transfer*, Vol. 18, 1975, pp. 1229–1242.

9 Kestin, J., "The Effect of Free-Stream Turbulence on Heat Transfer Rates," *Adv. Heat Transfer*, Vol. 3, 1966, pp. 1–32.

10 Kestin, J., and Wood, R., "The Influence of Turbulence on Mass Transfer from Cylinders," ASME *J. Heat Transfer*, Vol. 93, 1971, pp. 321–327.

11 Sunden, Bengt, "A Theoretical Investigation of the Effects of Freestream Turbulence on Skin Friction and Heat Transfer for a Bluff Body," *Int. J. Heat Mass Transfer*, Vol. 22, 1979, pp. 1125–1135.

12 Sreenivasan, K., and Ramachandran, A., "Effects of Vibration on Heat Transfer from a Horizontal Cylinder to a Normal Air Stream," *International Journal of Heat and Mass Transfer*, Vol. 3, 1961, pp. 60–67.

13 Saxena, V. C., and Laird, A. D. K., "Heat Transfer from a Cylinder Oscillating in a Cross-Flow," ASME *Journal of Heat Transfer*, Vol. 100, 1978, pp. 684–689.

14 Marziale, M. L., and Mayle, R. E., "Effect of an Oscillating Flow Direction on Leading Edge Heat Transfer," ASME Paper No. 83-GTJ-3.

15 Lebouche, M., and Martin, M., "Convection Force Autour du Cylindre; Sensibilité aux Pulsations de l'Ecoulement Externe," *Int. Journal Heat and Mass Transfer*, Vol. 18, 1975, pp. 1161–1175.

16 Simoneau, R. J., Morehouse, K. A., Van Fossen, G. J., and Behning, F., "Effect of a Rotor Wake on Heat Transfer from a Circular Cylinder," ASME Paper No. 84-HT-25, 1984.

17 Base, T. E., Patel, J. M., and Valaitis, G. C., "Heat Transfer from Cylinders in Unsteady Flow," *Canadian Journal of Chemical Engineering*, Vol. 59, 1981, pp. 247–250.

18 Borell, G. J., Kim, B. K., Ekhaml, W., Diller, T. E., and Telionis, D. P., "Pressure and Heat Transfer Measurements Around a Cylinder in Pulsating Crossflow," in: *Unsteady Turbulent Boundary Layers and Friction*, Eds. D. C. Wiggert and C. S. Martin, ASME, New York, 1984, pp. 17–23.

19 Brunson, F. W., Jr., "Local Heat Transfer Coefficient Around a Cylinder in Oscillating Flow," M.S. Thesis, Naval Postgraduate School, Monterey, California, Dec. 1981.

20 Lighthill, M. J., "The Response of Laminar Skin Friction and Heat Transfer to Fluctuations in the Stream Velocity," *Proc. Roy. Soc.*, Vol. A224, 1954, pp. 1–23.

21 Mori, Y., and Tokuda, S., "The Effect of Oscillation on Instantaneous Local Heat Transfer in Forced Convection from a Cylinder," *Proc. Third Int. Heat Transfer Conf.*, Am. Inst. Chem. Engrs., NY, 1966, pp. 49–56.

22 Ishigaki, Hiroshi, "Heat Transfer in a Periodic Boundary Layer Near a Two-Dimensional Stagnation Point," *J. Fluid Mech.*, Vol. 56, 1972, pp. 619–627.

23 Kasza, K. E., "Thermal Response Characteristics of Unsteady Stagnation Point Flows: A New Approach," *Int. J. Heat Mass Transfer*, Vol. 18, 1975, pp. 329–331.

24 Childs, E. P., and Mayle, R. E., "Heat Transfer on a Rotationally Oscillating Cylinder in Crossflow," *Int. J. Heat Mass Transfer*, Vol. 27, 1984, pp. 83–94.

25 Tavakoli, A., Kim, B., Borell, G. J., Diller, T. E., and Telionis, D. P., "Design and Evaluation of a Pulsating Flow Wind Tunnel," Technical Report No. VPI-E-83-41, VPI&SU, May 1983.

26 Sparrow, E. M., Stahl, T. J., and Traub, P., "Heat Transfer Adjacent to the Attached End of a Cylinder in Crossflow," *Int. J. Heat Mass Transfer*, Vol. 27, 1984, pp. 233–242.

27 Borell, G. J., and Diller, T. E., "A Convection Calibration Method for Local Heat Flux Gages," ASME Paper No. 84-HT-45, 1984.

28 Gardon, R., "An Instrument for the Direct Measurement of Intense Thermal Radiation," *Review of Scientific Instruments*, Vol. 24, 1953, pp. 366–370.

29 Eckert, E. R. G., and Drake, Robert M., *Analysis of Heat and Mass Transfer*, McGraw-Hill, NY, 1972.

30 Kraabel, J. S., "Heat Transfer to Air from a Yawed Cylinder," *Int. J. Heat Mass Transfer*, Vol. 25, No. 3, 1982, pp. 409–418.

31 Schmidt, E., and Wenner, K., "Heat Transfer over the Circumference of a Heated Cylinder in Transverse Flow," NACA TM 1050, 1943.

32 Hiwada, M., Kiyomi, N., Masaya, K., and Mabuchi, I., "Effects of Tunnel Blockage on Local Mass Transfer from a Circular Cylinder in Cross Flow," *Heat Transfer—Japanese Research*, Vol. 8, No. 3, 1979, pp. 37–51.

Downloaded 01 Jun 2010 to 171.66.16.71. Redistribution subject to ASME license or copyright; see http://www.asme.org/terms/Terms_Use.cfm

Effects of Tip Endwall Contouring on the Three-Dimensional Flow Field in an Annular Turbine Nozzle Guide Vane: Part 1—Experimental Investigation

E. Boletis
von Karman Institute
for Fluid Dynamics
1640 Rhode Saint Genèse, Belgium

Tip endwall contouring is one of the most effective methods to improve the performance of low aspect ratio turbine vanes [1]. In view of the wide variety of geometric parameters, it appears that only the physical understanding of the three-dimensional flow field will allow us to evaluate the probable benefits of a particular endwall contouring. The paper describes the experimental investigation of the three-dimensional flow through a low-speed, low aspect ratio, high-turning annular turbine nozzle guide vane with meridional tip endwall contouring. The full impact of the effects of tip contouring is evaluated by comparison with the results of a previous study in an annular turbine nozzle guide vane of the same blade and cascade geometry with cylindrical endwalls [12]. In parallel, the present experimental study provides a fully three-dimensional test case for comparison with advanced theoretical calculation methods [15]. The flow is explored by means of double-head, four-hole pressure probes in five axial planes from far upstream to downstream of the blade row. The results are presented in the form of contour plots and spanwise pitch-averaged distributions.

Introduction

Enormous efforts are devoted by the turbine aerodynamicist to combine overall turbine performance requirements with high aerodynamic efficiencies for the individual turbine engine components. Fuel consumption and size considerations dictate low aspect ratio blade design for the high-pressure turbine component while experience reveals that low blade aspect ratio is detrimental for the turbine aerodynamic efficiency. Secondary losses become of the same order of magnitude as the profile losses or even predominant. A number of aspects of turbine design needs to be reexamined and optimized on the basis of the overall loss reduction, and it appears that the consideration of the annulus flow path shape is of primary importance [1-3].

Meridional tip endwall contouring as an effective tool to reduce the overall losses in turbine nozzle guide vanes was first proposed by Dejc [1] in the early sixties. According to Dejc, the benefits of the method are due to the increase of the channel convergence, the decrease of the pitchwise pressure gradient at the front half of the blade passage, and the positive influence on the spanwise static pressure distribution at the blade trailing edge region. Basic contouring design rules

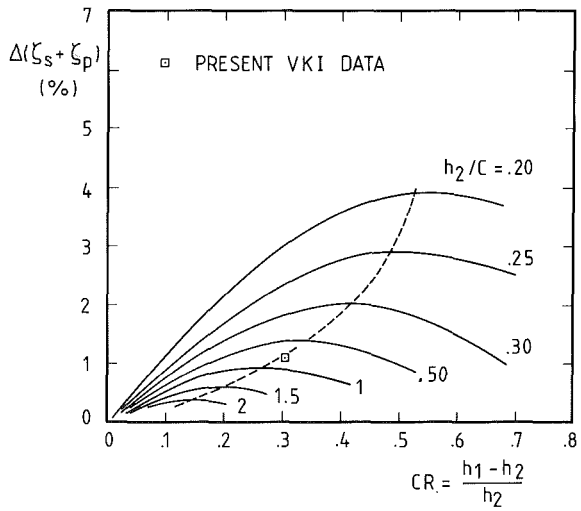


Fig. 1 Loss reduction with tip contouring according to Dejc [1]

reported by Dejc were followed by almost all investigators, in particular the curve indicating the optimum contraction ratio for a given aspect ratio, shown in Fig. 1 (straight cascade tests by Morris and Hoare [4], Kopper et al. [5]; annular cascade tests by Waterman and Tall [6], Haas [7], and present tests). It is important to note that the design considerations of Dejc are extracted for a certain family of blade profiles and vortex

Contributed by the Gas Turbine Division of THE AMERICAN SOCIETY OF MECHANICAL ENGINEERS and presented at the 30th International Gas Turbine Conference and Exhibit, Houston, Texas, March 18-21, 1985. Manuscript received at ASME Headquarters, December 21, 1984. Paper No. 85-GT-71.

Copyright © 1985 by ASME
Downloaded 01 Jun 2010 to 171.66.16.71. Redistribution subject to ASME license or copyright; see http://www.asme.org/terms/Terms_Use.cfm

distributions, and they may not necessarily be applied as general principles. This is evident from the discrepancy of results in the investigations reported in [4–7] with those of Dejc. In straight cascades, Morris and Hoare and Kopper et al. measured similar loss reductions of 0.4 percent with tip contouring compared to 1.5 percent due to Dejc. In annular cascades, Haas measured an overall loss reduction of 0.5 percent compared to 1.2 due to Dejc, while Waterman and Tall measured no loss reduction at all for a high leading-edge loaded blade. The tests in straight cascades showed a loss reduction mainly at the unprofiled half-span, while Haas indicated that tip contouring enabled the low momentum fluid at the tip to be contained at the tip region causing thereby a reduction of the radial loss migration. For the geometrical parameters of the present configuration (see Fig. 1), the "expected" full efficiency gain predicted by Dejc is about 1 percent. Performance tests in small full turbine stages showed some benefits of the stator tip endwall contouring on the overall stage efficiency [8–10]. However, Ewen et al. [8] pointed out that the measured increase in stage efficiency had to be attributed to a higher degree of reaction and improved rotor inlet conditions rather than to the reduction of stator secondary losses.

The foregoing discussion indicates that the evaluation of the wall contouring effects is a difficult task. In view of the wide variety of geometric parameters and the interrelation of the annulus design with the profile design, blade stacking, etc., simple rules of thumb will not always guarantee the best choice of the optimum endwall contour. Only the physical understanding of the three-dimensional flow field will allow us to evaluate the potential benefits of a particular endwall contouring. Unfortunately, none of the previous investigators report measurements of the fully three-dimensional velocity vector and in no case has the evolution of the flow field in the blade passage been demonstrated.

The present paper describes the three-dimensional flow field in a low-speed, annular turbine cascade with tip endwall contouring. The *full impact* of the effects of tip contouring is evaluated by comparison with the results of a previous study in an annular turbine nozzle guide vane of the same blade and cascade geometry with cylindrical endwalls [12]. In parallel, the present well-documented experimental study provides a fully three-dimensional test case for comparison with advanced theoretical calculation methods (see [15]).

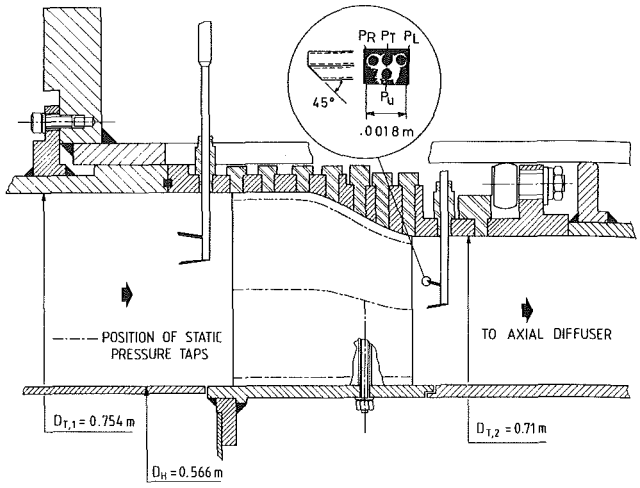


Fig. 2 Test section

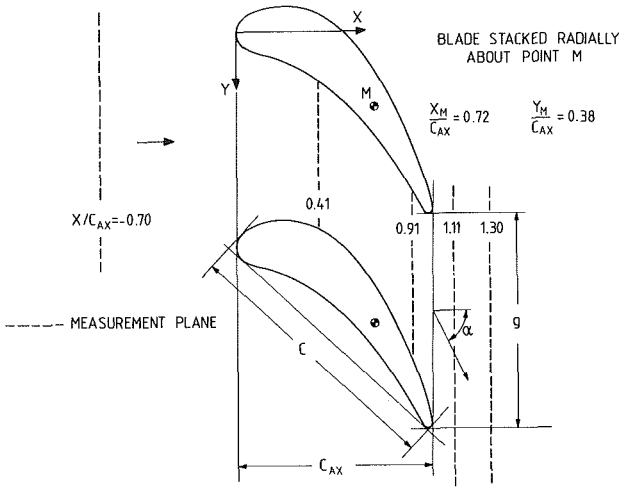


Fig. 3 Cascade geometry at midblade height

VKI Annular Cascade

Test Facility. The tests were carried out in the VKI open-loop, low-speed turbine test rig. Three different con-

Nomenclature

C = chord
CP_O = local total pressure coefficient $(P_{O1,MS} - P_{Ol})/(P_{O1,MS} - \bar{\bar{P}}_{s2})$
CP_s = local static pressure coefficient $(P_{O1,MS} - P_{sl})/(P_{O1,MS} - \bar{\bar{P}}_{s2})$
CP_s' = modified local static pressure coefficient $(P_{O1,MS} - P_{sl})/(P_{O1,MS} - \bar{P}_{s2}(r))$
CR = contraction ratio, $(H_1 - H_2)/H_2$
D = diameter
g = pitch
H = blade height
$H_{1,2}$ = boundary layer shape factor, $H_{1,2} = \delta^*/\theta$
N = number of blades
O = throat
P = pressure
Re = Reynolds number, $\mathrm{Re} = C^* V/\nu$
T = temperature
Tu = turbulence level, $Tu = \sqrt{\overline{v_{ax}'^2}}/V_{ax}$
V = velocity
v' = velocity fluctuation
X, Y = coordinates (Fig. 3)
α = flow angle in blade-to-blade plane (referred to axial direction)
γ = radial flow angle, $\gamma = \mathrm{arctg}\,(V_r/V_{ax})$
δ = boundary layer thickness
δ^* = boundary layer displacement thickness
θ = boundary layer momentum thickness
ν = kinematic viscosity
ρ = density
ξ = kinetic energy loss coefficient, $(V_{2,is}^2 - V_2^2)/V_{2,is}^2$

Subscripts

1 = upstream conditions
2 = downstream conditions
atm = atmospheric conditions
ax = axial direction
H = hub
l = local
MS = midspan
O = total conditions
p = profile
r = radial direction
s = static conditions, secondary flow
T = tip

Superscripts

$\bar{\ }$ = pitchwise mass-averaged value
$\bar{\bar{\ }}$ = pitch- and spanwise mass-averaged value

Downloaded 01 Jun 2010 to 171.66.16.71. Redistribution subject to ASME license or copyright; see http://www.asme.org/terms/Terms_Use.cfm

figurations were studied previously at the same test rig: (*i*) a single guide vane with cylindrical endwalls and with collateral inlet endwall boundary layers [12], which serves as reference case for the present tests; (*ii*) a single guide vane with skewed inlet endwall boundary layer generated by a rotating hub endwall upstream of the cascade [13]; and (*iii*) a guide vane followed by a rotating blade row [14].

The test section for the present configuration is presented in Fig. 2. The low aspect ratio guide vane ($H_2/C=0.6$) has a constant hub diameter of 0.566 m and tip diameters at inlet and outlet of 0.754 m and 0.710 m, respectively. The vane exit endwall diameters are identical with those of the reference tests [12]. The contraction ratio *CR*, defined as the ratio of difference in height (outlet-inlet) over the outlet blade height, is 0.306. This value is not far from the optimum one indicated by the dotted line in Fig. 1. The meridional contour is defined by a cubic function as in reference [4] and extends from $X/C_{ax}=0.38$ to 1.03 ($Y/H=a^*(X/C_{ax})^3 + b^*(X/C_{ax})^2 + C^*(X/C_{ax})+d$, where $a=2.2248$, $b=-4.7054$, $c=2.6123$, $d=0.8702$). This choice is in good agreement with the profiles proposed by Dejc and the trends indicated in [11]. A single blade is instrumented with pressure tappings along three quasi-streamlines at 1/22, 11/22 (midspan), and 21/22 of the blade height (see Fig. 2). The flow is surveyed with double-headed four-hole pressure probes as in all the previous studies. Details about the measurement procedure are given in [12].

Blade and Cascade Geometry. The blade geometry is shown in Fig. 3. The blade profile is identical to that used for the previous investigation with cylindrical endwalls. The blade is stacked radially about point M in Fig. 3. The most important geometrical characteristics are summarized in Table 1.

Test Program and Test Conditions. The flow was surveyed in five measurement planes shown in Fig. 3. The plane far upstream ($X/C_{ax}=-0.70$) and the planes downstream ($X/C_{ax}=1.11$ and 1.30) are situated at the same axial positions as in the annular cascade with cylindrical endwalls, while the positions of the two planes in the passage differ slightly from those of the tests with cylindrical endwalls ($X/C_{ax}=0.41$ and 0.91 instead of 0.40 and 0.90). The test conditions are similar to those of the reference tests. They are summarized in Table 2.

Table 1 Blade and cascade characteristics

Hub-to-tip diameter D_H/D_T at exit	0.8
Tip diameter D_T at inlet and exit	0.754 m; 0.710 m
Contraction ratio *CR*	0.306
Chord length *C*	0.12 m
Axial chord length C_{ax}	0.087 m
Aspect ratio H/C at exit	0.6
Number of blades *N*	21
Inlet blade angle α'	−7°
Pitch to chord ratio at hub, mean, tip (exit), g/C	0.705; 0.795; 0.885
arccos (O/g) at hub, mean and tip (measured values)	69.0; 67.9; 67.0°

The spanwise distribution of the upstream total pressure loss coefficient $\overline{CP}_O$ is shown in Fig. 4. The inlet endwall boundary layer characteristics are presented in Table 3 together with the corresponding values from the cylindrical endwall tests.

The differences in the absolute values of the displacement and the momentum thickness and the shape factor between the two tests can be attributed to far upstream geometrical changes.

The experimental accuracies associated with the four hole-probes are given in [12].

Effects of Tip Endwall Contouring on the Three-Dimensional Flow Field

Blade Pressure Distribution. The pressure gradients in an annular pressure cascade are severe in all three orthogonal directions. The pitchwise pressure gradient is the main driving force of the secondary flow, while the streamwise gradients are principally responsible for the growth of the endwall and blade boundary layers. Radial pressure gradients depend on (*a*) the *circumferential curvature* of cylindrical or contoured endwalls acting upon the tangential component of the velocity and (*b*) the *meridional curvature* of noncylindrical endwalls acting upon the axial component of the velocity. The aim of a proper design of a contoured endwall is (*a*) to diminish the pitchwise pressure gradient in the high turning regions (between $X/C_{ax}=0.30$ and 0.60 for the present blade geometry) and (*b*) to create a radial pressure gradient counteracting the one imposed by the blade design at the trailing edge region. The first one is dependent on the curvature of the front part of the contour, which is mainly a function of the desired channel convergence, while the second depends on the curvature of the rear part of the contour.

Figure 5 presents the blade pressure distributions along the axial direction for three quasi-streamlines at 1/22, 11/22 (midspan) and 21/22 of the blade height. The blade pressure is expressed in the form of the CP_s' coefficient defined as $CP_s'=(P_{O1,MS}-P_{sl})/(P_{O1,MS}-P_{s,2}(r))$. As there were no

Table 2 Test conditions

Upstream ($X/C_{ax}=-0.70$), midspan:	
Total pressure, P_{O1}	$P_{atm}+70$ mm H_2O
Total temperature, T_{O1}	288 K
Flow angle in blade-to-blade plane, α_1	0.7°
Radial flow angle, γ_1	0°
Turbulence, Tu_1	0.8%
Downstream ($X/C_{ax}=1.68$):	
Reynolds number, Re_2, at midspan	2.5×10^5
Static pressure at hub, P_{s2}	$P_{atm}-8$ mm H_2O

Note: As in [12], a trip wire is placed on the blade suction side at $X/C_{ax}=0.56$ ($X'/C=0.35$ in chordwise direction).

Table 3 Inlet endwall boundary layer characteristics

	δ/H_1	δ^*/H_1	θ/H_1	$H_{1,2}$	δ^*(mm)	θ(mm)	H_1(mm)
			Tip endwall				
Contoured	.16	.0212	.0154	1.38	1.991	1.445	94.
Cyl. [12]	.15	.025	.019	1.33	1.831	1.375	72.
			Hub endwall				
Contoured	.12	.0132	.0094	1.41	1.242	0.883	94.
Cyl. [12]	.11	.017	.010	1.67	1.235	0.740	72.

Downloaded 01 Jun 2010 to 171.66.16.71. Redistribution subject to ASME license or copyright; see http://www.asme.org/terms/Terms_Use.cfm

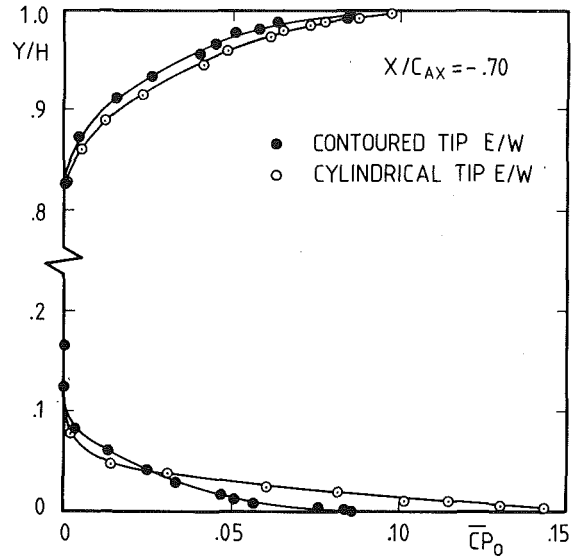


Fig. 4 Spanwise distribution of the total pressure loss coefficient at the far upstream plane ($X/C_{ax} = -0.70$)

Table 4 Total pressure loss

	Contoured			Cylindrical		
% span	0–50	50–100	0–100	0–50	50–100	0–100
$X/C_{ax}=1.11$	2.5%	2.1%	4.6%	2.8%	2.6%	5.4%
$X/C_{ax}=1.30$	3.6%	2.7%	6.3%	3.8%	3.1%	6.9%

experimental data for the reference case, the measured data of present tests are compared with the cylindrical tip endwall blade pressure distributions calculated with a time marching, three-dimensional, inviscid, rotational flow method by Van Hove [16]. The ability of the above numerical analysis to accurately predict the flow field in the passage of an inlet guide vane with cylindrical endwalls was demonstrated in [16].

The effects of tip contouring are extended throughout the blade passage. They are more significant at the tip region than at the hub and stronger at the blade suction side than at the pressure side. Over the first 60 percent of the axial chord the contour causes an important pressure rise on the suction side (CP_s' decrease) but a moderate change at the pressure side only. This results in an important unloading of the front part of the vane, which weakens the driving force of the secondary flows. At the rear part of the passage the effects of contouring are entirely different from those at the front part due to the opposite wall curvature. The blade suction side pressure decreases (CP_s' increases) significantly at the tip region, moderately at the midspan and increases almost null at the hub region. The most striking feature is the shift of the maximum suction side velocity toward the trailing edge at the blade tip causing a strong adverse pressure gradient at the rear blade side. No doubt, the blade boundary layer development will be significantly affected by this change. In the present configuration the outward pressure gradient caused by the contour is more important at about 80 percent of the axial chord than at the trailing edge.

Spatial Distribution

Flow Inside the Passage. Figure 6 presents the contour plots of total pressure, static pressure, flow angle at the blade-to-blade plane, and radial flow angle at $X/C_{ax}=0.41$ and 0.91 in comparison with the flow field patterns of the cylindrical tip endwall tests at $X/C_{ax}=0.40$ and 0.90. As in [12], the total and static pressures are presented in the form of pressure coefficients, CP_O and CP_s. The radial flow angle is calculated from the ratio of radial and axial velocity component

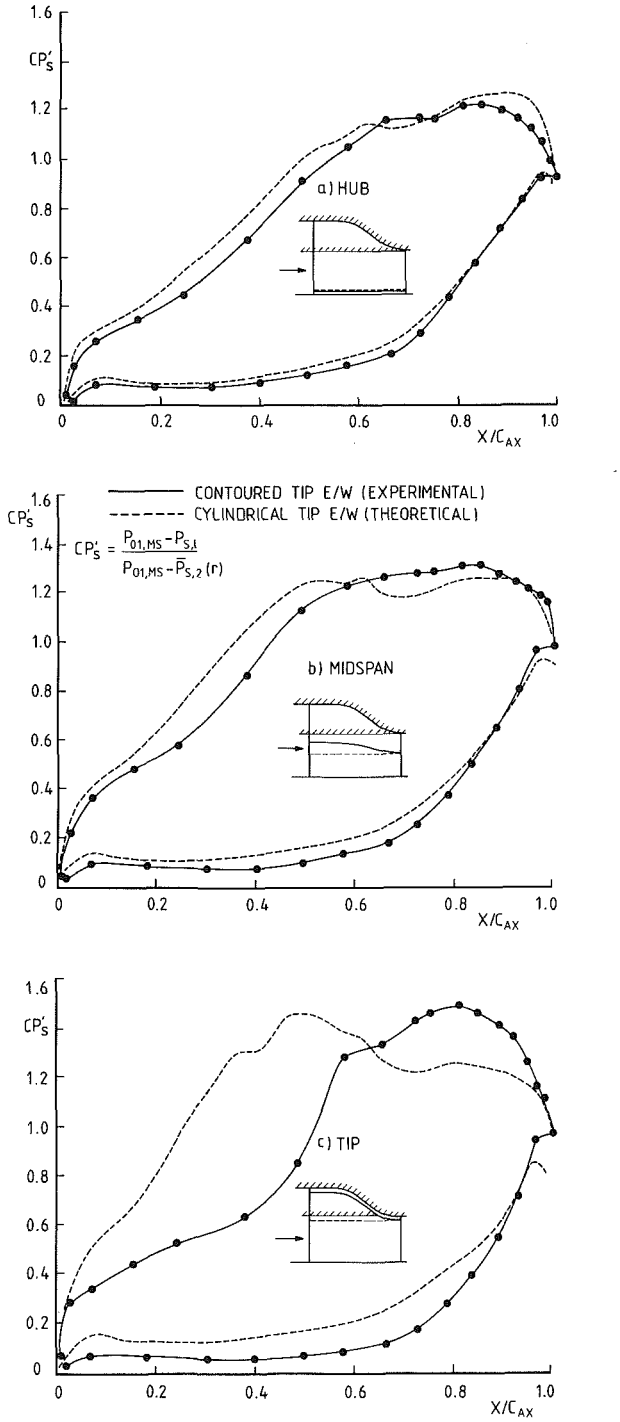


Fig. 5 Blade pressure distributions along three quasi-streamlines at hub (1/22 *H*), midspan, and tip (21/22 *H*)

$$\gamma = \text{arctg}(V_r/V_{ax})$$

The first measurement plane at $X/C_{ax}=0.41$ is situated just downstream of the starting point of the contour ($X/C_{ax}=0.38$). The static pressure field is characterized by important changes relative to the cylindrical tip endwall case. Both the absolute values and the relative circumferential position of the iso-CP_s values indicate a reduced pitchwise pressure gradient with contouring, especially at the tip region. Another important aspect of the static pressure field is the development of a strong radial pressure gradient with higher values of the static pressure at the tip than at the hub. This is a result of the tip wall curvature, and it may cause important

Downloaded 01 Jun 2010 to 171.66.16.71. Redistribution subject to ASME license or copyright; see http://www.asme.org/terms/Terms_Use.cfm

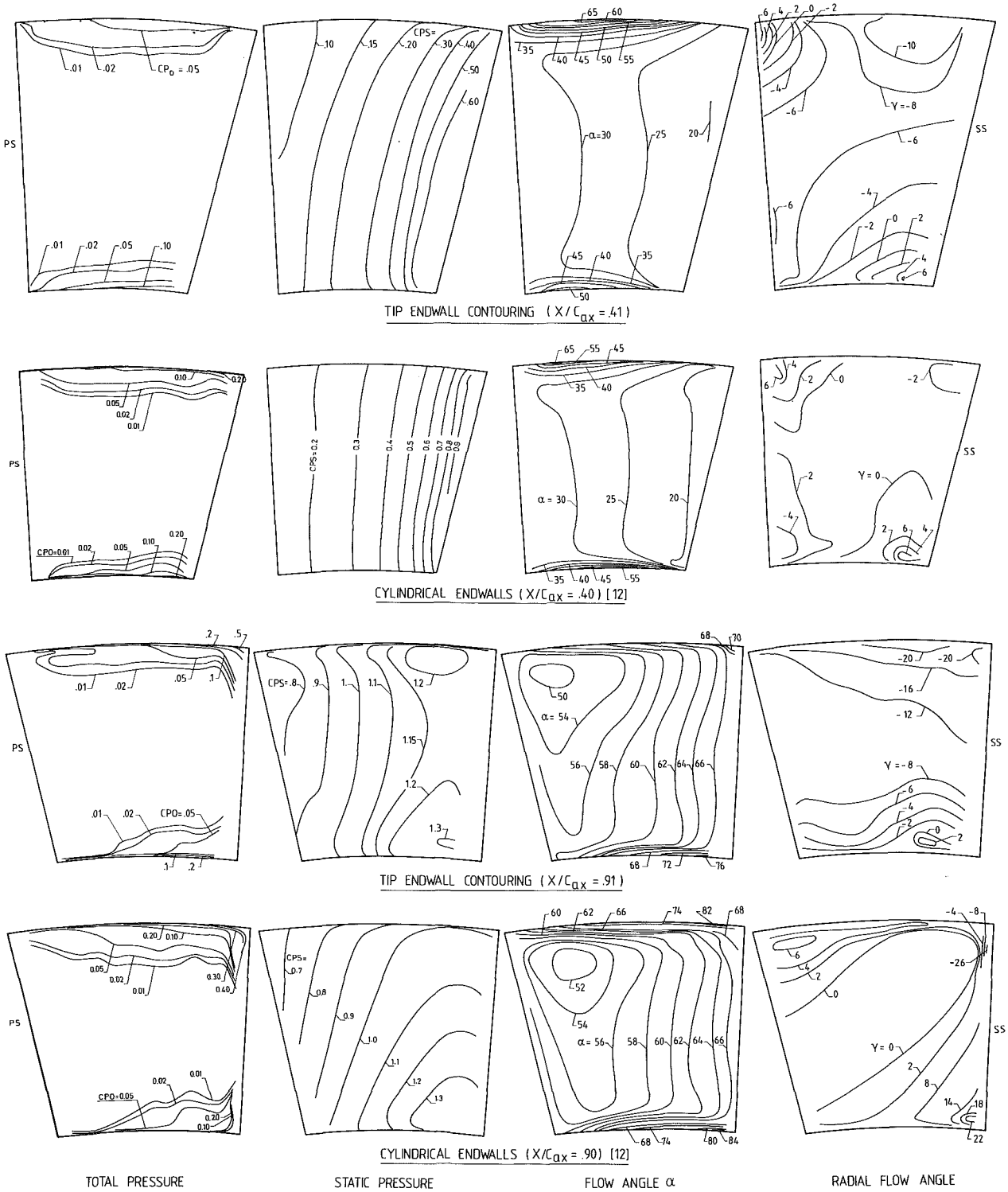


Fig. 6 Contour plots of total pressure, static pressure, flow angle α, and radial flow angle at the measurement planes X/C_{ax} = 0.41 (0.40) and X/C_{ax} = 0.91 (0.90)

modifications at the secondary flow evolution and the suction side boundary layer paths. With contouring the local total pressure loss values are smaller at both endwalls. This is to be attributed mainly to the reduced static pressure gradient and to a limited degree to the upstream endwall boundary layer differences. The contour plots for the flow angles α show only moderate overall changes, even at the endwall regions. This can only be explained by the fact that the direction of the wall streamlines is affected by both the transverse pressure gradient and the tip endwall curvature. The decrease of the overturning due to the reduced transverse pressure gradient is counteracted by the irrotational effect of the wall curvature, which tends to increase the angle (see [15]). The radial flow angle contour plots demonstrate that the endwall contraction imposes an inward movement of the flow particles. However, the radial motions associated with the secondary flow are observed clearly for both configurations.

The second measurement plane is situated at the rear part of the contour at $X/C_{ax} = 0.91$. We note for the datum case an important radial pressure gradient, in particular close to the

Downloaded 01 Jun 2010 to 171.66.16.71. Redistribution subject to ASME license or copyright; see http://www.asme.org/terms/Terms_Use.cfm

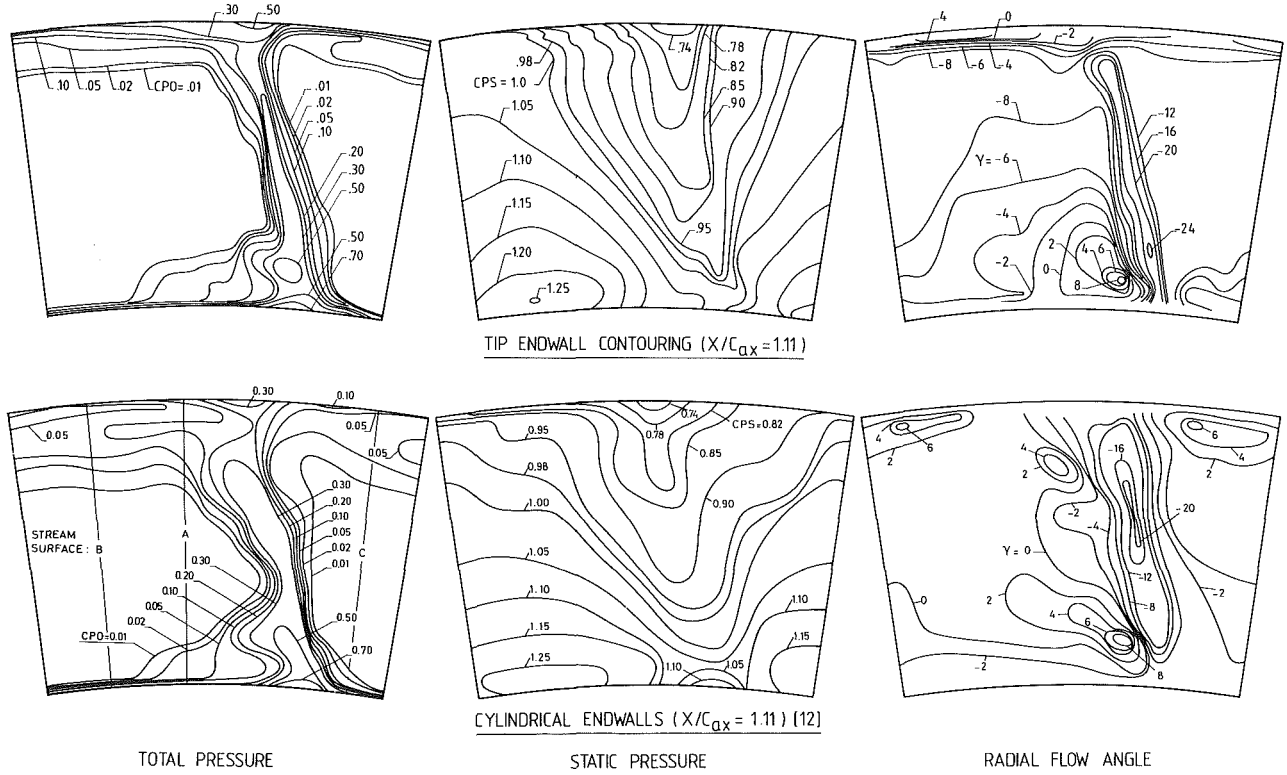


Fig. 7 Contour plots of total pressure, static pressure, and radial flow angle at the measurement plane $X/C_{ax} = 1.11$

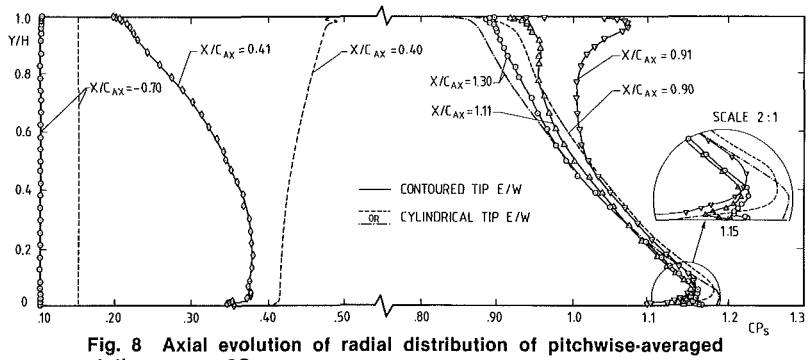


Fig. 8 Axial evolution of radial distribution of pitchwise-averaged static pressure CP_S

suction side. The endwall contouring reduces the static pressure at the suction side tip endwall corner such that the spanwise gradient at the upper half span is inverted, compared to that of the cylindrical endwall. This indicates possible changes at the radial migration of low-momentum material over the blade suction side. The loss distribution reflects the different evolution of the transverse pressure gradient between $X/C_{ax} = 0.41$ and 0.91. The maximum transverse pressure gradient for the cylindrical endwall case occurs at $X/C_{ax} = \sim 0.45$ but only at ~ 0.70 for the contoured endwall, such that the action on the tangential migration of the low-momentum boundary layer material is not yet fully effective in the latter case. Nevertheless, a strong increase of the corner loss is observed for the contoured endwall case and this loss core will take considerably higher proportions under the combined effect of the cross flow, the rear adverse pressure gradient and the increased length of the flow path. With the exception of the hub endwall suction side corner the radial flow angle is everywhere negative in the contoured stator passage.

Flow Downstream of the Blade Passage. Figure 7 presents the contour plots of total pressure, static pressure, and flow angle α at $X/C_{ax} = 1.11$ in comparison with the cylindrical endwall stator. The most striking feature of the flow field at $X/C_{ax} = 1.11$ is the overall diminution of the wake region. This is demonstrated in the total pressure contour plots by a circumferential reduction of the low-energy region of ~ 40 percent between 30 and 75 percent of the blade height. This has to be attributed to lower blade boundary layer losses and/or reduced radial migration of low-momentum boundary layer material. At the tip the iso-CP_O lines are less widely spread. The tip endwall loss region is half that of the reference case. Nevertheless the endwall losses at the vicinity of the endwall are stronger due to (*a*) the spreading out of the suction side corner loss (see measurement plane $X/C_{ax} = 0.91$) under the influence of the pitchwise static pressure gradient, and (*b*) the effect of the transition of the curved endwall into a cylindrical endwall causing in the endwall region an adverse static pressure gradient in axial direction. Compared to the data at $X/C_{ax} = 0.91$ the radial pressure gradient has significantly increased and the pressure field is not fundamentally different from that with cylindrical endwalls. However, the pressure gradients across the wake appear much

Downloaded 01 Jun 2010 to 171.66.16.71. Redistribution subject to ASME license or copyright; see http://www.asme.org/terms/Terms_Use.cfm

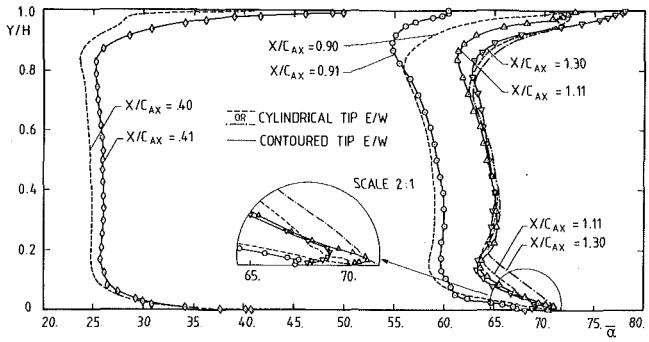


Fig. 9 Axial evolution of radial distribution of pitchwise-averaged flow angle α

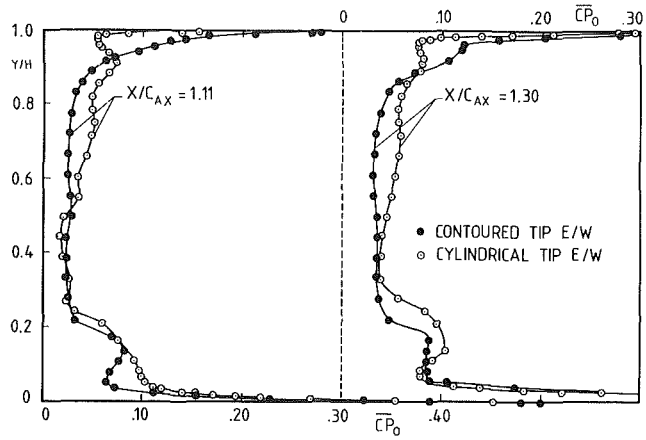


Fig. 10 Spanwise total pressure loss distribution at the two downstream planes

stronger due to the reduced wake width. The high negative radial flow angles in the wake regions indicate that the reduction of the wake width does not prevent entirely the radial migration of the low-momentum material. Also, the freestream flow is inclined toward the hub as was already observed in the blade passage.

Axial Evolution of the Spanwise Distributions of the Average Static Pressure and Flow Angle. Figure 8 presents the axial evolution of the spanwise distribution of the pitchwise integrated static pressure coefficient CP_s. The correspondent data of the tests with cylindrical tip endwall are also shown for comparison. At the far upstream plane $X/C_{ax} = -0.70$ the CP_s values are lower with contouring due to the reduction of the velocity magnitude. This is also the case for the lower 30 percent of the blade span at $X/C_{ax} = 0.41$. However, the increase of the static pressure due to the tip wall curvature modifies considerably the mid and upper part of the CP_s spanwise distribution at this plane. Proceeding further downstream to $X/C_{ax} = 0.91$, the opposite tip curvature counteracts the radial pressure gradient imposed by the blade design. This effect diminishes progressively with increasing downstream distance ($X/C_{ax} = 1.11$ and 1.30). At the last measurement plane the radial pressure gradient takes the same proportions as with cylindrical tip endwall.

Figure 9 presents the axial evolution of the spanwise distribution of the pitchwise integrated flow angle α. The effects of the tip contour are rather moderate. The most pronounced differences occur at the upper half-span at $X/C_{ax} = 0.91$ where the contouring causes a significant decrease of the overturning. This is an irrotational rather than a rotational flow effect (see [15]). Further downstream the flow overturning at the tip region increases rapidly becoming at $X/C_{ax} = 1.30$ about 6 deg bigger than that of the reference tests. At the lower half-span the position of the maximum flow underturning is somewhat lower than that of the reference tests.

It is important to note that the effects of endwall contouring on the static pressure and the flow angle are quite small at the last measurement plane ($X/C_{ax} = 1.30$). Since a rotor designed to match the present stator would typically be placed at this distance, it is expected that the mean inlet flow conditions to the rotor would not significantly be influenced by the endwall contouring at least over most of the blade height. Calculations have shown that the effect on the rotor incidence angle will be less than 5 deg except between $Y/H = 0.0$ to 0.03 and $Y/H = 0.97$ to 1.00 where the maximum differences amount up to 10 and 20 deg, respectively (this also includes changes of the total pressure loss distribution). The stage reaction would change little except perhaps close to the endwalls. However, an improvement of the inlet flow field to a downstream rotor could arise from the reduction of the tip endwall loss region and the wake width.

Spanwise Distributions of the Averaged Downstream Losses. Figure 10 presents the spanwise distributions of the averaged total pressure losses at the two downstream planes. Wall contouring reduces the losses over most of the blade height. Contrary to the reference case, the loss between $Y/H = 0.25$ and 0.80 is constant. This means that the overall radial migration of the tip losses is relatively small compared to the cylindrical endwall case. We note that a similar effect of tip contouring was also found by Haas [7]. Since the radial migration of low-momentum material through the wake is demonstrated clearly at both downstream planes, this might be due to a reduction in the spanwise migration of the low-momentum material over the blade suction side surface (see chapter on "Flow inside the passage"). A reduction of the loss is also evident between $Y/H = 0.05$ and 0.25 (lower half span secondary loss region). At $Y/H \geq 0.90$ the tip endwall loss is considerably higher with contouring.

The overall losses at the two downstream planes are $\overline{\overline{CP}}_O$ = 4.6 and 6.3 percent with tip contouring, while they are $\overline{\overline{CP}}_O$ = 5.4 and 6.9 percent with cylindrical tip endwall. The losses attributed to each half span are shown in Table 4.

Reduction in losses is shown at both halves, but that of the upper part is more prominent. The overall loss reduction with contouring (0.8 percent at $X/C_{ax} = 1.11$ and 0.6 percent at $X/C_{ax} = 1.30$) is a bit lower than the ~1 percent reduction indicated by Dejc for the same aspect ratio and contraction ratio (see Fig. 1).

We note that in addition to the direct measurement errors, integrated values may be in error due to a lack of measurement points in regions with high gradient and/or the integrating procedure. As is indicated in [17], there is no accurate way to determine how well the experimental procedure accounts for these errors, but a check is to see how close the conservation of mass is satisfied by comparing the measured mass flows at the exit of the cascade with the inlet mass flow. For all the four exit planes (present and reference tests), the value of the ratio of the mass flow over the inlet mass flow is measured between 1.03 and 1.06, which is considered satisfactory (see [14] and [17]).

Conclusions

1 The passage flow field is positively affected by tip contouring. The transverse pressure gradient is significantly decreased at the front part, while the radial pressure gradient imposed by the blade design is counteracted by the creation of a low static pressure region at the tip endwall suction side corner. Certainly, this causes a reduction of the inward migration of the low-momentum material over the blade suction side surface. The effects of the contraction and the tip endwall curvature extend over the whole blade height.

Downloaded 01 Jun 2010 to 171.66.16.71. Redistribution subject to ASME license or copyright; see http://www.asme.org/terms/Terms_Use.cfm

2 The exit flow field is characterized by a large reduction of the wake region from $Y/H = 0.25$ to 0.80. The overall losses decrease considerably compared to the cylindrical tip endwall case. However, the radial pressure gradients remain important and the radial flow angles in the wake region witness the spanwise migration of low-momentum material from tip to hub through the wake.

3 Since the effects of tip contouring on the flow angle and the static pressure decrease rapidly downstream of the stator trailing edge, the inlet flow conditions to a following blade row should only moderately be affected by changes at the total pressure loss distribution.

Acknowledgments

The author wishes to express his gratitude to Prof. C. H. Sieverding for supervising the present program. Mr. J. Dutton participated in the experimental work.

References

1 Dejc, E., et al., *Atlas of Axial Turbine Blade Characteristics*, Machinostroenie Publishing House, Moscow, 1965, CEGB Inf. Services, C. E. Trans. 4563.

2 Denton, J. D., "A Review of Current Research Activity on the Aerodynamics of Axial Flow Turbines," *Aerothermodynamics of Low Pressure Steam Turbines and Condensers*, VKI LS 1983-06.

3 Morgan, S., "Low Aspect Ratio Turbine Design in Rolls-Royce," *Secondary Flows and Endwall Boundary Layers in Axial Turbomachines*, VKI LS 1984-05.

4 Morris, A. W. H., and Hoare, R. G., "Secondary Loss Measurements in a Cascade of Turbine Blades with Meridional Wall Profiling," ASME Paper No. 75-WA/GT-13, 1975.

5 Kopper, F. C., Milano, R., and Vanco, M., "Experimental Investigation of Endwall Profiling in a Turbine Blade Cascade," *AIAA Journal*, Vol. 19, No. 8, Aug. 1981, pp. 1033–1040.

6 Waterman, W. F., and Tall, W. A., 'Measurement and Prediction of Three-Dimensional Viscous Flow in Low Aspect Ratio Turbine Nozzles," ASME Paper No. 76-GT-73, 1976.

7 Haas, J. E., "Analytical and Experimental Investigation of Stator Endwall Contouring in a Small Axial Flow Turbine: 1—Stator Performance," NASA TP 2023, 1982.

8 Ewen, J. S., Huber, F. W., and Mitchell, J. P., "Investigation of the Aerodynamic Performance of a Small Axial Turbine," ASME Paper No. 73-GT-3, 1973.

9 Due, H. F., Easterling, A. E., and Rogo, C., "Cascade Research on a Small, Axial, High Work Cooled Turbine," ASME Paper No. 75-GT-62, 1975.

10 Okapuu, U., "Some Results From Tests on a High Work Axial Gas Generator Turbine," ASME Paper No. 74-GT-81, 1974.

11 Boyle, R. J., Rholik, H. E., and Goldman, L. J., "Analytic Investigation of Effect of Endwall Contouring on Stator Performance," NASA TP 1943, 1981.

12 Sieverding, C. H., Van Hove, W., and Boletis, E., "Experimental Study of the Three-Dimensional Flow Field in an Annular Turbine Nozzle Guide Vane," ASME JOURNAL OF ENGINEERING FOR GAS TURBINES AND POWER, Vol. 106, No. 2, Apr. 1984, pp. 437–444; also VKI Preprint 1982-38.

13 Boletis, E., Sieverding, C. H., and Van Hove, W., "Effects of Skewed Inlet Endwall Boundary Layer on the Three-Dimensional Flow Field in an Annular Turbine Cascade," *Viscous Effects in Turbomachines*, AGARD CP 351, 1983, Paper 16; also VKI Preprint 1983-12.

14 Boletis, E., and Sieverding, C. H., "Experimental Study of the Flow Field Behind an Annular Turbine Nozzle Guide Vane With and Without Downstream Rotor," ASME Paper No. 84-GT-15, 1984; also VKI Preprint 1983-25.

15 Arts, T., "Effects of Tip Endwall Contouring on the Three-Dimensional Flow Field in an Annular Turbine Nozzle Guide Vane. Part II—Numerical Investigation," Paper to be presented at the 30th ASME Gas Turbine Conference, March 17–21, 1983, Houston, Texas; also VKI Preprint 1984-32.

16 Van Hove, W., "Calculation of a Three Dimensional, Inviscid, Rotational Flow in Axial Turbine Blade Rows," ASME JOURNAL OF ENGINEERING FOR GAS TURBINES AND POWER, Vol. 106, No. 2, Apr. 1984, pp. 430–436; also VKI preprint 1982-35.

17 Langston, L. S., Nice, M. L., and Hooper, R. M., "Three-Dimensional Flow Within a Turbine Cascade Passage," ASME JOURNAL OF ENGINEERING FOR POWER, Vol. 99, No. 1, Jan. 1977, pp. 21–28.

Downloaded 01 Jun 2010 to 171.66.16.71. Redistribution subject to ASME license or copyright; see http://www.asme.org/terms/Terms_Use.cfm

Short-Duration Measurements and Numerical Simulation of Heat Transfer Along the Suction Side of a Film-Cooled Gas Turbine Blade

C. Camci

T. Arts

von Karman Institute for Fluid Dynamics,
B-1640 Rhode Saint Genèse,
Belgium

This paper deals with an experimental investigation of heat transfer across the suction side of a high-pressure, film-cooled gas turbine blade and with an attempt to numerically predict this quantity both with and without film cooling. The measurements were performed in the VKI isentropic compression tube facility under well-simulated gas turbine conditions. Data measured in a stationary frame, with and without film cooling, are presented. The predictions of convective heat transfer, including streamwise curvature effects, are compared with the measurements. A new approach to determine the augmented mixing lengths near the ejection holes on a highly convex wall is discussed and numerical results agree well with experimentally determined heat transfer coefficients in the presence of film cooling.

Introduction

Current trends in the aircraft gas turbine industry are in the direction of increasing turbine entry temperature and pressure ratio in order to improve the engine efficiency. However, material properties often impose a limit to these thermodynamic inlet conditions. Over the last years, one of the popular methods to overcome the high temperature operation problems has been discrete hole external film cooling.

In gas turbine engines, local wall heat flux levels are dominated by complex three-dimensional flows originating from viscous effects. The existence of complicated three-dimensional flows and their interaction in a turbine cascade has been demonstrated by several authors, e.g., Sieverding [1]. Starting from the stagnation point, very thin and laminar boundary layers start to grow up. Around the stagnation zone, both high turbulence intensities and the three-dimensional flow structure are responsible for the highest heating rates on the blades [2]. Streamwise vortices develop on both sides of the profile. Along the suction side, where the flow is submitted to a strong favorable pressure gradient, amplification of the instabilities originating from the leading edge, breakdown of the streamwise vortices and hairpin eddy formation are the expected phases of a laminar to turbulent transition. The important streamwise curvature variations along this surface also affect the boundary layer development.

Several film cooling studies on turbine blades have been undertaken [3, 4]. Quantities such as adiabatic wall temperature T_{aw} and adiabatic effectiveness η, directly related to an adiabatic wall configuration, have most often been presented. Some typical stages of this approach are a detailed interpretation of convex curvature effects on the coolant film behavior [5], the effect of convex curvature on η compared with a flat-plate situation [5, 7], the rotational effects on suction-side film cooling [6]. Nevertheless, in the severe engine environment of a film-cooled airfoil, the large temperature differences existing between the mainstream and the blade surface induce a certain wall temperature pattern quite different from an adiabatic one. Considering the important spatial temperature variations due to internal cooling passages and the strongly varying heat flux distribution downstream of an ejection site, a more representative quantity is the convective heat transfer coefficient h, obtained from the local wall heat flux, the mainstream recovery temperature, and the local wall temperature at a prescribed coolant temperature and blowing rate. As a matter of fact, either an experimental or numerical determination of h is essential to perform any detailed heat conduction or stress analysis.

This paper deals with the theoretical and experimental investigation of heat transfer across the suction side of a high-pressure, film-cooled gas turbine blade. Spanwise-averaged convective heat transfer coefficient distributions are measured downstream of a double row of staggered cooling holes using a transient technique. Predictions are obtained from a two-dimensional boundary layer code (STAN5), taking into account the streamwise convex curvature effect and compared with the measurements. A new approach to determine the augmented mixing lengths downstream of the ejection holes is attempted and the predictions in the presence of coolant agree quite well with the measured heat transfer data in a given range of blowing rates and temperature ratios.

Contributed by the Gas Turbine Division of THE AMERICAN SOCIETY OF MECHANICAL ENGINEERS and presented at the 30th International Gas Turbine Conference and Exhibit, Houston, Texas, March 18-21, 1985. Manuscript received at ASME Headquarters, December 27, 1984. Paper No. 85-GT-111.

Copyright © 1985 by ASME
Downloaded 01 Jun 2010 to 171.66.16.71. Redistribution subject to ASME license or copyright; see http://www.asme.org/terms/Terms_Use.cfm

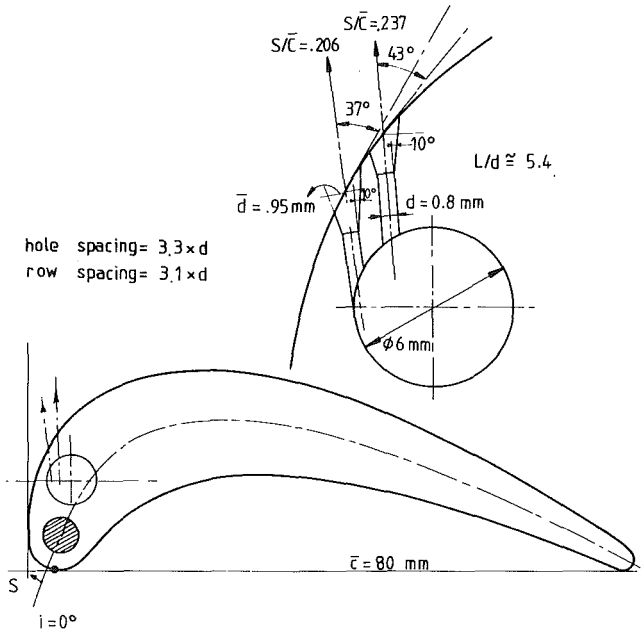


Fig. 1 Film-cooled turbine blade geometry

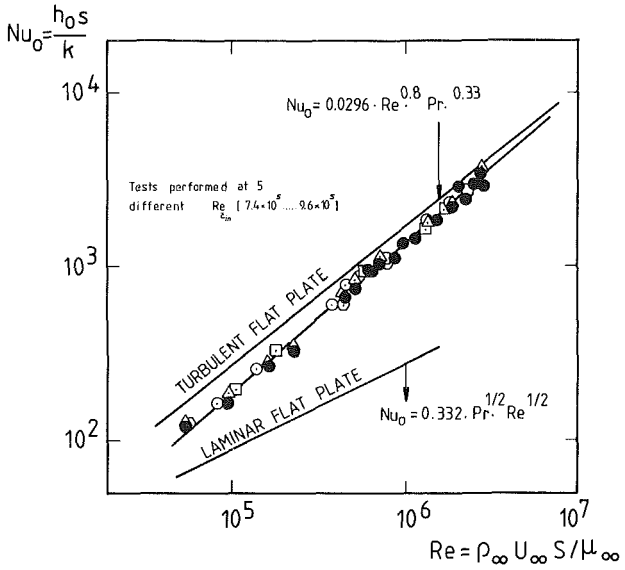


Fig. 2 Suction-side heat transfer without cooling

Experimental Apparatus

The experimental investigation was carried out in the VKI light piston isentropic compression tube facility. The same Reynolds and Mach numbers and wall to free-stream temperature ratios as encountered in actual aeroengines were generated. The coolant flow was supplied by a regenerative type cryogenic heat exchanger allowing a correct simulation of coolant to free-stream temperature ratio. The free-stream turbulence intensity was generated by a grid of parallel bars; the maximum turbulence level was 5.2 percent when the grid was installed one chord length upstream of the model [8]. Further details about this facility and its operating principles are described in [9, 10].

The coordinates of the blade and the cascade geometry were described by the authors in [13] and [8]. The local Ma number at the ejection site is 0.52. The details of measured and computed local Ma distributions were presented by the authors in [13]. The blade instrumented for heat transfer measurements was machined from a single block of low conductivity "Macor" glass ceramic and 45 platinum thin films were painted on its surface. This feature resulted in negligible conduction patterns and no artificial boundary layer disturbance, because of the smoothness of the surface. Two staggered rows of shaped holes are located on the suction side (Fig. 1). A circular cavity, drilled along the blade height, acts as a plenum. Three rows of holes are also present in the stagnation region but, for the present investigation, the leading edge plenum was filled with an insert to avoid any undesirable mainstream-plenum interaction. Pressure tap-

Nomenclature

$\bar{c}$ = chord length
c_p = specific heat of air at constant pressure
d = ejection hole diameter
$\bar{d}$ = exit hole diameter of the shaped hole
h_0, h = convective heat transfer coefficient without, with film cooling, $h = \dot{q}/(T_{0\infty} - T_w)$
i = incidence angle (positive in the counterclockwise direction)
k = thermal conductivity of air
l = Prandtl's mixing length, $l = [-u'v'/(\partial u/\partial y)]^{1/2}$
$\bar{l}_{\max}$ = maximum of the mixing length augmentation for film cooling on the turbine blade
m = blowing rate
$\delta\dot{m}$ = coolant mass flow rate, shed into a stream tube
$\dot{m}_{\text{old}}$ = mass flow rate per unit depth in a stream tube
Ma = local Mach number
Nu_o = local Nusselt number, $\text{Nu}_o = h_0 \cdot s/k$
Pr = molecular Prandtl number, $\text{Pr} = \mu \cdot c_p/k$
PD = penetration depth
$\overline{PD}$ = constant penetration depth, $\overline{PD} = 0.8 \times \delta$
$\dot{q}$ = wall heat flux rate
Re = local Reynolds number, $\text{Re} = \rho_\infty U_\infty s/\mu_\infty$
$1/R$ = curvature
s = curvilinear distance on the suction side
St_0, St = Stanton number without, with film cooling ($\text{St} = h/\rho_\infty U_\infty c_p$)
T = temperature
TU = turbulence intensity, $TU = \sqrt{\overline{u'^2}}/\text{U}$
U = velocity
u', v' = fluctuating velocity components
y = distance from the wall in a boundary layer
ρ = density
μ = absolute viscosity of air
δ = boundary layer thickness, $\delta_{.99}$
$\bar{\theta}$ = momentum thickness
κ = von Karman constant, $\kappa = 0.41$
θ = nondimensional coolant temperature, $\theta = \dfrac{T_{0\infty} - T_c}{T_{0\infty} - T_w}$
η = adiabatic wall effectiveness

Subscripts

aw = adiabatic wall
$\bar{c}$ = based on chord length
c = relative to coolant
ex = exit
in = inlet
o = total condition
r = recovery
w = wall
∞ = relative to free stream
$\bar{\theta}$ = based on momentum thickness

Downloaded 01 Jun 2010 to 171.66.16.71. Redistribution subject to ASME license or copyright; see http://www.asme.org/terms/Terms_Use.cfm

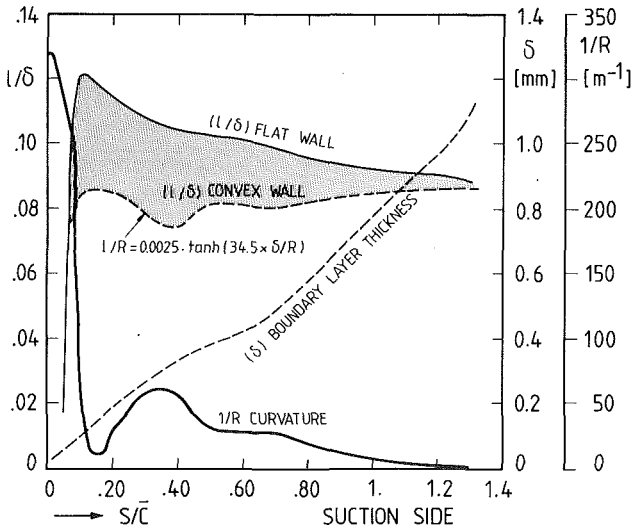


Fig. 3 Outer layer mixing length, curvature and boundary layer thickness on suction side

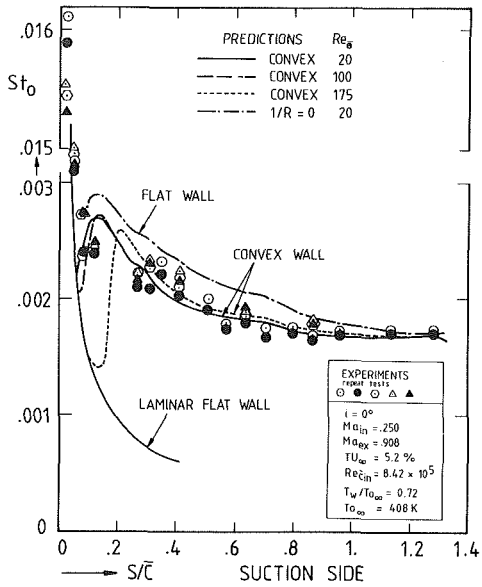


Fig. 4 Measured St_o number distribution and predictions without cooling

pings and fast response thermocouples provided the coolant characteristics at the plenum inlet and outlet.

The local heat flux is deduced from the corresponding time-dependent surface temperature evolution, provided by the thin films. The temperature/wall heat flux conversion is obtained from an electrical analogy, simulating a one-dimensional, semi-infinite body configuration. A detailed description of this transient technique is given in [11, 12] and the measurement uncertainties were quoted in [13]. The convective heat transfer coefficient is defined as the ratio of the measured wall heat flux over the difference between free-stream recovery and local wall temperature; a recovery factor equal to 0.896 is used [13]. Flow temperatures are measured using fine tungsten wires (5–10 μm) and thermocouples (20 μm).

Suction-Side Heat Transfer Without Film Cooling, Measurements

Heat transfer behavior in the stagnation region of the present model and downstream boundary layer development have been investigated by the authors [13]. Compared to the model having an identical external contour but without cooling holes, an early laminar/turbulent transition is observed, due to the tripping effect of the leading edge cooling holes. A turbulent boundary layer is fully established for $s/\bar{c} > 0.2$. The existence of a fully turbulent boundary layer is confirmed by examining the timewise variation and the order of magnitude of the heat flux signal traces. As a consequence of the present investigation, the coolant film ejected from the suction-side holes always interacts with a fully turbulent boundary layer.

The local Nusselt number along the suction side, in the absence of coolant, has been plotted as a function of local Reynolds number (Fig. 2) and compared with the laminar and turbulent flat-plate correlations [14]. The reduction of turbulent shear stress and turbulent kinetic energy levels, especially in the outer layer of a turbulent boundary layer developing on a convex surface, are closely related with wall heating rate reductions [15]. The actual data indeed show somewhat lower values than the turbulent flat-wall correlation. The largest deviations are observed near the leading edge, where the transition is artificially induced by the holes which are not ejecting ($0.05 < s/\bar{c} < 0.2$). Further downstream, the measured values tend to merge with the flat-plate correlation as strong convex curvature disappears. A full recovery near the trailing edge is, however, not expected [16].

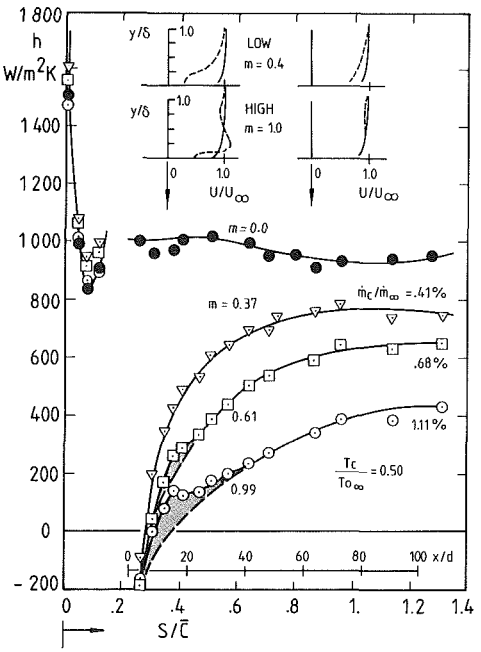


Fig. 5 Suction-side heat transfer with film cooling, effect of blowing rate

Suction-Side Heat Transfer Without Film Cooling, Predictions

A numerical prediction of convective heat transfer across the suction side has been attempted using a two-dimensional, finite difference boundary layer code (STAN5) developed by Crawford et al. [17]. The initial velocity and enthalpy profiles are obtained from a cylinder in crossflow solution. A streamwise curvature correction [16], based on mixing length modifications in the outer region of a turbulent boundary layer, has been implemented in the code. This outer layer mixing length is computed from the equation shown in Fig. 3, using the local wall curvature. As a result, small l/δ values are obtained compared to a flat-plate configuration. In the log

Downloaded 01 Jun 2010 to 171.66.16.71. Redistribution subject to ASME license or copyright; see http://www.asme.org/terms/Terms_Use.cfm

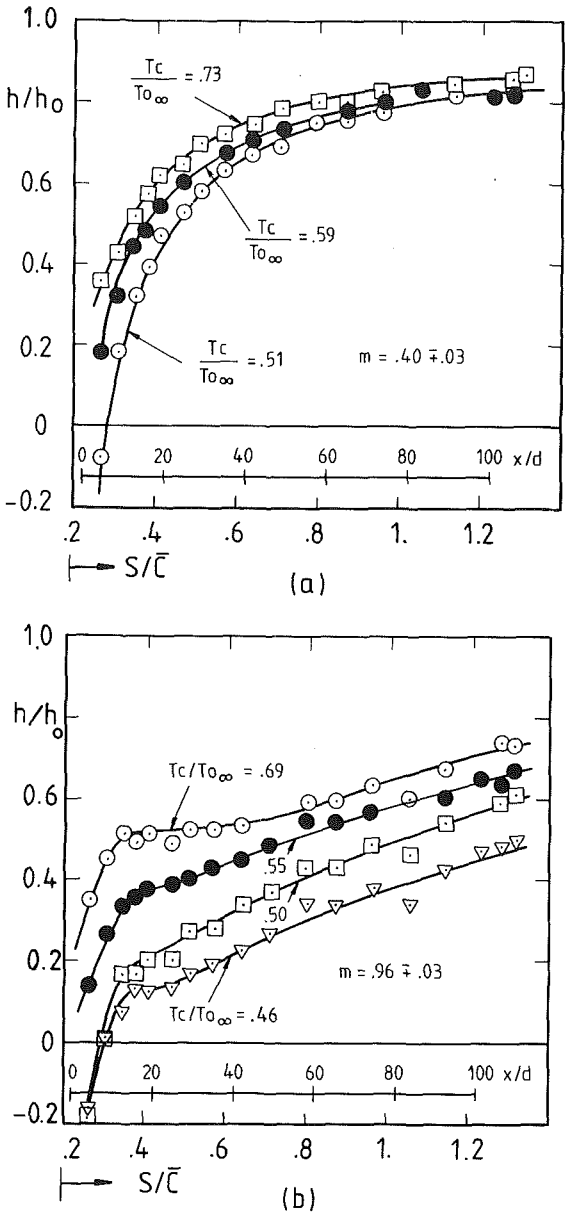


Fig. 6 Suction-side heat transfer with film cooling, effect of temperature ratio

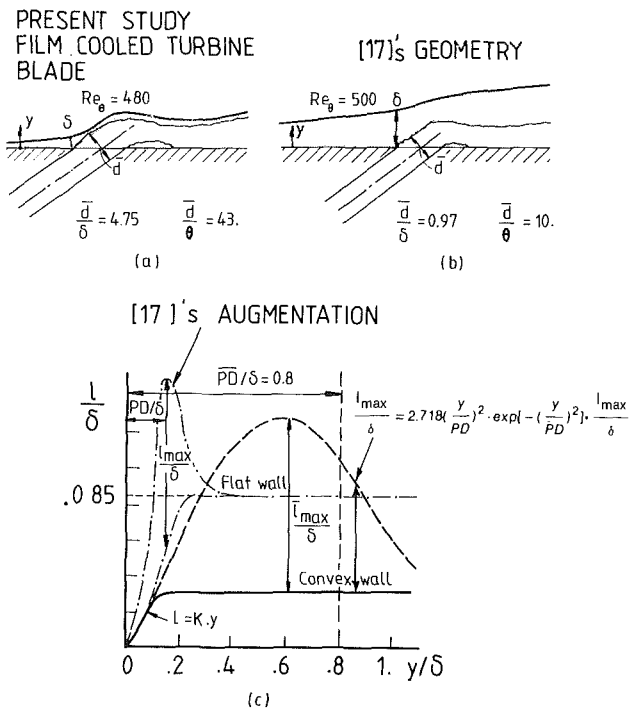


Fig. 7 Film-cooled boundary layer scaling on the turbine blade and mixing length augmentation

region, the shear stress correction was provided using a Richardson number formulation [16, 18]. As a matter of fact, for large convex curvature, the wall layer is structurally unchanged compared to a flat wall flow [16].

As already mentioned, an early boundary layer transition was forced by imposing a transitional Re_δ equal to 20 . . . 175. The predicted boundary layer thickness evolution is shown in Fig. 3. On the suction-side injection site, δ was computed to be 0.2 mm, i.e., almost five times smaller than a cooling hole diameter. Measured and computed local St_0 number distributions are compared in Fig. 4. These results clearly show the overprediction obtained without curvature correction and demonstrate the improvement obtained with a rather simple approach as the one presented above. Variations of transitional Re_δ between 20 . . . 175 . . .200 do not affect significantly the downstream convective wall heating rate level. The data scatter observed near the injection site is attributed to the disturbing influence of the relatively large diameter of cooling holes, although the injection plenum was filled with an insert.

Suction-Side Heat Transfer With Film Cooling, Measurements

Qualitative oil flow visualizations were performed in a low-speed environment; they demonstrated the spanwise uniformity of the coolant flow as well as the adequate film coverage, downstream of the ejection rows. It was also observed that the secondary flow region did not significantly affect the coolant field.

The influence of the blowing rate on the suction side convective heat transfer is shown in Fig. 5. The blowing rate was varied from 0.37 to 0.99 for a constant value of coolant to free-stream temperature ratio ($T_c/T_{0\infty} = 0.51$). In all cases, significant protection of the wall was achieved, especially close to the ejection holes ($x/d < 40$). Typical velocity profiles, near and far downstream of double rows of holes, have been extracted from [19, 20] (Fig. 5). For low blowing rates ($m = 0.40$), low mean velocity gradients near the wall and important momentum deficits above $y/\delta = 0.2$ are typically encountered. If m is raised up to 1.0, a velocity excess region is observed near the wall. Above this zone, the overall mean velocity gradient is very low compared to the preceding configuration. Since the turbulent kinetic energy production is related to the mean velocity gradient [19], higher heat flux levels are expected for low blowing rates whereas, except in the near wall region, a reduction in overall heat flux will be observed for $m = 1.0$. In the near wall region, the heat transfer augmentation observed for $x/d < 40$ may be related to the velocity excesses shown in Fig. 5. Very steep mean velocity gradients near the wall as well as an eventual jet penetration into the mainstream yields large shear stress and turbulent kinetic energy levels in this region. For most of the aforementioned studies, the approaching mainstream boundary layer thickness δ has the same order of magnitude as the injection hole diameter. Although the mean velocity profiles provide a good aid in the interpretation of the data presented in Fig. 5, the $\delta/\bar{d}$ ratio predicted for the present experiments is only 1/5, closer to a real situation. A

Downloaded 01 Jun 2010 to 171.66.16.71. Redistribution subject to ASME license or copyright; see http://www.asme.org/terms/Terms_Use.cfm

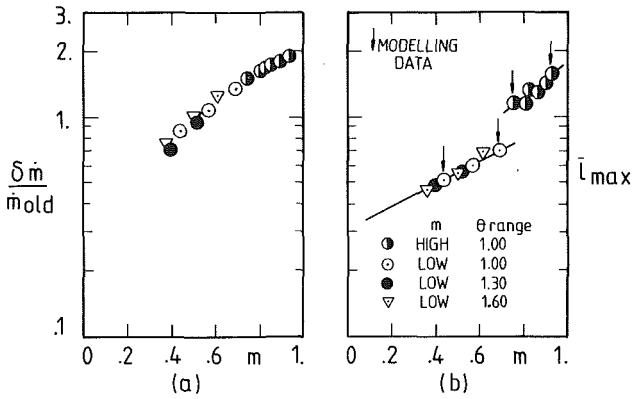


Fig. 8 Mass shed ratio and augmented mixing length

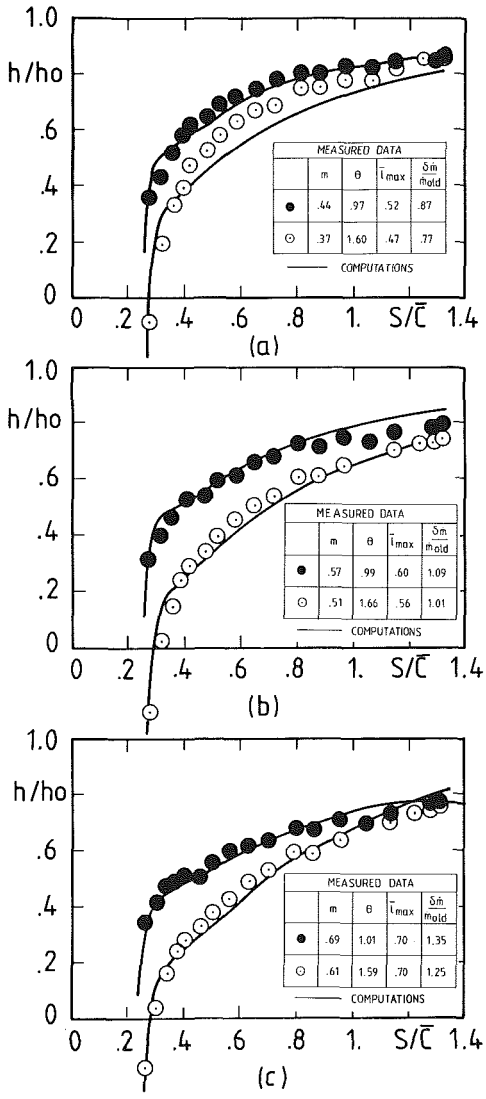


Fig. 9 Film cooling heat transfer, predictions $m < 0.69$

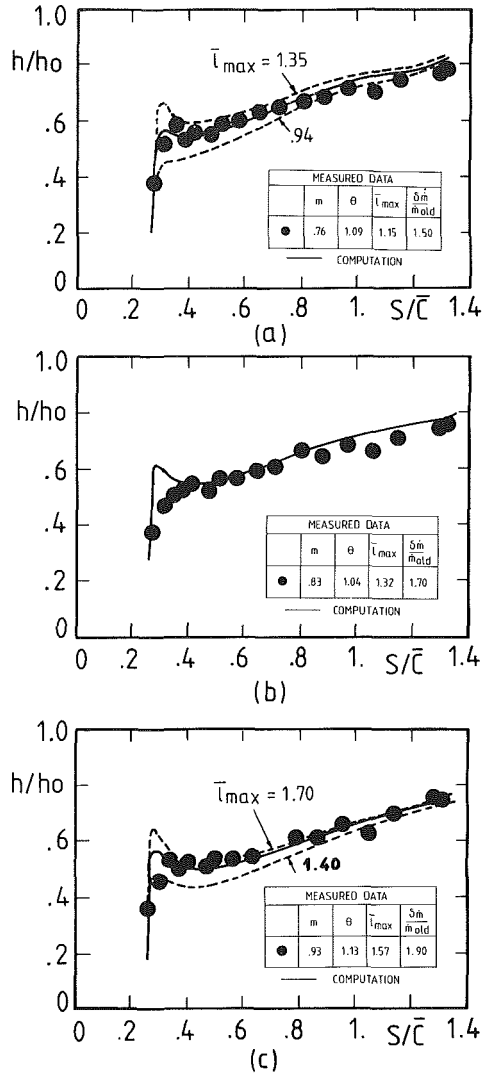


Fig. 10 Film cooling heat transfer, predictions $m > 0.76$

strong dominance of the new cold injected layers is therefore expected to take place.

Significant coolant temperature effects on convective heat transfer have also been observed. Figure 6(*a*) presents the results obtained for $m = 0.40$. Important h/h_0 reductions were achieved for $x/d < 40$ when the coolant temperature was lowered from wall temperature, to half of the mainstream level. The downstream values of h/h_0 smoothly increase and far downstream ($x/d = 100$) the heat flux level differences due to T_c variations are not as large as close to the ejection rows. Increasing m up to 0.96 provided the results presented in Fig. 6(*b*) with considerably lower heat transfer levels. Just downstream of the ejection side ($x/d < 40$), a local heat transfer augmentation, occurring almost independently of the coolant temperature level, is observed. This augmentation has been related to very high overall turbulent shear stress and turbulent kinetic energy levels near the wall, existing for such a blowing rate value. Another expected reason was "hot mainstream/wall" interaction due to severe coolant jet penetration into the mainstream. The penetrating coolant jets were expected to reduce the overall film cooling coverage just downtream of the ejection site, because of reduced lateral jet spread. In this zone, the wall has more chance to be influenced by the hot mainstream. Farther downstream, when the abrupt changes in the hydrodynamic structure start to decay, an almost linear h/h_0 rise takes place ($x/d = 30$). In contrast to the $m = 0.4$ case, the far downstream coolant temperature influence was very much pronounced. At $m = 0.96$, mainly because of considerably high momentum flux of the discrete coolant jets, the coolant layers tend to dominate even far downstream, as far as convective heat transfer is concerned.

Downloaded 01 Jun 2010 to 171.66.16.71. Redistribution subject to ASME license or copyright; see http://www.asme.org/terms/Terms_Use.cfm

Suction-Side Heat Transfer With Film Cooling, Computations

The numerical simulation of convective heat transfer across the suction side in the presence of discrete hole film cooling was attempted using the boundary layer code developed for full coverage film cooling on flat walls by Crawford et al. [17]. Because of the existence of curved high-speed and compressible coolant layers along the suction side of the blade, a number of modifications, related to the effect of streamwise curvature as Prandtl's mixing length turbulence augmentation near the ejection holes and to the coolant ejection into the boundary layer, have been introduced.

The ejection hole diameter d to momentum thickness $\bar{\theta}$ ratio has been one of the basic simulation parameters in the area of discrete hole film cooling. In the present case, the $d/\bar{\theta}$ ratio was computed to be 43 whereas the d/δ ratio was calculated to be 4.75 (Fig. 7(a)). Looking at the model used in [17], values respectively equal to 10 and 1 were observed (Fig. 7(b)).

As a matter of fact, the coolant layers on the present model are expected either to occupy a major portion of the boundary layer or to penetrate into the mainstream and reattach farther downstream to the wall, depending upon the blowing rate level, in contrast to the case presented in [17], where the boundary layer is almost equally dominated by both mainstream and coolant flows. Therefore, the blowing rate dependency of the augmented mixing length $\bar{l}_{max}$ and mass shed ratio $\delta\dot{m}/\dot{m}_{old}$, the two most importrant parameters modeling the ejected flow, is strongly needed.

In order to establish the relationship existing between mass shed ratio and blowing rate, it was assumed that all of the coolant was distributed in such a way that the penetration depth did not exceed the approach boundary layer thickness. The resulting $\delta\dot{m}/\dot{m}_{old}$ values are shown in Fig. 8(a). Although this approach does not simulate the most accurate coolant distribution across the boundary layer, it is expected to simulate the overall hydrodynamic nature of the coolant layers downstream of the ejection site. At least this approach adds the correct amount of coolant mass and momentum to the viscous flow field.

The augmentation mixing length $\bar{l}_{max}$, representing the maximum disturbance to the boundary layer due to ejection, has been considered in the present study, as a lumped quantity, responsible for the gross mixing length modifications in the viscous layers. Moreover, the wall heat flux augmentation due to the "hot mainstream/wall" interaction described in the preceding section was also expected to be simulated using this parameter, although no modifications were brought to the mass shed ratio. The exponential l_{max} variation used in [17] was found to be useful to simulate an augmentation which is spread over the entire boundary layer, with a PD located at 80 percent of the boundary layer thickness (Fig. 7(c)). $\bar{l}_{max}$ was decayed exponentially in the downstream direction with a time constant of two boundary layer thicknesses. Farther away from the ejection site the mixing length simulation takes only streamwise curvature effects into account.

The quantitative determination of $\bar{l}_{max}$ was performed by varying this quantity until a satisfactory simulation of the measured heat transfer data was obtained for two different blowing rates (m = 0.44, 0.69) (Fig. 8(b)). The straight line connecting these two modeling $\bar{l}_{max}$ values was used in the predictions, for different blowing rates, at three different coolant temperatures, when $m < 0.69$. However, $\bar{l}_{max}$ was found to be independent of the coolant temperature in this range. The low blowing rate data were predicted successfully as presented in Fig. 9. However, this line was not very satisfactory in simulating the high blowing rate data ($m >$ 0.69). Starting from the idea of "hot mainstream/wall" interaction, which may occur above a certain blowing rate, another $\bar{l}_{max}$ region with a stronger m dependency was established using again two sets of measured data. The second $\bar{l}_{max}$ relation (Fig. 8(a)) was used successfully to predict six more data sets (m = .76, .81, .83, .86, .90, .93) for θ = 1.0. Three of the predictions are shown in Fig. 10. The agreement is good.

Conclusions

Convective heat transfer in the boundary layer developing along the suction side of a high-pressure turbine rotor blade has been investigated, both in absence and presence of film cooling, under well-simulated mainstream conditions and δ/d.

The experimental investigation was performed using a sophisticated short duration technique. The measured data on the turbine blade, in the absence of the coolant flow, were compared to classical flat-plate correlations in order to determine the influence of curvature on heat transfer.

In the presence of cooling, the effect of blowing rate and temperature ratio was successively investigated and discussed with the aid of published hydrodynamic data. Important local differences in convective heat transfer behavior were observed at low and high blowing rates.

The numerical predictions were obtained from the STAN5/STANCOOL boundary layer code, including a number of modifications taking into account mixing lengths on a highly curved surface with film cooling. In the absence of film cooling, a streamwise curvature correction, affecting only the turbulent boundary layer was implemented. The boundary layer transition on the suction side of the film-cooled blade was quite early and abrupt compared to that of the blade without cooling holes, under identical free-stream conditions. This phenomenon shows the significance of a curvature correction procedure on a film-cooled blade even without ejection.

A new approach was attempted to determine the augmented mixing length $\bar{l}_{max}$ for film cooling, through quantitative wall heat flux measurements near the ejection site. Low and high blowing rate behavior of $\bar{l}_{max}$ has been evaluated on a two zone $\bar{l}_{max}$ versus m map. In spite of the simplicity of this modeling idea, computed and measured results compare quite well in a rather large blowing rate and coolant temperature range.

References

1 Marchal, P., and Sieverding, C. H., "Secondary Flows Within Turbomachinery Bladings," Paper 11, in *Secondary Flows in Turbomachines*, AGARD CP 214, 1977, also VKI Preprint 1977-11.

2 Kestin, J., and Wood, R. T., "The Mechanism Which Causes Free-Stream Turbulence to Enhance Stagnation Line Heat and Mass Transfer," *Heat Transfer*, Vol. 2, Amsterdam, Elsevier, 1970.

3 Lander, R. D., Fish, R. W., and Suo, M., "External Heat Transfer Distribution on Film Cooled Turbine Vanes," *Journal of Aircraft*, Vol. 9, No. 10, Oct. 1972, pp. 707-714.

4 Muska, J. F., Fish, R. W., and Suo, M., "The Additive Nature of Film Cooling From Rows of Holes," ASME JOURNAL OF ENGINEERING FOR POWER, Vol. 98, No. 4, Oct. 1976, pp. 457-463.

5 Ito, S., Goldstein, R., and Eckert, E.R.G., "Film Cooling of a Gas Turbine Blade," ASME JOURNAL OF ENGINEERING FOR POWER, Vol. 100, No. 3, July 1978, pp. 476-481.

6 Dring, R. P., Blair, M. F., and Joslyn, H. D., "An Experimental Investigation of Film Cooling on a Turbine Rotor Blade," ASME JOURNAL OF ENGINEERING FOR POWER, Vol. 102, No. 1, Jan. 1980, pp. 81-87.

7 Richards, B. E., Ville, J. P., Appels, C., and Salemi, C., "Film Cooling of Heated Turbine Surfaces at Simulated Conditions," Paper No. AIAA 77-947, AIAA/SAE 13th Joint Propulsion Conference, Florida, July 1977.

8 Consigny, H., and Richards, B. E., "Short Duration Measurements of Heat Transfer Rate to a Gas Turbine Blade," ASME JOURNAL OF ENGINEERING FOR POWER, Vol. 104, No. 3, July 1982, pp. 542-551.

9 Richards, B. E., "Heat Transfer Measurements Related to Hot Turbine Components in the von Karman Institute Hot Cascade Tunnel," in *Testing and Measurement Techniques in Heat Transfer and Combustion*, AGARD CP 281, 1980.

10 Jones, T. V., Schultz, D. L., and Hendley, A. D., "On the Flow in an Isentropic Free Piston Tunnel," ARC R&M 3731, Jan. 1973.

Downloaded 01 Jun 2010 to 171.66.16.71. Redistribution subject to ASME license or copyright; see http://www.asme.org/terms/Terms_Use.cfm

11 Schultz, D. L., and Jones, T. V., "Heat Transfer Measurements in Short Duration Hypersonic Facilities," AGARDograph 165, 1973.

12 Ligrani, P. M., Camci, C., and Grady, M.S., "Thin Film Heat Transfer Gauge Construction and Measurement Details," VKI TM 33, Nov. 1982.

13 Camci, C., and Arts, T., "Experimental Heat Transfer Investigation Around the Film-Cooled Leading Edge of a High-Pressure Gas Turbine Rotor Blade," ASME JOURNAL OF ENGINEERING FOR GAS TURBINES AND POWER, Vol. 107, No. 4, Oct. 1985, pp. 1016-1021; also VKI Preprint 1984-32.

14 Kays, W. M., and Crawford, M. E., *Convective Heat and Mass Transfer* (2d ed.), McGraw-Hill, 1980.

15 Gillis, J. C., and Johnston, J. P., "Turbulent Boundary Layer Flow and Structure of a Convex Wall and Its Redevelopment on a Flat Wall," *Journal of Fluid Mechanics*, Vol. 135, Oct. 1983, pp. 123-153.

16 Adams, E. W., and Johnston, J. P., "A Mixing Length Model for the Prediction of Convex Curvature Effects on Turbulent Boundary Layers," ASME JOURNAL OF ENGINEERING FOR GAS TURBINES AND POWER, Vol. 106, No. 1, Jan. 1984, pp. 142-148.

17 Crawford, M. E., Kays, W. M., and Moffat, R. J., "Full-Coverage Film Cooling. Part II: Heat Transfer Data and Numerical Simulation." ASME JOURNAL OF ENGINEERING FOR POWER, Vol. 102, No. 4, Oct. 1980, pp. 1006-1012.

18 So, R.M.C., "On the Curvature/Buoyancy Analogy for the Turbulent Shear Flows," *ZAMP*, Vol. 31, Fasc. 3, 1980.

19 Yavuzkurt, S., Moffat, R. J., and Kays, W. M., "Full-Coverage Film Cooling. Part 1—Three-Dimensional Measurements of Turbulent Structure," *J. Fluid Mechanics*, Vol. 101, No. 1, Nov. 1980, pp. 120-158.

20 Bergeles, G., Gosman, A. D., and Launder, B. E., "Near-Field Character of a Jet Discharged Through a Wall at 30 deg to a Mainstream," *AIAA Journal*, Vol. 15, No. 4, Apr. 1977, pp. 499-504.

Downloaded 01 Jun 2010 to 171.66.16.71. Redistribution subject to ASME license or copyright; see http://www.asme.org/terms/Terms_Use.cfm

Simulation of the Effects of Shock Wave Passing on a Turbine Rotor Blade

D. J. Doorly[1]

M. L. G. Oldfield

Department of Engineering Science,
Oxford University,
England

The unsteady effects of shock waves and wakes shed by the nozzle guide vane row on the flow over a downstream turbine rotor have been simulated in a transient cascade tunnel. At conditions representative of engine flow, both wakes and shock waves are shown to cause transient turbulent patches to develop in an otherwise laminar (suction-surface) boundary layer. The simulation technique employed, coupled with very high-frequency heat transfer and pressure measurements, and flow visualization, allowed the transition initiated by isolated wakes and shock waves to be studied in detail. On the profile tested, the comparatively weak shock waves considered do not produce significant effects by direct shock–boundary layer interaction. Instead, the shock initiates a leading edge separation, which subsequently collapses, leaving a turbulent patch that is convected downstream. Effects of combined wake- and shock wave–passing at high frequency are also reported.

Introduction

Although it is widely recognized that the flow around the compressor and turbine blades of an axial flow gas turbine engine is highly unsteady, the significance of the flow unsteadiness in determining the blade performance is only now beginning to be fully appreciated. This is largely because measurements have just recently been made that have indicated substantial effects caused by unsteadiness, since previous research concentrated on steady flow through model blade cascades, to allow the development of steady flow numerical prediction techniques. In order to further the understanding of flow in turbomachines, and develop better prediction techniques, there is now a need for a detailed study of the unsteady flow around the blades.

Causes of Flow Unsteadiness. The unsteadiness of the flow largely arises from the relative motion of the blade rows in the alternately stationary and rotating stages. For a compressor, or turbine stage, in which the flow is fully subsonic, the relative motion of the blades generates unsteadiness in two ways. In the first instance, the complete inviscid flow field around each blade is affected by the presence of, and flow fields around, the nearest blades belonging to the upstream and downstream stages, respectively. Studies such as [1–3], among others, have concerned the potential interaction of blade rows in incompressible flow and have shown that the unsteadiness due to the interaction is greater on the upstream blade than on the downstream blade, and decays rapidly with increasing axial spacing. This form of unsteadiness is thus of greater concern for the blades in the NGV (nozzle guide vane) row than for the turbine blades, and in particular it has been reported [4] that the unsteadiness generated by the downstream rotor may significantly affect the heat transfer rate to the NGV.

The second cause of the unsteadiness is "wake-passing," which describes the unsteady process whereby each blade of a given stage continuously "chops through" the wakes shed at the trailing edges of the blades of the stage upstream. The experiments described by [5] and [6] on single-stage axial flow compressors have shown that except for very small axial gaps (of order 5 percent axial chord, where the contributions of the wakes and the potential flow interaction are of equal amplitude) the unsteadiness due to the wakes is dominant.

Where the flow reaches transonic velocity in the blade passages, an additional source of unsteadiness arises through "shock-wave passing." This is the unsteady flow produced by the constant motion of the blades of one stage through the shock waves of the upstream blades.

In the first-stage turbine of a modern aircraft gas turbine, which is of immediate concern here, all three forms of flow unsteadiness are present. In addition, random turbulence of combustion chamber origin may still significantly add to the total unsteadiness in the flow to the first turbine rotor. Consequently, the boundary layer on the turbine blade in the engine responds to a very complex unsteady flow with a wake, shock wave, potential flow disturbance, and random freestream turbulence all acting.

Studies of Blade Boundary Layer. The type of boundary layer resulting from the unsteadiness in the free stream is of fundamental importance, as it determines the scale of the heat transfer and aerodynamic effects. Boundary layer studies on blades of low-speed axial flow compressors by [7–9], among others, demonstrated that the wakes from the stage upstream resulted in an unsteady transition of the blade boundary layer,

[1] Presently at Department of Mathematics, University College London

Contributed by the Gas Turbine Division of THE AMERICAN SOCIETY OF MECHANICAL ENGINEERS and presented at the 30th International Gas Turbine Conference and Exhibit, Houston, Texas, March 18–21, 1985. Manuscript received at ASME Headquarters, December 27, 1984. Paper No. 85-GT-112.

Copyright © 1985 by ASME
Downloaded 01 Jun 2010 to 171.66.16.71. Redistribution subject to ASME license or copyright; see http://www.asme.org/terms/Terms_Use.cfm

although no satisfactory interpretation of the nature of the transition process could be clearly established.

Boundary layer studies on the blades of low-speed turbines by [10] and [11] have also shown that the turbine blade boundary layer undergoes an unsteady transition caused by the wakes from the blades of the stage upstream. The effect of the wakes in forcing the transition process is cited in [12], and likewise in earlier experiments by [13], as a cause of the increased rotor profile loss over the loss of the equivalent profile tested in a cascade.

Effects of Combined Wakes and Shock Waves. The transition process initiated by the wakes is of central importance in the studies of the unsteady shock impingement. In the engine, the nozzle guide vane shock wave impinges on the turbine blade boundary layer either in rapid succession to the preceding wake, or even simultaneously with it.

Even where wakes and shock waves do not impinge simultaneously, study of the times required for the boundary layer to recover fully after the passing of each of these types of free-stream disturbance (both of which times have been measured in the experiments reported here) is necessary. The importance of the recovery time is in determining whether the actions of successive shock waves and wakes on the boundary layer may be treated separately, and to determine for what portions of each cycle the boundary layer response is controlled by one or other disturbance, or the product of both.

The maximum time taken for the boundary layer at a given point to recover fully after a single free-stream disturbance depends on:

(*a*) The position of the point on the blade surface
(*b*) The motion of the free-stream disturbance viewed as a trajectory in X (blade surface distance) versus T (time) space
(*c*) The evolution and trajectories of boundary layer features generated by the disturbance at locations upstream of the given point

In the work reported here, the production of boundary layer phenomena by shock waves, and their subsequent rearward convection, has been found to be of particular significance. The generation of such phenomena, together with the inherent stretching effect of the slower velocity in the boundary layer compared to the free-stream velocity, may considerably modify the period for which the boundary layer behavior is dominated by either wake or shock, or by the nonlinear superposition of both. Where wakes and shocks cause an otherwise laminar portion of the blade boundary layer to become turbulent for a transient period, the duration of this period, which is determined by these factors, determines the mean heat transfer level.

Problems of Experimental Studies of Shock Passing. The mechanical complexities involved in obtaining detailed measurements and flow visualization from a high-speed, high-temperature rotating turbine stage are severely limiting. In addition, however, the rotating turbine stage suffers from the disadvantage that it is not conveniently possible to vary the amplitude and time relationships of the unsteady disturbances (comprising the wakes, shock waves, and turbulence) independently. This is a cumbersome handicap in fundamental investigations of the blade boundary layer.

To date, the most detailed measurements of the effects of wake passing on unsteady transition have been provided by the authors of [14], who studied wake passing on the flat-plate boundary layer in incompressible flow. For this work, a large-diameter rotating "squirrel cage" arrangement mounted in a low-speed wind tunnel was used to generate wake-passing upstream of the flat plate.

An alternative procedure to the above, more suitable for the investigation of wake-passing and shock wave-passing in a high-speed cascade of stationary blades mounted in a wind tunnel, has been developed at Oxford, as reported briefly in [15].

This simulation technique allows studies to be made both of the unsteady effects of disturbances of a given type acting in isolation, and of the unsteady effects produced by combinations of two or more types of disturbance.

The objective has thus been to complement full three-dimensional, high-speed rotating studies (which produce a more exact simulation at the cost of a more complex flow), with a facility capable of providing more detailed information on the major contributions to the unsteady flow in an engine.

Relation to Other Studies. The results of the studies of wake-passing without associated shock wave-passing (i.e., for the simulation of subsonic NGV exit velocities) will be reported in [16].

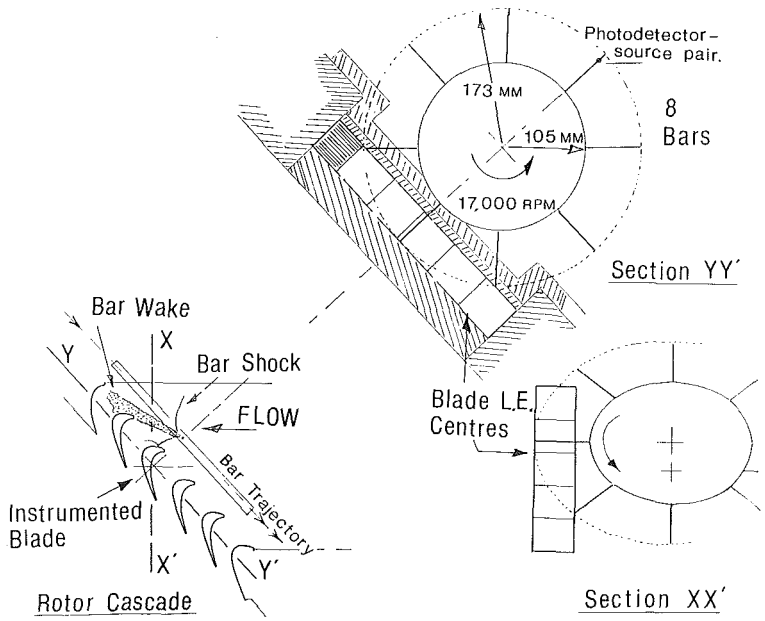


Fig. 1 Schematic of rotating bar system for the simulation of wake- and shock-wave passing in a cascade

Downloaded 01 Jun 2010 to 171.66.16.71. Redistribution subject to ASME license or copyright; see http://www.asme.org/terms/Terms_Use.cfm

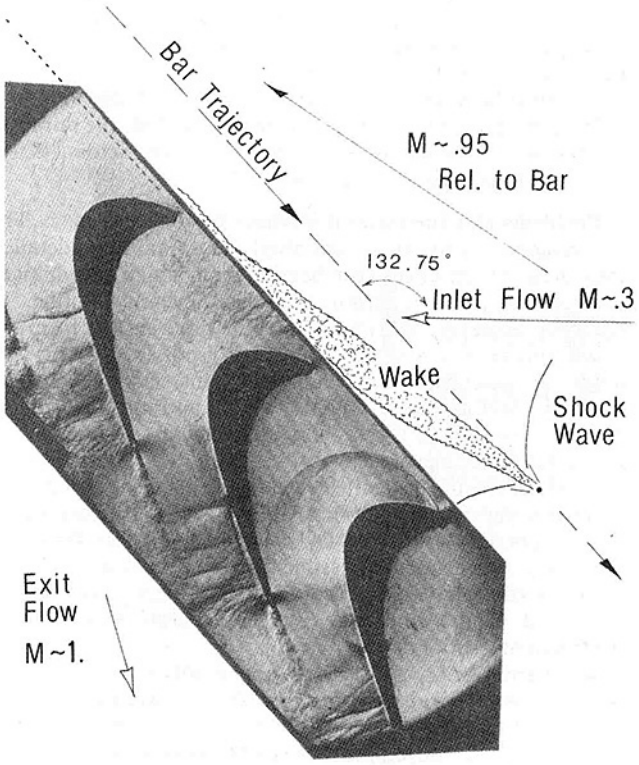


Fig. 2 Schlieren photograph of shock wave and wake (from 1.7-mm-dia bar) entering cascade

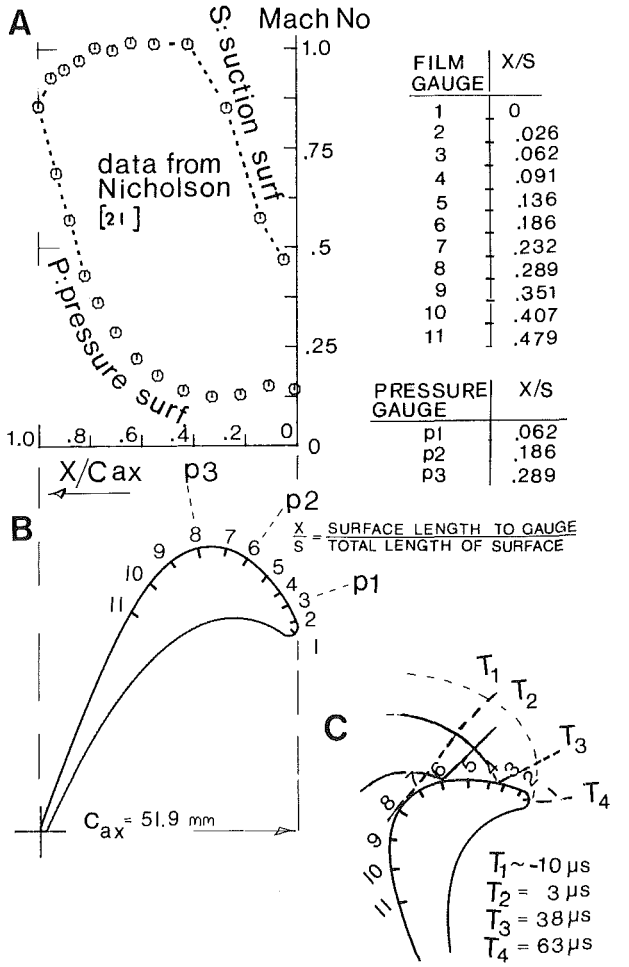


Fig. 3A: Blade Mach No. distribution [21]; B: gauge locations; C: impingement of shock wave on suction surface

The purpose of this paper is to report the effects produced by shock waves on the heat transfer and examine the unsteady results obtained with combined wakes and shock waves. Attention is confined to the suction surface of the blade, as the shock wave is effectively prevented by the geometry of the test blade from significantly affecting the pressure surface (for the comparatively weak shocks studied).

Subsequent results obtained with the unsteady flow simulation technique developed by the authors, but using a different transonic blade section, are to be reported in [17].

Experimental Arrangement

The arrangement of the wake generator, used to simulate wake-passing flow in a stationary cascade of rotor blades mounted in a wind tunnel, is shown schematically in Fig. 1. As described in [15], and more fully in [18], the correct relative velocity vector diagram of the rotor unsteady flow may be produced by moving a row of circular cylindrical bars at the correct velocity in front of the rotor cascade, which is mounted in a transient wind tunnel. Mounting the bars on the rim of the large diameter rotating disk (Fig. 1) approximates the ideal rectilinear motion of a "ladder" of bars past the cascade. The bars were chosen [18] primarily in order to simulate the wake of a typical upstream nozzle guide vane (or NGV) row, so that the shock simulation is not exact; in fact, it is, in general, impossible to model simultaneously the NGV wake and shock wave(s) strength and relative positions exactly using this arrangement. The advantages of the technique in allowing the effects of shock waves and wakes to be separately studied in great detail, and the capacity for subsequent independent variation in either shock wave or wake, are, however, considered by us to outweigh this disadvantage. The two sizes of bar chosen (actually stranded steel wire for mechanical reasons) measured 0.9 mm and 1.7 mm in diameter, representing low and high (wake-) loss NGV profiles, respectively.

The Isentropic Light Piston Tunnel (ILPT) at Oxford [19, 20] was the transient tunnel used for the tests. Prior to the run, the tunnel working section was evacuated, and the wake generator accelerated by a small air turbine up to a steady speed. The tunnel was then fired to give a (typically) 0.35 s steady flow, with a downstream variable area choked throat serving to maintain the cascade exit conditions. The inertia of the disk was sufficient to maintain the speed of the wake generator within 1 percent for the 15 ms interval when the high-frequency measurements were made.

The flow Reynolds number (based on a model blade chord of 67.8 mm and exit Mach number of 0.96) was 2.02×10^6; the free-stream total temperature was 432 K for the heat transfer measurements, corresponding to a gas-to-wall temperature ratio for the blade surface (at ambient initial conditions) of 1.5. Both the flow Reynolds number and gas-to-wall temperature ratio were equal to that of the engine blade at the design operating point. The surface Mach number distribution of the blade profile tested is reproduced in Fig. 3(*A*); the steady flow aerodynamics and heat transfer of this profile has been the subject of extensive studies reported in [21], [22], and of work to be published [23].

For the particular nozzle guide vane stage associated with this test rotor, the simulation of wake-passing flow at the design operating conditions of the engine required the bars to be moved at a Mach number of 0.94 relative to the Mach 0.32 cascade inlet flow. With 8 bars fitted to the wake-generator disk, the circumferential spacing of the bars at the cascade midspan was 116 mm, or two times the pitch of the rotor cascade. This corresponds approximately to the ratio of NGV pitch to rotor blade pitch in the engine.

In order to study the separate effects of wakes and shock waves on the boundary layer however, only two bars were

Downloaded 01 Jun 2010 to 171.66.16.71. Redistribution subject to ASME license or copyright; see http://www.asme.org/terms/Terms_Use.cfm

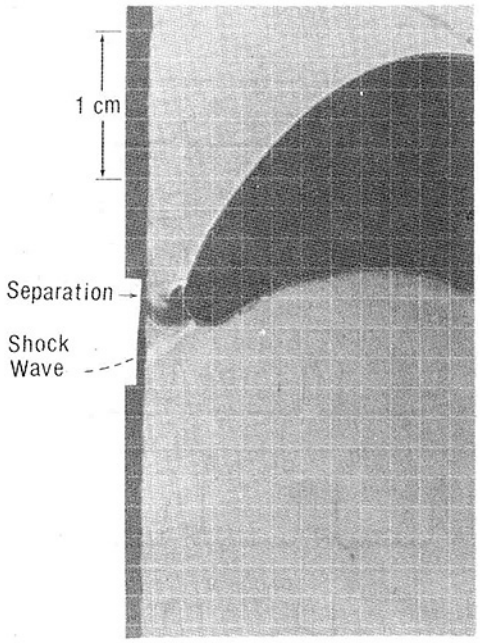


Fig. 4 Cycle time = 63 μs

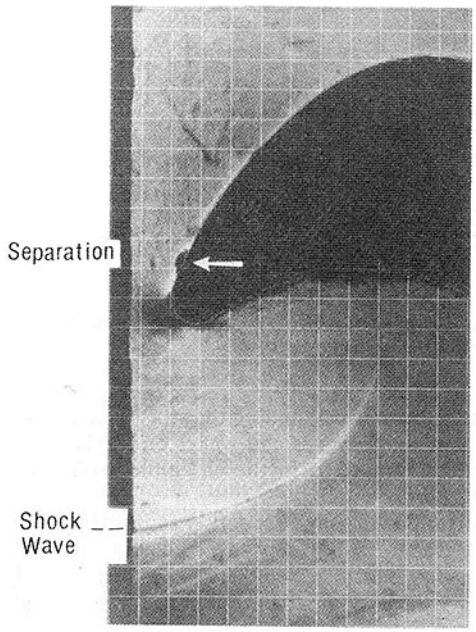


Fig. 5 Cycle time = 101 μs

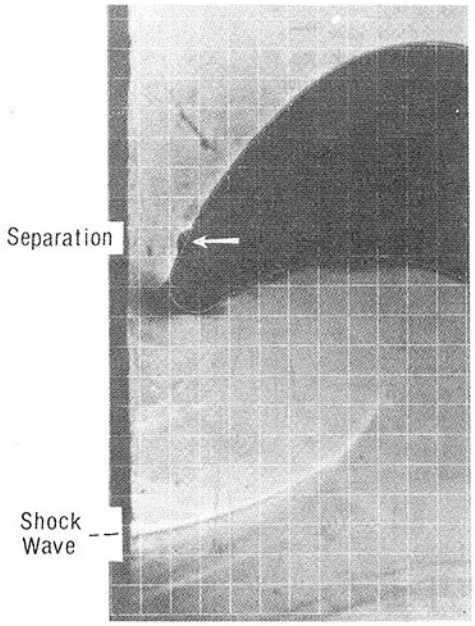


Fig. 6 Cycle time = 105 μs

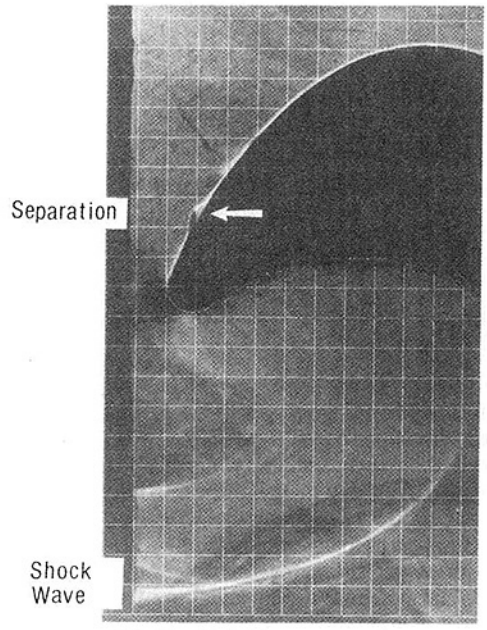


Fig. 7 Cycle time = 121 μs

fitted to the wake generator in the initial tests. This configuration effectively increases the spacing of successive disturbance cycles associated with each bar passing by a factor of four and allows complete relaxation of the boundary layer between cycles.

Schlieren Flow Visualization

The optical and electronic sequencing systems that allowed spark Schlieren photographs to be taken at any instant in a given cycle are described in [18]. Details of the photodetector-based, time-referencing system, used to define the start of each cycle accurately, and to relate the Schlieren photographs to the high-speed heat transfer and pressure measurements are also contained therein.

One of a sequence of Schlieren photographs is reproduced in Fig. 2. The wake from a 1.7-mm-dia bar is clearly visible as a highly turbulent band entering the top passage in the cascade, while the recompression shock wave shed by the bar is at this instant impinging on the suction surface of the bottom blade in the photograph.

The bar relative Mach number in the photo of Fig. 2 varied from 0.83 to 1.06 across the 50 mm span of the working section, with a nominal (mid-working section) value of 0.95. With the bar tip traveling slightly supersonically, only a weak bow shock wave standing well in front of the bar exists, whereas the recompression shock, behind the bar, is of significant strength. (Excellent Schlieren photographs of a cylinder in the transonic regime are contained in [24].)

The shock wave first impinges on the crown of the suction surface (between the positions of heat transfer gauges 7 and 8, Fig. 3(*C*)); the impingement point moves from there forward to the leading edge. The shock then effectively clears the blade, as the pressure surface curves rapidly away from the leading edge. Thus the shock does not impinge on the part of the suction surface downstream of the initial impingement point, and only lightly affects the pressure surface.

Downloaded 01 Jun 2010 to 171.66.16.71. Redistribution subject to ASME license or copyright; see http://www.asme.org/terms/Terms_Use.cfm

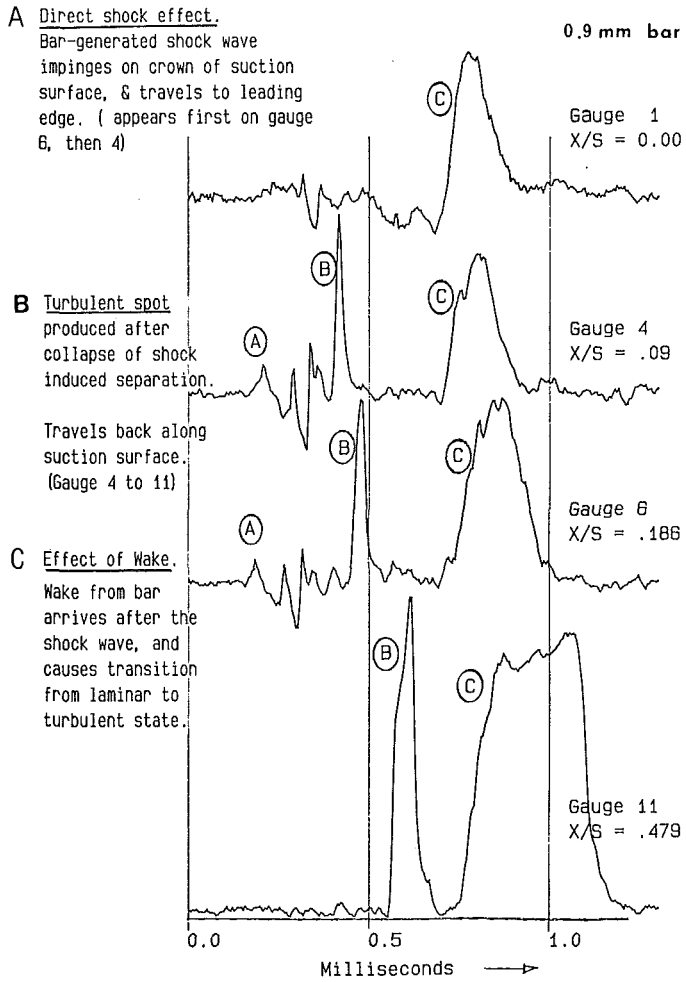


Fig. 8 Summary of effects of isolated wakes and shock waves on heat transfer

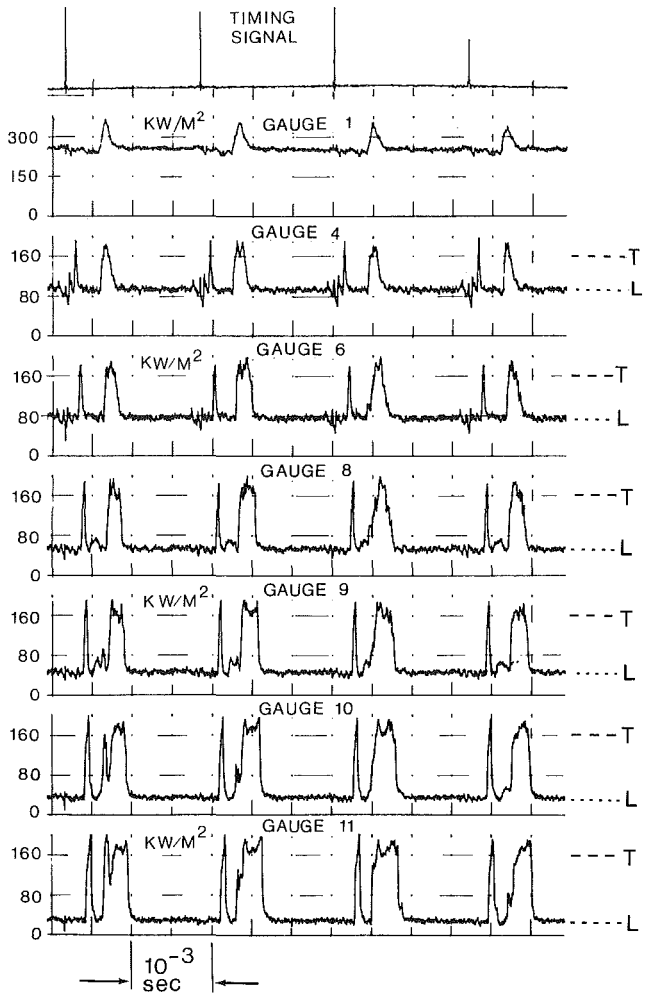


Fig. 9 Unaveraged heat transfer traces with isolated wake- and shock-wave passing (two 0.9 mm-dia-bars)

Analysis of the unsteady heat transfer records suggested that the direct impingement of the shock wave on the blade boundary layer produced little effect. A disturbance, in some way related to the shock wave (and considered in the next section), was found to propagate along the blade surface after the shock had passed. Reexamination of the sequences of Schlieren photographs uncovered the details of the shock interaction responsible for this phenomenon. Enlargements (Figs. 4–7) reveal that the interaction of the shock wave with the boundary layer at the leading edge results in the formation of a separation bubble at cycle time 63 μs. The sequence shows that the separation bubble is swept along the blade surface after the shock wave clears the leading edge. After progressing a short distance it appears to flatten and is absent in the next photograph of the sequence (cycle time 135 μs) and on succeeding photographs. (A smaller separation bubble was observed to be generated by the shock wave from the 0.9-mm-dia bar.)

Unsteady Heat Transfer Measurements

The locations of the thin film heat transfer gauges on the (machinable glass) model blade are marked on Fig. 3(*B*). Techniques for the measurement of surface heat transfer in a transient wind tunnel using thin film instrumented ceramic models and electronic analog circuitry are described in [25] and [26]. The 100 kHz bandwidth heat transfer instrumentation developed for this work is described in [27] and the data acquisition systems and heat transfer signal processing procedure are detailed in [28] and [18].

To clarify the discussion of the unsteady heat transfer signals (at the risk of spoiling the story!), the separate effects of isolated shock waves and wakes on the laminar boundary layer are summarized in the ensemble-averaged (over eight cycles) traces of Fig. 8.

A portion of the simultaneously sampled (at 200 kHz) heat transfer traces, with widely spaced wakes and shock waves (2 bars, dia 0.9 mm, fitted to the wake generator) is reproduced in Fig. 9. For comparison, the mean heat transfer rates associated with a *laminar* (marked *L*), and a fully *turbulent* (marked *T*) boundary layer (where the origin of transition for the latter was very close to the leading edge) are shown at each gauge position. At the top of the figure is the cycle reference time signal from the photodetector. Two large heat transfer disturbances during each cycle are evident, both involving a full transition from the laminar to the turbulent state. (That the transient high heat transfer level corresponds to that of a fully turbulent boundary layer is considered later, see Fig. 13.) The first, sharp spike-shaped transition is associated with the recompression shock wave from the bar, whereas the second "square" transition is associated with the wake. The sudden transition to turbulence, and relaxation back to a laminar state, induced by the shock wave appears first just after the leading edge; there is no noticeable effect at gauge 1, but the "spike" is already clearly defined by gauge 4.

Thereafter, the sudden transition and relaxation occurs at all downstream gauges at successively later times (Figs. 8 and 9). In contrast, the Schlieren photographs show that the shock does not impinge on the part of the suction surface downstream of the crown (i.e., gauge 8 and higher numbered

Downloaded 01 Jun 2010 to 171.66.16.71. Redistribution subject to ASME license or copyright; see http://www.asme.org/terms/Terms_Use.cfm

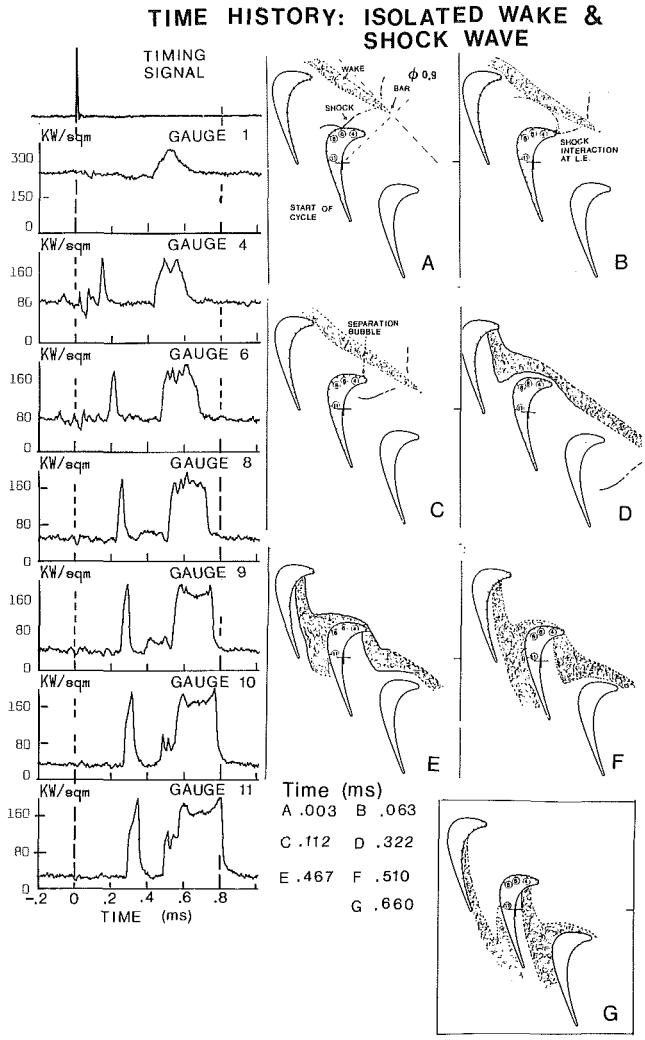


Fig. 10 Isolated wake- and shock-effects: relationship between measured heat transfer and position of shock wave and wake produced by bar (unaveraged traces: cycle 2, run 4159. 5 μs/sample). Diagrams of the flow (right) are labeled A, B, . . . G in order of increasing time.

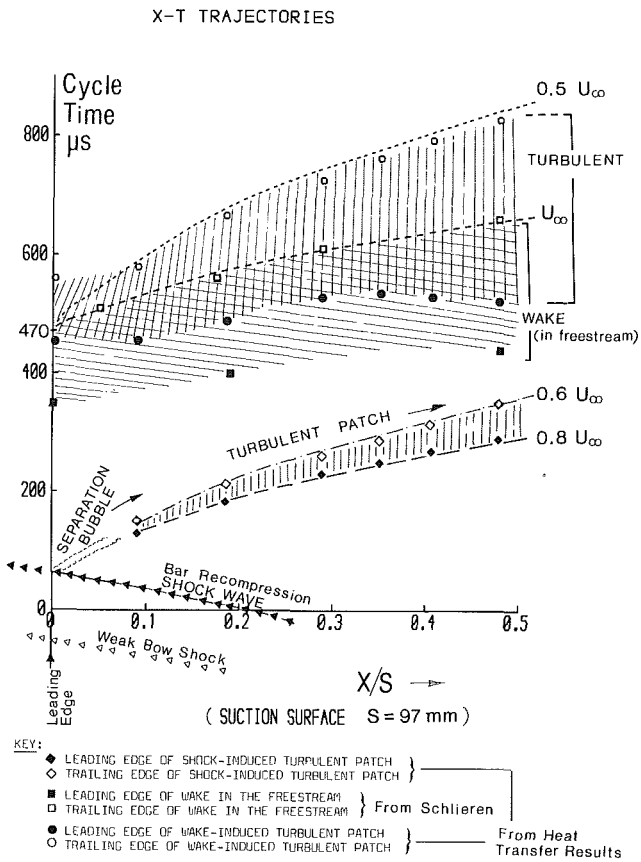


Fig. 11 Time response of boundary layer to shock and wake

gauges); further, the photographs show that the shock effectively travels upstream from point of first impingement on the crown (cycle time -10 μs) to the leading edge (cycle time 63 μs). The sharp transition at gauge 4 does not however begin until about 130 μs, i.e., at a time when the Schlieren photographs show that the shock wave has long cleared this surface of the blade.

These considerations led to the reexamination of the Schlieren photographs, which revealed the formation of the transient separation bubble by the shock wave at the leading edge. The unaveraged heat transfer traces corresponding to the second cycle in Fig. 9 have been plotted at an expanded scale in Fig. 10, together with tracings of the positions of the bar shock wave and wake at a number of successive instants. The portions of the wake and shock wave which have been traced directly from Schlieren photograhs for this size (dia 0.9 mm) bar are shown as full lines; the dotted lines show the positions predicted with the aid of a simple scheme described in [16].

On this expanded time scale it is possible to note that the direct impingement of the bar shock waves does produce a very slight oscillation in the heat transfer rate. This begins at ~ -0.1 ms, and corresponds in time exactly to the oscillations in the surface pressure measurements (see Fig. 12 later), which occur as the shock waves strike.

The upward spike in the heat transfer rate, beginning at gauge 4 at $+130$ μs cycle time, occurs after the collapse of the shock-induced separation. Consequently, the most likely explanation for this transient spike in heat transfer, from the laminar to the fully turbulent level and decrease back to the laminar level, is that a turbulent patch is left in the boundary layer after the collapse of the separation. This patch is convected down the blade surface, causing the spike in the heat transfer traces. Further support for the hypothesis that the formation of a turbulent patch in the boundary layer, caused indirectly by the bar shock wave, accounts for the observed transient heat transfer spike is provided by the observed rate of convection and spreading of the disturbance.

The convection and spreading of the heat transfer disturbance which develops after the decay of the shock-induced separation is shown in the X–T diagram of Fig. 11, obtained from the ensemble-averaged heat transfer traces. (The criterion used to define the instant at which the leading edge of the disturbance has reached a given point on the blade is that the heat transfer rate should have risen to 50 percent of the difference between the quiescent (laminar) level, and the maximum transient (turbulent) level attained.) The mean propagation velocity of the leading edge of the disturbance was found to be about 0.8 times the free-stream velocity, whereas the velocity of the trailing edge is about 0.6 times the free-stream velocity. This compares with propagation velocities of approximately 0.9 times, and 0.5 times the free-stream velocity for the leading and trailing edges, respectively, of turbulent spots in the flat-plate boundary layer [29] and [30]. Thus it was concluded that the transient spike in heat transfer rate was produced indirectly by the shock wave, by means of a turbulent patch remaining in the boundary layer after the collapse of the separation.

The arrival of the wake is later, and gives rise to characteristic "square wave" type transition from laminar to a quasi-steady turbulent state, and then reversal to laminar. (A value of 0.5 times the free-stream velocity was measured for

Downloaded 01 Jun 2010 to 171.66.16.71. Redistribution subject to ASME license or copyright; see http://www.asme.org/terms/Terms_Use.cfm

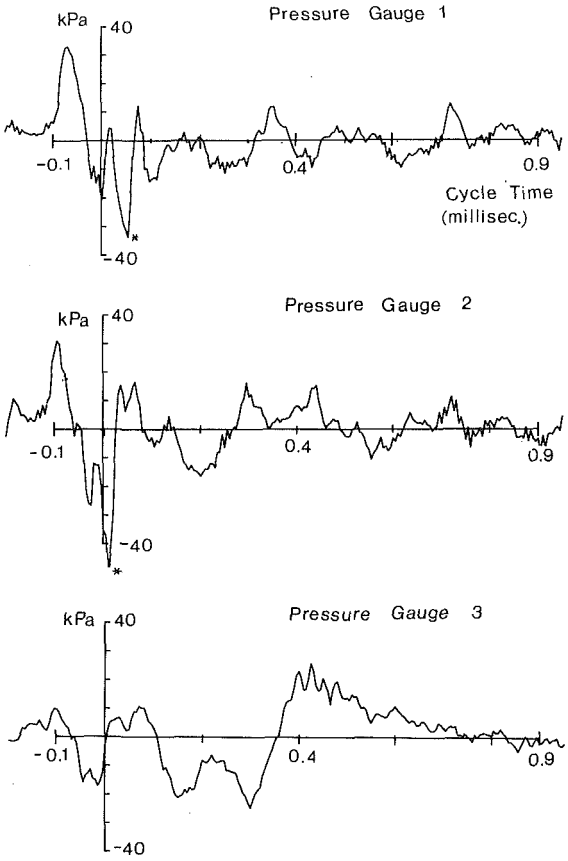


Fig. 12 Fluctuating surface pressure measurements with isolated wake- and shock-wave passing. The recompression shock from the bar impinges on gauge 2 at ~ 0.005 ms (marked *), and reaches gauge 1 at ~ 0.04 ms (also marked *). The pressure rise at gauge 2 at −0.1 ms is thought to be due to a weak bow shock wave from the bar tip. Mean levels: Upstream total pressure: 331 kPa
Gauge 1: 270 kPa
Gauge 2: 242 kPa
Gauge 3: 177 kPa

the propagation of the trailing edge of the turbulent boundary layer patch produced by the wake; the propagation of the leading edge of the wake-induced turbulent patch does not proceed uniformly, as the wake traveling in the free stream can inject turbulence ahead of that traveling in the boundary layer.)

The measurements clearly show that for points at increasing distances from the leading edge, there is an increasing delay between the time at which the disturbance in the free stream (whether the shock wave or wake) clears a given point, and the time at which the boundary layer fully recovers. The delay may be prolonged by the occurrence of some indirect response (such as the shock-induced leading edge separation), or be due merely to the fact that events are advected at a slower rate in the boundary layer than in the free stream.

The end result of this aspect of the unsteady boundary layer response on the heat transfer rate can be very considerable, in the case of shock- and wake-passing on an otherwise laminar boundary layer. The increased delay produced by this mechanism, before the boundary layer reverts to a laminar (low heat transfer) state, means that a greater proportion of each cycle is spent in the turbulent (high heat transfer) state, and consequently the mean heat transfer rate is much increased. The stretching of the turbulent patches may also decrease the transition length, by causing successive patches to merge at an earlier point on the blade surface to form a continuously turbulent boundary layer (see Fig. 14 later).

Very rapid jumps (of the order of 10 μs) from the laminar to the turbulent level of heat transfer are associated particularly with the shock-induced turbulent patch, but also with the wake. This suggests that the leading and trailing edge of the individual turbulent patches in the boundary layer caused by these disturbances may extend in a front roughly across the entire blade span, as the gauges extend across 20 percent of the span (and so are spanwise-averaging).

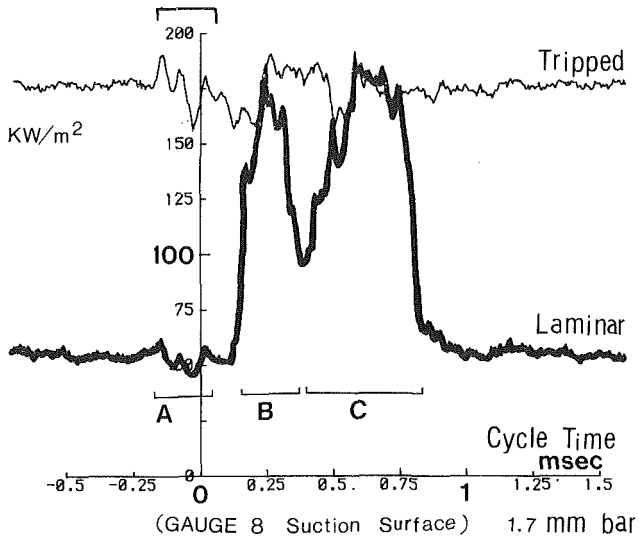


Fig. 13 ——— Shock-wave and wake-passing on a laminar boundary layer; ——— shock-wave and wake-passing on a tripped boundary layer (A, B, C refer to Fig. 8)

This feature contrasts with the unsteady heat transfer traces obtained in the case of "natural" transition initiated by relatively low (2 percent) intensity grid-generated turbulence. In this latter case (reported more fully in [18]), the transition is dominated by the irregular formation of turbulent spots at random locations across the span of the blade. The instantaneous heat transfer at a given gauge location is dependent on the fraction of the gauge covered by turbulent spots. Consequently, in the case of natural transition, where the gauge covering is virtually never complete in the initial transition zone, it is observed that the upward spikes in heat transfer rate do not attain the fully turbulent level. Apart from the clearly periodic nature of transition, and hence periodic heat transfer rate, caused by shock- and wake-passing, the complete spanwise extent of the turbulent patches, which is suggested by the heat transfer rate signals, further distinguishes the unsteady boundary layer with shock- and wake-passing flow, from that in natural transition.

Unsteady Pressure Measurements

Miniature Kulite type XCQ-062 pressure transducers with a frequency response of 0–100 kHz were used for the unsteady pressure measurements on the blade surface. The transducer faces were effectively mounted flush with the blade surface and were located at the positions shown in Fig. 3(*B*) in a model blade, corresponding to positions of three of the heat transfer gauges. It was found that the sensitivity of the pressure gauges did not alter during the 0.35 s warm (432 K) flow running time; experience where temperature sensitivity was a problem suggests that mounting the transducers in a brass model blade ensured that the sensors did not rise significantly in temperature during the run.

The fluctuating pressure traces in Fig. 12 (ensemble-averaged over nine cycles to reduce the noise), were obtained with two bars, diameter 1.7 mm fitted to the wake generator, and at a nominal relative Mach number of 0.91 (the larger bars being used to maximize the observed effects). All the pressure traces, particularly gauges 1 and 2, show a sharp rise in pressure which begins at about 100 μs before zero cycle time

Downloaded 01 Jun 2010 to 171.66.16.71. Redistribution subject to ASME license or copyright; see http://www.asme.org/terms/Terms_Use.cfm

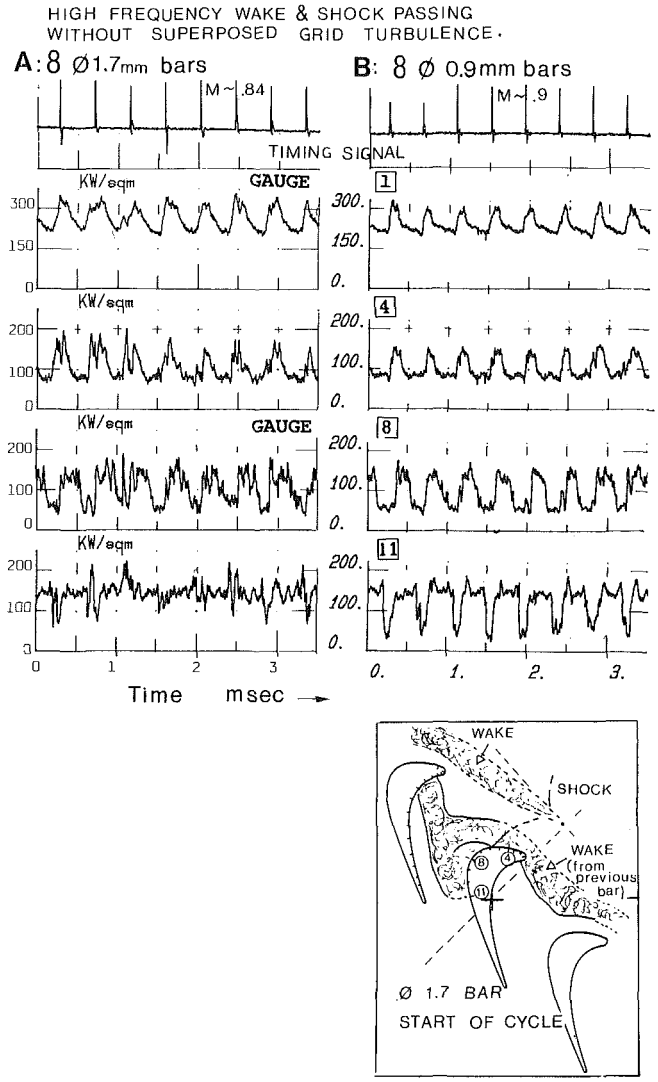


Fig. 14 Traces A show that the turbulent patches produced with the large bars fitted merge by gauge 11; traces B show that with the small bars, the patches do not merge by this point. Inset: Schlieren flow visualization shows that the shock wave from a bar moving in front of the cascade, and the wake from a previous bar interact simultaneously with the blade boundary layer.

at gauge 2, and later at 70 μs before zero cycle time at gauge 1. The pressure rise is not associated with the impingement of the recompression shock wave, which the Schlieren photographs show does not strike the blade near gauge 2 until about 3 μs after zero cycle time, and reaches gauge 1 approximately 30 μs later. Other Schlieren photographs [18] do however show a weak shock wave traveling well in front of the bar at a stand-off distance that corresponds almost exactly to a 100 μs lead over the recompression shock wave; this should account for the first pressure rise noted, and for the slight effect on the heat transfer traces of Figs. 8 and 10.

The second pressure rise, associated with the arrival of the recompression shock, is clearly visible; the time delay between the arrival of the shock over gauges 2 and 1 evident on the pressure traces agrees with that observed on the Schlieren photographs.

The leading edge of the wake, which follows the shock wave, arrives over the suction surface at about 300 μs cycle time, and the trailing edge of the wake has cleared pressure gauge 3 by about 600 μs. Only the signal from gauge 3 shows a marked rise in pressure which is associated with the wake.

Shock- and Wake-Passing on Tripped Boundary Layer

The effects of shock wave- and wake-passing on a laminar and a turbulent boundary layer at a given gauge position (gauge 8, X/S = 0.289), are compared in Fig. 13. For this test, the boundary layer was tripped by means of a strip of tape wrapped around the leading edge, extending across the entire span, and along the suction surface to an X/S of approximately 0.05. The traces (ensemble-averaged over eight cycles) were obtained with two large (1.7-mm-dia) bars fitted, again, to investigate the effects produced by stronger wakes and shock waves.

As on Fig. 8, which showed the ensemble-averaged effects of the shock and wake from the small (0.9-mm-dia) bar, the three major features are labeled A, B, and C. The mean heat transfer level from the tripped boundary layer was found to be practically identical to that occurring at the same gauge position, though where the early transition was instead produced by high (5 percent intensity) levels of grid turbulence [18]. Considering effects A, B, C in turn:

A: The direct action of the shock waves produces a more noticeable, though still small, effect on the tripped boundary layer than on the laminar boundary layer. (The shock waves considered are, however, comparatively weak.)

B: The turbulent patch produced indirectly by the bar shock wave causes momentarily the same heat transfer rate as the tripped boundary layer. This level is virtually identical with that associated with the turbulent patch caused by the shock from the small bar (e.g., Figs. 9 and 10). In comparison with the effects produced by the weaker shock from the smaller bar, however, this figure shows the larger bar results in a turbulent patch of considerably greater extent. This is expected, since the Schlieren records [18] show that the larger diameter bar results in a correspondingly larger separation bubble. Already by gauge 8, Fig. 13 shows that the trailing edge of the shock-induced turbulent patch is nearly overtaken by the wake-induced patch; the records [18] show that with the large bar, the patches have merged by gauge 11, which does not happen with the small bar (Figs. 8, 9, 10).

C: The wake causes a turbulent patch to develop in the laminar boundary layer; again, the extent of the patch produced by the wider wake from the larger bar is greater than that produced by the smaller bar. The wake has little effect on the tripped boundary layer.

Combined High-Frequency Wake- and Shock-Wave Passing

Extracts from the unsteady heat transfer measurements of the combined effects of wake- and shock-wave passing at high frequency are reproduced in Fig. 14. For these tests, eight bars were fitted to the wake-generator to model the actual close-spacing of the nozzle guide vanes in an engine. The diagram of the unsteady flow at a given instant, which has been traced from the Schlieren photographs of isolated wake-passing (with the 1.7-mm-dia bar), shows that at the engine-simulated spacing, both the shock wave and wake may directly impinge simultaneously on the blade boundary layer. In the absence of Schlieren photographs taken with eight bars fitted, it is not certain whether a transient separation is formed when the shock wave impinges simultaneously with the preceding wake. Heat transfer traces of isolated wakes and shock waves with high levels of free-stream turbulence suggest, however, that the turbulence in the wake may suppress formation of the separation (by such weak shock waves).

The results of a number of further studies of combinations of wake- and shock-wave passing, detailed in [18], have shown that even for the comparatively weak shock waves studied, the superposition of the shock wave with the wake noticeably alters the character of the unsteady transition on the early gauges (Nos. 4–8), from that associated with wake-passing alone.

Downloaded 01 Jun 2010 to 171.66.16.71. Redistribution subject to ASME license or copyright; see http://www.asme.org/terms/Terms_Use.cfm

The traces in Fig. 14, and the results described in previous sections, indicate that the wakes and shock waves essentially promote an unsteady transition, which leads eventually (within a distance depending on the disturbance type and level in the free stream), to a continuously turbulent boundary layer. In the case of shock-wave and wake-passing with the large (1.7-mm-dia) bars fitted, the traces marked "A" in Fig. 14 show that the boundary layer is continuously turbulent by gauge 11; in contrast, the turbulent patches, produced with the smaller bars fitted, have still not merged by this point, as shown by the traces "B."

The mean heat transfer rate at points on the suction surface where the turbulent patches have coalesced, forming a continuously turbulent boundary layer, was found to be almost the same as could be induced at the same point by initiating a "steady" transition with high levels of homogeneous free-stream turbulence, or by means of an artificial trip. This is suggested by the results of the tests with isolated wakes and shock waves; in all these cases, however, the origin of transition is similarly close to the leading edge on the test profile.

The character of the fully merged turbulent boundary layer is further affected by both the wakes and shock waves, with higher levels of unsteadiness resulting in higher fluctuations in heat transfer rate.

Conclusions

The impingement of an isolated shock wave on an otherwise laminar boundary layer on the suction surface of a representative turbine rotor blade was found to result in the formation of a separation bubble. Schlieren photographs showed the "bubble" progresses a short distance along the blade surface before collapsing. The unsteady heat transfer results indicated that a turbulent boundary layer patch remained after the disintegration of the bubble. It was thus concluded that the very high transient heat transfer rate associated with the shock was caused by this turbulent patch as it is swept down the boundary layer.

The significance of the development of transient disturbances in studies of both wake- and shock-wave passing has thus been demonstrated. In contrast the direct impingement of the shock was found to have little effect on the heat transfer rate. The effect of isolated shock waves and wakes on a tripped boundary layer was found to be slight, although the direct shock impingement resulted in a more noticeable fluctuation in the heat transfer rate than observed with a laminar boundary layer.

The effect of shock waves acting simultaneously with wakes, at high frequency, on the heat transfer rate to the blade suction surface has been studied. The results have shown that the successive disturbances produce turbulent boundary layer patches; depending on the extent of the free-stream disturbance, and the time history of the boundary layer response, the patches may eventually merge, forming a continuously turbulent boundary layer. The details of the interaction are considerably more complicated than those of either isolated wakes and shock waves; results of the further studies referred to indicate that the addition of even a comparatively weak shock wave may noticeably affect the transition process associated with a wake.

For these reasons, it is clear that shock wave-passing is a major source of the flow unsteadiness in the first stage turbine and may profoundly affect the heat transfer rate to the blades. As the contribution of shock wave-passing to the unsteadiness is of increasing importance with increasing nozzle guide vane exit Mach numbers, there is a need for a study of the effects of much stronger shock wave-passing than the comparatively weak shock wave-passing considered herein. Such studies seem likely to reveal more about the significance of unsteady separation as well as transition in determining the blade performance.

Acknowledgments

The authors are grateful to Rolls-Royce Limited, and the Science and Engineering Research Council of Great Britain for their support of this work.

References

1 Kemp, N. H., and Sears, W. R., "Aerodynamic Interference Between Moving Blade Rows," *J. Aero. Sci.*, Vol. 20, No. 9, Sept. 1953, pp. 585–597.

2 Parker, R., and Watson, J. F., "Interaction Effects Between Blade Rows in Turbomachines," *Proc. I. Mech. Eng.*, Vol. 186, No. 21, 1972.

3 Mitchell, N. A., "A Time-Marching Method for Unsteady Two-Dimensional Flow in a Blade Passage," *Int. J. Heat and Fluid Flow*, Vol. 2, No. 4, 1980.

4 Dunn, M. G., "Turbine Heat Flux Measurements: Influence of Slot Injection on Vane Trailing Edge Heat Transfer and Influence of Rotor on Vane Heat Transfer," ASME JOURNAL OF ENGINEERING FOR GAS TURBINES AND POWER, Vol. 107, No. 1, Jan. 1985, pp. 76–83.

5 Walker, G. J., and Oliver, A. R., "The Effect of Interaction Between Wakes from Blade Rows in an Axial Flow Compressor on the Noise Generated by Blade Interaction," ASME Paper No. 72-GT-15.

6 Gallus, H. E., Grollius, H., and Lambertz, J., "The Influence of Blade Number Ratio and Blade Row Spacing on Axial-Flow Compressor Stator Blade Dynamic Load and Stage Sound Pressure Level," ASME Paper No. 81-GT-165.

7 Walker, G. J., "The Unsteady Nature of Boundary Layer Transition on an Axial-Flow Compressor Blade," ASME Paper No. 74-GT-135, Zurich, 1974.

8 Evans, R. L., "Boundary Layer Transition and Separation on a Compressor Rotor Airfoil," ASME JOURNAL OF ENGINEERING FOR POWER, Vol. 104, Jan. 1982, pp. 251–253.

9 Larguier, R., "Experimental Analysis Methods for Unsteady Flows in Turbomachines," *Proc. 25th Annual International Gas Turbine Conference*, ASME, Mar. 1980.

10 Dring, R. P., Joslyn, H. D., Hardin, L. W., and Wagner, J. H., "Turbine Rotor-Stator Interaction," ASME Paper No. 82-GT-3.

11 Hodson, H. P., "Boundary Layer and Loss Measurements on the Rotor of an Axial-Flow Turbine," ASME Paper No. 83-GT-4, Phoenix, Ariz., Mar. 1983.

12 Hodson, H. P., D. Phil thesis, Cambridge University, 1983.

13 Samoilvich, G. S., and Yablokov, L. D., "Profile Losses With Unsteady Flow Through Turbomachine Cascades," *Teploenergetika*, Vol. 18, No. 4, 1971, pp. 73–75.

14 Pfeil, H., Herbst, R., and Schroeder, T., "Investigation of the Laminar-Turbulent Transition of Boundary Layers Disturbed by Wakes," ASME Paper No. 82-GT-124.

15 Doorly, D. J., and Oldfield, M. L. G., "Simulation of Wake-Passing in a Stationary Turbine Rotor Cascade," Paper submitted to the A.I.A.A. J.P.P.

16 Doorly, D. J., Oldfield, M. L. G., and Scrivener, C. T. J., "Wake-Passing in a Turbine Rotor Cascade," to be presented at the AGARD Symposium on Heat Transfer and Cooling in Gas Turbines, 1985.

17 Ashworth, D. A., LaGraff, J. E., Schultz, D. L., and Grindrod, K. J., "Unsteady Aerodynamic and Heat Transfer Processes in a Transonic Turbine Stage," ASME JOURNAL OF ENGINEERING FOR GAS TURBINES AND POWER, Vol. 107, No. 4, Oct. 1985, pp. 1022–1030.

18 Doorly, D. J., D. Phil thesis, Oxford University, 1983.

19 Jones, T. V., Schultz, D. L., and Hendley, A., "On the Flow in an Isentropic Light Piston Tunnel," ARC, R and M, 3731, 1973.

20 Jones, T. V., Schultz, D. L., Oldfield, M. L. G., and Daniels, L. C., "A New Transient Facility for the Measurement of Heat Transfer Rates," A.G.A.R.D., CP-229, *High-Temperature Problems in Gas Turbine Engines*, Ankara, 1979.

21 Nicholson, J. H., D. Phil thesis, 1981, Oxford University.

22 Schultz, D. L., Horton, G., and Forest, A., "Heat Transfer Measurements with Film Cooling on a Turbine Blade Profile in Cascade," to be presented at the ASME Gas Turbine Conference, Houston, Texas, 1985.

23 Horton, F. G., D. Phil thesis, to be published 1985, Oxford University.

24 Van Dyke, M., *An Album of Fluid Motions*, Van Dyke Press.

25 Schultz, D. L., and Jones, T. V., "Heat Transfer Measurements in Short Duration Hypersonic Facilities," A.G.A.R.D., AG-165, 1973.

26 Schultz, D. L., Jones, T. V., Oldfield, M. L. G., and Daniels, L. C., "Measurement of the Heat Transfer Rate to Turbine Blades and N.G.V.'s in a Transient Cascade," Paper EC-12, 6th International Heat Transfer Conference, Toronto, 1978.

27 Oldfield, M. L. G., Burd, H. J., and Doe, N. G., "Design of Wide-Bandwidth Analogue Circuits for Heat Transfer Instrumentation in Transient Tunnels," *Proc. 14th ICHMT Symposium on Heat and Mass Transfer in Rotating Machinery*, Dubrovnik, Aug. 1982.

28 Oldfield, M. L. G., Jones, T. V., and Schultz, D. L., "On-Line Computer for Transient Turbine Cascade Instrumentation," *I.E.E.E. Transactions on Aerospace and Electronic Systems*, Vol. AES-14, No. 5, Sept. 1978, pp. 738–749.

29 Wygnanski, I., Sokolov, M., and Friedman, D., "On a Turbulent Spot in a Laminar Boundary Layer," *J.F.M.*, Vol. 78, part 4, 1976, pp. 785–819.

30 Schubauer, G. B., and Klebanoff, P. S., "Contributions on the Mechanics of Boundary-Layer Transition," National Bureau of Standards, Report No. 1289, 1956.

Downloaded 01 Jun 2010 to 171.66.16.71. Redistribution subject to ASME license or copyright; see http://www.asme.org/terms/Terms_Use.cfm

T. Wang
Department of Mechanical Engineering,
Clemson University,
Clemson, S.C.

T. W. Simon
Department of Mechanical Engineering,
University of Minnesota,
Minneapolis, Minn.

J. Buddhavarapu
TSI, Inc.,
St. Paul, Minn.

Heat Transfer and Fluid Mechanics Measurements in Transitional Boundary Layer Flows

Experimental results are presented to document hydrodynamic and thermal development of flat-plate boundary layers undergoing natural transition. Local heat transfer coefficients, skin friction coefficients, and profiles of velocity, temperature, and Reynolds normal and shear stresses are presented. A case with no transition and transitional cases with 0.68 percent and 2.0 percent free-stream disturbance intensities were investigated. The locations of transition are consistent with earlier data. A late-laminar state with significant levels of turbulence is documented. In late-transitional and early-turbulent flows, turbulent Prandtl number and conduction layer thickness values exceed, and the Reynolds analogy factor is less than, values previously measured in fully turbulent flows.

Introduction

Transition from laminar to turbulent boundary layer flow effects significant increases in local wall shear stresses and convective heat transfer rates. These increases must be appropriately factored into the design of many types of equipment, e.g., compressor and gas turbine blades. Presently, the poor predictability of the location and streamwise coverage of transition on gas turbine blades results in either reduced longevity of the blade or reduced performance of the engine below design objectives. This inability to predict transition is partially due to a lack of experimental data, both heat transfer and hydrodynamic, which isolate the separate effects on transition. This, in turn, has retarded the endeavor to understand the transition process and to develop general prediction models. Some effects known to influence boundary layer transition are free-stream turbulence, acoustic disturbances, surface vibration, surface roughness, streamwise acceleration, cross-stream straining, film cooling injection, separation, compressibility effects, and streamwise curvature. Some characteristics of boundary layer transition that tend to exacerbate the difficulty in understanding the fundamentals are three-dimensionality, unsteadiness, interaction of several influences, and sensitivity to small influences not under the control of the experimenter or known to the designer. As much as 50–80 percent of a typical turbine blade surface is covered by flow undergoing transition [1]. It is therefore important that a program of systematic, well-controlled experimental studies be initiated to provide the data base necessary for developing improved transition prediction models.

The present experiment focuses on the effect of free-stream turbulence intensity and includes measurements of surface heat transfer rates as well as profiles of mean and turbulence quantities in the laminar, transitional, and turbulent flows. This test is the beginning of a series of tests that isolate the effects of free-stream turbulence intensity, streamwise acceleration, and streamwise curvature on transition. It is part of an ongoing series of experimental investigations on gas turbine heat transfer at the Heat Transfer Laboratory of the University of Minnesota.

As early as 1936, G. I. Taylor [2] analyzed free-stream turbulence effects on transition for flow past a sphere. His work is believed to be the first where the effects of free-stream disturbances on transition were discussed. Early experiments of boundary layer transition on a flat plate were made by Hall and Hislop [3]. Van Driest and Blumer [4] developed an early prediction model by assuming that the breakdown of laminar flow occurs whenever the maximum of the local cross-span vorticity in the boundary layer becomes sufficiently distant from the wall. Their model, which accounts for free-stream turbulence and streamwise acceleration effects, is still considered one of the better predictors of transition [5]. Several constants in their model were determined from existing experimental data. Later, as more data became available, these constants were adjusted somewhat, e.g., [6]. A forced-oscillation method for investigating boundary layer transition was introduced by Schubauer and Skramstad [7] to demonstrate the growth and evolution of disturbances in laminar flows. They concluded that when the free-stream turbulence intensity exceeds 0.1 percent, transition is caused directly by random disturbances and is not precluded by selective amplification of sinusoidal oscillations (as with lower-disturbance flows). Klebanoff, Tidstrom, and Sargent [8] observed that, in low-disturbance flows, an initially two-dimensional wave, the growth of which is predictable by linear theory of instability, develops three dimensions – a feature of strong nonlinear development. The termination of this development is indicated by a sudden increase in the wave amplitude. Spangler and Wells [9] studied the importance of

Contributed by the Gas Turbine Division of THE AMERICAN SOCIETY OF MECHANICAL ENGINEERS and presented at the 30th International Gas Turbine Conference and Exhibit, Houston, Texas, March 18–21, 1985. Manuscript received at ASME Headquarters, December 27, 1984. Paper No. 85-GT-113.

Copyright © 1985 by ASME
Downloaded 01 Jun 2010 to 171.66.16.71. Redistribution subject to ASME license or copyright; see http://www.asme.org/terms/Terms_Use.cfm

the frequency spectra and the origin of the disturbance (e.g., acoustic) on transition in low free-stream turbulence intensity flows (<0.10 percent). They determined the disturbance intensity, versus disturbance frequency, required to initiate transition. A review of the understanding and prediction of transition, current to 1969, was presented by Tani [10].

An empirical model for predicting the onset and end of transition was proposed by Hall and Gibbings [11]. It included the effects of free-stream turbulence and streamwise pressure gradient. Recently Abu-Ghannam and Shaw [12] developed an empirical relationship for the prediction of the start of transition, the end of transition and the development of momentum thickness, shape factor, intermittency factor, and skin friction coefficient during transition. The sole parameters in their model are the free-stream turbulence intensity and the free-stream acceleration.

In the gas turbine environment, free-stream turbulence intensities are in the range of 5–20 percent. To the authors' knowledge, few detailed transition studies have been conducted in such highly turbulent flows. Dyban, Epik, and Suprun [13] investigated the structure of laminar boundary layers developing under elevated free-stream turbulence intensities from 0.3 percent to 25.2 percent. They found a peak in oscillation magnitude within the boundary layer, believed to be caused by the penetration of free-stream fluctuations. This peak amplitude reached a maximum in the 4.5 percent free-stream turbulence intensity case. The waveform of this oscillation was not sinusoidal but more turbulentlike with energy distributed across a wide range of frequencies. They called the late-laminar boundary layers which show this behavior "pseudolaminar" to separate them from the laminar and transitional boundary layers, which are considered to be fundamentally different. The authors know of few other experiments where the turbulence (oscillation) development for natural transition through the laminar, pseudolaminar, transitional, and turbulent stages was documented [14, 15]. More on transition can be found in [16–19].

The foregoing studies are for isothermal flows. The following are studies of heat transfer in transitional flows: Junkhan and Serovy [20] conducted experiments on a constant-temperature flat plate to investigate the effect of free-stream turbulence intensity on heat transfer through transitional boundary layers. They found no effects of free-stream turbulence intensity within the laminar flow – only the well-documented effect on the location of transition. Simon and Moffat [21] measured heat transfer rates in a boundary layer that was undergoing transition on a convex-curved surface. They concluded that the onset of transition was delayed and that the evolution of transition was retarded by convex curvature. Recently, Blair [22, 23] conducted several tests on a uniformly heated flat wall where free-stream turbulence intensities were varied over the range 0.7 to 6.0 percent. He concluded that fully turbulent mean velocity profiles were established faster than fully turbulent mean temperature profiles. This indicates a breakdown of the Reynolds analogy and a larger effective turbulent Prandtl number in the very early turbulent flow than in a mature turbulent flow. He also showed that the transition Reynolds number is insensitive to streamwise acceleration for $\Lambda_\theta < 0.08$ over this turbulence intensity range. This is consistent with the van Driest and Blumer model.

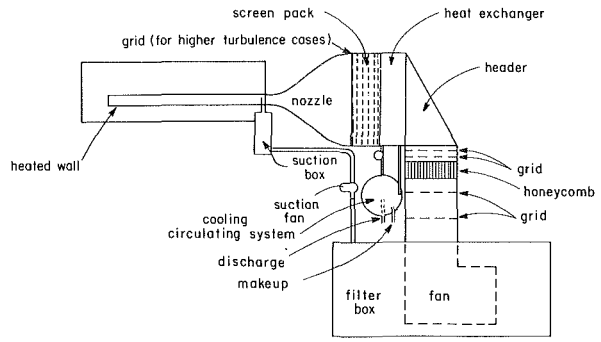


Fig. 1 Plan view of test facility

In the present study, Reynolds streamwise-normal stresses were measured in addition to surface heat transfer coefficients and mean velocity and temperature profiles to show the evolution of the turbulence structure inside laminar, transitional, and turbulent boundary layers during natural transition. Reynolds shear stresses were measured in the early-turbulent boundary layer. Two free-stream turbulence intensity levels, 0.68 and 2 percent, were investigated. The streamwise pressure gradients in the three tests were small, and believed to be insignificant, with $\Lambda_\theta < 0.02$. Values in excess of 0.05 are needed to have a perceptible effect on the location of transition for these free-stream turbulence intensity values [4].

Experimental Facility

The test program employed the open-circuit, boundary layer heat transfer facility shown in Fig. 1. Air is first drawn through 5-μm filter material to a large centrifugal blower, then forced through a finned-tube heat exchanger and screen pack assembly to enter the test region. Free-stream nominal velocities were 12 m/s and 35 m/s, uniform to ±0.2 percent across the tunnel cross-section, for the present experiment, and the free-stream temperature was nominally 25°C,

Nomenclature

c_p = specific heat
$C_f/2$ = skin friction coefficient
Pr = Prandtl number
Pr_t = turbulent Prandtl number
$\dot{q}''$ = heat flux
Re_x = x-Reynolds number
Re_{δ^*} = displacement thickness Reynolds number
Re_θ = momentum thickness Reynolds number
St = Stanton number
TI = turbulence intensity
$T^+ = \dfrac{(T_w - T)\sqrt{\tau_w/\rho}}{\dot{q}''/(\rho c_p)}$
u,v = streamwise and cross-stream velocity
u', v' = streamwise and cross-stream velocity fluctuations
$\bar{u}$ = streamwise mean velocity
U_τ = friction velocity ($\equiv\sqrt{\tau_w/\rho}$)
$U^+ \equiv \bar{u}/U_\tau$
x = streamwise distance
y = cross-stream distance from the wall
Y^+ = inner coordinate $\equiv \dfrac{yU_\tau}{\nu}$
Y_{cl}^+ = conduction layer thickness in inner coordinates
z = spanwise distance from center span

Greek

ρ = density
τ = shear stress
ν = kinematic viscosity
δ_{99} = boundary layer thickness based on 99 percent of the free-stream velocity
δ^* = displacement thickness
θ = momentum thickness
Λ_θ = acceleration parameter, $\dfrac{\theta^2}{\nu}\dfrac{dU_\infty}{dx}$

Subscripts

∞ = at free stream
w = at wall

Downloaded 01 Jun 2010 to 171.66.16.71. Redistribution subject to ASME license or copyright; see http://www.asme.org/terms/Terms_Use.cfm

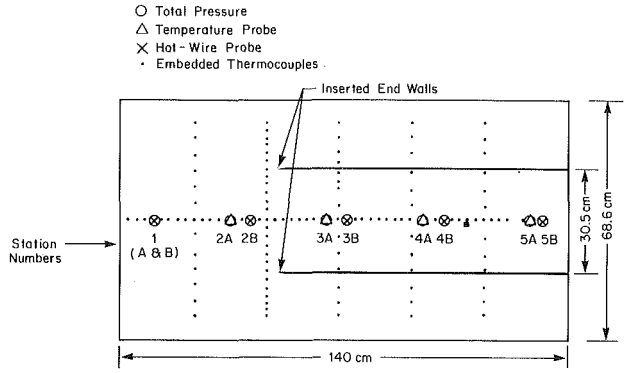


Fig. 2 Measurement locations – heated boundary layer flow data taken at "A" stations and isothermal flow data taken at "B" stations

Table 1 Measurement uncertainties

Variables	Range	Uncertainty
St in the laminar & turbulent region	$0.2 \sim 5.x10^{-3}$	± 2%
St in the transition region	$0.2 \sim 2.x10^{3}$	± 3%
Mean Velocity	0 ~ 35 m/s	± 2%
Mean Temperature	20 ~ 40 C	± 0.1°C
$\sqrt{\overline{u'^2}}/U_\infty$	0.1 ~ 11%	± 5%
$\overline{u'v'}/U_\tau^2$	0 ~ 1	± 10%
C_f (other than in transition)	$0.2 \sim 2.0x10^{-3}$	± 5%

uniform to ± 0.05°C and constant to within ± 0.2°C. The room temperature was held constant to within ± 0.5°C. The test region is rectangular, 11.4 cm × 68.6 cm (4.5 inches × 27 inches) in cross-section, and 1.4 m (55 inches) long. The test section was designed and constructed so that transition data with streamwise wall curvature could eventually be taken. For this straight-wall study, it was necessary to insert endwalls beginning with sharp leading edges after 50 cm of the streamwise length and continuing throughout the remainder of the test region. These inserted endwalls reduced the effective span from 68.6 cm to 30.5 cm as shown in Fig. 2. One side wall of the tunnel, 68.6 cm × 1.4 m, was heated to nominally 10°C above the oncoming air temperature with a heat flux of 240 W/m^2, uniform to ± 1.0 percent.

This is the heated, flat wall upon which data for the present study were taken. Strong suction was applied at the leading edge of this wall to remove the boundary layer which grows inside the nozzle. Therefore, the initial flow on the test wall simulated the classic sharp-leading-edge configuration. The heated test wall is flexible so that transition studies with varying degrees of streamwise curvature could later be taken. The description of this heated wall follows. It begins with the surface adjacent to the room (the outside) and proceeds to the test surface (the inside). A 15.2-cm (6-in.)-thick fiberglass insulation pad was installed on the outside of a 5-mm (3/16-in.)-thick polycarbonate plastic (Lexan) support wall to minimize heat transfer to the room. Attached to the inside of the support wall is a 1-mm (0.045-in.)-thick heating pad constructed of heater foil sandwiched between glass cloth and silicon rubber sheets. The foil provides Joule heating when energized with 60-cycle a-c current using variable transformer voltage control. Bonded to the heater is a 0.25-mm (10-mil)-thick rubber spacer within which 120, 3-mil, chromel-constantan thermocouple wires were embedded. These thermocouples are distributed along the wall center span, with a 2.54-cm (1-in.)-spacing and were uniformly distributed across the span at five streamwise locations (see Fig. 2). Covering the thermocouples, in contact with their junctions, and bonded to the spacer, is a 0.1-mm (4-mil)-thick sheet of stainless steel. Bonded to the stainless steel and providing the test surface is a 0.025-mm (1-mil)-thick sheet of reflective film. This film, type P-19 manufactured by the 3M Company, was added to reduce the uncertainty attributable to radiation exchange with the test wall.

The free-stream and boundary layer mean temperatures were measured with 3-mil thermocouples constructed of wire from the same manufacturing run as that of the embedded thermocouples. The thermocouples were calibrated in the tunnel against a calibrated, precision thermister known to be stable by continued comparison against a platinum resistance thermometer in the calibration laboratory. Mean velocity profiles were measured using 0.7-mm (28-mil)-o.d. boundary layer total pressure tubes, 0.063-mm (2.5-mil) wall static ports, and a ±9 cm H_2O maximum pressure, reluctance-type, diaphragm differential pressure transducer (Validyne DP-45). Mean velocity measurements were taken in both heated and isothermal flows. Small variations in properties were included in the data reduction; the mean of the wall and free-stream temperature was used for property evaluation. Reynolds normal stresses were obtained in the isothermal flow with a horizontal hot wire (TSI Model 1218, T1-5) maintained at a constant temperature. Reynolds shear stresses were taken in isothermal flows using a boundary layer X-wire (TSI Model 1243, T 1.5) with constant-temperature operation. The anemometer bridges were TSI Models 1050 and IFA-100. The pressure transducer and anemometer signals were digitized with an HP Model 3437A, 3-1/2 digit voltmeter. Because only one digitizer was available, the shear stress measurements were taken one-wire-at-a-time. This is essentially the rotating slant-wire technique [24]. Thermocouple EMF values were recorded with a Fluke Model 2205A multichannel scanner. The total power supplied to the heater was computed as the product of a power factor, the measured voltage across the heater, and the current through the heater computed from the measured voltage across a precision resistor. The power factor, measured prior to the test, was within 0.1 percent of 1.0. Data were reduced in an HP Series 200 Model 16 laboratory computer.

Corrections were made within the data reduction program for heat transfer through the fiberglass insulation, radiation exchange with the test wall, and streamwise conduction within the heated wall. A complete uncertainty analysis of the wall heat transfer data was also made within the data reduction program. This analysis employed the Kline and McClintock [25] methodology for computing the propagation of uncertainties and the Moffat [26] methodology for incorporating known contributors to bias error. Nominal values of wall heat flux uncertainty are presented along with other relevant uncertainties in Table 1. Details of the heater design, data reduction techniques, and wall heat flux uncertainty analysis can be found in [27, 28].

Experimental Results and Discussion

The results of the following three cases are presented herein:

A. The Laminar Baseline Case (Turbulence Intensity, $TI = 0.3$ percent). The laminar boundary layer extends over the entire test length. Transition correlations and the unsteadiness of the data indicate that transition is about to begin at the channel exit.

B. The Lower Free-Stream Turbulence Intensity Case ($TI = 0.68$ percent). The velocity is increased from that of Case A and the onset of transition is moved to about one-third of the test length.

C. The Higher Free-Stream Turbulence Intensity Case ($TI = 2.0$ percent). A coarse grid is inserted upstream of the

Downloaded 01 Jun 2010 to 171.66.16.71. Redistribution subject to ASME license or copyright; see http://www.asme.org/terms/Terms_Use.cfm

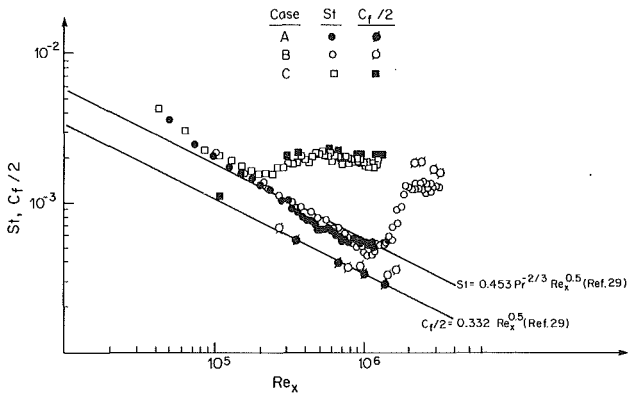


Fig. 3 Stanton numbers and skin friction coefficients versus x-Reynolds number

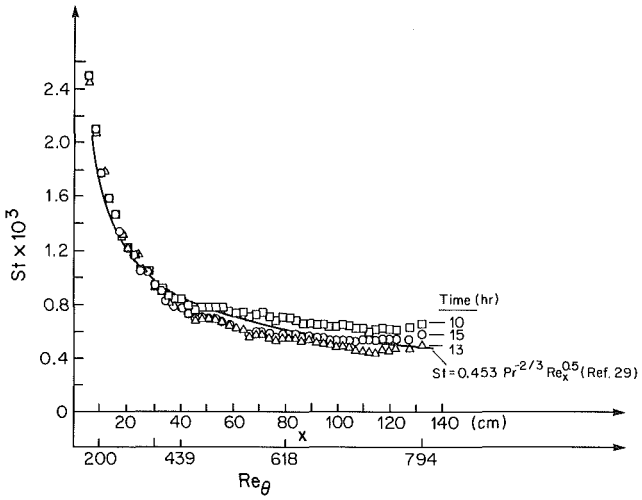


Fig. 4 Long-period unsteadiness of Stanton number data for Case A

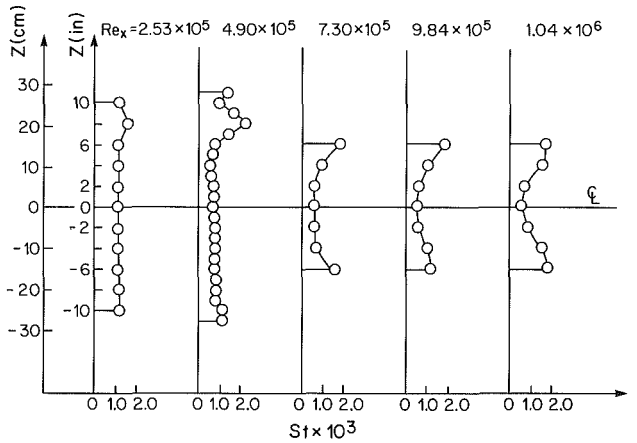


Fig. 5 Spanwise distributions of local Stanton number for Case A (baseline case)

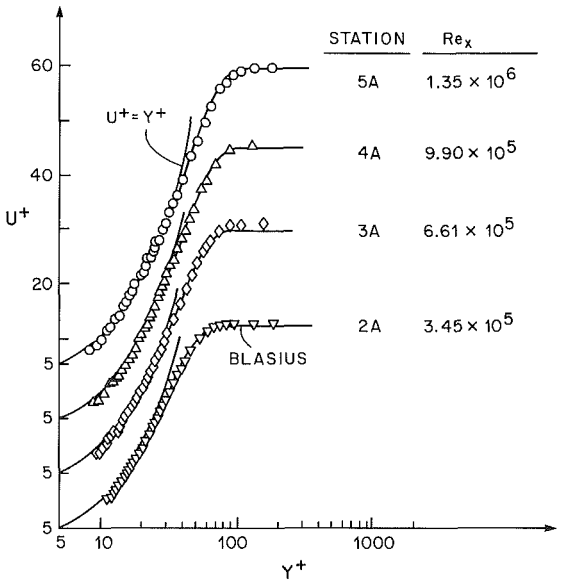


Fig. 6 Mean velocity profiles for Case A

nozzle and the free-stream velocity is reduced to move the onset of transition into the first one-third of the test length.

The Laminar Baseline Case – Case A. The test facility was first qualified by conducting an all-laminar boundary layer test. A comparison of the results to laminar boundary layer theory [29], Fig. 3, shows that the Stanton numbers and skin friction coefficient values for this case follow the laminar correlation well, except at the very end of the test where it appears that transition is near. Stanton numbers for this and the subsequent cases were calculated directly from the measured (and corrected) wall heat flux and the measured local free-stream velocity, free-stream temperature, and wall temperature. The wall temperature was taken as an average of five readings over a period of 15 min. Skin friction coefficients were computed from the wall shear stress; which, in turn, is calculated from the local near-wall velocity gradient $\tau_w = \mu(du/dy)_w$ and the local free-stream velocity. One unanticipated result in this experiment was the long-period unsteadiness shown in Fig. 4. Three sets of data were taken in one 15-hr run. The first was taken after a 10-hr stabilization period as was also required for case B and case C. As shown, the data fluctuated ±10 percent about the laminar line. The mean data of the 5-hr data-taking period follow the laminar correlation well. The curve labeled "15-hr" is the data shown on Fig. 3. The theoretical stability limit for laminar boundary layer flow for a flat plate is $Re_\theta = 200$ [30] which, for this case, corresponds to 10 cm of development length and an x-Reynolds number of 0.97×10^5. Note that the Stanton number data remain repeatable for the first 30 cm ($Re_\theta = 400$) within the 5-hr data-taking period. The unsteadiness of this flow is presumed to be due to the sensitivity of this boundary layer to small disturbances to the flow in the face of a low free-stream turbulence intensity of 0.3 percent. Possibilities would include the small variations in free-stream and wall temperatures (within the stated uncertainties) or small uncontrolled variations in tunnel vibration. Subsequent runs taken under these conditions over a period of one month showed that this long-period unsteadiness is repeatable. Long-period unsteadiness was not observable in cases B and C of this study, which have turbulence intensities of 0.68 and 2.0 percent, respectively.

Spanwise variations of Stanton number for five streamwise positions are shown on Fig. 5. At the first two positions, the heat transfer coefficient is very spanwise-uniform; the stable laminar boundary layer is two-dimensional. Transition appears to begin as streaks off center span. It symmetrically migrates toward the center span. Transition is believed to be triggered in the three-dimensional corner flow region near the end wall. It then is believed to propagate by acoustic disturbance toward the center as discussed in [31]. No spanwise data are shown for the region beyond the inserted endwalls (see Fig. 2).

At the end of the test section, the momentum thickness Reynolds number is approximately 800. According to the transition model of van Driest and Blumer [4], transition should begin about $Re_\theta = 890$ for a case having a free-stream

Downloaded 01 Jun 2010 to 171.66.16.71. Redistribution subject to ASME license or copyright; see http://www.asme.org/terms/Terms_Use.cfm

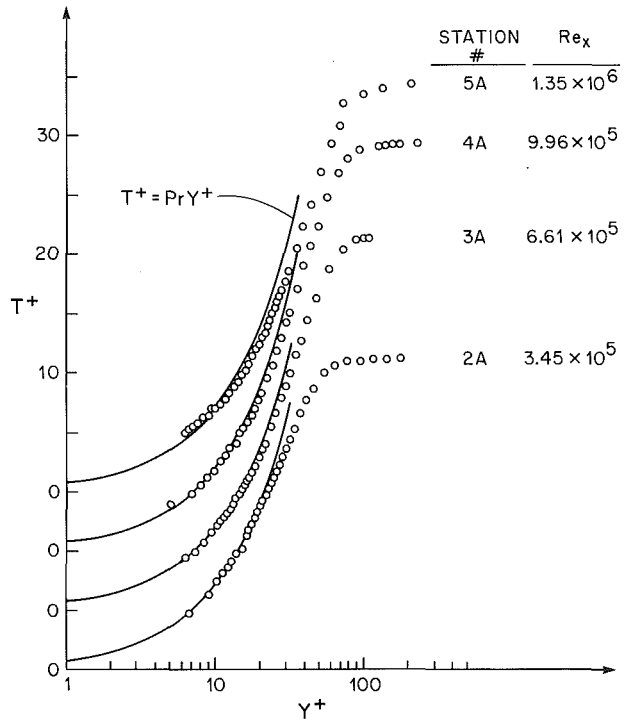


Fig. 7 Mean temperature profiles for Case A

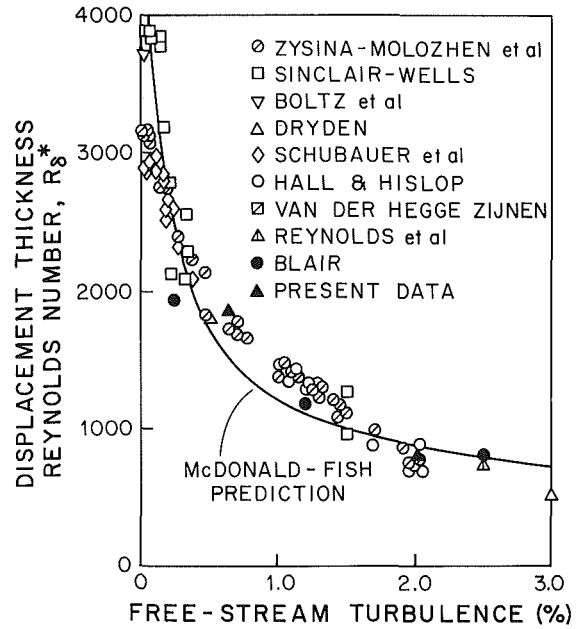


Fig. 8 Effect of free-stream turbulence on transition Reynolds number for zero pressure gradient flow (from [22])

turbulence intensity of 0.3 percent; the flow is very near transition.

Mean velocity and mean temperature profiles plotted in inner coordinates U^+ versus Y^+ and T^+ versus Y^+, are shown on Figs. 6 and 7, respectively. They appear to be typical laminar boundary layer profiles. Blasius velocity profiles are shown for comparison on Fig. 6. Mean velocity and temperature data were taken for this run and subsequent runs as time-averages over 30–40 s periods.

A thermal energy balance applied over the entire test length using the time-averaged Stanton numbers on the centerline assuming two-dimensional flow achieved closure to within 3 percent. This closure, the nearness of the Stanton number data to the laminar correlation, and the lack of premature

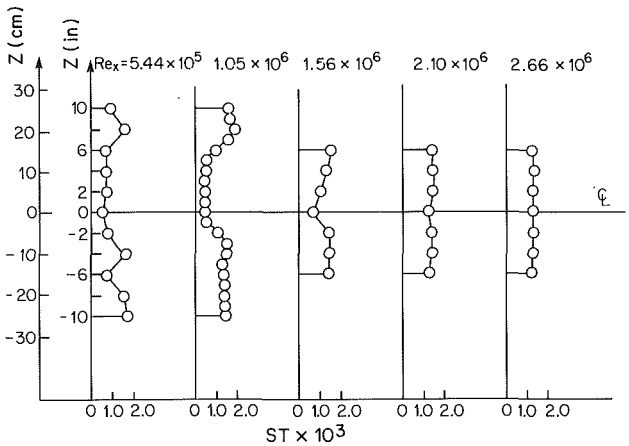


Fig. 9 Spanwise distribution of local Stanton number for Case B

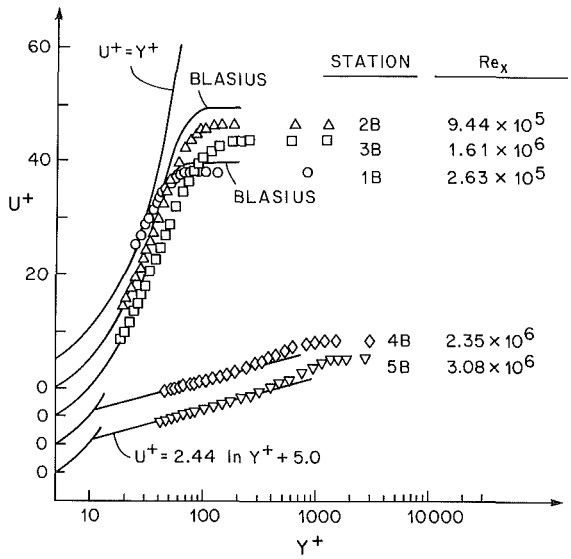


Fig. 10 Mean velocity profiles for Case B

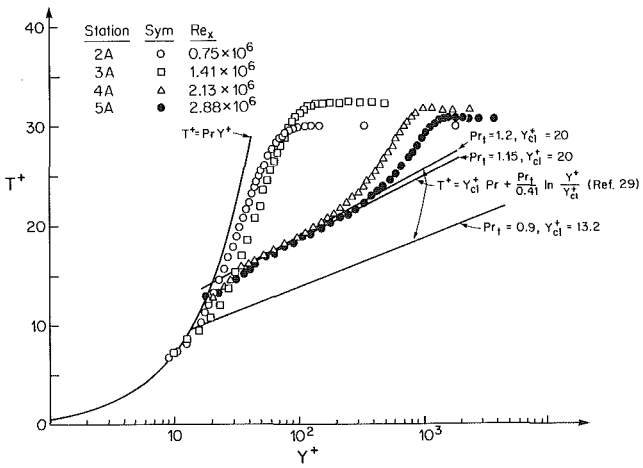


Fig. 11 Mean temperature profiles for Case B

transition in this case suggest that the facility is free of significant, uncontrolled disturbances, and that the measurements are free of significant bias error. A momentum balance was also attempted; the lack of closure was 30 percent. This poor closure is believed to be due to the sparsity and inaccuracy of the skin friction coefficients deduced from velocity profiles, the inability to measure time-averaged skin friction coefficients (as was done with the Stanton number

Downloaded 01 Jun 2010 to 171.66.16.71. Redistribution subject to ASME license or copyright; see http://www.asme.org/terms/Terms_Use.cfm

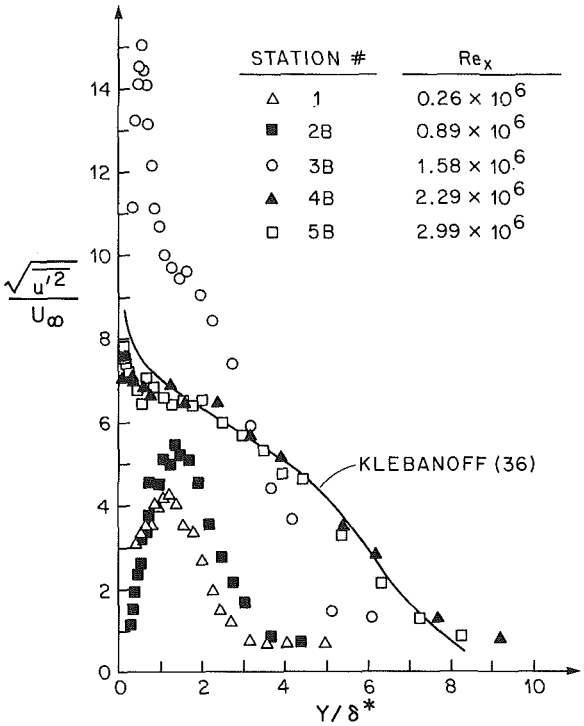


Fig. 12 Reynolds streamwise-normal stress profiles for Case B

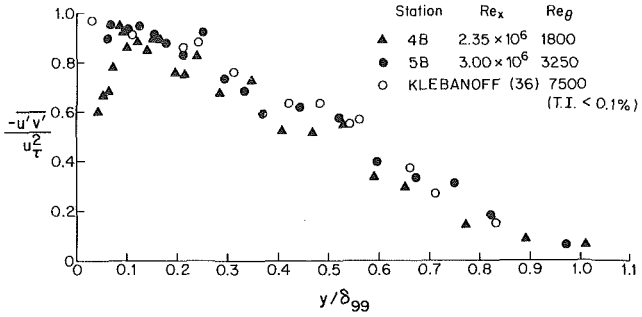


Fig. 13 Reynolds shear stress profiles for Case B

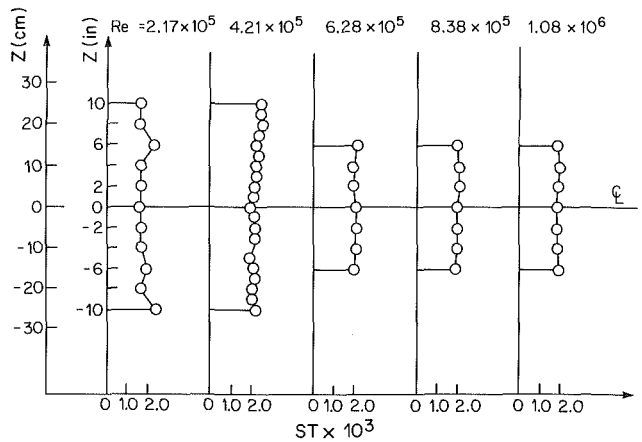


Fig. 14 Spanwise distributions of local Stanton number for Case C

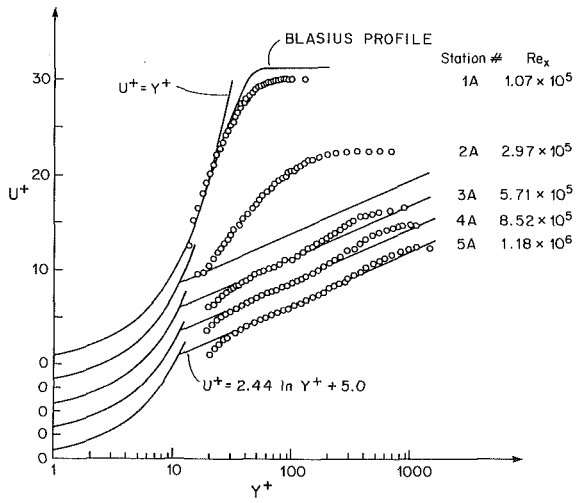


Fig. 15 Mean velocity profiles for Case C

data for the energy balance), and the inability to measure momentum thicknesses with low uncertainty. Note that because of the sparse skin friction data, a momentum balance from only the first profile station to the last could be taken. This required taking precise measurements of the momentum thickness in the very thin laminar boundary layer at the first station. Such a problem did not exist with the thermal energy balance, which was taken from the leading edge to the last station.

The Lower Free-Stream Turbulence Intensity Case – Case B. In the second case, the free-stream velocity was increased to nominally 35 m/s which moved the location of the beginning of transition to about one-third of the test length. The resulting free-stream turbulence intensity became 0.68 percent. Stanton number and skin friction coefficient data for this case are shown on Fig. 3. Transition, taken to be the beginning of the dramatic increase in heat transfer coefficient and shear stress, is shown to be at an x-Reynolds number of about 1.2×10^6. At this location the displacement thickness Reynolds number is 1890. Transition at this location is consistent with the van Driest and Blumer [4] model or the McDonald and Fish [32] model (shown on Fig. 8). The skin friction coefficient and Stanton number data follow the laminar correlation well. No significant change in the laminar data due to the increase in free-stream turbulence from that of case A is observable. Stanton number values have been previously shown to exceed $C_f/2$ values in a mature turbulent boundary layer [33, 34]. Spalding [33] showed that the value of the "Reynolds Analogy Factor," $2\,St/C_f$, for air is 1.2. The Reynolds analogy factor for the early-turbulent region of case B is about 0.75, however. This indicates a slower response of the heat transfer data in transition than that of the hydrodynamic data, as was observed by Blair [22]. It will subsequently be shown that the turbulent Prandtl number in the low-Reynolds-number turbulent flow for case B is considerably larger than 0.9, the value measured for mature turbulent boundary layers. Skin friction values for the laminar flow were calculated as discussed previously in case A. Two $C_f/2$ values, $Re_x = 1.4 \times 10^6$ and 1.6×10^6 (Fig. 3), were calculated assuming a laminar boundary layer though the profiles clearly indicate a beginning of transition (as will be discussed). The values shown, therefore, represent lower-bound values. $C_f/2$ values for turbulent flows were deduced from the law-of-the wall using the Clauser technique [35]. No direct measurements of wall shear stress were made.

Spanwise distributions of local Stanton number are shown in Fig. 9. At the first station, the boundary layer momentum thickness Reynolds number, 300, exceeded the stability limit of $Re_\theta = 200$, and is clearly showing signs of transition. These are observable as streaks of high local heat transfer coefficient off the center span. Downstream, these regions of early transition grow to effect transition on the centerline. A notable difference from the profiles shown for case A is the lack of symmetry. Transition at the center-span location is underway by the second profile and is complete by the fourth (Figs. 3 and 9). At the last station, effective turbulent cross-stream transport has restored two-dimensionality.

Downloaded 01 Jun 2010 to 171.66.16.71. Redistribution subject to ASME license or copyright; see http://www.asme.org/terms/Terms_Use.cfm

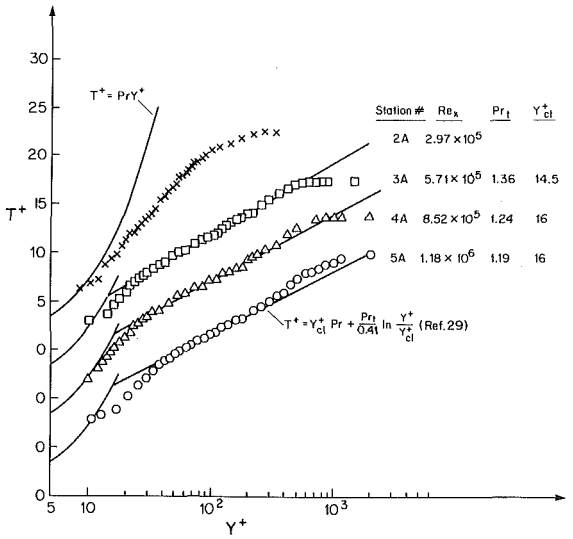


Fig. 16 Mean temperature profiles for Case C

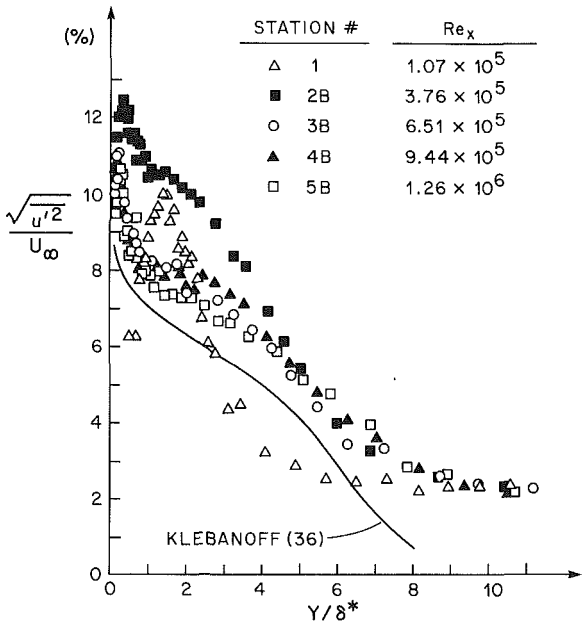


Fig. 17 Reynolds streamwise-normal stress profiles for Case C

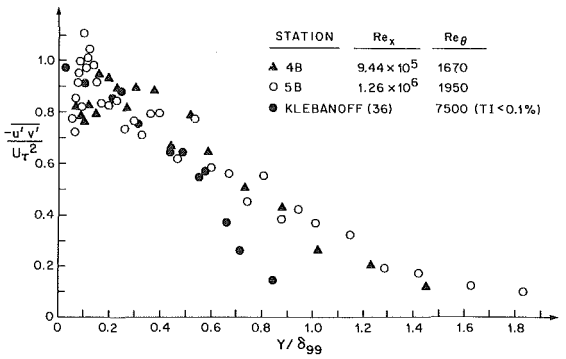


Fig. 18 Reynolds shear stress profiles for Case C

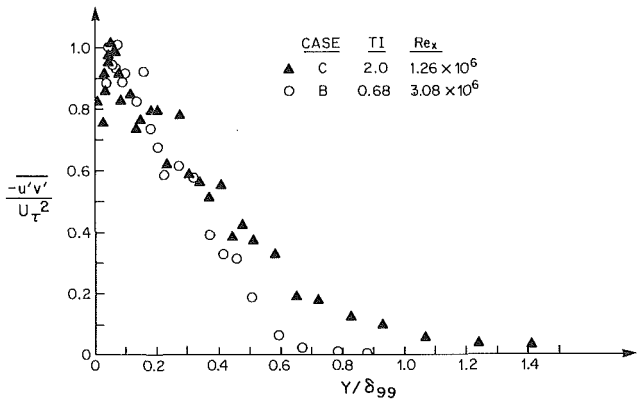


Fig. 19 Comparison of Reynolds shear stress profiles at Station 5B (Fig. 2) for Cases B and C

The local heat transfer data for this run were repeatable to within 1 percent over a 6-hr test period, beginning after the standard 10-hr equilibrium period. In a similar case they were repeatable to within 3 percent over a period of one month.

Mean velocity profiles are shown in Fig. 10. The two upstream profiles (Stations 1 and 2B) follow the $U^+ = Y^+$ correlation to $Y^+ = 20$, indicating laminarlike behavior even though there are signs of the beginning of transition at these locations as discussed above. The two downstream profiles (Stations 4B and 5B) follow the law-of-the wall relationship over a sufficient range of Y^+ that using the Clauser technique was deemed appropriate. The third profile (Station 3B), though reduced with a skin friction coefficient calculated from the near-wall velocity gradient, as done with the laminar profiles, is clearly not laminarlike. This profile also does not display the turbulent log-linear behavior with an appropriate choice of $C_f/2$ – it is clearly transitional. One method for finding the transition region $C_f/2$ is to force closure of the two-dimensional momentum integral equation through the transition region [22]. This method was tried and found to give values which appear unreasonably high for this case. This is believed to be attributable to the influence of the lack of two-dimensionality in the transition region for this low free-stream turbulence case.

Mean temperature profiles are shown on Fig. 11. The first profile (Station 2A), taken in the laminarlike flow, follows the near-wall correlation, $T^+ = \mathrm{Pr}\, Y^+$, well. The two downstream profiles (Stations 4A and 5A), taken in the turbulent flow, display thermal-log-law behavior. In fitting the log regions, the turbulent Prandtl number Pr_t and the conduction layer thickness Y^+_{cl} were considered free parameters. Best-fits were found with $Y^+_{cl} = 20$ and $\mathrm{Pr}_t = 1.20$ and 1.15 for $\mathrm{Re}_x = 2.1 \times 10^6$ and 2.9×10^6, respectively. These values of Pr_t are consistent with the trend in $2\,\mathrm{St}/C_f$ observed in Fig. 3 and the conclusion, also made by Blair [22], that Reynolds analogy is violated in the low-Reynolds number turbulent boundary layer. Figure 11 also shows that the conduction layer thickness is larger in the low-Reynolds-number turbulent flow than that observed in higher Reynolds number flows [29].

Profiles of Reynolds normal stresses, $\sqrt{\overline{u'^2}}/U_\infty$, are shown in Fig. 12. The two upstream profiles (Stations 1B and 2B) have some turbulencelike characteristics, although the mean velocity and temperature profiles and the Stanton numbers at this streamwise position appear laminarlike. The anemometer output signals were viewed on a storage oscilloscope. At the peak value, i.e., $y/\delta^* = 1.3$ for the first station, the waveform was turbulentlike, indicating a distribution of energy over a large range of frequencies. No intermittent nonturbulent behavior was observable. At the innermost y-position of station 1 data ($\mathrm{Re}_x = 2.63 \times 10^5$, $y/\delta^* = 0.3$), some intermittency was observed where a quiet signal was present about 5 percent of the time. These findings are consistent with the results of Dyban [13] et al. They termed such a boundary layer "pseudolaminar." It is believed that this turbulence is produced by nonlinear amplification of the free-stream disturbances. This process gives rise to streamwise vortices which concentrate in a thin layer termed the "shear layer" by Klebanoff et al. [8]. This shear layer is characterized by high-

Downloaded 01 Jun 2010 to 171.66.16.71. Redistribution subject to ASME license or copyright; see http://www.asme.org/terms/Terms_Use.cfm

frequency disturbances and turbulence intensities similar to the peaks of streamwise turbulence intensity shown in Fig. 12. The near-wall decay of turbulence intensity is presumed to be due to stabilizing viscous forces. The effect of these turbulentlike fluctuations on the transition process is presently unknown. Schubauer and Skramstad [7] observed weak oscillations preceding transition in a flow where disturbances were very small. Klebanoff, Tidstrom, and Sargent [8] observed that, in a laminar boundary layer disturbed by a vibrating ribbon, an initially two-dimensional wave develops into a three-dimensional pattern that is terminated by a sudden increase of wave amplitude. Profiles of rms values of these waves are similar (including a peak at $y/\delta^* = 1.3$) to those profiles of Fig. 12, which precede transition.

Transition is observable in the normal stress profiles as a very large increase in peak turbulence intensity concentrated near the wall where it is believed that turbulent bursts are agitating the flow (Station 3B profile of Fig. 12). The residue of the laminar profile peaks remains in the downstream profiles but soon becomes overshadowed by the intense near-wall peak (Stations 4B and 5B). The outer half of the transitional boundary layer profile (Station 3B) has a low turbulence intensity compared to fully turbulent profiles (i.e., Stations 4B and 5B). Though these last two stations are in the low-Reynolds-number turbulent flow, the normal stress profiles appear to have reached an equilibrium shape. This is evidence that the turbulence characteristics are established almost immediately after transition. The last two profiles appear similar to one measured in a mature turbulent boundary layer by Klebanoff [36]. Note that the Station 3B profile is different than either the laminar or turbulent profile and therefore cannot be reproduced from the two by way of an intermittency factor, as is often done in transitional flow modeling.

Reynolds shear stress profiles for the two downstream stations are shown on Fig. 13 [37]. The probe was too large to take similar profiles in the laminar and transitional boundary layers. These data and the Klebanoff [36] data, also shown, support the earlier conclusion that the turbulence characteristics rapidly assume those of a fully turbulent flow. The reduced shear-stress values near the wall in the $\mathrm{Re}_x = 2.35 \times 10^6$ profile are probably due to averaging by the probe over the length of the wire. This was not observable in the last station profile where the boundary layer was considerably thicker.

The Higher Free-Stream Turbulence Intensity Case – Case C. To set up the third case, a square grid constructed of 5-cm-wide metal strips on a 10-cm pitch was inserted between the screen pack and the nozzle. The free-stream velocity was then reduced to approximately 13 m/s to place the onset of transition into the first one-third of the test length. This gave free-stream turbulence intensities which decay from 2.1 to 1.9 percent over the test length; 2.0 percent was recorded in the transition region. Larger values of free-stream turbulence intensity, though more representative of the gas turbine environment, decay rapidly and are difficult to characterize and reproduce. This case is considered representative of cases with higher free-stream disturbance ($TI < 5$ percent).[1]

The Stanton number and skin friction coefficient data, Fig. 3, show that the onset of transition has been moved to approximately $\mathrm{Re}_x = 2.1 \times 10^5$ ($\mathrm{Re}_{\delta^*} = 788$). This is consistent with earlier data shown on Fig. 8 for 2 percent free-stream turbulence intensity. There also is some indication of a higher heat transfer coefficient in the late laminar flow due to the higher free-stream turbulence intensity, although the data for $\mathrm{Re}_x < 10^5$ seem to be insensitive to turbulence intensity. The two skin friction coefficient values at $\mathrm{Re}_x \approx 3 \times 10^5$ were found by forcing closure of the integral momentum equation over the transition region as previously done by Blair [22]. In contrast to case B, this technique was found to give values that appear reasonable on Fig. 3. It is believed that this model was successful in case C and not in case B, because case C was shown to be more two-dimensional. The data indicate that the x-Reynolds number at the end of transition is about twice that of the onset of transition for both cases B and C. This is consistent with the transition length model presented by Abu-Ghannam and Shaw [12]. The turbulent data ($\mathrm{Re}_x > 4 \times 10^5$) indicate a lower value of $2\ \mathrm{St}/C_f$ than 1.2, the accepted value for fully mature turbulent flow [33, 34], but a higher value than observed in case B. Also, it will be shown that turbulent Prandtl numbers are reduced somewhat from those of case B. A thermal energy balance yielded closure to within 5 percent over the full test length for this case and a momentum balance closed to within 4 percent from the first profile ($\mathrm{Re}_x \approx 10^5$) to the last ($\mathrm{Re}_x \approx 1.3 \times 10^6$). It should be noted, however, that the two $C_f/2$ values within the transition region ($\mathrm{Re}_x \approx 3.5 \times 10^5$) were chosen to force momentum balance closure over the transition region, $2.1 \times 10^5 < \mathrm{Re}_x < 5 \times 10^5$.

Spanwise distributions of Stanton number are shown in Fig. 14. The first distribution is in late-laminar flow. Transitional streaks are beginning to form off center span as was observed in case B. The second distribution is in late-transitional flow. It appears that transition near the center span is spanwise-uniform and that the flow remains two-dimensional throughout, for this high turbulence case.

Mean velocity profiles, Fig. 15, show behavior similar to that of case B. The upstream station (Station 1) is laminarlike, the next (Station 2B) is in transition, and the three downstream stations (3A, 4A, and 5A) are clearly turbulent – each with a longer log-linear region and a decreased wake strength than the last. A comparison of the Station 1 profile with the Blasius profile (Fig. 15) shows a lack of agreement at the edge of the boundary layer. This may be due to the nearness of the flow to transition (Fig. 3) or due to the higher free-stream turbulence level of Case C. Mean temperature profiles of case C, Fig. 16, show behavior similar to that of the case C velocity profiles. Note that the upstream profile (Station 2A) is in transition. The turbulent profiles (Stations 3A, 4A and 5A) show log-linear behavior. As in case B, the log regions were fit by assuming the turbulent Prandtl number, Pr_t, and the conduction layer thickness, Y_{cl}^+, to be free parameters. Best fits were achieved with $Y_{cl}^+ = 14.5$, 16, and 16, and $\mathrm{Pr}_t = 1.36$, 1.24, and 1.19 for Stations 3A, 4A, and 5A, respectively. Note that the conduction layers for the last two profiles are thinner than those of case B, but thicker than those of a mature turbulent boundary layer ($Y_{cl}^+ = 13.2$ [29]). Note also that the turbulent Prandtl numbers are higher than 0.9, the fully turbulent value, and less than those observed just after transition in case B.

Reynolds normal stress profiles, plotted in Fig. 17, continue to show a peak at $y/\delta^* = 1.3$ in the laminar flow (Station 1) as was observed in case B. The peaks and values throughout the profile are larger than the case B counterparts, however. The residue of the peak in the laminar profiles remains in the downstream profiles but soon becomes overshadowed by the near-wall peak. The three downstream profiles (3B, 4B, and 5B) are nearly the same, supporting the earlier conclusion that the turbulence quantities are rapidly established. Due to the higher free-stream turbulence, the values throughout the profile are higher than the case B values and those of Klebanoff [36], however.

Reynolds shear stress profiles are shown on Fig. 18. Though the scatter is large, the figure shows that the downstream profiles (Stations 4B and 5B) are essentially the same. Figure 18 also shows that the near-wall shear stress is approximately the same, in these coordinates, as that in the

[1] The upper limit of 5 percent was imposed based upon the findings of Dyban et al. [13] that the characteristics of "pseudolaminar" flows for $TI > 5$ percent are different than those for $TI < 5$ percent.

Downloaded 01 Jun 2010 to 171.66.16.71. Redistribution subject to ASME license or copyright; see http://www.asme.org/terms/Terms_Use.cfm

Klebanoff profile [36]. The shear stress near the edge of the boundary layer is considerably larger than Klebanoff's values, however – the free-stream turbulence for the Klebanoff data was very low ($TI < 0.1$ percent). Figure 19 compares the shear stress profiles from the last station for cases B and C. Although the near-wall values are essentially the same in these coordinates, the case C values near the edge of the boundary layer are considerably higher.

Conclusions and Recommendations

1 An unstable laminar flow is described as a separate flow from that of laminar or transitional flow. In this flow, turbulence intensities significantly higher than the free-stream turbulence intensity are observable in the boundary layer. Heat transfer rates appear to be somewhat sensitive to free-stream turbulence in this flow – a contrast to the lack of sensitivity to free-stream turbulence intensity in the early laminar flow. More investigation into the role of this boundary layer turbulence intensity on the process of transition is needed.

2 Increased free-stream turbulence intensity decreases the transition onset Reynolds number and the length of transition. The locations of the onset and end of transition in the present cases were consistent with results of earlier experiments. Onset of transition is taken to be the location where Stanton number data begin to rise sharply with increasing streamwise distance; the end of transition is the peak of the Stanton number curve.

3 Turbulent Prandtl number values in the early turbulent flow, just downstream of transition, are significantly higher than the 0.9 value known to apply to fully mature turbulent flows. These values decrease, somewhat, with higher free-stream disturbance levels. Temperature profiles in the early turbulent flow indicate a thicker conduction layer than observed in fully turbulent flows. This thickness decreases with increased free-stream disturbance levels.

4 Values of the Reynolds analogy factor, $2\,St/C_f$, in the early turbulent flow are significantly smaller than 1.2, the fully turbulent value.

5 Profiles of turbulent streamwise-normal and shear stresses develop rapidly to fully turbulent shapes immediately after transition.

6 Transition is characterized by a very large spike in streamwise turbulence intensity near the wall. This spike is considerably larger than the maximum value observed in turbulent normal stress profiles.

7 The effect of higher free-stream turbulence intensity is seen to penetrate to very near the wall in profiles of streamwise-normal stresses. The effect of higher free-stream disturbance on the shear stress profiles in the fully turbulent flow is seen predominantly in the outer portion of the boundary layer.

8 Long-period unsteadiness was observed in a low free-stream disturbance ($TI = 0.3$ percent) laminar flow downstream of the theoretical instability limit. Similar unsteadiness was not observed just before transition in higher-disturbance flows ($TI = 0.68$ and 2 percent).

Acknowledgments

This study was supported by the NASA-Lewis Research Center grant number NAG 3-286. The grant monitor is Dr. Raymond Gaugler. Additional support was provided by the Graduate School of the University of Minnesota.

References

1 Turner, A. B., "Local Heat Transfer Measurements on a Gas Turbine Blade," *J. of Mech. Engr. Sci.*, Vol. 13, No. 1, 1971, pp. 1-12.

2 Taylor, G. I., "Statistical Theory of Turbulence, Part V," *Proc. Roy. Soc.* (London), A156, 1936, pp. 307-317.

3 Hall, A., and Hislop, G. S., "Experiments on the Transition of the Laminar Boundary Layer on a Flat Plate," *British Aeronautical Research Committee*, R&M 1843, 1938.

4 van Driest, E. R., and Blumer, C. B., "Boundary Layer Transition: Freestream Turbulence and Pressure Gradient Effects," *AIAA Journal*, Vol. 1, No. 6, June 1963, pp. 1303-1306.

5 Hylton, L. D., Mihelc, M. S., Turner, E. R., Nealy, D. A., and York, R. E., "Analytical and Experimental Evaluation of the Heat Transfer Distribution Over the Surfaces of Turbine Vanes," NASA CR-168015, May 1983.

6 Wells, C. S., Jr., "Effects of Freestream Turbulence on Boundary Layer Transition," *AIAA Journal*, Vol. 5, No. 1, 1967, pp. 172-174.

7 Schubauer, G. B., and Skramstad, H. K., "Laminar Boundary Layer Oscillations on a Flat Plate," NACA Report, No. 909, 1948.

8 Klebanoff, P. S., Tidstrom, K. D., and Sargent, L. H., "The Three-Dimensional Nature of Boundary Layer Instability," *J. Fluid Mech.*, Vol. 12, pt. I, 1962, pp. 1-34.

9 Spangler, J. G., and Wells, C. S., Jr., "Effects of Freestream Disturbances on Boundary Layer Transition," *AIAA Journal*, Vol. 6, No. 3, 1968, pp. 543-545.

10 Tani, I., "Boundary Layer Transition," *Annual Rev. of Fluid Mech.*, Vol. I, 1969, edited by W. R. Sears, pp. 169-196.

11 Hall, D. J., and Gibbings, J. C., "Influence of Stream Turbulence and Pressure Gradient Upon Boundary Layer Transition," *J. of Mech. Engr. Div.*, Vol. 14, No. 2, 1972, pp. 134-146.

12 Abu-Ghannam, B. J., and Shaw, R., "Natural Transition of Boundary Layers—The Effects of Turbulence, Pressure Gradient, and Flow History," *J. of Mech. Engr. Sci.*, Vol. 22, No. 5, 1980, pp. 213-228.

13 Dyban, YE. P., Epik, E. YA., and Suprun, T. T., "Characteristics of the Laminar Boundary Layer in the Presence of Elevated Free-Stream Turbulence," *Fluid Mech.-Soviet Research*, Vol. 5, No. 4, 1976, pp. 31-36.

14 Clauser, M., and Clauser, F., "The Effect of Curvature on the Transition from Laminar to Turbulent Boundary Layer," NACA Tech. Note No. 613, 1937.

15 Liepmann, H. W., "Investigations on Laminar Boundary-Layer Stability and Transition on Curved Boundaries," NASA Wartime Advanced Confidential Rept. 3H3D, Aug. 1943.

16 Morkoven, M. W., "Instability, Transition to Turbulence and Predictability," AGARDograph, 236, 1978.

17 Reshotko, E., "Boundary Layer Stability and Transition," *Annual Rev. of Fluid Mech.*, Vol. 8, 1976, pp. 311-350.

18 Tani, I., "Three-Dimensional Aspects of Boundary Layer Transition," *Proc. Indian Acad. Sci.*, Vol. 4, Part 2, Aug. 1981, pp. 219-238.

19 "Laminar-Turbulent Transition," AGARD-CP224, May 1977.

20 Junkhan, G. H., and Serovy, G. K., "Effects of Free-Stream Turbulence and Pressure Gradient on Flat-Plate Boundary Layer Velocity Profiles and on Heat Transfer," ASME *Journal of Heat Transfer*, May 1967, pp. 169-176.

21 Simon, T. W., and Moffat, R. J., "Turbulent Boundary Layer Heat Transfer Experiments: A Separate Effects Study on Convexly Curved Wall," ASME *Journal of Heat Transfer*, Vol. 105, Nov. 1983, pp. 835-840.

22 Blair, M. F., "Influence of Free-Stream Turbulence on Boundary Layer Transition in Favorable Pressure Gradients," ASME JOURNAL OF ENGINEERING FOR POWER, Vol. 104, Oct. 1982, pp. 743-750.

23 Blair, M. F., "Influence of Free-Stream Turbulence on Turbulent Boundary-Layer Heat Transfer and Mean Profile Development, Part I—Experimental Data," ASME *Journal of Heat Transfer*, Vol. 105, Feb. 1983, pp. 33-40.

24 Perry, A. E., *Hot-Wire Anemometry*, Clarendon Press, Oxford, 1982.

25 Kline, S. J., and McClintock, F. A., "Describing Uncertainties in Single-Sample Experiments," *J. of Mech. Eng. Sci.*, Vol. 75, 1953, pp. 3-8.

26 Moffat, R. J., "Contributions to the Theory of Single-Sample Uncertainty Analysis," *J. of Fluids Engr.*, Vol. 104, 1982, pp. 250-260.

27 Wang, T., and Simon, T. W., "Using Uncertainty Analysis to Guide Test Program Development: A Case Study," Internal Report, Heat Transfer Lab., Dept. of Mech. Engr., University of Minnesota, Jan. 1984.

28 Wang, T., "An Experimental Investigation of Curvature and Free-Stream Turbulence Effects on Heat Transfer and Fluid Mechanics in Transitional Boundary Layers," Ph.D. thesis, Department of Mechanical Engineering, University of Minnesota, Dec. 1984.

29 Kays, W. M., and Crawford, M. E., *Convective Heat and Mass Transfer*, 2d ed., McGraw-Hill, New York, 1980.

30 Schlichting, H., *Boundary Layer Theory*, 7th ed., Chap. XVI, McGraw-Hill, New York, 1979.

31 Kachanov, Yu. S., and Levchenko, V. Ya., "The Resonant Interaction of Disturbances at Laminar-Turbulent Transition in a Boundary Layer," *J. of Fluid Mech.*, Vol. 138, 1984, pp. 209-247.

32 McDonald, H., and Fish, R. W., "Practical Calculations of Transitional Boundary Layers," *International Journal of Heat and Mass Transfer*, Vol. 16, 1973, pp. 1729-1744.

33 Spalding, D. B., "Contribution to the Theory of Heat Transfer Across a Turbulent Boundary Layer," *International Journal of Heat and Mass Transfer*, Vol. 17, No. 7, July 1964, pp. 743-761.

34 Simonich, J. C., and Bradshaw, P., "Effect of Free-Stream Turbulence on Heat Transfer through a Turbulent Boundary Layer," ASME *Journal of Heat Transfer*, Vol. 100, Nov. 1978, pp. 671-677.

35 Clauser, F. H., "The Turbulent Boundary Layer," *Advances in Applied Mechanics*, Vol. IV, 1956, Academic Press, New York, pp. 1-51.

36 Klebanoff, P. S., "Characteristics of Turbulence in a Boundary Layer with Zero Pressure Gradient," NACA Report, 1247, 1955.

37 Buddhavarapu, J., "An Experimental Study of Transitional Boundary Layers on a Flat Plate," M.S. thesis, Department of Mechanical Engineering, University of Minnesota, Sept. 1984.

Downloaded 01 Jun 2010 to 171.66.16.71. Redistribution subject to ASME license or copyright; see http://www.asme.org/terms/Terms_Use.cfm

Experimental Heat Transfer Investigation Around the Film-Cooled Leading Edge of a High-Pressure Gas Turbine Rotor Blade

C. Camci

T. Arts

von Karman Institute for Fluid Dynamics, B-1640 Rhode Saint Genèse, Belgium

This paper describes an experimental heat transfer investigation around the leading edge of a high-pressure film-cooled gas turbine rotor blade. The measurements were performed in the VKI isentropic compression tube facility using platinum thin film gauges painted on a blade made of machinable glass ceramic. Free-stream to wall temperature ratio, Reynolds, and Mach numbers were selected from actual aeroengines conditions. Heat transfer data obtained without and with film cooling in a stationary frame are presented. The effects of coolant to free-stream mass weight ratio and temperature ratio were successively investigated. Heat transfer modifications due to incidence angle variations were interpreted with the aid of inviscid flow calculation methods.

Introduction

A classic way to improve the thermal efficiency of a gas turbine cycle is to increase the turbine entry temperature. As a result, specific fuel consumption, size, and weight of aeroengines were significantly reduced during the two last decades. A 25/1 pressure ratio and an 1800 K TET are typical values encountered in high-performance jet engines [1]. An accurate knowledge of the convective heat flow across the blade surfaces is therefore an important, even essential, part of their design. The stagnation point of a turbine blade is probably the most critical area as it is exposed to an important level of heat flux. Considering the ever increasing temperature and pressure levels, external film cooling coupled with internal convective and impingement cooling have been a general practice in this portion of the blade. From a fluid dynamic point of view, the regions affected by film cooling, especially very close to the ejection holes, are characterized by a flow which is viscous, obviously nonadiabatic, and fully three dimensional. The coolant jets, interacting with the boundary layer, considerably alter its initial structure.

The objective of this paper is to present detailed heat transfer data measured around the film-cooled leading edge of a high-pressure turbine rotor blade in the VKI short-duration isentropic compression tube. In the high-speed, compressible flow environment of this facility, wall heat flux measurements were performed duplicating the same Reynolds and Mach numbers as well as wall to free-stream and coolant to free-stream temperature ratios existing in an aeroengine. Measurement results are presented as heat transfer coefficient distributions. The effects of incidence angle, coolant to free-stream mass weight ratio and coolant to free-stream temperature ratio were successively investigated.

Contributed by the Gas Turbine Division of THE AMERICAN SOCIETY OF MECHANICAL ENGINEERS and presented at the 30th International Gas Turbine Conference and Exhibit, Houston, Texas, March 18–21, 1985. Manuscript received at ASME Headquarters, December 27, 1984. Paper No. 85-GT-114.

Experimental Apparatus

Test Facility. Short-duration testing techniques were employed; they were provided by the VKI isentropic compression tube facility. The latter consists of a 5-m-long and 1-m-dia cylinder containing a lightweight piston, driven by a 250 bar air reservoir. As the piston moves, the gas in front of it is nearly isentropically compressed until it reaches a preset pressure, and hence temperature level. A fast-opening valve is then actuated, allowing the mainstream to flow through the test section until the piston has completed its stroke. The free-stream conditions may be varied between 300 and 600 K and between 0.5 and 7 bar. A 5 m^3 dump tank allows downstream pressure adjustments between 0.1 and 3 bar. Testing time is about 500 ms. Further details about this facility and its operating principles are described in [2, 3].

The Model. All measurements reported in this paper were carried out on the same rotor blade section as tested by Consigny and Richards [4]. The cascade geometry is fully described in this reference and summarized in Fig. 1. The blade instrumented for heat flux measurements was milled from "Macor" glass ceramic and 45 platinum thin films were painted on its surface. Three rows of cooling holes (d = 0.8 mm) are located around the leading edge; the row and hole spacing are both 2.48 mm. The hole axes are spanwise inclined at 30 deg from the tangential direction. A circular cavity (ϕ = 4.5 mm) drilled along the blade height acts as an injection plenum. A regenerative type of heat exchanger provides cooling air temperatures ranging between $-120°C$ and $+150°C$. Pressure tappings and miniature thermocouples provide continuously the coolant characteristics at the plenum inlet and outlet.

Copyright © 1985 by ASME

Downloaded 01 Jun 2010 to 171.66.16.71. Redistribution subject to ASME license or copyright; see http://www.asme.org/terms/Terms_Use.cfm

Table 1

RUN	$P_{0\infty}$	$T_{0\infty}$	$T_w/T_{0\infty}$	$T_c/T_{0\infty}$	P_{oc}	$\dot{m}_c/\dot{m}_\infty$	Ma_{inlet}	$Ma_{exit,s}$	$Re_{\bar{c}_{inlet}}$	TU_∞	i
	b	K			b	%				%	deg.
126	2.915	410.0	0.736				.240	.901	8.40 E5	5.2	0
112	2.901	409.2	0.724				.251	.905	8.42 E5	5.2	0
113	2.905	409.4	0.727				.251	.908	8.42 E5	5.2	0
187	3.330	409.2	0.719				.251	.923	9.65 E5	5.2	0
196	3.045	417.6	0.716				.316	.951	10.66 E5	0.8	+15
198	3.040	417.8	0.713				.310	.948	10.25 E5	0.8	+10
201	3.050	417.2	0.700				.271	.952	9.27 E5	0.8	0
206	3.050	417.9	0.706				.263	.945	8.99 E5	0.8	-10
202	2.885	417.3	0.705	.39	3.72	.87	.271	.952	9.27 E5	0.8	0
199	2.902	418.3	0.710	.39	3.65	.84	.310	.948	10.25 E5	0.8	+10
204	2.892	417.8	0.707	.38	3.69	.89	.263	.945	8.99 E5	0.8	-10
154	2.883	408.9	0.722	.52	3.28	.50	.251	.905	8.42 E5	5.2	0
155	2.895	409.5	0.727	.52	3.40	.62	.251	.905	8.42 E5	5.2	0
157	2.891	409.3	0.731	.49	3.92	1.01	.251	.905	8.42 E5	5.2	0
120	2.926	410.3	0.727	.59	4.02	.57	.251	.905	8.42 E5	5.2	0
125	2.892	409.3	0.735	.59	3.73	.46	.251	.905	8.42 E5	5.2	0
130	2.862	406.5	0.722	.70	3.69	.50	.251	.905	8.42 E5	5.2	0

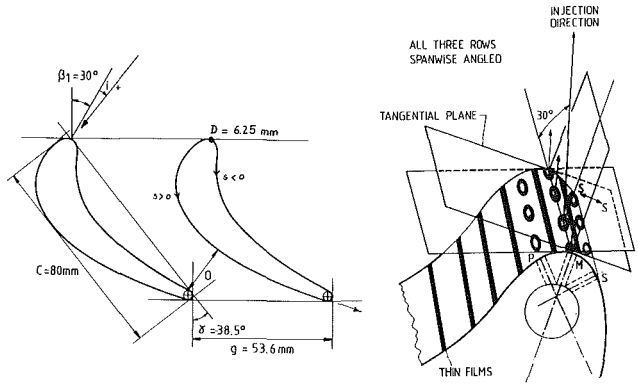


Fig. 1 Cascade geometry and cooling configuration

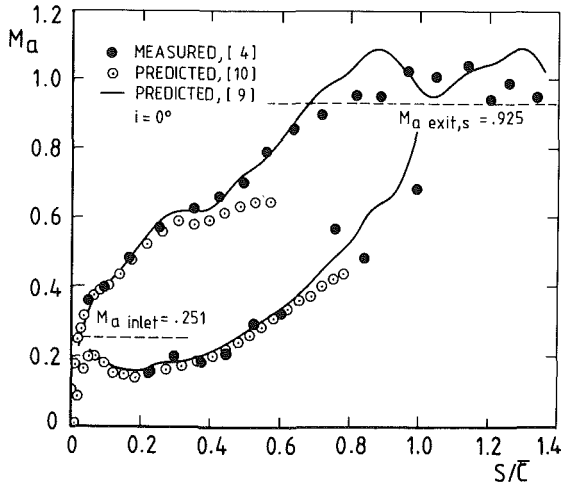


Fig 2 Blade velocity distribution

Turbulence Generation. The free-stream turbulence is generated by an upstream horizontal grid of parallel bars. The maximum turbulence level is 5.2 percent when the grid is installed at one chord length upstream of the model [4], but can be reduced by displacing the grid further upstream.

Measurement Technique. The local wall heat flux is deduced from the corresponding time dependent surface temperature evolution; the latter is obtained from platinum thin films (variable resistance thermometers) deposited on the surface. The temperature/wall heat flux conversion is obtained from an electrical analogy, simulating a semi-infinite body configuration. A detailed description of this transient technique is given in [5, 6]. The convective heat transfer coefficient is defined as the ratio of the measured wall heat flux over the difference between the free-stream recovery and local wall temperatures; a recovery factor of 0.896 is used [7] as if the boundary layer were turbulent everywhere on the blade surface. Local temperature of the wall is evaluated from measured thin film resistance, just before the mainstream flow establishment, taking into account near hole conduction effects because of slightly early start-up of injection process (~200 ms).

The uncertainties on the different measurements were estimated as following [8]:

Nomenclature

$\bar{c}$ = chord length
$\overline{C_d}$ = averaged discharge coefficient
d = ejection hole diameter
g = pitch
h_0, h = convective heat transfer coefficient, without/with film cooling
i = incidence angle (positive in the counterclockwise direction)
$\dot{m}$ = mass flow rate
m = blowing rate, $m = \dfrac{\rho_c U_c}{\rho_\infty U_\infty}$
M = leading edge midrow of ejection ($s/\bar{c} = 0.0$)
Ma = local Mach number
O = throat
p = pressure
P = leading edge pressure side row of ejection ($s/\bar{c} = -0.026$)
$\dot{q}$ = wall heat flux rate
Re = Reynolds number
s = curvilinear coordinate along the blade
S = leading edge suction side row of ejection ($s/\bar{c} = +0.026$)
T = temperature
TET = turbine entry temperature
TU = turbulence intensity
U = velocity
ρ = density
γ = stagger angle

Subscripts

c = relative to coolant
d = based on injection hole diameter
D = based on leading edge diameter
o = total condition
∞ = relative to free stream
oc = plenum chamber condition
r = recovery
s = isentropic
T = based on plenum chamber diameter

Downloaded 01 Jun 2010 to 171.66.16.71. Redistribution subject to ASME license or copyright; see http://www.asme.org/terms/Terms_Use.cfm

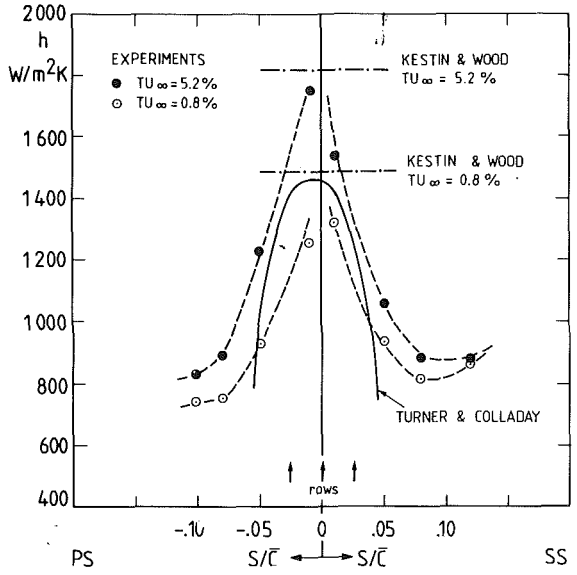


Fig. 3 Leading-edge heat transfer without cooling, effect of TU_∞

h = 1000 W/m²K ± 50 W/m²K (excluding $s/\bar{c}$ = ∓ 0.01 with cooling)
p = 2200 mm Hg ± 15 mm Hg
T = 100 K ± 0.5 K
$\dot{m}_c$ = 0.020 kg/s ± 0.0005 kg/s
$\dot{m}_c/\dot{m}_\infty$ = 2 ± 0.1%

Experimental Results and Discussion

The heat transfer behavior around the leading edge of a film-cooled rotor blade has been experimentally investigated over a range of coolant temperatures, coolant to free-stream mass weight ratios and incidence angles. The main parameters of this experimental program are summarized in Table 1.

Blade Velocity Distribution. Measured isentropic Mach number distributions around the blade are shown in Fig. 2 at zero incidence. The free-stream inlet Mach number was measured to be 0.251. Because of the relatively small leading edge radius, detailed static pressure measurements near the stagnation point could not be carried out. The flow accelerates quite regularly on the suction side up to nearly sonic conditions at the trailing edge. Along the pressure side, a velocity peak appears at $s/\bar{c} = -0.08$. More downstream, a favorable pressure gradient accelerates the flow up to the trailing edge.

A two-dimensional time marching method [9] provided an inviscid prediction of the mainstream flow (Fig. 2). Because of the weakness of this kind of approach to accurately model a very low velocity region, a singularity method [10] was also applied around the leading edge in order to carefully determine the stagnation point position. At $i = 0$, the latter was calculated to be at $s/\bar{c} = -0.019$ (Fig. 5 – point B), very close to the midrow of holes. This suggests that when no coolant is ejected, rows M and S may be considered as roughness elements for the suction side boundary layer. On the pressure side, the boundary layer is only affected by row P.

Leading-Edge Heat Transfer Without Film Cooling (i = 0 deg). Heat transfer coefficient distributions without coolant ejection are shown in Fig. 3 for $-0.10 < s/\bar{c} < +0.10$. In order to avoid any possible free-stream air circulation between rows M, P, and S, the coolant plenum chamber was filled with a flexible insert. In the absence of the latter, as has been demonstrated from surface oil flow visualizations, free-stream air penetrates in the plenum through row M and depending on the local static pressure, is ejected through rows P and S, affecting the local heat flux measurement.

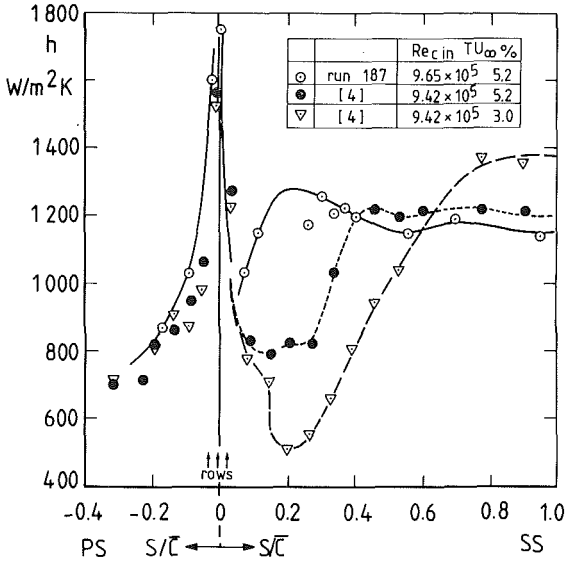


Fig. 4 Leading-edge heat transfer without cooling, effect of existence of holes

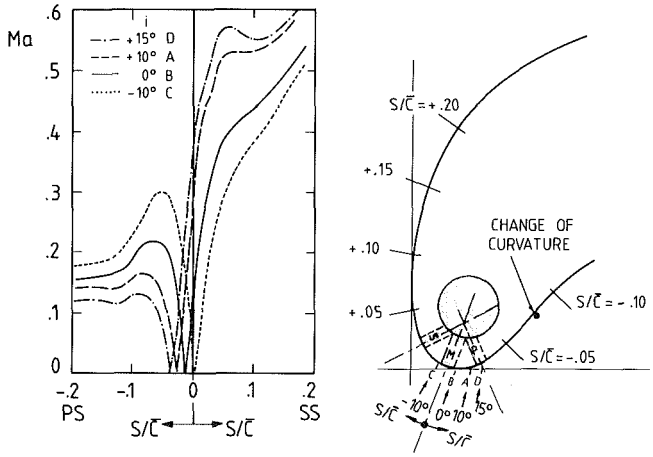


Fig. 5 Leading-edge velocity distribution, effect of incidence

Stagnation region heat transfer on a cylinder in crossflow is mainly dominated by a three-dimensional vortical structure [11]. These vortices have their vorticity axes parallel to the main flow, as visualized by [12]. The amount of heat transfer is proportional to the quantity $TU_\infty \mathrm{Re}^{1/2}$. Any increase of this product decreases the spacing of these vortices and, hence, enhances heat transfer. Looking at the gauges located at $s/\bar{c} = \mp 0.01$ (Fig. 3), enhancement of heat flux is clearly observed when TU_∞ is increased from 0.8 to 5.2 percent. Kestin and Wood's cylinder in crossflow correlation [13] provides similar trends. For $TU_\infty = 0.8$ percent, the present data are also compared with Turner and Colladay's cylinder in crossflow correlation [14, 15]. However, even at $i = 0$ deg, a smooth cylinder in crossflow is not an exact simulation of a turbine blade leading edge, because different accelerations exist on both sides of the stagnation line. Moreover, the present model displays three rows of holes acting as roughness elements.

The heat transfer distributions are affected by the existence of these holes, even when no coolant is ejected. This was demonstrated by comparing the present measurements with those by Consigny and Richards [4], performed on an identical, but smooth profile (Fig. 4). On the pressure side, at $TU_\infty = 5.2$ percent, nearly similar heat transfer levels were observed. The effect of the holes is not very pronounced. As a matter of fact, the boundary layer transition is mainly due to the curvature change, at $s/\bar{c} = -0.08$, where the breakdown

Downloaded 01 Jun 2010 to 171.66.16.71. Redistribution subject to ASME license or copyright; see http://www.asme.org/terms/Terms_Use.cfm

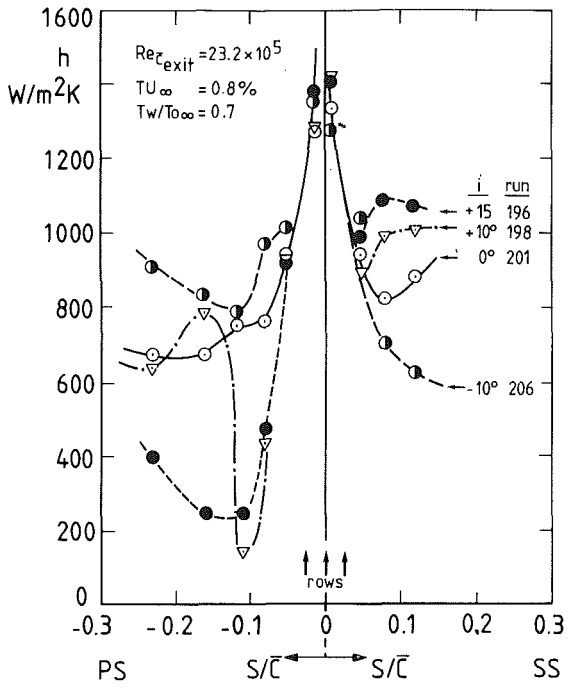


Fig. 6 Leading-edge heat transfer without cooling, effect of incidence

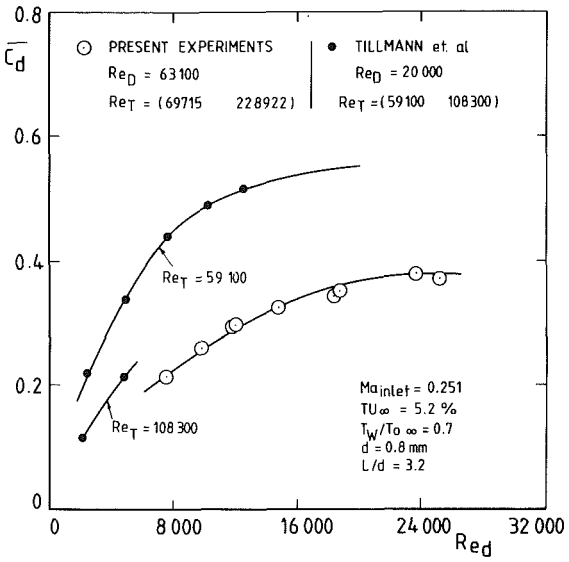


Fig. 7 Cooling holes discharge coefficients

of the three-dimensional vortices originating from the stagnation region may occur [16], due to the unfavorable pressure gradient (Fig. 2). Along the suction side a definite influence of the holes is observed on the transition process. The data obtained on the smooth blade demonstrate the relationship existing between turbulence intensity (3.0 . . . 5.2 percent) and transition onset and length (Fig. 4). Measurements on the present model suggest a very early transition induced by the presence of the cooling holes: The suction-side boundary layer appears to be fully turbulent at $s/\bar{c} = 0.25$. As already shown by other investigators [17, 18] free-stream turbulence variations only affect laminar or transitional boundary layers in the presence of a favorable pressure gradient in a significant way as shown in Fig. 4 for $-0.01 < s/\bar{c} < 0.20$.

Leading-Edge Heat Transfer Without Film Cooling ($i \neq 0$ deg). Leading-edge velocity distributions and stagnation point location were computed at different incidences using a Martensen method (Fig. 5). The corresponding heat transfer

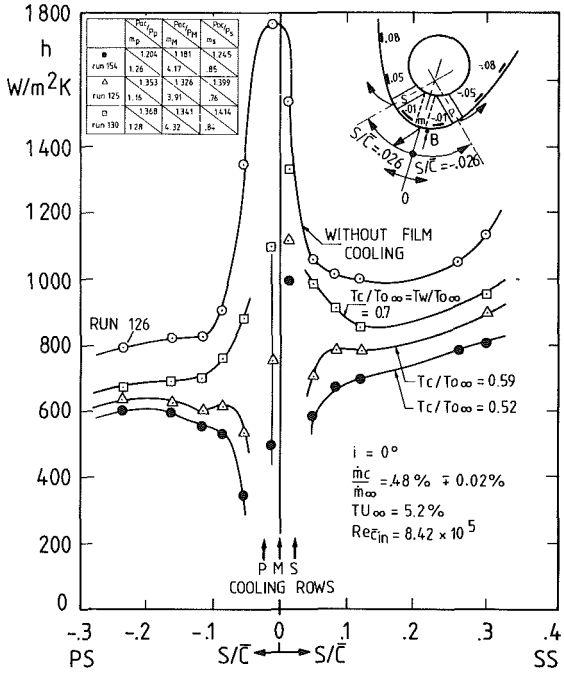


Fig. 8 Leading-edge heat transfer with film cooling, effect of temperature ratio

evolutions are presented in Fig. 6. At zero incidence, as a result of the tripping effect of rows M and S, the onset of suction-side boundary layer transition is observed at $s/\bar{c} = 0.08$. In this paper, we have defined the onset of transition location to be the first measurement point where h starts to increase in a pronounced way. Increasing the incidence to $+10$ deg and $+15$ deg moves the stagnation point respectively to points A and D whereas transition onset is displaced to $s/\bar{c} = 0.065$ and 0.050. At $i = -10$ deg, the stagnation point is located in C and only row S disturbs the suction-side boundary layer. On the pressure side, at $i = 0$ deg and $i = -10$ deg, transition is observed to occur at $s/\bar{c} = -0.08$, because of the adverse pressure gradient. In the latter case, a higher local free-stream velocity level, enhancing local Re number as well as the disturbing effect of rows M and P, is responsible for slightly higher heat transfer coefficient values. At $i = +15$ deg, the stagnation point D nearly coincides with row P and the unfavorable pressure gradient almost disappears; hence larger laminar and transitional regimes are expected. This behavior has been confirmed by the measurements (Fig. 6).

Leading-Edge Heat Transfer With Film Cooling ($i = 0$ deg). Because of different free-stream conditions around the leading edge, as well as different internal flows, the local discharge coefficients of the three rows differ from each other; moreover, local mass flow rate measurements through each row were not possible. As a result, a mean discharge coefficient $\overline{C_d}$ was evaluated from the total coolant mass flow rate, the coolant plenum total pressure as well as an averaged free-stream static pressure. The $\overline{C_d}$ distribution, obtained for a mass weight ratio range of 0.48 to 1.01 percent, is shown in Fig. 7. The present data show qualitative agreement with measurements obtained in a water tunnel on a cylinder with three cooling rows by Tillman et al. [19].

The effect of coolant temperature on the convective heat transfer coefficient distribution is shown in Fig. 8. The coolant to free-stream temperature ratio was varied from 0.5 to 0.7 for a constant mass weight ratio of 0.48 percent. From stagnation point location predictions as well as from qualitative oil flow visualizations, it appears that the suction-side wall heating is affected by the coolant jets from rows M

Downloaded 01 Jun 2010 to 171.66.16.71. Redistribution subject to ASME license or copyright; see http://www.asme.org/terms/Terms_Use.cfm

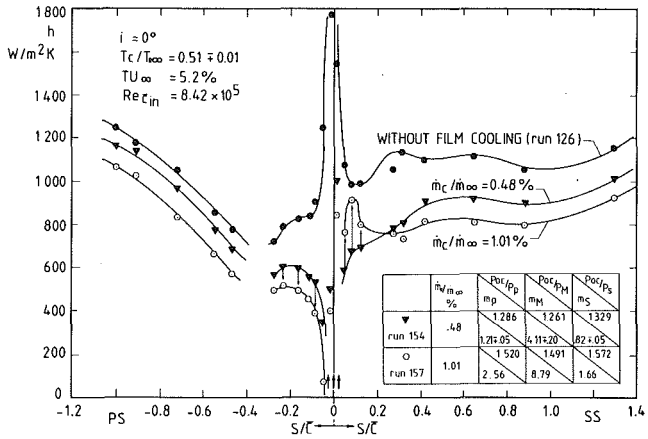


Fig. 9 Leading-edge heat transfer with film-cooling, effect of mass weight ratio

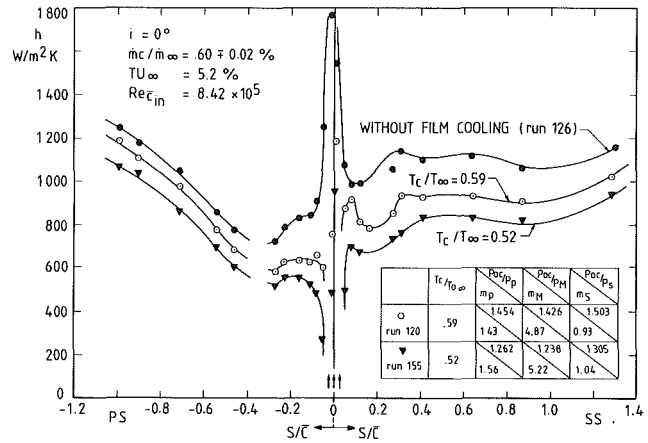


Fig. 10 Leading-edge heat transfer with film cooling

and S, whereas the pressure-side heat flux is only affected by row P.

The blowing rate m has been the most documented parameter in film-cooling research because of its governing role in the distribution of coolant fluid inside the viscous layers, normal to the wall. A given distribution establishes its specific mean velocity gradients and the associated turbulent shear stress and turbulent kinetic energy distributions. Unfortunately, because of a lack of detailed static pressure measurements, a very accurate determination of local m values was not obtained. An attempt to calculate local m values was made using the calculated local isentropic coolant mass flux rate, the averaged $\overline{C_d}$ and the predicted free-stream mass flux rate. Looking at Fig. 8, local blowing rate values of 4.17, 1.26, and 0.85 were respectively obtained for rows M, P, and S. On the suction side, highly penetrating jets from row M disturb the approaching mainstream boundary layer; downstream of this row, a separated coolant layer zone is observed ($s/\bar{c} = 0.01$), where a poor cooling efficiency is achieved. Reattachment is expected near row S due to the free-stream acceleration and strong convex curvature. Although this region does not seem to be submitted to the influence of a coolant film, the gauge located at $s/\bar{c} = -0.01$ provides a quite low heat transfer coefficient measurement. This observation may be attributed to the fact that, even with this low-conductivity material and short running times of the facility, local wall temperature measurements could be affected by conduction in between closely spaced ejection rows ($-0.01 < s/\bar{c} < +0.01$). This influence is mainly related with the local wall temperature measurement, rather than the wall heat flux measurement which is only sensitive to the time rate of change of wall temperature. The comparison of heat

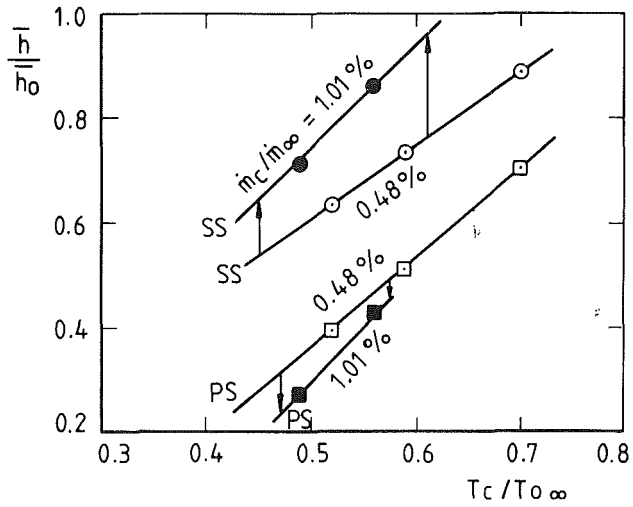


Fig. 11 Averaged leading-edge heat transfer

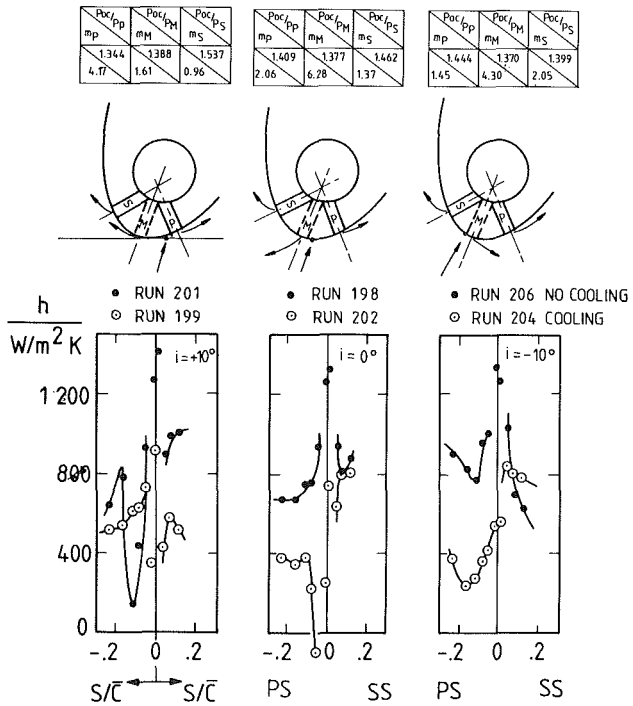


Fig. 12 Leading-edge heat transfer with film cooling, effect of incidence

transfer coefficients evaluated with an isothermal wall and with the locally measured wall temperatures displayed a quite negligible difference after three hole diameters downstream of rows P and S. In the showerhead region ($s/\bar{c} = \mp 0.01$), h measurement has some additional uncertainty because of the interrow heat conduction.

The effect of coolant mass weight ratio is shown in Fig. 9. This parameter was varied from 0.48 to 1.01 percent for a fixed value of coolant to free-stream temperature ratio of 0.51. Film cooling applied with a higher mass weight ratio provides a reduced heat transfer pattern along the pressure side. Although row P, ejecting along a concave surface, has a quite high blowing rate (2.56), the measured heat transfer pattern shows that the coolant remains attached to this concave surface, providing a correct wall protection. This behavior confirms the trends already observed in a low-speed environment [20]. For a high coolant mass weight ratio (1.01 percent), the blowing rate amounts to 8.79 across row M whereas a value of 1.66 is observed across row S. As might be expected, due to the high momentum flux of these jets, the

Downloaded 01 Jun 2010 to 171.66.16.71. Redistribution subject to ASME license or copyright; see http://www.asme.org/terms/Terms_Use.cfm

disturbed region is enlarged on the suction side and the reattachment point is moved more downstream. Behind row S, the first three gauges experience wall heat flux levels comparable to zero injection situation. From Fig. 9, there is experimental evidence that the jets ejected from row S separate from this convex surface. Coolant jet separation from convex surfaces at high blowing rates is, however, a well-known effect [20]. After reattachment, measured wall heat flux values far downstream ($s/\bar{c} > 0.25$) are lower than when moderate mass weight ratios (0.50 percent) are applied. In order to find the upper mass weight ratio limit before jet separation, heat transfer distributions were obtained for $\dot{m}_c/\dot{m}_\infty = 0.60$ percent and $T_c/T_{0\infty} = 0.52$ and 0.59 (Fig. 10). For the lowest coolant temperature ratio, the coolant ejected through row S is at the onset of separation: A slight heat transfer augmentation is observed only at $s/\bar{c} = +0.08$; the local blowing rates through rows M and S are respectively 5.22 and 1.04. Increasing the coolant temperature ratio, at an almost constant blowing rate, leads to a partially separated coolant flow situation. As a matter of fact, an increase of $T_c/T_{0\infty}$ results in a decrease of ρ_c/ρ_∞ and hence, at constant m, in an increase of U_c/U_∞ and moreover of the momentum flux ratio, leading to a more severe jet separation. On the pressure side, no coolant jet separation has been observed.

Although strong variations exit in this region, an attempt was made to define a leading edge heat transfer coefficient as a function of coolant mass weight ratio and coolant to free-stream temperature ratio (Fig. 11) using only four gauges located on both sides of the stagnation point B; $\bar{h}$ and $\bar{h}_0$ were obtained as arithmetical averages both on suction and pressure side. On an average basis, the cooling looks more effective on the pressure side than on the suction side. As the mass weight ratio increases, the suction side appears to be less protected because of jet separation. The strong influence of $T_c/T_{0\infty}$ is also demonstrated.

Leading-Edge Heat Transfer With Film Cooling ($i \neq 0$ deg). The effect of incidence variations upon leading-edge heat transfer in the presence of cooling was investigated for constant values of mass weight ratio, temperature ratio, and outlet Reynolds number. Results as well as estimated flow paths are given in Fig. 12 whereas aerodynamic predictions were given in Fig. 5. For $i = 10$ deg, the stagnation point is very close to row P. The ejection in such a low-velocity area provides a much higher local blowing rate (4.17) than at zero incidence ($m_p = 2.0$). On the pressure side the laminar region, observed between point A and $s/\bar{c} = -0.10$ without ejection, obviously disappears because of the disturbing nature of the coolant jets in the boundary layer. However, cooling along this surface is not as efficient as for the zero incidence configuration. The local blowing ratios across rows M and S are 1.61 and 0.96. The coolant layers provide a very efficient wall protection as a result of a very smooth coolant introduction into the suction-surface boundary layer.

For $i = -10$ deg, the position of the stagnation point (C) suggests that the suction surface boundary layer is only affected by jets issued from row S ($m_s = 2.05$). The cooling efficiency is rather poor, most probably because of a very small portion of fluid ejected through this row. Cooling of the pressure side through rows M and P provides heat transfer coefficient reductions to values equal to at least half of those obtained for the noncooled configuration in between C and $s/\bar{c} = -0.30$.

Conclusions

Convective heat transfer in the boundary layers developing around the leading edge of a H.P. turbine rotor blade has been investigated both in absence and presence of film cooling, using a sophisticated short-duration technique.

The quantitative wall heat transfer measurements documented the downstream development of the boundary layers as affected by the existence of the injection holes, even without coolant flow.

Important convective heat transfer reductions were obtained in the presence of cooling for realistic temperature ratios. It has been confirmed that a row situated on or very close to the stagnation point ejects at a relatively higher blowing rate, disturbing the downstream viscous layers in a more pronounced way.

Near hole external heat transfer coefficients were found to be slightly influenced from internal conduction paths, in between closely spaced cooling holes. However, the conduction pattern near the ejection site in the present low-conductivity model reveals much less significant flow of heat than that of the blade made of a conventional superalloy. This behavior provides some safety margin in wall temperature predictions, incorporating the heat transfer coefficients presented in this paper.

The effect of incidence variations on heat transfer with and without film cooling was interpreted with the aid of inviscid flow prediction methods. Predicted coolant trajectories were found to be consistent with the measured data.

References

1 Olsson, U., "Advanced Engine Technology and Its Influence on Aircraft Performance," *J. of Aircraft*, Vol. 19, No. 5, May 1982, pp. 380–384.

2 Richards, B. E., "Heat Transfer Measurements Related to Hot Turbine Components in the von Karman Institute Hot Cascade Tunnel," *Testing and Measurements Techniques in Heat Transfer and Combustion*, AGARD CP 281, May 1980.

3 Jones, T. V., Schultz, D. L., and Hendley, A. D., "On the Flow in an Isentropic Free Piston Tunnel," ARC R&M 3731, Jan. 1973.

4 Consigny, H., and Richards, B. E., "Short Duration Measurements of Heat Transfer Rate to a Gas Turbine Rotor Blade," ASME JOURNAL OF ENGINEERING FOR POWER, Vol. 104, No. 3, July 1983, pp. 542–551.

5 Schultz, S. L., and Jones T. V., "Heat Transfer Measurements in Short Duration Hypersonic Facilities," AGARD-ograph No. 165, Feb. 1973.

6 Ligrani, P. M., Camci, C., and Grady, M. S., "Thin Film Heat Transfer Gauge Construction and Measurement Details," VKI TM 33, Nov. 1982.

7 Schlichting, H., *Boundary Layer Theory* (7th ed.), McGraw-Hill, New York, 1979, pp. 714–715.

8 Kline, S. J., and McClintock, F. A., "Describing Uncertainties in Single Sample Experiments," *J. Mechanical Engin.*, Vol. 75, No. 1, Jan. 1953, pp. 3–8.

9 Arts, A., "Cascade Flow Calculations Using a Finite Volume Method," in *Numerical Methods for Flow in Turbomachinery*, VKI LS 1982-05, Apr. 1982.

10 Van Den Braembussche, R., "Calculation of Compressible Subsonic Flow in Cascades With Varying Blade Height," ASME JOURNAL OF ENGINEERING FOR POWER, Vol. 95, No. 4, Oct. 1973, pp. 345–351.

11 Kestin, J., and Wood, R. T., "The Mechanism Which Causes Free-Stream Turbulence to Enhance Stagnation Line Heat and Mass Transfer," *Heat Transfer*, Vol. 2, Elsevier, Amsterdam, 1970.

12 Sadeh, W. Z., Brauer, H. J., and Garrison, J. A., "Visualization Study of Vorticity Amplification in Stagnation Flow," Colorado State U., SQUID-CSU-1-PU, Oct. 1977.

13 Kestin, J., and Wood, R. T., "The Influence of Turbulence on Mass Transfer From Cylinders," ASME *Journal of Heat Transfer*, Vol. 93, No. 4, Nov. 1971, pp. 321–327.

14 Turner, A. B., "Local Heat Transfer Measurements on a Gas Turbine Blade," *J. Mech. Eng. Science*, Vol. 13, No. 1, 1971.

15 Colladay, R. S., "Turbine Cooling-Turbine Design and Application," NASA SP 2100, 1975.

16 Daniels, L. C., "Film Cooling of Gas Turbine Blades," Ph.D. Thesis, Oxford Univ. Eng. Lab. Report No. 1302/79, 1979.

17 Buyuktur, A. R., Kestin, J., and Maeder, P. F., "Influence of Combined Pressure Gradient and Turbulence on the Transfer of Heat From a Plate," *International Journal of Heat and Mass Transfer*, Vol. 7, 1964, p. 1175.

18 Junkhan, G. H., and Serovy, G. K., "Effects of Free-Stream Turbulence and Pressure Gradient on Flat Plate Boundary Layer Velocity Profiles and Heat Transfer," ASME *Journal of Heat Transfer*, Vol. 69, No. 2, May 1967, pp. 169–176.

19 Tillman, E. S., Hartell, E. L., and Jen, H. F., "The Prediction of Flow Through Leading Edge Holes in a Film-Cooled Airfoil With and Without Inserts," ASME Paper No. 84-GT-4, 1984.

20 Ito, S., Goldstein, R. J., and Eckert, E. R. G., "Film Cooling of a Gas Turbine Blade," ASME JOURNAL OF ENGINEERING FOR POWER, Vol. 100, No. 3, July 1978, pp. 476–481.

Downloaded 01 Jun 2010 to 171.66.16.71. Redistribution subject to ASME license or copyright; see http://www.asme.org/terms/Terms_Use.cfm

D. A. Ashworth
Rolls-Royce Ltd.,
Derby, England

J. E. LaGraff
Syracuse University,
Syracuse, N.Y.

D. L. Schultz

K. J. Grindrod

The University of Oxford,
England

Unsteady Aerodynamic and Heat Transfer Processes in a Transonic Turbine Stage

The effect of the interaction of the wake from a nozzle guide vane with the rotor may be simulated in part by means of a stationary rotor and a moving wake system. This technique is applied to a transonic rotor blade cascade, and the unsteady measurements of surface pressure and heat transfer rate are compared with baseline data obtained without the wake interaction. The wake-rotor interaction results in a change in inlet incidence angle and this effect is also examined in the steady-state case. It is found that the shock waves from the moving wake system have a major effect on the instantaneous heat transfer rates.

Introduction

Previous work by Doorly [1] and Dunn [2] has shown the importance of NGV rotor passing on heat transfer rates to rotor blades and nozzle guide vanes, respectively. In particular, Doorly has identified the phenomena observed on fast response heat transfer gauges associated with the impingement of the NGV trailing edge shock and the transit of the wake over the rotor blade surfaces. This investigation was carried out with a stationary rotor blade, the wakes themselves being generated by an array of bars rotated on an off-center disk upstream of the linear cascade. Dunn's study employed a complete rotor behind an NGV stage and was chiefly concerned with the influence of the rotor on the heat transfer rate to the NGV. Hodson [3] has made measurements of the unsteady blade pressures on a large-scale rotating turbine stage. The present study in which both heat transfer rates and a limited range of pressures have been measured was carried out on a highly loaded rotor profile for which the NGV exit flow included strong trailing edge shock waves. The rotor profile is the same as that currently fitted to the MIT transient blowdown facility, Epstein et al. [4]. In the present tests it was possible to vary the blade incidence and thus to examine the effect of this additional variable associated with rotor-wake interaction.

Experimental Apparatus

The measurements were made in the isentropic light piston cascade previously described by Schultz et al. [5]. This short duration ($\approx$ 0.5 s) facility produces correctly scaled gas/wall temperature ratios and full-scale engine Reynolds and blade Mach numbers that may be varied independently, thus enabling their separate influences to be determined. The test gas is compressed by what is in effect a single-stroke isentropic compressor, the compression ratio being, for example, 4.13 to attain a gas-total/wall temperature ratio of 1.5. The exit Mach number is set by the area of a second throat located downstream of the cascade and the Reynolds number by the predetermined pressure after compression. The aerodynamic design for the prototype cold-air turbine included 36 guide vanes and 61 rotor blades rotating at 9004 rpm (at T_o inlet 457.4 K). The wake generation system to simulate this wake-blade interaction is illustrated in Fig. 1. A linear cascade of five rotor blades in which the center blade is instrumented has upstream of it a disk with stranded steel cables held in root fixings around the perimeter. Correct scaling of the NGV and rotor pitch was obtained by using 16 bars and a cascade/cold air turbine scaling size factor of 1.3247. The trailing edge diameter of the NGV's was 1.2192 mm and the nearest wire diameter to 1.6151 mm was selected for the rotating "bars,"

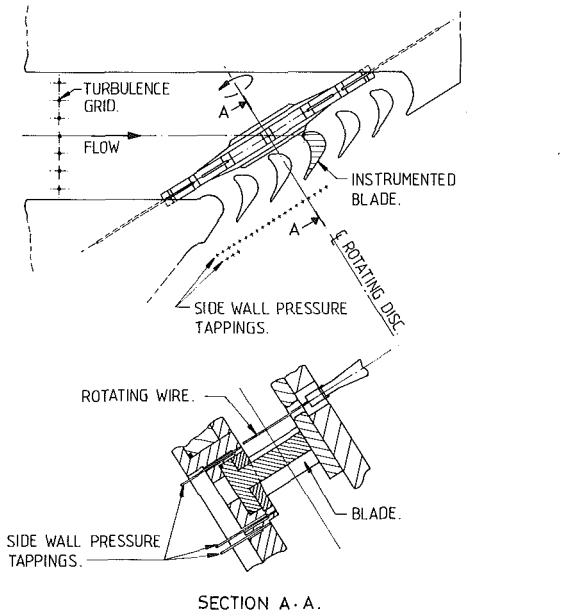


Fig. 1 Arrangement of rotating bar wake generator and cascade

Contributed by the Gas Turbine Division of THE AMERICAN SOCIETY OF MECHANICAL ENGINEERS and presented at the 30th International Gas Turbine Conference and Exhibit, Houston, Texas, March 18–21, 1985. Manuscript received at ASME Headquarters, January 7, 1985. Paper No. 85-GT-128.

Copyright © 1985 by ASME
Downloaded 01 Jun 2010 to 171.66.16.71. Redistribution subject to ASME license or copyright; see http://www.asme.org/terms/Terms_Use.cfm

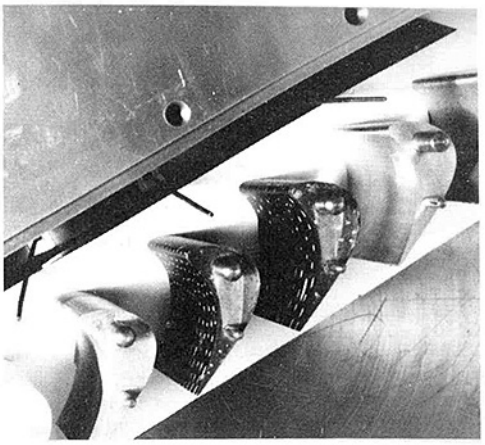


Fig. 2 View of Schlieren build showing bars protruding through sidewall slot. The polished back face is covered with paper for clarity.

which were located in a plane 14.333 mm upstream of the cascade blade leading edge. Previous experiments by Doorly [1] have shown that a wake velocity profile similar to that of an NGV (without downstream rotor) can be produced by a circular cylinder of diameter equal to the trailing edge diameter. The bars protruded through a slot in the sidewall, shown in cross-section in Fig. 1, extending almost the full 50-mm inlet span of the blades. A photograph showing the relationship of the bars protruding through the sidewall slot and the rotor blades is shown in Fig. 2. The cascade has an outlet span of 56.095 mm with an inlet span of 50 mm, the expansion being from blade leading edge to trailing edge on one sidewall only as shown in Fig. 1. Upstream and downstream static pressure taps were located 13.61 and 14.06 mm from the leading and trailing edges, respectively. The second throat enables the bars to be spun up to the correct speed, using an air-driven turbocharger as the driver, in a low background pressure. The rotor housing is vented to the dump tank and acts as a boundary layer bleed reservoir during the high-pressure part of the run.

Data from the 22 heat transfer gauges [6] or pressure transducers were recorded on a digital transient recorder sampling up to 8 channels at 500 kHz for each channel or directly into the A-D converter of the main computer at a lower rate of 400 Hz for each of 32 channels. The heat transfer rate measurement system has a bandwidth of 100 kHz, more than adequate to resolve the wake interaction phenomena, but three specially mounted pressure transducers (Kulite XCQ-062-50D) with a bandwidth of 600 kHz were required for the unsteady pressure measurements. Conventional semiconductor transducers (National Semiconductor Corp. type LX-1620D) operating in a differential mode and connected to 30 blade taps via short lengths of small bore (1.58 mm) tubing were used for the steady pressure survey where the bandwidth of approximately 2 kHz was more than adequate. The locations of heat transfer sensors and pressure taps on the blades is shown in Figs. 3(*a*) and (*b*) in terms of surface length x/s from the design stagnation point.

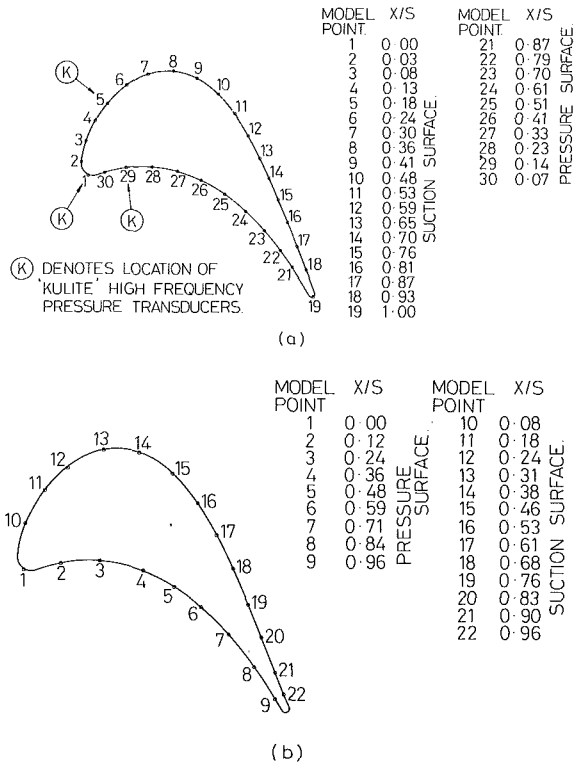


Fig. 3(*a*) Coordinates of pressure tappings on the blade profile; (*b*) coordinates of heat transfer gauges on the blade profile

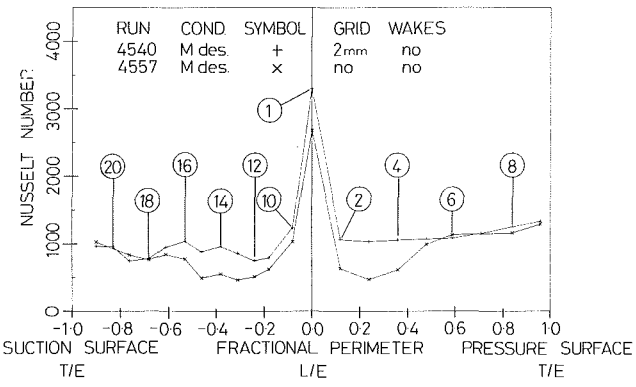


Fig. 4 Effect of free-stream turbulence level on mean heat transfer rate without wakes. Operating conditions are for nominal "design" case, see Table 1, M_e = 1.18, Re = 8.19 E5.

Nomenclature

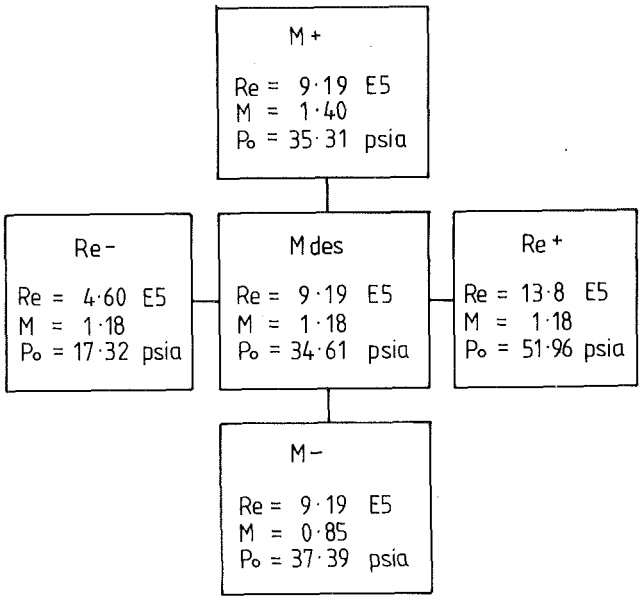
M = Mach number
Nu = Nusselt number
$\dot{q}$ = heat transfer rate W/m^2
Re = Reynolds number (based on inlet total conditions, isentropic exit Mach number and tangential chord)
T = temperature K
U = blade speed
C_2 = absolute velocity at exit from NGV, no wakes
V_2 = relative rotor inlet velocity, no wakes
C_2' = absolute velocity in NGV wake
V_2' = relative rotor inlet velocity with wake interaction
c = tangential chord
k = thermal conductivity W/mK
s = blade surface length
x = distance from leading edge to measurement point
β = incidence angle measured from turbine axis

Subscripts

amb = ambient
e = exit condition
1 = inlet (angle)
m = parameter at the selected measuring instant
o = total

Downloaded 01 Jun 2010 to 171.66.16.71. Redistribution subject to ASME license or copyright; see http://www.asme.org/terms/Terms_Use.cfm

Table 1



For To/Tamb = 1.5

Tangential chord = 41.18 mm (Axial cord = 34.82 mm)

Pitch = 34.30 mm

Inlet span = 50.00 mm

Experimental Results

Baseline Steady-State Results. The steady-state experimental results (without rotor generated wakes) will be presented in this section for surface heat transfer rate, surface pressure, and flow visualization. The effects of variations in free-stream turbulence levels, exit Mach number, Reynolds number, and flow incidence changes are examined. The heat transfer data are presented in terms of the dimensionless Nusselt number

$$\mathrm{Nu} = \frac{\dot{q}_m c}{(T_o - T_m)k}$$

where the local heat transfer rate $\dot{q}_m$ is measured at a time when the rising surface temperature is T_m.

A plot of $\dot{q}$ versus surface temperature rise is shown in Figs. 5(*a*) and (*b*) of [5]. If the Nusselt number is assumed constant at each instant throughout the usable portion of the test period a line may be drawn between Nu = 0, i.e., $T_o = T_m$ and $\dot{q}_m$, T_m defining Nu as above.

Mean Heat Transfer Without Wakes. Figure 4 shows a comparison of the distribution of mean Nusselt number over the blade surface for two values of free-stream turbulence, without wake induced unsteadiness. The free-stream conditions for temperature (432 K), Mach number (1.18), Reynolds number (9.19×10^5), and incidence angle (58.06 deg) were near nominal design values, Table 1. The turbulence levels stated have been measured by previous workers in the facility [7]. The 4 percent turbulence case was generated by a 15 mm between centers single array of 2-mm-dia circular cylinders parallel to the blade span and 208 mm upstream from the instrumented blade (Fig. 1). The low-turbulence case represented the best estimate of grid-free mainstream values, viz. < 0.8 percent [7]. In addition to the enhancement due to free-stream turbulence, the characteristic heat transfer rise associated with a transitional boundary layer on a turbine blade appears to have been brought forward. Figure 5 shows

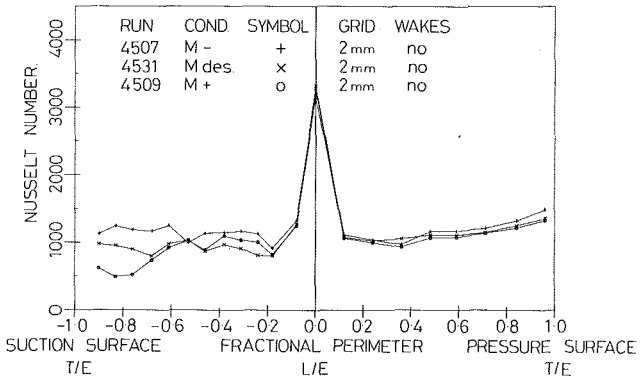


Fig. 5 Effect of off-design Mach number on distribution of mean heat transfer rate. Refer to Table 1 for nominal operating conditions.

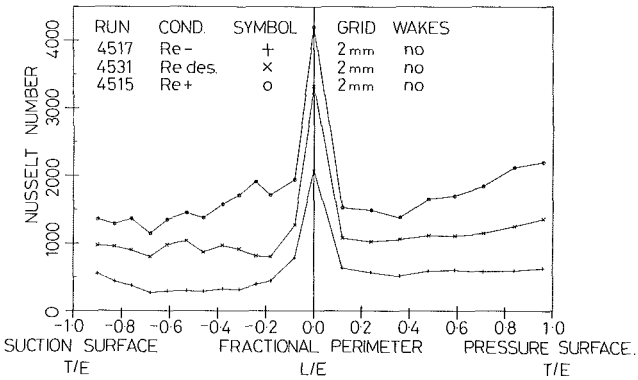


Fig. 6 Effect of Reynolds number on mean heat transfer rate

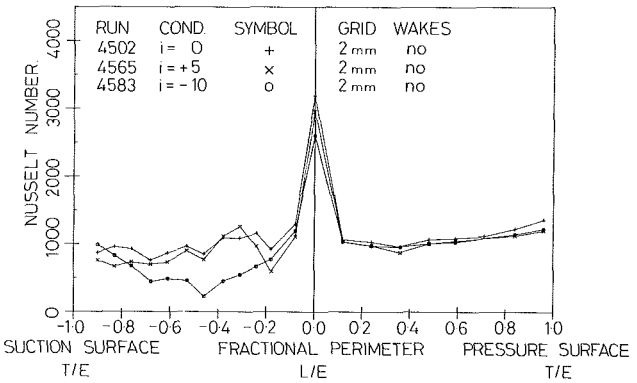


Fig. 7 Effects of incidence variation on mean heat transfer rate at the nominal "design" case, M_e = 1.18, Re = 8.19 E5

some effects due to changes in the exit Mach number to off-design conditions. The main effects appear to be on the suction surface; especially rearward of the approximate locations of the impingement point of the trailing edge shock [8] near $x/s = -0.6$. All other flow parameters in this test were kept near the design values and the grid turbulence generator was in place. The location of boundary layer transition at $x/s = -0.175$ appears to be unaffected by the exit Mach number variation.

The Reynolds number scaling effect (e.g., [3]) is shown clearly in Fig. 6 for design conditions, for $1.5 \times \mathrm{Re}_{\mathrm{design}}$ (Re^+) and $0.5 \times \mathrm{Re}_{\mathrm{design}}$ (Re^-). Incidence effects are shown in Fig. 7 for design Reynolds number and Mach number. The design incidence is 58.06 deg, see Fig. 1, and the off-design cases considered were +5 deg and −10 deg. The main effects again are confined to the suction surface where, as is shown in the next section, the pressure gradient near the

Downloaded 01 Jun 2010 to 171.66.16.71. Redistribution subject to ASME license or copyright; see http://www.asme.org/terms/Terms_Use.cfm

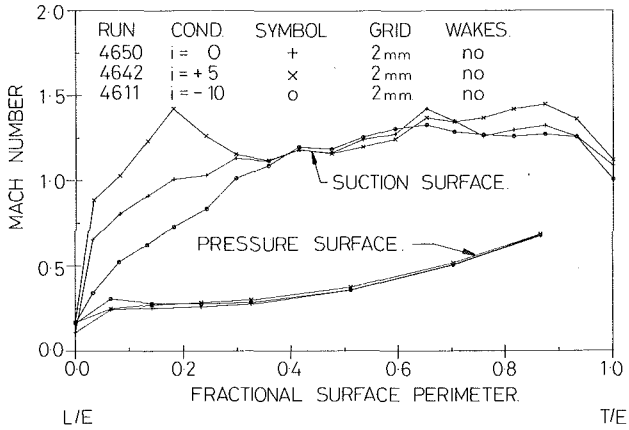


Fig. 8 Effect of incidence variations on mean surface Mach numbers at the nominal "design" case, M_e = 1.18, Re = 8.19 E5

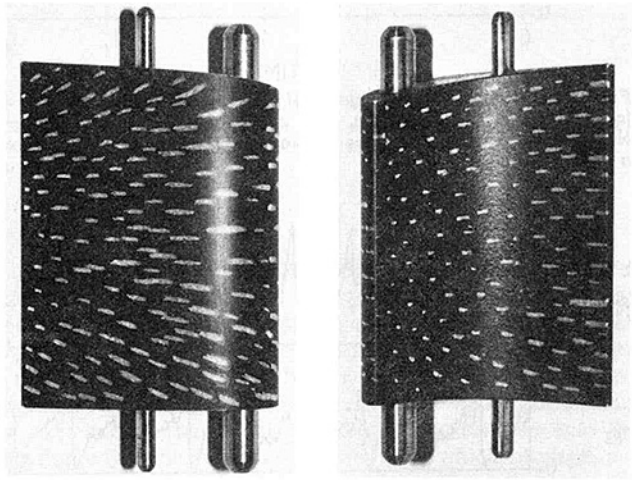
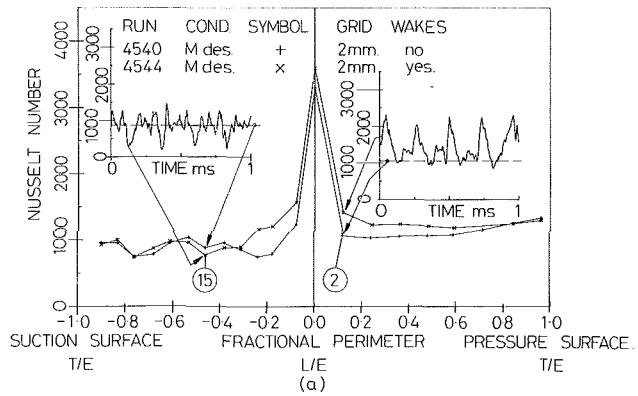


Fig. 9(*a*) Oil-dot surface flow visualization on the blade suction surface; and (*b*) oil-dot surface flow visualization on the blade pressure surface



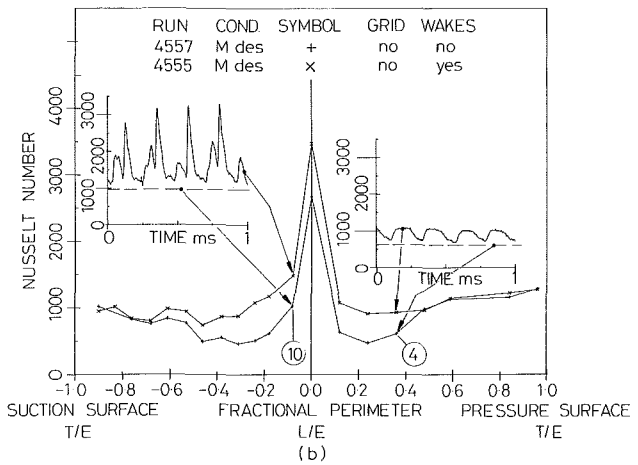


Fig. 10(*a*) Effect of wake interaction on mean heat transfer to blade with free-stream turbulence ≈ 4 percent, nominal "design" operating conditions. Inset are typical transient recorder signals at two *x/s* locations showing a 1 ms interval of the record together with the time-averaged value in the absence of wake interaction. (*b*) Effect of wake interaction on mean heat transfer to blade with low (≈ 0.8 percent $u'/\bar{U}$) free-stream turbulence at nominal "design" operating conditions. Inset are typical transient recorder signals together with the time-averaged value in the absence of wake interaction.

leading edge is strongly affected. It should be noted that the spacing of the heat transfer gauges between $-0.1 < 0 < +0.1$ *x/s* does not allow any deductions to be made about the movement of the stagnation point with incidence changes.

Surface Mach Number Distribution. The Effect of Incidence Variations. The reduced apparent blade incidence angle caused by the diminished velocity in a wake also results in a marked variation in the velocity distribution over the suction surface of the blade. In order to assess the importance of such incidence changes in the steady state, a series of tests was carried out at incidences of + 5 deg and − 10 deg from the nominal design value of β_1 = 58.06 deg. It should be noted that the results at (β_1 + 5 deg) were obtained in order to check the overall behavior of the profile with various inlet gas angles and only the (β_1 − 10 deg) value is applicable to the effects of wake-blade interaction. The general effect, shown in Fig. 8, is as anticipated and the effect of an increase in incidence angle to (β_1 + 5 deg) is a higher suction peak Mach number of 1.4 followed by a diffusion to 1.1 at 30 percent *x/s* consistent with the Nusselt number increase seen in Fig. 7 over the same range of *x/s*. There is a small increase in pressure surface Mach number near the leading edge which appears to have a negligible effect on the Nusselt number in this region. At an incidence of (β_1 − 10 deg) there is the expected marked reduction in suction surface Mach number for *x/s* < 30 percent coupled with a slightly higher Mach number near the front of the pressure surface, *x/s* < 15 percent.

Surface Flow Visualization. The "rapid-on, rapid-off" characteristic of the flow in the transient cascade offers advantages in surface flow visualization, since the starting and stopping processes are extremely short and do not smear the oil/titanium-dioxide mixture used. The extent of secondary flow on the suction surface is evident from Fig. 9(*a*), covering approximately 30 percent of the span at the trailing edge from each sidewall. The pressure surface, on the other hand (Fig. 9(*b*)), presents no unexpected phenomena and the conclusions are that there are no unexpected separations or unusual secondary flows likely to cause difficulties in the interpretation of either Nusselt or Mach number distributions over the blade surfaces.

Unsteady Heat Transfer With Wake Passing

The experiments conducted with the rotor-bar wake generator operating were confined to the design case of free-stream conditions, viz., M_e = 1.2, Re ≅ 9 × 10^5, incidence = 58.06 deg. All tests comparing the wake versus no-wake heat transfer distribution were also made with and without the free-stream turbulence generating grid in place.

Mean Heat Transfer Comparisons. Figures 10(*a*) and 10(*b*) show the effect of wakes on the mean heat transfer distribution with high and low free-stream turbulence, respectively. There is a significant enhancement of the mean Nusselt number beginning with the leading edge and ex-

Downloaded 01 Jun 2010 to 171.66.16.71. Redistribution subject to ASME license or copyright; see http://www.asme.org/terms/Terms_Use.cfm

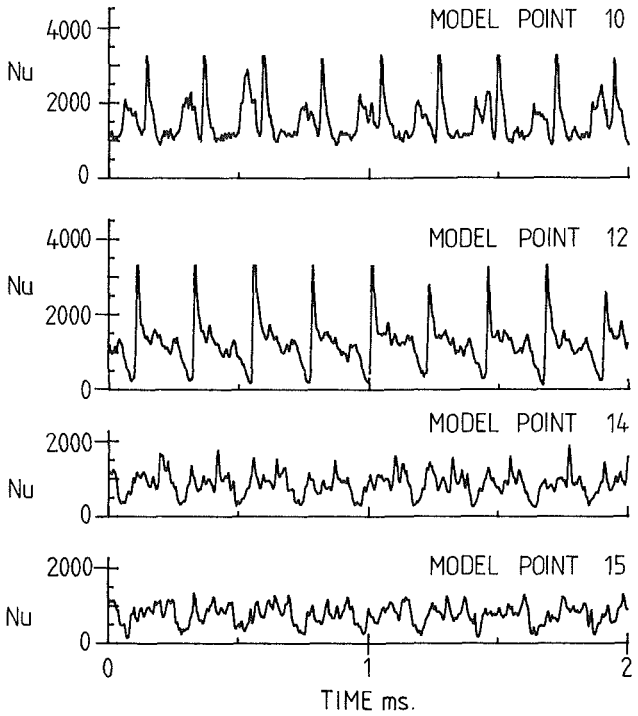


Fig. 11 Transient recorder signals of heat transfer rate for gauges 10, 12, 14, and 15 on the blade suction surface showing wake and shock impingement effects. Nominal "design" operating conditions, turbulence level ≈ 4 percent $u'/\bar{U}$.

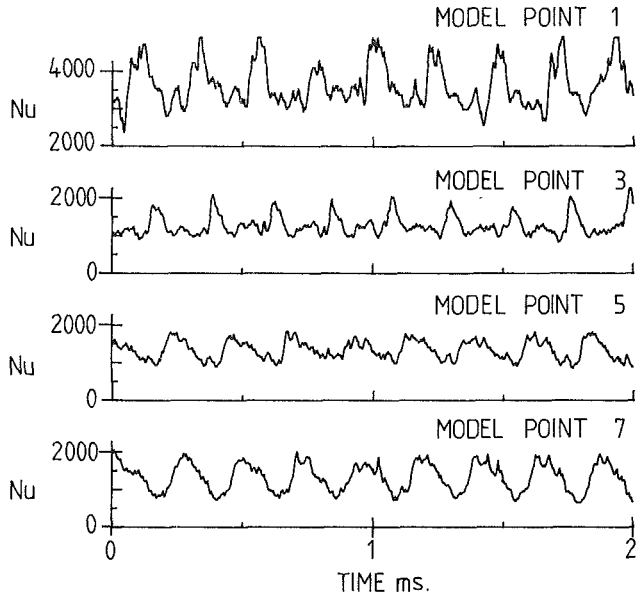


Fig. 12 Transient recorder signals of heat transfer rate for gauges at locations 1 (stagnation point), 3, 5, and 7 on the pressure surface. Nominal "design" operating conditions, turbulence level ≈ 4 percent $u'/\bar{U}$.

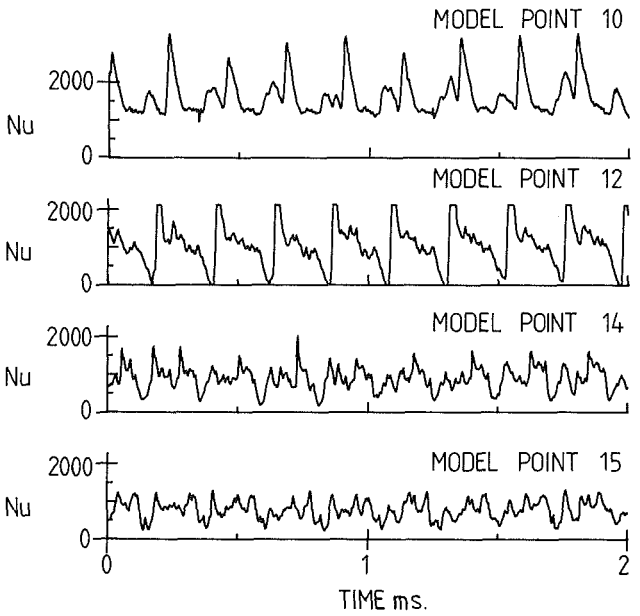


Fig. 13 Transient recorder signals of heat transfer rate for gauges at locations 10, 12, 14, and 15 on the suction surface showing separate wake and shock impingement effects. Nominal "design" operating conditions, low turbulence level $u'/\bar{U} \approx 0.8$ percent.

tending over much of the forward blade surface in both cases. It is interesting to compare the similarity of Figs. 4 and 10(*b*), i.e., the free-stream turbulence (whether grid generated isotropic or relatively low frequency discrete wake turbulence) appears to bring forward the point of onset and completion of transition. Beyond the 50 percent x/s point on the pressure surface and the 70 percent x/s point on the suction surface, the Nusselt number values come together. In comparison, Fig. 10(*a*) shows clearly a further heat transfer increase over the 4 percent turbulence case when the wake passing generator is in use. Qualitatively the distributions in Fig. 10(*a*) differ in the point where the two traces merge, cf. Figs. 10(*b*) and 4. The suction surface distributions may be explained by the earlier completion of transition when there is both free-stream isotropic turbulence and large-scale bar wake turbulence driving the transition process. In fact, it appears that for a time the wake-case heat transfer rate actually drops *below* the no-wake case. Possible reasons for this will be offered in the next section where detailed transient traces are examined. Inset in both Figs. 10(*a*) and 10(*b*) are examples of the instantaneous heat transfer at selected locations with wake interaction for comparison with the steady values shown by the dashed horizontal line.

Instantaneous Heat Transfer Comparisons. The mean heat transfer comparisons discussed in the previous section were averaged values because of the basic on-line-computer sampling rate of 400 Hz per channel and the line fitting process of the software. Detailed time resolved displays of the high-frequency (5000 Hz) wake passing events were obtained by direct digital recording on the eight-channel transient recorder at a 500 kHz sampling rate for 6 ms. At this rate, the bandwidth of the system is limited by the 100 kHz analogue circuits. Figures 11 and 12 present a 2 ms interval of time resolved data at the measured point of the mean data presented earlier (225 ms). Looking first at the grid-in or high free-stream turbulence case at design conditions, it will be seen in Fig. 11 that the output from four suction surface locations near the front of the blade has several features which stand out. One is the sharpness and magnitude of the disturbance created by the wake generator. The rise time of the spikelike disturbance is within 2–3 digitized sample points (4–6 μs); clearly near the limits of the analogue. The peak of the spike is nearly three times the mean value reported in the previous section. Another feature of interest on gauge 12 is the significant drop in heat transfer rate immediately before the sharp rise to values substantially below the mean. These strong spike disturbances are not evident, however, on gauge 14 ($x/s = 0.38$) or further back. It should be remembered that the relative Mach number of the rotating bar was about 1.17 corresponding to the stage design exit Mach number for this blade. The shock waves associated with the rotating bars sweep past the cascade and strike the suction surface near the point of maximum thickness as first observed by Doorly [10]. The present results confirm the results of Doorly [10] that the

Downloaded 01 Jun 2010 to 171.66.16.71. Redistribution subject to ASME license or copyright; see http://www.asme.org/terms/Terms_Use.cfm

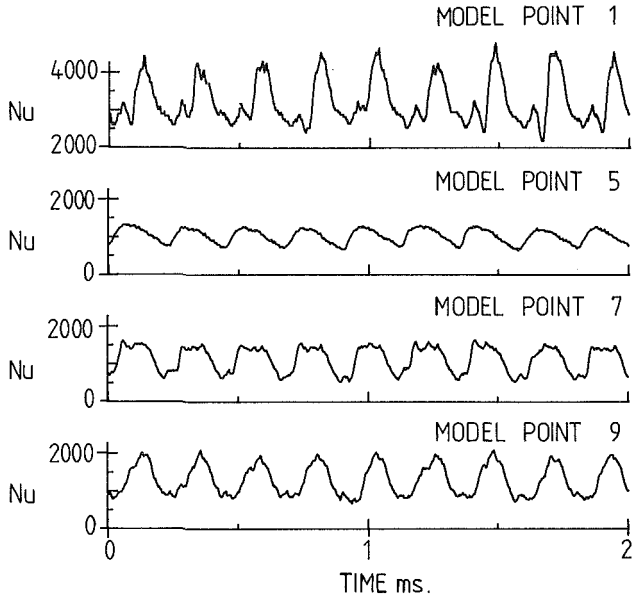


Fig. 14 Transient recorder signals of heat transfer rate for gauges at locations 1 (stagnation point), 5, 7, and 9 on the pressure surface. Nominal "design" operating conditions, low turbulence level $u'/\bar{U} \approx$ 0.8 percent.

shock waves very profoundly affect the transient heat transfer rate. The sharp fall in heat transfer (often to near zero) may be associated with a transient separation caused by the shock wave, followed by a very fast transient spike as the boundary layer reattaches turbulently. In the case of Doorly's experimental investigation the shock waves were considerably weaker and the bar shock induced separation only near the leading edge, the subsequent collapse of which resulted in a turbulent patch which was then swept downstream along the blade surface resulting in a characteristic transient rise in heat transfer. With the stronger shock waves in this investigation, *it may be observed, however, that the drop in heat transfer* and subsequent rise moves upstream toward the leading edge tied to the shock wave. Close examination of the disturbance trajectory (time location on gauges 10 and 12 of Fig. 11) indicates that the shock disturbance is moving toward the leading edge arriving first at gauge 12 ($x/s = -0.24$) then passing over 11 ($x/s = -0.18$), then 10 ($x/s = -0.08$).

Figure 12 shows some representative fast sweep traces for the pressure surface heat transfer (and stagnation point) at design conditions. The periodic disturbances can be seen to broaden and increase in amplitude as they move toward the trailing edge. Again the model of a turbulent wake being transported through the passage as suggested by Doorly [1] is consistent with the present results. The trajectory of a single disturbance appears to travel toward the trailing edge. The bar shock wave is not evident on the pressure surface, as would be expected from geometry. The stagnation point/leading edge gauge shows strong wake disturbances, mostly positive going from the mean values. The leading edge of the disturbance traversing the pressure surface starts out quite steep at the stagnation point with a less steep trailing edge. This pattern extends well back along the pressure surface albeit with a lessening of the gradients (see Fig. 12, gauge 7).

The low free-stream turbulence (no grid) case for wide bandwidth time resolved heat transfer measurements is shown in Figs. 13 and 14 for suction surface and pressure surface, respectively. No significant changes appear compared with the high turbulence case except the sharp drop on s/s gauge 12 actually which is to zero heat transfer rate. The traces have

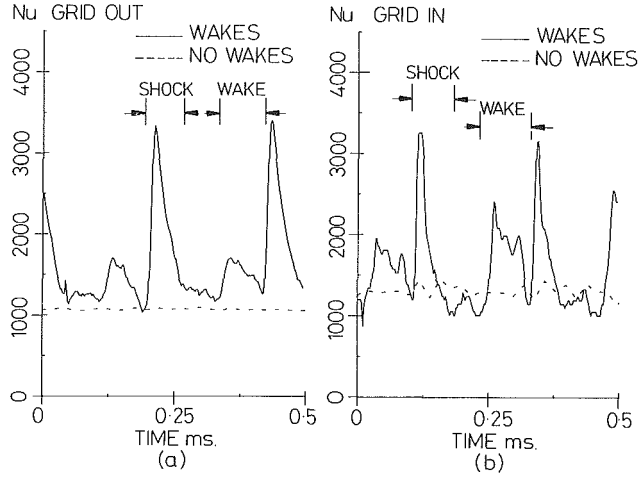


Fig. 15(*a*) Sample for gauge 10 over 0.5 ms of suction surface heat transfer rate with and without wake interaction at low free-stream turbulence level; and (*b*) nominal 4 percent turbulence level. Nominal "design" operating conditions of M and Re.

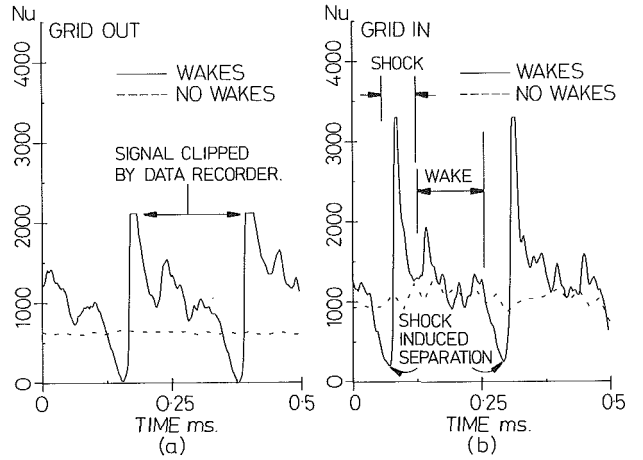


Fig. 16(*a*) Sample for gauge 12 over 0.5 ms of heat transfer rate with and without wake interaction at low turbulence level; and (*b*) nominal 4 percent turbulence level. Nominal "design" operating conditions of M and Re.

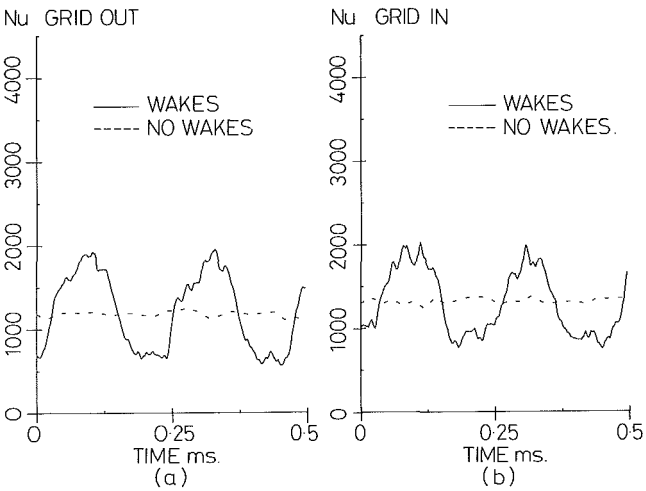


Fig. 17(*a*) Sample for gauge 8 over 0.5 ms of heat transfer with and without wake interaction at low turbulence level; and (*b*) with nominal 4 percent turbulence level. Nominal "design" operating conditions of M and Re.

Downloaded 01 Jun 2010 to 171.66.16.71. Redistribution subject to ASME license or copyright; see http://www.asme.org/terms/Terms_Use.cfm

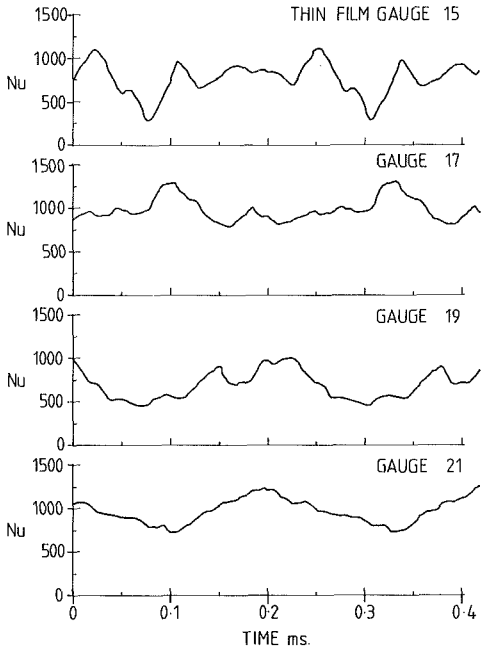


Fig. 18 Ensemble-averaged heat transfer rates for gauges 15, 17, 19, and 21 on the blade suction surface showing developments of wake footprint toward rear of blade (gauges 19 and 21). Nominal "design" operating conditions of M and Re.



Fig. 19 Schlieren photograph showing shock impingement and subsequent reflection and refraction in the flow field



Fig. 20 Schlieren photograph illustrating a wake entering the upper passage and shock-induced separation in the lower passage

less background fluctuation perhaps due to the delayed transition. Wake structure from gauge 15 (x/s = 0.46) onto the trailing edge is made more observable by ensemble averaging of the signals as will be discussed below. It is also instructive to directly compare the levels of several of the model point gauges with and without the wake generator. This will also be discussed below. The lower mean heat transfer on parts of the wakes-on data compared with the no-wakes case can be qualitatively explained by the drop in heat transfer associated with the separation caused by the shock wave.

Single-Channel, Time-Resolved Heat Transfer—Wakes Versus No Wakes. In order to make direct comparisons of the effect of wakes on the instantaneous heat transfer data, time resolved plots were made of a 1 ms segment of the isothermal wall heat transfer rate with and without the turbulence grid generator in place (Figs. 15, 16, and 17). The first figure (15(*a*)) is for no-grid and for suction surface heat transfer gauge No. 10 (x/s = −0.08). Again, as noted on the figure, the two distinct disturbance patterns are seen: the "shock" spike and the "wake." Also of note is that the wake disturbance is weaker on the no-grid trace than the grid-in case. Secondly, the instantaneous value between the disturbance does not drop to the no-wake level for the no-grid case but does in the grid-in case. In other words, the turbulence generated by the wakes alone fills in the space between the strong disturbance to maintain a level of heat transfer above that of the low free-stream turbulence case. In the case of high background turbulence with the grid in, the levels between the wake disturbances fall down to background levels.

Surface gauge No. 12 (x/s = −0.24), shown in Fig. 16, indicates the same general behavior but with some important differences. The wake disturbance is not as easily identified as it has by this time begun to spread out as it progresses through the passage. Secondly, the strong drop below mean levels before the shock disturbance is very apparent. In fact, the drop to zero levels of heat transfer is evident in the no-grid low turbulence case indicating the laminar boundary layer's inability to stay attached in the face of the strong shock pressure gradient. The clipping at the top of some of the shock spikes is caused by saturation of the instrumentation channel.

Figure 17 shows similar comparisons on a single pressure surface heat transfer gauge (No. 8, x/s = 0.84). The time resolved heat transfer shows a regular disturbance which oscillates between levels above and below the mean values. Looking again at Figs. 10 and 11, we see that mean values of heat transfer with and without wakes are nearly equal at this model point even though the instantaneous effects of wake passing are still quite strong.

Ensemble-Averaged Transient Heat Transfer. Figure 18 shows the ensemble average of ten cycles of wake passing at four model points well back on the suction surface (Nos. 15, 17, 19, 21 or x/s = −0.46, −0.61, −0.76, and −0.90,

Downloaded 01 Jun 2010 to 171.66.16.71. Redistribution subject to ASME license or copyright; see http://www.asme.org/terms/Terms_Use.cfm

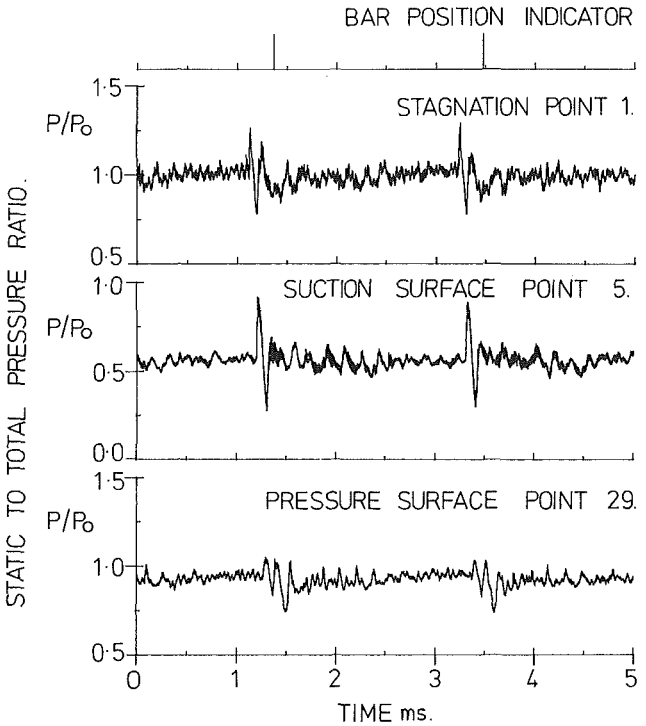


Fig. 21 Effect of wake interaction on pressure, expressed as static/total ratio at nominal stagnation point and two locations on the suction surface and the pressure surface. Time interval = 5 ms. Nominal "design" cascade conditions and bar relative speed.

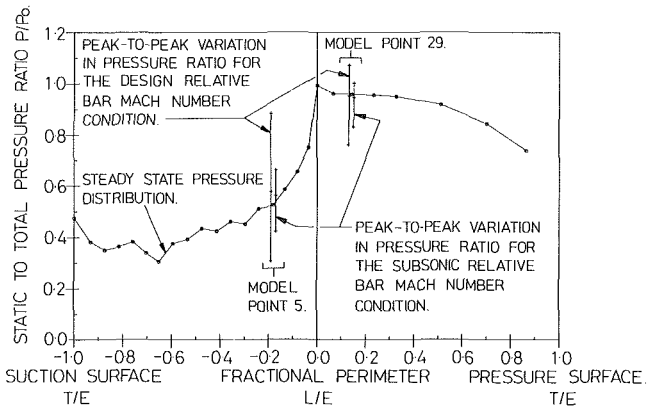


Fig. 22 Unsteady pressure, expressed as ratio static/total, caused by wake interaction superimposed on steady pressure ratio

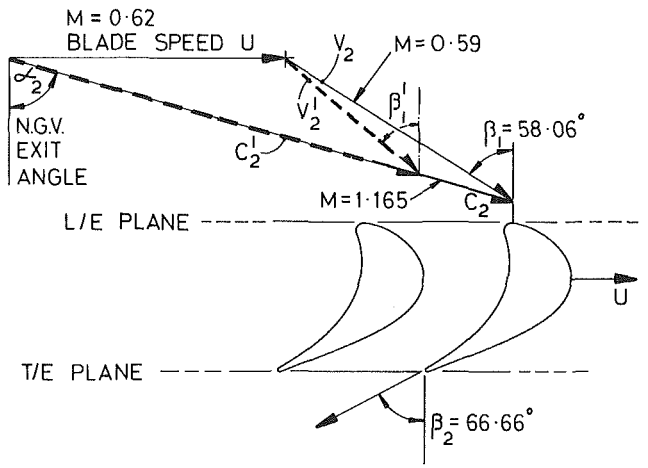


Fig. 23 Velocity triangles at inlet for steady nominal design case showing reduced incidence caused by the deficit in the wake

respectively). Without ensemble averaging, the traces near the back of the suction surface showed little obvious periodicity of wake passing events (e.g., see gauge 15 of Fig. 13(*a*)). The periodicity is clearly visible when ensemble averaged indicating that a coherent disturbance extends throughout the passage.

Flow Visualization—Schlieren. A double-pass Schlieren system, with the rear wall of the cascade fabricated from optically polished stainless steel, was used to study the distortion of the wakes as they traversed rotor passages and to observe the motion of the shock waves produced by the normally supersonic bars. All tests were done with the turbulence grid in place. The photographs were taken with increasing time delays from the start of flow such that a whole traverse of the passage by the wake was observed. Only two examples are included, since the wake distortion is similar to that reported by Doorly, i.e., the higher velocities over the suction surface leading to a stretching of the wake footprint relative to the pressure surface. In the present case, however, the reflected shock is much stronger than was evident in Doorly's experiments. An example of this may be seen in Fig. 19.

The shocks from the bar can be seen impinging the crown of the suction surface. The effect on heat transfer rate may be seen in, for example, Fig. 11 where the shock impingement on the suction surface heat transfer gauges results in large negative and positive fluctuations in level. This shock is reflected and curved in the nonuniform flow field and is again reflected from the pressure surface but is weaker here, and its effect on the heat transfer rate is not marked, Fig. 12, gauges 5 and 7 for instance not revealing any shock-induced phenomena. The shocks from the bar move forward toward the leading edge so that their arrival at heat transfer gauge 12 is sooner than their appearance on gauge 10, Fig. 11. The wake from the bar follows in time sequence and the combined shock-wake pair may be identified in Fig. 11. At heat transfer gauge location 12 on the suction surface the shock system apparently leads to separation of the boundary layer and heat transfer rate falls momentarily to zero, a phenomenon not observed elsewhere on the profile, Fig. 20.

Wake Interaction Effects on Surface Pressures

Steady-state measurements of pressure distribution have already been reported earlier in this paper. Measurements of unsteady pressures induced by the wake/shock phenomena were confined to three tapping points: on the stagnation line, suction surface and pressure surface. Only 2 rotating bars were used rather than 16, the correct number, in order to clarify the processes. Fast response transducers, Kulite type XCQ-062-50D were used with the diaphragms mounted flush with the blade surface. The time-resolved results for the two locations on the suction and pressure surfaces are shown in Fig. 21 where the effects of wake-blade interaction at a relative bar Mach number of 1.172 (the design value) last about 40–50 μs, roughly consistent with the wake passing time observed on the time-resolved heat transfer records. The shape of the time-resolved record, however, indicates that there is a region of decreased static pressure immediately following the expected increase. The static/total pressure ratios for this combination of p/p_o increase and decrease are shown superimposed on the steady-state values of p/p_o in Fig. 22. The increased pressure would be consistent with a surface Mach number of approximately 0.43, not out of line with a reduction of incidence of 10 deg, Fig. 23. A change of incidence of 10 deg indicates a reduction of absolute inlet Mach number from 1.165 to about 0.933 which is somewhat higher than expected from usual NGV losses. The data for surface

Downloaded 01 Jun 2010 to 171.66.16.71. Redistribution subject to ASME license or copyright; see http://www.asme.org/terms/Terms_Use.cfm

Mach number at an incidence of -10 deg shows a Mach number at $x/s = 0.475$, i.e., a p/p_o value of 0.857 only slightly less than the value of 0.883 observed, so that the *increase* in static/total pressure ratio is in reasonable agreement with a transient incidence change.

Conclusions

It must be emphasized that the simulation of an NGV by a rotating wake array outlined in this paper has yet to be verified by tests in which the rotor actually moves through the wakes from a stationary NGV ring. Such measurements on the identical blade geometry are planned in the blowdown facility described by Epstein et al. [4]. If it is found that midheight blade-wake interactions in this facility are closely replicated by the data presented here then there is a sound argument for continued use of the stationary rotor plus moving wake simulation. There are, however, several physical processes which cannot be modeled in this relatively simple manner. Among these are:

(*i*) The buoyancy forces on the NGV wake which is itself at a lower temperature than the mainstream.

(*ii*) The possible distortion of NGV passage flow by the periodic blockage arising from the rotor. Dunn et al. [2] have addressed this problem and observed the effect of the rotor on the heat transfer rate to an NGV.

(*iii*) The undoubtedly significant effect of wake-induced periodicity on the secondary flows such as the corner vortices in the rotor passage.

Despite these major shortcomings it is considered that the present study, together with that reported by Doorly and Oldfield [1], has highlighted some of the phenomena which will inevitably appear in "fully rotational" experiments and has established the nature and extent of unsteady effects on heat transfer rates and pressure distributions over the blade.

An extensive set of steady-state, i.e., no wake interaction, heat transfer, and aerodynamic data has been presented in Figs. 4–8. The effect of increasing the free-stream turbulence level from a low value ($<$ 1 percent) to approximately 4 percent was shown to be to move transition on the pressure surface forward from about 50 percent to about 10 percent x/s. On the suction surface a similarly large forward movement was noted, the transition region moving from around 50–60 percent to 30–40 percent x/s (Fig. 4). Variations in exit Mach number, on the other hand, had no effect on the location of boundary layer transition, although the strong passage shock which impinged on the suction surface at $x/s \approx 60$ percent at all exit Mach numbers caused a major reduction in trailing edge heat transfer rate (Fig. 5), possibly associated with boundary layer separation.

One of the most significant transient effects associated with wake blade interaction is the reduction in flow incidence angle and it has been demonstrated that there is (Fig. 7) a substantial reduction in heat transfer rate over the whole of the suction surface which begins at $x/s \approx 20$ percent. Comparison of these data with the unsteady (i.e., wake interaction) results in Fig. 10(*a*) shows that while there are momentary reductions in heat transfer rate below the mean value, the net effect of wake passing is to increase the heat transfer rate up to a location of $x/s = 35$ percent on the suction surface. Thereafter, the steady and unsteady heat transfer rates are, to a close approximation, the same. The increase in heat transfer rate (time averaged) caused by wake passing and shock boundary layer interaction apparently overrides any reduction due to transient incidence reductions.

The strong shock waves generated by the wake-producing bar when moving at the correct relative velocity has a profound effect on heat transfer rate. This is most clearly seen in Figs. 15 and 16 where a 2 ms segment of heat transfer rate data shows a 250 percent increase in rate preceded by a drop (occasionally to near zero). It is postulated that this reduction–enhancement process is a consequence of a boundary layer separation–reattachment process that occurs as the shock wave impinges on the suction surface of the blade and then moves forward, allowing turbulent reattachment with the resulting high heat transfer rate.

These phenomena require further investigation before the causes of the individual effects can be unambiguously identified. Some of them, notably the dominance of the shock boundary interaction, are a function of the transonic stage design. Nevertheless, it is believed that the method of simulation originally proposed by Doorly and Oldfield offers many advantages for fundamental studies.

Acknowledgments

This study was carried out with support from Rolls-Royce Ltd. and the Ministry of Defence, and the authors are grateful for their permission to publish the paper.

References

1 Doorly, D. J., and Oldfield, M. L. G., "Simulation of Wake Passing in a Stationary Turbine Rotor Cascade," submitted to the *Journal of Propulsion and Power*.

2 Dunn, M. G., "Turbine Heat Flux Measurements: Influence of Slot Injection on Vane Trailing Edge Heat Transfer and Influence of Rotor on Vane Heat Transfer," ASME JOURNAL OF ENGINEERING FOR GAS TURBINES AND POWER, Vol. 107, No. 1, Jan. 1985, pp. 76–83.

3 Hodson, H. P., "An Inviscid Blade-to-Blade Prediction of Wake Generated Unsteady Flows," ASME JOURNAL OF ENGINEERING FOR GAS TURBINES AND POWER, Vol. 107, No. 2, Apr. 1985, pp. 467–476.

4 Epstein, A. H., Guenette, G. R., and Norton, R. J. G., "The MIT Blowdown Turbine Facility," ASME Paper No. 84-GT-116.

5 Schultz, D. L., Jones, T. V., Oldfield, M. L. G., and Daniels, L. C., "A New Transient Cascade Facility for the Measurement of Heat Transfer Rates," AGARD Conference Proceedings No. 229, *High-Temperature Problems in Gas Turbine Engines*, 1977.

6 Schultz, D. L., and Jones, T. V., "Heat Transfer Measurements in Short Duration Hypersonic Facilities," AGARDOGRAPH No. 165, 1973.

7 Oldfield, M. L. G., Jones, T. V., and Schultz, D. L., "On-Line Computer for Transient Turbine Cascade Analysis," *IEEE Transactions on Aerospace and Electronic Systems*, Vol. AES-14, No. 5, Sept. 1978.

8 Haller, B. R., and Camus, J. J., "Aerodynamic Loss Penalty Produced by Film Cooling Transonic Turbine Blades," ASME JOURNAL OF ENGINEERING FOR GAS TURBINES AND POWER, Vol. 106, No. 1, Jan. 1984, pp. 198–205.

9 Lowery, G. W., and Vachon, R. I., "The Effect of Turbulence on Heat Transfer from Heated Cylinders," *International Journal of Heat Mass Transfer*, Vol. 18, 1975, p. 1229.

10 Doorly, D. J., and Oldfield, M. L. G., "Simulation of the Effects of Shock Wave Passing on a Turbine Rotor Blade," ASME JOURNAL OF ENGINEERING FOR GAS TURBINES AND POWER, Vol. 107, No. 4, Oct. 1985, pp. 998–1006.

Downloaded 01 Jun 2010 to 171.66.16.71. Redistribution subject to ASME license or copyright; see http://www.asme.org/terms/Terms_Use.cfm

S. H. Moustapha
Staff Aerodynamicist.

G. J. Paron
Senior Aerodynamicist.

Pratt & Whitney Canada, Inc.,
Montreal, Canada

J. H. T. Wade
Professor.
Department of Mechanical Engineering,
McMaster University,
Hamilton, Canada

Secondary Flows in Cascades of Highly Loaded Turbine Blades

Experimental measurements of the flow field in a low-speed, large-scale, annular cascade of highly loaded turbine rotor blades are presented. The blade has a turning angle of 128.5 deg, an aspect ratio of 0.88, and a Zweifel coefficient of 1. Detailed cascade tests consisted of inlet and exit flow parameter traverses, blade passage pressure distributions, and flow visualization. The results are presented in the form of contour plots and pitch-averaged radial distributions of losses and flow angles. The measurements are compared with the results obtained for the same blade section tested in a planar cascade. Distribution of the losses and flow angles revealed the presence of two large vortices that occupied a major portion of the trailing edge plane. A large high-loss core was visible in the center of the blade passage and coincided with regions of maximum flow underturning. The measured cascade secondary losses compared well with existing correlations.

Introduction

There are significant mechanical and cost benefits associated with the use of low rotor speed and low-aspect-ratio blades in the design of a high-pressure-ratio gas turbine. However, a serious disadvantage of this type of design is the low aerodynamic efficiency due to large flow turning and the resulting excessive secondary losses. The penalizing effects of secondary flow on turbine performance are due mainly to the associated vortices which cause dissipation of energy and tend to promote separation in the corner between the blades and the annulus walls. In particular it is the secondary flows which affect the gas exit angles and hence the incidence on a subsequent blade row. Considering the growing trend toward using high-turning-angle and low-aspect-ratio blades, it is evident that a successful turbine design requires a reasonably accurate assessment of the secondary losses and the resulting gas exit angles.

Over the past two decades a significant number of theoretical and experimental studies have been made to investigate the secondary flow phenomena. Examples of experimental investigation of secondary flow in turbine cascades are Came [1], Langston et al. [2, 3], Sjolander [4], Woods [5], Rohlik et al. [6], Camus et al. [7], Binder et al. [8], and Sieverding et al. [9]. Annular cascade data for blades with high turning angles are necessary since most of the available data have been derived from experiments conducted on rectilinear cascades or annular cascades with low turning.

The purpose of this study is to present and discuss the results of a series of tests carried out on an annular low-speed cascade of highly loaded turbine blades with a turning angle of 128.5 deg. The test rig had inlet and outlet ducts of hyperbolic shape to provide uniform flow at the blade-design angles. The measurements are compared with the results obtained for the same blade section tested in a planar cascade. The secondary losses at the exit plane of both cascades were analyzed and compared with the available data.

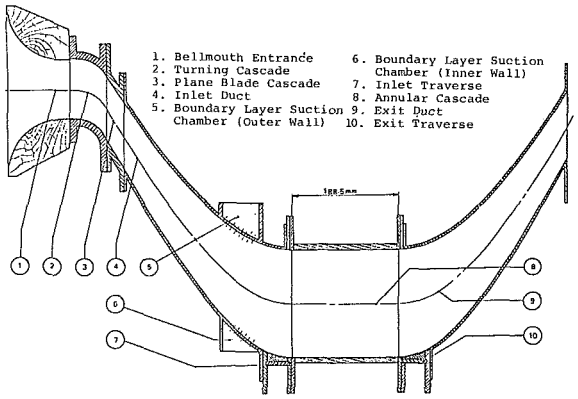


Fig. 1 A sectional view of the annular cascade rig in a plane through the center line

Experimental Apparatus

The experimental investigation of the secondary flow phenomena in turbine cascades requires accurate measurements of both the free-stream and the secondary flow. Many of the highly loaded turbine stages, considering the individual blade passage, are of such small scale as to prohibit a detailed analysis of the three-dimensional effects using even the most advanced measurement techniques. In order to minimize the probe size influence on the flow, and thus improve the accuracy of the measurements, large-scale models are called for. Annular cascades of large size, however, usually pass such a massive flow as to prohibit, from an economical viewpoint, the use of a complete annulus as a test section. To circumvent these difficulties a special annular test rig was designed [10] and constructed. Sufficient flexibility was built into the rig so that the inlet flow conditions could be tailored radially and circumferentially ac-

Contributed by the Gas Turbine Division of THE AMERICAN SOCIETY OF MECHANICAL ENGINEERS and presented at the 30th International Gas Turbine Conference and Exhibit, Houston, Texas, March 18-21, 1985. Manuscript received at ASME Headquarters, January 7, 1985. Paper No. 85-GT-135.

Copyright © 1985 by ASME
Downloaded 01 Jun 2010 to 171.66.16.71. Redistribution subject to ASME license or copyright; see http://www.asme.org/terms/Terms_Use.cfm

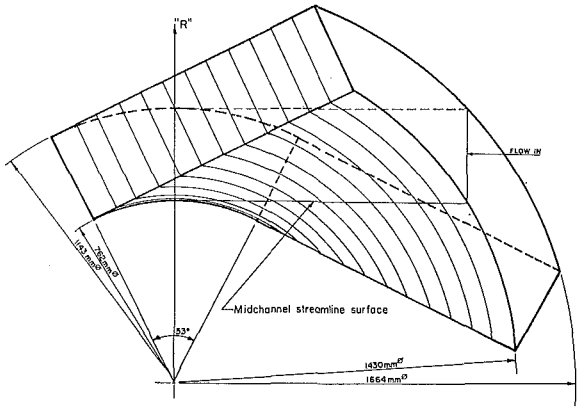


Fig. 2 A schematic drawing of the inlet duct

cording to the test requirements. A cross-sectional view of the test rig is shown in Fig. 1. The test facility is an open-circuit wind tunnel consisting of three main parts:

1 a large scale sector of an annular turbine blade cascade (8 in Fig. 1)
2 an inlet section: 1, 2, 3, and 4 in Fig. 1; and
3 an outlet section: 9 in Fig. 1.

The entrance to the inlet duct (4), which includes the bellmouth, the turning and plane-blade cascades, was designed with the object of turning the flow and ensuring that the streamline surfaces were planar and inclined to a plane passing through the blade leading edge at the design inlet angle (64 deg). In order to provide uniform inlet and exit flow angles, the inlet and outlet ducts (4 and 9) have walls of hyperboloidal shape. The inlet duct is shown in Fig. 2 with equidistant cross sections normal to the axial direction. The straight line generatrices of the inlet and outlet ducts are inclined to the design-blade inlet and exit angles. Two sliding circular arc segments (7 and 10 in Fig. 1), providing for circumferential traversing, are situated at the inner wall of both the inlet and the exit of the cascade. Inlet boundary-layer control is provided by means of suction chambers located on the inner and the outer walls of the inlet duct. Figure 3 is a photographic illustration of the test rig. References [11, 12, 13] give further information on the annular test rig and describe the effect of the inlet boundary layer on the secondary flows within the blade passage.

The cascade test section is a 45 deg segment of an annulus with an inner radius of 381.5 mm and an outer radius of 571.5 mm. The annular section housed four identical blades, three flow passages of 15 deg each, designed with the object of providing the proper working conditions in the center-blade passage, within which the measurements were to be made. Figure 4 shows the cascade test section which was manufactured from clear acrylic plastic to allow for observation of the flow within the test passage. The profiles of

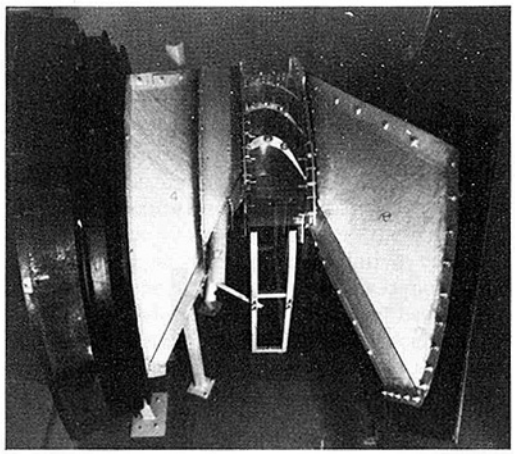


Fig. 3 A photograph of the annular cascade rig (side view)

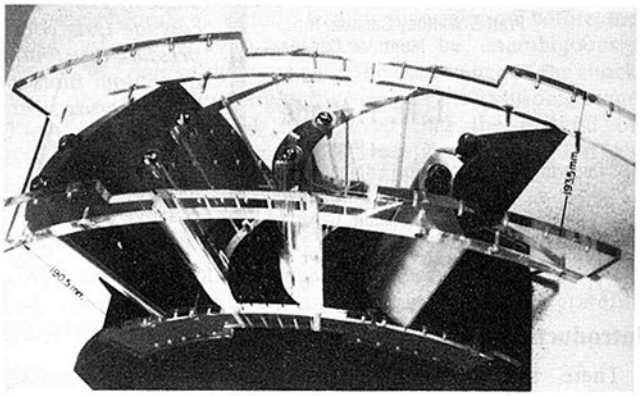


Fig. 4 A view of the annular cascade test section

the blades selected for testing are cylindrical and of the "flat-back" type (Fig. 5). The blades were installed with the leading edges in the radial direction and the trailing edges inclined at 6.5 deg to the radial direction. The reference direction for the circumferential locations was the radial line "R" (Fig. 2) which was the center of the test passage at the leading edge plane. The important geometrical characteristics of the cacade are as follows:

Blade chord 214 mm	Blade exit angle 64.5 deg
Blade axial chord 188.5 mm	Aspect ratio (H/C) 0.88
Blade inlet angle 64 deg	Pitch/axial chord (midspan) 0.66
Hub-to-tip ratio 0.66	Blade Zweifel coefficient 1.0

A two-dimensional (planar) test rig, geometrically similar to the annular rig, was built to test the same blade profile (Fig. 6). The purpose of those tests [14] was to investigate the effect of rig geometry on the secondary flow pattern at the cascade exit.

Nomenclature

C = blade chord
C_L = lift coefficient*
C_{p_o} = local total pressure loss coefficient*
C_{p_S} = local static pressure coefficient*
C_Z = Zweifel lift coefficient*
H = annular height
P = pressure
r = radial coordinate
R = radial reference direction (center of the cascade at inlet)
S = blade pitch
V = absolute flow velocity
X_S = secondary loss parameter*
Y_T = overall loss coefficient*
Y_P = profile loss coefficient
Y_S = secondary loss coefficient*
Z = blade loading parameter*
z = spanwise distance measured from the inner wall
α = gas angle measured from the axial direction
β = metal angle measured from the axial direction
δ^* = boundary layer displacement thickness
θ = circumferential location measured from the cascade center (R) at the inlet
ρ = air density

Subscripts

1 = passage inlet
2 = passage exit
a = axial
m = mean
o = stagnation
S = static

* Defined in Appendix 1

Downloaded 01 Jun 2010 to 171.66.16.71. Redistribution subject to ASME license or copyright; see http://www.asme.org/terms/Terms_Use.cfm

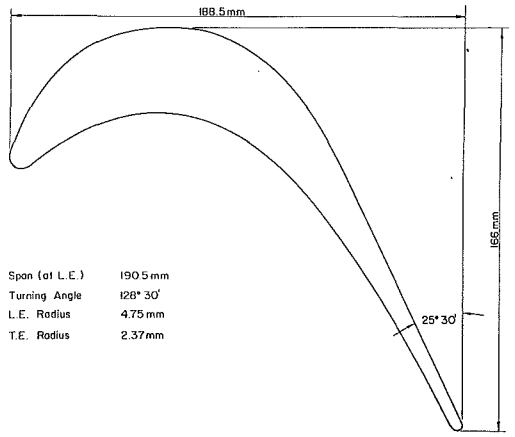


Fig. 5 The blade profile

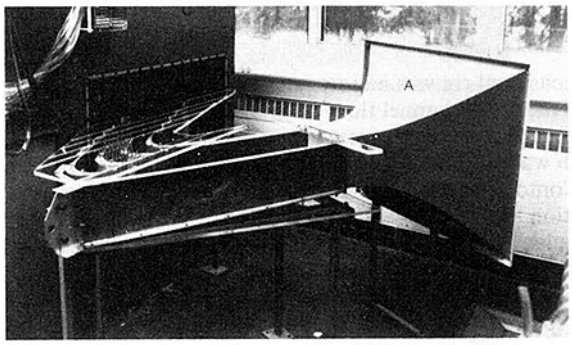


Fig. 6 Overall view of the planar cascade test facility

Experimental Procedure

The inlet and exit traverses in the annular rig were conducted at two measuring stations located at an axial distance of 27.5 mm upstream and downstream from the test section. The planar rig provided a second exit measuring station (*B* in Fig. 7) in order to evaluate the effect of flow mixing on secondary losses. The main flow field measurements were made using a United Sensor five-hole directional probe of the type DA/125/12F/10/CP. The flow field was traversed radially and circumferentially across more than one blade pitch by means of traversing gears which were mounted on the sliding arc segments (7 and 10 in Fig. 1) Two pitot probes of flattened tip type were used for boundary layer measurements at the inner and outer endwalls. Provisions were made for static pressure measurements on the walls of the center blade passage. A total of 130 static taps were used at seven axial stations in the test section. The flow visualization was performed by means of a low-speed smoke probe designed to combine two gas jets, one of anhydrous ammonia, the other of sulfur dioxide. Passage surface-flow visualization was obtained using a mixture of kerosene and lamp-black.

A series of tests was conducted on both annular [12, 13] and planar [14] rigs in which the inlet conditions were varied and the corresponding flow parameters (total pressure and flow angle) at the cascade exit were measured. The cascade inlet velocity range was 23 m/s to 47 m/s which corresponded to Reynolds numbers of 3×10^5 to 6×10^5 based on the blade chord. The test Reynolds numbers are representative of those found in typical high-pressure-ratio gas turbines. The inlet turbulence intensity, measured using a normal hot-wire probe, was about 4% root mean square.

Inlet Flow

Extensive tests were first conducted on both rigs in order to establish uniform inlet flow conditions across the center-blade

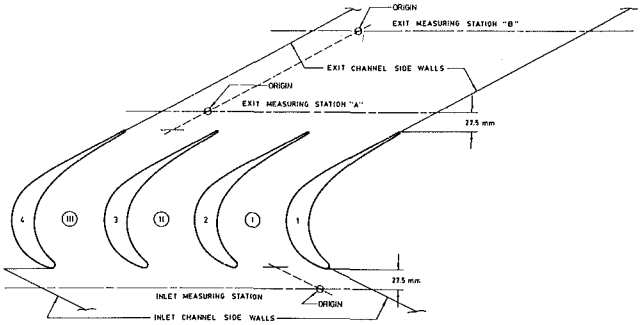


Fig. 7 Planar cascade inlet and exit measuring stations

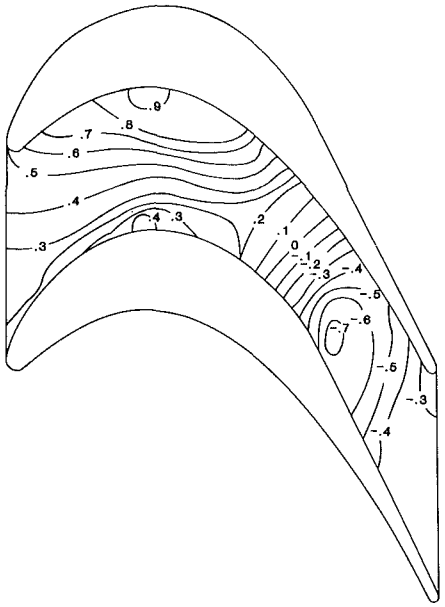


Fig. 8 Contours of the static pressure coefficients on the inner wall

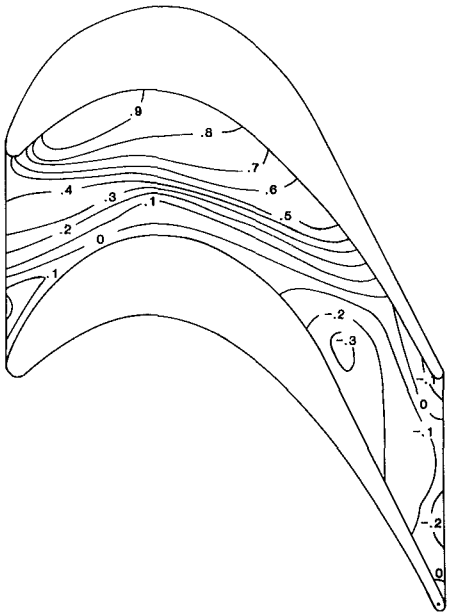


Fig. 9 Contours of the static pressure coefficients on the outer wall

passage in the spanwise and pitchwise directions respectively. The main flow was traversed in the pitchwise direction at 25%, 50%, and 75% span with an increment of 1 deg over a total angle of 45 deg. The variation in the inlet flow velocity, primarily due to the upstream effect of the blade leading

Downloaded 01 Jun 2010 to 171.66.16.71. Redistribution subject to ASME license or copyright; see http://www.asme.org/terms/Terms_Use.cfm

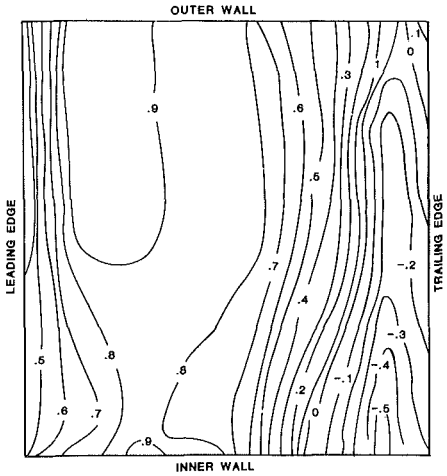


Fig. 10 Contours of the static pressure coefficients on the pressure surface of the blade

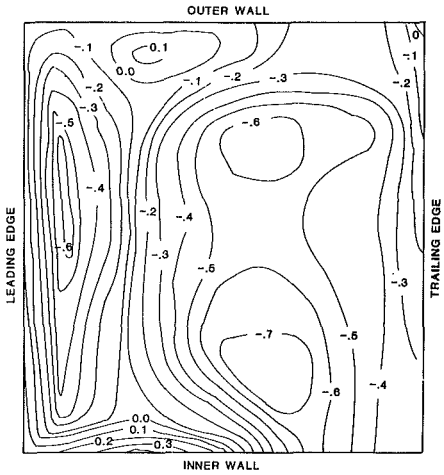


Fig. 11 Contours of the static pressure coefficients on the suction surface of the blade

edges, was found to be within 10% of the mean value at midspan with maximum velocity occurring at $\theta = 4$ deg. Main flow traverses in the radial direction, at several circumferential positions, indicated variations in velocity, but no more than 10% of the midspan value, over a spanwise range from 15% to 85%. The flow angle appeared to vary over a range of ± 1 deg in the radial direction. However, in the pitchwise direction, the upstream effect of the blades resulted in a periodic variation of the flow angles. In the passage center the angle was around 62 deg and in the leading edge regions the angles were about 56 deg. This corresponds to an induced negative incidence of 2–8 deg. The inlet boundary-layer thicknesses, for the results reported in the following sections, are 13% and 8% of the annular cascade height at the inner and outer walls respectively. For the planar cascade, the boundary-layer thicknesses are 8% and 12% of the span on the root and tip walls respectively. This corresponds to an average displacement thickness (as a ratio of the blade chord) of about 0.01 for the two rigs.

Blade-Passage Pressure Distributions

The surface pressures recorded in the center-blade passage are presented in the form of contour maps for the static pressure coefficient C_{p_S}. Isobaric contour maps of the static pressures on the inner and outer annular walls are shown in Figs. 8 and 9 respectively. The cross-channel gradient is noted to extend over a larger axial distance on the outer wall than on the inner wall. The zones of minimum pressure $C_{p_S} = -0.7$ and $C_{p_S} = -0.3$ on the root and the tip walls, respectively, are located upstream of the blade throat and are shifted away from the suction surface. Langston et al. [2] observed a similar situation and associated it with the local separation occurring in the vicinity of the suction side upstream of the throat region. Sjolander [4] found that the shear-stress trajectories in the endwall regions were essentially parallel to the pressure gradient, indicating that the energy of the fluid is so small that the inertial effects are unimportant. Thus, the endwall pressure gradient is indicative of the direction of the endwall shear stress and consequently the cross-channel flow. Accordingly, the cross-channel flow on the outer wall is expected to extend over most of the passage, whereas on the inner wall the cross-channel flow is expected to extend over the first 60% of the axial chord. This was confirmed by the surface flow visualization tests performed on both endwalls. For the planar rig, with a constant pitch/chord ratio in the spanwise direction, pressure contours on both endwalls were similar to those on the outer wall of the annular rig. The orientation of the pressure gradient for the two-dimensional rig was almost parallel to the pitchwise direction and the cross-channel flow extended over most of the passage. The local minimum pressure zones, with equal magnitude on both walls, were also detached from the blade suction surface.

Contour maps of the isobars on the blade pressure and suction sides are given in Figs. 10 and 11 respectively for the annular rig. On the pressure surface of the blade, the pressure varies slightly over the first 50% of the blade axial chord. The upper portion has a more uniform pressure distribution than the lower portion of the blade. The radial gradients of the pressure are more noticeable in the lower region near the leading edge. In the region between 50% axial chord and the trailing edge, the pressure falls rapidly and the pressure gradient is nearly axial with slight distortions near the inner wall.

On the suction surface of the blade (Fig. 11), the flow field may be divided into three distinct regions. A two-dimensional flow region is located between the leading edge and 30% axial chord and extends over most of the blade span. The flow accelerates rapidly from the leading edge toward a low-pressure zone ($C_{p_S} = -0.6$) located at about 12% axial chord. Beyond this zone, a steep adverse pressure gradient is observed and suggests a two-dimensional flow separation. The second region is three-dimensional in nature and starts on the inner wall. As shown in Fig. 8, the cross-channel pressure gradient drives the endwall low momentum fluid toward the suction surface and inner wall junction at about 30% axial chord ($C_{p_S} = 0.4$). This boundary layer fluid then migrates upward, as reflected by the negative slope of the C_{p_S} lines, toward a low-pressure zone ($C_{p_S} = -0.7$). Here it separates from the blade suction surface to form the inner-wall passage vortex at about 20% span. The third region is again three-dimensional and originates on the outer wall at about 30% axial chord. The flow behavior is similar to that in the inner-wall region with the low-momentum fluid ($C_{p_S} = 0.1$) detached from the outer wall. The radially inward migration of the low-momentum fluid (C_{p_S} with positive slope) is due to a lower pressure gradient when compared to the inner wall. The outer wall passage vortex, associated with the three-dimensional flow separation, is found at the same axial chord location as on the inner wall but is displaced inward (about 27% from the outer wall) due to the tip-to-root pressure gradient. The flow visualization studies permitted the observance of the endwall boundary layer fluid overturning and rolling over the blade suction surface (Figs. 12 and 13).

The pressure distributions on the blade surfaces at different spanwise locations are shown in Fig. 14 for both rigs. The curve plotted in Fig. 14(*c*) at midspan is the result of a two-dimensional potential flow calculation [15]. The pressure

Downloaded 01 Jun 2010 to 171.66.16.71. Redistribution subject to ASME license or copyright; see http://www.asme.org/terms/Terms_Use.cfm

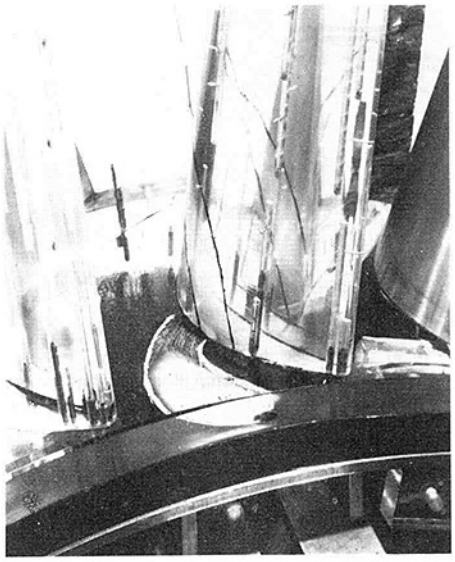


Fig. 12 Flow visualization using smoke deposits

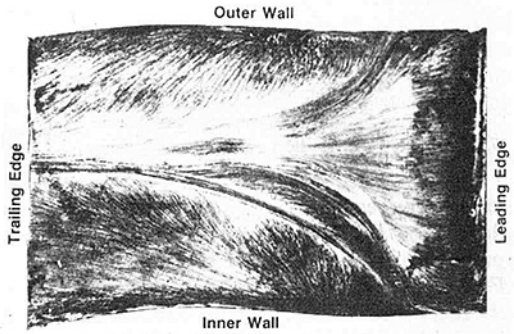


Fig. 13 Flow visualization using lamp-black and kerosene showing flow traces on the blade suction surface

distributions measured on the pressure surface of the blade, for the annular and planar rig, are similar and compared reasonably well with the analysis at 50% span. However, on the suction surface, large discrepancies occur between the annular and planar rig distributions.

For the two-dimensional rig, the maximum blade loading is at midspan and slight unloadings take place near the inner and outer walls due to secondary flows. For the three-dimensional rig, the maximum blade loading occurred at 75% span due to the varying pitch/chord ratio. High blade unloadings are observed toward both endwalls, which means that the three-dimensional effects are not confined to the immediate vicinity of the endwalls. The deviation of the experimental results from the potential flow solution over the rear portion of the blade suction surface corresponds to areas of three-dimensional separation.

Exit Flow Parameters

The local-loss-coefficient maps at the exit plane of the planar and annular cascades are given in Fig. 15. The repeatability of the loss pattern in each blade passage demonstrated the flow periodicity for the two cascades. A typical three-dimensional representation of the local-pressure-loss coefficient is shown in Fig. 16 for the annular rig. Normally, for large-aspect-ratio blades, a high-loss region is visible at each blade end corresponding to the inlet inner and outer wall boundary layers. Results for the planar rig (Fig. 15*a*) show that there are two high-loss cores (C_{p_Q} = 0.6) close and parallel to the projection of the blade suction surface at 32% and 65% of the blade span. This means that the effect of

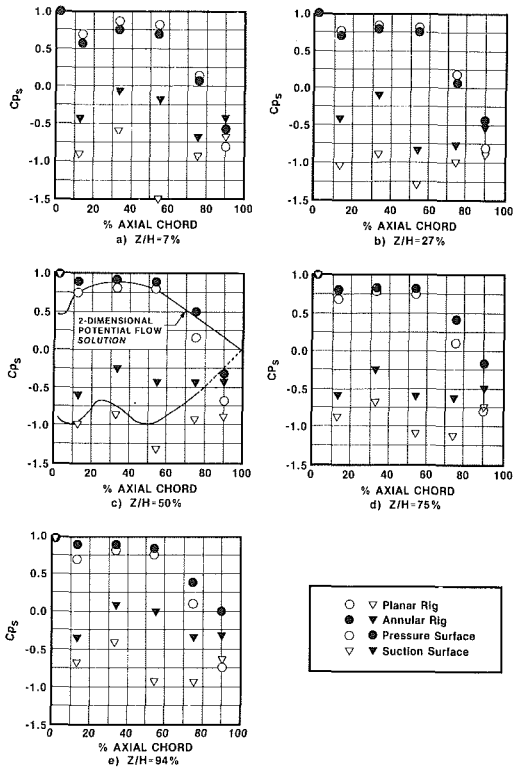


Fig. 14 Blade surface pressure distributions

low-aspect-ratio and high-turning-angle blades is to displace radially inward the two endwall loss regions which are associated with the secondary vortices. For the annular rig (Fig. 15*b*), a large high-loss core (C_{p_Q} = 0.6) is visible at the middle of the blade passage between 48% and 77% span. The high loss region is seen to enclose two higher peak zones: C_{p_Q} = 0.7 and 0.8 at 53% and 70% span respectively. These are the two passage vortices associated with the observed three-dimensional flow separation (Fig. 11) at 20% and 73% span. The varying pitch/chord ratio, the orientation of the blades in the annulus, and the radial pressure gradients occurring in the annular rig would all have a combined effect on the merging of the two passage vortices and the radial position of the resulting high-loss core. The evidence provided by the contour maps in Fig. 15 made it quite clear that the material in the vortex core came from the suction surface of the blades. This was consistent with the observed origin of the core as a rolling of both inlet inner and outer wall boundary layers over the suction surface of the blades and eventually moving to the blade passage (Figs. 12, 13).

Came [1] found that the loss peaks increased in size with the upstream boundary-layer thickness and showed that the loss core was moved farther from the endwalls as flow turning was increased. The experimental results of Woods [5] indicated that the loss peak was shifted from a spanwise location of 15% to about 24% as the aspect ratio was reduced from 1.036 to 0.592.

Figure 15(*b*) revealed also the presence of two loss peaks located at the junctions of the blade trailing edges and the inner wall. At the outer wall, similar regions were also apparent but with a loss magnitude smaller than that for the inner wall. The reason for the difference in magnitude between the losses at the inner and the outer wall may be attributed to two factors. The first factor was the thicker boundary layer measured at the cascade exit inner wall when compared to that measured on the outer wall. The second factor is the spanwise pressure gradient in the annular cascade. This gradient is responsible for sweeping some of the

Downloaded 01 Jun 2010 to 171.66.16.71. Redistribution subject to ASME license or copyright; see http://www.asme.org/terms/Terms_Use.cfm

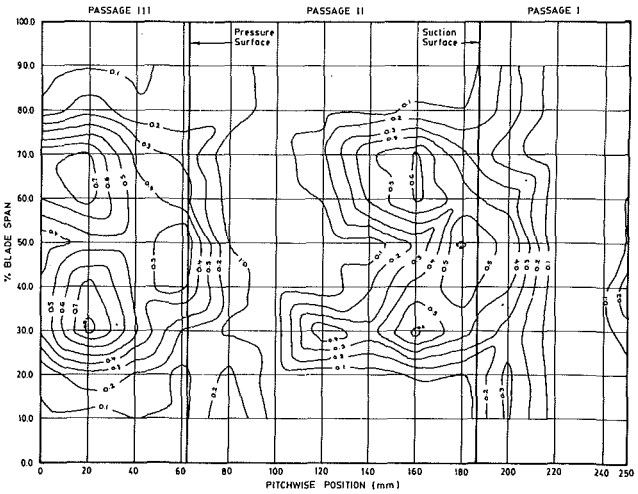


Fig. 15(*a*) Total pressure loss contours for the planar rig

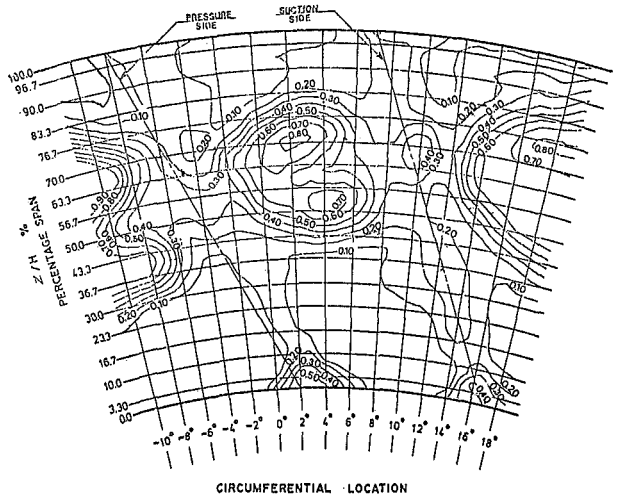


Fig. 15(*b*) Total pressure loss contours for the annular rig

low-energy air in the inlet outer-wall boundary layer down to the trailing edge resulting in larger hub than tip losses. Rohlik et al. [6] observed this fact in their tests which were carried out on an annular cascade.

The spanwise distribution of the pitchwise averaged total pressure-loss coefficient for both rigs is shown in Fig. 17. The spanwise location of the two loss peaks for the planar rig versus the location of the single loss peak for the annular rig is evident in Fig. 17 and corresponds to the peaks presented in the loss contours. It is of interest to note from Fig. 17 that the exact extent of the profile losses is difficult to define, as both profile and secondary losses interact with each other for low-aspect-ratio and high-turning-angle cascades.

The secondary flow vectors at the cascade exit were obtained by projecting the components of velocity perpendicular to the direction of the blade exit angle onto the plane of the exit measuring station. The secondary flow pattern depicted in Fig. 18 for the annular rig is consistent with the total pressure-loss distribution (Fig. 15*b*), where the areas of high loss coincide closely with the vortex cores. Figure 19 shows the spanwise distribution of the exit flow angle deviation for the two rigs. The following features can be seen:

1 Two areas of overturning are observed, one near the inner wall and one near the outer wall.
2 The peak losses in Fig. 17 are coincident with the regions of high underturning shown in Fig. 19.
3 For the annular cascade, the merging of the two vortices at a spanwise location of approximately 60% is obviously the reason for the larger underturning (about 14 deg) when compared to the planar cascade maximum underturning values (5 and 7 deg).
4 Flow-angle distribution (Fig. 19) is in agreement with the recent results obtained on a similar blade profile [16] but with a larger aspect ratio (1.3) and tested in a rotating rig. From the results [16], a single large vortex was apparent between 35% and 65% with a maximum underturning of 10 deg.

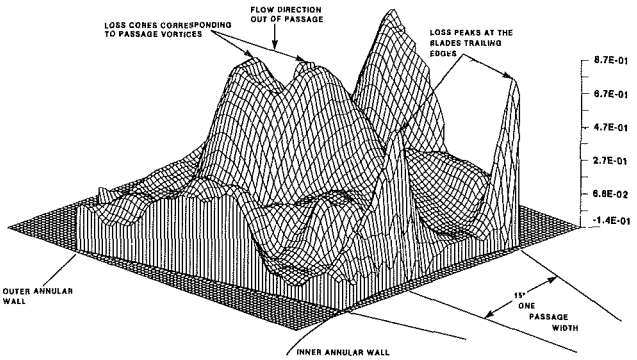


Fig. 16 A typical three-dimensional illustration of the variation of C_{p_o}

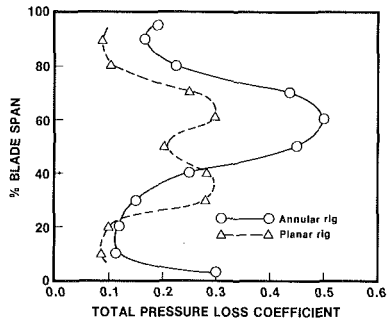


Fig. 17 Spanwise distribution of the total pressure-loss coefficient

Losses—A Comparison With Existing Correlations

The comparison of the cascade secondary losses with the existing data and correlations required the calculation of the integrated overall loss coefficient and the secondary loss coefficient. The effect of the exit measuring position and the differentiation between profile and secondary losses are further considered.

The effect of the exit measuring station position on the measured losses was accounted for by estimating the mixing losses. Most of the cascade data reported in the literature included the mixing losses, in which case the measurements were taken at a distance downstream from the cascade of the same order of magnitude as the chord length. Came [1] in his preliminary tests noted a rising trend for both the profile and secondary losses downstream of the cascade up to a distance of 1.2 C. Data presented by Langston et al. [2] indicated an increase in the measured losses of about 15% over a distance between 0.2 C and 0.4 C downstream of the exit plane. For the planar rig, the flow was traversed in the plane of exit measuring station B (located at a streamwise distance of 1.5 C from the cascade exit) and the measured losses increased by approximately 47% from those measured at 0.33 C. It was estimated that the measured losses for both rigs should be increased by 20% to account for the effect of mixing. This adjustment was necessary to compare the measured losses with the existing data and correlations which were based on a downstream location between 0.7 C and 1 C.

Ideally the test results should be analyzed to separate the profile loss, endwall boundary loss, and secondary loss. The

Downloaded 01 Jun 2010 to 171.66.16.71. Redistribution subject to ASME license or copyright; see http://www.asme.org/terms/Terms_Use.cfm

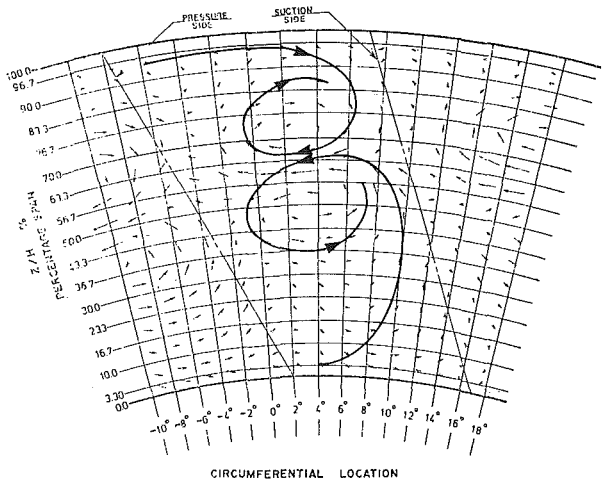


Fig. 18 Secondary flow velocities in the exit plane of the annular cascade

boundary-layer thickness at the exit from the cascade was found to be very small in comparison with the inlet boundary layer (less than 1% of the cascade height). The exit boundary layer, being negligibly small, was therefore not included in the total loss coefficient. For high-aspect-ratio blades, the secondary losses are determined by subtracting the measured midspan (profile) loss from the measured fullspan loss. The fullspan loss is determined from the spanwise integration of the pitchwise area-averaged distribution. Due to the low-aspect-ratio blades used in the present tests and the subsequent merging of the two vortices, the differentiation between the profile and the secondary loss was not possible. In order to calculate the secondary loss, the profile loss was therefore estimated using the modified Ainley and Mathieson method [17, 19]. The measured total losses, after allowing for mixing, and the derived secondary losses are given in Appendix 3 for the two cascades.

Figure 20 shows the variation of the secondary loss parameter with the relative upstream boundary-layer displacement thickness for the annular and planar test results. Also shown in Fig. 20 are the test results reported in [1], the Dunham and Came [1, 21] correlations, and the nominal loss value used in turbine-performance predictions [18]. The secondary loss parameter for the experimental results is defined according to the recent dependence on aspect ratio as suggested by Kacker and Okapuu [19] and a correction for large turning angles as proposed by Moustapha [20]. These updates for the secondary loss parameter were introduced because the Dunham and Came correlations overestimated the secondary losses at low-aspect ratio and high turning angles, when compared to experimental data.

From Fig. 20 it can be seen that the present test results agree quite well with the available correlations. The effect of the inlet boundary-layer thickness on increasing the secondary losses [13, 14] is also seen for both rigs. With the same mean blade loading parameter (Z) and aspect ratio, the annular and planar cascade performance comparison shows larger secondary losses for the former.

Conclusions

In order to study the performance of a highly loaded annular cascade of turbine blades, a special test rig of hyperboloidal inlet and exit ducts was constructed and tested. The measurements were compared with the results obtained for the same blade section tested in a planar cascade at similar test conditions. The analysis of extensive test results leads to the following general conclusions:

1 The study of the total pressure loss contours at the cascade exit indicated the presence of two loss peaks at about 35% and 65% span for the planar rig. The two loss peaks merged together for the annular cascade to produce a large high-loss core in the middle of the passage.

2 According to the exit flow vectors for the annular cascade, two large vortices were detected coinciding with the high-loss core. The two counter rotating vortices merged into a band of high underturning. A similar pattern was observed for the planar cascade but with lower underturning.

3 The varying pitch/chord ratio, the radial pressure gradient and the orientation of the blades in the annular cascade would all have a combined effect on the blade loading, the radial position of the high-loss core, the maximum flow underturning and accordingly the measured secondary losses when compared to the planar cascade.

4 A comparison of the measured secondary loss parameter with existing prediction models indicated good agreement between the test results and the correlations.

Finally, the present tests demonstrated that the flow field in a highly loaded, turbine annular cascade is complex in nature and mainly dominated by secondary flows. Analytical models are needed to obtain a reliable estimate of the flow overturning and underturning for this class of turbine blades to permit the design of incidence-free airfoils.

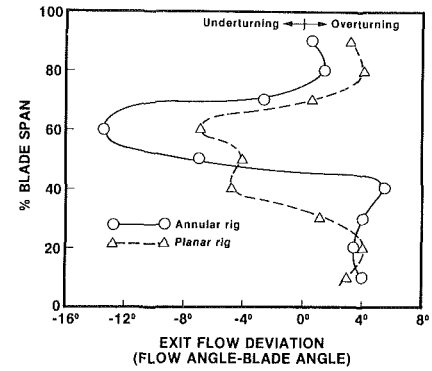


Fig. 19 Spanwise distribution of the exit flow angle

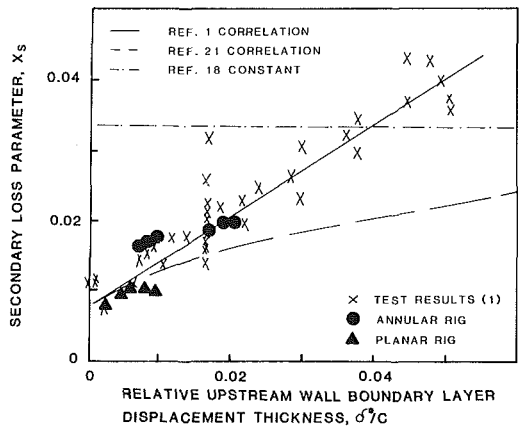


Fig. 20 Variation of the gross secondary loss with inlet displacement thickness

Acknowledgments

This research was carried out under a grant from the Natural Sciences and Engineering Research Council Canada. The model turbine blades were manufactured using the facilities of the Division of Mechanical Engineering of the National Research Council of Canada.

Downloaded 01 Jun 2010 to 171.66.16.71. Redistribution subject to ASME license or copyright; see http://www.asme.org/terms/Terms_Use.cfm

References

1 Came, P. M., "Secondary Loss Measurements in a Cascade of Turbine Blades," *I. Mech. Eng. Conference Publication 3*, 1973, p. 75.

2 Langston, L. S., Nice, H. L., and Hooper, R. M., "Three Dimensional Flow Within a Turbine Cascade Passage," ASME JOURNAL OF ENGINEERING FOR POWER, 1977, p. 21.

3 Langston, L. S., "Cross Flows in a Turbine Cascade Passage," ASME JOURNAL OF ENGINEERING FOR POWER, Vol. 102, No. 4, Oct. 1980; Paper No. 80-GT-5.

4 Sjolander, S. A., "The End Wall Boundary Layer in an Annular Cascade of Turbine Nozzle Guide Vanes," Carleton University, TRME/A 75-4, Dec. 1975.

5 Woods, J. R., "An Investigation of Secondary Flow Phenomena and Associated Losses in a High-Deflection Turbine Cascade," Ph.D. Thesis, Naval Postgraduate School, Monterey, California, Sept. 1972.

6 Rohlik, H. E., Kofskey, M. G., Allen, H. W., and Herzig, H. Z., "Secondary Flows and Boundary Layer Accumulations in Turbine Nozzles," NACA Report 1168, 1954.

7 Camus, J. J., Denton, J. D., Soulis, J. V., and Scrivener, C. T. J., "An Experimental and Computational Study of Transonic Three-Dimensional Flow in a Turbine Cascade," ASME JOURNAL OF ENGINEERING FOR GAS TURBINES AND POWER, Vol. 106, No. 2, Apr. 1984, pp. 414–420; Paper No. 83-GT-12.

8 Binder, A., and Romey, R., "Secondary Flow Effects and Mixing of the Wake Behind a Turbine Stator," ASME JOURNAL OF ENGINEERING FOR POWER, Vol. 105, No. 1, Jan. 1983, pp. 40–46; Paper No. 82-GT-46.

9 Sieverding, C. H., Van Hove, W., and Boletis, E., "Experimental Study of the Three-Dimensional Flow Field in an Annular Turbine Nozzle Guidevane," ASME JOURNAL OF ENGINEERING FOR GAS TURBINES AND POWER, Vol. 106, No. 2, Apr. 1984, pp. 437–448; Paper No. 83-GT-120.

10 Myachin, E. V., "A Three-Dimensional Test Rig for the Investigation of the Secondary Flow in High Turning Turbine Blade Cascades," *Mech. Eng. Dept. Report*, McMaster University, Canada, 1973.

11 El Shammaa, S. A., Moustapha, S. H., and Wade, J. H. T., "Secondary Flow in Cascades of High Turning Angle Turbine Blades," *First Parsons International Turbine Conference*, Trinity College, Dublin, June 1984.

12 Moustapha, S. H., "Secondary Flow in an Annular Cascade of High Turning Angle Turbine Blades," Ph.D. Thesis, Department of Mechanical Engineering, McMaster University, Canada, Mar. 1978.

13 El Shammaa, S. A., "The Effect of Inlet Boundary Layer on the Secondary Flow in an Annular Cascade," Ph.D. Thesis, Department of Mechanical Engineering, McMaster University, Oct. 1978.

14 Paron, G. J., "Secondary Flow in a Two-Dimensional Cascade of High Turning Angle Turbine Blades," M. Eng. Thesis, Department of Mechanical Engineering, McMaster University, Canada, Apr. 1981.

15 Stannard, J. H., "The Aerodynamic Design and Testing of High Turning Angle Turbine Blades," Ph.D. Thesis, Department of Mechanical Engineering, McMaster University, Canada, 1975.

16 Moustapha, S. H., Okapuu, U., and Williamson, R. G., "The Influence of Rotor Blade Aerodynamics Loading on the Performance of a Highly Loaded Turbine Stage," submitted for presentation at the 31st International Gas Turbine Conference and Exhibit, Düsseldorf, West Germany, June 1986.

17 Ainley, D. G., and Mathieson, G. C. R., "A Method of Performance Estimation for Axial Flow Turbines," British ARC, R & M 2974, 1951.

18 Dunham, J., and Came, P. M., "Improvement to the Ainley/Mathieson Method of Turbine Performance Prediction," ASME JOURNAL OF ENGINEERING FOR POWER, Vol. 92, No. 3, July 1970, pp. 252–256.

19 Kacker, S. C., and Okapuu, U., "A Mean Line Prediction Method for Axial Flow Turbine Efficiency," ASME JOURNAL OF ENGINEERING FOR POWER, Vol. 103, No. 1, Jan. 1981; Paper No. 81-GT-58.

20 Moustapha, S. H., "Secondary Losses at Large Turning Angles," Pratt and Whitney Canada Inc., Internal Report, Feb. 1981.

21 Dunham, J., "A Review of Cascade Data on Secondary Losses in Turbines," *Journal of Mech. Eng. Sciences*, Vol. 12, No. 1, 1970, p. 48.

APPENDIX 1

C_L = Lift coefficient

$$C_L = 2\frac{S}{C}(\tan\alpha_1 - \tan\alpha_2)\cos\alpha_m$$

where

$$\alpha_m = \tan^{-1}[0.5(\tan\alpha_1 + \tan\alpha_2)]$$

C_Z = Zweifel lift coefficient

$$C_Z = 2\frac{S}{C_a}\cos^2\alpha_2(\tan\alpha_1 - \tan\alpha_2)$$

C_{p_o} = Local total pressure-loss coefficient

$$C_{p_o} = \frac{P_{o1m} - P_o}{0.5\,\rho\,V_{1m}^2}$$

C_{p_S} = Local static pressure coefficient

$$C_{p_S} - \frac{P_{S1m} - P_S}{0.5\,\rho\,V_{1m}^2}$$

X_S = Secondary loss parameter

$$X_S = \frac{H}{C}\frac{Y_S}{Z}\frac{\cos\beta_1}{\cos\alpha_2}$$ as defined in [18]

Y_T = Overall loss coefficient

$$Y_T = \frac{\Delta P_T}{P_{o2m} - P_{S2m}}$$

where

$$\Delta P_T = \frac{\int_S\int_H [P_{o1m} - P_o(r,\theta)]V_a(r,\theta)\,r\,dr\,d\theta}{\int_S\int_H V_a(r,\theta)\,r\,dr\,d\theta}$$

while

$$P_{o2m} = P_{o1m} - \Delta P_T$$

and

$$P_{S2m} = P_{S1m} - \Delta P_S$$

ΔP_S defined in a manner similar to ΔP_T

Y_S = Secondary loss coefficient

$$Y_S = Y_T - Y_p$$

Z = Blade-loading parameter

$$\left(\frac{C_L}{S/C}\right)^2\frac{\cos^2\alpha_2}{\cos^3\alpha_m}$$

APPENDIX 2

Blade coordinates (in cms)

Axial Distance	Pressure Surface	Suction Surface
0.00	11.28	11.28
0.38	10.72	12.23
1.13	11.10	13.58
1.86	11.64	14.56
3.02	12.29	15.58
4.15	12.74	16.16
5.28	13.01	16.46
6.41	13.08	16.57
7.54	12.95	16.51
8.29	12.73	16.37
9.80	11.98	15.80
11.31	10.79	14.66
12.82	9.15	12.70
13.95	7.85	10.51
15.08	5.95	8.14
16.21	4.10	5.77
17.34	2.18	3.40
18.09	0.69	1.82
18.85	0.24	0.24

APPENDIX 3

Measured cascade losses (at $\delta^*/C = 0.01$)

Losses	Annular rig	Planar rig
Y_T (measured)	0.23	0.15
Y_p [17, 19]	0.07	0.07
$Y_S = (Y_T - Y_P)$	0.16	0.08

Downloaded 01 Jun 2010 to 171.66.16.71. Redistribution subject to ASME license or copyright; see http://www.asme.org/terms/Terms_Use.cfm

Turbulence Production Due to Secondary Vortex Cutting in a Turbine Rotor

A. Binder
Research Engineer.
DFVLR-Propulsion Institute,
Cologne, W. Germany

Measurements of the unsteady flow field near and within a turbine rotor were made by means of a Laser-2-Focus velocimeter. The testing was performed in a single-stage cold-air turbine at part-load and near-design conditions. Random unsteadiness and flow angle results indicate that the secondary vortices of the stator break down after being cut and deformed by the rotor blades. A quantitative comparison shows that some of the energy contained in these secondary vortices is thereby converted into turbulence energy in the front part of the rotor. An attempt is made to explain this turbulence energy production as caused by the vortex breakdown.

Introduction

In recent years many experimental and theoretical studies on the unsteady flow in turbomachines have been presented. Kerrebrock and Mikolajczak [15] were among the first to show that unsteady phenomena significantly affect turbomachinery flow.

A basic requirement for experimental investigations in this field is a measurement system which uses high-response instrumentation. There are several techniques presently available which can be used for measuring highly fluctuating flows. These include transducers, hot wire and hot film anemometers, and the nonintrusive laser measurement techniques.

The flow interactions between the stationary and rotating blade rows of a turbomachine include potential, wake, and secondary-flow effects, all of which occur simultaneously. The potential influence of a blade extends both upstream and downstream, but decays much faster with increasing distance than the blade wake which may be convected far downstream. The present investigation is concerned with the wake and secondary-flow phenomena which occur due to the interaction between a stationary and a rotating blade row. In the test turbine used for the measurements described in this paper the stator-rotor axial gap was large enough to exclude the potential-flow interaction effects. The flow field downstream of the stator blade row consists of several different types of flow regions, namely an almost inviscid region with low random unsteadiness, the stator blade wake, the hub and casing boundary layers, and secondary flow regions. The wake is characterized by a velocity defect, strong radial velocity components [17], and high random unsteadiness levels. The boundary layer and secondary flow regions also exhibit high levels of random unsteadiness. The unsteady interaction caused by the periodic striking of rotor blades on these regions at different levels of flow unsteadiness have been investigated by Pfeil [21] and Hodson [11]. Their results show a very strong influence on the rotor boundary layer transition behavior, and thus on the character of the rotor blade boundary layer. This, in turn, may influence loss generation and heat transfer.

Proceeding from the results of Meyer [19] and Kerrebrock and Mikolajcak [15], Hodson [12] and the author et al. [2] described in independent studies the existence of two counterrotating circulation regions (with radial axis of rotation) at both sides of the chopped stator wakes. These regions are a consequence of the velocity defect inside the wake.

The results presented in this paper show a marked increase in random flow unsteadiness at the entrance of the rotor blade row where the wakes and the secondary vortices from the upstream stator are chopped. An attempt is made here to show and explain a connection between the chopping of the secondary vortices and the increase in flow turbulence in the rotor entrance region.

Experimental Apparatus

Turbine Test Facility. A cold air turbine test facility already mentioned in previous papers [1, 2] was used during this investigation.

For the tests a transonic stage with low aspect ratio (especially in the stator) and a high hub-to-tip ratio was used (Fig. 1). The stator-rotor axial gap was such that there were

Table 1 Geometric parameters

	Stator	Rotor
Chord (midspan)	0.0975 m	0.0678 m
Number	20	31
Tip diameter	0.45 m	0.45 m
Hub diameter (see Fig. 1)	0.34 m	0.34 m
Hub diameter (rotor exit)	–	0.3354 m
Axial gap (midspan)	0.0598 m	
Hub-to-tip ratio	0.756	0.756
Inlet metal angle (midspan)	90 deg	42.4 deg
Exit metal angle (midspan)	21.1 deg	147.5 deg

Contributed by the Gas Turbine Division of THE AMERICAN SOCIETY OF MECHANICAL ENGINEERS and presented at the 30th International Gas Turbine Conference and Exhibit, Houston, Texas, March 18–21, 1985. Manuscript received at ASME Headquarters, January 16, 1985. Paper No. 85-GT-193.

Copyright © 1985 by ASME
Downloaded 01 Jun 2010 to 171.66.16.71. Redistribution subject to ASME license or copyright; see http://www.asme.org/terms/Terms_Use.cfm

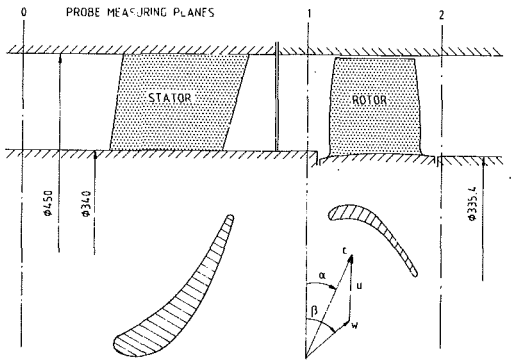


Fig. 1 Turbine geometry

no measurable upstream potential interactions between the blade rows. For details about the turbine geometry see Table 1.

All conventional probes, i.e., total-pressure probes, direction probes, total-temperature probes, and five-hole probes, were mounted in radial traversing devices which also allowed the probes to be rotated about their axes. In order to make a circumferential traverse of the stator exit flow, the upstream part of the casing together with the stator vanes was rotated circumferentially, thereby moving the stator exit flow past the probes in plane 1.

Laser Measurement Technique. For the tests reported in this paper, Laser-2-Focus (L2F) measurements were done in the rotor region between the probe measuring planes 1 and 2 (Fig. 1). In this region circular windows were mounted at the rotor casing. The L2F-velocimeter was mounted in a traversing device which was adjustable in both the axial and radial directions of the turbine. For traversing of the flow field behind the stator in the circumferential direction, the upstream part of the casing together with the stator vanes was rotated in the circumferential direction.

In Fig. 2 the L2F-measurement locations are shown. For the operating point OP2 (see the section on test conditions) 12 equidistant L2F-locations in the pitchwise direction were measured at the axial L2F-station 1. These locations are fixed to the stator, and thus are in the stationary reference frame.

Due to the moving rotor blades the flow velocity at these L2F-locations is unsteady [2]. As shown in the literature [6, 14], such unsteady velocities can be separated into a periodic fluctuating velocity and a random fluctuating velocity.

L2F-velocimetry is a nonintrusive measurement technique which offers the opportunity to obtain information on the phase-lock averaged (periodic fluctuating) two-dimensional flow vector magnitude and direction, as well as on the random velocity fluctuations parallel and perpendicular to the two-dimensional flow vector.

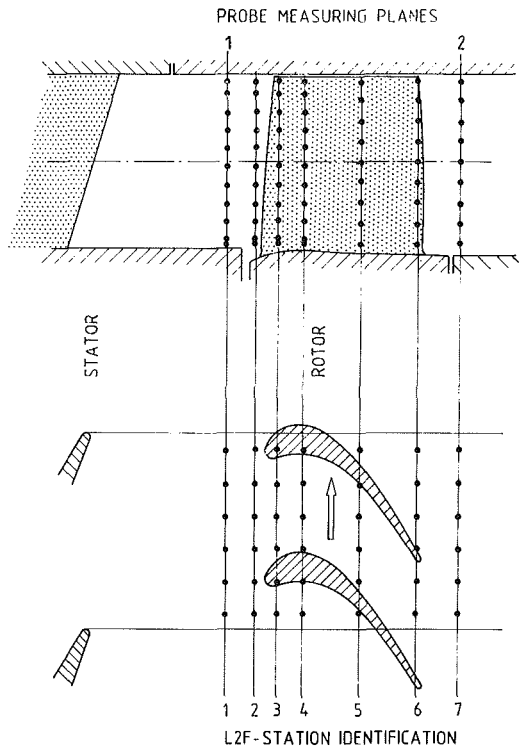


Fig. 2 L2F locations

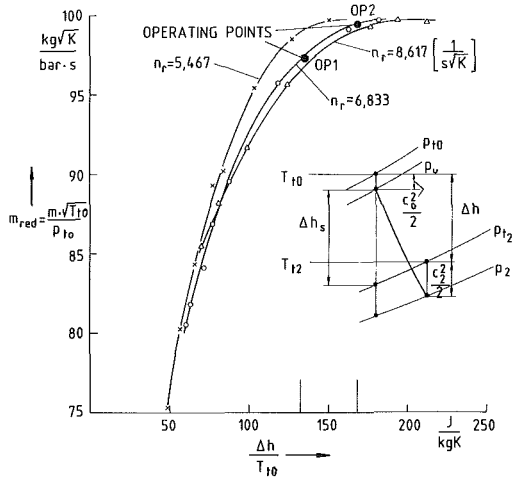


Fig. 3 Performance map

It should be noted that the L2F-instrument provided no information on the velocity or its fluctuation in the radial direction of the turbine. Detailed descriptions of the L2F-velocimeter and the measurement sampling technique are

Nomenclature

c = absolute velocity
c' = absolute velocity fluctuation (random part)
$\overline{c'^2}$ = mean square of c'
h = enthalpy (Δh = enthalpy drop)
i = incidence
m = mass flow rate
n = rotor speed
n_r = reduced rotor speed $n_r = n/\sqrt{T_{t0}}$
p = pressure
r = radius
T = temperature
t = time
Tu = turbulence intensity
u = rotational velocity
w = relative velocity
α = absolute flow angle (yaw)
β = relative flow angle (yaw)
ϕ = coordinate in circumferential direction

Subscripts and Superscripts

i = 0, 1, 2 number of probe measuring plane
l = longitudinal fluctuation velocity
t = total
tr = transverse fluctuation velocity
per = period
p = pitchwise averaged
a = average over the entire measuring plane
$\hat{}$ = time integrated

Downloaded 01 Jun 2010 to 171.66.16.71. Redistribution subject to ASME license or copyright; see http://www.asme.org/terms/Terms_Use.cfm

given in [23, 24]. Schodl [21] also gives a detailed description of the experimental uncertainty inherent in the L2F-technique. Using the assumptions of [23], the uncertainty in the described measurements was ± 0.5 deg in flow angle and $\pm 1\%$ in the absolute velocity.

Test Conditions. The measurements described in this paper were made at two distinct operating conditions (Fig. 3).

The first operating point OP1 was chosen so far below the design point that an entire subsonic flow field would be expected. As seen in Table 2 the turbine was designed for a reduction in enthalpy of $\Delta h/T_{t0} = 217$ J/kg K.

The second operating point OP2 was selected near the design point, where the turbine operated in the transonic flow region. Due to test cost limitations it was not possible to make the measurements exactly at design conditions.

Table 2 Operating and design conditions

Design conditions:	
Total temperature (turbine inlet)	450K
Total pressure (turbine inlet)	4 bar
Rotor speed	8850 rpm
Mass flow rate	18 kg/s
Stage reaction ratio ($\Delta h_{rotor}/\Delta h$)	0.43
$\Delta h/T_{t0}$	217 J/kg K
Operating conditions:	
Total temperature (turbine inlet)	347K
Rotor speed ($n_r = 6.979$)	7800 rpm
m_{red} (OP1)	97 kg$\sqrt{K}$/s bar
m_{red} (OP2)	99 kg$\sqrt{K}$/s bar
$\Delta h/T_{t0}$(OP1)	132 J/kg K
$\Delta h/T_{t0}$(OP2)	168 J/kg K

Table 3 Possible denominator for the random velocity fluctuation

Total temperature (turbine inlet)	347 K
Δh in Table 2	
For OP1:	
Absolute velocity c_a (L2F station 1)	287.3 m/s
Absolute velocity c_a (L2F station 7)	124.9 m/s
Relative velocity $(c_{rel})_a$(L2F station 1)	152.2 m/s
Relative velocity $(c_{rel})_a$ (L2F station 7)	218.2 m/s
For OP2:	
Absolute velocity c_a (L2F station 1)	301.5 m/s
Relative velocity $(c_{rel})_a$ (L2F station 1)	166.2 m/s

The rotor speed was selected so that both tests were run at nearly the same rotor inlet flow angles as shown in a later section. Further information on the two operating points and on the design point can be found in Table 2.

Results and Discussions

By means of total temperature measurements (thermistor probe) which were made in probe measuring plane 1, and L2F-velocity measurements in the same axial plane, the Mach numbers of the absolute and relative flow were calculated. The radial distribution of the time and pitchwise averaged absolute and relative Mach numbers are shown in Figs 4(*a*) and 4(*b*). The Mach numbers of the operating point OP2 were higher than those of OP1 over the whole blade span. The stator vane was designed so that the peak suction surface Mach number exceeds 1 when the outlet Mach number exceeds 0.88. Therefore, transonic flow regions occurred in the stator vane passages with OP2.

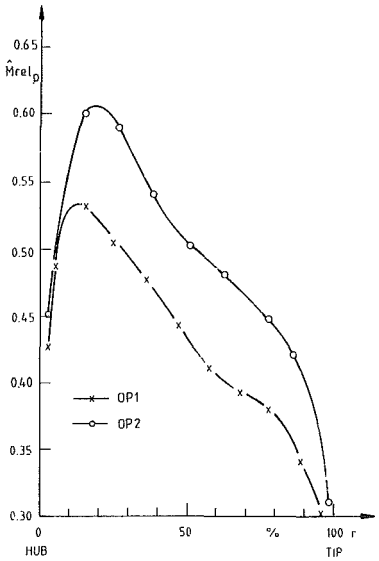


Fig. 4(*b*) Stator outlet-rotor inlet flow (L2F-plane 1) relative Mach number $\hat{M}_{rel,p}$

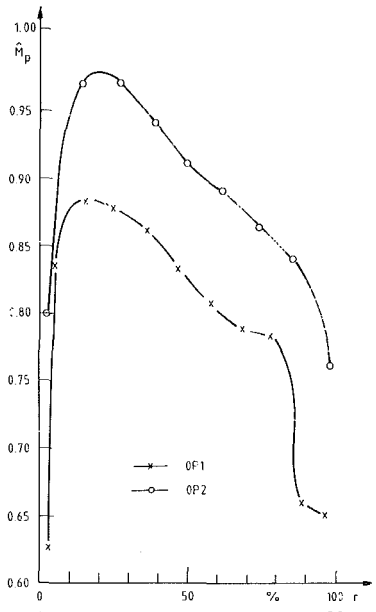


Fig. 4(*a*) Stator outlet-rotor inlet flow (L2F-plane 1) absolute Mach number $\hat{M}_p$

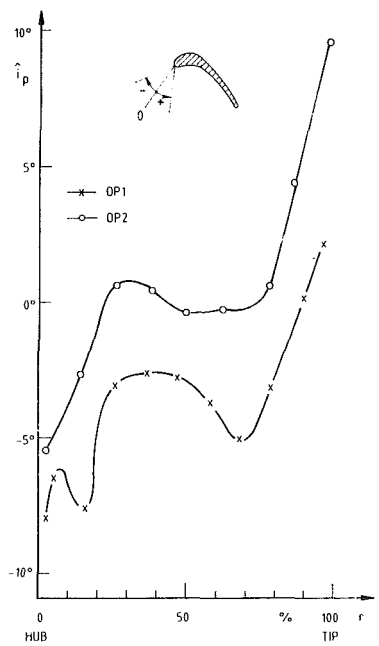


Fig. 4(c) Stator outlet-rotor inlet flow (L2F-plane 1) incidence $\hat{i}_p$

Downloaded 01 Jun 2010 to 171.66.16.71. Redistribution subject to ASME license or copyright; see http://www.asme.org/terms/Terms_Use.cfm

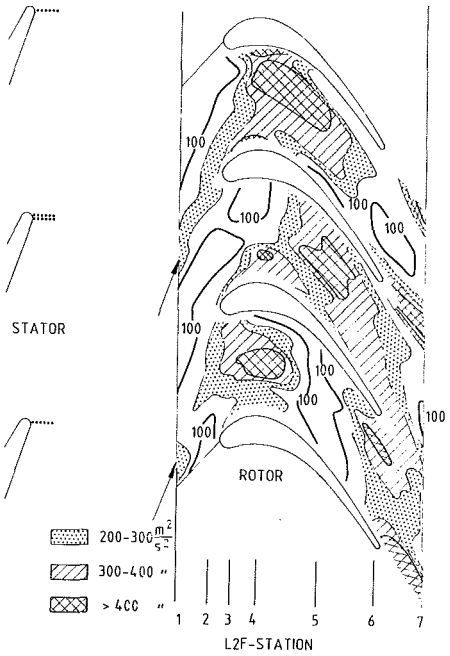


Fig. 5 Instantaneous pattern of random velocity fluctuation $c_l'^2$ (m^2/s^2) for operating point OP1 (midspan)

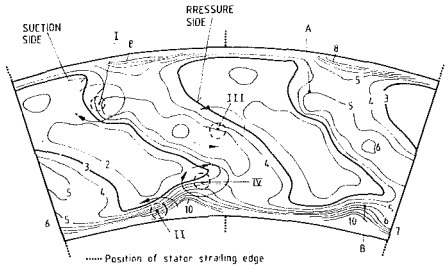


Fig. 6(*a*) Contours of time-integrated mean-square or relative turbulence intensity $\hat{T}u$ (%) for OP2 (L2F-plane 1)

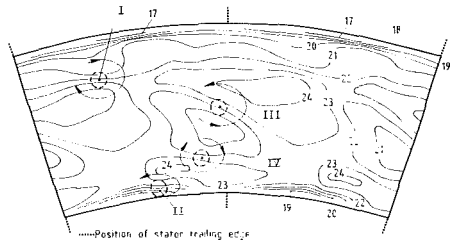


Fig. 6(*b*) Contours of time-integrated absolute flow angle (yaw) for OP2 (L2F-plane 1)

Figure 4(*c*) shows a negative flow incidence to the rotor for both operating points, except near the tip where it is positive. The distribution of the incidence over the blade height is influenced by the operating point and the secondary vortices which occur behind the stator. A detailed description of the secondary flows measured behind the stator is given in a later section.

In a previous publication the author et al. [2] describe some effects of the stator wake rotor blade interaction. The cutting of the stator wakes by the rotor was demonstrated using instantaneous patterns of the random velocity fluctuation. One of the most interesting, but in detail unexplained, features of the flow was the considerable increase in random velocity fluctuation within the chopped wake segments near the rotor entrance. In this paper an extensive evaluation of the L2F-measurements is presented, and an attempt is made to explain this flow behavior. The contour plot presented in [2] is repeated here for convenience and is shown in Fig. 5.

The stator wakes which are marked with arrows in the absolute flow direction were cut up by the rotor blades. The maximum random unsteadiness within the stator wakes (dotted area) in L2F-station 1 was between $200 < \overline{c_l'^2} < 300$ m^2/s^2. In the first part of the rotor the random velocity fluctuations (parallel to the flow vector), considerably increase to $\overline{c_l'^2} > 400$ only within the intersected parts of the wakes, even in the middle of the blade channel. There was, however, no noticeable increase of random velocity fluctuations in the regions of lower unsteadiness outside the stator wakes.

Separated rotor blade boundary layers and blade vibrations were not the reason for this increase of random fluctuations, because these effects would lead at first to an increase of unsteadiness near the blade surfaces and not in the middle of the channel. Blade vibrations would also occur in the regions of low random fluctuation between the wakes. Another aspect which could lead to an increase of the measured random velocity fluctuations is a cycle-to-cycle fluctuation in the periodic velocity component. Due to the measurement sampling technique [23, 24], this cycle-to-cycle fluctuation in the periodic velocity component would be added to the random velocity fluctuations everywhere. Therefore, one would see an increase in the random fluctuations between the wakes. No such increase was observed, thus the cycle-to-cycle fluctuations are negligible.

Two papers were found in the literature [5, 12] that showed in great detail measurements of the random unsteadiness after wake cutting. Dunker [5] measured the turbulence intensity distribution in an axial compressor stator at midspan by means of an L2F-velocimeter. Hodson [10] used a rotating hot-wire anemometer in a turbine rotor and measured the flow velocity only at midspan. Neither Dunker nor Hodson measured an increase in random unsteadiness within the intersected wakes.

One essential difference between those test facilities and the turbine used in these tests was the aspect ratio of the wake generating blade rows. The aspect ratio of Dunker's compressor rotor was 1.71; that of Hodson's turbine stator was 1.5. In those blade rows the secondary flow effects near midspan can be considered negligible. The turbine used in the present tests has an aspect ratio of 0.56 for the wake generating blade row. As shown in [1], downstream of this turbine stator there are very strong secondary vortices, even in the middle of the blade height. Figures 6(*a*) and 6(*b*) show the secondary vortices behind the stator and their positions relative to the wake for operating point OP2. Both turbulence intensity (equation (1)) and absolute flow angle (yaw) were measured by the L2F in plane 1. The dotted lines indicate the position of the stator trailing edges (Fig. 5). The figures represent two stator blade passages.

$$\hat{T}u[\%] = \frac{\sqrt{\hat{c}_l'^2}}{\hat{c}} \cdot 100 \tag{1}$$

By means of the explanations given in [1], which show that a three-dimensional vortex motion can be identified by two-dimensional flow angle measurements, and the contours of constant flow angles (isoclinal plot) in Fig. 6(*b*) the vortices can be clearly identified. A real vortex is a combination of a solid body rotation in the center and a free vortex motion at a particular distance from the vortex axis. In [1] it is shown that a solid body rotation can be identified by straight parallel lines in the isoclinal contour plots. A free vortex rotation is

Downloaded 01 Jun 2010 to 171.66.16.71. Redistribution subject to ASME license or copyright; see http://www.asme.org/terms/Terms_Use.cfm

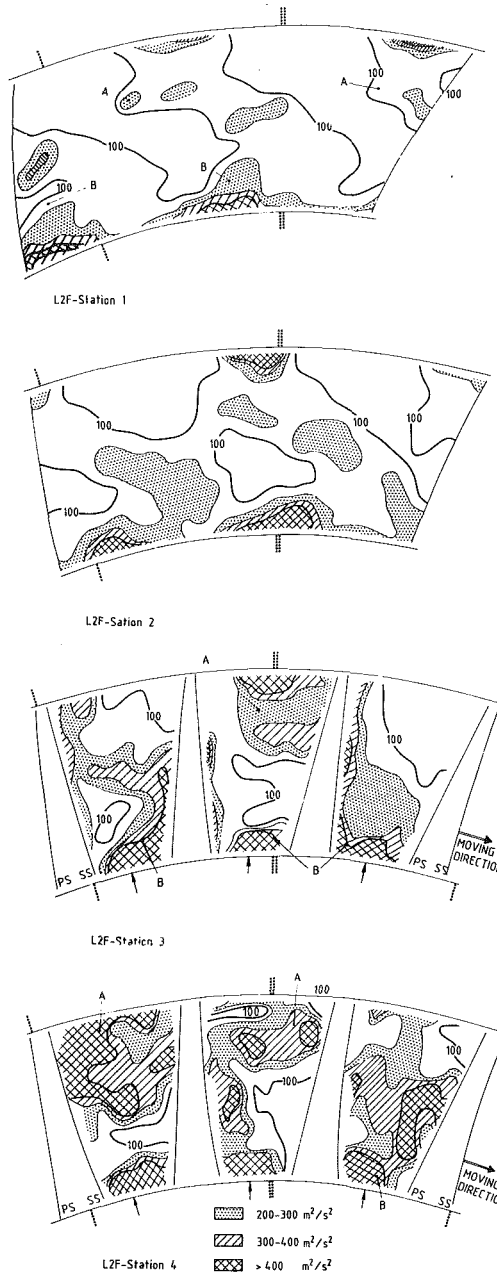


Fig. 7 Instantaneous pattern of random velocity fluctuation $\overline{c_l'^2}$ (m^2/s^2) for OP1 (L2F plane 1 to 4)

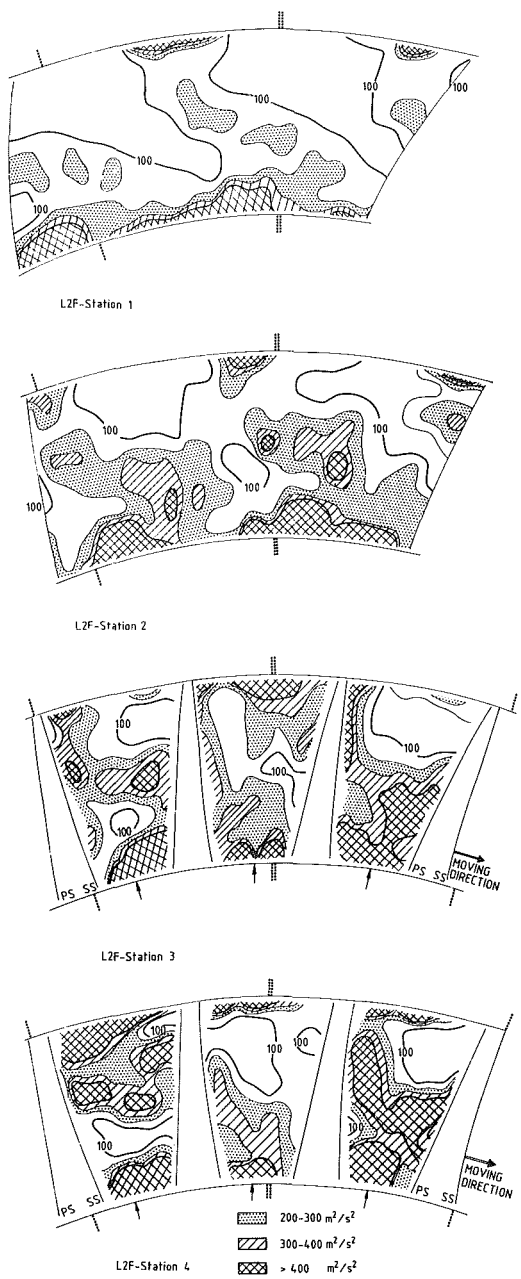


Fig. 8 Instantaneous pattern of random velocity fluctuation $\overline{c_l'^2}$ (m^2/s^2) for OP2 (L2F plane 1 to 4)

characterized by two ovals, each with its center at a fixed distance from the vortex axis.

The vortices I and II are the well-known passage vortices that arose within the stator blade passage. The vortical motion led to an overturning of the flow (Fig. 6*b*) near the walls (hub and casing) and to an underturning of the flow (higher values of the flow angle) on the side opposite the vortex center. Two additional vortices III and IV existed in the wake. Such vortices (see [1]) are associated with trailing shed vorticity. An experimental description of secondary flows is given in [16] and in theoretical form in Reference [14]. These four vortices which were found by means of the isoclinal plot in Fig. 6(*b*) are presented in the turbulence intensity contours in Fig. 6(*a*). In this figure the dark contour line approximately indicates the boundary between the "core flow" which is free from the viscous effects of the wake, endwall boundary layers, and secondary loss regions. The vortices had their centers within or adjacent to the stator wake. At the suction side of the wake in Fig. 6(*a*), two regions *A* and *B* were found which have a higher turbulence level than the "core flow." These regions *A* and *B* arose inside the stator vane passages due to swirling motion of the passage vortices I and II. Behind the blade row, these high fluctuating regions *A* and *B* are in or near the centers of the passage vortices I and II, as shown in [1] and [18]. In the present measurements (Fig. 6*a*) the region *A* corresponds to vortex I and region *B* lies almost in between vortices II and IV. By means of these regions *A* and *B* the approximate positions of the passage vortices can be found without use of the isoclinal (yaw angle) contours.

All vortices described above have a vorticity vector approximately in the absolute flow direction (see arrows of Fig. 5). There were only very small differences in position and intensity of the secondary vortices behind the stator for different operating conditions [1]. Corresponding positions of the vortices were also found for operating point OP1.

In the next figures an attempt is made to follow the wake and secondary flow regions *A* and *B* in the axial flow

Downloaded 01 Jun 2010 to 171.66.16.71. Redistribution subject to ASME license or copyright; see http://www.asme.org/terms/Terms_Use.cfm

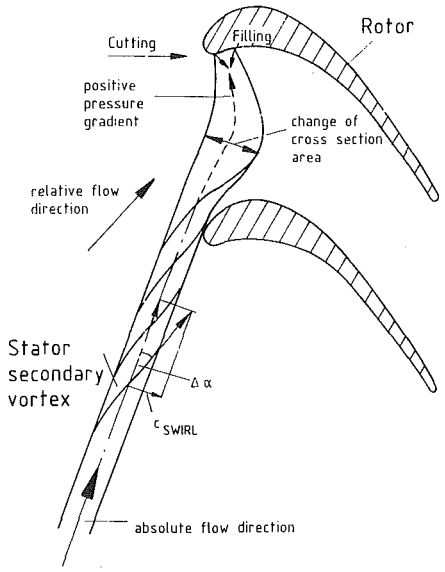


Fig. 9 Stator secondary vortex cutting and deformation by the rotor

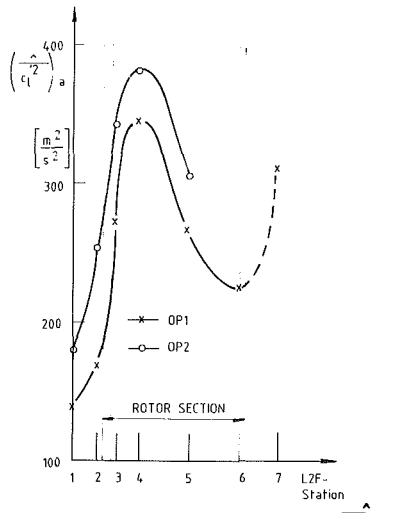


Fig. 10(*a*) Random velocity fluctuation $(\hat{c_l'^2})_a$

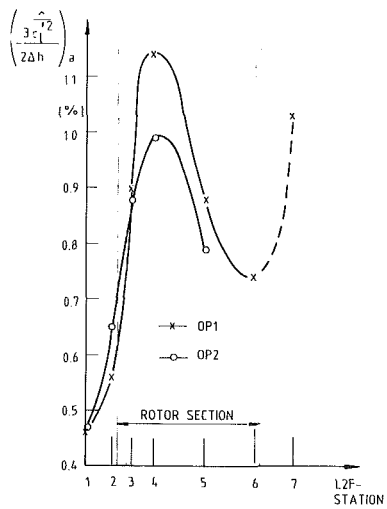


Fig. 10(*b*) Reduced random fluctuating energy

direction. For the L2F-stations 1 to 4 the instantaneous plots of the random velocity fluctuations are given in Figs. 7 and 8, for the same position of the rotor to the stator as shown in Fig. 5. Each of the three rotor blade passages shown in these figures had a different position relative to the stator vanes because of the different blade numbers (Table 1). The double-dotted lines indicate the position of the middle stator vane trailing edge of Fig. 5. The contours of operating point OP1 are shown in Fig. 7, those of operating point OP2 in Fig. 8. The random velocity fluctuations are given in terms of $\overline{c_l'^2}$ without a denominator because it is difficult to select the proper one. In Table 3 some representative values are given which can be used as a denominator to allow a comparison with other results.

In plane 1 the random unsteadiness $\overline{c_l'^2}$ for operating point OP1 (Fig. 7) had a maximum value between $200 < \overline{c_l'^2} < 300$ in the wakes. At the suction side of the wakes the two secondary loss accumulation regions *A* and *B*, discussed with regard to Fig. 6(*a*), are clearly visible. The very high unsteadiness accumulations near the hub were a consequence of a radial flow within the wakes directed toward the hub. This radial flow was caused by an inbalance of radial pressure forces due to the lower tangential velocity inside the wakes. As a consequence the highly fluctuating material from the wakes migrated to the hub, and thus increased the size of the high fluctuation regions.

At L2F station 2 (OP1) the random unsteadiness distribution showed a similar behavior to that in plane 1. The regions of $\overline{c_l'^2} > 100$ were more extended due to a mixing process in the flow. There was only a small increase in unsteadiness near the hub and casing.

In the L2F plane 3 (Fig. 7) there was a considerable increase in random unsteadiness. This increase in random unsteadiness was limited to those regions of the wakes where secondary vortices were found in the upstream plane. The secondary loss regions *A* and *B* were still visible in this L2F plane, and especially in these regions a considerable increase of random unsteadiness was found. The high random fluctuating region *B* of the wake on the right (near the hub) was intersected by the rotor blades.

The flow pattern in L2F plane 4 (Fig. 7) showed a further increase in random velocity fluctuation, especially in the wake near midspan where the trailing shed vortices were located (see Fig. 6). The secondary flow regions *A* and *B* were also found in this plane. The region *A* of the wake on the left is extremely extended.

By examining the difference in random unsteadiness of the secondary flow region *A* (passage vortex I) between L2F plane 1 and 4, a difference of approximately $\overline{c_l'^2} \sim 200$ m^2/s^2 was recognized. As already shown in Fig. 5, there was no noticeable increase of $\overline{c_l'^2}$ between the wakes in the low random fluctuating regions. However, the regions of low fluctuations in planes 3 and 4 were found to be somewhat smaller than in plane 1 due to mixing-out of the wake fluid.

In all rotor blade channels (L2F station 3 and 4) near the hub high random unsteadiness regions can be recognized. These regions may be caused by leading edge vortices (horseshoe vortices) [18] which arise near the leading edges of the rotor blades at the hub due to a separation of the incoming wall boundary layers. Another reason for the increase in unsteadiness near the hub may be the joints in the wall (indicated by arrows). The rotor blades were milled with their platforms. These platforms forming the hub are interrupted by joints. These joints may disturb the flow in the hub regions and therefore increase the turbulence.

A similar behavior of the flow described for operating point OP1 was found for OP2 (Fig. 8), but with the essential difference that the random unsteadiness already started to increase in L2F plane 2 and not in plane 3 as for OP1. The differences between the rotor inlet conditions of OP1 and OP2 which can cause such different behavior was found to be

Downloaded 01 Jun 2010 to 171.66.16.71. Redistribution subject to ASME license or copyright; see http://www.asme.org/terms/Terms_Use.cfm

the higher relative Mach number (Fig. 4*b*) and the difference in incidence (Fig. 4*c*).

Summarizing the results of Figs. 7 and 8, it can be said that an increase in random unsteadiness was found in the first part of the rotor (OP1) or very near the leading edge (OP2) of the rotor blades. The production of the unsteadiness was found to occur in the regions containing the stator secondary vortices. These vortices were located in or very near the stator wakes. A considerable increase in random unsteadiness in the region of a vortex can be explained by a breakdown process, whereby the vortical motion breaks down and is converted into energy in the form of random fluctuations.

It should, perhaps, be noted that in Figs. 7 and 8 only the contours of the random velocity fluctuations parallel to the (two-dimensional) flow vector $\overline{c_l'^2}$ were shown, although the L2F technique also yielded the random fluctuations perpendicular to the flow vector $\overline{c_{tr}'^2}$. This was done because the distributions of $\overline{c_{tr}'^2}$ showed, in addition to the described phenomena, local regions of high unsteadiness at some locations within the rotor blade channel, namely, the blade tip region and near to the suction surface. This different behavior of $\overline{c_l'^2}$ and $\overline{c_{tr}'^2}$ at some locations needs further investigation.

By means of the results of [2, 12, 13], which showed the deformation and cutting of the wakes, a schematic figure (Fig. 9) for the deformation of the vortices was developed, and some possible reasons for a vortex breakdown were found. As shown in Fig. 9, the secondary vortex had its axis in the absolute flow direction. The secondary vortices behind the stator had a maximum swirl angle $\Delta\alpha$ of the order of 3.5 deg, this being determined from the measured difference of 7 deg between overturning and underturning (overturning 19 deg, underturning 26 deg). This swirl angle was found in Fig. 6(*b*) for the passage vortex I. The absolute velocity in this region was approximately 280 m/s. Therefore, for OP2 the maximum swirl velocity was $c_{\text{swirl}} \sim 17$ m/s.

The relative flow direction with respect to the rotor blade led to a cutting of the stator vortex by the rotor blade. Near the vortex axis the static pressure is lower than outside the vortex core. This pressure difference gives rise to a motion at the pressure side of the blade which leads to a filling of the vortex. By this filling process the pressure difference inside the vortex decays and the vortex breaks up. This filling motion cannot be separated from wake effects which initiate a motion in the same direction [2] because the wake has approximately the same position as the vortex.

The "classical vortex breakdown" [8, 9] which has been observed in swirling flows requires vortices with a high swirl angle $\Delta\alpha$. Swirl angles $\Delta\alpha$ of about 40 deg have been measured in such flows. Another necessary condition for this vortex breakdown is a positive pressure gradient in the direction of the vortex axis (in the flow direction). In the case of the turbine rotor flow, there is a positive pressure gradient in the absolute flow direction to the stagnation point of the rotor blade. However, the small inlet swirl angle $\Delta\alpha$ of 3.5 deg was not sufficient to enable swirl angles of 40 deg in the deceleration regions. If existing, such high swirling flows must be found in the flow angle measurements made by the L2F. For both operating points no such high swirling flow regions were recognized near the stagnation point of the rotor blades. Therefore, the classical vortex breakdown seems a very unlikely explanation for the observed phenomena.

As a vortex first reaches a rotor blade channel, it becomes bowed because the relative velocity in the middle of the passage is higher than near the rotor blade leading edges. The downstream boundary of the vortex (on the right) which moves into the rotor blade channel is accelerated, while the upstream part (on the left) has not yet reached the inlet and remains unaccelerated. This leads to a considerable increase and deformation of the vortex cross-sectional area which may also cause the vortex breakdown.

A final and definite explanation of the flow mechanisms involved in the vortex breadown with the corresponding generation of increased random unsteadiness cannot be given, but summarized below are the two possible reasons already discussed:

1 The vortex cutting and filling.

2 The considerable increase and deformation of the vortex cross-sectional area as the vortex moves into the rotor.

Finally, the considerable increase in random unsteadiness is shown by time and area-averaged values of the random velocity fluctuations (Fig. 10). The distributions are plotted against the axial position of the turbine. The dark strips indicate the rotor leading and trailing edge regions. The width is caused by the radial variation of the leading and trailing edge locations.

Figure 10(*a*) shows the averaged random unsteadiness parallel to the flow vector $\overline{c_l'^2}$ which was shown in the previous contour plots. There was a significant production of random unsteadiness near the leading edge (OP2) or in the first part of the rotor. The maximum was reached in L2F station 4 for both operating points. Downstream of this station a very strong dissipation of random unsteadiness occurs until L2F plane 6. The growth of unsteadiness behind the rotor was caused by rotor wake and secondary flows. The distribution behind the rotor was estimated by a dashed line because only one L2F station exists behind the rotor.

An attempt was made to quantify the influence of the turbulence production on the overall performance of the turbine. Using the random velocity fluctuations parallel to the flow vector $\overline{c_l'^2}$ and the assumption of isotropic turbulence, the random fluctuating energy is estimated as approximately equal to 1.5 times $\overline{c_l'^2}$. If one relates the random fluctuating energy to the enthalpy drop of the turbine stage, the significance of the random unsteadiness increase is clearly visible (Fig. 10*b*). It was found that the turbulence energy behind the stator (L2F station 1) was approximately 0.5% of the total turbine enthalpy drop. Behind the region of unsteadiness increase, the energy contained in turbulence was of the order of 1.1% for OP1 (1.0 for OP2). As shown, the major part of this turbulence increase was caused by the stator secondary-vortex breakdown. This means that an increase of turbulence of approximately 0.6% for OP1 (0.5 for OP2) in the first part of the rotor was a result of stator secondary motions. The energy contained in the turbulence of the flow remains useless in the turbine. It contributes, therefore, to an increase of losses in the turbine rotor although the secondary vortices which break down were generated in the stator.

In addition to the abovementioned loss generation from turbulence production, some other disadvantages were considered. These include the influence of the turbulence on the boundary layer development, and therefore on the heat transfer and the profile losses [11, 21]. Another factor that can be considered is the effects on the secondary flow in the rotor. The secondary vortices generated in the rotor rotate counter to the stator secondary vortices, and therefore they would be expected to reduce one another [16]. However, the rotor secondary motion develops after breakdown of the stator vortices. This leads possibly to additional losses.

Summary

The L2F velocimeter was used to obtain data from the unsteady flow field within a turbine rotor for two operating points.

The nonuniform stator outlet flow impinging on the rotor blade row contained the stator wakes and secondary vortices located within or adjacent to the wakes.

After cutting of the wakes and the stator secondary vortices by the rotor blades, the random unsteadiness was increased considerably in the regions associated with stator secondary

Downloaded 01 Jun 2010 to 171.66.16.71. Redistribution subject to ASME license or copyright; see http://www.asme.org/terms/Terms_Use.cfm

flow. This random unsteadiness production was explained by means of a vortex breakdown process. Two possible reasons for this breakdown were presented: the vortex cutting and filling, and the strong deformation of the vortex cross-sectional area.

The energy of the vortex motion is converted into random fluctuation energy during breakdown. This conversion is considered part of the rotor losses, although the secondary vortices were generated in the stator. This vortex breakdown may also affect other aspects of the flow, e.g., boundary layer behavior, heat transfer, and the generation of secondary flows in the rotor blade channels.

Acknowledgments

The author wishes to express his gratitude to the members of the turbine group of the DFVLR propulsion institute for their support in evaluating the test results, the preparation of the final version of the manuscript, and for very helpful discussion. The author also thanks Dr. R. Schodl for his support with the L2F measurement system, W. Karnatschke who has done the L2F measurements, and D. L. Tweedt for his assistance in correcting this paper.

References

1 Binder, A., and Romey, R., "Secondary Flow Effects and Mixing of the Wake Behind a Turbine Stator," ASME JOURNAL OF ENGINEERING FOR POWER, Vol. 105, No. 1, Jan. 1983, pp. 40–46.

2 Binder, A., et al., "An Experimental Investigation Into the Effects of Wakes on the Unsteady Turbine Rotor Flow," ASME Paper No. 84-GT-178, 1984.

3 Denton, J. D., and Usui, S., "Use of a Tracer Gas Technique to Study Mixing in a Low Speed Turbine," ASME Paper No. 81-GT-86, 1981.

4 Dring, R. P., et al., "Turbine Rotor-Stator Interaction," ASME JOURNAL OF ENGINEERING FOR POWER, Vol. 104, No. 3, Aug. 1982; Paper No. 82-GT-3.

5 Dunker, R. J., "Flow Measurements in the Stator Row of a Single-Stage Transonic Axial-Flow Compressor with Controlled Diffusion Stator Blades," AGARD-CP-351, *Viscous Effects in Turbomachines*, 1983.

6 Evans, R. L., "Turbulence and Unsteadiness Measurements Downstream of a Moving Blade Row," ASME JOURNAL OF ENGINEERING FOR POWER, Vol. 97, 1974, pp. 131–139.

7 Gallus, H. E., Grollius, H., and Lambertz, J., "The Influence of Blade Number Ratio and Blade Row Spacing on Axial-Flow Compressor Stator Blade Dynamic Load and Stage Sound Pressure Level," ASME JOURNAL OF ENGINEERING FOR POWER, Vol. 104, 1982, pp. 633–641.

8 Hall, M. G., "Vortex Breakdown," *Annual Review Fluid Mechanics*, Vol. 4, 1972, pp. 195–218.

9 Hall, M. G., "The Structure of Concentrated Vortex Cores," *Progress in Aeronautical Sciences*, Vol. 7, 1966, pp. 53–110.

10 Hawthorne, W. R., "Rotational Flow Through Cascades, PT I: The Components of Vorticity," *Q. Journal Mech. and Applied Math.*, Vol. VIII, Pt. 3, 1955, pp. 266–279.

11 Hodson, H. P., "Boundary Layer and Loss Measurements in the Rotor of an Axial-Flow Turbine," ASME JOURNAL OF ENGINEERING FOR POWER, Vol. 106, 1984, pp. 391–399.

12 Hodson, H. P., "Measurements of Wake-Generated Unsteadiness in the Rotor Passages of Axial Flow Turbines," ASME Paper No. 84-GT-189, Amsterdam, 1984.

13 Hodson, H. P., "An Inviscid Blade-to-Blade Prediction of a Wake-Generated Unsteady Flow," ASME Paper No. 84-GT-43, Amsterdam, 1984.

14 Joslyn, H. D., Dring, R. P., and Sharma, O. P., "Unsteady Three-Dimensional Turbine-Aerodynamics," ASME JOURNAL OF ENGINEERING FOR POWER, Apr. 1983, Vol. 105, pp. 322–331.

15 Kerrebrock, K. L., and Mikolajczak, A. A., "Intra-Stator Transport of Rotor Wakes and Its Effects on Compressor Performance," ASME JOURNAL OF ENGINEERING FOR POWER, Oct. 1970, p. 359.

16 Lakshminarayana, B., and Horlock, J. H., "Generalized Expressions for Secondary Vorticity Using Intrinsic Coordinates," *Journal of Fluid Mechanics*, Vol. 59, 1973, pp. 97–115.

17 Lakshminarayana, B., and Davino, R., "Mean Velocity and Decay Characteristics of the Guidevane and Stator Blade Wake of an Axial Flow Compressor," ASME JOURNAL OF ENGINEERING FOR POWER, Vol. 102, 1980, pp. 50–60.

18 Marchal, Ph., and Sieverding, C. H., "Secondary Flows Within Turbomachinery Bladings," AGARD-CP-214, *Secondary Flows in Turbomachines*, 1977.

19 Meyer, R. X., "The Effect of Wakes on the Transient Pressure and Velocity Distributions in Turbomachines," ASME *Journal of Basic Engineering*, Oct. 1958, pp. 1544–1552.

20 Okiishi, T. H., Hathaway, M. D., and Hansen, J. L., "Note on Blade Wake Interaction Influence on Compressor Stator Aerodynamic Performance," ASME JOURNAL OF ENGINEERING FOR GAS TURBINES AND POWER, Vol. 107, No. 2, Apr. 1985, pp. 549–551.

21 Pfeil, H., Herbst, R., and Schröder, T., "Investigation of the Laminar-Turbulent Transition of Boundary Layers Disturbed by Wakes," ASME JOURNAL OF ENGINEERING FOR POWER, Vol. 105, 1983, pp. 130–137.

22 Richter, H., and Koschel, W., "Untersuchung der Schwingungserregung einer Axialturbinenstufe mit verstellbaren Leitschaufeln," *VDI*, Vol. 487, 1983, pp. 89–99.

23 Schodl, R., "Entwicklung des Laser-Zwei-Focus-Verfahrens für die berührungslose Messung der Strömungsvektoren, insbesondere in Turbomaschinen," Diss. TH Aachen, 1977.

24 Schodl, R., "A Laser-Two-Focus (L2F) Velocimeter for Automatic Flow Vector Measurements in the Rotating Components on Turbomachines," ASME *Journal of Fluids Engineering*, Vol. 102, No. 4, Dec. 1980.

Downloaded 01 Jun 2010 to 171.66.16.71. Redistribution subject to ASME license or copyright; see http://www.asme.org/terms/Terms_Use.cfm

Journal of Engineering for Gas Turbines and Power

Discussion

Holographic Measurements and Theoretical Predictions of the Unsteady Flow in a Transonic Annular Cascade[1]

S. G. Newton[2]

1 Since the phase of unsteady pressure is important with respect to stability, it would be interesting to see phase data presented. Does the statement in Section 2 that the phase was unreliable imply low coherence between unsteady pressure and blade motion?

2 In Section 4 it should perhaps be emphasized that the calculations were performed with a large amount of artificial viscosity, the density being upwinded by one element.

3 (*i*) If an appropriate oblique shock solution were compared with Fig. 8 then the Mach number jump would closely match the Finsup value. (*ii*) A solution with the shock on the suction surface trailing edge could result in errors, since the cusp will be highly loaded and the implementation of the Kutta condition is in doubt.

4 In Section 5 the leading edge shock is described as normal (as shown in Fig. 6), but it is also described as weak. In the strict sense a normal shock must be strong, i.e., subsonic downstream of the shock. Furthermore, if the leading edge shock is attached, there can be no series of weak shocks from adjacent blades. There seems to be an inconsistency between this and the requirement for the Mach number ahead of the leading edge to be close to unity.

5 The 315 deg position sketch in Fig. 18 (β = 180 deg) appears to differ from that of Fig. 14 (photograph of hologram); the same is true for the 90 deg position case of Figs. 15 and 14 (β = 135 deg).

6 If one plots out shock position on the blade surface both the leading edge shock intersection with the suction surface and the trailing edge shock intersection with the pressure surface appear harmonic only over the first 180 deg of the motion. This observation is based only on approximate measurements from Figs. 17 and 18, but does seem to be consistent with the discussion in Section 7.

Author's Closure

I should like to thank Dr. Newton for the points he raises on the paper. I shall comment briefly on these and where I make no comment I am in agreement with him.

1 The problem here was more of the instrumentation being unable to measure the pressure phase accurately after the signal was filtered. In saying this, however, it is implied that we had little knowledge of coherence save that which was obtained by viewing the unfiltered signals on an oscilloscope: They then looked to be coherent.

4 Firstly I see nothing wrong in describing a weak normal shock as "weak." Secondly, the upstream shock to which we refer is shown at the 45 deg position of Fig. 15 as an extension of the leading edge shock. As this lies in front of the passage shock above it will weaken it.

5 It is difficult to make any direct comparisons between the sketches and the photographs. The sketches were made by looking around a three-dimensional hologram; it is only then that the true shock positions can be found. The optical distortions which exist can best be illustrated by the position of the blade mounting pin in the center of Fig. 14. This should be at 50 percent chord with the chord as a diameter.

The Effects of Reynolds Number on the Efficiency of Centrifugal Compressor Stages[1]

C. Rodgers.[2] The asymptotic trend of equation (22) toward a constant C = 5.0 for impeller width-to-diameter ratios (b_2/D_2) greater than 0.06 would appear to be inconsistent with the trend of increased passage curvature losses in very high specific speed impellers.

Additional test data are required for such impellers in order to refine the author's excellent correlation of Reynolds number effects.

Author's Closure

I agree with Mr. Rodgers that additional test data are needed for stages with high width-to-diameter ratio (b_2/D_2), in order to refine the correlation given in the paper. I do not agree, however, that the constant value of c given for wide impellers is inconsistent. Firstly, roughly half of the Reynolds-dependent friction losses occur in the diffuser and are unaffected by the curvature of the impeller passages. Secondly, it is not clear that the additional losses due to passage curvature in the impeller are strongly dependent on the Reynolds number.

Combined-Cycle System With Novel Bottoming Cycle[3]

G. J. Silvestri, Jr.[4] This paper, which is an extension of a concept presented in ASME Paper No. 83-JPGC-GT-3, applies principles used in ammonia absorption refrigeration to power generation cycles. The data which are presented indicate substantial improvements in energy conversion efficiency and significantly lower power costs.

The choice of working fluid and operating conditions raises

[1]By M. R. D. Davies and P. J. Bryanston-Cross, published in the April 1985 issue of the JOURNAL OF ENGINEERING FOR GAS TURBINES AND POWER, Vol. 107, No. 2, pp. 450-457.

[2]Rolls-Royce Limited, Derby, England

[1]By M. V. Casey, published in the April 1985 issue of the JOURNAL OF ENGINEERING FOR GAS TURBINES AND POWER, Vol. 107, No. 2, pp. 541-548.

[2]Turbomach, San Diego, CA

[3]By A. I. Kalina, published in the October 1984 issue of the JOURNAL OF ENGINEERING FOR GAS TURBINES AND POWER, Vol. 106, No. 4, pp. 737-742.

[4]Steam Turbine Generator Division, Westinghouse Electric Corporation, Orlando, FL 32817.

Copyright © 1985 by ASME
Downloaded 01 Jun 2010 to 171.66.16.71. Redistribution subject to ASME license or copyright; see http://www.asme.org/terms/Terms_Use.cfm